Coupling of continuous and hybridizable discontinuous Galerkin methods for weakly compressible fluid-structure interaction

Andrea La Spina

Bericht Nr. 50 (2021)
Lehrstuhl für Numerische Mechanik
Professor Dr.-Ing. Wolfgang A. Wall
Technische Universität München

Berichte können bezogen werden über:

Lehrstuhl für Numerische Mechanik
Technische Universität München
Boltzmannstrasse 15
D-85747 Garching bei München
http://www.lnm.mw.tum.de

TECHNISCHE UNIVERSITÄT MÜNCHEN

Fakultät für Maschinenwesen

Coupling of continuous and hybridizable discontinuous Galerkin methods for weakly compressible fluid-structure interaction

Andrea La Spina

Vollständiger Abdruck der von der Fakultät für Maschinenwesen der Technischen Universität München zur Erlangung des akademischen Grades eines

Doktor-Ingenieurs (Dr.-Ing.)

genehmigten Dissertation.

Vorsitzender: Prof. Dr.-Ing. Steffen Marburg

Prüfer der Dissertation:

1. Prof. Dr.-Ing. Wolfgang A. Wall
2. Prof. Dr. Antonio Huerta

Die Dissertation wurde am 01.02.2021 bei der Technischen Universität München eingereicht und durch die Fakultät für Maschinenwesen am 09.03.2021 angenommen.

Abstract

The interest in the simulation of fluid-structure interaction (FSI) phenomena has increased significantly over the years. Despite the constant growth in available computing resources, the demand for more robust and efficient computational methods does not cease.

This thesis proposes novel schemes for the solution of FSI problems with weakly compressible flows. Special attention is devoted to the spatial discretization of the fluid problem by means of the hybridizable discontinuous GALERKIN (HDG) method and to the coupling of the fluid field with the structural one, discretized by means of the continuous GALERKIN (CG) method.

The first part of the thesis presents a weakly compressible formulation of the NAVIER–STOKES equations for viscous flows interacting with nonlinear elastic solid bodies in a CG framework. An analytical study reveals the beneficial effect of the introduction of a weak compressibility against potential instabilities caused by the artificial added mass effect. Two classical FSI benchmarks highlight the enhanced robustness and the improved efficiency in terms of computational time of the proposed approach compared to a fully incompressible solver.

Two HDG formulations are then derived for the solution of the fluid equations, the first featuring the velocity and the pressure as primal variables, while the latter solving for the density and the momentum. The adoption of the VOIGT notation to strongly enforce the symmetry of the stress tensor allows the use of an equal-order approximation for all the variables and improves the computational efficiency of the HDG method, by reducing the stored quantities and the size of the local problems. Optimal and superoptimal convergence rates are achieved on weakly compressible POISEUILLE and TAYLOR–COUETTE flows, for which analytical solutions are available in literature. Spatial and temporal convergence studies on a problem with manufactured solution finally show the capability of the method to preserve the expected convergence rates, even with arbitrarily deforming domains.

Next, a novel strategy to couple HDG and CG discretizations by means of NITSCHE's method is proposed. Its key feature is the minimal intrusiveness in terms of computer implementation with regards to existing finite elements libraries, achieved by exploiting the definition of the numerical flux and the trace of the solution on the mesh faces to impose the transmission conditions. The proposed approach is tested for the solution of thermal and linear elastic problems featuring multiple materials with compressible and nearly incompressible behaviors.

The final part of the thesis exploits the achievements of the previous chapters to present two FSI formulations coupling weakly compressible flow problems solved by means of the HDG method and nonlinear structural problems solved by means of the CG method. The first formulation revisits the partitioned DIRICHLET–NEUMANN scheme in the context of hybrid HDG-CG discretizations, while the second formulation exploits NITSCHE's method to monolithically solve the coupled problem. The spatial and temporal convergence properties are assessed on a problem with manufactured solution and several benchmarks confirm the advantages of the proposed formulations in terms of robustness and efficiency, as well as their capability to solve problems of engineering interest.

Zusammenfassung

Das Interesse an Simulationen von Fluid-Struktur-Interaktion (FSI) ist in den letzten Jahren stark angestiegen. Trotz einer stetigen Zunahme der verfügbaren Rechenleistung besteht weiterhin ein Bedarf an leistungsfähigeren numerischen Methoden zur Bearbeitung solcher komplexen Problemstellungen.

Diese Dissertation schlägt neue Ansätze zur Lösung von FSI-Problemen für schwach-kompressible Strömungen vor. Der besondere Fokus liegt hierbei auf der räumlichen Diskretisierung des Fluidfeldes mittels der hybridisierten diskontinuierlichen GALERKIN (HDG) Methode und auf der Kopplung von Fluid- und Strukturfeld. Das Strukturfeld ist hierbei mit der kontinuierlichen GALERKIN (CG) Methode diskretisiert.

Der erste Teil dieser Arbeit präsentiert eine schwach-kompressible Formulierung der NAVIER–STOKES Gleichungen für viskose Strömungen in Interaktion mit nichtlinear-elastischen Festkörpern auf Basis eines CG Ansatzes. Eine analytische Studie zeigt zunächst die Vorteile der eingeführten schwachen Kompressibilität in Bezug auf die Vorbeugung potenzieller Instabilitäten durch den sogenannten Effekt der virtuellen Masse. Die verbesserte Robustheit und Recheneffizienz des neuen Lösungsansatzes, in Gegenüberstellung zu einem kompressiblen Löser, wird anhand zweier etablierten Benchmark-Probleme dargelegt.

Anschließend werden zwei HDG Formulierungen zur Lösung der Fluidgleichungen hergeleitet. Die erste Formulierung beinhaltet hierbei die Geschwindigkeits- und Druck-Primärvariablen und die zweite Formulierung löst nach der Dichte und nach dem Impuls. Die Verwendung der VOIGT-Notation stellt die Symmetrie des Spannungstensors sicher und ermöglicht Approximationen der Lösungsfelder unter Verwendung gleich hoher Polynomgrade. Dieses Vorgehen steigert die Effizienz des HDG Ansatzes durch eine Reduktion der zu speichernden Variablen und der Größe der lokalen Probleme. Optimale und superoptimale Konvergenzraten werden für schwach-kompressible POISEUILLE- und TAYLOR–COUETTE-Strömungen erreicht, für welche Referenzlösungen in der Literatur existieren. Räumliche und zeitliche Konvergenzstudien für eine Problemstellung mit konstruierter Lösung bestätigen die erwarteten Konvergenzraten, auch für willkürlich deformierte Gebiete.

In einem nächsten Schritt wird ein auf der NITSCHE-Methode basierender Ansatz zur Kopplung der HDG- und CG-Diskretisierung vorgeschlagen. Hauptmerkmal ist die verringerte Notwendigkeit zur Änderung von bestehenden Implementierungen in Bezug auf Finite-Elemente Bibliotheken. Diese wird durch Ausnutzung der Definition des numerischen Flusses und der Spur der Lösung auf den Netzflächen erreicht, um Übertragungsbedingungen sicherzustellen. Das beschriebene Vorgehen wird für die Lösung von thermischen und linear-elastischen Problemen, für Materialien mit kompressiblen und nahe-inkompressiblen Eigenschaften, vorgestellt.

Der abschließende Teil dieser Arbeit nutzt die Ergebnisse der vorherigen Kapitel und stellt zwei FSI Formulierungen vor. Diese behandeln schwach-kompressible Strömungen unter Nutzung der HDG Methode und nichtlineare Strukturprobleme mittels der CG Methode.

Die erste Formulierung greift auf ein partitioniertes DIRICHLET–NEUMANN Schema im Kontext einer hybriden HDG-CG Diskretisierung zurück, während der zweite Ansatz die NITSCHE-Methode zur monolithischen Lösung des gekoppelten Problems verwendet. Räumliche und zeitliche Konvergenzeigenschaften werden anhand einer Problemstellung mit konstruierter Lösung bewertet. Mehrere Vergleichsprobleme bestätigen die Vorteile der vorgeschlagenen Formulierungen hinsichtlich Robustheit und Effizienz sowie ihrer Fähigkeit tatsächliche Ingenieursfragestellungen beantworten zu können.

Contents

List of Figures

List of Tables

List of Symbols

Primal variables

$\boldsymbol{v}$	Velocity vector
p	Pressure
ρ	Density
$\boldsymbol{\rho v}$	Momentum vector
$\boldsymbol{u}$	Displacement vector
T	Temperature

Mixed variables

$\boldsymbol{L}$	Scaled strain rate vector in VOIGT notation
$\boldsymbol{Q}$	Scaled linear strain vector in VOIGT notation
$\boldsymbol{q}$	Scaled temperature gradient vector

Hybrid variables

$\hat{\boldsymbol{v}}$	Trace of velocity vector
$\hat{p}$	Trace of pressure
$\hat{\rho}$	Trace of density
$\widehat{\boldsymbol{\rho v}}$	Trace of momentum vector
$\hat{\boldsymbol{u}}$	Trace of displacement vector
$\hat{T}$	Trace of temperature

Postprocessed variables

$\boldsymbol{v}^\star$	Postprocessed velocity vector
$\boldsymbol{u}^\star$	Postprocessed displacement vector
$T^\star$	Postprocessed temperature

ALE variables

$\boldsymbol{d}$	ALE mesh displacement vector

$\boldsymbol{a}$	ALE mesh velocity vector
$\boldsymbol{c}$	ALE convective velocity vector
$\boldsymbol{\varphi}$	ALE mapping

Derived variables

$\boldsymbol{\omega}$	Vorticity tensor
$\boldsymbol{\omega}_\mathrm{V}$	Vorticity vector in VOIGT notation
ε	Strain rate tensor or linear strain tensor
ε_V	Strain rate vector or linear strain vector in VOIGT notation
$\boldsymbol{E}$	GREEN–LAGRANGE strain tensor
$\boldsymbol{\sigma}$	CAUCHY stress tensor
$\boldsymbol{\sigma}_\mathrm{V}$	CAUCHY stress vector in VOIGT notation
$\boldsymbol{P}$	First PIOLA–KIRCHHOFF stress tensor
$\boldsymbol{F}$	Deformation gradient tensor
J	Determinant of the deformation gradient
ψ	Strain energy density function

Forcing terms

$\boldsymbol{b}$	Body force vector
$\boldsymbol{f}$	Force vector
s	Heat source
$\boldsymbol{t}$	Traction vector
f	Thermal flux

Residuals

$\mathcal{R}_\mathrm{C}$	Residual of continuity equation
$\boldsymbol{\mathcal{R}}_\mathrm{M}$	Residual of momentum equation

Material parameters

$p^\texttt{ref}$	Reference pressure
$\rho^\texttt{ref}$	Reference density
ε	Compressibility coefficient
θ	Compressibility factor
m	Characteristic mass
μ	Dynamic viscosity or second LAMÉ parameter
λ	Second coefficient of viscosity or first LAMÉ parameter

E	YOUNG's modulus
ν	POISSON's ratio
$\mathbf{D}$	Material matrix in VOIGT notation
K	Bulk modulus
κ	Thermal conductivity

Stabilization parameters

$\tau_{\texttt{SUPG}}$	SUPG stabilization parameter
$\tau_{\texttt{PSPG}}$	PSPG stabilization parameter
τ_{v}	Stabilization parameter of velocity
τ_{p}	Stabilization parameter of pressure
τ_{ρ}	Stabilization parameter of density
$\tau_{\rho v}$	Stabilization parameter of momentum
$\tau_{\rho v}^{c}$	Stabilization parameter of momentum (convective part)
$\tau_{\rho v}^{d}$	Stabilization parameter of momentum (diffusive part)
τ_{u}	Stabilization parameter of displacement
τ_{T}	Stabilization parameter of temperature
C_{v}	Scaling factor for stabilization of velocity
C_{p}	Scaling factor for stabilization of pressure
C_{ρ}	Scaling factor for stabilization of density
$C_{\rho v}^{c}$	Scaling factor for stabilization of momentum (convective part)
$C_{\rho v}^{d}$	Scaling factor for stabilization of momentum (diffusive part)
C_{u}	Scaling factor for stabilization of displacement
C_{T}	Scaling factor for stabilization of temperature

Algorithm parameters

η	Convergence tolerance
ω	Relaxation parameter
γ	NITSCHE's penalty parameter

Spatial domain and its discretization

x, y, z	Cartesian coordinates
r, θ, z	Cylindrical coordinates
Ω	Spatial domain
$\partial\Omega$	Domain boundary
Σ	Mesh skeleton
Γ	Internal skeleton

Γ^D	DIRICHLET portion of the boundary
Γ^N	NEUMANN portion of the boundary
Γ^I	Interface portion of the boundary
$\boldsymbol{n}$	Outward-pointing unit normal vector
$\mathbf{N}$	Normal operator in VOIGT notation
$\mathbf{T}$	Tangent operator in VOIGT notation
k	Polynomial degree of approximation
r	Level of mesh refinement
h	Characteristic element size
l	Representative length scale
$\boldsymbol{\xi}$	Coordinates of quadrature points in reference element
$\widehat{\boldsymbol{\xi}}$	Coordinates of quadrature points in reference face
$\boldsymbol{\psi}$	Matrix of element shape functions
$\widehat{\boldsymbol{\psi}}$	Matrix of face shape functions

Temporal domain and its discretization

t	Time instant
t_i	Initial time
t_f	Final time
Δt	Time step size
BDFo	BDF order
α	BDF coefficients for first derivatives
β	BDF coefficients for second derivatives
$\alpha_{\texttt{v}}$	General time integration coefficient for the velocity
$\alpha_{\texttt{p}}$	General time integration coefficient for the pressure
$C_{\texttt{inst}}$	Instability constant

Discrete variables

$\mathbf{v}$	Discrete velocity vector
$\dot{\mathbf{v}}$	Time derivative of discrete velocity vector
$\bar{\mathbf{v}}$	Combination of previous discrete velocity values and derivatives
$\mathbf{p}$	Discrete pressure
$\dot{\mathbf{p}}$	Time derivative of discrete pressure
$\bar{\mathbf{p}}$	Combination of previous discrete pressure values and derivatives
$\mathbf{V}$	Discrete velocity-pressure vector
$\boldsymbol{\rho}$	Discrete density
$\mathbf{w}$	Discrete momentum vector
$\mathbf{U}$	Discrete density-momentum vector

$\mathbf{u}$	Discrete displacement vector
$\mathbf{T}$	Discrete temperature
$\mathbf{L}$	Discrete scaled strain rate vector in VOIGT notation
$\mathbf{Q}$	Discrete scaled linear strain vector in VOIGT notation
$\mathbf{q}$	Discrete scaled temperature gradient vector
$\hat{\mathbf{v}}$	Discrete trace of velocity vector
$\hat{\mathbf{p}}$	Discrete trace of pressure
$\widehat{\mathbf{V}}$	Discrete trace of velocity-pressure vector
$\hat{\boldsymbol{\rho}}$	Discrete trace of density
$\hat{\mathbf{w}}$	Discrete trace of momentum vector
$\widehat{\mathbf{U}}$	Discrete trace of density-momentum vector
$\hat{\mathbf{u}}$	Discrete trace of displacement vector
$\hat{\mathbf{T}}$	Discrete trace of temperature
$\mathbf{d}$	Discrete ALE mesh displacement vector
$\mathbf{M}$	Discrete mass matrix
$\mathbf{G}$	Discrete gradient operator
$\boldsymbol{\mathcal{M}}$	Discrete added mass operator
$\mathbf{K}$	Discrete left hand side matrix
$\mathbf{f}$	Discrete right hand side vector
$\mathbf{r}$	Discrete residual vector

Indices

n	Time step index
i	Coupling iteration index
j	NEWTON iteration index
e	Element index
f	Face index
b	BDF index

Dimensions

$\mathtt{n}^{\mathtt{el}}$	Number of elements
$\mathtt{n}^{\mathtt{en}}$	Number of element nodes
$\mathtt{n}^{\mathtt{fn}}$	Number of face nodes
$\mathtt{n}^{\mathtt{eq}}$	Number of element quadrature points
$\mathtt{n}^{\mathtt{fq}}$	Number of face quadrature points
$\mathtt{n}^{\mathtt{dof}}$	Number of degrees of freedom
$\mathtt{n}_{\mathtt{sd}}$	Number of spatial dimensions
$\mathtt{m}_{\mathtt{sd}}$	Number of non-redundant tensor components in VOIGT notation

$\mathtt{q}_{\mathtt{sd}}$	Number of redundant tensor components in VOIGT notation

Spaces

$\mathbb{R}$	Space of real numbers
$\mathcal{P}$	Space of polynomial functions
$\mathcal{L}$	LEBESGUE space
$\mathcal{H}$	SOBOLEV space

Standard matrices and vectors

$\mathbf{I}$	Identity tensor
$\mathbf{E}$	Identity vector in VOIGT notation
$\mathbf{0}$	Zero vector or tensor

Operators

$\cdot$	Dot product
$:$	Double-dot product
$\otimes$	Tensor product
$\boldsymbol{\nabla}$	Gradient operator
$\boldsymbol{\nabla}\cdot$	Divergence operator
$\boldsymbol{\nabla}\times$	Curl operator
$\boldsymbol{\nabla}^{\mathtt{S}}$	Symmetric part of gradient operator
$\boldsymbol{\nabla}^{\mathtt{W}}$	Skew-symmetric part of gradient operator
$\boldsymbol{\nabla}_{\mathtt{S}}$	Symmetric part of gradient operator in VOIGT notation
$\boldsymbol{\nabla}_{\mathtt{W}}$	Skew-symmetric part of gradient operator in VOIGT notation
$\sum$	Summation operator
A	Assembly operator
$\delta_{\mathtt{i},\mathtt{j}}$	KRONECKER delta
$\odot^{T}$	Transpose operator
$\odot^{-T}$	Transpose of inverse operator
$\lvert\odot\rvert$	Determinant or absolute operator
$\lVert\odot\rVert$	EUCLIDean norm operator
$[\![\odot]\!]$	Jump operator
$\mathrm{tr}\left(\odot\right)$	Trace operator
$\mathrm{eig}\left(\odot\right)$	Eigenvalue operator
$\max\left(\odot\right)$	Maximum operator
$\mathrm{V}\left(\odot\right)$	VOIGT operator
$\mathrm{V}^{-1}\left(\odot\right)$	Inverse VOIGT operator

$\mathrm{hull}\left\{\odot\right\}$	Convex hull operator

Subscripts and superscripts

$\odot_{\mathcal{F}}$	Fluid quantity
$\odot_{\mathcal{S}}$	Structure quantity
$\odot_{\mathcal{I}}$	Fluid-structure interface quantity
$\odot_{\texttt{HDG}}$	HDG quantity
$\odot_{\texttt{CG}}$	CG quantity
$\odot_{\texttt{I}}$	HDG-CG interface quantity
$\odot_{\texttt{V-P}}$	Velocity-pressure formulation
$\odot_{\texttt{D-M}}$	Density-momentum formulation
$\odot^{\texttt{inc}}$	Incompressible (fluid)
$\odot^{\texttt{wcomp}}$	Weakly compressible (fluid)
$\odot_{\texttt{ninc}}$	Nearly incompressible (structure)
$\odot_{\texttt{comp}}$	Compressible (structure)
$\odot_{\texttt{i}}$	Interior DOFs
$\odot_{\texttt{I}}$	Interface DOFs
$\odot^{0}$	Initial field
$\odot^{D}$	DIRICHLET quantity
$\odot^{N}$	NEUMANN quantity
$\odot^{I}$	Interface quantity
$\odot^{\texttt{Left}}$	Left portion
$\odot^{\texttt{Right}}$	Right portion
$\odot^{\star}$	Postprocessed variable
$\odot_{\texttt{V}}$	Variable in VOIGT notation
$\odot_{\texttt{lump}}$	Variable obtained with a lumped mass matrix
$\odot^{\texttt{ref}}$	Reference value
$\odot_{\texttt{max}}$	Maximum value within a time step
$\odot_{\texttt{mean}}$	Mean value within a time step
$\odot_{\texttt{avg}}$	Average value over all time steps

Problem-specific variables

$\bar{t}$	Time period
$t_{\texttt{cpu}}$	CPU time
ε^{*}	Dimensionless compressibility coefficient
L	Channel length
R	Channel half-height
U	Channel exit mean velocity

H	Cylinder height
r_1	Inner wall radius
r_2	Outer wall radius
ω_1	Inner wall angular velocity
ω_2	Outer wall angular velocity
C_1	Coefficient 1
C_2	Coefficient 2
$\bar{d}$	Maximum mesh displacement
$\sigma_{\mathtt{VM}}$	VON MISES stress
$\bar{y}$	Neutral axis location
$\bar{h}$	Beam layer thickness
V	Shear force
M	Bending moment
δ	Temporal variation of interface displacement
δ_0	Initial interface displacement
t_0	Time shift
f	Interface position
Q	User-provided function
q	User-provided exponent
a	Horizontal displacement function
b	Vertical displacement function
ξ	Auxiliary variable 1
χ	Auxiliary variable 2
R	Auxiliary function 1
S	Auxiliary function 2
A	Auxiliary function 3
B	Auxiliary function 4
C	Auxiliary function 5
$\Omega_{\mathcal{C}}$	Circular block domain
$f_{\mathtt{L}}$	Lift force
$f_{\mathtt{D}}$	Drag force
$\mathtt{M}$	Mean value of compared quantity
$\mathtt{A}$	Average value of compared quantity
$\mathtt{F}$	Frequency of compared quantity
$\bar{v}$	Maximum inflow velocity
τ	Auxiliary variable
$V_{\mathtt{pump}}$	Net volume pumped

List of Abbreviations

ALE	Arbitrary LAGRANGEan–EULERian
BDF	Backward Differentiation Formula
CG	Continuous GALERKIN
CPU	Central Processing Unit
DG	Discontinuous GALERKIN
DOFs	Degrees Of Freedom
FEM	Finite Element Method
FSI	Fluid-Structure Interaction
HDG	Hybridizable Discontinuous GALERKIN
PDEs	Partial Differential Equations
PDMS	Polydimethylsiloxane
PSPG	Pressure-Stabilizing PETROV–GALERKIN
SUPG	Streamline-Upwind PETROV–GALERKIN

1 Introduction

Fluid-structure interaction (FSI) denotes the multiphysics coupling of fluid flows and deformable structures. In a typical FSI scenario, a fluid exerts stresses on a solid body which undergoes a deformation that can lead to a substantial modification of the flow itself, establishing a relation of mutual influence.

Fluid-structure interaction phenomena occur frequently, both in nature and in the industrial world. A classical occurrence in nature is represented by the interaction of the blood flow in the human circulatory system, which has attracted the interest of scientists for decades [13, 14, 39, 64, 157]. In particular, the understanding of aneurysm in arteries constitutes an active area of research [15, 44, 110, 156], as well as the comprehension of the pumping motion of the human heart [105, 161, 165]. FSI is also omnipresent in a vast range on engineering applications. In civil engineering, the design of dams [2, 172], lock gates [128] and storage tanks [101, 143] needs to carefully take into account FSI phenomena involving the interaction of the solid structure with water during a seismic event. Moreover, the underestimation of wind loading on large span bridges can lead to disastrous failures, like the notorious collapse of the Tacoma Narrows bridge in 1940 [99]. FSI also plays a major role in the prevention of the rupture of components susceptible to fatigue, like aircraft wings [87] and turbine blades [16, 80, 170]. In the naval sector then, FSI simulations are often performed to improve the hydrodynamic behavior of marine propellers [113, 139, 171] against cavitation erosion and the consequent performance decay and to accurately design yacht sails [47, 129, 158]. Finally, a promising application of FSI in the aerospace industry is the manufacturing of effective and reliable parachute systems for safe landing on the Martian soil [81].

Although the simulation of fluid-structure interaction problems has been under investigation for decades, there is still much room for improvement in terms of development of robust, efficient and scalable numerical methods. Some related issues are addressed in this thesis, with special emphasis on the devising of appropriate spatial discretization and coupling techniques for the simulation of FSI problems involving weakly compressible flows and nonlinear elastic structures undergoing large deformations.

1.1 Background

The numerical techniques developed for the solution of fluid-structure interaction problems can be catalogued based on many different features, for instance, with respect to the fluid compressibility, the spatial discretization, the kinematical description and the solution scheme. A brief literature review of these key aspects in the context of FSI is given in the following.

Fluid compressibility

The characteristics of the fluid and the structure involved in FSI problems can be disparate. In aerodynamics, the coupling may involve a light compressible fluid and a stiff structure like an aircraft wing [49], or it may involve a light incompressible fluid and an extremely flexible structure such as a parachute [153, 155]. In hemodynamics instead, incompressible fluids and deformable structures with similar densities are usually coupled [133]. Among many other features, the flow compressibility plays a crucial role on the construction of the FSI solver.

Compressibility effects primarily arise from the variation of the fluid density, which in general depends on pressure and temperature. The MACH number, defined as the ratio of the fluid velocity and the speed of sound, describes the influence of compressibility on a flow field. Although in the real world every fluid exhibits a certain level of compressibility, it is a common practice to consider a flow incompressible when the MACH number is smaller than 0.3, as explained in the book of ANDERSON [5]. In the incompressible regime, the speed of sound is much larger than the fluid velocity and fast pressure waves lead to a rapid pressure equalization. The flow is consequently defined incompressible, since no density variations due to compression can take place. On the one hand, fluid-structure interaction problems with incompressible flows are widely solved in both academia and industry and the works of TUREK and HRON [159], KÜTTLER *et al.* [93] and BURMAN and FERNÁNDEZ [21] represent just some representative applications. On the other hand, fluid-structure interaction scenarios featuring fully compressible flows have been successfully considered for the simulation of air-blast loading of structures by KAMBOUCHEV *et al.* [88], explosions in vessels by SORIA and CASADEI [147], steam explosions in nuclear power plants by CASADEI *et al.* [23] and the dynamic collapse of cylindrical shells submerged in water by FARHAT *et al.* [51].

In addition, a weakly compressible behavior of the fluid flow is sometimes considered. In the context of smoothed particle hydrodynamics techniques, linearised equations of state relating the fluid density and pressure are commonly introduced in order to avoid the complexity of the implicit computation of pressure in meshless methods. The results obtained with the numerical simulation of the deformation of an elastic plate under the effect of a rapidly varying fluid flow using a weakly compressible model have been validated by ANTOCI *et al.* [6] against suitable laboratory experiments. VICCIONE *et al.* [163] also considered weakly compressible fluids to simulate a two-dimensional flow impacting onto a rigid vertical wall, by means of a so-called weakly compressible smoothed particle hydrodynamics technique. The same authors moreover studied in [162] the influence of compressibility in terms of accuracy and efficiency on a current generated by a three-dimensional dam break over a rectangular channel. Weakly compressible fluids have also been considered by DE ROSIS *et al.* [42], who solved FSI problems by coupling the lattice BOLTZMANN and the finite element methods and by MITSUME *et al.* [107], who simulated a dam break problem with an elastic obstacle by coupling the moving particle simulation and the finite element methods.

The beneficial effects of the introduction of a weak compressibility in the flow field for the simulation of coupled problems in terms of accuracy, robustness and efficiency have been examined by LA SPINA *et al.* [95] in the context of finite element methods. The present work builds upon these findings and systematically makes use of a weakly compressible model for the simulation of fluid-structure interaction problems.

Spatial discretization

A fundamental distinction among the techniques employed to solve fluid-structure interaction problems is based on the spatial discretization strategies adopted. The discretization can be considered the process of transferring continuous mathematical operators into discrete counterparts, making them suitable for numerical evaluation and implementation on digital computers.

Among many other techniques developed so far, the finite element method (FEM) is one of the most successful spatial discretization approaches for the solution of the partial differential equations (PDEs) underlying many physical phenomena, including fluid-structure interaction. The classical FEM is also known as continuous GALERKIN (CG) method and its development is usually credited to GALERKIN, although its first formulation can be attributed to RITZ. As opposed to primitive discretization techniques, the CG method possesses useful properties like geometric flexibility and high-order accuracy. Moreover, the standard continuous GALERKIN method provides computationally efficient discretizations with a very limited number of degrees of freedom (DOFs) for the solution of a wide variety of physical problems. For an overview on CG methods, the interested reader is referred to the textbooks of STRANG and FIX [152], HUGHES [82] and LARSON and BENGZON [100]. The theoretical foundation of the finite element method is also outlined in the book of ZIENKIEWICZ *et al.* [173], while its application for the solution of fluid and structural problems can be found in [175] and [174], respectively.

In 1973, REED and HILL [134] introduced the discontinuous GALERKIN method (DG) for the solution of steady-state neutron transport problems. The DG method works over a trial space of functions that are only piecewise continuous and the information among neighbour elements is exchanged through the numerical fluxes, defined on their respective boundaries. An overview of the evolution of DG methods since their introduction can be found in the article of COCKBURN *et al.* [33]. The interest in DG methods has increased over the last decades in the computational fluid dynamics community and the works of PERSSON *et al.* [132], KRANK *et al.* [89] and FEHN *et al.* [52] constitute some representative applications. The distinctive properties of DG methods are the intrinsic stabilization of the convection terms in conservation laws, the ability to construct high-order discretizations on unstructured meshes and the flexibility in performing polynomial adaptivity, in addition to the standard mesh size adaptivity. Despite their beneficial features, DG methods are often criticised because of their high computational cost, given by the duplication of the DOFs at the element interfaces and the inability to apply static condensation techniques to reduce the final problem size.

More recently, hybridizable discontinuous GALERKIN methods (HDG) have gained a lot of attention owing to their reduced computational cost with respect to classical matrix-based DG approaches, thanks to the reduced number of global DOFs in the associated linear systems, especially for high-degree polynomial approximations. The HDG method is a mixed method, since it treats the solution derivatives as independent unknowns, defining the so-called mixed variable, and it introduces a hybrid variable on the mesh skeleton, allowing the possibility to perform a static condensation to reduce the problem size. In addition, the possibility to obtain a superconvergent solution through an efficient element-by-element postprocessing allows to obtain an improved approximation of the solution and to drive efficient degree adaptive procedures, as shown by GIORGIANI *et al.* [68, 69] and SEVILLA and HUERTA [141].

The HDG method has been mostly developed by COCKBURN, NGUYEN and PERAIRE who applied it persistently for the solution of a great variety of physical problems. COCKBURN and GOPALAKRISHNAN [28] derived new hybridization techniques for linear second order elliptic problems in the context of DG methods, paving the way for the development of the HDG method. The name hybridizable discontinuous GALERKIN has been first introduced by COCKBURN *et al.* [36], who highlighted the efficiency features of the method, given by the fact that the only globally coupled DOFs are those approximating the solution on the boundaries of the elements. They moreover pointed out that, for symmetric second order elliptic problems, the HDG method provides sparse, symmetric and positive definite matrices, making the solution of this kind of problems particularly efficient. Given the promising features of the newly derived method, a number of HDG strategies has been later proposed for the solution of several physical problems. A brief overview of the relevant works regarding HDG methods for fluid and structural problems, as well as for fluid-structure interaction problems, is given in the following.

Regarding flow problems, COCKBURN and GOPALAKRISHNAN [29] developed the first HDG method for the STOKES problem and proposed four different hybridization strategies, differing by the choice of the globally coupled unknowns. NGUYEN *et al.* [120] then proposed a velocity-pressure-gradient formulation for the STOKES equations, considering the trace of the velocity on the faces and the mean of the pressure on the elements as global variables. They moreover applied an augmented LAGRANGEan method to further reduce the globally coupled unknowns to the numerical trace of the velocity only. Three different HDG formulations for the solution of the STOKES problem have been compared by COCKBURN *et al.* [37], namely velocity-pressure-gradient, velocity-pressure-stress and velocity-pressure-vorticity. The authors concluded that the velocity-pressure-gradient formulation provides the best approximation, for similar computational complexity. An alternative velocity-vorticity formulation of the STOKES equations in a three-dimensional space has been studied by COCKBURN and CUI [27], who moreover showed how to hybridize the method to avoid the construction of the divergence-free velocity spaces and recover an approximation for the pressure. Then, COCKBURN and SHI [31] provided sufficient conditions for the superconvergence of the velocity field and they later offered in [32] an overview on HDG methods for STOKES flow, by discussing the existing formulations and describing how to systematically construct superconvergent methods. Afterwards, GATICA and SEQUEIRA [60] performed a priori and a posteriori error analysis of an augmented HDG method for a class of nonlinear STOKES models arising in quasi-NEWTONian fluids. More recently, GIACOMINI *et al.* [67] proposed a superconvergent HDG method for the approximation of the CAUCHY formulation of the STOKES equation using the same degree of polynomials for the mixed and the primal variables. Making use of the VOIGT notation to strongly enforce the symmetry of the stress tensor, the authors remedied the suboptimal behavior of classical HDG methods for formulations involving the symmetric part of the gradient of the primal variable and obtained a gain in computational efficiency, given the reduced size of the local problems and the reduced quantity of stored information.

The preliminary work on the STOKES problem opened the possibility to solve the complete NAVIER–STOKES equations for both compressible and incompressible flows. PERAIRE *et al.* [130] presented the first HDG method for the compressible EULER and NAVIER–STOKES equations. As numerical examples, the authors considered an inviscid flow over an airfoil, a COUETTE flow on a square domain and a laminar flow over an airfoil. Optimal convergence rates were obtained for the conserved quantities as well as the viscous stresses and the heat fluxes, but no superconvergence property was reported. The compressible HDG method has been then extended by MORO *et al.* [112] to deal with relevant problems in aeronautics, by applying shock capturing strategies and including a SPALART–ALLMARAS turbulence model, suitable for high-order computations. Later, FERNANDEZ *et al.* [55] presented a HDG method for implicit large-eddy simulation of transitional turbulent flows. The approach proved to be high-order accurate and highly competitive in terms of computational cost at high REYNOLDS numbers. NGUYEN *et al.* [121] presented the first application of the HDG method for the solution of the incompressible NAVIER–STOKES equations instead. The formulation considered the velocity gradient, the pressure and the velocity in the local problems and the trace of the velocity and the mean of the pressure on the element boundaries as globally coupled variables. In an extensive set of two-dimensional steady and unsteady numerical examples, the authors showed optimal convergence of the local variables and superconvergence of the exactly divergence-free postprocessed velocity field. A space-time HDG method has been instead proposed by RHEBERGEN and COCKBURN [135] to deal with deforming domains. The authors observed irregular rates of convergence for the pressure when using the same polynomial approximation in space and in time and they restored the optimal convergence by taking a polynomial approximation in time one degree higher than in space. Later, GIORGIANI *et al.* [69] proposed an adaptive degree technique for the solution of the incompressible NAVIER–STOKES equations, driven by a posteriori error estimator of the velocity, based on the superconvergence features of the HDG method. Both steady and unsteady examples in two dimensions showed the effectiveness and the efficiency of the technique, given the local elemental nature of the error estimator. CESMELIOGLU *et al.* [26] then provided an analysis of a HDG method for the steady incompressible NAVIER–STOKES equations and they proved, under the assumption of a small source term, the well posedness of the problem and the superconvergence properties of the method. To the best of the author's knowledge, no HDG formulation has been proposed so far for the simulation of fluid flows in the weakly compressible regime and this work presents the first approaches to tackle this kind of problems.

Regarding structural problems, SOON *et al.* [146] proposed the first HDG method for linear elasticity. The formulation provided symmetric and definite positive stiffness matrices and exhibited optimal convergence for the displacement and the stress and superconvergence for the postprocessed displacement field, for polynomial degrees of approximation greater or equal than two. Moreover, the authors showed numerical evidence of the locking-free behavior of the HDG method and its good performance in the presence of singularities. CELIKER *et al.* [25] then presented a new class of HDG methods for TIMOSHENKO beams, featuring the displacement and the bending moment at the element boundaries as globally coupled DOFs. The method provided optimal convergence rates with respect to the displacement, the rotation, the bending moment and the shear force. Later, a displacement gradient-velocity-pressure HDG formulation for linear elastodynamics has been introduced by NGUYEN *et al.* [122] for compressible and nearly incompressible solids. The authors obtained optimal convergence for the primal and mixed variables and superconvergence for the postprocessed displacement and velocity fields. Moreover, the HDG method produced more accurate approximations than the standard CG method for the same number of global DOFs. Similar to what done for the STOKES problem, COCKBURN and SHI [30] provided a systematic way of devising superconvergent HDG methods for linear elasticity based on weak stress symmetry formulations. The relevant HDG formulations derived for both fluid and structural mechanics have been summarized by NGUYEN and PERAIRE [117], who moreover presented novel formulations for nonlinear elastostatics and elastodynamics for the simulations of elastic bodies undergoing large deformation. FU *et al.* [59] then provided a first a priori error analysis of the HDG formulation for linear elasticity and acknowledged a loss of superconvergence for some types of meshes and some values of the polynomial degree of approximation. A superconvergent HDG method for linear elasticity, capable of using the same degree of approximation for both the primal and mixed variables, has been introduced by SEVILLA *et al.* [142]. Exploiting the VOIGT notation for second-order symmetric tensors, the approach produced optimal convergence of the stress and superconvergence of the displacement field, even for low-order polynomial approximations. More recently, TERRANA *et al.* [154] simulated both thin and thick nonlinear elastic structures by means of a novel three-field HDG formulation, featuring the material position vector, the deformation gradient and the first PIOLA-KIRCHHOFF stress tensor as independent variables. Various shell problems showed optimal convergence for the displacement field and an improved accuracy after the postprocessing.

The first reported work regarding the application of the HDG method in the context of fluid-structure interaction is attributed to SHELDON *et al.* [144]. The authors systematically discretized all the subproblems by means of the HDG method, namely the fluid field governed by the incompressible NAVIER–STOKES equations, the structural field governed by the equations of nonlinear elastodynamics and the mesh motion solved with a linear elastic model. The convergence properties of the single components have been examined through the method of manufactured solutions and the complete FSI model has been tested against the benchmark by TUREK and HRON [159]. SHELDON *et al.* [145] later presented an improved formulation in terms of computational efficiency, by abolishing the previous two-hybrid-field formulation for the structural problem and keeping only the trace of the velocity as globally coupled variable. Moreover, only linear polynomial approximations were considered for the mesh problems, independently of the polynomial approximation of the fluid and the structure. These changes approximately halved the number of the global DOFs for high-order FSI computations.

The coupling of HDG and CG methods can be of particular interest in the context of multiphysics and multimaterial problems in which different regions of the computational domain feature distinct physical properties, for which specific discretizations need to be devised. The first attempt to couple HDG and CG discretizations has been performed by PAIPURI *et al.* [127] in the context of conjugate heat transfer problems. Such an approach requires the introduction of an appropriate projection operator to enforce the transmission conditions in the HDG local problems. The consequent coupling of local and global DOFs of the HDG problem with the ones of the CG discretization makes the implementation of this strategy in existing FEM libraries rather intrusive. More recently, LA SPINA *et al.* [96] proposed a hybrid coupling of HDG and CG discretizations based on NITSCHE's method, exploiting the definition of the numerical flux and the trace of the solution on the mesh faces to impose the transmission conditions between the subdomains. Such a strategy does not affect the core structure of HDG and CG discretizations, being therefore minimally-intrusive and suitable to be integrated in existing codes.

With regards to the spatial discretization, the contribution of this thesis consists in the derivation of two HDG formulations for the simulation of weakly compressible flows and in the development of a novel minimally-intrusive technique for the coupling of HDG and CG discretizations. The aforementioned HDG-CG coupling can be found at LA SPINA *et al.* [96] in the context of thermal and linear elastic problems, while its application for the solution of FSI problems can be found at LA SPINA *et al.* [97], as well as one of the two HDG formulations for the fluid field.

Kinematical description

An important aspect in the simulation of multiphysics problems is the choice of an appropriate kinematical description. Three different types of description of motion are commonly adopted in continuum mechanics, namely the LAGRANGEan, the EULERian and the arbitrary LAGRANGEan-EULERian (ALE) description.

With the LAGRANGEan description, the nodes of the mesh follow the associated material particles during the motion. This approach is usually used in structural mechanics with large displacements and deformations and it is particularly useful in the treatment of history-dependent constitutive models for materials with elasto-plastic and visco-plastic behavior and it moreover facilitates the tracking of free surfaces and interfaces between different materials. The main drawback of this algorithm is its inability to follow large distortions of the computational domain without recourse to frequent remeshing operations. A further distinction can be made between the total LAGRANGEan and the updated LAGRANGEan approach. In the first case the discrete equations are formulated with respect to the initial configuration, while in the second case the static and kinematic variables are computed with respect to the current configuration. LAGRANGEan algorithms are omnipresent in solid mechanics, but some notable early applications concern vehicle crash tests by AMBRÒSIO and PEREIRA [3] and metal forming operations by JUNG-HO and NOBORU [86].

With the EULERian description, the individual material particles are not directly tracked and the quantities of interest, such as the velocity and the pressure, are described as fields within a control volume. This approach is usually used in pure flow problems and it is particularly useful for the simulation of turbulent flows, in which large distortions in the fluid motion occur. The main disadvantage of this strategy is the difficulty to deal with free surfaces and interfaces between different materials or different media, as it happens in fluid-structure interaction problems.

Arbitrary LAGRANGEan-EULERian methods aim to alleviate the major drawbacks experienced by traditional LAGRANGEan and EULERian formulations when dealing with mobile and deforming boundaries. By combining the advantages of the classical kinematical descriptions, ALE algorithms consider a computational mesh which can move with a velocity independent of the velocity of the material particles. In particular, the mesh inside the domain is deformed attempting to deliver minimally distorted elements, while on the interface it moves along with the materials to precisely track their relative movements. The ALE description has been usually applied to describe fluid problems on deforming domains, as done by BRAESS and WRIGGERS [17], SOULI and ZOLÉSIO [148] and NITHIARASU [123] for the simulation of free surface flows and, among many others, by SOULI *et al.* [149], WALL *et al.* [168] and HRON and TUREK [79] in the context of FSI problems. Moreover, the ALE description has been also adopted in solid mechanics by RODRIGUEZ-FERRAN *et al.* [136] for hyper-elasto-plasticity, by GHOSH and KIKUCHI [66] for elastic-visco-plastic solids and by MOVAHHEDY *et al.* [114] for the modelling of the orthogonal metal cutting process. A comprehensive overview on ALE methods for fluid dynamics, structural mechanics and coupled problems, as well as the numerical implementation details, can be found at DONEA *et al.* [46].

Regarding the kinematical description of motion, in this thesis the total LAGRANGEan approach is adopted for the structural field, the EULERian description for simple fluid simulations and the ALE method to deal with flows on deformable domains.

Solution scheme

Two different solution schemes can be adopted for the numerical solution of fluid-structure interaction problems, namely partitioned and monolithic schemes. Each approach comes along with specific advantages and drawbacks that are briefly discussed in following.

Partitioned schemes solve one subproblem at a time and the interface information is exchanged between the fluid and the structure at each single-field solution. The exchange of the interface state is performed only once per time step in the so-called loosely-coupled staggered approaches, while the solution of the flow and structural problems are repeated within one time step until a convergence criterion is satisfied in the strongly-coupled staggered approaches. Partitioned schemes allow the use of well-established and optimised single-field solvers and this is of particular interest when widely used commercial codes need to be included in the coupling algorithm. However, these techniques may suffer stability and convergence issues, especially related to the artificial added mass effect. This phenomenon has been analyzed by CAUSIN *et al.* [24] and FÖRSTER *et al.* [58] in the context of incompressible flows and the instability has been shown to be relaxed for compressible fluids by VAN BRUMMELEN [160], by means of an analysis based on the particular setting of a two-dimensional panel-model problem. In a more general setting, LA SPINA *et al.* [95] analytically demonstrated how the introduction of a weak compressibility in the flow field alleviates the constraints of the instability condition of the artificial added mass effect, thanks to the reduction of the maximal eigenvalue of the so-called added mass operator.

The exchange of the information on the interface between the fluid and the structure is often based on a DIRICHLET–NEUMANN scheme, in which the fluid field is considered as the DIRICHLET partition with prescribed interface velocities, while the structural field is considered as the NEUMANN partition loaded with interface tractions. Different variants of this approach have been used, for instance, by GERBEAU and VIDRASCU [63], by MICHLER *et al.* [106] and by KÜTTLER and WALL [91, 92]. A reverse approach, namely the NEUMANN–DIRICHLET scheme, has been instead proposed by KÜTTLER *et al.* [93] as a possible remedy for the so-called incompressibility dilemma, referring to the treatment of FSI problems with fully enclosed fluids. Despite the possibility to solve a number of academic examples, the method usually fails to solve real world problems, because the response of stiff structures to varying interface displacements is too sensitive for any numerical approach to find the equilibrium. Alternative methods to transfer the information among the subproblems rely on the so-called ROBIN transmission conditions and have been adopted by NOBILE and VERGARA [126], by BADIA *et al.* [10, 12], by GERARDO-GIORDA *et al.* [62] and by FERNÁNDEZ *et al.* [54].

Remarkable examples of loosely-coupled schemes can be found in the work of FARHAT *et al.* [50], who proposed two different schemes with provable second order accuracy in time. The astonishing computational efficiency and numerical stability of these carefully designed schemes have been shown with regards to the simulation of the aeroelastic response of a complete F-16 configuration to a gravity excitation. Later, FARHAT *et al.* [51] presented two loosely-coupled staggered schemes, namely explicit-explicit and implicit-explicit ones, for highly nonlinear compressible fluid-structure interaction problems. They validated the results with the simulation of the dynamic collapse of a cylindrical shell submerged in water and they showed that subiteration-free integrators can be designed to achieve high numerical stability and robustness, as long as the fluid can be justifiably modelled as a compressible medium.

As already pointed out, strongly-coupled schemes iterate the solution of the subproblems in each time step until some convergence criterion is satisfied, usually measured in terms of the difference between the interface displacement in two consecutive iterations. MATTHIES and STEINDORF [102] introduced a strongly-coupled partitioned scheme based on a block-NEWTON method, by approximating the derivatives with the iterative solvers for the subsystems. Later, WALL *et al.* [169] proposed a strong coupling approach to treat FSI problems with free surfaces, useful to simulate typical scenarios in offshore engineering and naval architecture. An alternative technique for strongly-coupled FSI problems with partitioned solvers has been presented by VIERENDEELS *et al.* [164], who approximated the JACOBIan from reduced order models built up during the coupling iterations. A review on strongly-coupled algorithms has been given by DEGROOTE [43], which special emphasis on the techniques required when using at least one of the solvers as a black box. Finally, the work of KÜTTLER and WALL [91] focused on strong coupling schemes based on the DIRICHLET–NEUMANN partitioning and discussed and compared different methods for the relaxation of the fixed-point FSI solver. After considering several alternatives, the authors concluded that the dynamic relaxation based on AITKEN's method is at the same time extremely simple to implement and astonishingly efficient in terms of computational time saved. A systematic comparison and classification of partitioned schemes for FSI can be found in the thesis of KÜTTLER [90].

As opposed to partitioned algorithms, monolithic schemes simultaneously solve the fluid and the structural equations within one system of nonlinear equations. On the one hand, the development of such approaches demands more effort since it requires an ad hoc implementation, in the sense that already existing and well-established single-field solvers cannot be directly employed. Moreover, the adoption of efficient preconditioners is needed when solving computationally demanding problems. On the other hand, monolithic schemes often outperform partitioned strategies in terms of computational cost and robustness. MAYR *et al.* [104] proposed a monolithic approach capable to allow an independent choice of the time integration method for the fluid and the structure, tailored to the needs of the single field. The authors moreover increased the performance of the strategy by adopting specific predictors for the subproblems. More recently, SHELDON *et al.* [144, 145] developed monolithic schemes for the solution of FSI problems by means of the HDG method. The development of suitable preconditioners has been then addressed by several authors. Among them, HEIL [76] derived efficient preconditioners from block-triangular approximations of the JACOBIan matrix, allowing a rapid iterative solution of the linear systems arising from the applications of NEWTON's method. BADIA *et al.* [11] then analyzed different modular and non-modular preconditioners for FSI problems with pronounced added mass effect and acknowledged the non-modular ILUT preconditioner to achieve great efficiency. Later, GEE *et al.* [61] proposed two efficient preconditioners for the solution of the monolithic system of equations, by applying algebraic multigrid techniques. In conclusion, a fair comparison between partitioned and monolithic FSI schemes can be found in the works of HEIL *et al.* [77] and KÜTTLER *et al.* [94]

In the present thesis, a strongly-coupled scheme based on the DIRICHLET–NEUMANN partitioning is revisited for hybrid HDG-CG discretizations and its potential instabilities are resolved with the introduction of a weak compressibility in the flow field. Moreover, a novel fluid-structure interaction monolithic scheme based on NITSCHE's method is presented. Both the partitioned and the monolithic schemes can be found in the recent work by LA SPINA *et al.* [97].

1.2 Goals

The main objective of this thesis is providing robust and efficient spatial discretization techniques for the simulation of weakly compressible fluid flows interacting with nonlinear elastic structures undergoing large deformations.

In order to relax the potential instabilities of the artificial added mass effect, causing the failure of FSI simulations involving fluid and structures with similar densities, a weakly compressible model needs to be derived and tested for the flow field. On the one hand, an analytical analysis shall firmly corroborate the beneficial effects of the introduction of a weak compressibility in the fluid for this multiphysics problem. On the other hand, the capability of the model to provide robust and efficient FSI algorithms and to ensure at the same time accurate solutions needs to be assessed on widely used benchmarks.

The most appropriate spatial discretization method shall be employed for each field. While the standard continuous GALERKIN method provides computationally efficient discretizations with a very limited number of degrees of freedom for the solution of structural problems, an alternative discretization method is preferable for the fluid field to tackle a number of intrinsic issues. Among them, the CG method typically lacks stability when convective effects dominate, requiring the use of special stabilization techniques to properly treat high REYNOLDS number flows. Moreover, an appropriate combination of interpolation spaces for the solution variables needs to be selected to treat the saddle-point nature of the fluid problem in the incompressible limit, unless additional stabilization strategies are adopted. The hybridizable discontinuous GALERKIN method, by combining robustness of discontinuous GALERKIN approaches in convection-dominated flows with higher-order accuracy and efficient implementations, constitutes a promising option for the discretization of the fluid problem. Therefore, novel HDG formulations need to be derived, implemented and tested for the simulation of flows in the weakly compressible regime.

Given the hybrid nature of the discretization strategy employed in the subdomains, a suitable technique is required for the imposition of the coupling conditions on the interface. A method for coupling HDG and CG discretizations, enforcing the transmission conditions in the HDG local problems, is already available in literature. However, the resulting coupling of local and global degrees of freedom between the two discretizations makes the implementation of this strategy in existing finite element libraries rather intrusive and inefficient. A novel coupling strategy, preserving the core structure of HDG and CG matrices, shall therefore be developed. This goal can be achieved by solely relying on the CG unknown and on the HDG hybrid variable defined on the mesh faces, to impose the transmission conditions between the subdomains on a global level. Such a strategy needs to be derived and its convergence properties tested first on simple physical phenomena, like thermal and linear elastic problems.

After addressing these key challenges, robust and efficient HDG-CG formulations for the simulation of weakly compressible fluid-structure interaction problems shall be at hand. A partitioned DIRICHLET–NEUMANN scheme can be revisited in the context of hybrid discretizations, while a monolithic scheme can be formulated by extending the novel HDG-CG coupling strategy to the solution of FSI problems. The spatial and temporal convergence features of the proposed schemes shall then be investigated and compared on a problem with manufactured solution. The application of such strategies in two- and three-dimensional benchmarks shall produce reliable solutions and exhibit enhanced robustness and efficiency properties.

1.3 Outline

The remainder of the thesis is organized as follows. In Chapter 2, the governing equations of weakly compressible flows and nonlinear elastic structures are first introduced in Sections 2.1 and 2.2, respectively. The interface conditions and the partitioned algorithm for the solution of the coupled problem are then presented in Section 2.3. The added mass operator, which plays a crucial role on the stability of the numerical scheme, is first recalled with regards to incompressible flows in Section 2.4, while a novel analytical derivation of the same operator in the context of weakly compressible flows is performed in Section 2.5. A comparison of the two operators and a brief discussion follows in Section 2.6. Finally, the role of the compressibility for FSI solvers in terms of robustness, accuracy and computational efficiency is examined on two classical benchmarks in Section 2.7.

Chapter 3 is devoted to the discretization of the fluid problem by means of the HDG method. The governing equations are briefly recalled in Section 3.1 and the adopted VOIGT notation is introduced in Section 3.2. Then, a first scheme featuring the velocity and the pressure as primal variables is formulated in Section 3.3 for simple steady-state flows using the EULERian description of motion. A second density-momentum formulation is derived instead in Section 3.4 for general unsteady flows with the arbitrary LAGRANGEan–EULERian description of motion to deal with deforming domains. In Section 3.5, a weakly compressible POISEUILLE flow, equipped with analytical solution, is employed for the assessment of the convergence properties and for a comparison of the proposed HDG formulations. A second example considers instead a weakly compressible TAYLOR–COUETTE flow in three dimensions, while a last example, exercising all the terms in the fluid partial differential equations, is then presented to verify the capability of the chosen method to preserve the expected spatial and temporal convergence rates on both fixed and moving computational meshes.

The coupling of HDG and CG discretization is addressed in Chapter 4. First, simple thermal problems are considered in Section 4.1. More precisely, the single HDG and CG formulations are introduced in Sections 4.1.1 and 4.1.2, respectively, whereas an approach already existing in literature is recalled in Section 4.1.3 and its disadvantages in terms of computer implementation are discussed. A novel hybrid coupling of HDG and CG discretizations based on NITSCHE's method is proposed in Section 4.1.4 in the context of thermal problems and in Section 4.2 for the solution of elastic problems involving compressible and nearly incompressible materials. A comparison of the two approaches and the properties of the proposed method are presented in Section 4.3 on an extensive set of two- and three-dimensional numerical examples.

The techniques developed and presented in Chapters 2, 3 and 4 are then employed to formulate novel robust and efficient schemes for the solution of FSI problems in Chapter 5. The problem statement is recalled in Section 5.1, whereas a hybrid partitioned DIRICHLET–NEUMANN scheme is presented in Section 5.2 and a monolithic NITSCHE-based scheme is proposed in Section 5.3. The spatial and temporal convergence properties of the proposed approaches are analyzed in the first numerical example of Section 5.4. The remaining examples then apply the FSI strategies for the solution of two- and three-dimensional benchmarks and highlight their enhanced robustness and efficiency features.

Finally, the conclusions of this work are drawn in Chapter 6. In particular, a summary of the achievements is outlined in Section 6.1, whereas an outlook for potential future research is offered in Section 6.2.

2 Role of compressibility for FSI solvers

This chapter introduces the equations governing the flow of incompressible and weakly compressible fluids and the motion of nonlinear elastic structures undergoing large deformations, upon which the content of this thesis is built.

More precisely, the flow of viscous fluid substances is described by the NAVIER–STOKES equations. Although the first appropriate description of the dynamic behavior of fluids is attributed to NEWTON, the mathematical equations of inviscid flows were subsequently derived in the 18th century by BERNOULLI and EULER. The governing equations of viscous flows used nowadays were instead independently formulated by the French engineer NAVIER and the British physicist and mathematician STOKES at the beginning of the 19th century. The first type of flow considered here is treated with the incompressible version of the NAVIER–STOKES equations, whereas the weakly compressible flow is modelled with the isentropic limit of the fully compressible NAVIER–STOKES equations under isothermal conditions.

The deformation of the structure obeys to the laws of nonlinear elastodynamics. A large number of great scientists devoted themselves in the past centuries to the development of the modern theory of elasticity. GALILEI and HOOKE built the mathematical foundations of such theory in the 17th century, whereas fundamental contributions were later brought by COULOMB, YOUNG, POISSON, CAUCHY, LAMÉ and ST. VENANT, among many others. Here, the solid body is assumed to have a hyperelastic behavior, hence accounting for geometrical and potentially material nonlinearities.

In the second part of the chapter, the partitioned algorithm by KÜTTLER and WALL [91] adopted for the coupling of the fluid and the structural subproblems is outlined. As anticipated in the introduction, partitioned schemes suffer the instability of the artificial added mass effect. While this phenomenon has been well understood in the context of incompressible flows with the works by CAUSIN *et al.* [24] and FÖRSTER *et al.* [58], the analysis and the numerical examples presented here highlight fundamental differences that make the adoption of the weakly compressible assumption a favourable approach when using partitioned schemes for the solution of FSI problems characterized by a strong coupling between the fluid and the structural field.

Sections 2.1 and 2.2 introduce the governing equations of fluid flows and nonlinear structural problems, respectively, as well as the associated weak forms in a CG framework. The coupling strategy of the single fields is then exposed in Section 2.3. It follows an analytical study on the role of compressibility in fluid-structure interaction problems with respect to the artificial added mass effect. In particular, the added mass operator for incompressible flows is first recalled in Section 2.4, while the same operator is derived in the context of weakly compressible flows in Section 2.5. The two operators are then compared in Section 2.6. The analytical findings are finally numerically tested on two benchmarks in Section 2.7. The content of this chapter is mainly based on the work of LA SPINA *et al.* [95].

2.1 Fluid problem

In this section, the governing equations of fluid flows with incompressible and weakly compressible behaviors are exposed together with the associated finite element discretization in a classical CG framework.

Let $\Omega_{\mathcal{F}} \in \mathbb{R}^{\mathrm{n_{sd}}}$ be an open bounded domain, with $\mathrm{n_{sd}}$ denoting the number of spatial dimensions, and let the boundary $\partial\Omega_{\mathcal{F}}$ be partitioned into a DIRICHLET portion $\Gamma_{\mathcal{F}}^{D}$ and a NEUMANN portion $\Gamma_{\mathcal{F}}^{N}$ such that $\partial\Omega_{\mathcal{F}} = \Gamma_{\mathcal{F}}^{D} \cup \Gamma_{\mathcal{F}}^{N}$ and $\Gamma_{\mathcal{F}}^{D} \cap \Gamma_{\mathcal{F}}^{N} = \emptyset$. The flow of an incompressible fluid within a deformable region $\Omega_{\mathcal{F}}$ in the time span (t_i, t_f) can be described by the NAVIER–STOKES equations with the arbitrary LAGRANGEan–EULERian description of motion

$$\begin{cases} \rho_{\mathcal{F}} \dfrac{\partial \boldsymbol{v}_{\mathcal{F}}}{\partial t} + \rho_{\mathcal{F}} \boldsymbol{\nabla} \boldsymbol{v}_{\mathcal{F}} \boldsymbol{c}_{\mathcal{F}} - \boldsymbol{\nabla} \cdot \boldsymbol{\sigma}_{\mathcal{F}} \left(\boldsymbol{\nabla} \boldsymbol{v}_{\mathcal{F}}, p_{\mathcal{F}} \right) = \rho_{\mathcal{F}} \boldsymbol{b}_{\mathcal{F}} & \text{in } \Omega_{\mathcal{F}} \times (t_i, t_f), \\ \boldsymbol{\nabla} \cdot \boldsymbol{v}_{\mathcal{F}} = 0 & \text{in } \Omega_{\mathcal{F}} \times (t_i, t_f), \\ \boldsymbol{v}_{\mathcal{F}} = \boldsymbol{v}_{\mathcal{F}}^{0} & \text{in } \Omega_{\mathcal{F}} \times (t_i), \\ \boldsymbol{v}_{\mathcal{F}} = \boldsymbol{v}_{\mathcal{F}}^{D} & \text{on } \Gamma_{\mathcal{F}}^{D} \times (t_i, t_f), \\ \boldsymbol{\sigma}_{\mathcal{F}} \left(\boldsymbol{\nabla} \boldsymbol{v}_{\mathcal{F}}, p_{\mathcal{F}} \right) \boldsymbol{n}_{\mathcal{F}} = \boldsymbol{t}_{\mathcal{F}}^{N} & \text{on } \Gamma_{\mathcal{F}}^{N} \times (t_i, t_f). \end{cases} \tag{2.1}$$

The variables $\boldsymbol{v}_{\mathcal{F}}$ and $p_{\mathcal{F}}$ represent the unknown velocity and pressure fields, $\rho_{\mathcal{F}}$ is a constant fluid density and $\boldsymbol{b}_{\mathcal{F}}$ a prescribed body force. Moreover, $\boldsymbol{\sigma}_{\mathcal{F}}$ denotes the CAUCHY stress tensor that, for NEWTONian viscous flows, is linearly related to the strain rate tensor

$$\boldsymbol{\varepsilon}_{\mathcal{F}} \left(\boldsymbol{\nabla} \boldsymbol{v}_{\mathcal{F}} \right) = \boldsymbol{\nabla}^{\mathrm{S}} \boldsymbol{v}_{\mathcal{F}} = \frac{1}{2} \left(\boldsymbol{\nabla} \boldsymbol{v}_{\mathcal{F}} + \left(\boldsymbol{\nabla} \boldsymbol{v}_{\mathcal{F}} \right)^{T} \right), \tag{2.2}$$

by means of the relationship

$$\boldsymbol{\sigma}_{\mathcal{F}} \left(\boldsymbol{\nabla} \boldsymbol{v}_{\mathcal{F}}, p_{\mathcal{F}} \right) = 2 \mu_{\mathcal{F}} \boldsymbol{\varepsilon}_{\mathcal{F}} \left(\boldsymbol{\nabla} \boldsymbol{v}_{\mathcal{F}} \right) - p_{\mathcal{F}} \mathbf{I}_{\mathrm{n_{sd}}}, \tag{2.3}$$

with $\mu_{\mathcal{F}}$ being the dynamic viscosity and $\mathbf{I}_{\mathrm{n_{sd}}}$ the $\mathrm{n_{sd}} \times \mathrm{n_{sd}}$ identity tensor. The term $\boldsymbol{c}_{\mathcal{F}}$ is referred to as ALE convective velocity and represents the velocity of the fluid relative to the moving background mesh according to

$$\boldsymbol{c}_{\mathcal{F}} = \boldsymbol{v}_{\mathcal{F}} - \boldsymbol{a}_{\mathcal{F}}. \tag{2.4}$$

The mesh velocity $\boldsymbol{a}_{\mathcal{F}}$ is computed as the time derivative of the mesh displacement $\boldsymbol{d}_{\mathcal{F}}$

$$\boldsymbol{a}_{\mathcal{F}} = \frac{d \boldsymbol{d}_{\mathcal{F}}}{dt}. \tag{2.5}$$

The incompressible fluid problem (2.1) is finally completed with suitable initial and boundary conditions. In particular, an initial divergence free velocity field $\boldsymbol{v}_{\mathcal{F}}^{0}$ is imposed in the fluid domain $\Omega_{\mathcal{F}}$, whereas a given velocity $\boldsymbol{v}_{\mathcal{F}}^{D}$ and an external traction $\boldsymbol{t}_{\mathcal{F}}^{N}$ are prescribed on the DIRICHLET portion $\Gamma_{\mathcal{F}}^{D}$ and on the NEUMANN portion $\Gamma_{\mathcal{F}}^{N}$ of the boundary with outward-pointing normal vector $\boldsymbol{n}_{\mathcal{F}}$, respectively.

An isothermal weakly compressible fluid flow is governed by the isentropic limit of the compressible NAVIER–STOKES equations given by

$$\begin{cases} \dfrac{\partial \rho_{\mathcal{F}} \boldsymbol{v}_{\mathcal{F}}}{\partial t} + \boldsymbol{\nabla} \cdot \left(\rho_{\mathcal{F}} \boldsymbol{v}_{\mathcal{F}} \otimes \boldsymbol{v}_{\mathcal{F}}\right) - \boldsymbol{\nabla} \left(\rho_{\mathcal{F}} \boldsymbol{v}_{\mathcal{F}}\right) \boldsymbol{a}_{\mathcal{F}} - \boldsymbol{\nabla} \cdot \boldsymbol{\sigma}_{\mathcal{F}} \left(\boldsymbol{\nabla} \boldsymbol{v}_{\mathcal{F}}, p_{\mathcal{F}}\right) = \rho_{\mathcal{F}} \boldsymbol{b}_{\mathcal{F}}, \\ \dfrac{\partial \rho_{\mathcal{F}}}{\partial t} + \boldsymbol{\nabla} \cdot \left(\rho_{\mathcal{F}} \boldsymbol{v}_{\mathcal{F}}\right) - \boldsymbol{\nabla} \rho_{\mathcal{F}} \cdot \boldsymbol{a}_{\mathcal{F}} = 0, \\ \rho_{\mathcal{F}} = \rho_{\mathcal{F}} \left(p_{\mathcal{F}}\right). \end{cases} \tag{2.6}$$

The first equation is referred to as momentum equation and ensures the balance of the linear momentum in accordance with NEWTON's second law of motion [115], whereas the second equation is denoted continuity equation and states the conservation of mass. The third equation represents an equation of state relating the fluid pressure with the density, which is no longer assumed constant. Since no temperature changes are taken into account, the energy equation is decoupled from the other equations and its conservation is automatically ensured through the equation of state. The linear relationship

$$\rho_{\mathcal{F}} = \rho_{\mathcal{F}}^{\mathtt{ref}} + \varepsilon_{\mathcal{F}} \left(p_{\mathcal{F}} - p_{\mathcal{F}}^{\mathtt{ref}}\right) \tag{2.7}$$

is used throughout this thesis, with $\varepsilon_{\mathcal{F}}$ being a (small) compressibility coefficient and $\rho_{\mathcal{F}}^{\mathtt{ref}}$ denoting the reference density computed at the reference pressure $p_{\mathcal{F}}^{\mathtt{ref}}$. Alternative and more sophisticated equations of state can however be adopted, possibly requiring the evaluation of additional parameters. Equation (2.7) is not explicitly written in the following analysis in order to keep the formulation as general as possible. Since the fluid velocity does not constitute a solenoidal field in the weakly compressible regime, i.e. $\boldsymbol{\nabla} \cdot \boldsymbol{v}_{\mathcal{F}} \neq 0$, the CAUCHY stress in (2.6) takes the more general form

$$\boldsymbol{\sigma}_{\mathcal{F}} \left(\boldsymbol{\nabla} \boldsymbol{v}_{\mathcal{F}}, p_{\mathcal{F}}\right) = 2\mu_{\mathcal{F}} \boldsymbol{\varepsilon}_{\mathcal{F}} \left(\boldsymbol{\nabla} \boldsymbol{v}_{\mathcal{F}}\right) + \lambda_{\mathcal{F}} \left(\boldsymbol{\nabla} \cdot \boldsymbol{v}_{\mathcal{F}}\right) \mathbf{I}_{\mathrm{n_{sd}}} - p_{\mathcal{F}} \mathbf{I}_{\mathrm{n_{sd}}}, \tag{2.8}$$

with $\lambda_{\mathcal{F}}$ being the so-called second coefficient of viscosity, whose value can be extrapolated by means of the widely accepted STOKES hypothesis [151]

$$\frac{2}{3}\mu_{\mathcal{F}} + \lambda_{\mathcal{F}} = 0. \tag{2.9}$$

The strong form of the weakly compressible flow problem with the ALE description of motion in the primitive variables velocity and pressure is then given by

$$\begin{cases} \rho_{\mathcal{F}} \left(p_{\mathcal{F}}\right) \dfrac{\partial \boldsymbol{v}_{\mathcal{F}}}{\partial t} + \rho_{\mathcal{F}} \left(p_{\mathcal{F}}\right) \boldsymbol{\nabla} \boldsymbol{v}_{\mathcal{F}} \boldsymbol{c}_{\mathcal{F}} & \\ \quad - \boldsymbol{\nabla} \cdot \left[2\mu_{\mathcal{F}} \boldsymbol{\nabla}^{\mathrm{S}} \boldsymbol{v}_{\mathcal{F}} + \lambda_{\mathcal{F}} \left(\boldsymbol{\nabla} \cdot \boldsymbol{v}_{\mathcal{F}}\right) \mathbf{I}_{\mathrm{n_{sd}}} - p_{\mathcal{F}} \mathbf{I}_{\mathrm{n_{sd}}}\right] = \rho_{\mathcal{F}} \left(p_{\mathcal{F}}\right) \boldsymbol{b}_{\mathcal{F}} & \text{in } \Omega_{\mathcal{F}} \times (t_i, t_f), \\ \dfrac{\partial \rho_{\mathcal{F}} \left(p_{\mathcal{F}}\right)}{\partial p_{\mathcal{F}}} \dfrac{\partial p_{\mathcal{F}}}{\partial t} + \dfrac{\partial \rho_{\mathcal{F}} \left(p_{\mathcal{F}}\right)}{\partial p_{\mathcal{F}}} \boldsymbol{\nabla} p_{\mathcal{F}} \cdot \boldsymbol{c}_{\mathcal{F}} & \\ \qquad + \rho_{\mathcal{F}} \left(p_{\mathcal{F}}\right) \boldsymbol{\nabla} \cdot \boldsymbol{v}_{\mathcal{F}} = 0 & \text{in } \Omega_{\mathcal{F}} \times (t_i, t_f), \\ \boldsymbol{v}_{\mathcal{F}} = \boldsymbol{v}_{\mathcal{F}}^0 & \text{in } \Omega_{\mathcal{F}} \times (t_i), \\ p_{\mathcal{F}} = p_{\mathcal{F}}^0 & \text{in } \Omega_{\mathcal{F}} \times (t_i), \\ \boldsymbol{v}_{\mathcal{F}} = \boldsymbol{v}_{\mathcal{F}}^D & \text{on } \Gamma_{\mathcal{F}}^D \times (t_i, t_f), \\ p_{\mathcal{F}} = p_{\mathcal{F}}^D & \text{on } \Gamma_{\mathcal{F}}^D \times (t_i, t_f), \\ \left[2\mu_{\mathcal{F}} \boldsymbol{\nabla}^{\mathrm{S}} \boldsymbol{v}_{\mathcal{F}} + \lambda_{\mathcal{F}} \left(\boldsymbol{\nabla} \cdot \boldsymbol{v}_{\mathcal{F}}\right) \mathbf{I}_{\mathrm{n_{sd}}} - p_{\mathcal{F}} \mathbf{I}_{\mathrm{n_{sd}}}\right] \boldsymbol{n}_{\mathcal{F}} = \boldsymbol{t}_{\mathcal{F}}^N & \text{on } \Gamma_{\mathcal{F}}^N \times (t_i, t_f), \end{cases} \tag{2.10}$$

where the momentum equation is rearranged by assuming the mass conservation to be exactly fulfilled. With this algebraic manipulation, the problem (2.10) constitutes a straightforward extension of the incompressible counterpart (2.1) and only the inclusion of a relatively small number of terms is required to simulate the effect of a weak flow compressibility. Moreover, as opposed to the incompressible model, in which the pressure appears solely under the gradient operator and acts as a LAGRANGE multiplier of the incompressibility constraint, here the pressure assumes a clear physical meaning and directly affects the fluid density through the equation of state (2.7). This physical model allows to impose a function $p_{\mathcal{F}}^{D}$ on the DIRICHLET portion of the boundary and requires the specification of the initial field $p_{\mathcal{F}}^{0}$ to evolve in time.

The weak form of the weakly compressible flow problem is obtained by multiplying the governing equations by suitable weighting functions and integrating over the computational domain. After integration by parts of the stress term and by exploiting the boundary conditions, the weak form of the CG approximation of problem (2.10) reads: given $(\boldsymbol{v}_{\mathcal{F}}^{0}, p_{\mathcal{F}}^{0})$ in $\Omega_{\mathcal{F}} \times (t_i)$, find $(\boldsymbol{v}_{\mathcal{F}}, p_{\mathcal{F}}) \in [\mathcal{V}^h(\Omega_{\mathcal{F}})]^{\mathtt{n_{sd}}} \times \mathcal{V}^h(\Omega_{\mathcal{F}})$ such that

$$\begin{aligned}
&\left(\boldsymbol{w}, \rho_{\mathcal{F}}(p_{\mathcal{F}}) \frac{\partial \boldsymbol{v}_{\mathcal{F}}}{\partial t}\right)_{\Omega_{\mathcal{F}}} + \left(\boldsymbol{w}, \rho_{\mathcal{F}}(p_{\mathcal{F}}) \boldsymbol{\nabla} \boldsymbol{v}_{\mathcal{F}} \left(\boldsymbol{v}_{\mathcal{F}} - \frac{d\boldsymbol{d}_{\mathcal{F}}}{dt}\right)\right)_{\Omega_{\mathcal{F}}} \\
&\quad + \left(\boldsymbol{\nabla}\boldsymbol{w}, 2\mu_{\mathcal{F}} \boldsymbol{\nabla}^{\mathrm{S}} \boldsymbol{v}_{\mathcal{F}} + \lambda_{\mathcal{F}}\left(\boldsymbol{\nabla}\cdot\boldsymbol{v}_{\mathcal{F}}\right)\mathbf{I}_{\mathtt{n_{sd}}} - p_{\mathcal{F}}\mathbf{I}_{\mathtt{n_{sd}}}\right)_{\Omega_{\mathcal{F}}} - \left(\boldsymbol{w}, \rho_{\mathcal{F}}(p_{\mathcal{F}})\boldsymbol{b}_{\mathcal{F}}\right)_{\Omega_{\mathcal{F}}} \\
&\quad + \sum_{e=1}^{\mathtt{n}_{\mathcal{F}}^{\mathtt{el}}} \left(\boldsymbol{\nabla}\boldsymbol{w}\left(\boldsymbol{v}_{\mathcal{F}} - \frac{d\boldsymbol{d}_{\mathcal{F}}}{dt}\right), \tau_{\mathtt{SUPG}} \boldsymbol{\mathcal{R}}_{\mathrm{M}}\left(\boldsymbol{v}_{\mathcal{F}}, p_{\mathcal{F}}\right)\right)_{\Omega_{\mathcal{F}}^{e}} = \left\langle \boldsymbol{w}, \boldsymbol{t}_{\mathcal{F}}^{N}\right\rangle_{\Gamma_{\mathcal{F}}^{N}},
\end{aligned} \tag{2.11a}$$

$$\begin{aligned}
&\left(w, \frac{\partial \rho_{\mathcal{F}}(p_{\mathcal{F}})}{\partial p_{\mathcal{F}}} \frac{\partial p_{\mathcal{F}}}{\partial t}\right)_{\Omega_{\mathcal{F}}} + \left(w, \frac{\partial \rho_{\mathcal{F}}(p_{\mathcal{F}})}{\partial p_{\mathcal{F}}} \boldsymbol{\nabla} p_{\mathcal{F}} \cdot \left(\boldsymbol{v}_{\mathcal{F}} - \frac{d\boldsymbol{d}_{\mathcal{F}}}{dt}\right)\right)_{\Omega_{\mathcal{F}}} \\
&\quad + \left(w, \rho_{\mathcal{F}}(p_{\mathcal{F}}) \boldsymbol{\nabla}\cdot\boldsymbol{v}_{\mathcal{F}}\right)_{\Omega_{\mathcal{F}}} + \sum_{e=1}^{\mathtt{n}_{\mathcal{F}}^{\mathtt{el}}} \left(\boldsymbol{\nabla} w, \tau_{\mathtt{PSPG}} \boldsymbol{\mathcal{R}}_{\mathrm{M}}\left(\boldsymbol{v}_{\mathcal{F}}, p_{\mathcal{F}}\right)\right)_{\Omega_{\mathcal{F}}^{e}} = 0,
\end{aligned} \tag{2.11b}$$

for all $(\boldsymbol{w}, w) \in [\mathcal{V}_0^h(\Omega_{\mathcal{F}})]^{\mathtt{n_{sd}}} \times \mathcal{V}_0^h(\Omega_{\mathcal{F}})$. The precise definition of the finite element spaces for the test functions and the solution variables is given in Appendix A.

The last terms in the left hand sides provide a remedy for the deficiency of the continuous GALERKIN approach, arising in convection-dominated flows and in the vicinity of the incompressible limit. More precisely, the streamline-upwind PETROV–GALERKIN (SUPG) term introduced by BROOKS and HUGHES [19] in the momentum equation stabilizes the formulation at high REYNOLDS number flows, whereas the pressure-stabilizing PETROV–GALERKIN (PSPG) term introduced by HUGHES *et al.* [83] in the continuity equation allows the use of equal-order interpolations for velocity and pressure. The corresponding stabilization parameters are denoted with $\tau_{\mathtt{SUPG}}$ and $\tau_{\mathtt{PSPG}}$, while $\boldsymbol{\mathcal{R}}_{\mathrm{M}}$ refers to the residual of the momentum equation. A detailed analysis on these parameters can be found in the textbooks by DONEA and HUERTA [45] and by ZIENKIEWICZ *et al.* [175] or in the thesis of WALL [166]. It is worth highlighting that the introduced stabilization terms are weighted residuals and therefore ensure the consistency of the CG formulation.

Only the weak form of the weakly compressible flow problem is reported here, for the sake of brevity. However, the incompressible counterpart is fully recovered by considering a vanishing compressibility, i.e. $\partial\rho_{\mathcal{F}}(p_{\mathcal{F}})/\partial p_{\mathcal{F}} = \varepsilon_{\mathcal{F}} = 0$, and by neglecting the term $\lambda_{\mathcal{F}}\left(\boldsymbol{\nabla}\cdot\boldsymbol{v}_{\mathcal{F}}\right)\mathbf{I}_{\mathtt{n_{sd}}}$.

2.2 Structure problem

Analogously to the fluid field, the structural domain is denoted with $\Omega_{\mathcal{S}} \in \mathbb{R}^{\mathrm{n_{sd}}}$ and its boundary $\partial\Omega_{\mathcal{S}}$ is partitioned into a DIRICHLET portion $\Gamma_{\mathcal{S}}^{D}$ and a NEUMANN portion $\Gamma_{\mathcal{S}}^{N}$ such that $\partial\Omega_{\mathcal{S}} = \Gamma_{\mathcal{S}}^{D} \cup \Gamma_{\mathcal{S}}^{N}$ and $\Gamma_{\mathcal{S}}^{D} \cap \Gamma_{\mathcal{S}}^{N} = \emptyset$. The total LAGRANGEan approach is adopted to describe the structural motion, hence all the quantities and mathematical operators are referred to the undeformed configuration. However, no special notation is introduced to distinguish the operators associated to either the material or the spatial coordinates for the sake of readability. The strong form of a nonlinear elastodynamic problem can then be written as

$$\begin{cases} \rho_{\mathcal{S}} \dfrac{d^2 \boldsymbol{u}_{\mathcal{S}}}{dt^2} - \boldsymbol{\nabla} \cdot \boldsymbol{P}_{\mathcal{S}} \left(\boldsymbol{\nabla} \boldsymbol{u}_{\mathcal{S}} \right) = \rho_{\mathcal{S}} \boldsymbol{b}_{\mathcal{S}} & \text{in } \Omega_{\mathcal{S}} \times (t_i, t_f), \\ \boldsymbol{u}_{\mathcal{S}} = \boldsymbol{u}_{\mathcal{S}}^{0} & \text{in } \Omega_{\mathcal{S}} \times (t_i), \\ \dfrac{d\boldsymbol{u}_{\mathcal{S}}}{dt} = \dot{\boldsymbol{u}}_{\mathcal{S}}^{0} & \text{in } \Omega_{\mathcal{S}} \times (t_i), \\ \boldsymbol{u}_{\mathcal{S}} = \boldsymbol{u}_{\mathcal{S}}^{D} & \text{on } \Gamma_{\mathcal{S}}^{D} \times (t_i, t_f), \\ \boldsymbol{P}_{\mathcal{S}} \left(\boldsymbol{\nabla} \boldsymbol{u}_{\mathcal{S}} \right) \boldsymbol{n}_{\mathcal{S}} = \boldsymbol{t}_{\mathcal{S}}^{N} & \text{on } \Gamma_{\mathcal{S}}^{N} \times (t_i, t_f). \end{cases} \tag{2.12}$$

The first equation states the dynamic equilibrium of inertial, internal and external forces, whereas the following ones impose the initial and the boundary conditions. The variable $\boldsymbol{u}_{\mathcal{S}}$ represents the unknown displacement field, whereas $\rho_{\mathcal{S}}$ is a constant solid density and $\boldsymbol{b}_{\mathcal{S}}$ a prescribed body force per unit undeformed volume.

The internal forces are expressed in terms of the first PIOLA–KIRCHHOFF stress tensor $\boldsymbol{P}_{\mathcal{S}}$ that, for hyperelastic materials, is computed as

$$\boldsymbol{P}_{\mathcal{S}} \left(\boldsymbol{\nabla} \boldsymbol{u}_{\mathcal{S}} \right) = \frac{\partial \psi_{\mathcal{S}} \left(\boldsymbol{F}_{\mathcal{S}} \right)}{\partial \boldsymbol{F}_{\mathcal{S}}}, \tag{2.13}$$

with $\boldsymbol{F}_{\mathcal{S}}$ being the deformation gradient and $\psi_{\mathcal{S}}$ the strain energy density function. The former is directly related to the displacement gradient through the expression

$$\boldsymbol{F}_{\mathcal{S}} = \boldsymbol{\nabla} \boldsymbol{u}_{\mathcal{S}} + \mathbf{I}_{\mathrm{n_{sd}}}, \tag{2.14}$$

while the latter is defined as

$$\psi_{\mathcal{S}} \left(\boldsymbol{F}_{\mathcal{S}} \right) = \begin{cases} \mu_{\mathcal{S}} \boldsymbol{E}_{\mathcal{S}} : \boldsymbol{E}_{\mathcal{S}} + \dfrac{\lambda_{\mathcal{S}}}{2} \left[\mathrm{tr} \left(\boldsymbol{E}_{\mathcal{S}} \right) \right]^2 & \text{ST. VENANT–KIRCHHOFF}, \\ \dfrac{\mu_{\mathcal{S}}}{2} \left[\mathrm{tr} \left(\boldsymbol{F}_{\mathcal{S}}^{T} \boldsymbol{F}_{\mathcal{S}} \right) - 2 \ln \left(|\boldsymbol{F}_{\mathcal{S}}| \right) - \mathrm{n_{sd}} \right] + \dfrac{\lambda_{\mathcal{S}}}{2} \left[\ln \left(|\boldsymbol{F}_{\mathcal{S}}| \right) \right]^2 & \text{Neo-HOOKE}, \end{cases} \tag{2.15}$$

for the two popular material models adopted in this thesis.

The ST. VENANT–KIRCHHOFF is the simplest hyperelastic material model and represents an extension of the linear elastic model to the geometrically nonlinear regime. In fact, the GREEN–LAGRANGE strain tensor $\boldsymbol{E}_{\mathcal{S}}$ is computed as

$$\begin{aligned} \boldsymbol{E}_{\mathcal{S}} \left(\boldsymbol{\nabla} \boldsymbol{u}_{\mathcal{S}} \right) &= \frac{1}{2} \left(\boldsymbol{F}_{\mathcal{S}}^{T} \boldsymbol{F}_{\mathcal{S}} - \mathbf{I}_{\mathrm{n_{sd}}} \right) \\ &= \frac{1}{2} \left(\boldsymbol{\nabla} \boldsymbol{u}_{\mathcal{S}} + \left(\boldsymbol{\nabla} \boldsymbol{u}_{\mathcal{S}} \right)^{T} + \left(\boldsymbol{\nabla} \boldsymbol{u}_{\mathcal{S}} \right)^{T} \boldsymbol{\nabla} \boldsymbol{u}_{\mathcal{S}} \right), \end{aligned} \tag{2.16}$$

and stems from the infinitesimal strain tensor

$$\varepsilon_{\mathcal{S}}\left(\boldsymbol{\nabla} \boldsymbol{u}_{\mathcal{S}}\right)=\frac{1}{2}\left(\boldsymbol{\nabla} \boldsymbol{u}_{\mathcal{S}}+\left(\boldsymbol{\nabla} \boldsymbol{u}_{\mathcal{S}}\right)^{T}\right), \tag{2.17}$$

with the inclusion of the second order terms to account for geometrical nonlinearities. The Neo-HOOKEan model considers instead a nonlinear stress-strain relationship and is suited for the behavior of plastic and rubber-like solids undergoing large deformations.

The LAMÉ parameters $\mu_{\mathcal{S}}$ and $\lambda_{\mathcal{S}}$ can the be evaluated from the YOUNG modulus $E_{\mathcal{S}}$ and the POISSON ratio $\nu_{\mathcal{S}}$ of the material through the relations

$$\mu_{\mathcal{S}}=\frac{E_{\mathcal{S}}}{2\left(1+\nu_{\mathcal{S}}\right)}, \qquad \lambda_{\mathcal{S}}=\frac{\nu_{\mathcal{S}} E_{\mathcal{S}}}{\left(1+\nu_{\mathcal{S}}\right)\left(1-2 \nu_{\mathcal{S}}\right)}. \tag{2.18}$$

The coefficient $\mu_{\mathcal{S}}$ is strictly positive and coincides with the shear modulus, thus describing material's response to shear stress. The parameter $\lambda_{\mathcal{S}}$ is closely related to the bulk modulus

$$K_{\mathcal{S}}=\frac{2}{3} \mu_{\mathcal{S}}+\lambda_{\mathcal{S}}, \tag{2.19}$$

which describes the material response to a uniform hydrostatic pressure and therefore provides a direct measure of the solid compressibility.

For convenience, fluid-structure interaction problems are solved in this thesis considering solely compressible solids, for which the POISSON ratio is bounded in the interval $0 \leq \nu_{\mathcal{S}}<0.5$, hence resulting in a finite value of the bulk modulus, i.e. $K_{\mathcal{S}}<\infty$. It is well-known that low-order displacement-based CG formulations fail to provide locking-free approximations for (nearly) incompressible materials, for which $\nu_{\mathcal{S}} \rightarrow 0.5$. A number of possible remedies, discussed in Chapter 4, have been proposed in the literature to circumvent this issue. A novel strategy involving a hybrid HDG-CG discretization is proposed in Section 4.2 to solve elastic problems featuring multiple materials with compressible and nearly incompressible behaviors.

Owing to the presence of the second temporal derivative, the structural problem (2.12) requires not only an initial displacement field $\boldsymbol{u}_{\mathcal{S}}^{0}$, but also an initial velocity $\dot{\boldsymbol{u}}_{\mathcal{S}}^{0}$. Finally, the DIRICHLET and NEUMANN boundary conditions are expressed in terms of displacements $\boldsymbol{u}_{\mathcal{S}}^{D}$ imposed on $\Gamma_{\mathcal{S}}^{D}$ and tractions $\boldsymbol{t}_{\mathcal{S}}^{N}$ imposed on $\Gamma_{\mathcal{S}}^{N}$, respectively. The outward-pointing unit normal vector to the structural boundary is denoted with $\boldsymbol{n}_{\mathcal{S}}$.

Analogously to the fluid field, the weak form of the CG approximation of the structural problem (2.12) is obtained by multiplying the governing equation by an appropriate test function, integrating over the computational domain and performing an integration by parts of the term under the divergence operator. It thus reads: given $(\boldsymbol{u}_{\mathcal{S}}^{0}, \dot{\boldsymbol{u}}_{\mathcal{S}}^{0})$ in $\Omega_{\mathcal{S}} \times (t_i)$, find $\boldsymbol{u}_{\mathcal{S}} \in [\mathcal{V}^{h}(\Omega_{\mathcal{S}})]^{\mathrm{n_{sd}}}$ such that

$$\left(\boldsymbol{v}, \rho_{\mathcal{S}} \frac{d^{2} \boldsymbol{u}_{\mathcal{S}}}{d t^{2}}\right)_{\Omega_{\mathcal{S}}}+\left(\boldsymbol{\nabla} \boldsymbol{v}, \boldsymbol{P}_{\mathcal{S}}\left(\boldsymbol{\nabla} \boldsymbol{u}_{\mathcal{S}}\right)\right)_{\Omega_{\mathcal{S}}}=\left(\boldsymbol{v}, \rho_{\mathcal{S}} \boldsymbol{b}_{\mathcal{S}}\right)_{\Omega_{\mathcal{S}}}+\left\langle\boldsymbol{v}, \boldsymbol{t}_{\mathcal{S}}^{N}\right\rangle_{\Gamma_{\mathcal{S}}^{N}}, \tag{2.20}$$

for all $\boldsymbol{v} \in [\mathcal{V}_{0}^{h}(\Omega_{\mathcal{S}})]^{\mathrm{n_{sd}}}$.

2.3 Fluid-structure coupling

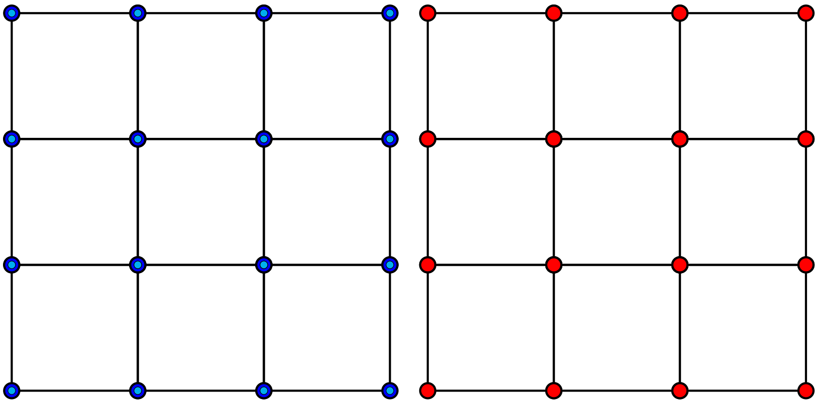

Figure 2.1: Degrees of freedom of the CG-CG discretization

Let the whole domain Ω be split into two non-overlapping subdomains $\Omega_{\mathcal{F}}$ and $\Omega_{\mathcal{S}}$ such that $\Omega = \Omega_{\mathcal{F}} \cup \Omega_{\mathcal{S}}$, with interface $\Gamma^I = \Omega_{\mathcal{F}} \cap \Omega_{\mathcal{S}}$. The fluid subdomain is divided into $\mathtt{n}^{\mathtt{el}}_{\mathcal{F}}$ disjoint elements as

$$\Omega_{\mathcal{F}} = \bigcup_{e=1}^{\mathtt{n}^{\mathtt{el}}_{\mathcal{F}}} \Omega^e_{\mathcal{F}}, \quad \Omega^e_{\mathcal{F}} \cap \Omega^f_{\mathcal{F}} = \emptyset \quad \text{for} \quad e \neq f, \tag{2.21}$$

while the structural subdomain is divided into $\mathtt{n}^{\mathtt{el}}_{\mathcal{S}}$ elements as

$$\Omega_{\mathcal{S}} = \bigcup_{e=1}^{\mathtt{n}^{\mathtt{el}}_{\mathcal{S}}} \Omega^e_{\mathcal{S}}, \quad \Omega^e_{\mathcal{S}} \cap \Omega^f_{\mathcal{S}} = \emptyset \quad \text{for} \quad e \neq f. \tag{2.22}$$

Figure 2.1 depicts the degrees of freedom of the discretization, for a polynomial degree of approximation $k = 1$ in the whole domain. More precisely, the blue circles denote the CG DOFs of the fluid problem corresponding to the velocity $\mathbf{v}_{\mathcal{F}}$ and the pressure $\mathbf{p}_{\mathcal{F}}$, collected in the vector $\mathbf{V}_{\mathcal{F}} = \begin{bmatrix}\mathbf{v}_{\mathcal{F}} & \mathbf{p}_{\mathcal{F}}\end{bmatrix}^T$ for simplicity, whereas the red circles refer to the CG DOFs of the structural problem, corresponding to the displacement $\mathbf{u}_{\mathcal{S}}$. Finally, the DOFs in cyan refer to the fluid mesh displacement $\mathbf{u}_{\mathcal{F}}$ in the ALE framework.

It is worth mentioning that the deformation of the fluid computational mesh is evaluated as a function of the structural displacement at the interface, by means of a unique ALE mapping φ. The grid motion strategy is an artificial problem, hence not affecting the physics of the coupled problem, and its sole purpose is to generate a proper mesh for the solution of the fluid problem. With this regard, several techniques have been proposed in the last decades and they are not discussed here, because of secondary importance for the purposes of this thesis. However, a comprehensive literature survey on this topic can be found at DONEA *et al.* [46].

In order to couple the fluid problem, whose weak form has been derived Section 2.1, and the structural problem, whose weak form has been presented in Section 2.2, the following kinematic and dynamic continuity conditions have be enforced at the fluid-structure interface

$$\begin{cases} \boldsymbol{v}_{\mathcal{F}} - \dfrac{d\boldsymbol{u}_{\mathcal{S}}}{dt} = \mathbf{0} & \text{on } \Gamma^I \times (t_i, t_f), \\ \boldsymbol{t}_{\mathcal{F}} \left(\boldsymbol{\nabla} \boldsymbol{v}_{\mathcal{F}}, p_{\mathcal{F}} \right) + \boldsymbol{t}_{\mathcal{S}} \left(\boldsymbol{\nabla} \boldsymbol{u}_{\mathcal{S}} \right) = \mathbf{0} & \text{on } \Gamma^I \times (t_i, t_f). \end{cases} \tag{2.23}$$

The first equality denotes the no-slip condition, prohibiting a fluid flow across the interface and a relative tangential movement of the fluid and the structure at the same location. The second relation enforces then the equilibrium of the fluid and the structural forces at the interface and directly follows from NEWTON's third law of motion [115].

The coupling of the fluid and the structural solvers is performed by means of the partitioned DIRICHLET–NEUMANN scheme outlined by KÜTTLER and WALL [91]. In the following, the terms $\mathbf{K}$ and $\mathbf{f}$ denote the left hand side matrices and right hand side vectors, respectively, arising from the discretization of the associated weak forms, whereas the symbol $\mathop{\mathsf{A}}$ stands for the assembly operator of the elemental contributions. Moreover, owing to the nonlinear nature of the governing equations, the single-field problems are linearised and solved in terms solution increments (indicated with δ) by means of the NEWTON–RAPHSON method until convergence. Assuming all the quantities referred to the time step $n+1$ and denoting by i the coupling iteration count, the matrix form of the coupling algorithm can be schematized as:

1. Start with a predicted interface structural displacement $\left[\mathbf{u}_{\mathcal{S}}^i\right]$.
2. Update the fluid mesh by means of the ALE mapping $\left[\mathbf{d}_{\mathcal{F}}^i\right] = \boldsymbol{\varphi}\left(\left[\mathbf{u}_{\mathcal{S}}^i\right]\right)$.
3. Compute the fluid solution $\left[\mathbf{V}_{\mathcal{F}}^i\right]$ by solving the problem
$$\left[\mathbf{K}_{\mathcal{F}\mathcal{F}}\right] \left[\delta \mathbf{V}_{\mathcal{F}}^i\right] = \left[\mathbf{f}_{\mathcal{F}}\right], \tag{2.24}$$
with
$$\left[\mathbf{K}_{\mathcal{F}\mathcal{F}}\right] = \mathop{\mathsf{A}}_{e=1}^{\mathrm{n}_{\mathcal{F}}^{\mathrm{el}}} \left\{ \left[\mathbf{K}_{VV}\right]_e \right\}, \qquad \left[\mathbf{f}_{\mathcal{F}}\right] = \mathop{\mathsf{A}}_{e=1}^{\mathrm{n}_{\mathcal{F}}^{\mathrm{el}}} \left\{ \left[\mathbf{f}_{V}\right]_e \right\}, \tag{2.25}$$
and $\left[\mathbf{V}_{\mathcal{I}}^D(\mathbf{u}_{\mathcal{S}}^i)\right]$ being strongly imposed as a DIRICHLET condition on the interface.
4. Compute a new structural solution $\left[\bar{\mathbf{u}}_{\mathcal{S}}^{i+1}\right]$ by solving the problem
$$\left[\mathbf{K}_{\mathcal{S}\mathcal{S}}\right] \left[\delta \bar{\mathbf{u}}_{\mathcal{S}}^{i+1}\right] = \left[\mathbf{f}_{\mathcal{S}}\right] + \left[\mathbf{f}_{\mathcal{I}}^N(\mathbf{V}_{\mathcal{F}}^i)\right], \tag{2.26}$$
with
$$\left[\mathbf{K}_{\mathcal{S}\mathcal{S}}\right] = \mathop{\mathsf{A}}_{e=1}^{\mathrm{n}_{\mathcal{S}}^{\mathrm{el}}} \left\{ \left[\mathbf{K}_{uu}\right]_e \right\}, \qquad \left[\mathbf{f}_{\mathcal{S}}\right] = \mathop{\mathsf{A}}_{e=1}^{\mathrm{n}_{\mathcal{S}}^{\mathrm{el}}} \left\{ \left[\mathbf{f}_{u}\right]_e \right\}, \tag{2.27}$$
and $\left[\mathbf{f}_{\mathcal{I}}^N(\mathbf{V}_{\mathcal{F}}^i)\right]$ denoting the NEUMANN coupling vector on the interface.
5. Check the convergence of the interface displacement residual $\left\|\left[\mathbf{r}_{\mathcal{I}}^{i+1}\right]\right\| < \eta$ with
$$\left[\mathbf{r}_{\mathcal{I}}^{i+1}\right] = \left[\bar{\mathbf{u}}_{\mathcal{S}}^{i+1}\right] - \left[\mathbf{u}_{\mathcal{S}}^i\right]. \tag{2.28}$$
Continue with next time step if the algorithm is converged, otherwise return to step 2 with
$$\left[\mathbf{u}_{\mathcal{S}}^{i+1}\right] = \omega^{i+1} \left[\bar{\mathbf{u}}_{\mathcal{S}}^{i+1}\right] + \left(1 - \omega^{i+1}\right) \left[\mathbf{u}_{\mathcal{S}}^i\right], \tag{2.29}$$
where the relaxation parameter is either kept constant or updated by means of AITKEN's Δ^2 method
$$\omega^{i+1} = -\omega^i \left[\mathbf{r}_{\mathcal{I}}^i\right]^T \left(\left[\mathbf{r}_{\mathcal{I}}^{i+1}\right] - \left[\mathbf{r}_{\mathcal{I}}^i\right]\right) / \left\|\left[\mathbf{r}_{\mathcal{I}}^{i+1}\right] - \left[\mathbf{r}_{\mathcal{I}}^i\right]\right\|^2. \tag{2.30}$$

2.4 Incompressible added mass operator

The artificial added mass effect is a well-known phenomenon in the fluid-structure interaction community. It is particular evident in the context of loosely-coupled partitioned schemes and it imposes a lower bound on the time step size to allow stable computations. The resulting instability is defined artificial added mass effect since the fluid forces acting on the structural interface contain an artificial and incorrect contribution, acting as an extra mass on the structural interface degrees of freedom. This phenomenon has been first investigated by CAUSIN *et al.* [24] on a simplified model problem in the context of incompressible flows. Although the model problem considered therein represents an extreme simplification of real world applications, it is nonetheless able to realistically predict the stability and the convergence properties of the FSI solver. Later, FÖRSTER *et al.* [58] offered a general discrete representation of the added mass operator and derived different instability conditions for various temporal discretization schemes.

By adopting a classical DIRICHLET–NEUMANN coupling scheme and discretizing the governing equations by means of finite elements in a CG framework, the coupling force vector can be expressed in terms of the interface acceleration as

$$\mathbf{f}_{\mathtt{I}} = m_{\mathcal{F}} \boldsymbol{\mathcal{M}} \dot{\mathbf{v}}_{\mathtt{I}}, \tag{2.31}$$

with $m_{\mathcal{F}}$ denoting a characteristic fluid mass and $\dot{\mathbf{v}}_{\mathtt{I}}$ being the aforementioned interface acceleration. $\boldsymbol{\mathcal{M}}$ is the artificial added mass operator, which can be interpreted as a geometrical operator mapping a dimensionless interface acceleration onto an also dimensionless interface force. Henceforth, the subscripts $\odot_{\mathtt{i}}$ and $\odot_{\mathtt{I}}$ are adopted to refer to the interior and the interface degrees of freedom, respectively. By only considering the relevant features and neglecting secondary effects, such as the motion of the fluid domain and all nonlinearities, and assuming a regular mesh as well as a lumped mass matrix approximation, the added mass operator for incompressible flows derived by FÖRSTER *et al.* [58] can be written as

$$\boldsymbol{\mathcal{M}}^{\mathtt{inc}}_{\mathtt{lump}} = \mathbf{I}_{\mathtt{II}} + 2\mathbf{G}_{\mathtt{I}} \left(\mathbf{G}_{\mathtt{i}}^{T} \mathbf{G}_{\mathtt{i}} \right)^{-1} \mathbf{G}_{\mathtt{I}}^{T}, \tag{2.32}$$

with $\mathbf{G}$ denoting the discrete gradient operator and its transpose $\mathbf{G}^T$ being the discrete divergence operator. The first term in (2.32) represents the forces required to accelerate the fluid masses adjacent to the interface, whereas the second term yields forces generated by the effect of incompressibility.

2.5 Weakly compressible added mass operator

As opposed to fluid-structure interaction problems involving incompressible flows, which are heavily affected by the artificial added mass effect, compressible flows are much less influenced by this detrimental phenomenon and related instabilities have rarely been reported in literature (for example by JAIMAN *et al.* [85]). Moreover, it is often claimed that no artificial added mass effect arises even when driving a (weakly) compressible flow solver close to the incompressible limit, i.e. at low MACH number. A first analysis conducted by VAN BRUMMELEN [160] on a simple two-dimensional model problem highlighted the beneficial role of compressibility, whereas a later study by LA SPINA *et al.* [95] derived an expression of the discrete weakly compressible added mass operator in a more general setting and supported the analytical findings with numerical examples in both two and three dimensions. As anticipated in the introduction of this chapter, the analysis presented here is mainly based on the publication just mentioned.

In order to derive the added mass operator for weakly compressible flows, it turns out to be useful to rewrite the fluid governing equations by means of material time derivatives as

$$\begin{cases} \rho \dfrac{D\boldsymbol{v}}{Dt} - \boldsymbol{\nabla} \cdot \left[2\mu \boldsymbol{\nabla}^{\mathrm{S}} \boldsymbol{v} + \lambda \left(\boldsymbol{\nabla} \cdot \boldsymbol{v} \right) \mathbf{I}_{\mathrm{n_{sd}}} - p \mathbf{I}_{\mathrm{n_{sd}}} \right] = \rho \boldsymbol{b}, \\ \hfill \dfrac{\partial \rho}{\partial p} \dfrac{Dp}{Dt} + \rho \boldsymbol{\nabla} \cdot \boldsymbol{v} = 0, \end{cases} \tag{2.33}$$

where the subscript $\odot_{\mathcal{F}}$ is omitted for the sake of simplicity. Equations (2.33) are equipped with a suitable equation of state relating density and pressure changes. If the simple linear relation (2.7) is considered, the partial derivative of the density with respect to the pressure simply stems from the compressibility coefficient, i.e. $\partial \rho / \partial p = \varepsilon$.

Some assumptions and simplifications can be introduced to further simplify the analysis, while preserving the relevant features. First, external loads are omitted without loss of generality. It is then acknowledged that the artificial added mass effect is independent of the nonlinearities of the system, as well as of the fluid mesh movement. Moreover, viscous terms have a much lower impact than mass terms for small time step sizes, for which the artificial added mass manifests, and they can therefore be reasonably neglected. No structural damping is considered, as done throughout this thesis. Finally, density variations in time are small in the vicinity of the incompressible limit and it is therefore justified to linearise the system with respect to the fluid density, that is subsequently updated by means of the equation of state. Given these assumptions, the governing equations (2.33) can be rewritten as

$$\begin{cases} \rho \dfrac{D\boldsymbol{v}}{Dt} + \boldsymbol{\nabla} p = \mathbf{0}, \\ \theta \dfrac{Dp}{Dt} + \boldsymbol{\nabla} \cdot \boldsymbol{v} = 0, \end{cases} \tag{2.34}$$

where a compressibility factor $\theta = \varepsilon / \rho$ has been introduced.

Upon the finite element discretization, the discrete system of equations reads

$$\begin{cases} \mathbf{M} \dot{\mathbf{v}} + \mathbf{G} \mathbf{p} = \mathbf{0}, \\ \theta \mathbf{M}_{\mathrm{p}} \dot{\mathbf{p}} - \mathbf{G}^T \mathbf{v} = \mathbf{0}, \end{cases} \tag{2.35}$$

with $\mathbf{M}$ denoting the standard fluid mass matrix, whereas $\mathbf{M}_{\mathrm{p}}$ is a mass matrix associated to the pressure degrees of freedom. Moreover, $\mathbf{G}$ and $\mathbf{G}^T$ are the aforementioned discrete gradient and divergence operators, respectively, while the vectors $\mathbf{v}$ and $\mathbf{p}$ represent the unknown velocity and pressure DOFs. Finally, the over-set dots represent the material time derivatives, according to the LAGRANGEan description adopted in (2.34). It is worth pointing out that the ongoing analysis is performed in a CG framework, but the findings are independent of the particular discretization technique adopted. As a matter of fact, the trends arising in the numerical examples in Section 2.7 are also observed in the FSI problems in Section 5.4, where the HDG method is instead adopted to discretize the fluid equations.

For a general time discretization scheme, the velocity and the pressure at the time step $n+1$ can be written as

$$\begin{cases} \mathbf{v} = \alpha_\mathrm{v} \Delta t \dot{\mathbf{v}} + \bar{\mathbf{v}}, \\ \mathbf{p} = \alpha_\mathrm{p} \Delta t \dot{\mathbf{p}} + \bar{\mathbf{p}}, \end{cases} \tag{2.36}$$

with $\dot{\mathbf{v}}$ and $\dot{\mathbf{p}}$ denoting the time derivatives at the same time, while $\bar{\mathbf{v}}$ and $\bar{\mathbf{p}}$ refer to a linear combination of values and time derivatives computed in the previous time steps. The time step level is not explicitly indicated in order to not overload the notation. The parameters α_v and α_p depend then on the specific time integrator adopted. More precisely, for implicit integrators $\alpha_\mathrm{v} \neq 0$ and $\alpha_\mathrm{p} \neq 0$, while explicit methods exhibit $\alpha_\mathrm{v} = \alpha_\mathrm{p} = 0$.

By considering both the spatial and the temporal discretization in (2.35) and (2.36), the fully discretized problem

$$\begin{cases} \mathbf{M}\dot{\mathbf{v}} + \alpha_\mathrm{p} \Delta t \mathbf{G} \dot{\mathbf{p}} + \mathbf{G}\bar{\mathbf{p}} = \mathbf{0}, \\ \theta \mathbf{M}_\mathrm{p} \dot{\mathbf{p}} - \alpha_\mathrm{v} \Delta t \mathbf{G}^T \dot{\mathbf{v}} - \mathbf{G}^T \bar{\mathbf{v}} = \mathbf{0}, \end{cases} \tag{2.37}$$

leads to the linear system

$$\begin{bmatrix} \mathbf{M} & \alpha_\mathrm{p} \Delta t \mathbf{G} \\ -\alpha_\mathrm{v} \Delta t \mathbf{G}^T & \theta \mathbf{M}_\mathrm{p} \end{bmatrix} \begin{bmatrix} \dot{\mathbf{v}} \\ \dot{\mathbf{p}} \end{bmatrix} = \begin{bmatrix} -\mathbf{G}\bar{\mathbf{p}} \\ \mathbf{G}^T \bar{\mathbf{v}} \end{bmatrix}. \tag{2.38}$$

In order to derive the discrete added mass operator for weakly compressible flows, it is convenient to split the velocity degrees of freedom belonging to the interface from the remaining ones. The system (2.38) is therefore rewritten as

$$\begin{bmatrix} \mathbf{M}_{\mathtt{ii}} & \mathbf{M}_{\mathtt{iI}} & \alpha_\mathrm{p} \Delta t \mathbf{G}_{\mathtt{i}} \\ \mathbf{M}_{\mathtt{Ii}} & \mathbf{M}_{\mathtt{II}} & \alpha_\mathrm{p} \Delta t \mathbf{G}_{\mathtt{I}} \\ -\alpha_\mathrm{v} \Delta t \mathbf{G}_{\mathtt{i}}^T & -\alpha_\mathrm{v} \Delta t \mathbf{G}_{\mathtt{I}}^T & \theta \mathbf{M}_\mathrm{p} \end{bmatrix} \begin{bmatrix} \dot{\mathbf{v}}_{\mathtt{i}} \\ \dot{\mathbf{v}}_{\mathtt{I}} \\ \dot{\mathbf{p}} \end{bmatrix} = \begin{bmatrix} -\mathbf{G}_{\mathtt{i}}\bar{\mathbf{p}} \\ -\mathbf{G}_{\mathtt{I}}\bar{\mathbf{p}} + \mathbf{f}_{\mathtt{I}} \\ \mathbf{G}^T \bar{\mathbf{v}} \end{bmatrix}, \tag{2.39}$$

with $\mathbf{f}_{\mathtt{I}}$ being the interface force vector to be passed to the structural solver. Solving the system (2.39) in terms of the interior acceleration $\dot{\mathbf{v}}_{\mathtt{i}}$ and the time derivative of the pressure $\dot{\mathbf{p}}$ and replacing back their expressions in the system allows to obtain the following definition of the coupling vector

$$\begin{aligned} \mathbf{f}_{\mathtt{I}} = \Bigg[& \left(\mathbf{M}_{\mathtt{Ii}} \mathbf{M}_{\mathtt{ii}}^{-1} \mathbf{G}_{\mathtt{i}} - \mathbf{G}_{\mathtt{I}}\right) \left(\frac{\theta}{\alpha_\mathrm{v} \alpha_\mathrm{p} \Delta t^2} \mathbf{M}_\mathrm{p} + \mathbf{G}_{\mathtt{i}}^T \mathbf{M}_{\mathtt{ii}}^{-1} \mathbf{G}_{\mathtt{i}} \right)^{-1} \left(\mathbf{G}_{\mathtt{i}}^T \mathbf{M}_{\mathtt{ii}}^{-1} \mathbf{M}_{\mathtt{iI}} - \mathbf{G}_{\mathtt{I}}^T \right) \\ & \qquad - \mathbf{M}_{\mathtt{Ii}} \mathbf{M}_{\mathtt{ii}}^{-1} \mathbf{M}_{\mathtt{iI}} + \mathbf{M}_{\mathtt{II}} \Bigg] \dot{\mathbf{v}}_{\mathtt{I}} \\ - \Bigg[& \left(\mathbf{M}_{\mathtt{Ii}} \mathbf{M}_{\mathtt{ii}}^{-1} \mathbf{G}_{\mathtt{i}} - \mathbf{G}_{\mathtt{I}}\right) \left(\frac{\theta}{\alpha_\mathrm{v} \alpha_\mathrm{p} \Delta t^2} \mathbf{M}_\mathrm{p} + \mathbf{G}_{\mathtt{i}}^T \mathbf{M}_{\mathtt{ii}}^{-1} \mathbf{G}_{\mathtt{i}} \right)^{-1} \mathbf{G}^T \frac{1}{\alpha_\mathrm{v} \Delta t} \Bigg] \bar{\mathbf{v}} \\ + \Bigg[& \left(\mathbf{M}_{\mathtt{Ii}} \mathbf{M}_{\mathtt{ii}}^{-1} \mathbf{G}_{\mathtt{i}} - \mathbf{G}_{\mathtt{I}}\right) \left(\frac{\theta}{\alpha_\mathrm{v} \alpha_\mathrm{p} \Delta t^2} \mathbf{M}_\mathrm{p} + \mathbf{G}_{\mathtt{i}}^T \mathbf{M}_{\mathtt{ii}}^{-1} \mathbf{G}_{\mathtt{i}} \right)^{-1} \mathbf{G}_{\mathtt{i}}^T \mathbf{M}_{\mathtt{ii}}^{-1} \mathbf{G}_{\mathtt{i}} \\ & \qquad - \mathbf{M}_{\mathtt{Ii}} \mathbf{M}_{\mathtt{ii}}^{-1} \mathbf{G}_{\mathtt{i}} + \mathbf{G}_{\mathtt{I}} \Bigg] \bar{\mathbf{p}}. \end{aligned} \tag{2.40}$$

The first contribution shows the dependency of the interface force on the interface acceleration and the term in square brackets can therefore be interpreted as a mass. The second and the third contributions depend on the history of velocity and pressure, respectively. Assuming a regular mesh and employing a lumped mass matrix, the off-diagonal terms $\mathbf{M}_{\mathtt{iI}}$ and $\mathbf{M}_{\mathtt{Ii}}$ vanish, whereas the mass attributed to an internal node is twice the mass of an interface node which has half the support of the former, i.e. $\mathbf{M}_{\mathtt{ii}} = 2m_{\mathcal{F}}\mathbf{I}_{\mathtt{ii}}$ and $\mathbf{M}_{\mathtt{II}} = m_{\mathcal{F}}\mathbf{I}_{\mathtt{II}}$. The lumped version of the coupling force vector can therefore be written as

$$\begin{aligned}\mathbf{f}_{\mathtt{I,\,lump}} = &\left[2m_{\mathcal{F}}\mathbf{G}_{\mathtt{I}}\left(\frac{2m_{\mathcal{F}}\theta}{\alpha_{\mathrm{v}}\alpha_{\mathrm{p}}\Delta t^2}\mathbf{M}_{\mathrm{p}} + \mathbf{G}_{\mathtt{i}}^T\mathbf{G}_{\mathtt{i}}\right)^{-1}\mathbf{G}_{\mathtt{I}}^T + m_{\mathcal{F}}\mathbf{I}_{\mathtt{II}}\right]\dot{\mathbf{v}}_{\mathtt{I}} \\ &+ \left[2m_{\mathcal{F}}\mathbf{G}_{\mathtt{I}}\left(\frac{2m_{\mathcal{F}}\theta}{\alpha_{\mathrm{v}}\alpha_{\mathrm{p}}\Delta t^2}\mathbf{M}_{\mathrm{p}} + \mathbf{G}_{\mathtt{i}}^T\mathbf{G}_{\mathtt{i}}\right)^{-1}\mathbf{G}^T\frac{1}{\alpha_{\mathrm{v}}\Delta t}\right]\bar{\mathbf{v}} \\ &- \left[\mathbf{G}_{\mathtt{I}}\left(\frac{2m_{\mathcal{F}}\theta}{\alpha_{\mathrm{v}}\alpha_{\mathrm{p}}\Delta t^2}\mathbf{M}_{\mathrm{p}} + \mathbf{G}_{\mathtt{i}}^T\mathbf{G}_{\mathtt{i}}\right)^{-1}\mathbf{G}_{\mathtt{i}}^T\mathbf{G}_{\mathtt{i}} - \mathbf{G}_{\mathtt{I}}\right]\bar{\mathbf{p}}.\end{aligned} \tag{2.41}$$

Two limit cases are worth analysing: the incompressible limit and the time step size limit.

In the incompressible limit the flow compressibility vanishes, i.e. $\theta \to 0$ (and therefore $\varepsilon \to 0$), corresponding to an infinite speed of sound. In such a case, the pressure mass matrix $\mathbf{M}_{\mathrm{p}}$ does not offer any contribution and the force vector reduces to

$$\lim_{\theta\to 0}\mathbf{f}_{\mathtt{I,\,lump}} = \left[m_{\mathcal{F}}\mathbf{I}_{\mathtt{II}} + 2m_{\mathcal{F}}\mathbf{G}_{\mathtt{I}}\left(\mathbf{G}_{\mathtt{i}}^T\mathbf{G}_{\mathtt{i}}\right)^{-1}\mathbf{G}_{\mathtt{I}}^T\right]\dot{\mathbf{v}}_{\mathtt{I}}. \tag{2.42}$$

This expression is obtained by recalling that the flow velocity is divergence-free in all time steps in the incompressible limit, thus

$$\lim_{\theta\to 0}\mathbf{G}^T\bar{\mathbf{v}} = \mathbf{0}. \tag{2.43}$$

It is therefore clear that the incompressible added mass operator (2.32) is fully recovered from a weakly compressible approach for a vanishing compressibility coefficient.

However, as long as even a small compressibility is taken into account, i.e. $\theta > 0$ (and therefore $\varepsilon > 0$), the full definition of the force vector (2.41) needs to be considered. To derive the expression of the added mass operator for weakly compressible flows, the vanishing time step size limit is analyzed. In such a circumstance, the force vector simplifies to

$$\lim_{\Delta t\to 0}\mathbf{f}_{\mathtt{I,\,lump}} = m_{\mathcal{F}}\mathbf{I}_{\mathtt{II}}\dot{\mathbf{v}}_{\mathtt{I}}. \tag{2.44}$$

This expression is obtained by considering that

$$\lim_{\Delta t\to 0}\bar{\mathbf{p}} = \mathbf{p} = \text{const}, \tag{2.45}$$

according to (2.36). Hence, the added mass operator for weakly compressible flows results in

$$\boldsymbol{\mathcal{M}}_{\mathtt{lump}}^{\mathtt{wcomp}} = \mathbf{I}_{\mathtt{II}}. \tag{2.46}$$

2.6 Discussion

A loosely-coupled FSI scheme has been proven by FÖRSTER *et al.* [58] to be unconditionally unstable if

$$\frac{m_{\mathcal{F}}}{m_{\mathcal{S}}} \max\left[\mathrm{eig}\left(\boldsymbol{\mathcal{M}}\right)\right] > C_{\mathtt{inst}}, \tag{2.47}$$

with $m_{\mathcal{F}}$ and $m_{\mathcal{S}}$ denoting a characteristic fluid and structural mass, respectively, and $C_{\mathtt{inst}}$ being a constant coefficient dependent on the specific time integration method adopted. Unfortunately, this coefficient turns out to be smaller for higher temporal accuracy. The inequality (2.47) allows to establish fundamental differences regarding the robustness of fluid-structure interaction solvers involving incompressible and weakly compressible flows.

Replacing the incompressible added mass operator (2.32) in (2.47), the instability condition reads

$$\frac{m_{\mathcal{F}}}{m_{\mathcal{S}}} \max\left[\mathrm{eig}\left(\mathbf{I}_{\mathtt{II}} + 2\mathbf{G}_{\mathtt{I}}\left(\mathbf{G}_{\mathtt{i}}^{T}\mathbf{G}_{\mathtt{i}}\right)^{-1}\mathbf{G}_{\mathtt{I}}^{T}\right)\right] > C_{\mathtt{inst}}. \tag{2.48}$$

It is therefore clear that partitioned schemes with incompressible flows can be safely adopted only in the case that the fluid is much lighter than the structure and if the maximal eigenvalue of the added mass operator is not much larger than unity. However, the incompressible contribution $2\mathbf{G}_{\mathtt{I}}\left(\mathbf{G}_{\mathtt{i}}^{T}\mathbf{G}_{\mathtt{i}}\right)^{-1}\mathbf{G}_{\mathtt{I}}^{T}$ can be rather large and, in the case of a fluid entirely enclosed by DIRICHLET boundaries (except of course the fluid-structure interface), its maximal eigenvalue tends to infinity.

Replacing instead the weakly compressible added mass operator (2.46) in (2.47), the instability condition reduces to

$$\frac{m_{\mathcal{F}}}{m_{\mathcal{S}}} \max\left[\mathrm{eig}\left(\mathbf{I}_{\mathtt{II}}\right)\right] = \frac{m_{\mathcal{F}}}{m_{\mathcal{S}}} > C_{\mathtt{inst}}. \tag{2.49}$$

Consequently, also the weakly compressible model exhibits a mass ratio for which the scheme gets unconditionally unstable. However, the condition (2.49) is much more permissive than the incompressible counterpart (2.48), explaining why artificial added mass effects are rarely observed in simulations involving (weakly) compressible flows. Moreover, from the analysis in Section 2.5 it is clear that if the limit mass ratio in (2.49) is not reached by a particular problem, then time step size reduction will eventually stabilize the partitioned scheme. It is therefore obvious why potential stability issues in the weakly compressible case can frequently be handled in the standard way, i.e. by time step size reduction. Such simple approach has been shown by FÖRSTER *et al.* [58] not to work in the incompressible case.

The present analysis rigorously refers to loosely-coupled partitioned schemes, however analogous considerations apply to the convergence of strongly-coupled partitioned schemes, in which the exchange of the interface information is repeated within a time step until a convergence criterion is met. In fact, although it is sometimes claimed that the added mass related instability can be always overcome by subiterating over the single fields to converge to the solution of the corresponding monolithic system, VAN BRUMMELEN [160] pointed out how the artificial added mass effect directly affects the stability and the convergence of the subiteration process. The artificial added mass operator defines indeed an upper bound for the contraction number of the problem and if this value is greater than one, the iterative procedure will inevitably fail. The findings of the present analysis are thus confirmed in the following numerical examples by using a strongly-coupled partitioned scheme and examining the number of coupling iterations required, as well as the values of the relaxation parameter (when a dynamic relaxation is adopted).

2.7 Numerical examples

The numerical examples presented here aim to experimentally investigate the influence of the flow compressibility for FSI solvers in terms of accuracy, robustness and efficiency. The first example is a popular two-dimensional benchmark that allows to perform a series of tests with increasing difficulty for the coupling algorithm, by simply varying the structural density. The performance of the weakly compressible formulation is then assessed considering both a fixed and a dynamic relaxation of the fixed-point FSI solver. The second example is a widely used three-dimensional benchmark that mimics hemodynamic conditions and highlights the artificial added mass phenomenon. Special emphasis is devoted to the efficiency of the proposed formulation considering different compressibility levels and time step sizes. The simulations associated with the presented numerical examples have been performed with the parallel multiphysics research code `BACI` [167].

2.7.1 Lid-driven cavity with flexible bottom

The first numerical example is a two-dimensional lid-driven cavity with flexible bottom. It was introduced by WALL [166] as a modification of the well-known lid-driven cavity used in fluid dynamics and it has been used for several numerical studies by MOK and WALL [109], KÜTTLER *et al.* [91], FÖRSTER *et al.* [58] and MAYR *et al.* [104], among others. The goal of this example is to investigate the role of compressibility for FSI solvers in a simple setting with an increasing difficulty for the coupling algorithm. In fact, the structural configuration is set up in such a way that its main resistance against the fluid forces stems from its density, which can be easily varied.

The fluid domain is a unit square, while the structure on the bottom has a thickness of $0.002\ m$ and is clamped ($\boldsymbol{u}_{\mathcal{S}}^{D} = \mathbf{0}$) on its left and right edges. On the top side of the cavity, an oscillatory velocity is prescribed according to

$$\begin{cases} v_{\mathcal{F}x}^{D}\left(x,1,t\right) = 1 - \cos\left(2\pi t/\bar{t}\right)\ m/s, \\ v_{\mathcal{F}y}^{D}\left(x,1,t\right) = 0\ m/s, \end{cases} \tag{2.50}$$

with period $\bar{t} = 5\ s$, whereas no-slip boundary conditions ($\boldsymbol{v}_{\mathcal{F}}^{D} = \mathbf{0}$) are applied on the left and right sides. Two unconstrained nodes are considered at each side of the cavity, to allow free inflow and outflow of the fluid. The geometry and the boundary conditions of the problem are sketched in Figure 2.2.

The fluid is first assumed incompressible with density $\rho_{\mathcal{F}} = 1\ kg/m^3$ and dynamic viscosity $\mu_{\mathcal{F}} = 0.01\ kg/(m \cdot s)$. Then, the weakly compressible formulation is adopted taking the same viscosity and a reference density $\rho_{\mathcal{F}}^{\mathtt{ref}} = 1\ kg/m^3$, evaluated at the reference pressure $p_{\mathcal{F}}^{\mathtt{ref}} = 0$ N/m^2. Three different compressibility coefficients are considered, i.e. $\varepsilon_{\mathcal{F}} = [0.001, 0.01, 0.1]$ s^2/m^2. The structure is modelled as a ST. VENANT–KIRCHHOFF material with YOUNG's modulus $E_{\mathcal{S}} = 250\ N/m^2$ and POISSON's ratio $\nu_{\mathcal{S}} = 0$. Three structural densities are considered, i.e. $\rho_{\mathcal{S}} = [5000, 500, 50]\ kg/m^3$, producing an increasing difficulty for the partitioned algorithm.

The fluid mesh consists of 32×32 linear stabilized quadrilateral elements, while the structure is discretized with 32 linear quadrilateral elements. The computational mesh is shown in Fig-

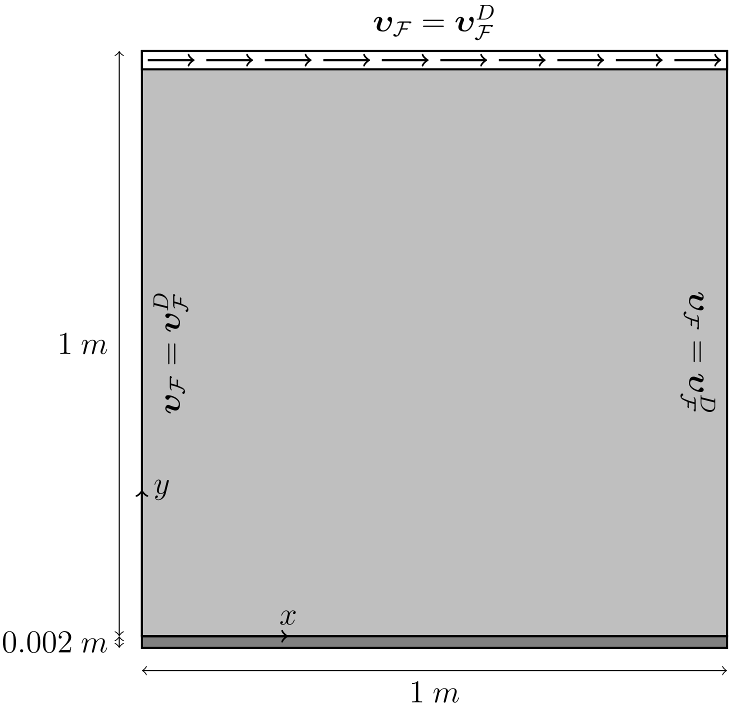

Figure 2.2: Geometry and boundary conditions for lid-driven cavity with flexible bottom

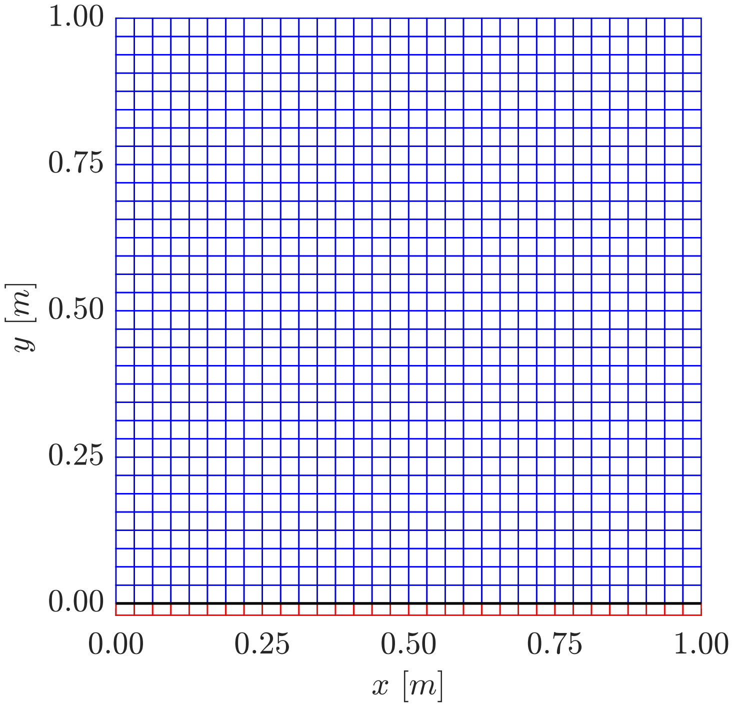

Figure 2.3: Computational mesh for lid-driven cavity with flexible bottom

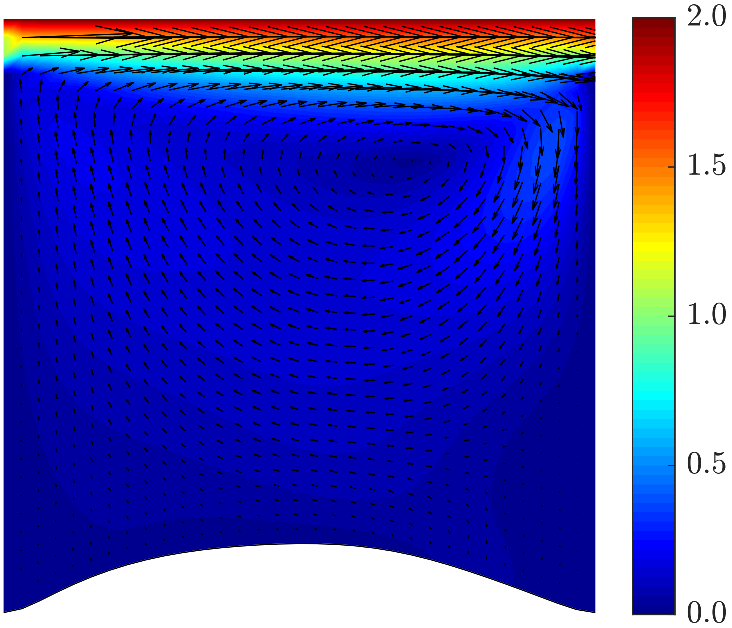

Figure 2.4: Solution of fluid velocity for lid-driven cavity with flexible bottom

ure 2.3, with a magnification factor of 10 on the structural thickness for a better visualization. The time span analyzed is $t \in (0, 15)\ s$ and the time step size is taken as $\Delta t = 0.1\ s$. It is worth recalling that the spatial discretization is performed with the CG method for both subdomains, whereas the first order backward differentiation formula (BDF1) is used for the evolution in time. Two relaxation techniques are considered in this example:

1. constant relaxation,

2. dynamic relaxation by means of AITKEN's Δ^2 method.

For the first case the relaxation parameter is chosen as $\omega = 0.825$ by a trial and error approach, while the convergence tolerance for the coupling iterations is set as $\eta = 10^{-7}$ for both cases.

The fluid velocity field obtained with $\varepsilon_{\mathcal{F}} = 0.01\ s^2/m^2$ and $\rho_{\mathcal{S}} = 500\ kg/m^3$ is exemplarily depicted in Figure 2.4 on the deformed domain at time $t = 7.5\ s$, in which the prescribed velocity reaches a maximum. In Figure 2.5, the vertical displacement over time of the top center point of the membrane is plotted for the three structural densities considered. In all the configurations, the weakly compressible model produces physical results very similar to the incompressible counterparts, with only minimal differences.

The average number of coupling iterations (evaluated over all time steps) required to meet the convergence criterion for constant relaxation is summarized in Table 2.1. On the one hand, for the most challenging scenario, i.e. $\rho_{\mathcal{S}} = 50\ kg/m^3$, neither the weakly compressible formulation nor the incompressible formulation is able to converge, as also reported by KÜTTLER *et al.* [91]. On the other hand, for the intermediate structural density, the average number of coupling iterations drastically drops from 12.2 with the incompressible formulation to 2.7 with the weakly compressible formulation with $\varepsilon_{\mathcal{F}} = 0.1\ s^2/m^2$, saving about 78% of iterations. No appreciable differences are observed instead when the fluid-structure coupling is very weak.

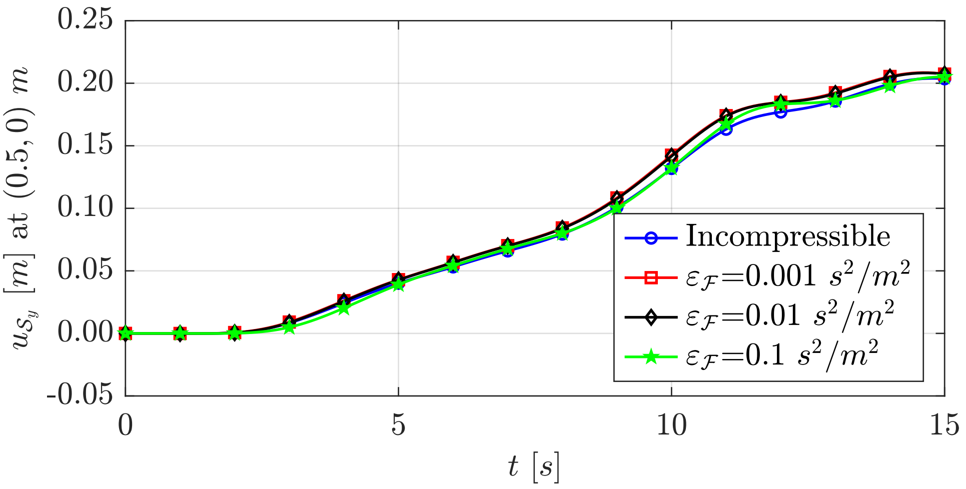

(a) $\rho_{\mathcal{S}} = 5000\ kg/m^3$

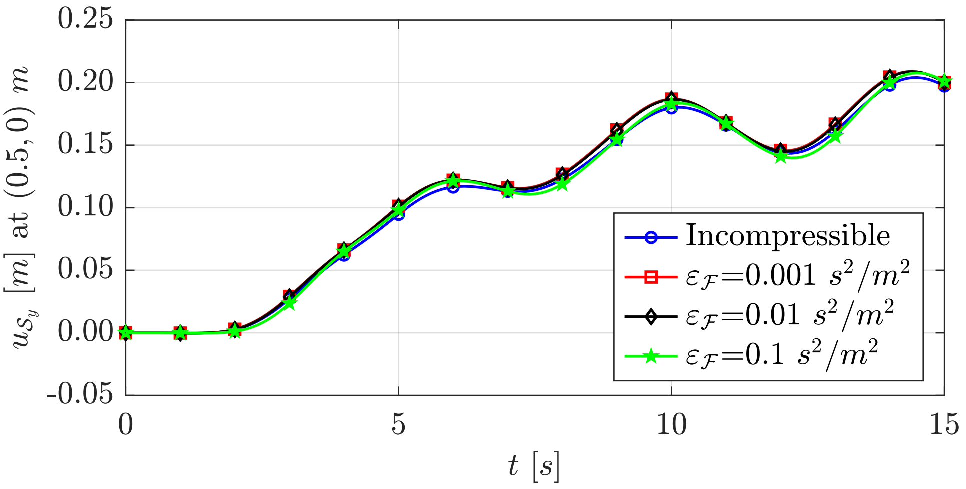

(b) $\rho_{\mathcal{S}} = 500\ kg/m^3$

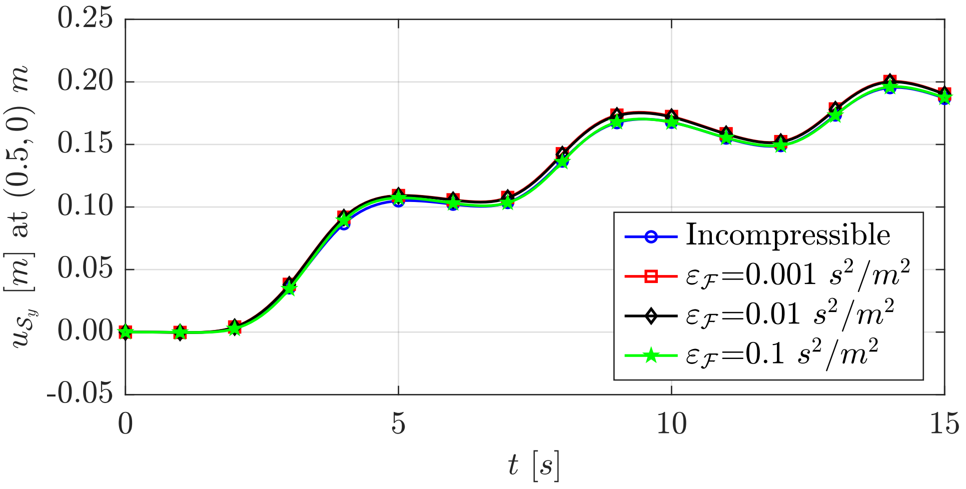

(c) $\rho_{\mathcal{S}} = 50\ kg/m^3$

Figure 2.5: Plot of structural displacement for lid-driven cavity with flexible bottom

As opposed to the first case, the coupling algorithm is always able to convergence when the relaxation parameter is dynamically updated via AITKEN's Δ^2 method. The average number of coupling iterations and the average relaxation parameter computed over all time steps are reported in Table 2.2. A general trend can be observed: the weakly compressible formulation accelerates the convergence of the iterative scheme that resolves the fluid-structure coupling and the higher the compressibility, the more iterations can be saved. Moreover, the advantages are more accentuated in the most challenging cases. In fact, by comparing the data associated to the incompressible and the most compressible case, the saving of coupling iterations is about 33% and 48% for $\rho_{\mathcal{S}} = 5000\ kg/m^3$ and $\rho_{\mathcal{S}} = 50\ kg/m^3$, respectively. The reduction of coupling iterations comes along with a systematic increase of the relaxation parameter. Comparing again the incompressible formulation and the weakly compressible one with $\varepsilon_{\mathcal{F}} = 0.1\ s^2/m^2$, the average relaxation parameter increases by 71% for $\rho_{\mathcal{S}} = 50\ kg/m^3$, by 35% for $\rho_{\mathcal{S}} = 500\ kg/m^3$ and by just 5% for $\rho_{\mathcal{S}} = 5000\ kg/m^3$. Figure 2.6 then shows the evolution of the mean relaxation parameter, evaluated over the coupling iterations within each time step in order to homogeneously compare the results. From the plots it can be observed that the relaxation parameter exhibits at the same time a higher value and a minor oscillating behavior when decreasing the strength of the FSI coupling. In the limit case, when $\varepsilon_{\mathcal{F}} = 0.1\ s^2/m^2$ and $\rho_{\mathcal{S}} = 5000\ kg/m^3$, the relaxation parameter remains constant and equal to $\omega = 1$ during the entire simulation (Figure 2.6(a)). Given the improved robustness and efficiency features of AITKEN's Δ^2 method, this relaxation strategy will be henceforth applied for the solution of FSI problems with partitioned schemes.

	$\rho_{\mathcal{S}} = 5000\ kg/m^3$		$\rho_{\mathcal{S}} = 500\ kg/m^3$		$\rho_{\mathcal{S}} = 50\ kg/m^3$	
	ω	i_{avg}	ω	i_{avg}	ω	i_{avg}
Incompressible	0.825	2.2	0.825	12.2	0.825	–
$\varepsilon_{\mathcal{F}} = 0.001\ s^2/m^2$	0.825	2.2	0.825	9.3	0.825	–
$\varepsilon_{\mathcal{F}} = 0.01\ s^2/m^2$	0.825	2.3	0.825	3.7	0.825	–
$\varepsilon_{\mathcal{F}} = 0.1\ s^2/m^2$	0.825	2.4	0.825	2.7	0.825	–

Table 2.1: Relaxation parameter and coupling iterations for lid-driven cavity with flexible bottom via constant relaxation

	$\rho_{\mathcal{S}} = 5000\ kg/m^3$		$\rho_{\mathcal{S}} = 500\ kg/m^3$		$\rho_{\mathcal{S}} = 50\ kg/m^3$	
	ω_{avg}	i_{avg}	ω_{avg}	i_{avg}	ω_{avg}	i_{avg}
Incompressible	0.95	1.5	0.67	2.9	0.30	7.7
$\varepsilon_{\mathcal{F}} = 0.001\ s^2/m^2$	0.96	1.5	0.69	3.0	0.31	7.6
$\varepsilon_{\mathcal{F}} = 0.01\ s^2/m^2$	0.97	1.3	0.78	2.9	0.35	6.5
$\varepsilon_{\mathcal{F}} = 0.1\ s^2/m^2$	1.00	1.0	0.91	1.9	0.51	4.0

Table 2.2: Relaxation parameter and coupling iterations for lid-driven cavity with flexible bottom via dynamic relaxation

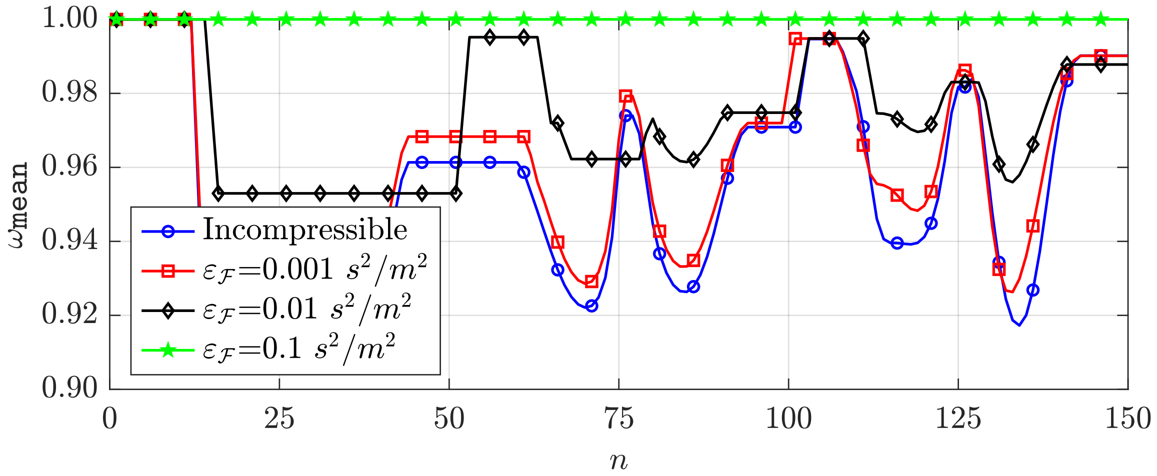

(a) $\rho_{\mathcal{S}} = 5000\ kg/m^3$

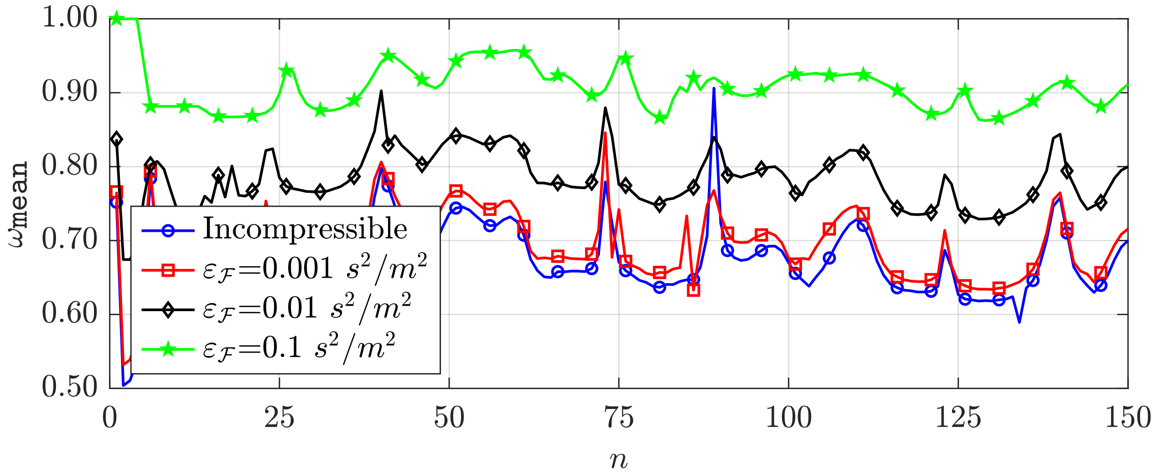

(b) $\rho_{\mathcal{S}} = 500\ kg/m^3$

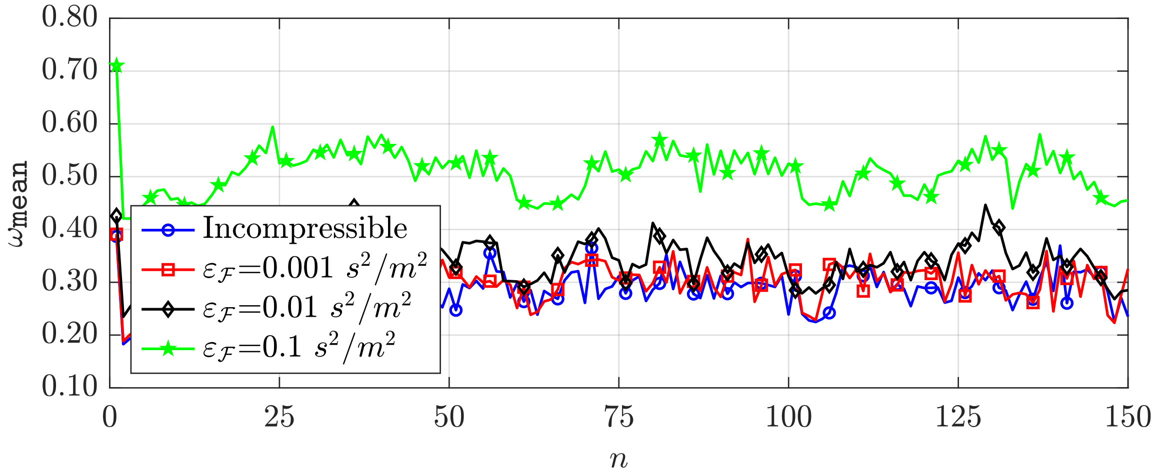

(c) $\rho_{\mathcal{S}} = 50\ kg/m^3$

Figure 2.6: Plot of relaxation parameter for lid-driven cavity with flexible bottom

2.7.2 Pressure wave in flexible tube

The second numerical example simulates a three-dimensional pressure wave in a flexible tube. It was originally proposed by NOBILE [125] and FORMAGGIA *et al.* [57] and it has been later used by GERBEAU and VIDRASCU [63], by FERNÁNDEZ and MOUBACHIR [53] and by MAYR *et al.* [104], among others. This fluid-structure interaction problem arises from the modelling of blood flow in large arteries and constitutes a classical benchmark in hemodynamics. The main feature is represented by the similar fluid and structural densities, i.e. $\rho_{\mathcal{F}}/\rho_{\mathcal{S}} \approx 1$, producing therefore a challenging scenario with respect to the artificial added mass effect, as explained in Section 2.6.

The fluid domain is constituted by a straight cylinder of radius $0.5\ cm$ and length $5\ cm$ and it is surrounded by a solid tube with a thickness of $0.1\ cm$. The fluid, initially at rest, is loaded with the surface traction

$$\begin{cases} t^N_{\mathcal{F}x}(0,y,z,t) = 1.3332 \cdot 10^4\ g/(cm \cdot s^2), \\ t^N_{\mathcal{F}y}(0,y,z,t) = 0\ g/(cm \cdot s^2), \\ t^N_{\mathcal{F}z}(0,y,z,t) = 0\ g/(cm \cdot s^2), \end{cases} \tag{2.51}$$

for the duration of $3 \cdot 10^{-3}\ s$, imposed as a NEUMANN boundary condition at the inlet. The structure is clamped at both ends ($\boldsymbol{u}^D_{\mathcal{S}} = \mathbf{0}$). The geometry and the boundary conditions of the problem are depicted in Figure 2.7.

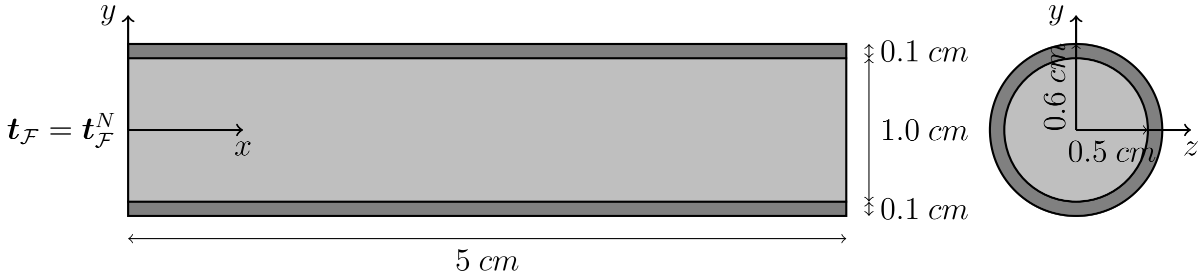

Figure 2.7: Geometry and boundary conditions for pressure wave in flexible tube

To compare the accuracy and the performance of the weakly compressible formulation against the incompressible one, the fluid is first considered incompressible with density $\rho_{\mathcal{F}} = 1\ g/cm^3$ and dynamic viscosity $\mu_{\mathcal{F}} = 0.03\ g/(cm \cdot s)$ and the weakly compressible model is then employed with the same viscosity and a reference density $\rho^{\mathtt{ref}}_{\mathcal{F}} = 1\ cm/m^3$, evaluated at the reference pressure $p^{\mathtt{ref}}_{\mathcal{F}} = 0\ g/(cm \cdot s^2)$. Three different orders of magnitude are considered for the compressibility coefficient, i.e. $\varepsilon_{\mathcal{F}} = [10^{-7}, 10^{-6}, 10^{-5}]\ s^2/cm^2$. These parameters are in the range where the solution starts to globally alter the physical behavior compared to the incompressible formulation for this particular example. The constitutive behavior of the structure is described by a ST. VENANT–KIRCHHOFF material with YOUNG's modulus $E_{\mathcal{S}} = 3 \cdot 10^6$ $g/(cm \cdot s^2)$, POISSON's ratio $\nu_{\mathcal{S}} = 0.3$ and density $\rho_{\mathcal{S}} = 1.2\ g/cm^3$.

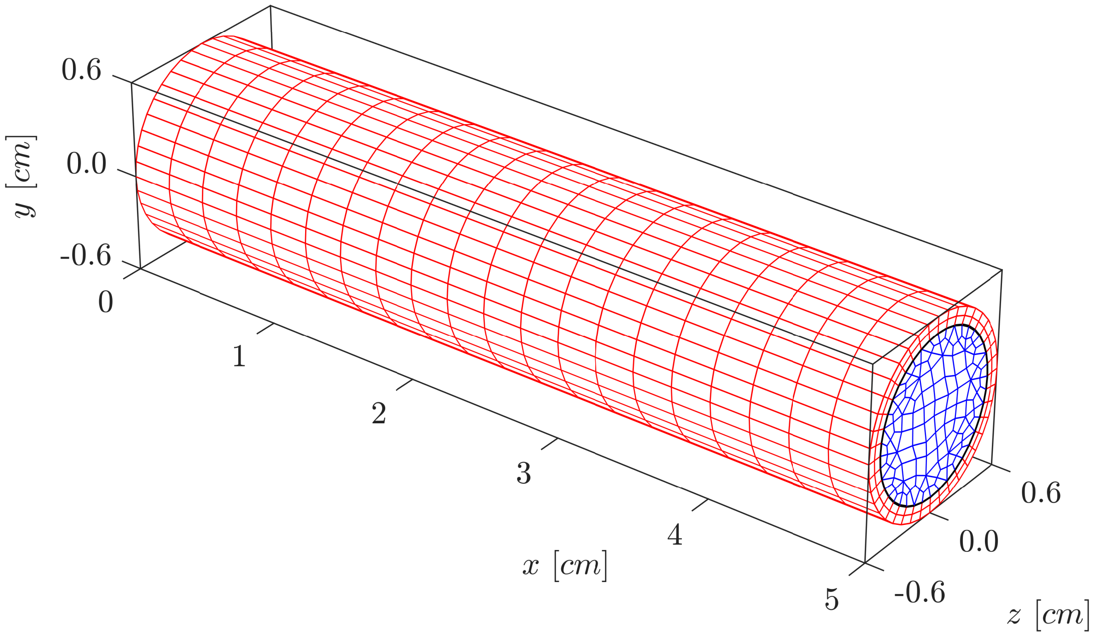

Figure 2.8: Computational mesh for pressure wave in flexible tube

The fluid domain is discretized with 2480 linear stabilized hexahedral elements, while the structural mesh consists of 1600 linear hexahedral elements, with 2 elements over the thickness. The computational mesh adopted for this example is depicted in Figure 2.8. The fluid and structural meshes are denoted in blue and red, respectively, whereas the interface is shown in black. The time interval analyzed is $t \in (0, 0.015)\ s$ and, in order to investigate the role the time step size on the efficiency of the coupling scheme, the time span is divided into a progressively increasing number of steps, i.e. $\Delta t = 0.015/\,[10, 30, \ldots, 150]\ s$. The time integration is performed with BDF1 and the convergence tolerance considered for the coupling iterations is $\eta = 10^{-7}$. Given the enhanced efficiency of dynamic relaxation techniques observed in the previous example, AITKEN's Δ^2 method is adopted here to accelerate the fixed-point FSI solver.

As a consequence of the boundary conditions, a pressure wave travels along the axis of the tube. In Figure 2.9 the pressure field is shown for the different compressibility levels considered at two time instants corresponding to $1/3$ and $2/3$ of the total time span, i.e. $t = 0.005\ s$ and $t = 0.010\ s$. The deformation of the fluid domain is magnified by a factor of 10 for a better visualization. Moreover, the temporal evolution of the fluid pressure at the center of the tube (with coordinates $(2.5, 0, 0)\ cm$) and of the structural radial displacement at the point $(2.5, 0.6, 0)\ cm$ is depicted in Figure 2.10. The data associated to Figures 2.9 and 2.10 refer to the solution obtained with the smallest time step size considered, i.e. $\Delta t = 10^{-4}\ s$. As expected, the weakly compressible formulation slightly changes the dynamics of the problem and this change is proportional to the compressibility considered. For this setting, it is clear that the flow compressibility induces a decrease in the pressure wave speed and, as a consequence, the peaks of the curves in Figure 2.10 progressively shift to the right. The results obtained with $\varepsilon_{\mathcal{F}} = 10^{-7}\ s^2/cm^2$ and $\varepsilon_{\mathcal{F}} = 10^{-6}\ s^2/cm^2$ still accurately reproduce the global physical behavior of the system with engineering accuracy, whereas the mismatch with the incompressible reference becomes excessive for larger compressibility coefficients. It also worth pointing out that an acceptably accurate

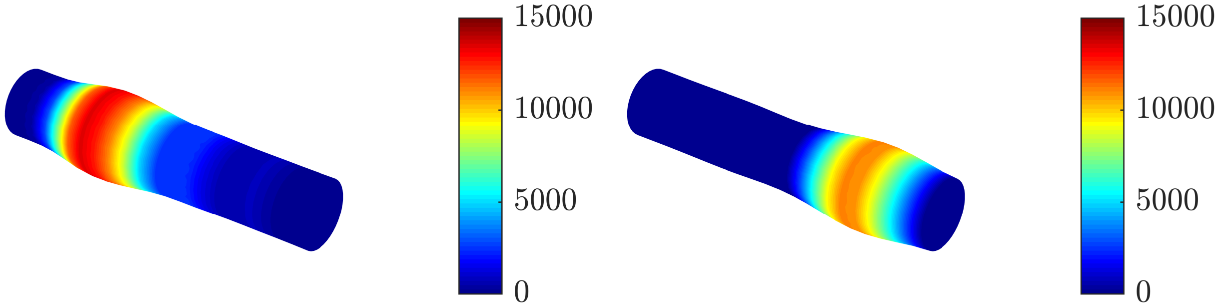

(a) Incompressible at $t = 0.005\ s$ (b) Incompressible at $t = 0.010\ s$

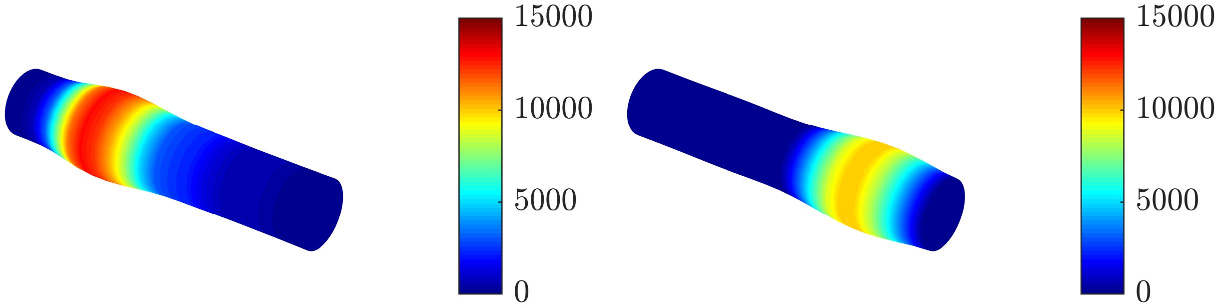

(c) $\varepsilon_{\mathcal{F}} = 10^{-7}\ s^2/cm^2$ at $t = 0.005\ s$ (d) $\varepsilon_{\mathcal{F}} = 10^{-7}\ s^2/cm^2$ at $t = 0.010\ s$

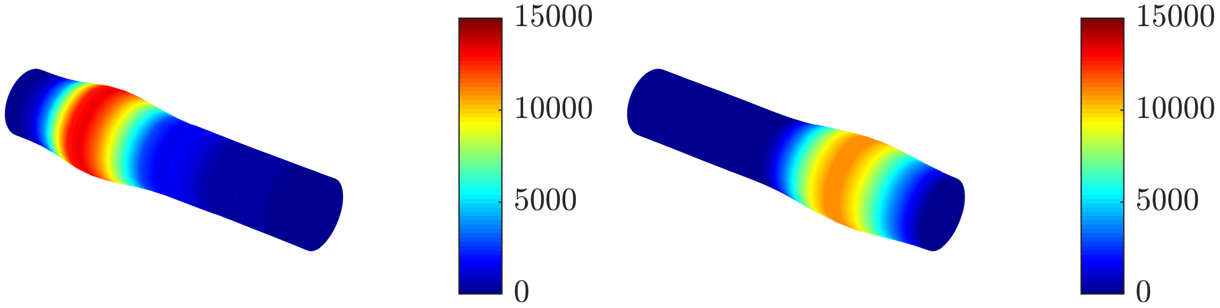

(e) $\varepsilon_{\mathcal{F}} = 10^{-6}\ s^2/cm^2$ at $t = 0.005\ s$ (f) $\varepsilon_{\mathcal{F}} = 10^{-6}\ s^2/cm^2$ at $t = 0.010\ s$

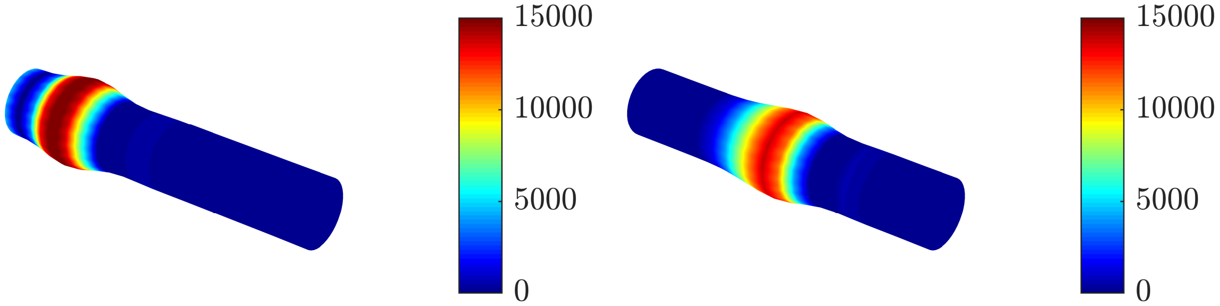

(g) $\varepsilon_{\mathcal{F}} = 10^{-5}\ s^2/cm^2$ at $t = 0.005\ s$ (h) $\varepsilon_{\mathcal{F}} = 10^{-5}\ s^2/cm^2$ at $t = 0.010\ s$

Figure 2.9: Solution of fluid pressure for pressure wave in flexible tube

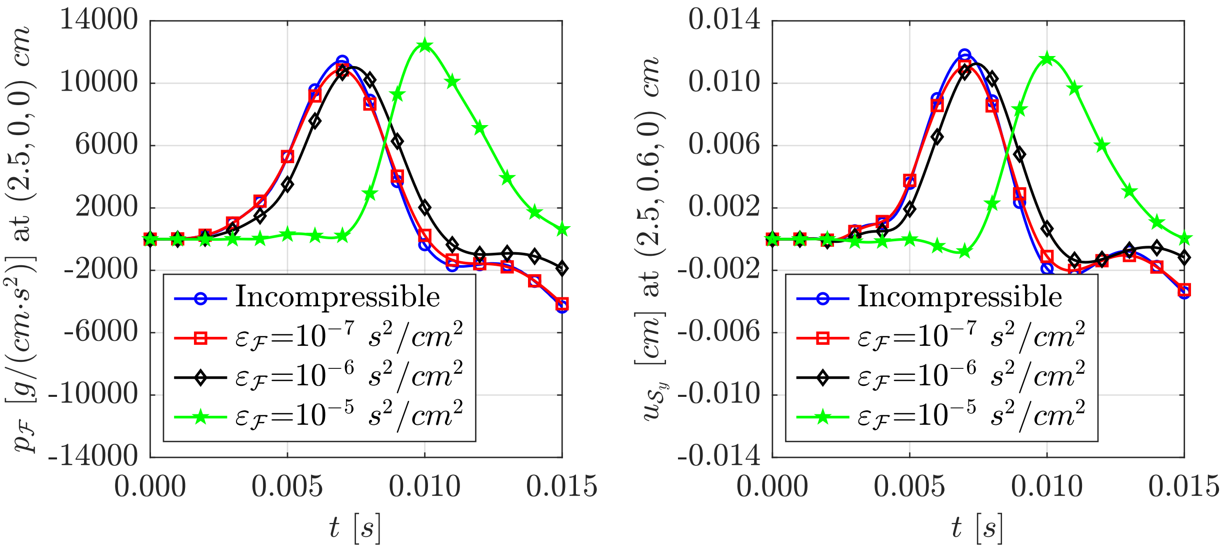

(a) Fluid pressure (b) Structural displacement

Figure 2.10: Plot of fluid pressure and structural displacement for pressure wave in flexible tube

solution is obtained when at least 100 steps are considered for the discretization of the time span considered here.

The average value of the relaxation parameter and the average number of coupling iterations required to meet the convergence tolerance are reported in Table 2.3, for the various compressibility levels and time step sizes considered. As observed in the previous example, the relaxation parameter increases and at the same time the number of coupling iterations decreases, when increasing the flow compressibility. Additionally, these changes are more accentuated for smaller time step sizes. For instance, comparing the incompressible and the most compressible case, the average relaxation parameter increases by a factor of 2.4 for the largest time step size and by a factor of 8.0 for the smallest time step size considered. Analogously, up to 72% of coupling iterations are saved when dividing the time span in 10 steps, while the saving reaches a maximum of 96% when considering 150 steps. Moreover, while in the incompressible case the average number of coupling iterations does not decrease when decreasing the time step size, by adopting the weakly compressible formulation the coupling iterations systematically decrease for sufficiently small time step sizes, as expected from the findings discussed in Section 2.6.

The remarkable speedup offered by the weakly compressible formulation can be deduced from Table 2.4, in which the CPU time t_{cpu} spent is reported for all the compressibility coefficients and the time step sizes considered as ratio of the CPU time spent by the incompressible FSI solver $t_{\mathrm{cpu}}^{\mathrm{inc}}$. One the one hand, the computational time required to solve the problem is approximately the same in the incompressible and weakly compressible case when just a few time steps are considered. On the other hand, the computational time saved increases dramatically for small time step sizes. For instance, with $\Delta t = 10^{-4}$ s, the weakly compressible model requires only 26%, 19% and 17% of the computational time spent by the incompressible model, for $\varepsilon_{\mathcal{F}} = 10^{-7}$ s^2/cm^2, $\varepsilon_{\mathcal{F}} = 10^{-6}$ s^2/cm^2 and $\varepsilon_{\mathcal{F}} = 10^{-5}$ s^2/cm^2, respectively. The data in Table 2.4 therefore highlight how the increase of the computational cost of the fluid solver due to the weak compressibility has only a marginal effect compared to the decrease of the computational time induced by the reduction of the number of coupling iterations. The evolution over the time steps of the mean relaxation parameter, the maximum number of coupling iterations and the CPU time spent with $\Delta t = 10^{-4}\ s$ is detailed in Figure 2.11.

Overall, the value of the compressibility coefficient plays an important role in the accuracy and efficiency of the FSI problem. It can qualitatively be stated that $\varepsilon_{\mathcal{F}}$ has to be sufficiently large to accurately reproduce the physical behavior of the system but, at the same time, it should be chosen as small as possible to benefit from the advantages of the weakly compressible formulation. The numerical experiments presented here suggest that a good trade-off between accuracy and speedup can be achieved when the maximum relative variation in the fluid density is between 10^{-3} and 10^{-2}.

	$\Delta t = t_f/10\ s$		$\Delta t = t_f/30\ s$		$\Delta t = t_f/50\ s$		$\Delta t = t_f/70\ s$	
	ω_{avg}	i_{avg}	ω_{avg}	i_{avg}	ω_{avg}	i_{avg}	ω_{avg}	i_{avg}
Incompressible	0.37	14.3	0.16	24.2	0.13	25.8	0.11	26.1
$\varepsilon_{\mathcal{F}} = 10^{-7}\ s^2/cm^2$	0.51	10.1	0.29	14.9	0.29	12.0	0.33	9.1
$\varepsilon_{\mathcal{F}} = 10^{-6}\ s^2/cm^2$	0.61	8.2	0.57	6.6	0.63	4.4	0.66	3.3
$\varepsilon_{\mathcal{F}} = 10^{-5}\ s^2/cm^2$	0.87	4.0	0.83	3.1	0.82	2.4	0.83	2.0
	$\Delta t = t_f/90\ s$		$\Delta t = t_f/110\ s$		$\Delta t = t_f/130\ s$		$\Delta t = t_f/150\ s$	
	ω_{avg}	i_{avg}	ω_{avg}	i_{avg}	ω_{avg}	i_{avg}	ω_{avg}	i_{avg}
Incompressible	0.11	25.4	0.11	26.5	0.11	27.3	0.11	27.8
$\varepsilon_{\mathcal{F}} = 10^{-7}\ s^2/cm^2$	0.37	7.1	0.40	5.6	0.44	4.3	0.46	3.4
$\varepsilon_{\mathcal{F}} = 10^{-6}\ s^2/cm^2$	0.68	2.8	0.69	2.3	0.69	2.0	0.71	1.7
$\varepsilon_{\mathcal{F}} = 10^{-5}\ s^2/cm^2$	0.84	1.7	0.85	1.3	0.86	1.0	0.88	1.0

Table 2.3: Relaxation parameter and coupling iterations for pressure wave in flexible tube

	$\Delta t = t_f/10\ s$	$\Delta t = t_f/30\ s$	$\Delta t = t_f/50\ s$	$\Delta t = t_f/70\ s$
	$t_{\text{cpu}}/t_{\text{cpu}}^{\text{inc}}$	$t_{\text{cpu}}/t_{\text{cpu}}^{\text{inc}}$	$t_{\text{cpu}}/t_{\text{cpu}}^{\text{inc}}$	$t_{\text{cpu}}/t_{\text{cpu}}^{\text{inc}}$
Incompressible	100%	100%	100%	100%
$\varepsilon_{\mathcal{F}} = 10^{-7}\ s^2/cm^2$	116%	79%	57%	44%
$\varepsilon_{\mathcal{F}} = 10^{-6}\ s^2/cm^2$	87%	43%	30%	26%
$\varepsilon_{\mathcal{F}} = 10^{-5}\ s^2/cm^2$	59%	26%	22%	20%
	$\Delta t = t_f/90\ s$	$\Delta t = t_f/110\ s$	$\Delta t = t_f/130\ s$	$\Delta t = t_f/150\ s$
	$t_{\text{cpu}}/t_{\text{cpu}}^{\text{inc}}$	$t_{\text{cpu}}/t_{\text{cpu}}^{\text{inc}}$	$t_{\text{cpu}}/t_{\text{cpu}}^{\text{inc}}$	$t_{\text{cpu}}/t_{\text{cpu}}^{\text{inc}}$
Incompressible	100%	100%	100%	100%
$\varepsilon_{\mathcal{F}} = 10^{-7}\ s^2/cm^2$	39%	34%	29%	26%
$\varepsilon_{\mathcal{F}} = 10^{-6}\ s^2/cm^2$	24%	22%	20%	19%
$\varepsilon_{\mathcal{F}} = 10^{-5}\ s^2/cm^2$	19%	19%	16%	17%

Table 2.4: CPU time for pressure wave in flexible tube

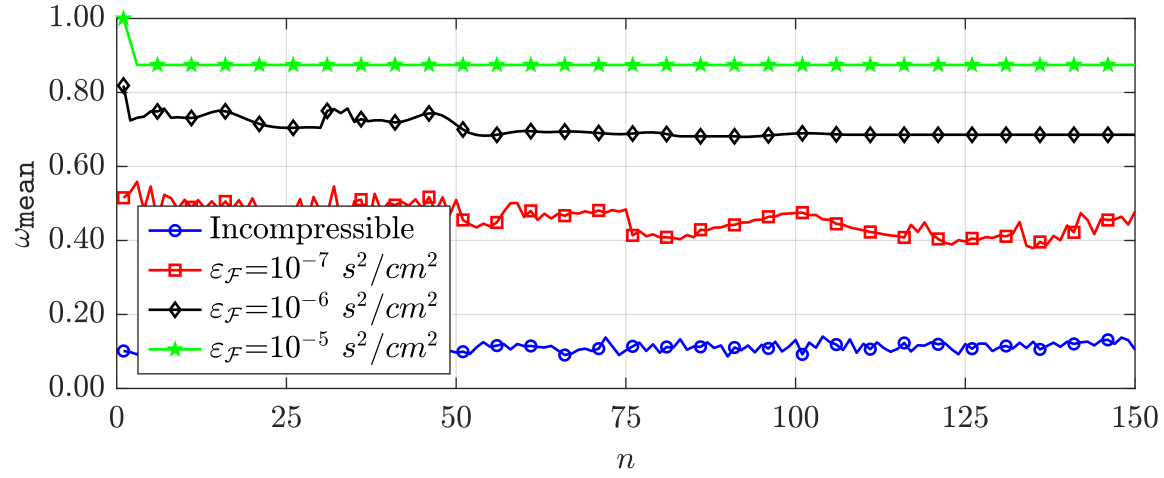

(a) Relaxation parameter

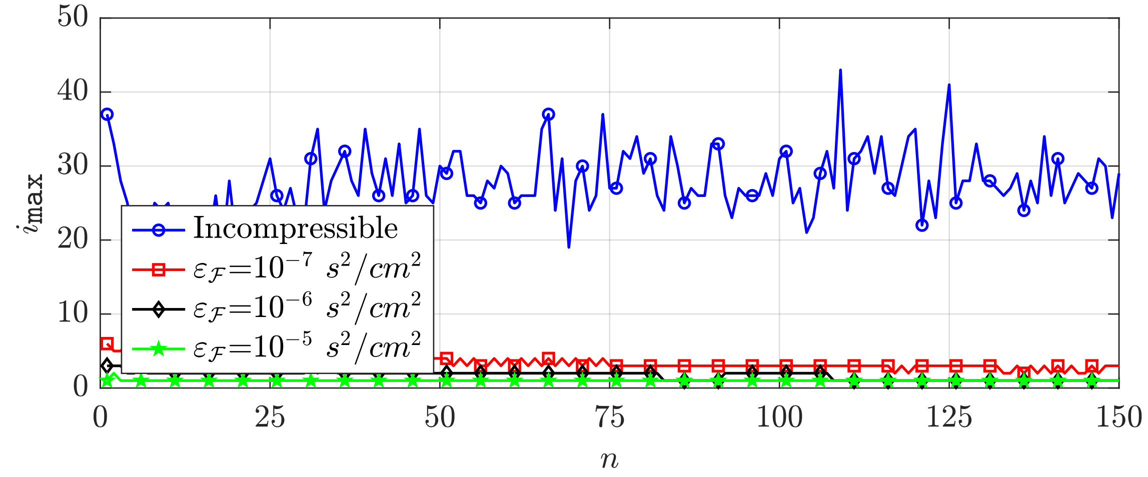

(b) Coupling iterations

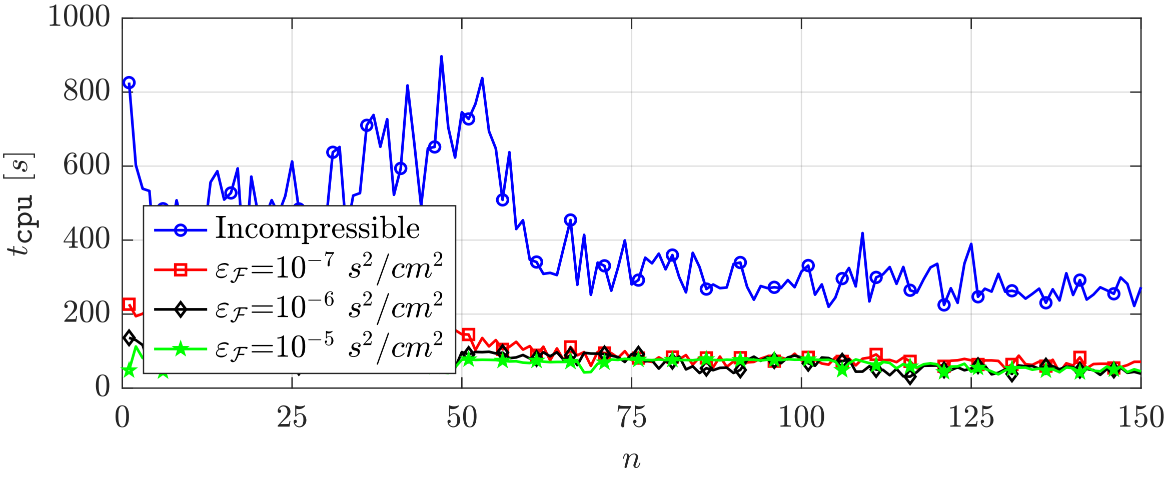

(c) CPU time

Figure 2.11: Plot of relaxation parameter, coupling iterations and CPU time for pressure wave in flexible tube

3 HDG formulations for weakly compressible flows

This chapter is devoted to the discretization of the equations governing the behavior of weakly compressible flows by means of the HDG method. The derivation of suitable spatial discretization strategies for the solution of fluid problems constitutes a fundamental ingredient towards the design of robust and efficient coupled algorithms for the simulation of fluid-structure interaction problems, that is the objective of this thesis.

As already anticipated in the introduction, a variety of HDG formulations have been proposed in literature for solving flow problems in both the incompressible and the compressible regime. For the incompressible regime, the velocity and pressure fields constitute the preferred choice as primal unknowns in the interior of the elements. The trace of the velocity on the mesh skeleton and the mean value of the pressure over either the interior or the boundary of the elements are usually selected as global variables. Alternative options, featuring different combinations of vorticity, velocity, pressure and harmonic velocity potentials have been investigated by COCKBURN and GOPALAKRISHNAN [29]. To obtain a first-order problem, several choices have been adopted for the definition of the mixed variable. The velocity gradient has been adopted, among others, by NGUYEN *et al.* [120, 121], RHEBERGEN and COCKBURN [135], GIORGIANI *et al.* [69] and SHELDON *et al.* [144, 145], whereas alternative formulations involving either the vorticity or the stress tensor have been analyzed by COCKBURN *et al.* [37]. For the fully compressible regime instead, the conserved quantities (namely, density, momentum and energy) are commonly taken as primal variables, their trace representation as hybrid variables and their gradient as mixed variables, as done for instance by PERAIRE *et al.* [130] and FERNANDEZ *et al.* [55]. The aforementioned formulations have been mainly developed for the solution of pure flow problems on fixed domains and a few applications dealing with deforming domains can be found in the works of RHEBERGEN and COCKBURN [135] and SHELDON *et al.* [144, 145]. Here, two original and computationally efficient HDG formulations are presented for the simulation of weakly compressible flows. Such formulations feature a scaled strain rate tensor in VOIGT notation as mixed variable following GIACOMINI *et al.* [67] and consider either the velocity and the pressure or the density and the momentum as primal variables and the corresponding trace representation as hybrid variables, whereas the postprocessing is performed in terms of the flow velocity in both cases. The second formulation is moreover designed to deal with deforming meshes, to be easily embedded in FSI solvers.

After recalling the governing equations for weakly compressible flows in fixed and moving domains in Section 3.1 and introducing the VOIGT notation in Section 3.2, the two HDG formulations are proposed. In particular, the velocity-pressure formulation is presented in Section 3.3 and the density-momentum formulation is presented in Section 3.4. Finally, the convergence properties are experimentally assessed in Section 3.5. The content of this chapter is partially based on the work of LA SPINA *et al.* [97].

3.1 Problem statement

Let $\Omega \in \mathbb{R}^{\mathtt{n_{sd}}}$ be an open bounded domain, with $\mathtt{n_{sd}}$ denoting the number of spatial dimensions, and let the boundary $\partial\Omega$ be partitioned into a DIRICHLET portion Γ^D and a NEUMANN portion Γ^N such that $\partial\Omega = \Gamma^D \cup \Gamma^N$ and $\Gamma^D \cap \Gamma^N = \emptyset$. The flow of a weakly compressible fluid within a fixed region Ω in the time span (t_i, t_f) is described by the equations

$$\begin{cases} \dfrac{\partial \rho}{\partial t} + \boldsymbol{\nabla} \cdot (\boldsymbol{\rho v}) = 0 & \text{in } \Omega \times (t_i, t_f), \\ \dfrac{\partial \boldsymbol{\rho v}}{\partial t} + \boldsymbol{\nabla} \cdot (\boldsymbol{\rho v} \otimes \boldsymbol{v}) - \boldsymbol{\nabla} \cdot \boldsymbol{\sigma}(\boldsymbol{\nabla v}, p) = \rho \boldsymbol{b} & \text{in } \Omega \times (t_i, t_f), \\ \rho = \rho(p) & \text{in } \Omega \times (t_i, t_f), \end{cases} \tag{3.1}$$

equipped with suitable initial and boundary conditions, whose expression depends on the specific formulation adopted. As opposed to the previous chapter where multiple physics were taken into account, no subscript is used here to refer to the fluid quantities. It is worth recalling that the unknown quantities $\boldsymbol{v}$, p, ρ, $\boldsymbol{\rho v}$ refer to velocity, pressure, density and momentum, respectively, whereas $\boldsymbol{\sigma}$ denotes the CAUCHY stress tensor and $\boldsymbol{b}$ an applied body force. The first two equations in (3.1) express the conservation of the mass and the momentum, respectively, while the third equation defines a dependence between fluid pressure and density ensuring the conservation of energy. The linear relationship (2.7) is adopted and recalled here for completeness

$$\rho = \rho^{\mathtt{ref}} + \varepsilon \left(p - p^{\mathtt{ref}}\right), \tag{3.2}$$

with $\rho^{\mathtt{ref}}$ denoting the reference density evaluated at the reference pressure $p^{\mathtt{ref}}$ and ε being a (small) constant isothermal compressibility coefficient.

In order to derive the arbitrary LAGRANGEan–EULERian description of the flow, the ALE convective velocity, defined as the velocity of the fluid relative to the moving background mesh (whose velocity is indicated here with $\boldsymbol{a}$), is introduced

$$\boldsymbol{c} = \boldsymbol{v} - \boldsymbol{a}. \tag{3.3}$$

Using the ALE time derivative (i.e. the time derivative with respect to the reference configuration), the governing equations of the fluid problem under analysis on a deforming domain $\Omega(t)$ can be written as

$$\begin{cases} \dfrac{\partial \rho}{\partial t} + \rho \boldsymbol{\nabla} \cdot \boldsymbol{a} + \boldsymbol{\nabla} \cdot (\rho \boldsymbol{c}) = 0 & \text{in } \Omega(t) \times (t_i, t_f), \\ \dfrac{\partial \boldsymbol{\rho v}}{\partial t} + \boldsymbol{\rho v} \boldsymbol{\nabla} \cdot \boldsymbol{a} + \boldsymbol{\nabla} \cdot (\boldsymbol{\rho v} \otimes \boldsymbol{c}) - \boldsymbol{\nabla} \cdot \boldsymbol{\sigma}(\boldsymbol{\nabla v}, p) = \rho \boldsymbol{b} & \text{in } \Omega(t) \times (t_i, t_f), \\ \rho = \rho(p) & \text{in } \Omega(t) \times (t_i, t_f). \end{cases} \tag{3.4}$$

It is worth highlighting that no specific notation is adopted here to distinguish the quantities associated to the EULERian and the ALE description of motion to not overload the notation. It is therefore implicitly assumed that the mathematical operators in (3.1) are computed on a fixed computational mesh, whereas the counterparts in (3.4) are computed with respect to a potentially deforming mesh.

3.2 VOIGT notation

The VOIGT notation is a well-known strategy in mathematics and its main idea consists in replacing symmetric tensors with equivalent vectors of reduced size. This is achieved by rearranging the diagonal and off-diagonal components of a $\mathtt{n_{sd}} \times \mathtt{n_{sd}}$ tensor into a vector of size $\mathtt{m_{sd}} \times 1$, with $\mathtt{m_{sd}} = \mathtt{n_{sd}}(\mathtt{n_{sd}} + 1)/2$ denoting the number of non-redundant components.

According to the arrangement adopted by FISH and BELYTSCHKO [56], the VOIGT operator V in two and three dimensions can be defined as

$$\begin{cases} \mathrm{V}\left(\begin{bmatrix}\sigma_{xx} & \sigma_{xy}\\ \sigma_{xy} & \sigma_{yy}\end{bmatrix}\right) = \begin{bmatrix}\sigma_{xx} & \sigma_{yy} & \sigma_{xy}\end{bmatrix}^T & \text{in 2D,}\\ \mathrm{V}\left(\begin{bmatrix}\sigma_{xx} & \sigma_{xy} & \sigma_{xz}\\ \sigma_{xy} & \sigma_{yy} & \sigma_{yz}\\ \sigma_{xz} & \sigma_{yz} & \sigma_{zz}\end{bmatrix}\right) = \begin{bmatrix}\sigma_{xx} & \sigma_{yy} & \sigma_{zz} & \sigma_{xy} & \sigma_{xz} & \sigma_{yz}\end{bmatrix}^T & \text{in 3D.}\end{cases} \tag{3.5}$$

An inverse operator V^{-1} that, given a $\mathtt{m_{sd}} \times 1$ vector in VOIGT notation, returns the associated full $\mathtt{n_{sd}} \times \mathtt{n_{sd}}$ symmetric tensor can analogously be defined as

$$\begin{cases} \mathrm{V}^{-1}\left(\begin{bmatrix}\sigma_{xx} & \sigma_{yy} & \sigma_{xy}\end{bmatrix}^T\right) = \begin{bmatrix}\sigma_{xx} & \sigma_{xy}\\ \sigma_{xy} & \sigma_{yy}\end{bmatrix} & \text{in 2D,}\\ \mathrm{V}^{-1}\left(\begin{bmatrix}\sigma_{xx} & \sigma_{yy} & \sigma_{zz} & \sigma_{xy} & \sigma_{xz} & \sigma_{yz}\end{bmatrix}^T\right) = \begin{bmatrix}\sigma_{xx} & \sigma_{xy} & \sigma_{xz}\\ \sigma_{xy} & \sigma_{yy} & \sigma_{yz}\\ \sigma_{xz} & \sigma_{yz} & \sigma_{zz}\end{bmatrix} & \text{in 3D.}\end{cases} \tag{3.6}$$

This operator allows, for instance, to perform the pull-back operation to transform the CAUCHY stress into the first PIOLA–KIRCHHOFF stress. Its role will be exploited in Section 5.2 in the context of fluid-structure interaction problems solved by means of the partitioned DIRICHLET–NEUMANN coupling, but its definition is reported here for consistency.

For a NEWTONian fluid, the CAUCHY stress in equation (3.4) is related to the strain rate tensor

$$\boldsymbol{\varepsilon}\left(\boldsymbol{\nabla v}\right) = \boldsymbol{\nabla}^{\mathrm{S}}\boldsymbol{v} = \frac{1}{2}\left(\boldsymbol{\nabla v} + \left(\boldsymbol{\nabla v}\right)^T\right), \tag{3.7}$$

according to the stress-strain rate relationship

$$\boldsymbol{\sigma}\left(\boldsymbol{\nabla v}, p\right) = 2\mu\boldsymbol{\varepsilon}\left(\boldsymbol{\nabla v}\right) + \lambda\,\mathrm{tr}\left(\boldsymbol{\varepsilon}\left(\boldsymbol{\nabla v}\right)\right)\mathbf{I}_{\mathtt{n_{sd}}} - p\mathbf{I}_{\mathtt{n_{sd}}}, \tag{3.8}$$

with μ and λ denoting the fluid dynamic viscosity and the second coefficient of viscosity, respectively. The stored vectors in VOIGT notation reduce to

$$\boldsymbol{\sigma}_{\mathrm{V}} = \begin{cases} \begin{bmatrix}\sigma_{xx} & \sigma_{yy} & \sigma_{xy}\end{bmatrix}^T & \text{in 2D,}\\ \begin{bmatrix}\sigma_{xx} & \sigma_{yy} & \sigma_{zz} & \sigma_{xy} & \sigma_{xz} & \sigma_{yz}\end{bmatrix}^T & \text{in 3D,}\end{cases} \tag{3.9}$$

and

$$\boldsymbol{\varepsilon}_{\mathrm{V}} = \begin{cases} \begin{bmatrix}\varepsilon_{xx} & \varepsilon_{yy} & 2\varepsilon_{xy}\end{bmatrix}^T & \text{in 2D,}\\ \begin{bmatrix}\varepsilon_{xx} & \varepsilon_{yy} & \varepsilon_{zz} & 2\varepsilon_{xy} & 2\varepsilon_{xz} & 2\varepsilon_{yz}\end{bmatrix}^T & \text{in 3D,}\end{cases} \tag{3.10}$$

with $2\varepsilon_{xy}$, $2\varepsilon_{xz}$ and $2\varepsilon_{yz}$ denoting the off-diagonal terms of the strain rate tensor according to the engineering notation. The strain rate vector can therefore be computed as

$$\boldsymbol{\varepsilon}_{\mathrm{V}} = \boldsymbol{\nabla}_{\mathtt{S}} \boldsymbol{v}, \tag{3.11}$$

with $\boldsymbol{\nabla}_{\mathtt{S}}$ being a $\mathtt{m}_{\mathtt{sd}} \times \mathtt{n}_{\mathtt{sd}}$ operator, accounting for the symmetric part of the gradient and whose definition is

$$\boldsymbol{\nabla}_{\mathtt{S}} = \begin{cases} \begin{bmatrix} \partial/\partial x & 0 & \partial/\partial y \\ 0 & \partial/\partial y & \partial/\partial x \end{bmatrix}^T & \text{in 2D,} \\ \begin{bmatrix} \partial/\partial x & 0 & 0 & \partial/\partial y & \partial/\partial z & 0 \\ 0 & \partial/\partial y & 0 & \partial/\partial x & 0 & \partial/\partial z \\ 0 & 0 & \partial/\partial z & 0 & \partial/\partial x & \partial/\partial y \end{bmatrix}^T & \text{in 3D.} \end{cases} \tag{3.12}$$

As opposed to the strain rate tensor, the so-called vorticity tensor corresponds to the skew-symmetric part of the velocity gradient according to

$$\boldsymbol{\omega}\left(\boldsymbol{\nabla} \boldsymbol{v}\right) = \boldsymbol{\nabla}^{\mathtt{W}} \boldsymbol{v} = \frac{1}{2}\left(\boldsymbol{\nabla} \boldsymbol{v} - \left(\boldsymbol{\nabla} \boldsymbol{v}\right)^T\right). \tag{3.13}$$

The associated quantity in VOIGT notation can be computed as

$$\boldsymbol{\omega}_{\mathrm{V}} = \boldsymbol{\nabla}_{\mathtt{W}} \boldsymbol{v}, \tag{3.14}$$

with $\boldsymbol{\nabla}_{\mathtt{W}}$ being a $\mathtt{q}_{\mathtt{sd}} \times \mathtt{n}_{\mathtt{sd}}$ operator defined as

$$\boldsymbol{\nabla}_{\mathtt{W}} = \begin{cases} \begin{bmatrix} -\partial/\partial y & \partial/\partial x \end{bmatrix} & \text{in 2D,} \\ \begin{bmatrix} 0 & -\partial/\partial z & \partial/\partial y \\ \partial/\partial z & 0 & -\partial/\partial x \\ -\partial/\partial y & \partial/\partial x & 0 \end{bmatrix} & \text{in 3D,} \end{cases} \tag{3.15}$$

with $\mathtt{q}_{\mathtt{sd}} = \mathtt{m}_{\mathtt{sd}} - \mathtt{n}_{\mathtt{sd}}$ denoting the number of redundant tensor components. The constitutive law (3.8) can then be expressed in matrix form as

$$\boldsymbol{\sigma}_{\mathrm{V}} = \mathbf{D} \boldsymbol{\varepsilon}_{\mathrm{V}} - \mathbf{E} p, \tag{3.16}$$

with $\mathbf{D}$ denoting the $\mathtt{m}_{\mathtt{sd}} \times \mathtt{m}_{\mathtt{sd}}$ material matrix

$$\mathbf{D} = \begin{cases} \begin{bmatrix} 2\mu + \lambda & \lambda & 0 \\ \lambda & 2\mu + \lambda & 0 \\ 0 & 0 & \mu \end{bmatrix} & \text{in 2D,} \\ \begin{bmatrix} 2\mu + \lambda & \lambda & \lambda & 0 & 0 & 0 \\ \lambda & 2\mu + \lambda & \lambda & 0 & 0 & 0 \\ \lambda & \lambda & 2\mu + \lambda & 0 & 0 & 0 \\ 0 & 0 & 0 & \mu & 0 & 0 \\ 0 & 0 & 0 & 0 & \mu & 0 \\ 0 & 0 & 0 & 0 & 0 & \mu \end{bmatrix} & \text{in 3D,} \end{cases} \tag{3.17}$$

and $\mathbf{E}$ representing the equivalent form of the identity matrix, rewritten in VOIGT notation as a $\mathtt{m_{sd}} \times 1$ vector as

$$\mathbf{E} = \begin{cases} \begin{bmatrix} 1 & 1 & 0 \end{bmatrix}^T & \text{in 2D,} \\ \begin{bmatrix} 1 & 1 & 1 & 0 & 0 & 0 \end{bmatrix}^T & \text{in 3D.} \end{cases} \tag{3.18}$$

Moreover, the normal projection of the stress can be computed by premultiplying $\boldsymbol{\sigma}_{\mathrm{V}}$ by $\mathbf{N}^T$ with $\mathbf{N}$ being the $\mathtt{m_{sd}} \times \mathtt{n_{sd}}$ matrix

$$\mathbf{N} = \begin{cases} \begin{bmatrix} n_x & 0 & n_y \\ 0 & n_y & n_x \end{bmatrix}^T & \text{in 2D,} \\ \begin{bmatrix} n_x & 0 & 0 & n_y & n_z & 0 \\ 0 & n_y & 0 & n_x & 0 & n_z \\ 0 & 0 & n_z & 0 & n_x & n_y \end{bmatrix}^T & \text{in 3D,} \end{cases} \tag{3.19}$$

whereas the tangential projection of the velocity, for instance, can be retrieved by premultiplying $\boldsymbol{v}$ by the $\mathtt{q_{sd}} \times \mathtt{n_{sd}}$ matrix $\mathbf{T}$ with

$$\mathbf{T} = \begin{cases} \begin{bmatrix} -n_y & n_x \end{bmatrix} & \text{in 2D,} \\ \begin{bmatrix} 0 & -n_z & n_y \\ n_z & 0 & -n_x \\ -n_y & n_x & 0 \end{bmatrix} & \text{in 3D.} \end{cases} \tag{3.20}$$

Given the main concepts of the VOIGT notation and the associated definition of the differential operators and the geometrical projections, the governing equations of the fluid problem (3.4) can be rewritten, together with the initial and the boundary conditions, as

$$\begin{cases} \dfrac{\partial \rho}{\partial t} + \rho \boldsymbol{\nabla} \cdot \boldsymbol{a} + \boldsymbol{\nabla} \cdot (\rho \boldsymbol{c}) = 0 & \text{in } \Omega(t) \times (t_i, t_f), \\ \dfrac{\partial \boldsymbol{\rho v}}{\partial t} + \boldsymbol{\rho v} \boldsymbol{\nabla} \cdot \boldsymbol{a} + \boldsymbol{\nabla} \cdot (\boldsymbol{\rho v} \otimes \boldsymbol{c}) - \boldsymbol{\nabla}_{\mathrm{S}}^T \boldsymbol{\sigma}_{\mathrm{V}}(\boldsymbol{\nabla}_{\mathrm{S}} \boldsymbol{v}, p) = \rho \boldsymbol{b} & \text{in } \Omega(t) \times (t_i, t_f), \\ \rho = \rho(p) & \text{in } \Omega(t) \times (t_i, t_f), \\ (\boldsymbol{v}, p) - (\boldsymbol{v}^0, p^0) = \mathbf{0} \quad \text{or} \quad (\rho, \boldsymbol{\rho v}) - (\rho^0, \boldsymbol{\rho v}^0) = \mathbf{0} & \text{in } \Omega(t) \times (t_i), \\ (\boldsymbol{v}, p) - \left(\boldsymbol{v}^D, p^D\right) = \mathbf{0} \quad \text{or} \quad (\rho, \boldsymbol{\rho v}) - \left(\rho^D, \boldsymbol{\rho v}^D\right) = \mathbf{0} & \text{on } \Gamma^D(t) \times (t_i, t_f), \\ \mathbf{N}^T \boldsymbol{\sigma}_{\mathrm{V}}(\boldsymbol{\nabla}_{\mathrm{S}} \boldsymbol{v}, p) = \boldsymbol{t}^N & \text{on } \Gamma^N(t) \times (t_i, t_f). \end{cases} \tag{3.21}$$

The pairs $(\boldsymbol{v}^0, p^0)$ and $(\rho^0, \boldsymbol{\rho v}^0)$ define the initial conditions for the fluid unknowns, while the quantities $(\boldsymbol{v}^D, p^D)$ and $(\rho^D, \boldsymbol{\rho v}^D)$ and $\boldsymbol{t}^N$ denote the DIRICHLET and the NEUMANN boundary data applied on Γ^D and Γ^N, respectively. The exact expression of these conditions depends on the formulation adopted. In the following sections, two HDG formulations are presented in detail for the solution of flow problems, the first featuring the velocity and the pressure and the second featuring the density and the momentum field as primal unknowns.

3.3 Velocity-pressure formulation

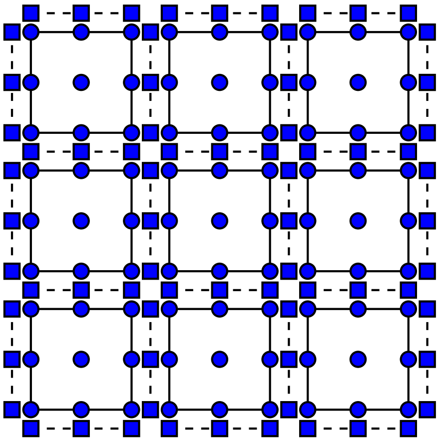

Figure 3.1: Degrees of freedom of the HDG discretization for velocity-pressure formulation

The first HDG formulation proposed for the solution of weakly compressible flows features the fluid velocity and pressure as primal independent variables. On the one hand, it can be considered the HDG counterpart of the CG formulation presented in Chapter 2 in the context of fluid-structure interaction problems. On the other hand, it consists of the extension of the work of GIACOMINI *et al.* [67] to accommodate a weak compressibility. To the best of the author's knowledge, no such formulation has been proposed in the literature so far. For the sake of simplicity, the velocity-pressure formulation is presented and its numerical properties analyzed only with respect to steady-state and non-convective flows on fixed domains, such that the only source of nonlinearity stems from the compressibility of the fluid.

The broken computational domain is defined by partitioning the fluid domain Ω in $\mathtt{n}^{\mathtt{el}}$ disjoint subdomains Ω^e such that

$$\Omega = \bigcup_{e=1}^{\mathtt{n}^{\mathtt{el}}} \Omega^e, \quad \Omega^e \cap \Omega^f = \emptyset \quad \text{for} \quad e \neq f. \tag{3.22}$$

The internal interface is then constituted by the union of the internal element boundaries as

$$\Gamma = \left[\bigcup_{e=1}^{\mathtt{n}^{\mathtt{el}}} \partial\Omega^e \right] \setminus \partial\Omega. \tag{3.23}$$

Henceforth, with the term mesh skeleton is indicated instead the union of the internal interface just defined and the NEUMANN portion of the boundary, i.e. $\Sigma = \Gamma \cup \Gamma^N$.

The degrees of freedom of a typical HDG discretization are sketched in Figure 3.1 for a polynomial degree of approximation $k = 2$. The local DOFs, constituted by the so-called mixed and primal variables, are depicted with the circles, whereas the global DOFs, constituted by the hybrid variables defined on the mesh skeleton, are denoted with the squares.

The second-order problem (3.21) can be rewritten as a system of first-order equations over the broken computational domain as

$$\left\{\begin{aligned} \boldsymbol{L}+\mathbf{D}^{1/2}\boldsymbol{\nabla}_{\mathrm{S}}\boldsymbol{v} &= \mathbf{0} && \text{in } \Omega^e,\\ \boldsymbol{\nabla}_{\mathrm{S}}^{T}\left(\mathbf{D}^{1/2}\boldsymbol{L}+\mathbf{E}p\right) &= \rho\,(p)\,\boldsymbol{b} && \text{in } \Omega^e,\\ \boldsymbol{\nabla}\cdot\left(\rho\,(p)\,\boldsymbol{v}\right) &= 0 && \text{in } \Omega^e,\\ \boldsymbol{v} &= \boldsymbol{v}^D && \text{on } \partial\Omega^e\cap\Gamma^D,\\ p &= p^D && \text{on } \partial\Omega^e\cap\Gamma^D,\\ \boldsymbol{v} &= \hat{\boldsymbol{v}} && \text{on } \partial\Omega^e\setminus\Gamma^D,\\ p &= \hat{p} && \text{on } \partial\Omega^e\setminus\Gamma^D,\\ -\mathbf{N}^T\left(\mathbf{D}^{1/2}\boldsymbol{L}+\mathbf{E}p\right) &= \boldsymbol{t}^N && \text{on } \partial\Omega^e\cap\Gamma^N,\\ [\![\boldsymbol{v}\otimes\boldsymbol{n}]\!] &= \mathbf{0} && \text{on } \Gamma,\\ [\![p\boldsymbol{n}]\!] &= \mathbf{0} && \text{on } \Gamma,\\ \left[\!\!\left[\widehat{\mathbf{N}^T\left(\mathbf{D}^{1/2}\boldsymbol{L}+\mathbf{E}p\right)}\right]\!\!\right] &= \mathbf{0} && \text{on } \Gamma,\\ \left[\!\!\left[\widehat{\rho\,(p)\,\boldsymbol{v}\cdot\boldsymbol{n}}\right]\!\!\right] &= 0 && \text{on } \Gamma. \end{aligned}\right. \tag{3.24}$$

The variable $\boldsymbol{L}$ is the mixed variable and physically represents the strain rate vector in VOIGT notation as in (3.11), scaled by the quantity $-\mathbf{D}^{1/2}$, with $\mathbf{D}$ being the material matrix defined in (3.17). This scaling allows to retrieve the symmetry of the STOKES problem in the incompressible formulation presented by GIACOMINI *et al.* [67] and it is kept here for consistency. The same consideration holds, for instance, in the context of linear elastic problems, as demonstrated in the antecedent work by SEVILLA *et al.* [142]. The variables $\boldsymbol{v}$ and p in (3.24) define the solution of the velocity and the pressure within the elements Ω^e and are in the following referred to as primal variables. Finally, the quantities $\hat{\boldsymbol{v}}$ and $\hat{p}$ represent the trace of the velocity and the pressure on the mesh skeleton Σ and are referred to as hybrid variables. It is worth highlighting that, owing to the specific choice of the unknowns, the fluid density does not constitute an independent variable, but it is computed as a function of the pressure level according to the equation of state (3.2).

The first set of equations in problem (3.24) represents the local problems that allow to compute the elemental variables in terms of the unknown traces. The last equations constitute the transmission conditions and define the global problem to effectively compute the hybrid variables. More precisely, the conditions enforce the continuity of the primal variables and the equilibrium of the normal fluxes across the internal interface Γ. Given the discontinuous nature of the HDG approximation, the jump operator $[\![\odot]\!]$ sums values from two adjacent elements Ω^e and Ω^f and reads

$$[\![\odot]\!] = \odot^e + \odot^f, \tag{3.25}$$

according to the definition introduced by MONTLAUR *et al.* [111]. On the one hand, the continuity of the solution is automatically satisfied due to the boundary conditions $\boldsymbol{v}=\hat{\boldsymbol{v}}$ and $p=\hat{p}$ imposed in the local problems together with the unique definition of the hybrid variables $\hat{\boldsymbol{v}}$ and $\hat{p}$ on each face of the mesh skeleton. On the other hand, the equilibrium of the flux across the internal interface is taken into account by introducing the following definition of the numerical normal fluxes

$$\widehat{\mathbf{N}^T\left(\mathbf{D}^{1/2}\boldsymbol{L}+\mathbf{E}p\right)} = \begin{cases} \mathbf{N}^T\left(\mathbf{D}^{1/2}\boldsymbol{L}+\mathbf{E}p^D\right)+\tau_v\left(\boldsymbol{v}-\boldsymbol{v}^D\right) & \text{on } \partial\Omega^e\cap\Gamma^D, \\ \mathbf{N}^T\left(\mathbf{D}^{1/2}\boldsymbol{L}+\mathbf{E}\hat{p}\right)+\tau_v\left(\boldsymbol{v}-\hat{\boldsymbol{v}}\right) & \text{on } \partial\Omega^e\setminus\Gamma^D, \end{cases} \tag{3.26a}$$

$$\widehat{\rho\left(p\right)\boldsymbol{v}\cdot\boldsymbol{n}} = \begin{cases} \rho\left(p^D\right)\boldsymbol{v}^D\cdot\boldsymbol{n}+\tau_p\left(p-p^D\right) & \text{on } \partial\Omega^e\cap\Gamma^D, \\ \rho\left(\hat{p}\right)\hat{\boldsymbol{v}}\cdot\boldsymbol{n}+\tau_p\left(p-\hat{p}\right) & \text{on } \partial\Omega^e\setminus\Gamma^D. \end{cases} \tag{3.26b}$$

The terms τ_v and τ_p are stabilization parameters for the momentum and the continuity equation, respectively. The crucial role played by the stabilization with respect to the stability, the accuracy and the convergence properties of HDG methods has been investigated for instance by COCKBURN *et al.* [35–37] and NGUYEN *et al.* [118, 119, 121]. Dimensional analysis provides a practical choice for the stabilization parameters

$$\tau_v = C_v\frac{\mu}{l}, \qquad \tau_p = C_p\frac{1}{|\boldsymbol{v}|}, \tag{3.27}$$

with l being a representative length scale of the problem under analysis and C_v and C_p being suitable positive scaling factors.

Exploiting the definition of the numerical normal fluxes (3.26) and after integration by parts, the weak form the HDG local problems reads: given $(\boldsymbol{v}^D, p^D)$ on Γ^D and $(\hat{\boldsymbol{v}}, \hat{p})$ on Σ, find $(\boldsymbol{L}, \boldsymbol{v}, p) \in [\mathcal{W}^h(\Omega^e)]^{\mathtt{m}_{\mathtt{sd}}} \times [\mathcal{W}^h(\Omega^e)]^{\mathtt{n}_{\mathtt{sd}}} \times \mathcal{W}^h(\Omega^e)$ for $e = 1, \dots, \mathtt{n}^{\mathtt{el}}$ such that

$$\begin{aligned} &-\left(\boldsymbol{W},\boldsymbol{L}\right)_{\Omega^e}+\left(\boldsymbol{\nabla}_{\mathtt{S}}^T\mathbf{D}^{1/2}\boldsymbol{W},\boldsymbol{v}\right)_{\Omega^e} = \\ &\qquad\left\langle\mathbf{N}^T\mathbf{D}^{1/2}\boldsymbol{W},\boldsymbol{v}^D\right\rangle_{\partial\Omega^e\cap\Gamma^D}+\left\langle\mathbf{N}^T\mathbf{D}^{1/2}\boldsymbol{W},\hat{\boldsymbol{v}}\right\rangle_{\partial\Omega^e\setminus\Gamma^D}, \end{aligned} \tag{3.28a}$$

$$\begin{aligned} &\left(\boldsymbol{w},\boldsymbol{\nabla}_{\mathtt{S}}^T\left(\mathbf{D}^{1/2}\boldsymbol{L}+\mathbf{E}p\right)\right)_{\Omega^e}+\left\langle\boldsymbol{w},\tau_v\boldsymbol{v}\right\rangle_{\partial\Omega^e}-\left(\boldsymbol{w},\rho\left(p\right)\boldsymbol{b}\right)_{\Omega^e} = \\ &\qquad\left\langle\boldsymbol{w},\tau_v\boldsymbol{v}^D\right\rangle_{\partial\Omega^e\cap\Gamma^D}+\left\langle\boldsymbol{w},\tau_v\hat{\boldsymbol{v}}\right\rangle_{\partial\Omega^e\setminus\Gamma^D}, \end{aligned} \tag{3.28b}$$

$$\begin{aligned} &-\left(\boldsymbol{\nabla}w,\rho\left(p\right)\boldsymbol{v}\right)_{\Omega^e}+\left\langle w,\tau_p p\right\rangle_{\partial\Omega^e} = \\ &\qquad-\left\langle w,\rho\left(p^D\right)\boldsymbol{v}^D\cdot\boldsymbol{n}-\tau_p p^D\right\rangle_{\partial\Omega^e\cap\Gamma^D}-\left\langle w,\rho\left(\hat{p}\right)\hat{\boldsymbol{v}}\cdot\boldsymbol{n}-\tau_p\hat{p}\right\rangle_{\partial\Omega^e\setminus\Gamma^D}, \end{aligned} \tag{3.28c}$$

for all $(\boldsymbol{W}, \boldsymbol{w}, w) \in [\mathcal{W}^h(\Omega^e)]^{\mathtt{m}_{\mathtt{sd}}} \times [\mathcal{W}^h(\Omega^e)]^{\mathtt{n}_{\mathtt{sd}}} \times \mathcal{W}^h(\Omega^e)$. It is worth noting that the local boundary conditions, imposing either the DIRICHLET data on $\partial\Omega^e \cap \Gamma^D$ or the trace of the solution on $\partial\Omega^e \setminus \Gamma^D$, are applied in a weak sense in each equation in (3.28). Moreover, the parameters τ_v and τ_p defined in (3.27) ensure dimensional consistency. It is also worth anticipating that the local problems (3.28) are used to substitute the respective variables in the global problem (3.29) to obtain a final system involving only the traces of the solution.

The HDG global problem is obtained by replacing the definitions (3.26) in the transmission conditions (3.24) across the mesh skeleton and by embedding the NEUMANN boundary condition. Hence, its weak form reads: find $(\hat{\boldsymbol{v}}, \hat{p}) \in [\widehat{\mathcal{W}}^h(\Sigma)]^{\mathtt{n}_{\mathtt{sd}}} \times \widehat{\mathcal{W}}^h(\Sigma)$ such that

$$-\sum_{e=1}^{\mathtt{n}^{\mathtt{el}}}\left\langle\hat{\boldsymbol{w}},\mathbf{N}^T\left(\mathbf{D}^{1/2}\boldsymbol{L}+\mathbf{E}\hat{p}\right)+\tau_v\left(\boldsymbol{v}-\hat{\boldsymbol{v}}\right)\right\rangle_{\partial\Omega^e\setminus\Gamma^D} = \sum_{e=1}^{\mathtt{n}^{\mathtt{el}}}\left\langle\hat{\boldsymbol{w}},\boldsymbol{t}^N\right\rangle_{\partial\Omega^e\cap\Gamma^N}, \tag{3.29a}$$

$$\sum_{e=1}^{\mathtt{n}^{\mathtt{el}}}\left\langle\hat{w},\tau_p\left(p-\hat{p}\right)\right\rangle_{\partial\Omega^e\setminus\Gamma^D} = 0, \tag{3.29b}$$

for all $(\hat{\boldsymbol{w}}, \hat{w}) \in [\widehat{\mathcal{W}}^h(\Sigma)]^{\mathtt{n}_{\mathtt{sd}}} \times \widehat{\mathcal{W}}^h(\Sigma)$. It is worth noting that the term $\rho(\hat{p})\hat{\boldsymbol{v}} \cdot \boldsymbol{n}$ does not appear in the global problem, since its value is uniquely defined across adjacent elements, owing to the unique definition of the hybrid variables on each face of the mesh skeleton.

The linear system associated with the discretization of the local problems (3.28) by means of a isoparametric formulation with equal interpolation for the local variables possesses the following structure

$$\begin{bmatrix} \mathbf{K}_{LL} & \mathbf{K}_{Lv} & \mathbf{0} \\ \mathbf{K}_{vL} & \mathbf{K}_{vv} & \mathbf{K}_{vp} \\ \mathbf{0} & \mathbf{K}_{pv} & \mathbf{K}_{pp} \end{bmatrix}_e \begin{bmatrix} \delta\mathbf{L} \\ \delta\mathbf{v} \\ \delta\mathbf{p} \end{bmatrix}_e = \begin{bmatrix} \mathbf{f}_L \\ \mathbf{f}_v \\ \mathbf{f}_p \end{bmatrix}_e - \begin{bmatrix} \mathbf{K}_{L\hat{v}} & \mathbf{0} \\ \mathbf{K}_{v\hat{v}} & \mathbf{0} \\ \mathbf{K}_{p\hat{v}} & \mathbf{K}_{p\hat{p}} \end{bmatrix}_e \begin{bmatrix} \delta\hat{\mathbf{v}} \\ \delta\hat{\mathbf{p}} \end{bmatrix}_e, \tag{3.30}$$

for $e = 1, \ldots, \mathtt{n}^{\mathtt{el}}$. Owing to the dimensions of the local unknowns, i.e. the mixed variable and the primal variables, the solution of this system implies for each element the inversion of a matrix of size $(\mathtt{m}_{\mathtt{sd}} + \mathtt{n}_{\mathtt{sd}} + 1)\mathtt{n}^{\mathtt{en}}$, with $\mathtt{n}^{\mathtt{en}}$ denoting the number of element nodes in Ω^e, function of the polynomial degree of approximation k. It is worth highlighting that the adoption of the VOIGT notation allows to reduce the size of the systems (3.30), since only the $\mathtt{m}_{\mathtt{sd}}$ non-redundant components of the (scaled) strain rate tensor are stored, instead of $\mathtt{n}_{\mathtt{sd}} \times \mathtt{n}_{\mathtt{sd}}$, as done in most HDG formulations published in literature. This strategy therefore produces a gain in computational efficiency, owing to a reduced size of the local problems and the quantity of stored information. However, the elemental nature of the problems (3.30) allows to easily solve them in parallel, whereas most of the computational time is spent for the solution of the global problem presented below, when direct solvers are used. Moreover, the adoption of the VOIGT notation ensures the optimal convergence of order $k + 1$ of the mixed variable, as opposed to the suboptimal behavior exhibited by classical HDG formulations involving the symmetric part of the gradient of the primal variable. Such a detrimental loss of convergence has been experienced by the same author before the implementation of the strong imposition of the symmetry of the stress tensor, which followed the publication of the works by SEVILLA *et al.* [142] and GIACOMINI *et al.* [67].

Analogously to what has been done for the local problems, the discretization of the global problem (3.29) produces a system of the form

$$\sum_{e=1}^{\mathtt{n}^{\mathtt{el}}} \left\{ \begin{bmatrix} \mathbf{K}_{\hat{v}L} & \mathbf{K}_{\hat{v}v} & \mathbf{0} \\ \mathbf{0} & \mathbf{0} & \mathbf{K}_{\hat{p}p} \end{bmatrix}_e \begin{bmatrix} \delta\mathbf{L} \\ \delta\mathbf{v} \\ \delta\mathbf{p} \end{bmatrix}_e + \begin{bmatrix} \mathbf{K}_{\hat{v}\hat{v}} & \mathbf{K}_{\hat{v}\hat{p}} \\ \mathbf{0} & \mathbf{K}_{\hat{p}\hat{p}} \end{bmatrix}_e \begin{bmatrix} \delta\hat{\mathbf{v}} \\ \delta\hat{\mathbf{p}} \end{bmatrix}_e \right\} = \sum_{e=1}^{\mathtt{n}^{\mathtt{el}}} \begin{bmatrix} \mathbf{f}_{\hat{v}} \\ \mathbf{f}_{\hat{p}} \end{bmatrix}_e. \tag{3.31}$$

The expressions of the matrices and vectors just presented are detailed in Appendix C. As usual in HDG methods, the final global system is obtained by replacing the solution of the local problems (3.30) in the global problem (3.31) and, for this velocity-pressure formulation (denoted by the subscript $\odot_{\mathtt{V-P}}$), it reads

$$\left[\mathbf{K}_{\mathtt{V-P}}\right] \left[\delta\widehat{\mathbf{V}}\right] = \left[\mathbf{f}_{\mathtt{V-P}}\right], \tag{3.32}$$

with

$$\left[\mathbf{K}_{\mathtt{V-P}}\right] = \mathop{\mathsf{A}}_{e=1}^{\mathtt{n}^{\mathtt{el}}} \left\{ \left[\mathbf{K}_{\widehat{V}\widehat{V}}\right]_e - \left[\mathbf{K}_{\widehat{V}L} \quad \mathbf{K}_{\widehat{V}V}\right]_e \begin{bmatrix} \mathbf{K}_{LL} & \mathbf{K}_{LV} \\ \mathbf{K}_{VL} & \mathbf{K}_{VV} \end{bmatrix}_e^{-1} \begin{bmatrix} \mathbf{K}_{L\widehat{V}} \\ \mathbf{K}_{V\widehat{V}} \end{bmatrix}_e \right\}, \tag{3.33}$$

and

$$\left[\mathbf{f}_{\mathtt{V-P}}\right] = \mathop{\mathsf{A}}_{e=1}^{\mathtt{n}^{\mathtt{el}}} \left\{ \left[\mathbf{f}_{\widehat{V}}\right]_e - \left[\mathbf{K}_{\widehat{V}L} \quad \mathbf{K}_{\widehat{V}V}\right]_e \begin{bmatrix} \mathbf{K}_{LL} & \mathbf{K}_{LV} \\ \mathbf{K}_{VL} & \mathbf{K}_{VV} \end{bmatrix}_e^{-1} \begin{bmatrix} \mathbf{f}_{L} \\ \mathbf{f}_{V} \end{bmatrix}_e \right\}, \tag{3.34}$$

where the fluid velocity and pressure DOFs have been grouped in the variable $\mathbf{V} = \begin{bmatrix}\mathbf{v} & \mathbf{p}\end{bmatrix}^T$ for the sake of brevity.

It is worth highlighting that the problem under analysis features a nonlinear behavior, owing to the weak flow compressibility. As a consequence, the matrices $\mathbf{K}$ stem from the linearization of the problem with respect to the unknown variables, whereas the vectors $\mathbf{f}$ represent the residuals (scaled by a factor -1) of the weak forms in (3.28) and (3.29). Thus, in the philosophy of the NEWTON–RAPHSON method, the system (3.32) is assembled and solved in a succession of iterations until a convergence criterion is fulfilled, expressed either in terms of the norm of the residuals or in terms of the norm of the solution increments.

As shown in the numerical examples in Section 3.5, this velocity-pressure formulation succeeds to provide optimal convergence of order $k+1$ for the scaled strain rate, the velocity and the pressure field. However, a key feature of the HDG method is to exploit the accuracy of the mixed variable to construct an enhanced approximation of the solution, converging in a superoptimal fashion, i.e. converging with order $k+2$. More precisely, a postprocessed velocity field $\boldsymbol{v}^\star$ is sought in the richer space $[\mathcal{W}^h_\star(\Omega^e)]^{\mathtt{n_{sd}}}$, whose definition is given in Appendix A. The weak form of the postprocessing procedure thus reads: given $(\boldsymbol{L}, \boldsymbol{v})$ in Ω^e, $\boldsymbol{v}^D$ on Γ^D and $\hat{\boldsymbol{v}}$ on Σ, find $\boldsymbol{v}^\star \in [\mathcal{W}^h_\star(\Omega^e)]^{\mathtt{n_{sd}}}$ for $e = 1, \dots, \mathtt{n}^{\mathtt{el}}$ such that

$$\begin{aligned}
-\left(\boldsymbol{\nabla}_{\mathtt{S}}\boldsymbol{w}^\star, \mathbf{D}^{1/2}\boldsymbol{\nabla}_{\mathtt{S}}\boldsymbol{v}^\star\right)_{\Omega^e} &= \left(\boldsymbol{\nabla}_{\mathtt{S}}\boldsymbol{w}^\star, \boldsymbol{L}\right)_{\Omega^e}, && \text{(3.35a)}\\
\left(\boldsymbol{u}_{\mathtt{T}}, \boldsymbol{v}^\star\right)_{\Omega^e} &= \left(\boldsymbol{u}_{\mathtt{T}}, \boldsymbol{v}\right)_{\Omega^e}, && \text{(3.35b)}\\
\left(\boldsymbol{u}_{\mathtt{R}}, \boldsymbol{\nabla}_{\mathtt{W}}\boldsymbol{v}^\star\right)_{\Omega^e} &= \left\langle \boldsymbol{u}_{\mathtt{R}}, \mathbf{T}\boldsymbol{v}^D\right\rangle_{\partial\Omega^e\cap\Gamma^D} && \text{(3.35c)}\\
&\quad + \left\langle \boldsymbol{u}_{\mathtt{R}}, \mathbf{T}\hat{\boldsymbol{v}}\right\rangle_{\partial\Omega^e\setminus\Gamma^D},
\end{aligned}$$

for all $(\boldsymbol{w}^\star, \boldsymbol{u}_{\mathtt{T}}, \boldsymbol{u}_{\mathtt{R}}) \in [\mathcal{W}^h_\star(\Omega^e)]^{\mathtt{n_{sd}}} \times [\mathcal{U}^h(\Omega^e)]^{\mathtt{n_{sd}}} \times [\mathcal{U}^h(\Omega^e)]^{\mathtt{q_{sd}}}$. The first equation in (3.35) directly follows from the definition of the mixed variable in (3.24) and represents a least-squares fit to the accurate variable $\boldsymbol{L}$. The last two equations are introduced to remove the underdetermination of the problem by constraining the rigid motions, consisting of $\mathtt{n_{sd}}$ translations and $\mathtt{q_{sd}}$ rotations. From a physical point of view, the first condition enforces the average value of the postprocessed velocity $\boldsymbol{v}^\star$ to equal the average value of the velocity field $\boldsymbol{v}$ already computed. Then, the left hand side of the second condition represents the mean vorticity in the interior of element Ω^e, whereas its right hand side denotes the circulation of the flow around the element boundary $\partial\Omega^e$. It is worth pointing out that the postprocessing problem in (3.35) is formally identical to the one proposed by GIACOMINI *et al.* [67] for incompressible flows. However, the material matrix $\mathbf{D}$ defined in (3.17) includes the second coefficient of viscosity λ, whose role cannot be neglected for the computation of the CAUCHY stress in (3.8), since the velocity field is not divergence-free in the (weakly) compressible regime.

It is worth emphasizing that the postprocessing procedure (3.35), introduced here for steady-state problems, can also be adopted for unsteady flows without modifications. In that case, the postprocessing problem does not have to be solved at all time levels, but only at the time steps where a more accurate solution is desired. Although not addressed in this thesis, it is then worth reminding that the mismatch between the primal and the postprocessed solution can provide a reliable and inexpensive error estimator that can be further exploited to drive efficient degree adaptive procedures, as shown by GIORGIANI *et al.* [68, 69] and SEVILLA and HUERTA [141].

3.4 Density-momentum formulation

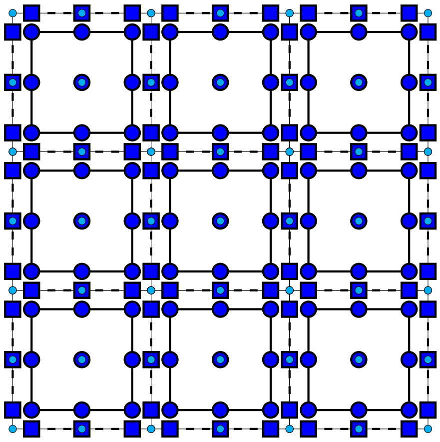

Figure 3.2: Degrees of freedom of the HDG discretization for density-momentum formulation

The second HDG formulation presented for the solution of weakly compressible flows considers the fluid density and momentum as primal independent variables. As opposed to the first strategy in Section 3.3, the formulation presented here deals with unsteady flows and tackles all the nonlinearities, represented by the convection and the weak compressibility. Moreover, potentially deforming domains are considered by means of the ALE description of motion.

The time-varying computational domain $\Omega(t)$ under analysis is partitioned in $\mathtt{n}^{\mathtt{el}}$ disjoint elements $\Omega^e(t)$ such that

$$\Omega\left(t\right)=\bigcup_{e=1}^{\mathtt{n}^{\mathtt{el}}}\Omega^{e}\left(t\right),\quad \Omega^{e}\left(t\right)\cap\Omega^{f}\left(t\right)=\emptyset\quad\text{for}\quad e\neq f, \tag{3.36}$$

while the deforming internal interface is given by

$$\Gamma\left(t\right)=\left[\bigcup_{e=1}^{\mathtt{n}^{\mathtt{el}}}\partial\Omega^{e}\left(t\right)\right]\setminus\partial\Omega\left(t\right). \tag{3.37}$$

Figure 3.2 depicts the degrees of freedom of this HDG formulation for a degree $k=2$. The local DOFs represented by the blue circles are constituted here by the scaled strain rate tensor, the density and the momentum in the interior of the elements, whereas the global DOFs denoted with the blue squares stem from the trace of the density and the momentum on the mesh skeleton. The small circles in cyan refer to the displacement of the ALE mesh. The displacement is imposed by means of user-defined functions in the numerical examples of this chapter. In the context of fluid-structure interaction, instead, the deformation of the fluid mesh is determined by a suitable mapping as a function of the interface structural displacement, as done in Chapters 2 and 5. It is worth pointing out that a lower polynomial degree k can be adopted for the geometrical representation of the ALE mesh compared to the degree of approximation of the HDG unknowns, as long as the same set of quadrature points is selected for the integration of the terms presented in the following.

The strong form of the density-momentum formulation of the complete weakly compressible flow problem (3.21) is

$$\left\{\begin{array}{rl}
\boldsymbol{L} + \mathbf{D}^{1/2}\boldsymbol{\nabla}_{\mathrm{S}}\boldsymbol{v} = \mathbf{0} & \text{in } \Omega^e(t) \times (t_i, t_f),\\
\dfrac{\partial \rho}{\partial t} + \rho \boldsymbol{\nabla}\cdot\boldsymbol{a} + \boldsymbol{\nabla}\cdot(\rho\boldsymbol{c}) = 0 & \text{in } \Omega^e(t) \times (t_i, t_f),\\
\dfrac{\partial \boldsymbol{\rho v}}{\partial t} + \boldsymbol{\rho v}\boldsymbol{\nabla}\cdot\boldsymbol{a} + \boldsymbol{\nabla}\cdot(\boldsymbol{\rho v}\otimes\boldsymbol{c}) \qquad\qquad & \\
+\boldsymbol{\nabla}_{\mathrm{S}}^T\left(\mathbf{D}^{1/2}\boldsymbol{L} + \mathbf{E}p(\rho)\right) = \rho\boldsymbol{b} & \text{in } \Omega^e(t) \times (t_i, t_f),\\
\rho = \rho^0 & \text{in } \Omega^e(t) \times (t_i),\\
\boldsymbol{\rho v} = \boldsymbol{\rho v}^0 & \text{in } \Omega^e(t) \times (t_i),\\
\rho = \rho^D & \text{on } \partial\Omega^e(t) \cap \Gamma^D(t) \times (t_i, t_f),\\
\boldsymbol{\rho v} = \boldsymbol{\rho v}^D & \text{on } \partial\Omega^e(t) \cap \Gamma^D(t) \times (t_i, t_f),\\
\rho = \hat{\rho} & \text{on } \partial\Omega^e(t) \setminus \Gamma^D(t) \times (t_i, t_f),\\
\boldsymbol{\rho v} = \widehat{\boldsymbol{\rho v}} & \text{on } \partial\Omega^e(t) \setminus \Gamma^D(t) \times (t_i, t_f),\\
-\mathbf{N}^T\left(\mathbf{D}^{1/2}\boldsymbol{L} + \mathbf{E}p(\rho)\right) = \boldsymbol{t}^N & \text{on } \partial\Omega^e(t) \cap \Gamma^N(t) \times (t_i, t_f),\\
[\![\rho\boldsymbol{n}]\!] = \mathbf{0} & \text{on } \Gamma(t) \times (t_i, t_f),\\
[\![\boldsymbol{\rho v}\otimes\boldsymbol{n}]\!] = \mathbf{0} & \text{on } \Gamma(t) \times (t_i, t_f),\\
[\![\widehat{\rho\boldsymbol{c}\cdot\boldsymbol{n}}]\!] = 0 & \text{on } \Gamma(t) \times (t_i, t_f),\\
\left[\!\!\left[\widehat{(\boldsymbol{\rho v}\otimes\boldsymbol{c})\,\boldsymbol{n}}\right]\!\!\right] = \mathbf{0} & \text{on } \Gamma(t) \times (t_i, t_f),\\
\left[\!\!\left[\widehat{\mathbf{N}^T\left(\mathbf{D}^{1/2}\boldsymbol{L} + \mathbf{E}p(\rho)\right)}\right]\!\!\right] = \mathbf{0} & \text{on } \Gamma(t) \times (t_i, t_f).
\end{array}\right. \tag{3.38}$$

The mixed variable $\boldsymbol{L}$ preserves the definition in Section 3.3 and stems from the VOIGT representation of the scaled strain rate tensor. The primal variables are the density ρ and the momentum $\boldsymbol{\rho v}$, whereas $\hat{\rho}$ and $\widehat{\boldsymbol{\rho v}}$ are the corresponding trace variables defined on the mesh skeleton $\Sigma(t) = \Gamma(t) \cup \Gamma^N(t)$.

The initial and the DIRICHLET boundary conditions are imposed in the local problems and they are consistently expressed in terms of the density and the momentum field. In this formulation, the velocity and the pressure are not independent variables. The former is computed as the ratio of the momentum and the density, whereas the latter is evaluated from the equation of state (3.2). Moreover, the velocity of the computational mesh $\boldsymbol{a}$, which is independent of the velocity of the material particles, is computed as the time derivative of the mesh displacement $\boldsymbol{d}$. As usual in HDG methods, the NEUMANN boundary condition and the transmission conditions are imposed in the global problem and they stem from the last equations in (3.38). The continuity of the primal variables is automatically fulfilled, due to the local boundary conditions and the unique definition of the hybrid variables on each face. Moreover, it is worth highlighting that no continuity of the mesh velocity needs to be enforced, since its approximation is continuous by construction over the whole computational domain, as shown in Figure 3.2. The numerical normal fluxes of the terms under the divergence operator are defined as

$$\widehat{\rho \boldsymbol{c} \cdot \boldsymbol{n}} = \begin{cases} \left(\boldsymbol{\rho v}^D - \rho^D \boldsymbol{a}\right) \cdot \boldsymbol{n} + \tau_\rho \left(\rho - \rho^D\right) & \text{on } \partial\Omega^e\left(t\right) \cap \Gamma^D\left(t\right), \\ \left(\widehat{\boldsymbol{\rho v}} - \hat{\rho} \boldsymbol{a}\right) \cdot \boldsymbol{n} + \tau_\rho \left(\rho - \hat{\rho}\right) & \text{on } \partial\Omega^e\left(t\right) \setminus \Gamma^D\left(t\right), \end{cases} \tag{3.39a}$$

$$\widehat{\left(\boldsymbol{\rho v} \otimes \boldsymbol{c}\right) \boldsymbol{n}} = \begin{cases} \left[\boldsymbol{\rho v}^D \otimes \left(\dfrac{\boldsymbol{\rho v}^D}{\rho^D} - \boldsymbol{a}\right)\right] \boldsymbol{n} + \tau^c_{\rho v} \left(\boldsymbol{\rho v} - \boldsymbol{\rho v}^D\right) & \text{on } \partial\Omega^e\left(t\right) \cap \Gamma^D\left(t\right), \\ \left[\widehat{\boldsymbol{\rho v}} \otimes \left(\dfrac{\widehat{\boldsymbol{\rho v}}}{\hat{\rho}} - \boldsymbol{a}\right)\right] \boldsymbol{n} + \tau^c_{\rho v} \left(\boldsymbol{\rho v} - \widehat{\boldsymbol{\rho v}}\right) & \text{on } \partial\Omega^e\left(t\right) \setminus \Gamma^D\left(t\right), \end{cases} \tag{3.39b}$$

$$\widehat{\mathbf{N}^T \left(\mathbf{D}^{1/2} \boldsymbol{L} + \mathbf{E} p\left(\rho\right)\right)} = \begin{cases} \mathbf{N}^T \left(\mathbf{D}^{1/2} \boldsymbol{L} + \mathbf{E} p\left(\rho^D\right)\right) + \tau^d_{\rho v} \left(\boldsymbol{\rho v} - \boldsymbol{\rho v}^D\right) & \text{on } \partial\Omega^e\left(t\right) \cap \Gamma^D\left(t\right), \\ \mathbf{N}^T \left(\mathbf{D}^{1/2} \boldsymbol{L} + \mathbf{E} p\left(\hat{\rho}\right)\right) + \tau^d_{\rho v} \left(\boldsymbol{\rho v} - \widehat{\boldsymbol{\rho v}}\right) & \text{on } \partial\Omega^e\left(t\right) \setminus \Gamma^D\left(t\right). \end{cases} \tag{3.39c}$$

The stabilization parameters τ_ρ, $\tau^c_{\rho v}$ and $\tau^d_{\rho v}$ account for the compressibility, the convection and the diffusion, respectively, and their magnitude can be estimated through the relations

$$\tau_\rho = C_\rho \frac{1}{\varepsilon \left|\boldsymbol{v}\right|}, \qquad \tau^c_{\rho v} = C^c_{\rho v} \left|\boldsymbol{v}\right|, \qquad \tau^d_{\rho v} = C^d_{\rho v} \frac{\mu}{\rho^{\texttt{ref}} l}, \tag{3.40}$$

with l being a representative length scale and C_ρ, $C^c_{\rho v}$ and $C^d_{\rho v}$ denoting suitable positive scaling factors. Without loss of generality, a unique parameter $\tau_{\rho v} = \tau^c_{\rho v} + \tau^d_{\rho v}$ is henceforth considered for the stabilization of the momentum equation.

Special attention is devoted to the imposition of appropriate boundary conditions. More precisely, four types of physical boundary conditions are considered in the numerical examples in Section 3.5 for pure flow problems and in Section 5.4 for fluid-structure interaction problems, namely:

- Inflow condition: the momentum profile, corresponding to the mass flow rate per unit volume, is imposed via the DIRICHLET boundary condition $\boldsymbol{\rho v} = \boldsymbol{\rho v}^D$.

- Outflow condition: the density evaluated at the given pressure level p^D is imposed via the DIRICHLET boundary condition $\rho = \rho^D = \rho(p^D)$, whereas the momentum is extrapolated. Alternatively, a stress-free condition can be considered via the homogeneous NEUMANN boundary condition $\boldsymbol{\sigma n} = \boldsymbol{t}^N = \boldsymbol{0}$.

- No-slip condition: each momentum component is forced to be zero via the homogeneous DIRICHLET boundary condition $\boldsymbol{\rho v} = \boldsymbol{\rho v}^D = \boldsymbol{0}$. In case of a boundary moving at a given speed $\boldsymbol{v}^D$, as it happens in FSI problems, only the density needs to be computed by considering the DIRICHLET boundary condition $\boldsymbol{\rho v} = \rho \boldsymbol{v}^D$.

- Free-slip condition: only the normal component of the momentum is forced to be zero via the DIRICHLET boundary condition $\boldsymbol{\rho v} \cdot \boldsymbol{n} = \boldsymbol{\rho v}^D \cdot \boldsymbol{n} = \boldsymbol{0}$, while the tangential component remains unconstrained.

Rigorously, the DIRICHLET portion of the boundary Γ^D should be split into two partitions Γ^D_ρ and $\Gamma^D_{\rho v}$, given the possibility to impose boundary conditions on either the density or the momentum in distinct regions. However, a unique definition of such boundary is adopted throughout this thesis for the sake of readability.

Following the same rationale of Section 3.3 and expliciting all the unknowns involved, the weak form of the HDG local problems reads: given $(\rho^0, \boldsymbol{\rho v}^0)$ in $\Omega^e(t) \times (t_i)$, $(\rho^D, \boldsymbol{\rho v}^D)$ on $\Gamma^D(t)$ and $(\hat{\rho}, \widehat{\boldsymbol{\rho v}})$ on $\Sigma(t)$, find $(\boldsymbol{L}, \rho, \boldsymbol{\rho v}) \in [\mathcal{W}^h(\Omega^e)]^{\mathtt{m_{sd}}} \times \mathcal{W}^h(\Omega^e(t)) \times [\mathcal{W}^h(\Omega^e(t))]^{\mathtt{n_{sd}}}$ for $e = 1, \dots, \mathtt{n_{el}}$ such that

$$
\begin{aligned}
&-(\boldsymbol{W}, \boldsymbol{L})_{\Omega^e(t)} + \left(\boldsymbol{\nabla}_{\mathtt{S}}^T \mathbf{D}^{1/2} \boldsymbol{W}, \frac{\boldsymbol{\rho v}}{\rho}\right)_{\Omega^e(t)} = \\
&\qquad \left\langle \mathbf{N}^T \mathbf{D}^{1/2} \boldsymbol{W}, \frac{\boldsymbol{\rho v}^D}{\rho^D} \right\rangle_{\partial\Omega^e(t) \cap \Gamma^D(t)} + \left\langle \mathbf{N}^T \mathbf{D}^{1/2} \boldsymbol{W}, \frac{\widehat{\boldsymbol{\rho v}}}{\hat{\rho}} \right\rangle_{\partial\Omega^e(t) \setminus \Gamma^D(t)},
\end{aligned}
\tag{3.41a}
$$

$$
\begin{aligned}
&\left(w, \frac{\partial \rho}{\partial t}\right)_{\Omega^e(t)} + \left(w, \rho \boldsymbol{\nabla} \cdot \frac{d\boldsymbol{d}}{dt}\right)_{\Omega^e(t)} - \left(\boldsymbol{\nabla} w, \boldsymbol{\rho v} - \rho \frac{d\boldsymbol{d}}{dt}\right)_{\Omega^e(t)} + \langle w, \tau_\rho \rho \rangle_{\partial\Omega^e(t)} = \\
&\qquad - \left\langle w, \left(\boldsymbol{\rho v}^D - \rho^D \frac{d\boldsymbol{d}}{dt}\right) \cdot \boldsymbol{n} - \tau_\rho \rho^D \right\rangle_{\partial\Omega^e(t) \cap \Gamma^D(t)} \\
&\qquad - \left\langle w, \left(\widehat{\boldsymbol{\rho v}} - \hat{\rho} \frac{d\boldsymbol{d}}{dt}\right) \cdot \boldsymbol{n} - \tau_\rho \hat{\rho} \right\rangle_{\partial\Omega^e(t) \setminus \Gamma^D(t)},
\end{aligned}
\tag{3.41b}
$$

$$
\begin{aligned}
&\left(\boldsymbol{w}, \frac{\partial \boldsymbol{\rho v}}{\partial t}\right)_{\Omega^e(t)} + \left(\boldsymbol{w}, \boldsymbol{\rho v} \boldsymbol{\nabla} \cdot \frac{d\boldsymbol{d}}{dt}\right)_{\Omega^e(t)} - \left(\boldsymbol{\nabla} \boldsymbol{w}, \boldsymbol{\rho v} \otimes \left(\frac{\boldsymbol{\rho v}}{\rho} - \frac{d\boldsymbol{d}}{dt}\right)\right)_{\Omega^e(t)} \\
&\qquad + \left(\boldsymbol{w}, \boldsymbol{\nabla}_{\mathtt{S}}^T \left(\mathbf{D}^{1/2} \boldsymbol{L} + \mathbf{E} p(\rho)\right)\right)_{\Omega^e(t)} + \langle \boldsymbol{w}, \tau_{\rho v} \boldsymbol{\rho v} \rangle_{\partial\Omega^e(t)} - (\boldsymbol{w}, \rho \boldsymbol{b})_{\Omega^e(t)} = \\
&\qquad - \left\langle \boldsymbol{w}, \left[\boldsymbol{\rho v}^D \otimes \left(\frac{\boldsymbol{\rho v}^D}{\rho^D} - \frac{d\boldsymbol{d}}{dt}\right)\right] \boldsymbol{n} - \tau_{\rho v} \boldsymbol{\rho v}^D \right\rangle_{\partial\Omega^e(t) \cap \Gamma^D(t)} \\
&\qquad - \left\langle \boldsymbol{w}, \left[\widehat{\boldsymbol{\rho v}} \otimes \left(\frac{\widehat{\boldsymbol{\rho v}}}{\hat{\rho}} - \frac{d\boldsymbol{d}}{dt}\right)\right] \boldsymbol{n} - \tau_{\rho v} \widehat{\boldsymbol{\rho v}} \right\rangle_{\partial\Omega^e(t) \setminus \Gamma^D(t)},
\end{aligned}
\tag{3.41c}
$$

for all $(\boldsymbol{W}, w, \boldsymbol{w}) \in [\mathcal{W}^h(\Omega^e(t))]^{\mathtt{m_{sd}}} \times \mathcal{W}^h(\Omega^e(t)) \times [\mathcal{W}^h(\Omega^e(t))]^{\mathtt{n_{sd}}}$.

The weak form of the HDG global problem reads: find $(\hat{\rho}, \widehat{\boldsymbol{\rho v}}) \in \widehat{\mathcal{W}}^h(\Sigma(t)) \times [\widehat{\mathcal{W}}^h(\Sigma(t))]^{\mathtt{n_{sd}}}$ such that

$$
\sum_{e=1}^{\mathtt{n_{el}}} \langle \hat{w}, \tau_\rho (\rho - \hat{\rho}) \rangle_{\partial\Omega^e(t) \setminus \Gamma^D(t)} = 0,
\tag{3.42a}
$$

$$
\begin{aligned}
&- \sum_{e=1}^{\mathtt{n_{el}}} \left\langle \hat{\boldsymbol{w}}, \mathbf{N}^T \left(\mathbf{D}^{1/2} \boldsymbol{L} + \mathbf{E} p(\hat{\rho})\right) + \tau_{\rho v} (\boldsymbol{\rho v} - \widehat{\boldsymbol{\rho v}}) \right\rangle_{\partial\Omega^e(t) \setminus \Gamma^D(t)} = \\
&\qquad \sum_{e=1}^{\mathtt{n_{el}}} \langle \hat{\boldsymbol{w}}, \boldsymbol{t}^N \rangle_{\partial\Omega^e(t) \cap \Gamma^N(t)},
\end{aligned}
\tag{3.42b}
$$

for all $(\hat{w}, \hat{\boldsymbol{w}}) \in \widehat{\mathcal{W}}^h(\Sigma(t)) \times [\widehat{\mathcal{W}}^h(\Sigma(t))]^{\mathtt{n_{sd}}}$.

After linearization and discretization of the local problems by means of a isoparametric formulation, the increments of the local variables can be computed as function of the increments of the global variables within each NEWTON iteration through the solution of the linear system

$$\begin{bmatrix} \mathbf{K}_{LL} & \mathbf{K}_{L\rho} & \mathbf{K}_{Lw} \\ \mathbf{0} & \mathbf{K}_{\rho\rho} & \mathbf{K}_{\rho w} \\ \mathbf{K}_{wL} & \mathbf{K}_{w\rho} & \mathbf{K}_{ww} \end{bmatrix}_e \begin{bmatrix} \delta\mathbf{L} \\ \delta\boldsymbol{\rho} \\ \delta\mathbf{w} \end{bmatrix}_e = \begin{bmatrix} \mathbf{f}_L \\ \mathbf{f}_\rho \\ \mathbf{f}_w \end{bmatrix}_e - \begin{bmatrix} \mathbf{K}_{L\hat{\rho}} & \mathbf{K}_{L\hat{w}} \\ \mathbf{K}_{\rho\hat{\rho}} & \mathbf{K}_{\rho\hat{w}} \\ \mathbf{K}_{w\hat{\rho}} & \mathbf{K}_{w\hat{w}} \end{bmatrix}_e \begin{bmatrix} \delta\hat{\boldsymbol{\rho}} \\ \delta\hat{\mathbf{w}} \end{bmatrix}_e , \tag{3.43}$$

for $e = 1, \dots, \mathtt{n}^{\mathtt{el}}$, with $\mathbf{w}$ denoting the discrete momentum and $\hat{\mathbf{w}}$ its trace representation. The discretization of the global problem leads to the matrix problem

$$\sum_{e=1}^{\mathtt{n}^{\mathtt{el}}} \left\{ \begin{bmatrix} \mathbf{0} & \mathbf{K}_{\hat{\rho}\rho} & \mathbf{0} \\ \mathbf{K}_{\hat{w}L} & \mathbf{0} & \mathbf{K}_{\hat{w}w} \end{bmatrix}_e \begin{bmatrix} \delta\mathbf{L} \\ \delta\boldsymbol{\rho} \\ \delta\mathbf{w} \end{bmatrix}_e + \begin{bmatrix} \mathbf{K}_{\hat{\rho}\hat{\rho}} & \mathbf{0} \\ \mathbf{K}_{\hat{w}\hat{\rho}} & \mathbf{K}_{\hat{w}\hat{w}} \end{bmatrix}_e \begin{bmatrix} \delta\hat{\boldsymbol{\rho}} \\ \delta\hat{\mathbf{w}} \end{bmatrix}_e \right\} = \sum_{e=1}^{\mathtt{n}^{\mathtt{el}}} \begin{bmatrix} \mathbf{f}_{\hat{\rho}} \\ \mathbf{f}_{\hat{w}} \end{bmatrix}_e . \tag{3.44}$$

It is worth noting that the discretized problems (3.43) and (3.44) feature the same size of their counterparts in the velocity-pressure formulation presented in Section 3.3 and they differ in the physical meaning of the chosen unknowns and in the definition of the matrices and vectors, detailed in Appendix C. The global system of this density-momentum formulation (denoted by the subscript $\odot_{\mathtt{D-M}}$) resulting from the replacement of the local problems (3.43) in the global problem (3.44) can then be written as

$$\left[\mathbf{K}_{\mathtt{D-M}}\right] \left[\delta\widehat{\mathbf{U}}\right] = \left[\mathbf{f}_{\mathtt{D-M}}\right] , \tag{3.45}$$

with

$$\left[\mathbf{K}_{\mathtt{D-M}}\right] = \mathop{\mathsf{A}}_{e=1}^{\mathtt{n}^{\mathtt{el}}} \left\{ \left[\mathbf{K}_{\widehat{U}\widehat{U}}\right]_e - \left[\mathbf{K}_{\widehat{U}L} \quad \mathbf{K}_{\widehat{U}U}\right]_e \begin{bmatrix} \mathbf{K}_{LL} & \mathbf{K}_{LU} \\ \mathbf{K}_{UL} & \mathbf{K}_{UU} \end{bmatrix}_e^{-1} \begin{bmatrix} \mathbf{K}_{L\widehat{U}} \\ \mathbf{K}_{U\widehat{U}} \end{bmatrix}_e \right\}, \tag{3.46}$$

and

$$\left[\mathbf{f}_{\mathtt{D-M}}\right] = \mathop{\mathsf{A}}_{e=1}^{\mathtt{n}^{\mathtt{el}}} \left\{ \left[\mathbf{f}_{\widehat{U}}\right]_e - \left[\mathbf{K}_{\widehat{U}L} \quad \mathbf{K}_{\widehat{U}U}\right]_e \begin{bmatrix} \mathbf{K}_{LL} & \mathbf{K}_{LU} \\ \mathbf{K}_{UL} & \mathbf{K}_{UU} \end{bmatrix}_e^{-1} \begin{bmatrix} \mathbf{f}_{L} \\ \mathbf{f}_{U} \end{bmatrix}_e \right\}, \tag{3.47}$$

where the fluid density and momentum DOFs have been grouped in the variable $\mathbf{U} = \begin{bmatrix} \boldsymbol{\rho} & \mathbf{w} \end{bmatrix}^T$ for the sake of brevity.

The same postprocessing procedure of Section 3.3, with the right hand side velocity substituted by the ratio of the momentum and the density, allows to compute a superconvergent velocity field $\boldsymbol{v}^\star$. Its weak form reads: given $(\boldsymbol{L}, \rho, \boldsymbol{\rho v})$ in $\Omega^e(t)$, $(\rho^D, \boldsymbol{\rho v}^D)$ on $\Gamma^D(t)$ and $(\hat{\rho}, \widehat{\boldsymbol{\rho v}})$ on $\Sigma(t)$, find $\boldsymbol{v}^\star \in [\mathcal{W}^h_\star(\Omega^e(t))]^{\mathtt{n_{sd}}}$ for $e = 1, \dots, \mathtt{n}^{\mathtt{el}}$ such that

$$-\left(\boldsymbol{\nabla}_{\mathtt{S}}\boldsymbol{w}^\star, \mathbf{D}^{1/2}\boldsymbol{\nabla}_{\mathtt{S}}\boldsymbol{v}^\star\right)_{\Omega^e(t)} = \left(\boldsymbol{\nabla}_{\mathtt{S}}\boldsymbol{w}^\star, \boldsymbol{L}\right)_{\Omega^e(t)} , \tag{3.48a}$$

$$\left(\boldsymbol{u}_{\mathtt{T}}, \boldsymbol{v}^\star\right)_{\Omega^e(t)} = \left(\boldsymbol{u}_{\mathtt{T}}, \frac{\boldsymbol{\rho v}}{\rho}\right)_{\Omega^e(t)} , \tag{3.48b}$$

$$\begin{aligned} \left(\boldsymbol{u}_{\mathtt{R}}, \boldsymbol{\nabla}_{\mathtt{W}}\boldsymbol{v}^\star\right)_{\Omega^e(t)} &= \left\langle \boldsymbol{u}_{\mathtt{R}}, \mathbf{T}\frac{\boldsymbol{\rho v}^D}{\rho^D} \right\rangle_{\partial\Omega^e(t)\cap\Gamma^D(t)} \\ &+ \left\langle \boldsymbol{u}_{\mathtt{R}}, \mathbf{T}\frac{\widehat{\boldsymbol{\rho v}}}{\hat{\rho}} \right\rangle_{\partial\Omega^e(t)\setminus\Gamma^D(t)} , \end{aligned} \tag{3.48c}$$

for all $(\boldsymbol{w}^\star, \boldsymbol{u}_{\mathtt{T}}, \boldsymbol{u}_{\mathtt{R}}) \in [\mathcal{W}^h_\star(\Omega^e(t))]^{\mathtt{n_{sd}}} \times [\mathcal{U}^h(\Omega^e(t))]^{\mathtt{n_{sd}}} \times [\mathcal{U}^h(\Omega^e(t))]^{\mathtt{q_{sd}}}$.

3.5 Numerical examples

The numerical studies aim to assess the convergence properties of the proposed HDG formulations for weakly compressible flow problems. The first and the second numerical examples consider weakly compressible POISEUILLE and TAYLOR–COUETTE flows, respectively, for which analytical solutions are available in literature, offering the possibility to assess the convergence properties of the proposed formulations on physically meaningful settings. The last example is a purely artificial problem, whose solution is obtained through the method of manufactured solutions. Spatial and temporal convergence studies are carried out on both fixed and moving meshes, in order to verify the capability of the chosen method to solve fluid problems on deformable domains, which is crucial in the context of multiphysics problems. The HDG velocity-pressure formulation has been solely implemented in `MATLAB`, whereas the HDG density-momentum formulation has been implemented not only in `MATLAB`, but also in the research code `BACI` [167], to deal with larger problems in both two and three dimensions.

3.5.1 Weakly compressible POISEUILLE flow

The first numerical example considers a steady-state isothermal POISEUILLE flow of a weakly compressible NEWTONian fluid in a straight channel. This configuration is simulated by neglecting the time derivatives and the convective terms in the governing equations. HOUSIADAS and GEORGIOU [78] derived an analytical solution by representing the primary flow variables as asymptotic expansions of the compressibility coefficient, which is assumed to be a small parameter, and perturbing them with respect to that coefficient. The solution is then found up to the first order in ε. The authors considered also a pressure-dependent viscosity, but this feature is neglected here because unimportant in this context. The goal of this example is to investigate the convergence properties of the HDG formulations for weakly compressible flows and to assess their robustness with respect to the compressibility level on a simple and physically meaningful setting.

The analytical solution in terms of velocity and pressure reads

$$\begin{cases} v_x\left(x,y\right) = \dfrac{3}{2}U\left[1-\left(\dfrac{y}{R}\right)^2\right] \\ \qquad\qquad - \dfrac{9}{2}\dfrac{\mu L U^2}{\rho^{\mathtt{ref}} R^2}\left(1-\dfrac{x}{L}\right)\left[1-\left(\dfrac{y}{R}\right)^2\right]\varepsilon, \\ v_y\left(x,y\right) = 0, \\ p\left(x,y\right) = p^{\mathtt{ref}} + 3\dfrac{\mu L U}{R^2}\left(1-\dfrac{x}{L}\right) \\ \qquad\qquad - \dfrac{3}{2}\dfrac{\mu^2 U^2}{\rho^{\mathtt{ref}} R^2}\left\{3\left(\dfrac{L}{R}\right)^2\left(1-\dfrac{x}{L}\right)^2 - \left[1-\left(\dfrac{y}{R}\right)^2\right]\right\}\varepsilon, \end{cases} \tag{3.49}$$

with L and R denoting the length and the half-height of the channel, respectively, and U representing the mean velocity at the outflow. No body force is present in this pressure-driven flow, while a (small) residual of order $\mathcal{O}\left(\varepsilon^2\right)$ is added in the right hand side of the continuity equation

$$\mathcal{R}_{\mathrm{C}}\left(x,y\right) = \frac{27\mu^2U^3}{4\rho^{\mathtt{ref}}R^8}\left(R^2-y^2\right)\left\{6R^2\left(L-x\right) - \frac{\mu U}{\rho^{\mathtt{ref}}}\left[9\left(L-x\right)^2 - R^2 + y^2\right]\varepsilon\right\}\varepsilon^2. \tag{3.50}$$

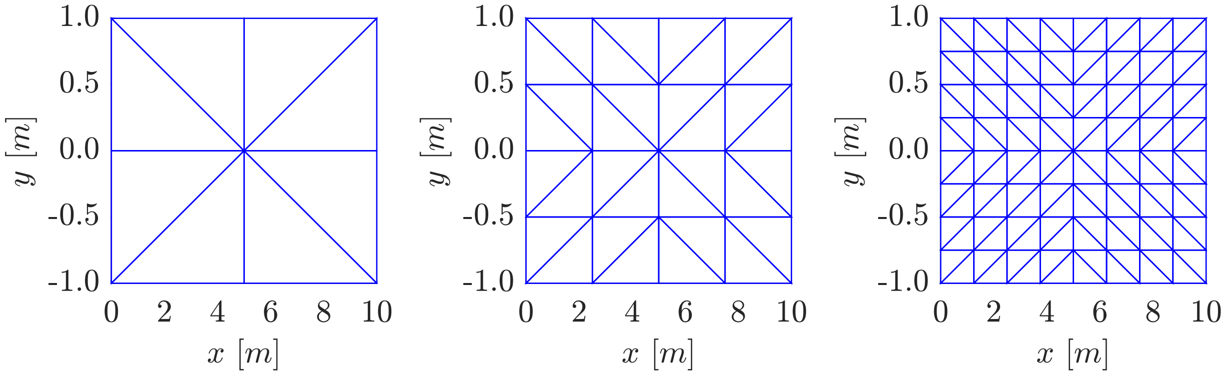

(a) First level of refinement (b) Second level of refinement (c) Third level of refinement

Figure 3.3: Computational mesh for weakly compressible POISEUILLE flow

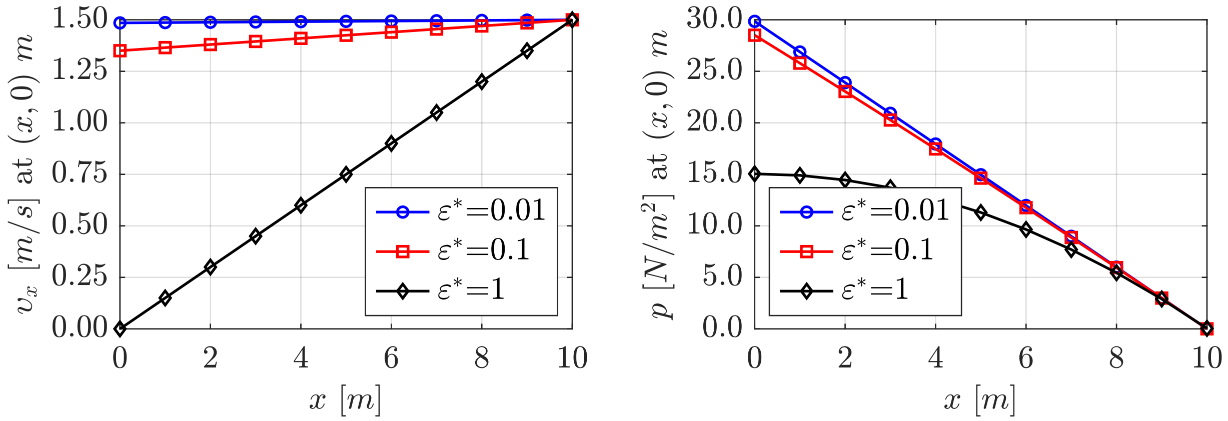

(a) Velocity (b) Pressure

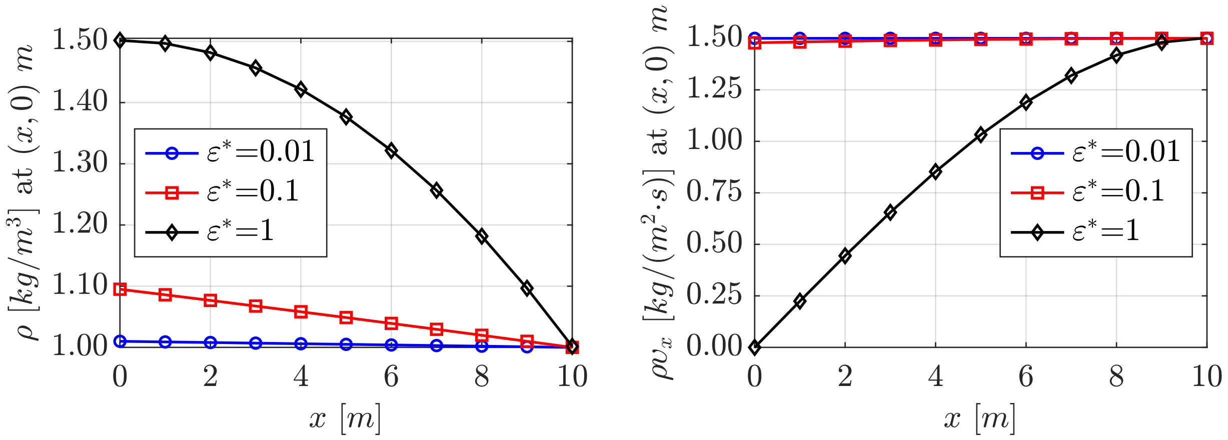

(c) Density (d) Momentum

Figure 3.4: Plot of velocity, pressure, density and momentum for weakly compressible POISEUILLE flow

Clearly, the classical incompressible POISEUILLE flow in a channel is fully recovered when the compressibility coefficient vanishes

$$\begin{cases} v_x^{\texttt{inc}}(x,y) = \dfrac{3}{2}U\left[1-\left(\dfrac{y}{R}\right)^2\right], \\ v_y^{\texttt{inc}}(x,y) = 0, \\ p^{\texttt{inc}}(x,y) = p^{\texttt{ref}} + 3\dfrac{\mu L U}{R^2}\left(1-\dfrac{x}{L}\right). \end{cases} \tag{3.51}$$

In the incompressible limit, the axial velocity assumes a simple parabolic profile in y-direction and it remains constant and equal to $1.5U$ along the x-axis. The pressure field varies linearly along the channel at reaches its reference value at the exit.

The computational domain is the rectangle $\Omega = (0, L) \times (-R, R)$ with $L = 10\ m$ and $R = 1\ m$. The analytical solution is derived by HOUSIADAS and GEORGIOU [78] applying no-slip and no-penetration boundary conditions along the walls at $y = \pm R$, considering a zero pressure value at the exit corners and enforcing a unit dimensionless mass flow rate at the outflow. In the following experiments however, solely DIRICHLET boundary conditions, corresponding to the restriction of the analytical solution (3.49) to the domain boundary, are imposed on $\Gamma^D = \partial\Omega$.

The mean velocity at the channel exit is considered as $U = 1\ m/s$, whereas the fluid viscosity is taken as $\mu = 1\ kg/(m \cdot s)$ and the reference density as $\rho^{\texttt{ref}} = 1\ kg/m^3$, evaluated at the reference pressure $p^{\texttt{ref}} = 0\ N/m^2$. A dimensionless compressibility coefficient can be defined as

$$\varepsilon^* = 3\frac{\mu L U}{\rho^{\texttt{ref}} R^2}\varepsilon. \tag{3.52}$$

To investigate the role of the compressibility level on the convergence of the HDG formulations, three different orders of magnitude are considered for the dimensionless compressibility coefficient, i.e. $\varepsilon^* = [0.01, 0.1, 1]$.

The evolution of the analytical primal variables along the horizontal axis is plotted in Figure 3.4 for the compressibility levels analyzed. The x-component of the velocity (Figure 3.4(a)) varies linearly and reaches by construction the value $1.5\ m/s$ at the outflow, corresponding to the mean velocity $U = 1\ m/s$. Regarding the pressure (Figure 3.4(b)), it decreases quadratically along the axis down to its reference value $p^{\texttt{ref}} = 0\ N/m^2$ at the exit corners. Moreover, the average pressure drop required to drive the flow decreases with the compressibility. In fact, the fluid pressure approaches the value of $30\ N/m^2$ at the inflow as $\varepsilon^* \to 0$, while it drops to about $15\ N/m^2$ for $\varepsilon^* = 1$. The density is then equal to its reference value $\rho^{\texttt{ref}} = 1\ kg/m^3$ at the exit corners and its variation along the channel obviously increases with the flow compressibility (Figure 3.4(c)). Finally, the axial momentum (Figure 3.4(d)) is nearly constant for sufficiently small compressibility coefficients. Clearly, the solution (3.49) has a physical meaning if the mass flow rate at the inflow is positive, hence $\varepsilon^* = 1$ constitutes an upper limit of validity for the solution itself in terms of the compressibility coefficient. Although this last case lacks physical meaningfulness, the performance of the HDG formulations is investigated for this extreme case too.

The meshes used for the spatial convergence studies are obtained by splitting a regular $2^r \times 2^r$ Cartesian grid, with r denoting the level of mesh refinement, into a total of $2 \cdot 2^{2r}$ triangles, giving element sizes of $h = L/2^r$. Figure 3.3 displays the first three meshes, contracted in the x-direction for compactness.

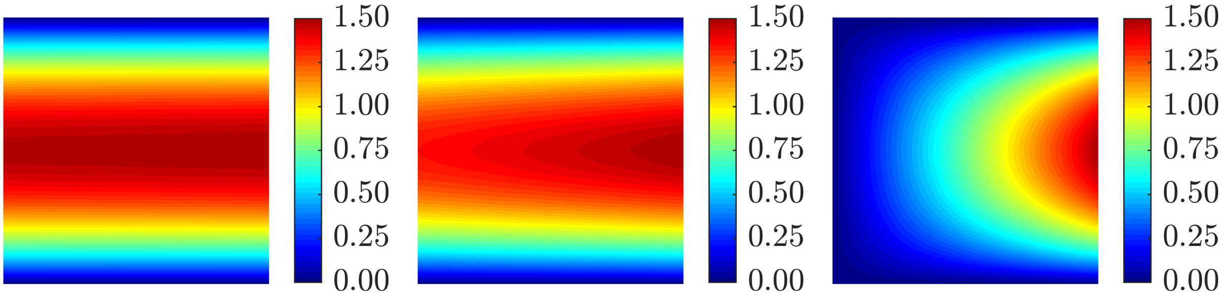

(a) Velocity with $\varepsilon^* = 0.01$ (b) Velocity with $\varepsilon^* = 0.1$ (c) Velocity with $\varepsilon^* = 1$

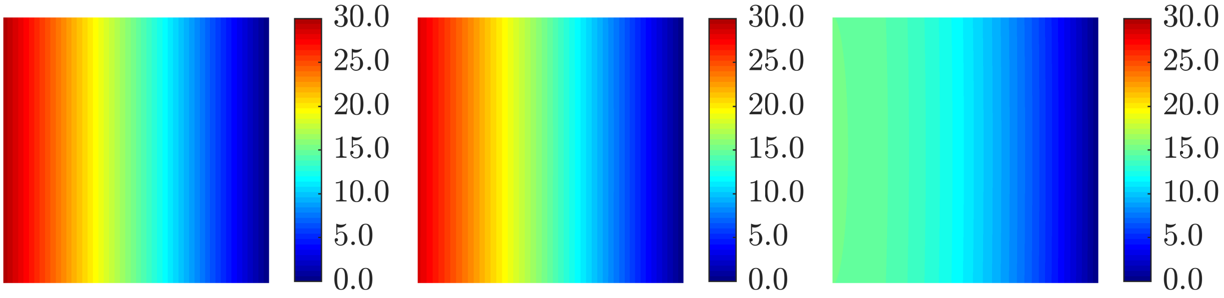

(d) Pressure with $\varepsilon^* = 0.01$ (e) Pressure with $\varepsilon^* = 0.1$ (f) Pressure with $\varepsilon^* = 1$

Figure 3.5: Solution of velocity and pressure for weakly compressible POISEUILLE flow via velocity-pressure formulation

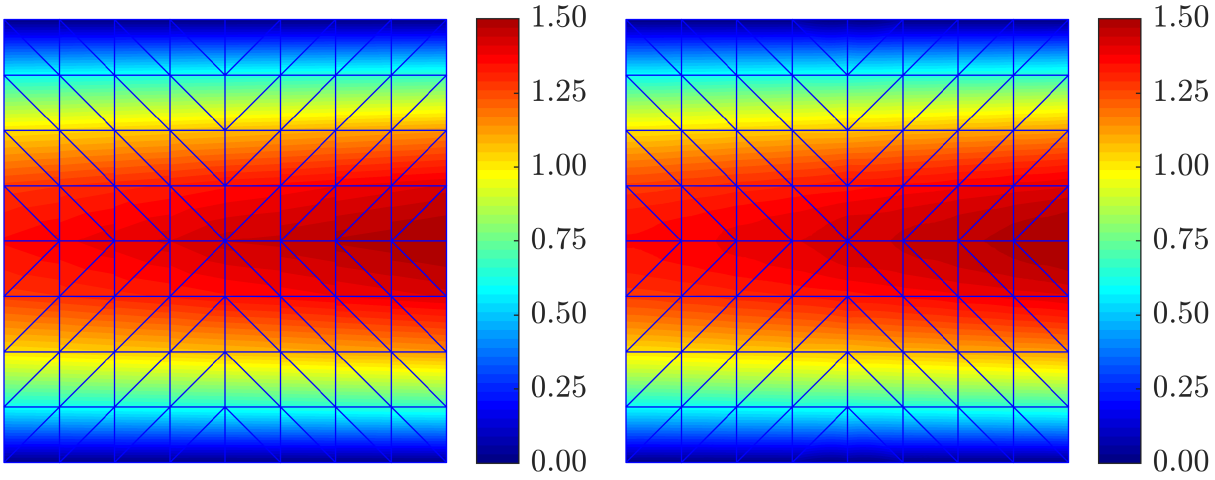

(a) Velocity with $\varepsilon^* = 0.1$ (b) Postprocessed velocity with $\varepsilon^* = 0.1$

Figure 3.6: Solution of velocity and postprocessed velocity for weakly compressible POISEUILLE flow via velocity-pressure formulation

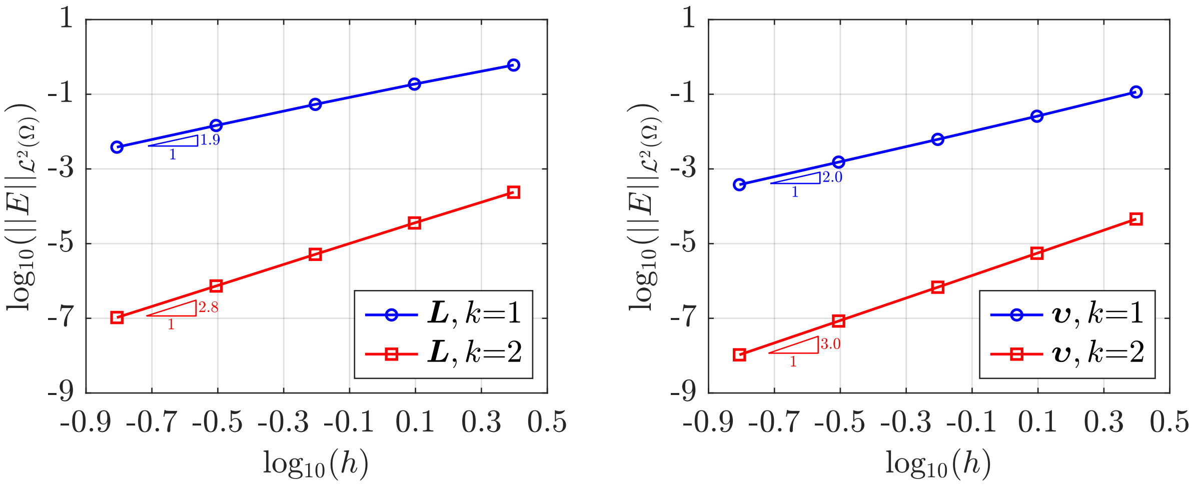

(a) Scaled strain rate (b) Velocity

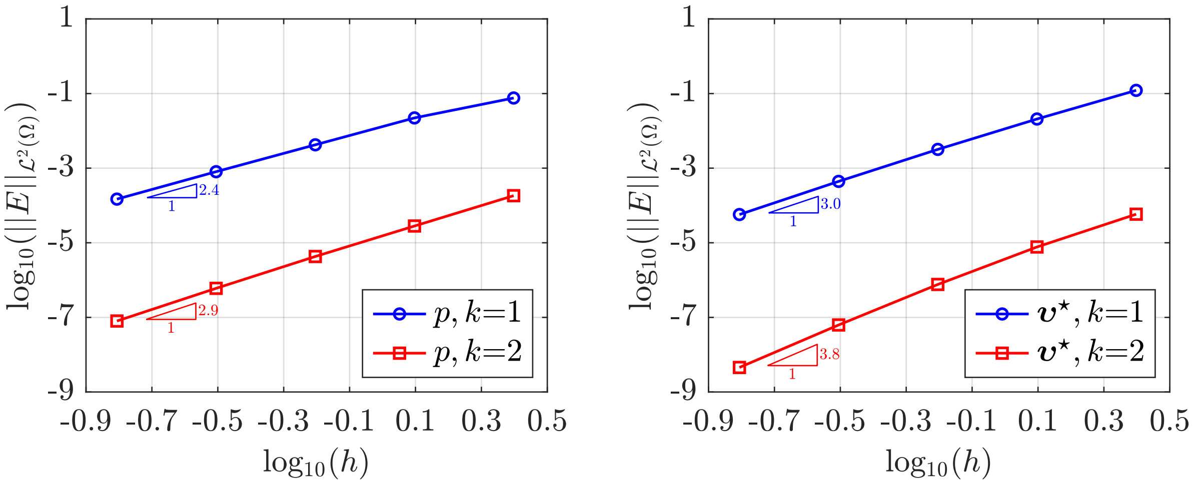

(c) Pressure (d) Postprocessed velocity

Figure 3.7: Spatial convergence study for weakly compressible POISEUILLE flow via velocity-pressure formulation with $\varepsilon^* = 0.01$

Two formulations are considered in the following:

1. HDG velocity-pressure formulation according to Section 3.3,
2. HDG density-momentum formulation according to Section 3.4.

The stabilization parameters adopted for the velocity-pressure formulation are computed according to (3.27), choosing $l = R$ as representative length scale and $|\boldsymbol{v}| = U$ as characteristic velocity and considering $C_v = 10$ and $C_p = 10$ as scaling factors, obtaining therefore $\tau_v = 10$ and $\tau_p = 10$. The polynomial degrees of approximation used in the spatial convergence studies are $k = [1, 2]$, whereas the levels of mesh refinement considered are $r = [2, 3, \ldots, 6]$. It is worth noting that the analytical solution in terms of velocity and pressure (3.49) belongs to the space of cubic polynomials $\mathcal{P}^3(\Omega)$, hence the analytical solution is fully recovered up to machine precision for any $k \geq 3$. The solution of the velocity and the pressure obtained with $r = 5$ and $k = 2$

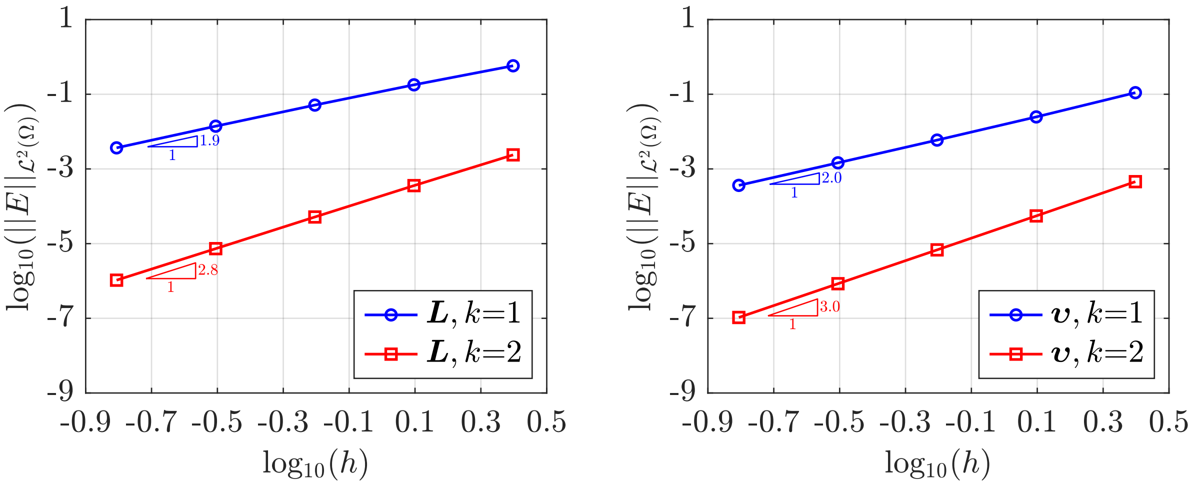

(a) Scaled strain rate (b) Velocity

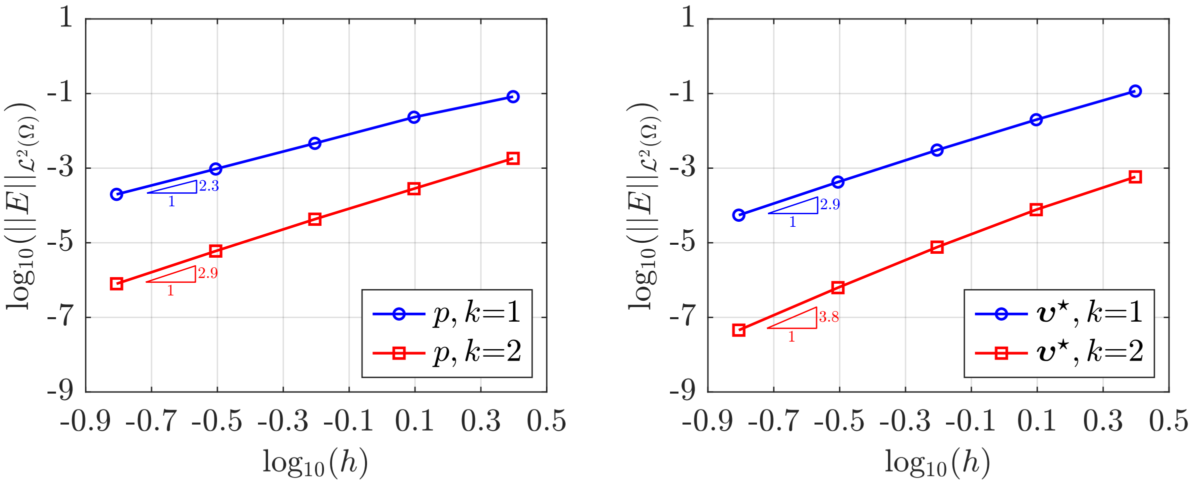

(c) Pressure (d) Postprocessed velocity

Figure 3.8: Spatial convergence study for weakly compressible POISEUILLE flow via velocity-pressure formulation with $\varepsilon^* = 0.1$

is displayed in Figure 3.5 for the various dimensionless compressibility coefficients considered. The velocity field is almost indistinguishable from the classical incompressible POISEUILLE flow when $\varepsilon^* = 0.01$, whereas a variation in the magnitude along the horizontal axis is appreciable for $\varepsilon^* \geq 0.1$. In the limit case of $\varepsilon^* = 1$, the velocity field is completely unphysical and its value along the horizontal axis ranges from $0\ m/s$ at the inflow to $1.5\ m/s$ at the outflow. Regarding the pressure field, the variation along the channel is almost linear for $\varepsilon^* = 0.01$ and the quadratic behavior can be appreciated for higher dimensionless compressibility coefficients. The improvement of the approximation of the velocity field given by the local HDG postprocessing (3.35) is exemplarily shown in Figure 3.6 for the intermediate dimensionless compressibility coefficients ($\varepsilon^* = 0.1$) for a relatively coarse solution, i.e. $r = 3$ and $k = 1$. It can be observed how the discontinuities across the element boundaries, more evident close to the horizontal axis in Figure 3.6(a), are smoother with the quadratic representation of the postprocessed velocity in

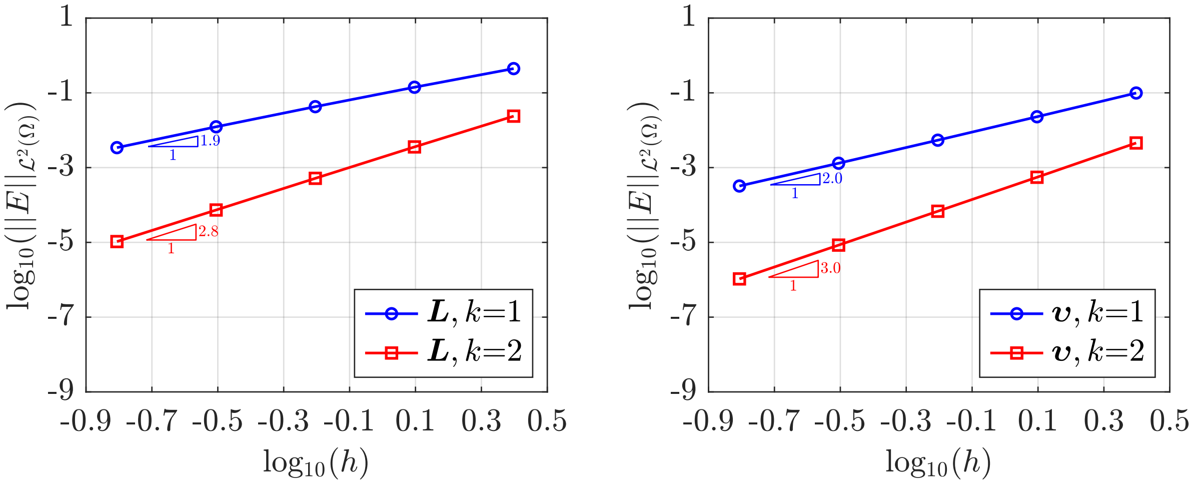

(a) Scaled strain rate

(b) Velocity

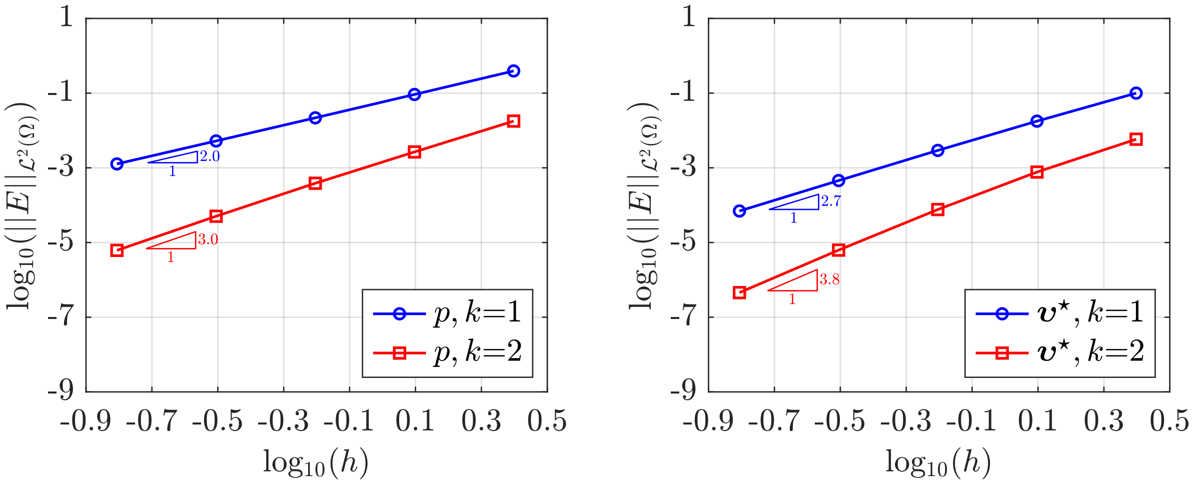

(c) Pressure

(d) Postprocessed velocity

Figure 3.9: Spatial convergence study for weakly compressible POISEUILLE flow via velocity-pressure formulation with $\varepsilon^* = 1$

Figure 3.6(b). The convergence of the absolute error measured in the $\mathcal{L}^2$ norm as a function of the characteristic element size h is reported in Figures 3.7, 3.8 and 3.9 for $\varepsilon^* = 0.01$, 0.1 and 1, respectively. Optimal convergence rates with order $k+1$ are obtained for the primal variables $\boldsymbol{v}$ and p for all the compressibility levels. The mixed variable $\boldsymbol{L}$ also convergences in an optimal fashion, thanks to the adoption of the VOIGT notation. As a matter of fact, a suboptimal behavior is observed for the mixed variable when its symmetry is satisfied only in a weak sense. Moreover, the optimal convergence of the mixed and the primal variables allows to construct a velocity field $\boldsymbol{v}^\star$ superconverging with order $k+2$, through the inexpensive local postprocessing in (3.35). It is worth noting that the velocity and the pressure errors decrease by orders of magnitude for $k \geq 2$ and $k \geq 1$, respectively, when approaching the incompressible limit, since $\boldsymbol{v}^{\texttt{inc}} \in \mathcal{P}^2(\Omega)$ and $p^{\texttt{inc}} \in \mathcal{P}^1(\Omega)$.

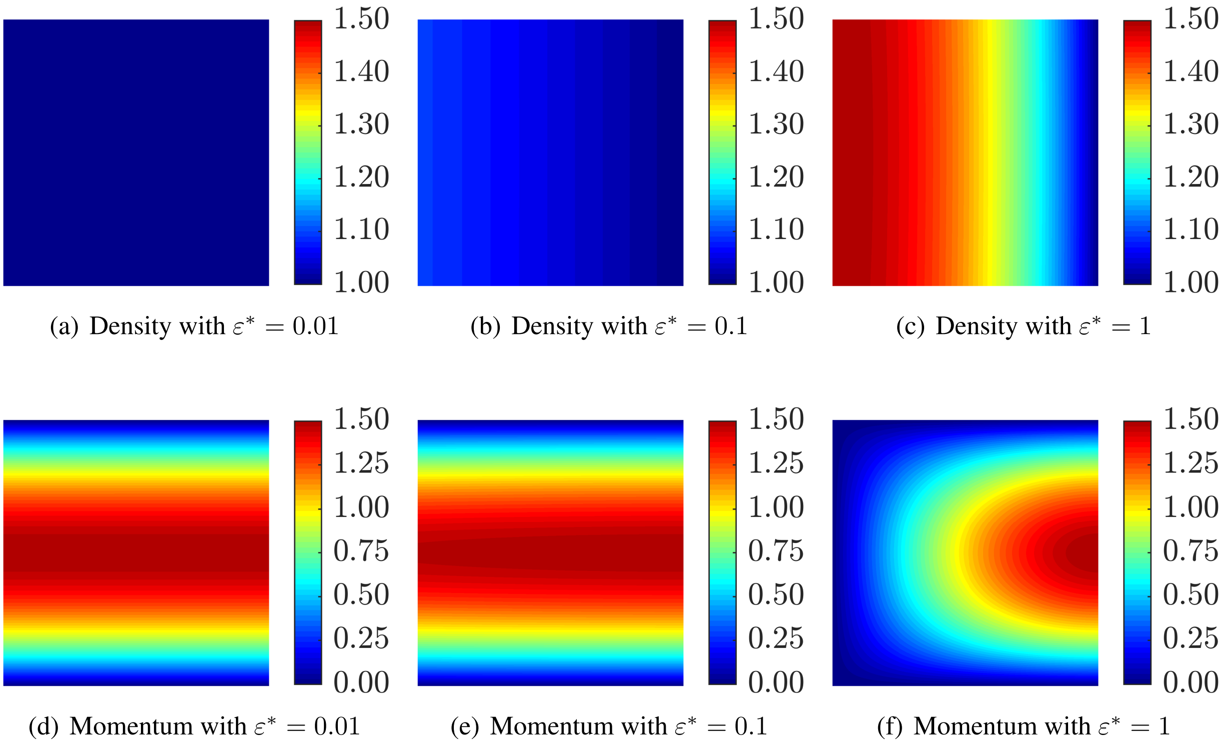

(a) Density with $\varepsilon^* = 0.01$ (b) Density with $\varepsilon^* = 0.1$ (c) Density with $\varepsilon^* = 1$

(d) Momentum with $\varepsilon^* = 0.01$ (e) Momentum with $\varepsilon^* = 0.1$ (f) Momentum with $\varepsilon^* = 1$

Figure 3.10: Solution of density and momentum for weakly compressible POISEUILLE flow via density-momentum formulation

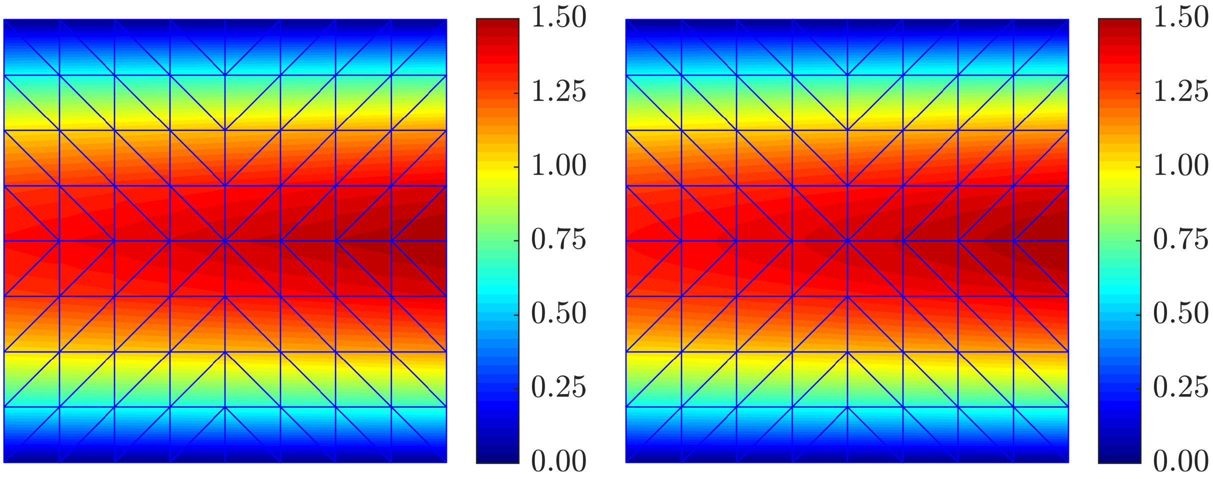

(a) Velocity with $\varepsilon^* = 0.1$ (b) Postprocessed velocity with $\varepsilon^* = 0.1$

Figure 3.11: Solution of velocity and postprocessed velocity for weakly compressible POISEUILLE flow via density-momentum formulation

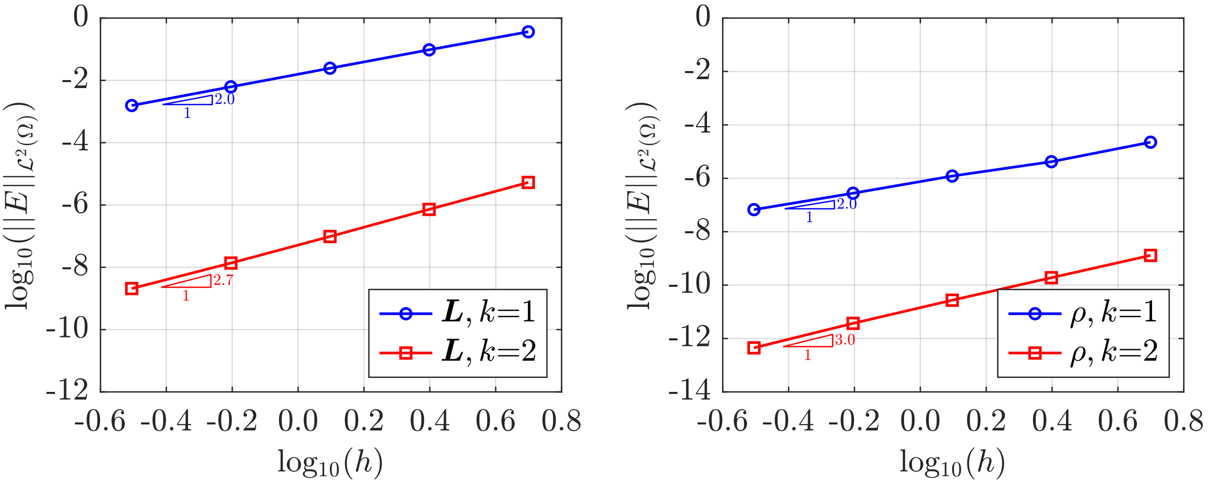

(a) Scaled strain rate

(b) Density

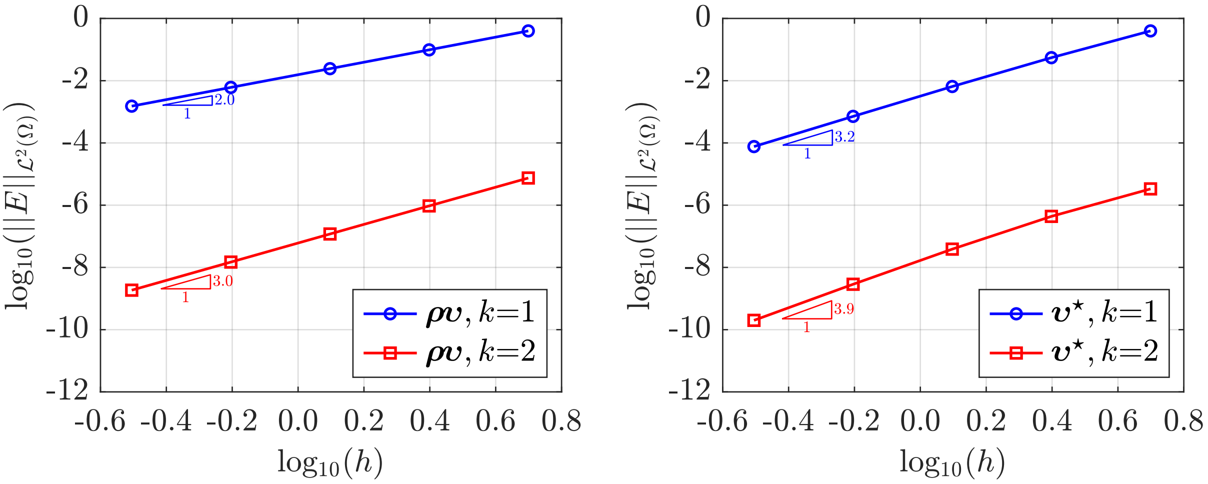

(c) Momentum

(d) Postprocessed velocity

Figure 3.12: Spatial convergence study for weakly compressible POISEUILLE flow via density-momentum formulation with $\varepsilon^* = 0.01$

The stabilization parameters adopted for the density-momentum formulation are computed according to (3.40), considering $C_\rho = 10/3$ and $C^d_{\rho v} = 1$ as scaling factors. It is worth highlighting that no stabilization of the convective part is needed, since no convection is taken into account in a POISEUILLE flow. This choice returns the stabilization parameters $\tau_\rho = 100/\varepsilon^*$ and $\tau_{\rho v} = 1$ for the density and the momentum, respectively. Variable ranges of polynomial degrees for the different compressibility coefficients are considered, in order to clearly visualize the convergence rates in the asymptotic regime by avoiding the errors to reach the machine precision for excessively coarse meshes. In fact, the solution belongs to the space of quadratic polynomials $\mathcal{P}^2(\Omega)$ in the incompressible limit when $\varepsilon^* \to 0$ (equation (3.51)). On the contrary, the pressure in (3.49) belongs to $\mathcal{P}^2(\Omega)$ for every $\varepsilon^* > 0$ and so does the density, according to the equation of state (3.2). The velocity in (3.49) belongs to $\mathcal{P}^3(\Omega)$ instead, hence the momentum belongs to $\mathcal{P}^5(\Omega)$, since it is computed as the product of the density and the velocity. As a consequence,

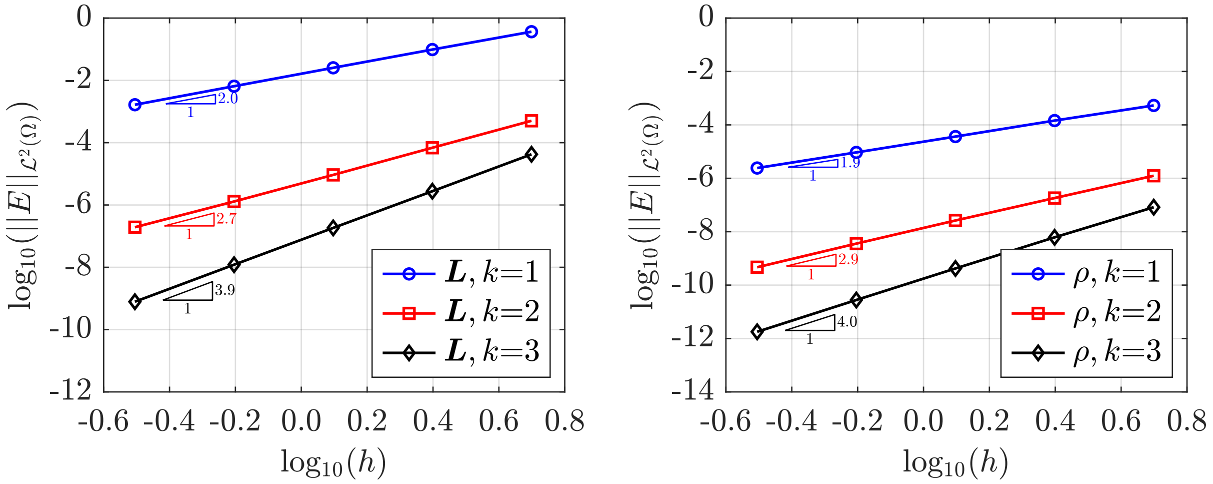

(a) Scaled strain rate
(b) Density

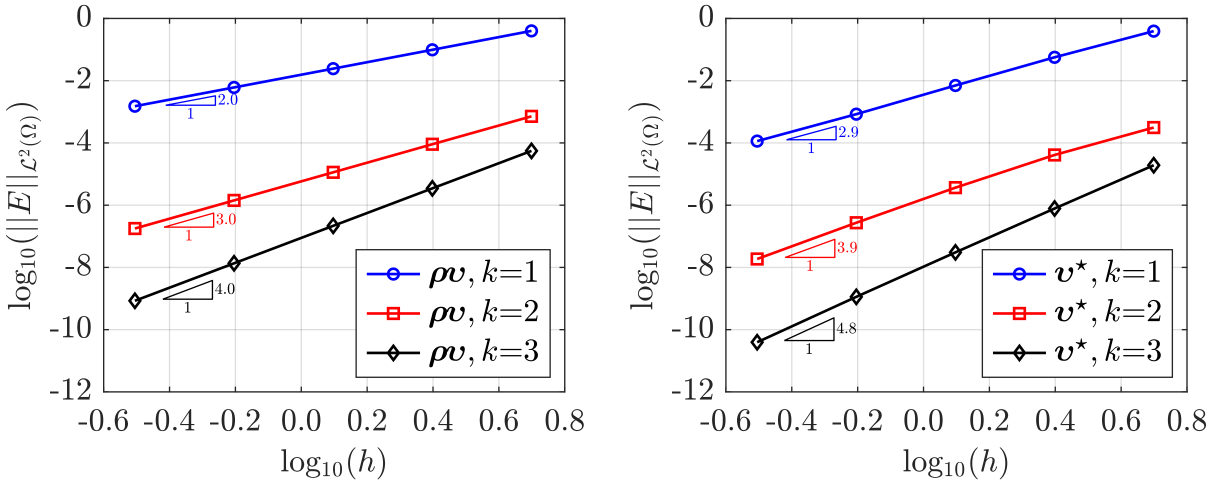

(c) Momentum
(d) Postprocessed velocity

Figure 3.13: Spatial convergence study for weakly compressible POISEUILLE flow via density-momentum formulation with $\varepsilon^* = 0.1$

the analytical solution is fully recovered up to machine precision for any $k \geq 5$, regardless of the compressibility coefficient. Therefore, the polynomial degrees of approximation used in the spatial convergence studies are $k = [1, 2]$ for $\varepsilon^* = 0.01$, $k = [1, 2, 3]$ for $\varepsilon^* = 0.1$ and $k = [1, 2, 3, 4]$ for $\varepsilon^* = 1$. The first five levels of mesh refinement are considered, i.e. $r = [1, 2, \ldots, 5]$. The solution of the density and the momentum obtained with $r = 5$ and $k = 2$ is displayed in Figure 3.10 for the various dimensionless compressibility coefficients considered. The density variation with respect to the reference value is about 1% for $\varepsilon^* = 0.01$, 10% for $\varepsilon^* = 0.1$ and 50% for $\varepsilon^* = 1$, in which the maximum value of the density reaches $1.5\ kg/m^3$. The momentum field is almost indistinguishable from the velocity field in Figure 3.5 for $\varepsilon^* = 0.01$, since the density is nearly constant. Similarly to what observed for the velocity-pressure formulation, the momentum field lacks physical meaningfulness for $\varepsilon^* = 1$. The velocity, obtained as the ratio of the momentum and the density, and the postprocessed velocity constructed by means

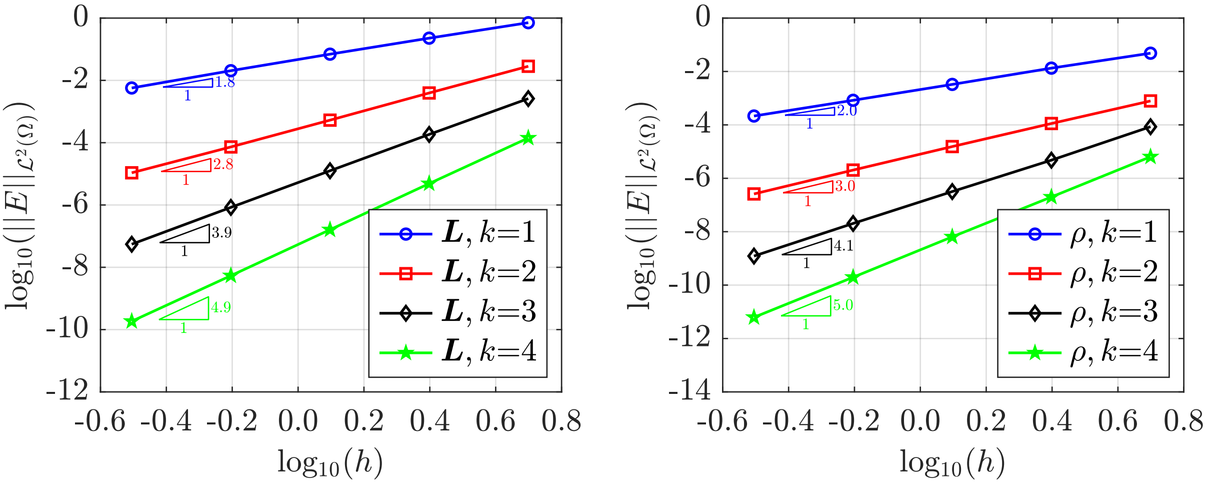

(a) Scaled strain rate

(b) Density

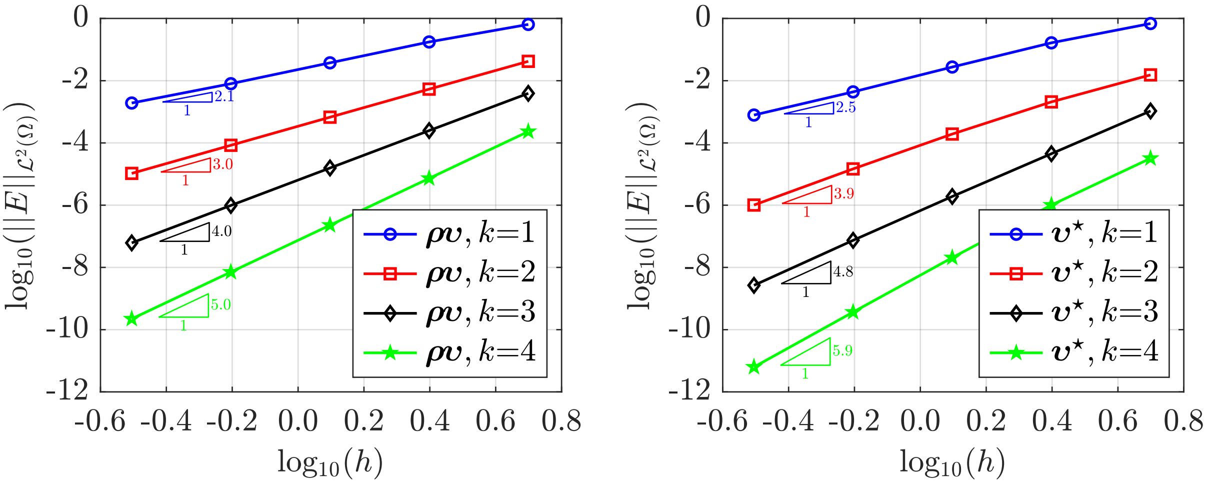

(c) Momentum

(d) Postprocessed velocity

Figure 3.14: Spatial convergence study for weakly compressible POISEUILLE flow via density-momentum formulation with $\varepsilon^* = 1$

of the local postprocessing (3.48) are compared in Figure 3.11 with the same settings adopted for the velocity-pressure formulation. The improvement of the solution is more remarkable than in the velocity-pressure formulation and the postprocessed velocity in Figure 3.11(b) computed on a coarse mesh is almost indistinguishable from the accurate velocity field in Figure 3.5(b). The convergence plots are shown in Figures 3.12, 3.13 and 3.14 for $\varepsilon^* = 0.01$, 0.1 and 1, respectively. As expected, the primal variables ρ and $\boldsymbol{\rho v}$ and the mixed variable $\boldsymbol{L}$ convergence optimally with order $k+1$, whereas the postprocessed velocity $\boldsymbol{v}^\star$ converges in a superoptimal fashion with order $k+2$. Analogously to the velocity-pressure formulation, the density and the momentum errors decrease by several orders of magnitude as $\varepsilon^* \rightarrow 0$ for $k \geq 0$ and $k \geq 2$, respectively, since $\rho^{\texttt{inc}} \equiv \rho^{\texttt{ref}} \in \mathcal{P}^0(\Omega)$ and $\boldsymbol{\rho v}^{\texttt{inc}} \equiv \rho^{\texttt{ref}} \boldsymbol{v}^{\texttt{inc}} \in \mathcal{P}^2(\Omega)$. Overall, both HDG formulations provide high-order accurate solutions and robust results with respect to the flow compressibility.

3.5.2 Weakly compressible TAYLOR–COUETTE flow

The second numerical example considers a weakly compressible TAYLOR–COUETTE flow. Its analytical solution has been derived by ROJAS FREDINI and LIMACHE [137] and adopted by the same authors to compare different smoothed particle hydrodynamics techniques. The goal of this example is to assess the convergence properties of the HDG density-momentum formulation in a three-dimensional setting.

The analytical solution in terms of velocity and pressure in cylindrical coordinates reads

$$\begin{cases} v_r\left(r,\theta,z\right) = 0, \\ v_\theta\left(r,\theta,z\right) = C_1\dfrac{1}{r} + C_2 r, \\ v_z\left(r,\theta,z\right) = 0, \\ p\left(r,\theta,z\right) = p^{\mathtt{ref}} + \dfrac{\rho^{\mathtt{ref}}}{\varepsilon}\left\{ e^{\varepsilon/2\left[C_1^2\left(1/r_1^2-1/r^2\right)+4C_1C_2\ln\left(r/r_1\right)+C_2^2\left(r^2-r_1^2\right)\right]} - 1\right\}, \end{cases} \tag{3.53}$$

where the coefficients C_1 and C_2 are given by

$$C_1 = -\frac{\left(\omega_2-\omega_1\right) r_2^2 r_1^2}{r_2^2 - r_1^2}, \qquad C_2 = \frac{\omega_2 r_2^2 - \omega_1 r_1^2}{r_2^2 - r_1^2}. \tag{3.54}$$

The parameters r_1 and r_2 denote the inner and outer radius of the rotating coaxial cylinders, respectively, whereas ω_1 and ω_2 refer to the corresponding angular velocities. No body force nor artificial residuals are added, since the provided solution exactly satisfies the governing equations. Moreover, as opposed to the previous example, both the weak compressibility and the convection are included in this flow configuration. The classical incompressible TAYLOR–COUETTE flow is recovered by taking the limit of (3.53) as the compressibility coefficient approaches zero

$$\begin{cases} v_r^{\mathtt{inc}}\left(r,\theta,z\right) = 0, \\ v_\theta^{\mathtt{inc}}\left(r,\theta,z\right) = C_1\dfrac{1}{r} + C_2 r, \\ v_z^{\mathtt{inc}}\left(r,\theta,z\right) = 0, \\ p^{\mathtt{inc}}\left(r,\theta,z\right) = p^{\mathtt{ref}} + \dfrac{\rho^{\mathtt{ref}}}{2}\left[C_1^2\left(\dfrac{1}{r_1^2}-\dfrac{1}{r^2}\right) + 4C_1C_2\ln\left(\dfrac{r}{r_1}\right) + C_2^2\left(r^2-r_1^2\right)\right]. \end{cases} \tag{3.55}$$

Interestingly, the compressibility level does not change the velocity field but it only affects the pressure profile. Moreover, the solutions (3.53) and (3.55) are not influenced by the viscosity.

The computational domain Ω is represented by a hollow cylinder with height $H = 4$, inner radius $r_1 = 1$ and outer radius $r_2 = 2$. The inner wall is considered fixed with $\omega_1 = 0$, while the outer wall rotates with angular velocity $\omega_2 = 1/2$. For the general case $\omega_1 \neq \omega_2$ considered here, the tangential velocity varies along the radial distance in a nonlinear fashion, whereas in the co-rotating case $\omega_1 = \omega_2$ the variation is linear and the flow assumes a rigid-like motion. DIRICHLET boundary conditions, corresponding to the analytical solution (3.53), are imposed on $\Gamma^D = \partial\Omega$. More precisely, the Cartesian components of the given solution are imposed and their values are computed through standard coordinate system transformations.

In the following simulations, the viscosity is $\mu = 1$ and the reference density $\rho^{\mathtt{ref}} = 1$, evaluated at the reference pressure $p^{\mathtt{ref}} = 0$, with a compressibility coefficient $\varepsilon = 0.1$.

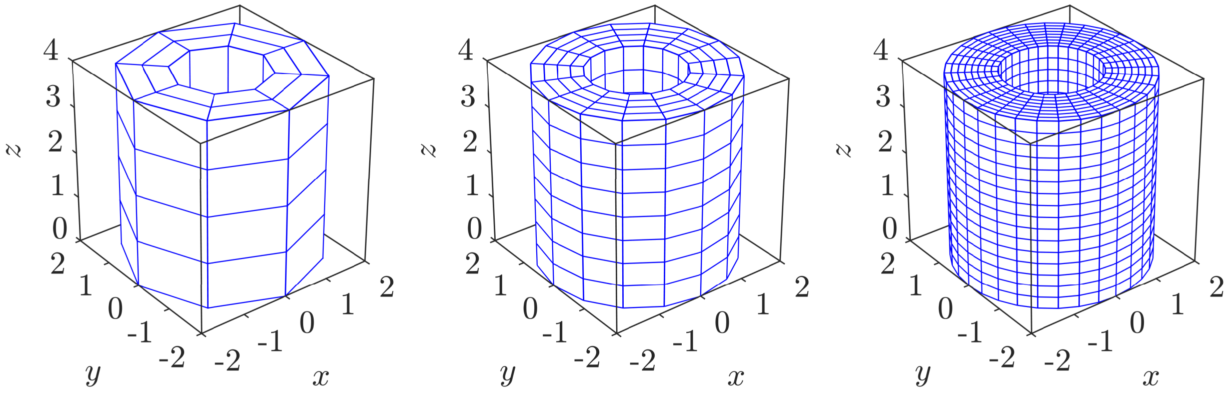

(a) First level of refinement (b) Second level of refinement (c) Third level of refinement

Figure 3.15: Computational mesh for weakly compressible TAYLOR–COUETTE flow

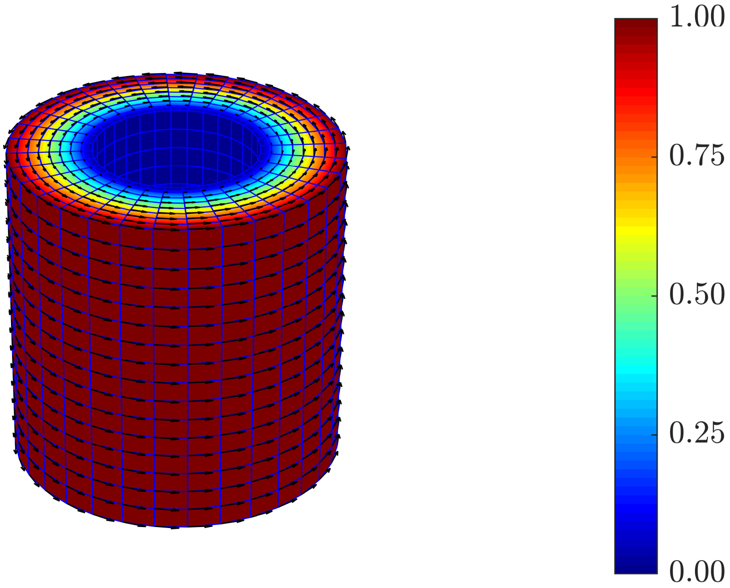

Figure 3.16: Solution of velocity for weakly compressible TAYLOR–COUETTE flow

Structured meshes are considered for the convergence study, by splitting the volume into a total number of 2^{3r+3} geometrically linear hexahedral elements, with r referring to the level of mesh refinement, obtaining a characteristic element size of $h = (r_2 - r_1)/2^r$. The first three levels of mesh refinement are shown in Figure 3.15. The polynomial degrees of approximation are $k = [1, 2]$, whereas the mesh levels are $r = [1, 2, \ldots, 5]$ for $k = 1$ and $r = [1, 2, \ldots, 4]$ for $k = 2$, for a maximum number of global DOFs close to 13000000. The stabilization parameters are considered constant and equal to $\tau_\rho = 100$ and $\tau_{\rho v} = 10$.

Figure 3.16 displays the velocity field computed with $r = 3$ and $k = 1$. Its magnitude ranges from 0 on the inner wall to 1 on the outer wall, whereas the weak compressibility induces a maximum density variation of about 2%. Finally, Figure 3.17 shows the optimal convergence of the fluid unknowns in the $\mathcal{L}^2$ norm, confirming the capability of the proposed formulation to accurately solve also three-dimensional problems.

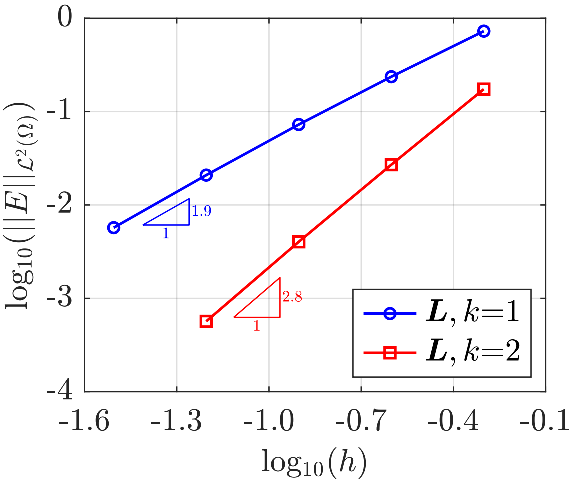

(a) Scaled strain rate

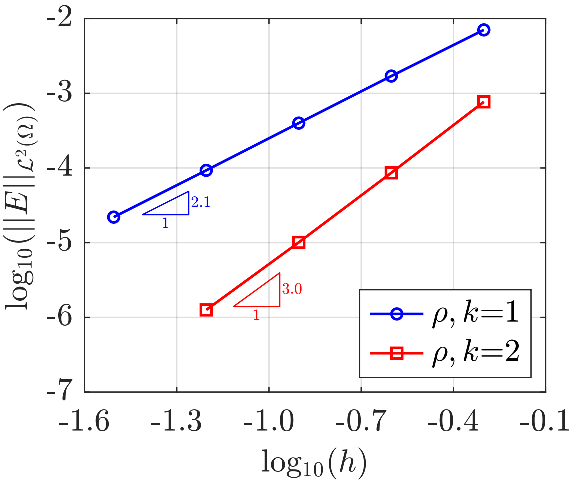

(b) Density

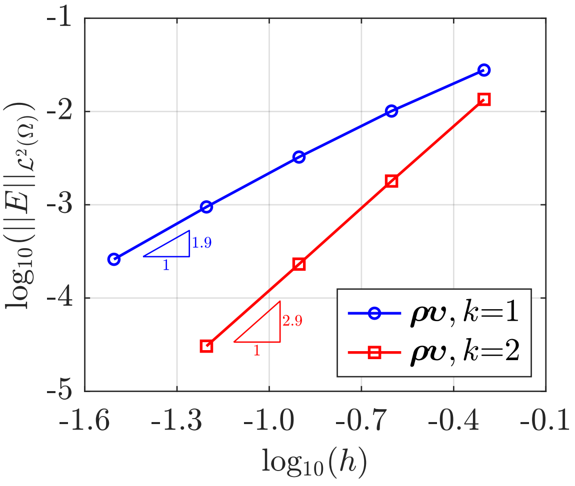

(c) Momentum

Figure 3.17: Spatial convergence study for weakly compressible TAYLOR–COUETTE flow

3.5.3 Fluid problem with manufactured solution

This numerical example considers a two-dimensional weakly compressible flow with analytical solution. The solution is generated through the method of manufactured solutions and it is built in such a way that all the terms included in the fluid partial differential equations (3.38) are exercised, including the time-dependent terms. Moreover, this solution tackles all nonlinearities, i.e. the convection and the weak compressibility. The main goal of this example is to assess the spatial and temporal convergence properties of the HDG density-momentum formulation in a general setting and to make sure that the deformation of the fluid mesh, according to the ALE representation of the motion, does not deteriorate the convergence rates of the fluid unknowns.

The analytical solution in terms of velocity and pressure reads

$$\begin{cases} v_x(x,y,t) = \sin(\pi x)\sin(\pi y)\sin(\pi t) \\ \qquad\qquad - \dfrac{\pi}{8\rho^{\mathtt{ref}}}\left[4\sin(\pi x)\sin(\pi y)\cos(\pi t)\right. \\ \qquad\qquad\qquad \left. + \left(\sin(2\pi x) + 2\pi x\cos(2\pi y)\right)\sin^2(\pi t)\right]\varepsilon, \\ v_y(x,y,t) = \cos(\pi x)\cos(\pi y)\sin(\pi t) \\ \qquad\qquad + \dfrac{\pi}{8\rho^{\mathtt{ref}}}\left[4\cos(\pi x)\cos(\pi y)\cos(\pi t)\right. \\ \qquad\qquad\qquad \left. - \left(\sin(2\pi y) + 2\pi y\cos(2\pi x)\right)\sin^2(\pi t)\right]\varepsilon, \\ p(x,y,t) = \pi\cos(\pi x)\sin(\pi y)\sin(\pi t)\,. \end{cases} \tag{3.56}$$

It is obtained by adding to the divergence-free velocity field in

$$\begin{cases} v_x^{\mathtt{inc}}(x,y,t) = \sin(\pi x)\sin(\pi y)\sin(\pi t)\,, \\ v_y^{\mathtt{inc}}(x,y,t) = \cos(\pi x)\cos(\pi y)\sin(\pi t)\,, \\ p^{\mathtt{inc}}(x,y,t) = \pi\cos(\pi x)\sin(\pi y)\sin(\pi t)\,, \end{cases} \tag{3.57}$$

specific $\mathcal{O}(\varepsilon)$ terms, such that the residual of the continuity equation in (3.38) is of order $\mathcal{O}(\varepsilon^2)$

$$\begin{aligned} \mathcal{R}_{\mathtt{C}}(x,y,t) = \Bigg\{ & \frac{\pi^3}{8\rho^{\mathtt{ref}}}\sin(\pi x)\sin(\pi y)\sin(\pi t) \\ & \cdot\left[4\sin(\pi x)\sin(\pi y)\cos(\pi t) + \left(\sin(2\pi x) + 2\pi x\cos(2\pi y)\right)\sin^2(\pi t)\right] \\ & + \frac{\pi^3}{8\rho^{\mathtt{ref}}}\cos(\pi x)\cos(\pi y)\sin(\pi t) \\ & \cdot\left[4\cos(\pi x)\cos(\pi y)\cos(\pi t) - \left(\sin(2\pi y) + 2\pi y\cos(2\pi x)\right)\sin^2(\pi t)\right] \\ & + \frac{\pi^2}{\rho^{\mathtt{ref}}}\left(p^{\mathtt{ref}} - \pi\cos(\pi x)\sin(\pi y)\sin(\pi t)\right) \\ & \cdot\left[\cos(\pi x)\sin(\pi y)\cos(\pi t) + \left(\cos^2(\pi x) + \cos^2(\pi y) - 1\right)\sin^2(\pi t)\right] \Bigg\}\,\varepsilon^2. \end{aligned} \tag{3.58}$$

Of course, if $\varepsilon = 0$, the incompressible solution (3.57) is recovered and the residual (3.58) vanishes. In order to cancel out any imbalance, a proper body force is then added in the right hand side of the momentum equation in (3.38). The computation of this term is technical and the symbolic toolbox of `MATLAB` is used for this purpose.

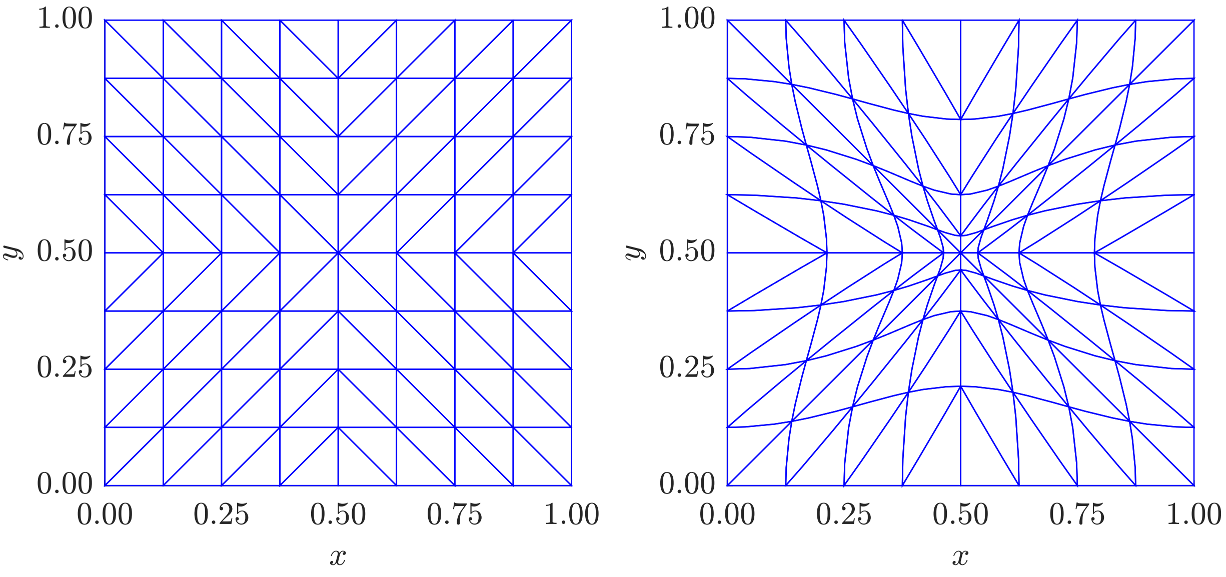

(a) Fixed mesh (b) Moving mesh at $t = 0.5$

Figure 3.18: Computational mesh for fluid problem with manufactured solution

The domain is the unit square $\Omega = (0,1) \times (0,1)$ and the initial conditions in $\Omega \times (0)$ and the boundary conditions imposed on $\Gamma^D = \partial\Omega$ are computed from the analytical solution (3.56). In particular, the density is evaluated from the equation of state (3.2) using the expression of the pressure in (3.56), while the momentum field is obtained as the product of the density just derived and the velocity field in (3.56).

The reference density is taken as $\rho^{\mathtt{ref}} = 1$, evaluated at the reference pressure $p^{\mathtt{ref}} = 0$, whereas the viscosity is chosen as $\mu = 0.1$. The variation in the compressibility level is unimportant for the present numerical experiment and therefore a unique compressibility coefficient $\varepsilon = 0.1$ is considered in the convergence studies.

Uniform meshes of triangular elements are considered for the domain by splitting a regular $2^r \times 2^r$ Cartesian grid into a total of $2 \cdot 2^{2r}$ triangles, giving element sizes of $h = 1/2^r$. The time span under analysis is $t \in (0, 0.5)$ instead. The stabilization parameters for the density and the momentum are considered constant on all faces and equal to $\tau_\rho = 100$ and $\tau_{\rho v} = 1$, respectively. In order to validated the HDG formulation in the ALE form, two scenarios are considered:

1. the problem is solved on a fixed mesh,
2. the problem is solved on a moving mesh, whose displacement is prescribed according to

$$\begin{cases} d_x(x,y,t) = \dfrac{1}{4}\sin(2\pi x)\left[1-\cos(2\pi y)\right]\left[1-\cos(2\pi t)\right]\bar{d}, \\[2ex] d_y(x,y,t) = \dfrac{1}{4}\left[1-\cos(2\pi x)\right]\sin(2\pi y)\left[1-\cos(2\pi t)\right]\bar{d}, \end{cases} \tag{3.59}$$

with $\bar{d} = 1/8$. The third level of refinement of the fixed and the moving mesh at $t = 0.5$ is shown in Figure 3.18.

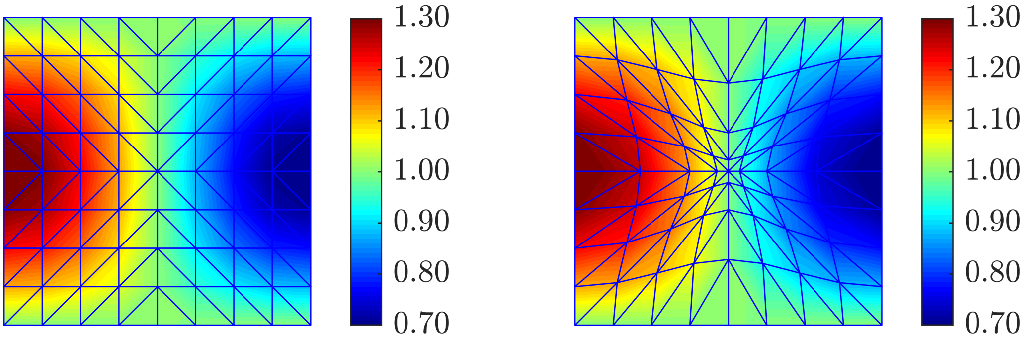

(a) Density ($k = 1$) on fixed mesh (b) Density ($k = 1$) on moving mesh

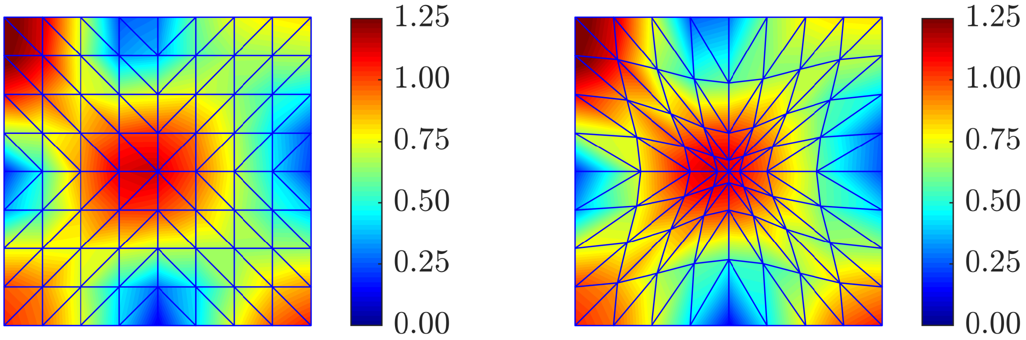

(c) Momentum ($k = 1$) on fixed mesh (d) Momentum ($k = 1$) on moving mesh

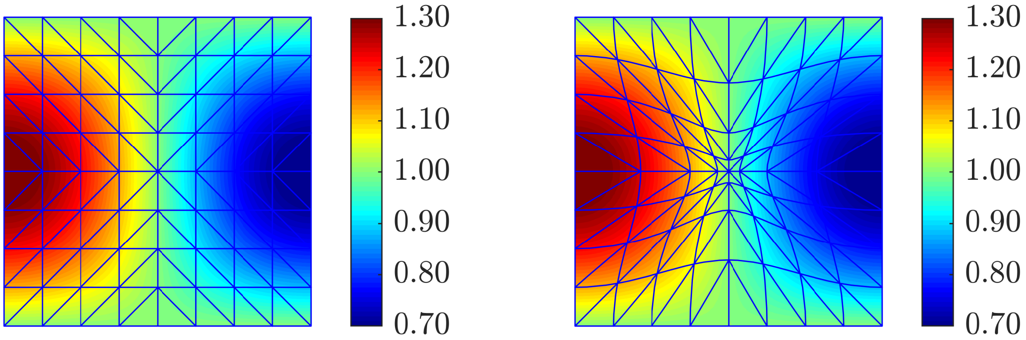

(e) Density ($k = 3$) on fixed mesh (f) Density ($k = 3$) on moving mesh

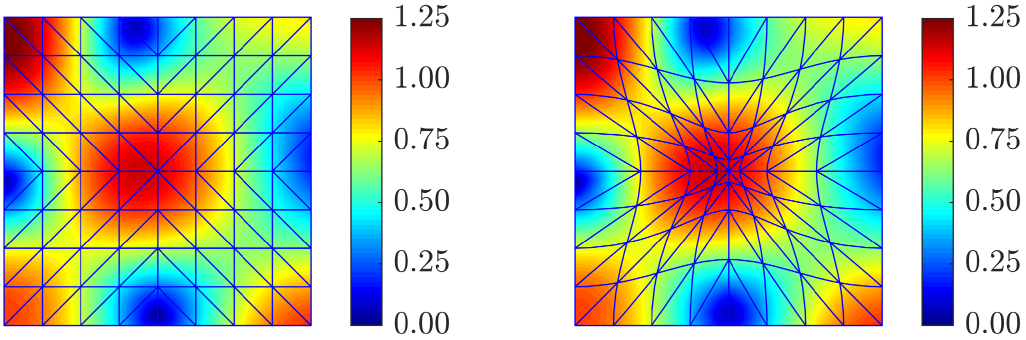

(g) Momentum ($k = 3$) on fixed mesh (h) Momentum ($k = 3$) on moving mesh

Figure 3.19: Solution of density and momentum for fluid problem with manufactured solution

The polynomial degrees considered for both the approximation of the fluid unknowns and the mesh displacement are $k = [1, 3, 5]$, whereas the integration in time is performed with the fourth order backward differentiation formula (BDF4). The level of mesh refinement considered is $r = [1, 2, \dots, 6]$ for $k = 1$, $r = [1, 2, \dots, 5]$ for $k = 3$ and $r = [1, 2, \dots, 4]$ for $k = 5$. This choice guarantees the achievement of the asymptotic regime in the spatial convergence. In order to keep the temporal error sufficiently small compared to the one associated to the spatial discretization, the time step sizes considered are $\Delta t = [2^{-5}, 2^{-7}, 2^{-9}]$ for $k = [1, 3, 5]$, respectively. The approximations of the density and the momentum fields obtained with $k = 1$ (top) and $k = 3$ (bottom) on the third level of mesh refinement for the fixed mesh (left) and the moving mesh (right) are shown in Figure 3.19. For the compressibility level considered, the maximum variation of the density from the reference value is about $\pm 30\%$. On the one hand, the improvement of the approximation of the solution when increasing the polynomial degree is clearly observed by comparing the solutions obtained with $k = 1$ and $k = 3$. On the other hand, no differences can be captured by comparing the plots on the left with the plots on the right for a sufficiently accurate solution, confirming the correct implementation of the ALE framework. The convergence of the error at the final simulation time in the $\mathcal{L}^2$ norm as a function of the characteristic element size h for the mixed and the primal variables is reported in Figure 3.20 for the first case (left) and the second case (right). As expected, the errors in the second case are systematically larger than the corresponding ones in the first case, since they are evaluated on distorted meshes. In particular, the errors differs by about 0.5, 1 and 2 orders of magnitude for the finest meshes used for k equal to 1, 3 and 5, respectively. However, the optimal convergence rate of $k + 1$ is nicely preserved in both cases. The capability of the method to retain the optimal convergence on moving meshes is a crucial feature in order to accurately solve fluid-structure interaction problems.

The temporal convergence studies are performed by discretizing the time span in a progressively increasing number of intervals. The time step sizes $\Delta t = [1/4, 1/8, \dots, 1/256]$ are therefore considered and the backward differentiation formulas are adopted, with the order BDFo ranging from 1 to 4. It is worth pointing out that, since no adaptive time stepping procedure has been implemented, the BDF schemes with BDF$o > 2$ are initialized by providing the analytical solution at the times $t = -n\Delta t$ with $n = [1, 2, \dots, \text{BDF}o - 1]$. Of course this is not possible for general problems, since analytical solutions are usually not available. The spatial discretization error is kept negligible compared to the temporal one, by choosing sufficiently fine meshes ($r = [3, 4, 5, 6]$ for BDF$o = [1, 2, 3, 4]$, respectively) with a polynomial degree of approximation $k = 5$. The $\mathcal{L}^2$ error of the mixed and the primal variables is shown in Figure 3.21 for the fixed mesh (left) and the moving mesh (right). Despite some differences in the error evolution, the theoretical convergence rates are observed for the two cases considered.

In conclusion, the proposed HDG density-momentum formulation accurately simulates fluid flows on arbitrary deforming domains with high-order accuracy and it will be henceforth employed for the solution of fluid-structure interaction problems with weakly compressible fluids.

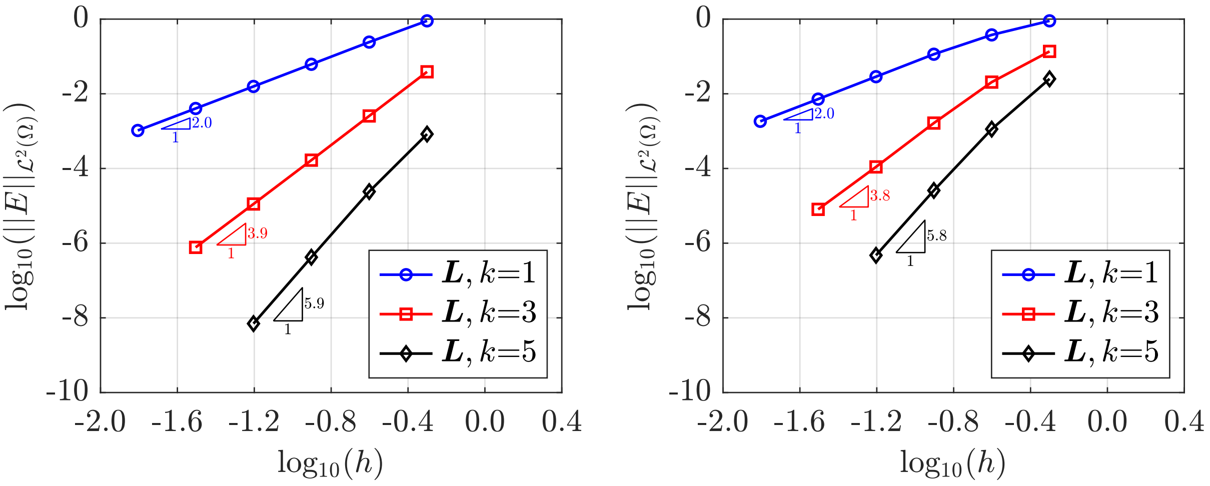

(a) Scaled strain rate on fixed mesh (b) Scaled strain rate on moving mesh

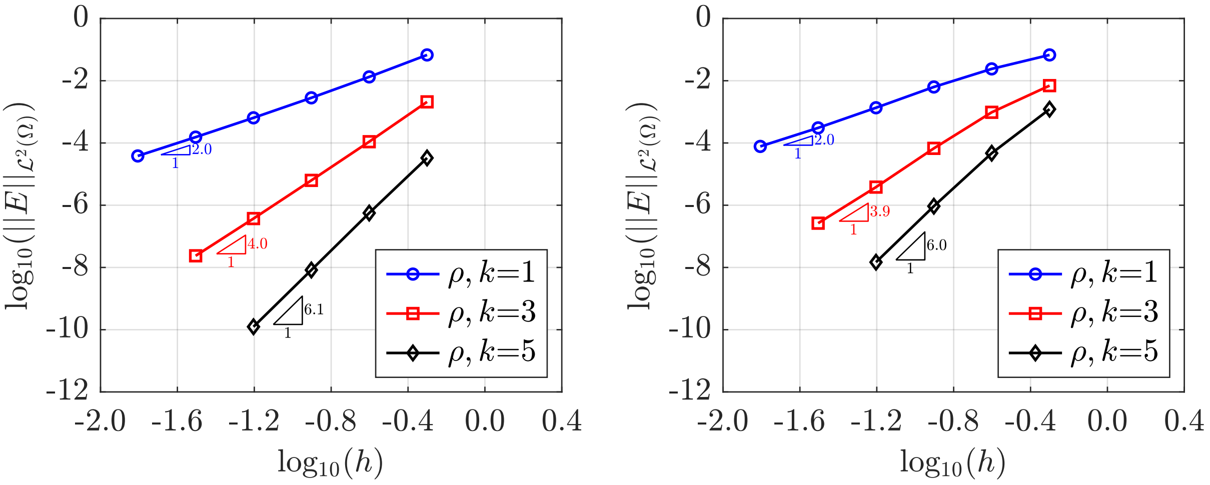

(c) Density on fixed mesh (d) Density on moving mesh

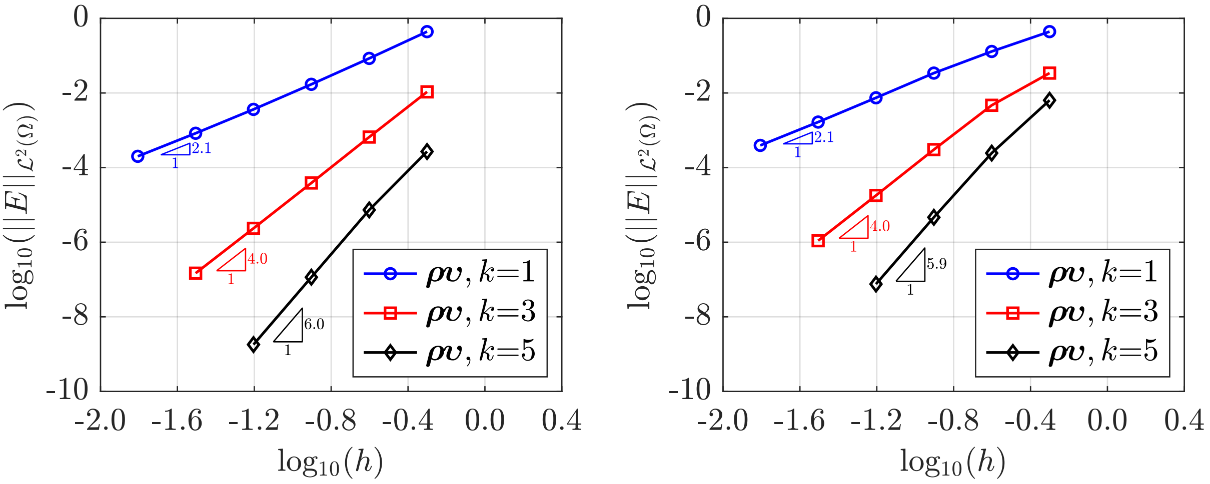

(e) Momentum on fixed mesh (f) Momentum on moving mesh

Figure 3.20: Spatial convergence study for fluid problem with manufactured solution

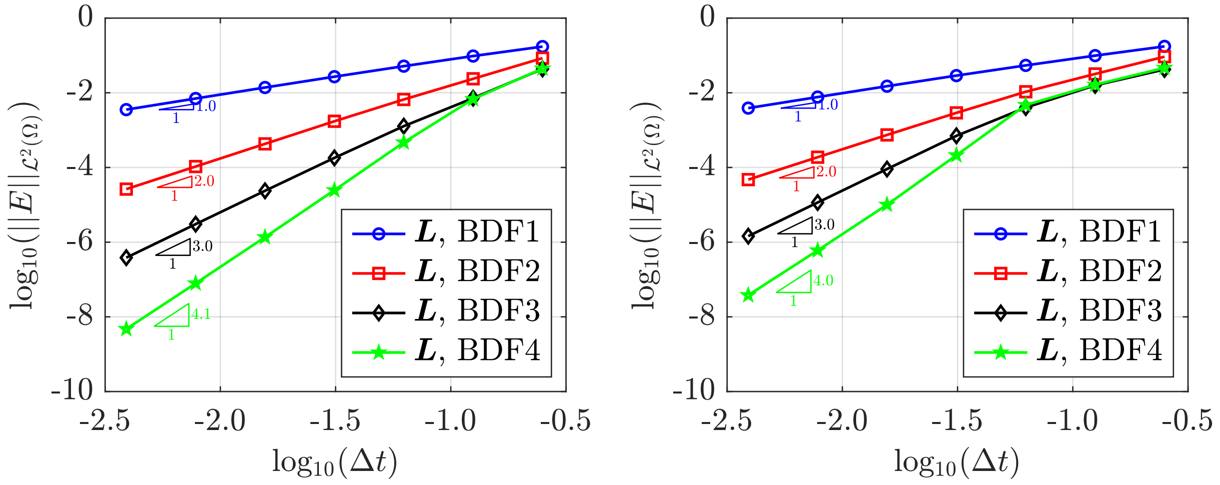

(a) Scaled strain rate on fixed mesh (b) Scaled strain rate on moving mesh

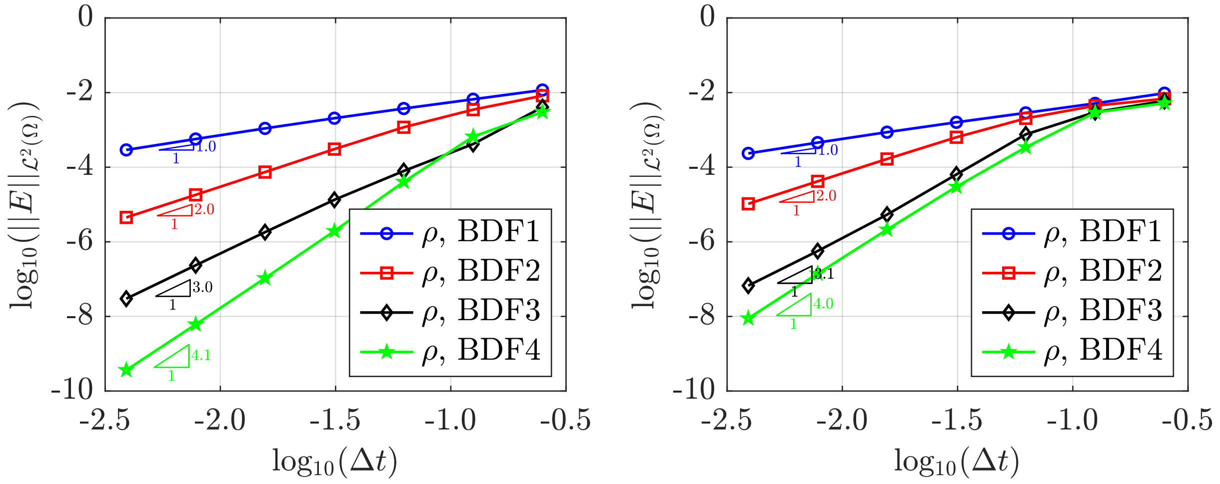

(c) Density on fixed mesh (d) Density on moving mesh

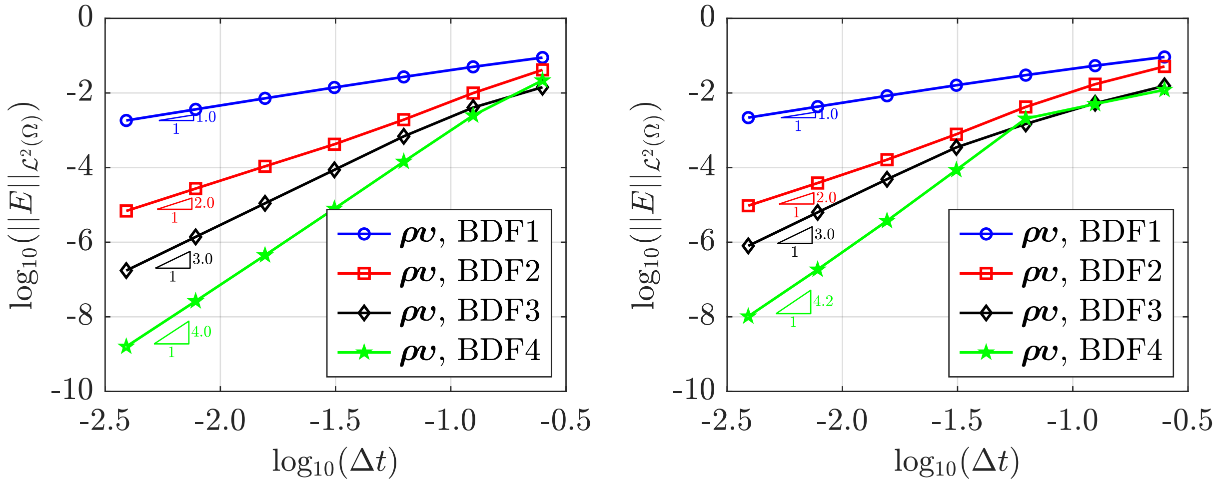

(e) Momentum on fixed mesh (f) Momentum on moving mesh

Figure 3.21: Temporal convergence study for fluid problem with manufactured solution

4 Coupling of HDG and CG discretizations

This chapter addresses the coupling of HDG and CG discretizations. Given the hybrid nature of the discretization, non-trivial strategies need to be devised. The design of efficient techniques for the coupling of HDG and CG methods constitutes a fundamental step towards the development of robust and efficient formulations for the simulation of fluid-structure interaction problems, which is the ultimate goal of this thesis. Given the complex nature of the equations governing weakly compressible fluid flows interacting with nonlinear elastic structures, the development of coupling strategies in the context of steady, linear and single-physics problems has been considered a fundamental checkpoint. On the one hand, POISSON's equation constitutes a classical prototype of linear elliptic PDEs and, owing to its computationally inexpensive nature, serves as a benchmark for the test of many numerical methods. On the other hand, the equations of linear elasticity allow to solve many problems of engineering interest. Moreover, the CG discretization of such equations simply stems from the linearised version of the equations adopted for the solid field in Chapter 2, whereas their HDG discretization presents several similarities with the formulation adopted for the simulation of weakly compressible flows in Chapter 3.

As already anticipated in the introduction, the CG method provides computationally efficient discretizations for moderate accuracy requirements, whereas the HDG method provides a flexible framework to construct high-order discretizations capable of efficiently exploiting parallel computing architectures and to devise adaptive strategies for nonuniform polynomial degree approximations. The coupling of such strategies is of special interest in the context of elastic problems featuring multiple materials with compressible and nearly incompressible behaviors, for which low-order displacement-based CG formulations fail to provide locking-free approximations. To remedy this issue, several approaches have been proposed such as mixed formulations by ARNOLD *et al.* [8], STENBERG [150] and ARNOLD and WINTHER [7], equilibrium formulations by DE ALMEIDA and MAUNDER [41] and the use of the nonconforming CROUZEIX–RAVIART element by CROUZEIX and RAVIART [40]. Moreover, the adoption of DG strategies has proven to be effective for the solution of (nearly) incompressible elasticity by HANSBO and LARSON [75], COCKBURN *et al.* [34] and BRAMWELL *et al.* [18], among others. Here, reliable solutions are obtained by adopting a HDG approximation in the nearly incompressible region, restricting the CG solver in the compressible part and coupling the two discretizations by means of NITSCHE's method.

The coupling of HDG and CG discretizations is performed in Section 4.1 for the solution of steady thermal problems with two distinct strategies. The proposed NITSCHE-based coupling is used for the solution of elasticity problems involving compressible and nearly incompressible materials in Section 4.2. The convergence properties and the advantages of the proposed coupling are assessed in the numerical examples in Section 4.3. The content of this chapter is mainly based on the work of LA SPINA *et al.* [96].

4.1 HDG-CG coupling for thermal problems

The coupling of HDG and CG discretizations is first presented in the context of thermal problems. The steady-state distribution of the temperature field T in a homogeneous medium Ω, characterized by a thermal conductivity κ and subjected to the heat source s, is described by the POISSON equation

$$\begin{cases} -\boldsymbol{\nabla} \cdot (\kappa \boldsymbol{\nabla} T) = s & \text{in } \Omega, \\ T = T^D & \text{on } \Gamma^D, \\ \kappa \boldsymbol{\nabla} T \cdot \boldsymbol{n} = f^N & \text{on } \Gamma^N. \end{cases} \tag{4.1}$$

The terms T^D and f^N denote the temperature and the thermal flux enforced on the DIRICHLET portion Γ^D and on the NEUMANN portion Γ^N of the domain boundary $\partial\Omega$, respectively. POISSON's equation is a second-order scalar elliptic partial differential equation and constitutes one of the most important equations in mathematics and engineering. Depending on the physical attributes of the variables involved, it can also be applied in other fields such as fluid dynamics, electromagnetism and astronomy. Both the HDG and CG approximation of the heat equation is presented in the following, together with two alternative HDG-CG coupling strategies.

4.1.1 HDG approximation

The HDG computational domain $\Omega_{\texttt{HDG}}$ is assumed to be partitioned in $\texttt{n}_{\texttt{HDG}}^{\texttt{el}}$ disjoint subdomains $\Omega_{\texttt{HDG}}^{e}$ such that

$$\Omega_{\texttt{HDG}} = \bigcup_{e=1}^{\texttt{n}_{\texttt{HDG}}^{\texttt{el}}} \Omega_{\texttt{HDG}}^{e}, \quad \Omega_{\texttt{HDG}}^{e} \cap \Omega_{\texttt{HDG}}^{f} = \emptyset \quad \text{for} \quad e \neq f. \tag{4.2}$$

Moreover, the union of the internal element boundaries constitutes the internal interface, i.e.

$$\Gamma_{\texttt{HDG}} = \left[\bigcup_{e=1}^{\texttt{n}_{\texttt{HDG}}^{\texttt{el}}} \partial\Omega_{\texttt{HDG}}^{e} \right] \setminus \partial\Omega_{\texttt{HDG}}, \tag{4.3}$$

and the union of the internal interface with the boundary faces belonging to $\Gamma_{\texttt{HDG}}^{N}$ constitutes the mesh skeleton, on which the hybrid variable is defined.

The strong form of the HDG problem is obtained by rewriting (4.1) over the broken computational domain as

$$\begin{cases} \boldsymbol{q}_{\texttt{HDG}} + \sqrt{\kappa} \boldsymbol{\nabla} T_{\texttt{HDG}} = \boldsymbol{0} & \text{in } \Omega_{\texttt{HDG}}^{e}, \\ \boldsymbol{\nabla} \cdot \left(\sqrt{\kappa} \boldsymbol{q}_{\texttt{HDG}} \right) = s & \text{in } \Omega_{\texttt{HDG}}^{e}, \\ T_{\texttt{HDG}} = T^D & \text{on } \partial\Omega_{\texttt{HDG}}^{e} \cap \Gamma_{\texttt{HDG}}^{D}, \\ T_{\texttt{HDG}} = \hat{T}_{\texttt{HDG}} & \text{on } \partial\Omega_{\texttt{HDG}}^{e} \setminus \Gamma_{\texttt{HDG}}^{D}, \\ -\sqrt{\kappa} \boldsymbol{q}_{\texttt{HDG}} \cdot \boldsymbol{n}_{\texttt{HDG}} = f^N & \text{on } \partial\Omega_{\texttt{HDG}}^{e} \cap \Gamma_{\texttt{HDG}}^{N}, \\ [\![T_{\texttt{HDG}} \boldsymbol{n}_{\texttt{HDG}}]\!] = \boldsymbol{0} & \text{on } \Gamma_{\texttt{HDG}}, \\ \left[\!\!\left[\widehat{\sqrt{\kappa} \boldsymbol{q}_{\texttt{HDG}} \cdot \boldsymbol{n}_{\texttt{HDG}}} \right]\!\!\right] = 0 & \text{on } \Gamma_{\texttt{HDG}}. \end{cases} \tag{4.4}$$

The variable $\boldsymbol{q}_{\texttt{HDG}}$ denotes the mixed variable, that allows to reduce the second-order problem to a system of first-order equations, whereas $\hat{T}_{\texttt{HDG}}$ is the hybrid variable, representing the trace of the solution on the mesh skeleton. The last two equations in (4.4) are the transmission conditions, ensuring the continuity of the solution and the equilibrium of the normal flux across the interface $\Gamma_{\texttt{HDG}}$. As already pointed out for the HDG formulations for weakly compressible flows in Chapter 3, the continuity of the solution is fulfilled in a weak sense by the uniqueness of the hybrid variable along the interface between two adjacent elements. An appropriate definition of the trace of the numerical normal flux is needed to handle the second condition. For pure HDG problems, it is considered

$$\widehat{\sqrt{\kappa}\boldsymbol{q}_{\texttt{HDG}} \cdot \boldsymbol{n}_{\texttt{HDG}}} = \begin{cases} \sqrt{\kappa}\boldsymbol{q}_{\texttt{HDG}} \cdot \boldsymbol{n}_{\texttt{HDG}} + \tau_T \left(T_{\texttt{HDG}} - T^D\right) & \text{on } \partial\Omega^e_{\texttt{HDG}} \cap \Gamma^D_{\texttt{HDG}}, \\ \sqrt{\kappa}\boldsymbol{q}_{\texttt{HDG}} \cdot \boldsymbol{n}_{\texttt{HDG}} + \tau_T \left(T_{\texttt{HDG}} - \hat{T}_{\texttt{HDG}}\right) & \text{on } \partial\Omega^e_{\texttt{HDG}} \setminus \Gamma^D_{\texttt{HDG}}, \end{cases} \tag{4.5}$$

with τ_T being a stabilization parameter, playing a crucial role on the stability and the convergence of the method. According to COCKBURN *et al.* [36], the optimal convergence of the HDG method for the POISSON equation is ensured by computing the stabilization parameter according to

$$\tau_T = C_T \frac{\kappa}{l}, \tag{4.6}$$

with C_T being a positive constant scaling factor and l denoting a representative length scale.

The weak form of the HDG approximation is then obtained by performing a single integration by parts on the mixed variable equation and a double integration by parts on the primal variable equation and exploiting the definition (4.5), as explained in the tutorial by SEVILLA and HUERTA [140]. The resulting local problem provides the expression of $(\boldsymbol{q}_{\texttt{HDG}}, T_{\texttt{HDG}})$ as a function of the unknown hybrid variable $\hat{T}_{\texttt{HDG}}$ and its weak form reads: given T^D on $\Gamma^D_{\texttt{HDG}}$ and $\hat{T}_{\texttt{HDG}}$ on $\Gamma_{\texttt{HDG}} \cup \Gamma^N_{\texttt{HDG}}$, find $(\boldsymbol{q}_{\texttt{HDG}}, T_{\texttt{HDG}}) \in [\mathcal{W}^h(\Omega^e_{\texttt{HDG}})]^{\texttt{n}_{\texttt{sd}}} \times \mathcal{W}^h(\Omega^e_{\texttt{HDG}})$ for $e = 1, \dots, \texttt{n}^{\texttt{el}}_{\texttt{HDG}}$ such that

$$\begin{aligned} &- \left(\boldsymbol{w}, \boldsymbol{q}_{\texttt{HDG}}\right)_{\Omega^e_{\texttt{HDG}}} + \left(\boldsymbol{\nabla} \cdot \left(\sqrt{\kappa}\boldsymbol{w}\right), T_{\texttt{HDG}}\right)_{\Omega^e_{\texttt{HDG}}} = \\ &\qquad \left\langle \sqrt{\kappa}\boldsymbol{w} \cdot \boldsymbol{n}_{\texttt{HDG}}, T^D \right\rangle_{\partial\Omega^e_{\texttt{HDG}} \cap \Gamma^D_{\texttt{HDG}}} + \left\langle \sqrt{\kappa}\boldsymbol{w} \cdot \boldsymbol{n}_{\texttt{HDG}}, \hat{T}_{\texttt{HDG}} \right\rangle_{\partial\Omega^e_{\texttt{HDG}} \setminus \Gamma^D_{\texttt{HDG}}}, \end{aligned} \tag{4.7a}$$

$$\begin{aligned} &\left(w, \boldsymbol{\nabla} \cdot \left(\sqrt{\kappa}\boldsymbol{q}_{\texttt{HDG}}\right)\right)_{\Omega^e_{\texttt{HDG}}} + \left\langle w, \tau_T T_{\texttt{HDG}} \right\rangle_{\partial\Omega^e_{\texttt{HDG}}} = \left(w, s\right)_{\Omega^e_{\texttt{HDG}}} \\ &\qquad + \left\langle w, \tau_T T^D \right\rangle_{\partial\Omega^e_{\texttt{HDG}} \cap \Gamma^D_{\texttt{HDG}}} + \left\langle w, \tau_T \hat{T}_{\texttt{HDG}} \right\rangle_{\partial\Omega^e_{\texttt{HDG}} \setminus \Gamma^D_{\texttt{HDG}}}, \end{aligned} \tag{4.7b}$$

for all $(\boldsymbol{w}, w) \in [\mathcal{W}^h(\Omega^e_{\texttt{HDG}})]^{\texttt{n}_{\texttt{sd}}} \times \mathcal{W}^h(\Omega^e_{\texttt{HDG}})$. The weak form of the global problem returns the solution of the hybrid variable and reads: find $\hat{T}_{\texttt{HDG}} \in \widehat{\mathcal{W}}^h(\Gamma_{\texttt{HDG}} \cup \Gamma^N_{\texttt{HDG}})$ such that

$$-\sum_{e=1}^{\texttt{n}^{\texttt{el}}_{\texttt{HDG}}} \left\langle \hat{w}, \sqrt{\kappa}\boldsymbol{q}_{\texttt{HDG}} \cdot \boldsymbol{n}_{\texttt{HDG}} + \tau_T \left(T_{\texttt{HDG}} - \hat{T}_{\texttt{HDG}}\right) \right\rangle_{\partial\Omega^e_{\texttt{HDG}} \setminus \Gamma^D_{\texttt{HDG}}} = \sum_{e=1}^{\texttt{n}^{\texttt{el}}_{\texttt{HDG}}} \left\langle \hat{w}, f^N \right\rangle_{\partial\Omega^e_{\texttt{HDG}} \cap \Gamma^N_{\texttt{HDG}}}, \tag{4.8}$$

for all $\hat{w} \in \widehat{\mathcal{W}}^h(\Gamma_{\texttt{HDG}} \cup \Gamma^N_{\texttt{HDG}})$.

The discretization of the weak form of the local problem in (4.7) by means of a isoparametric formulation for the mixed, primal and hybrid variables produces a linear system of the form

$$\begin{bmatrix} \mathbf{K}_{11} & \mathbf{K}_{12} \\ \mathbf{K}^T_{12} & \mathbf{K}_{22} \end{bmatrix}_e \begin{bmatrix} \mathbf{q}_{\texttt{HDG}} \\ \mathbf{T}_{\texttt{HDG}} \end{bmatrix}_e = \begin{bmatrix} \mathbf{f}_1 \\ \mathbf{f}_2 \end{bmatrix}_e - \begin{bmatrix} \mathbf{K}_{13} \\ \mathbf{K}_{23} \end{bmatrix}_e \left[\hat{\mathbf{T}}_{\texttt{HDG}}\right]_e, \tag{4.9}$$

for $e = 1, \dots, \mathtt{n}^{\mathtt{el}}_{\mathtt{HDG}}$. The subscripts $\odot_1$, $\odot_2$ and $\odot_3$ refer to the unknowns $\mathbf{q}_{\text{HDG}}$, $\mathbf{T}_{\text{HDG}}$ and $\hat{\mathbf{T}}_{\text{HDG}}$, respectively. The expressions of the matrices and vectors are detailed in Appendix C. Analogously, the resulting system for the global problem is given by

$$\sum_{e=1}^{\mathtt{n}^{\mathtt{el}}_{\mathtt{HDG}}} \left\{ \begin{bmatrix} \mathbf{K}_{13}^T & \mathbf{K}_{23}^T \end{bmatrix}_e \begin{bmatrix} \mathbf{q}_{\text{HDG}} \\ \mathbf{T}_{\text{HDG}} \end{bmatrix}_e + \begin{bmatrix} \mathbf{K}_{33} \end{bmatrix}_e \begin{bmatrix} \hat{\mathbf{T}}_{\text{HDG}} \end{bmatrix}_e \right\} = \sum_{e=1}^{\mathtt{n}^{\mathtt{el}}_{\mathtt{HDG}}} \begin{bmatrix} \mathbf{f}_3 \end{bmatrix}_e . \tag{4.10}$$

Replacing the solution of the local problem (4.9) in the global problem (4.10), the linear system which is actually solved in the computation can be written as

$$\begin{bmatrix} \mathbf{K}_{\text{HDG}} \end{bmatrix} \begin{bmatrix} \hat{\mathbf{T}}_{\text{HDG}} \end{bmatrix} = \begin{bmatrix} \mathbf{f}_{\text{HDG}} \end{bmatrix}, \tag{4.11}$$

with

$$\begin{bmatrix} \mathbf{K}_{\text{HDG}} \end{bmatrix} = \mathop{\mathsf{A}}_{e=1}^{\mathtt{n}^{\mathtt{el}}_{\mathtt{HDG}}} \left\{ \begin{bmatrix} \mathbf{K}_{33} \end{bmatrix}_e - \begin{bmatrix} \mathbf{K}_{13}^T & \mathbf{K}_{23}^T \end{bmatrix}_e \begin{bmatrix} \mathbf{K}_{11} & \mathbf{K}_{12} \\ \mathbf{K}_{12}^T & \mathbf{K}_{22} \end{bmatrix}_e^{-1} \begin{bmatrix} \mathbf{K}_{13} \\ \mathbf{K}_{23} \end{bmatrix}_e \right\}, \tag{4.12a}$$

$$\begin{bmatrix} \mathbf{f}_{\text{HDG}} \end{bmatrix} = \mathop{\mathsf{A}}_{e=1}^{\mathtt{n}^{\mathtt{el}}_{\mathtt{HDG}}} \left\{ \begin{bmatrix} \mathbf{f}_3 \end{bmatrix}_e - \begin{bmatrix} \mathbf{K}_{13}^T & \mathbf{K}_{23}^T \end{bmatrix}_e \begin{bmatrix} \mathbf{K}_{11} & \mathbf{K}_{12} \\ \mathbf{K}_{12}^T & \mathbf{K}_{22} \end{bmatrix}_e^{-1} \begin{bmatrix} \mathbf{f}_1 \\ \mathbf{f}_2 \end{bmatrix}_e \right\}. \tag{4.12b}$$

It is worth highlighting that the HDG stiffness matrix $\mathbf{K}_{\text{HDG}}$ preserves the symmetry of the original POISSON problem (4.1), as shown for instance by SEVILLA and HUERTA [140].

4.1.2 CG approximation

The CG computational domain Ω_{CG} is considered partitioned in $\mathtt{n}^{\mathtt{el}}_{\mathtt{CG}}$ elements with

$$\Omega_{\text{CG}} = \bigcup_{e=1}^{\mathtt{n}^{\mathtt{el}}_{\mathtt{CG}}} \Omega^e_{\text{CG}}, \quad \Omega^e_{\text{CG}} \cap \Omega^f_{\text{CG}} = \emptyset \quad \text{for} \quad e \neq f. \tag{4.13}$$

The strong form of the governing equations in the CG framework can simply be written by referring to the appropriate unknown temperature field T_{CG} as

$$\begin{cases} -\boldsymbol{\nabla} \cdot (\kappa \boldsymbol{\nabla} T_{\text{CG}}) = s & \text{in } \Omega_{\text{CG}}, \\ T_{\text{CG}} = T^D & \text{on } \Gamma^D_{\text{CG}}, \\ \kappa \boldsymbol{\nabla} T_{\text{CG}} \cdot \boldsymbol{n}_{\text{CG}} = f^N & \text{on } \Gamma^N_{\text{CG}}. \end{cases} \tag{4.14}$$

The weak form of the CG approximation is thus obtained by multiplying the governing equation in (4.14) with a suitable test function and integrating by parts the term under the divergence operator. It then reads: find $T_{\text{CG}} \in \mathcal{V}^h(\Omega_{\text{CG}})$ such that

$$(\boldsymbol{\nabla} v, \kappa \boldsymbol{\nabla} T_{\text{CG}})_{\Omega_{\text{CG}}} = (v, s)_{\Omega_{\text{CG}}} + \langle v, f^N \rangle_{\Gamma^N_{\text{CG}}}, \tag{4.15}$$

for all $v \in \mathcal{V}^h_0(\Omega_{\text{CG}})$. Standard finite element discretization gives rise to the symmetric problem

$$\begin{bmatrix} \mathbf{K}_{\text{CG}} \end{bmatrix} \begin{bmatrix} \mathbf{T}_{\text{CG}} \end{bmatrix} = \begin{bmatrix} \mathbf{f}_{\text{CG}} \end{bmatrix}, \tag{4.16}$$

with

$$\begin{bmatrix} \mathbf{K}_{\text{CG}} \end{bmatrix} = \mathop{\mathsf{A}}_{e=1}^{\mathtt{n}^{\mathtt{el}}_{\mathtt{CG}}} \left\{ \begin{bmatrix} \mathbf{K}_{44} \end{bmatrix}_e \right\}, \qquad \begin{bmatrix} \mathbf{f}_{\text{CG}} \end{bmatrix} = \mathop{\mathsf{A}}_{e=1}^{\mathtt{n}^{\mathtt{el}}_{\mathtt{CG}}} \left\{ \begin{bmatrix} \mathbf{f}_4 \end{bmatrix}_e \right\}, \tag{4.17}$$

with the subscript $\odot_4$ referring to the unknown $\mathbf{T}_{\text{CG}}$.

4.1.3 Local-global coupling

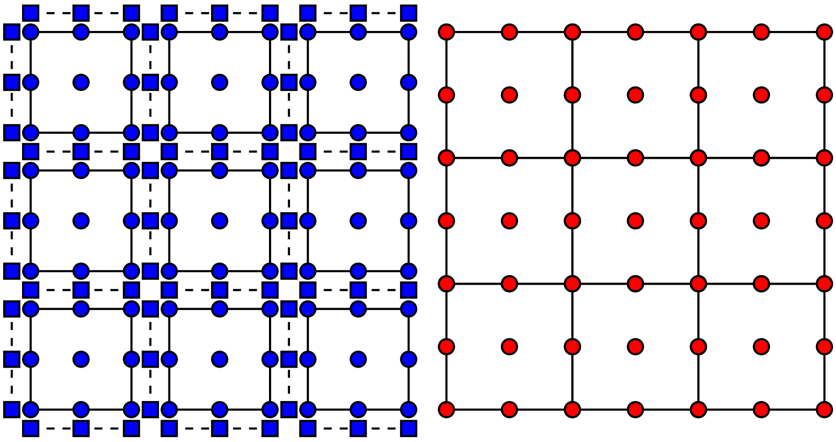

Figure 4.1: Degrees of freedom of the HDG-CG discretization for local-global coupling

Let the computational domain Ω be split into two non-overlapping subdomains $\Omega_{\texttt{HDG}}$ and $\Omega_{\texttt{CG}}$ such that $\Omega = \Omega_{\texttt{HDG}} \cup \Omega_{\texttt{CG}}$, with interface $\Gamma^I = \Omega_{\texttt{HDG}} \cap \Omega_{\texttt{CG}}$. Each subdomain is then subdivided into a set of disjoints elements, as in (4.2) and (4.13). Only matching meshes (with a potential nonuniform degree of approximation) are considered in this thesis and $\mathtt{n}_{\mathtt{I}}^{\mathtt{el}}$ denotes in the following the number of elements adjacent to the interface, belonging either to the HDG or the CG subdomain. The boundary of the whole domain is split into a DIRICHLET portion $\Gamma^D = \Gamma^D_{\texttt{HDG}} \cup \Gamma^D_{\texttt{CG}}$ and a NEUMANN portion $\Gamma^N = \Gamma^N_{\texttt{HDG}} \cup \Gamma^N_{\texttt{CG}}$.

The degrees of freedom of the coupled problem are displayed in Figure 4.1, in which the HDG and CG unknowns are depicted in blue and red, respectively. Moreover, the HDG local DOFs are represented with circles, whereas the HDG global DOFs are denoted with squares. It is worth noting that the HDG global DOFs are suppressed on the interface, given the local nature of the HDG-CG coupling discussed in the following.

The strong form of the coupling strategy is obtained by merging the HDG strong form (4.4) and the CG strong form (4.14) and considering the additional coupling conditions at the interface

$$\begin{cases} T_{\texttt{HDG}} = T_{\texttt{CG}} & \text{on } \Gamma^I, \\ \sqrt{\kappa}\boldsymbol{q}_{\texttt{HDG}} \cdot \boldsymbol{n}_{\texttt{HDG}} = \kappa \boldsymbol{\nabla} T_{\texttt{CG}} \cdot \boldsymbol{n}_{\texttt{CG}} & \text{on } \Gamma^I. \end{cases} \tag{4.18}$$

The first condition ensures the continuity of the temperature field, while the second enforces the equilibrium of the normal fluxes across the interface. It is worth reminding that the unit normal vector takes opposite directions on the interface Γ^I, i.e. $\boldsymbol{n}_{\texttt{HDG}} = -\boldsymbol{n}_{\texttt{CG}}$.

The key point of the presented coupling strategy is the imposition of the first coupling condition as a DIRICHLET boundary condition on the HDG local problem and the enforcement of the second coupling condition as a NEUMANN boundary condition of the CG problem. A novel definition of the numerical normal flux is therefore introduced, namely

$$\widehat{\sqrt{\kappa}\boldsymbol{q}_{\mathtt{HDG}}\cdot\boldsymbol{n}_{\mathtt{HDG}}} = \begin{cases} \sqrt{\kappa}\boldsymbol{q}_{\mathtt{HDG}}\cdot\boldsymbol{n}_{\mathtt{HDG}} + \tau_T\left(T_{\mathtt{HDG}} - T^D\right) & \text{on } \partial\Omega^e_{\mathtt{HDG}}\cap\Gamma^D_{\mathtt{HDG}},\\ \sqrt{\kappa}\boldsymbol{q}_{\mathtt{HDG}}\cdot\boldsymbol{n}_{\mathtt{HDG}} + \tau_T\left(T_{\mathtt{HDG}} - \hat{T}_{\mathtt{HDG}}\right) & \text{on } \partial\Omega^e_{\mathtt{HDG}}\setminus\Gamma^D_{\mathtt{HDG}}\setminus\Gamma^I,\\ \sqrt{\kappa}\boldsymbol{q}_{\mathtt{HDG}}\cdot\boldsymbol{n}_{\mathtt{HDG}} + \tau_T\left(T_{\mathtt{HDG}} - T_{\mathtt{CG}}\right) & \text{on } \partial\Omega^e_{\mathtt{HDG}}\cap\Gamma^I. \end{cases} \tag{4.19}$$

From a practical point of view, the HDG hybrid variable $\hat{T}_{\mathtt{HDG}}$ is replaced by the CG unknown $T_{\mathtt{CG}}$ at the interface.

The HDG local problems (4.7) are modified according to the new definition (4.19) and they read: given T^D on $\Gamma^D_{\mathtt{HDG}}$, $\hat{T}_{\mathtt{HDG}}$ on $\Gamma_{\mathtt{HDG}}\cup\Gamma^N_{\mathtt{HDG}}$ and $T_{\mathtt{CG}}$ on Γ^I, find $(\boldsymbol{q}_{\mathtt{HDG}}, T_{\mathtt{HDG}}) \in [\mathcal{W}^h(\Omega^e_{\mathtt{HDG}})]^{\mathtt{n_{sd}}} \times \mathcal{W}^h(\Omega^e_{\mathtt{HDG}})$ for $e = 1, \dots, \mathtt{n}^{\mathtt{el}}_{\mathtt{HDG}}$ such that

$$\begin{aligned} -\left(\boldsymbol{w}, \boldsymbol{q}_{\mathtt{HDG}}\right)_{\Omega^e_{\mathtt{HDG}}} + \left(\boldsymbol{\nabla}\cdot\left(\sqrt{\kappa}\boldsymbol{w}\right), T_{\mathtt{HDG}}\right)_{\Omega^e_{\mathtt{HDG}}} &= \\ \left\langle\sqrt{\kappa}\boldsymbol{w}\cdot\boldsymbol{n}_{\mathtt{HDG}}, T^D\right\rangle_{\partial\Omega^e_{\mathtt{HDG}}\cap\Gamma^D_{\mathtt{HDG}}} &+ \left\langle\sqrt{\kappa}\boldsymbol{w}\cdot\boldsymbol{n}_{\mathtt{HDG}}, \hat{T}_{\mathtt{HDG}}\right\rangle_{\partial\Omega^e_{\mathtt{HDG}}\setminus\Gamma^D_{\mathtt{HDG}}\setminus\Gamma^I} \\ + \left\langle\sqrt{\kappa}\boldsymbol{w}\cdot\boldsymbol{n}_{\mathtt{HDG}}, T_{\mathtt{CG}}\right\rangle_{\partial\Omega^e_{\mathtt{HDG}}\cap\Gamma^I}&, \end{aligned} \tag{4.20a}$$

$$\begin{aligned} \left(w, \boldsymbol{\nabla}\cdot\left(\sqrt{\kappa}\boldsymbol{q}_{\mathtt{HDG}}\right)\right)_{\Omega^e_{\mathtt{HDG}}} + \left\langle w, \tau_T T_{\mathtt{HDG}}\right\rangle_{\partial\Omega^e_{\mathtt{HDG}}} &= \left(w, s\right)_{\Omega^e_{\mathtt{HDG}}} \\ + \left\langle w, \tau_T T^D\right\rangle_{\partial\Omega^e_{\mathtt{HDG}}\cap\Gamma^D_{\mathtt{HDG}}} &+ \left\langle w, \tau_T \hat{T}_{\mathtt{HDG}}\right\rangle_{\partial\Omega^e_{\mathtt{HDG}}\setminus\Gamma^D_{\mathtt{HDG}}\setminus\Gamma^I} \\ + \left\langle w, \tau_T T_{\mathtt{CG}}\right\rangle_{\partial\Omega^e_{\mathtt{HDG}}\cap\Gamma^I}&, \end{aligned} \tag{4.20b}$$

for all $(\boldsymbol{w}, w) \in [\mathcal{W}^h(\Omega^e_{\mathtt{HDG}})]^{\mathtt{n_{sd}}} \times \mathcal{W}^h(\Omega^e_{\mathtt{HDG}})$. It is clear that, while standard local problems are performed for the interior HDG elements, a special treatment of the interface elements is needed to include the coupling conditions. Although this necessity does not represent a critical issue for the simple `MATLAB` implementations exploited in this chapter, it may constitute a severe limitation for large and structured codes like `BACI`, in which independent and difficult to access libraries are adopted for the single discretizations.

The HDG global problem remains substantially unchanged, with the only difference that the global DOFs are removed not only on the DIRICHLET portion of the boundary, but also on the interface. The definition of the numerical normal flux is added as an external thermal flux acting on the CG side of the interface. The resulting global problem thus reads: find $(\hat{T}_{\mathtt{HDG}}, T_{\mathtt{CG}}) \in \widehat{\mathcal{W}}^h(\Gamma_{\mathtt{HDG}}\cup\Gamma^N_{\mathtt{HDG}}) \times \mathcal{V}^h(\Omega_{\mathtt{CG}})$ such that

$$\begin{aligned} -\sum_{e=1}^{\mathtt{n}^{\mathtt{el}}_{\mathtt{HDG}}} \left\langle\hat{w}, \sqrt{\kappa}\boldsymbol{q}_{\mathtt{HDG}}\cdot\boldsymbol{n}_{\mathtt{HDG}} + \tau_T\left(T_{\mathtt{HDG}} - \hat{T}_{\mathtt{HDG}}\right)\right\rangle_{\partial\Omega^e_{\mathtt{HDG}}\setminus\Gamma^D_{\mathtt{HDG}}\setminus\Gamma^I} &= \\ \sum_{e=1}^{\mathtt{n}^{\mathtt{el}}_{\mathtt{HDG}}} \left\langle\hat{w}, f^N\right\rangle_{\partial\Omega^e_{\mathtt{HDG}}\cap\Gamma^N_{\mathtt{HDG}}}&, \end{aligned} \tag{4.21a}$$

$$\begin{aligned} \left(\boldsymbol{\nabla}v, \kappa\boldsymbol{\nabla}T_{\mathtt{CG}}\right)_{\Omega_{\mathtt{CG}}} - \left\langle v, \sqrt{\kappa}\boldsymbol{q}_{\mathtt{HDG}}\cdot\left(-\boldsymbol{n}_{\mathtt{CG}}\right) + \tau_T\left(T_{\mathtt{HDG}} - T_{\mathtt{CG}}\right)\right\rangle_{\Gamma^I} &= \left(v, s\right)_{\Omega_{\mathtt{CG}}} \\ &+ \left\langle v, f^N\right\rangle_{\Gamma^N_{\mathtt{CG}}}, \end{aligned} \tag{4.21b}$$

for all $(\hat{w}, v) \in \widehat{\mathcal{W}}^h(\Gamma_{\mathtt{HDG}}\cup\Gamma^N_{\mathtt{HDG}}) \times \mathcal{V}^h_0(\Omega_{\mathtt{CG}})$.

The discretization of the weak forms (4.20) and (4.21) leads to a linear system of the form

$$\begin{bmatrix} \bar{\mathbf{K}}_{\mathtt{HDG}} & \bar{\mathbf{K}}_{\mathtt{I}} \\ \bar{\mathbf{K}}_{\mathtt{I}}^{T} & \bar{\mathbf{K}}_{\mathtt{CG}} \end{bmatrix} \begin{bmatrix} \hat{\mathbf{T}}_{\mathtt{HDG}} \\ \mathbf{T}_{\mathtt{CG}} \end{bmatrix} = \begin{bmatrix} \bar{\mathbf{f}}_{\mathtt{HDG}} \\ \bar{\mathbf{f}}_{\mathtt{CG}} \end{bmatrix}, \tag{4.22}$$

with

$$\left[\bar{\mathbf{K}}_{\mathtt{HDG}}\right] = \mathop{\Large\mathsf{A}}_{e=1}^{n^{\mathtt{el}}_{\mathtt{HDG}}} \left\{ \left[\bar{\mathbf{K}}_{33}\right]_e - \left[\bar{\mathbf{K}}_{13}^{T} \quad \bar{\mathbf{K}}_{23}^{T}\right]_e \begin{bmatrix} \mathbf{K}_{11} & \mathbf{K}_{12} \\ \mathbf{K}_{12}^{T} & \mathbf{K}_{22} \end{bmatrix}_e^{-1} \begin{bmatrix} \bar{\mathbf{K}}_{13} \\ \bar{\mathbf{K}}_{23} \end{bmatrix}_e \right\}, \tag{4.23a}$$

$$\left[\bar{\mathbf{K}}_{\mathtt{I}}\right] = \mathop{\Large\mathsf{A}}_{e=1}^{n^{\mathtt{el}}_{\mathtt{I}}} \left\{ \qquad - \left[\bar{\mathbf{K}}_{13}^{T} \quad \bar{\mathbf{K}}_{23}^{T}\right]_e \begin{bmatrix} \mathbf{K}_{11} & \mathbf{K}_{12} \\ \mathbf{K}_{12}^{T} & \mathbf{K}_{22} \end{bmatrix}_e^{-1} \begin{bmatrix} \bar{\mathbf{K}}_{14} \\ \bar{\mathbf{K}}_{24} \end{bmatrix}_e \right\}, \tag{4.23b}$$

$$\left[\bar{\mathbf{K}}_{\mathtt{CG}}\right] = \mathop{\Large\mathsf{A}}_{e=1}^{n^{\mathtt{el}}_{\mathtt{CG}}} \left\{ \left[\bar{\mathbf{K}}_{44}\right]_e - \left[\bar{\mathbf{K}}_{14}^{T} \quad \bar{\mathbf{K}}_{24}^{T}\right]_e \begin{bmatrix} \mathbf{K}_{11} & \mathbf{K}_{12} \\ \mathbf{K}_{12}^{T} & \mathbf{K}_{22} \end{bmatrix}_e^{-1} \begin{bmatrix} \bar{\mathbf{K}}_{14} \\ \bar{\mathbf{K}}_{24} \end{bmatrix}_e \right\}, \tag{4.23c}$$

and

$$\left[\bar{\mathbf{f}}_{\mathtt{HDG}}\right] = \mathop{\Large\mathsf{A}}_{e=1}^{n^{\mathtt{el}}_{\mathtt{HDG}}} \left\{ \left[\mathbf{f}_{3}\right]_e - \left[\bar{\mathbf{K}}_{13}^{T} \quad \bar{\mathbf{K}}_{23}^{T}\right]_e \begin{bmatrix} \mathbf{K}_{11} & \mathbf{K}_{12} \\ \mathbf{K}_{12}^{T} & \mathbf{K}_{22} \end{bmatrix}_e^{-1} \begin{bmatrix} \mathbf{f}_{1} \\ \mathbf{f}_{2} \end{bmatrix}_e \right\}, \tag{4.24a}$$

$$\left[\bar{\mathbf{f}}_{\mathtt{CG}}\right] = \mathop{\Large\mathsf{A}}_{e=1}^{n^{\mathtt{el}}_{\mathtt{CG}}} \left\{ \left[\mathbf{f}_{4}\right]_e - \left[\bar{\mathbf{K}}_{14}^{T} \quad \bar{\mathbf{K}}_{24}^{T}\right]_e \begin{bmatrix} \mathbf{K}_{11} & \mathbf{K}_{12} \\ \mathbf{K}_{12}^{T} & \mathbf{K}_{22} \end{bmatrix}_e^{-1} \begin{bmatrix} \mathbf{f}_{1} \\ \mathbf{f}_{2} \end{bmatrix}_e \right\}. \tag{4.24b}$$

The barred terms refer to a modified version of the corresponding terms in the single subproblems introduced in Sections 4.1.1 and 4.1.2 and their expression is also reported in Appendix C. The invasive nature of this coupling is especially evident from the complicated pattern of the matrices in (4.23) and the right hand side vectors in (4.24). In particular, the matrices arising from the discretization of the local problems (with indices 1 and 2) spread outside the HDG block of the linear system and their communication is required for the computation of $\bar{\mathbf{K}}_{\mathtt{CG}}$ and $\bar{\mathbf{f}}_{\mathtt{CG}}$, as well as for the off-diagonal block $\bar{\mathbf{K}}_{\mathtt{I}}$.

Overall, this coupling strategy, first introduced by PAIPURI *et al.* [127] to solve conjugate heat transfer problems, slightly reduces the number of the globally coupled degrees of freedom and it does not need additional parameters to enforce the transmission conditions. Moreover, this strategy possesses optimal convergence properties and superconvergent rates can be obtained for the HDG solution through classical postprocessing techniques. However, the implementation of this formulation is rather invasive, especially with respect to monolithic frameworks, and the required communication of the local HDG matrices in the CG subproblem and on the interface might compromise the efficiency of parallel implementations.

Nevertheless, a staggered version of this coupling strategy, preserving the core structure of the single solvers and exchanging the coupling information solely through the right hand side vectors, hence circumventing the major drawbacks of this approach, will be successfully exploited in Section 5.2 for the solution of fluid-structure interaction problems by means of the popular DIRICHLET–NEUMANN partitioning.

4.1.4 NITSCHE-based coupling

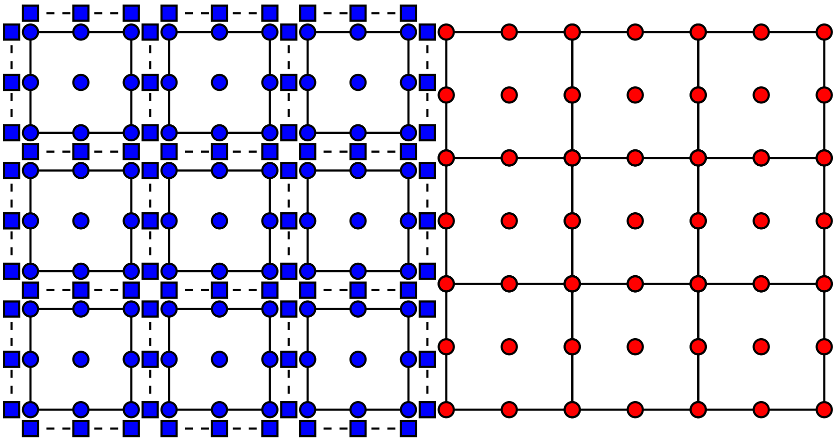

Figure 4.2: Degrees of freedom of the HDG-CG discretization for NITSCHE-based coupling

An alternative strategy for the coupling of HDG and CG discretizations is presented in this section with the purpose of keeping the implementation changes to a minimum in existing single-field codes. The main idea is to rely solely on the global variables, i.e. the trace of the temperature $\hat{T}_{\text{HDG}}$ in the HDG subdomain and the temperature field T_{CG} in the CG subdomain, to enforce the transmission conditions. Contrary to the previous strategy, the coupling here takes place only on a global level, not requiring any change in the HDG local problems.

The definition of the computational domain and its splitting introduced in Section 4.1.3 is considered here. A sketch of the degrees of freedom is offered in Figure 4.2. It is worth noting that, as opposed to the local-global coupling, the HDG global DOFs are preserved on the interface, since they are essential for the exchange of information among the fields. Of course, this results in a slightly increased number of total DOFs. However, this choice provides a much more flexible framework for the coupled discretization, allowing an easy treatment of nonuniform polynomial approximations as well as nonconforming meshes at the interface, although the latter feature is not explored in this thesis. Moreover, the preservation of the trace on the interface allows for a straightforward adoption of the HDG discretization in a coupled problem, without the need of rearranging the degrees of freedom.

The strong form of the NITSCHE-based coupling consists of the strong form of the HDG and CG subproblems (4.4) and (4.14), together with the following modified version of the coupling conditions

$$\begin{cases} \hat{T}_{\text{HDG}} = T_{\text{CG}} & \text{on } \Gamma^I, \\ \widehat{\sqrt{\kappa}\boldsymbol{q}_{\text{HDG}} \cdot \boldsymbol{n}_{\text{HDG}}} = \widehat{\kappa \boldsymbol{\nabla} T_{\text{CG}} \cdot \boldsymbol{n}_{\text{CG}}} & \text{on } \Gamma^I. \end{cases} \tag{4.25}$$

The HDG numerical flux is the same as the single-field formulation and it is recalled here for completeness

$$\widehat{\sqrt{\kappa}\boldsymbol{q}_{\texttt{HDG}} \cdot \boldsymbol{n}_{\texttt{HDG}}} = \begin{cases} \sqrt{\kappa}\boldsymbol{q}_{\texttt{HDG}} \cdot \boldsymbol{n}_{\texttt{HDG}} + \tau_T \left(T_{\texttt{HDG}} - T^D\right) & \text{on } \partial\Omega^e_{\texttt{HDG}} \cap \Gamma^D_{\texttt{HDG}}, \\ \sqrt{\kappa}\boldsymbol{q}_{\texttt{HDG}} \cdot \boldsymbol{n}_{\texttt{HDG}} + \tau_T \left(T_{\texttt{HDG}} - \hat{T}_{\texttt{HDG}}\right) & \text{on } \partial\Omega^e_{\texttt{HDG}} \setminus \Gamma^D_{\texttt{HDG}}, \end{cases} \tag{4.26}$$

whereas the trace of the CG numerical normal flux on the interface is defined as

$$\widehat{\kappa\boldsymbol{\nabla}T_{\texttt{CG}} \cdot \boldsymbol{n}_{\texttt{CG}}} = \kappa\boldsymbol{\nabla}T_{\texttt{CG}} \cdot \boldsymbol{n}_{\texttt{CG}} - \frac{\gamma}{h}\left(T_{\texttt{CG}} - \hat{T}_{\texttt{HDG}}\right) \text{ on } \Gamma^I. \tag{4.27}$$

where h denotes a characteristic element size of the mesh discretization on Γ^I and γ is a sufficiently large positive parameter, commonly used to enforce coercivity of the discrete bilinear form in CG discretizations with NITSCHE's imposition of essential boundary conditions. From a practical point of view, the definition (4.27) allows the imposition of the flux equilibrium via a NEUMANN boundary condition in the HDG global problem and it ensures the continuity of the solution via a weak DIRICHLET boundary condition in the CG problem.

The weak form of the HDG local problems remains unchanged and with the inclusion of the trace at the interface it now reads: given T^D on $\Gamma^D_{\texttt{HDG}}$ and $\hat{T}_{\texttt{HDG}}$ on $\Gamma_{\texttt{HDG}} \cup \Gamma^N_{\texttt{HDG}} \cup \Gamma^I$, find $(\boldsymbol{q}_{\texttt{HDG}}, T_{\texttt{HDG}}) \in [\mathcal{W}^h(\Omega^e_{\texttt{HDG}})]^{\texttt{n}_{\texttt{sd}}} \times \mathcal{W}^h(\Omega^e_{\texttt{HDG}})$ for $e = 1, \dots, \texttt{n}^{\texttt{el}}_{\texttt{HDG}}$ such that

$$\begin{aligned} -\left(\boldsymbol{w}, \boldsymbol{q}_{\texttt{HDG}}\right)_{\Omega^e_{\texttt{HDG}}} + \left(\boldsymbol{\nabla}\cdot\left(\sqrt{\kappa}\boldsymbol{w}\right), T_{\texttt{HDG}}\right)_{\Omega^e_{\texttt{HDG}}} &= \\ \left\langle \sqrt{\kappa}\boldsymbol{w}\cdot\boldsymbol{n}_{\texttt{HDG}}, T^D\right\rangle_{\partial\Omega^e_{\texttt{HDG}}\cap\Gamma^D_{\texttt{HDG}}} &+ \left\langle \sqrt{\kappa}\boldsymbol{w}\cdot\boldsymbol{n}_{\texttt{HDG}}, \hat{T}_{\texttt{HDG}}\right\rangle_{\partial\Omega^e_{\texttt{HDG}}\setminus\Gamma^D_{\texttt{HDG}}}, \end{aligned} \tag{4.28a}$$

$$\begin{aligned} \left(w, \boldsymbol{\nabla}\cdot\left(\sqrt{\kappa}\boldsymbol{q}_{\texttt{HDG}}\right)\right)_{\Omega^e_{\texttt{HDG}}} + \left\langle w, \tau_T T_{\texttt{HDG}}\right\rangle_{\partial\Omega^e_{\texttt{HDG}}} &= (w, s)_{\Omega^e_{\texttt{HDG}}} \\ + \left\langle w, \tau_T T^D\right\rangle_{\partial\Omega^e_{\texttt{HDG}}\cap\Gamma^D_{\texttt{HDG}}} &+ \left\langle w, \tau_T \hat{T}_{\texttt{HDG}}\right\rangle_{\partial\Omega^e_{\texttt{HDG}}\setminus\Gamma^D_{\texttt{HDG}}}, \end{aligned} \tag{4.28b}$$

for all $(\boldsymbol{w}, w) \in [\mathcal{W}^h(\Omega^e_{\texttt{HDG}})]^{\texttt{n}_{\texttt{sd}}} \times \mathcal{W}^h(\Omega^e_{\texttt{HDG}})$.

Exploiting the definition of the CG numerical normal flux in (4.27), the weak form of the global problem reads: find $(\hat{T}_{\texttt{HDG}}, T_{\texttt{CG}}) \in \widehat{\mathcal{W}}^h(\Gamma_{\texttt{HDG}} \cup \Gamma^N_{\texttt{HDG}} \cup \Gamma^I) \times \mathcal{V}^h(\Omega_{\texttt{CG}})$ such that

$$\begin{aligned} -\sum_{e=1}^{\texttt{n}^{\texttt{el}}_{\texttt{HDG}}} \Bigg\{ &\left\langle \hat{w}, \sqrt{\kappa}\boldsymbol{q}_{\texttt{HDG}}\cdot\boldsymbol{n}_{\texttt{HDG}} + \tau_T\left(T_{\texttt{HDG}} - \hat{T}_{\texttt{HDG}}\right)\right\rangle_{\partial\Omega^e_{\texttt{HDG}}\setminus\Gamma^D_{\texttt{HDG}}} \\ &- \left\langle \hat{w}, \kappa\boldsymbol{\nabla}T_{\texttt{CG}}\cdot(-\boldsymbol{n}_{\texttt{HDG}}) - \frac{\gamma}{h}\left(T_{\texttt{CG}} - \hat{T}_{\texttt{HDG}}\right)\right\rangle_{\partial\Omega^e_{\texttt{HDG}}\cap\Gamma^I}\Bigg\} = \sum_{e=1}^{\texttt{n}^{\texttt{el}}_{\texttt{HDG}}} \left\langle \hat{w}, f^N\right\rangle_{\partial\Omega^e_{\texttt{HDG}}\cap\Gamma^N_{\texttt{HDG}}}, \end{aligned} \tag{4.29a}$$

$$\begin{aligned} \left(\boldsymbol{\nabla}v, \kappa\boldsymbol{\nabla}T_{\texttt{CG}}\right)_{\Omega_{\texttt{CG}}} &- \left\langle v, \kappa\boldsymbol{\nabla}T_{\texttt{CG}}\cdot\boldsymbol{n}_{\texttt{CG}} - \frac{\gamma}{h}\left(T_{\texttt{CG}} - \hat{T}_{\texttt{HDG}}\right)\right\rangle_{\Gamma^I} \\ &- \left\langle \kappa\boldsymbol{\nabla}v\cdot\boldsymbol{n}_{\texttt{CG}}, T_{\texttt{CG}} - \hat{T}_{\texttt{HDG}}\right\rangle_{\Gamma^I} = (v, s)_{\Omega_{\texttt{CG}}} + \left\langle v, f^N\right\rangle_{\Gamma^N_{\texttt{CG}}}, \end{aligned} \tag{4.29b}$$

for all $(\hat{w}, v) \in \widehat{\mathcal{W}}^h(\Gamma_{\texttt{HDG}} \cup \Gamma^N_{\texttt{HDG}} \cup \Gamma^I) \times \mathcal{V}^h_0(\Omega_{\texttt{CG}})$. It is worth noting that the symmetry of the POISSON problem is preserved for both the HDG and the CG discretization, as well as for the overall coupled problem.

An alternative approach for the weak imposition of boundary conditions, not requiring the introduction of the penalty term to guarantee the stability of the numerical method, has been presented by BURMAN [20] and relies on a non-symmetric formulation of the discrete equation. On the one hand, such an approach would avoid the evaluation of the additional parameter γ, which is strongly problem-dependent and not known a priori, which might negatively effect the condition number of the resulting linear system when an excessively large value is adopted. On the other hand, however, the convergence rate of the error in the $\mathcal{L}^2$ norm is proven to be suboptimal by half an order in h.

The linear system arising from the discretization of the coupled problem has the form

$$\begin{bmatrix} \tilde{\mathbf{K}}_{\mathtt{HDG}} & \tilde{\mathbf{K}}_{\mathtt{I}} \\ \tilde{\mathbf{K}}_{\mathtt{I}}^T & \tilde{\mathbf{K}}_{\mathtt{CG}} \end{bmatrix} \begin{bmatrix} \hat{\mathbf{T}}_{\mathtt{HDG}} \\ \mathbf{T}_{\mathtt{CG}} \end{bmatrix} = \begin{bmatrix} \tilde{\mathbf{f}}_{\mathtt{HDG}} \\ \tilde{\mathbf{f}}_{\mathtt{CG}} \end{bmatrix}. \tag{4.30}$$

Even though the structure of the block matrix in (4.30) is formally similar to the one presented in Section 4.1.3, its construction is extremely different. In fact, the matrices and the vectors involved in the NITSCHE-based coupling are

$$\left[\tilde{\mathbf{K}}_{\mathtt{HDG}}\right] = \operatorname*{\mathcal{A}}_{e=1}^{\mathtt{n}^{\mathtt{el}}_{\mathtt{HDG}}} \left\{ \left[\tilde{\mathbf{K}}_{33}\right]_e - \left[\mathbf{K}_{13}^T \quad \mathbf{K}_{23}^T\right]_e \begin{bmatrix} \mathbf{K}_{11} & \mathbf{K}_{12} \\ \mathbf{K}_{12}^T & \mathbf{K}_{22} \end{bmatrix}_e^{-1} \begin{bmatrix} \mathbf{K}_{13} \\ \mathbf{K}_{23} \end{bmatrix}_e \right\} \cong \left[\mathbf{K}_{\mathtt{HDG}}\right], \tag{4.31a}$$

$$\left[\tilde{\mathbf{K}}_{\mathtt{I}}\right] = \operatorname*{\mathcal{A}}_{e=1}^{\mathtt{n}^{\mathtt{el}}_{\mathtt{I}}} \left\{ \left[\tilde{\mathbf{K}}_{34}\right]_e \right\}, \tag{4.31b}$$

$$\left[\tilde{\mathbf{K}}_{\mathtt{CG}}\right] = \operatorname*{\mathcal{A}}_{e=1}^{\mathtt{n}^{\mathtt{el}}_{\mathtt{CG}}} \left\{ \left[\tilde{\mathbf{K}}_{44}\right]_e \right\} \cong \left[\mathbf{K}_{\mathtt{CG}}\right], \tag{4.31c}$$

and

$$\left[\tilde{\mathbf{f}}_{\mathtt{HDG}}\right] = \operatorname*{\mathcal{A}}_{e=1}^{\mathtt{n}^{\mathtt{el}}_{\mathtt{HDG}}} \left\{ \left[\mathbf{f}_3\right]_e - \left[\mathbf{K}_{13}^T \quad \mathbf{K}_{23}^T\right]_e \begin{bmatrix} \mathbf{K}_{11} & \mathbf{K}_{12} \\ \mathbf{K}_{12}^T & \mathbf{K}_{22} \end{bmatrix}_e^{-1} \begin{bmatrix} \mathbf{f}_1 \\ \mathbf{f}_2 \end{bmatrix}_e \right\} \equiv \left[\mathbf{f}_{\mathtt{HDG}}\right], \tag{4.32a}$$

$$\left[\tilde{\mathbf{f}}_{\mathtt{CG}}\right] = \operatorname*{\mathcal{A}}_{e=1}^{\mathtt{n}^{\mathtt{el}}_{\mathtt{CG}}} \left\{ \left[\mathbf{f}_4\right]_e \right\} \equiv \left[\mathbf{f}_{\mathtt{CG}}\right]. \tag{4.32b}$$

It can be observed that no changes are required for the computation of the right hand side vectors in (4.32) compared to the ones of the single discretizations in (4.12) and (4.17). Regarding the left hand side, both $\tilde{\mathbf{K}}_{\mathtt{HDG}}$ and $\tilde{\mathbf{K}}_{\mathtt{CG}}$ feature the usual structure of the matrices of the HDG and CG global problems, respectively, and only a small number of terms arising from the definition (4.27) have to be included in $\tilde{\mathbf{K}}_{33}$ and $\tilde{\mathbf{K}}_{44}$. The off-diagonal block $\tilde{\mathbf{K}}_{\mathtt{I}}$ is responsible for the coupling and it simply stems from the discretization of $\langle \hat{w}, \kappa \boldsymbol{\nabla} T_{\mathtt{CG}} \cdot (-\boldsymbol{n}_{\mathtt{HDG}}) - \gamma h^{-1} T_{\mathtt{CG}} \rangle$ along the interface Γ^I. It is worth highlighting that the computation of this block is extremely simple and it can be performed by looping over the elements adjacent to the interface and, as opposed to the local coupling strategy in Section 4.1.3, no information related to the local solvers needs to be transferred. As a consequence, the proposed NITSCHE-based coupling is not only minimally-intrusive and suitable to be integrated in existing finite element libraries, but, owing to the reduced amount of data to communicate, it also better preserves the speedup of parallel implementations.

4.2 HDG-CG coupling for elastic problems

In this section, the NITSCHE-based coupling of HDG and CG discretizations is exploited for the solution of structural problems featuring multiple materials with compressible and nearly incompressible behaviors. In static conditions, the displacement field $\boldsymbol{u}$ of an elastic structure Ω subjected to a volume force $\boldsymbol{f}$ is obtained by the solution of the following problem

$$\begin{cases} -\boldsymbol{\nabla} \cdot \boldsymbol{\sigma}\left(\boldsymbol{\nabla} \boldsymbol{u}\right) = \boldsymbol{f} & \text{in } \Omega, \\ \boldsymbol{u} = \boldsymbol{u}^D & \text{on } \Gamma^D, \\ \boldsymbol{\sigma}\left(\boldsymbol{\nabla} \boldsymbol{u}\right) \boldsymbol{n} = \boldsymbol{t}^N & \text{on } \Gamma^N, \end{cases} \tag{4.33}$$

with $\boldsymbol{u}^D$ and $\boldsymbol{t}^N$ denoting an imposed displacement and traction applied on Γ^D and Γ^N, respectively. Then, $\boldsymbol{\sigma}$ is the CAUCHY stress which, in the linear elastic regime, is related to the linear strain tensor

$$\boldsymbol{\varepsilon}\left(\boldsymbol{\nabla} \boldsymbol{u}\right) = \frac{1}{2}\left(\boldsymbol{\nabla} \boldsymbol{u} + \left(\boldsymbol{\nabla} \boldsymbol{u}\right)^T\right), \tag{4.34}$$

according to HOOKE's law

$$\boldsymbol{\sigma}\left(\boldsymbol{\nabla} \boldsymbol{u}\right) = 2\mu \boldsymbol{\varepsilon}\left(\boldsymbol{\nabla} \boldsymbol{u}\right) + \lambda \operatorname{tr}\left(\boldsymbol{\varepsilon}\left(\boldsymbol{\nabla} \boldsymbol{u}\right)\right) \mathbf{I}_{\mathtt{n_{sd}}}. \tag{4.35}$$

The LAMÉ parameters μ and λ can be expressed by the more commonly used YOUNG's modulus E and POISSON's ratio ν through the following relations

$$\mu = \frac{E}{2\left(1+\nu\right)}, \qquad \lambda = \frac{\nu E}{\left(1+\nu\right)\left(1-2\nu\right)}. \tag{4.36}$$

Henceforth, the material is assumed to be homogeneous and isotropic in the whole domain Ω. Thus, the above mentioned material coefficients depend neither on the spatial coordinates nor on the direction of the main strains.

Owing to the symmetry of the stress and strain tensors, only their $\mathtt{m_{sd}}$ non-redundant components are considered, analogously to what has been done in Chapter 3 for the stress and strain rate tensors for weakly compressible flows. Thus, the stored vectors in VOIGT notation are

$$\boldsymbol{\sigma}_{\mathrm{V}} = \begin{cases} \begin{bmatrix} \sigma_{xx} & \sigma_{yy} & \sigma_{xy} \end{bmatrix}^T & \text{in 2D}, \\ \begin{bmatrix} \sigma_{xx} & \sigma_{yy} & \sigma_{zz} & \sigma_{xy} & \sigma_{xz} & \sigma_{yz} \end{bmatrix}^T & \text{in 3D}, \end{cases} \tag{4.37}$$

and

$$\boldsymbol{\varepsilon}_{\mathrm{V}} = \begin{cases} \begin{bmatrix} \varepsilon_{xx} & \varepsilon_{yy} & 2\varepsilon_{xy} \end{bmatrix}^T & \text{in 2D}, \\ \begin{bmatrix} \varepsilon_{xx} & \varepsilon_{yy} & \varepsilon_{zz} & 2\varepsilon_{xy} & 2\varepsilon_{xz} & 2\varepsilon_{yz} \end{bmatrix}^T & \text{in 3D}, \end{cases} \tag{4.38}$$

with $2\varepsilon_{xy}$, $2\varepsilon_{xz}$ and $2\varepsilon_{yz}$ denoting the off-diagonal terms of the strain tensor according to the engineering definition. The constitutive law (4.35) can therefore be expressed in matrix form as

$$\boldsymbol{\sigma}_{\mathrm{V}} = \mathbf{D} \boldsymbol{\varepsilon}_{\mathrm{V}}, \tag{4.39}$$

with $\mathbf{D}$ being the elasticity tensor

$$\mathbf{D} = \begin{cases} \begin{bmatrix} 2\mu+\lambda & \lambda & 0 \\ \lambda & 2\mu+\lambda & 0 \\ 0 & 0 & \mu \end{bmatrix} & \text{in 2D,} \\ \begin{bmatrix} 2\mu+\lambda & \lambda & \lambda & 0 & 0 & 0 \\ \lambda & 2\mu+\lambda & \lambda & 0 & 0 & 0 \\ \lambda & \lambda & 2\mu+\lambda & 0 & 0 & 0 \\ 0 & 0 & 0 & \mu & 0 & 0 \\ 0 & 0 & 0 & 0 & \mu & 0 \\ 0 & 0 & 0 & 0 & 0 & \mu \end{bmatrix} & \text{in 3D.} \end{cases} \tag{4.40}$$

It is worth noting that the definition of $\mathbf{D}$ is formally identical to the one in (3.17), but with a different physical interpretation of the variables involved. In fact, while in flow problems μ and λ denote the viscosity and the second coefficient of viscosity of the fluid, in elasticity problems μ and λ refer to the aforementioned LAMÉ parameters and they describe the material resistance to simple shear and to a change in volume caused by a change in pressure, respectively. As a matter of fact, in the incompressible limit $\nu \to 0.5$ and consequently $\lambda \to \infty$, according to (4.36). Given these considerations, the linear elastic problem (4.33) can be rewritten as

$$\begin{cases} -\boldsymbol{\nabla}_{\texttt{S}}^T \boldsymbol{\sigma}_{\text{V}}\left(\boldsymbol{\nabla}_{\texttt{S}}\boldsymbol{u}\right) = \boldsymbol{f} & \text{in } \Omega, \\ \boldsymbol{u} = \boldsymbol{u}^D & \text{on } \Gamma^D, \\ \mathbf{N}^T \boldsymbol{\sigma}_{\text{V}}\left(\boldsymbol{\nabla}_{\texttt{S}}\boldsymbol{u}\right) = \boldsymbol{t}^N & \text{on } \Gamma^N, \end{cases} \tag{4.41}$$

with the symbols $\boldsymbol{\nabla}_{\texttt{S}}$ and $\mathbf{N}$ denoting the symmetric part of the gradient and the normal operator in VOIGT notation, already defined (3.12) and (3.19).

The strong form of the HDG approximation of problem (4.41) follows the formulation recently proposed by SEVILLA *et al.* [142] and reads

$$\begin{cases} \boldsymbol{Q}_{\texttt{HDG}} + \mathbf{D}_{\texttt{HDG}}^{1/2}\boldsymbol{\nabla}_{\texttt{S}}\boldsymbol{u}_{\texttt{HDG}} = \mathbf{0} & \text{in } \Omega_{\texttt{HDG}}^e, \\ \boldsymbol{\nabla}_{\texttt{S}}^T \mathbf{D}_{\texttt{HDG}}^{1/2}\boldsymbol{Q}_{\texttt{HDG}} = \boldsymbol{f} & \text{in } \Omega_{\texttt{HDG}}^e, \\ \boldsymbol{u}_{\texttt{HDG}} = \boldsymbol{u}^D & \text{on } \partial\Omega_{\texttt{HDG}}^e \cap \Gamma_{\texttt{HDG}}^D, \\ \boldsymbol{u}_{\texttt{HDG}} = \hat{\boldsymbol{u}}_{\texttt{HDG}} & \text{on } \partial\Omega_{\texttt{HDG}}^e \setminus \Gamma_{\texttt{HDG}}^D, \\ -\mathbf{N}_{\texttt{HDG}}^T \mathbf{D}_{\texttt{HDG}}^{1/2}\boldsymbol{Q}_{\texttt{HDG}} = \boldsymbol{t}^N & \text{on } \partial\Omega_{\texttt{HDG}}^e \cap \Gamma_{\texttt{HDG}}^N, \\ \llbracket \boldsymbol{u}_{\texttt{HDG}} \otimes \boldsymbol{n}_{\texttt{HDG}} \rrbracket = \mathbf{0} & \text{on } \Gamma_{\texttt{HDG}}, \\ \left\llbracket \widehat{\mathbf{N}_{\texttt{HDG}}^T \mathbf{D}_{\texttt{HDG}}^{1/2}\boldsymbol{Q}_{\texttt{HDG}}} \right\rrbracket = \mathbf{0} & \text{on } \Gamma_{\texttt{HDG}}. \end{cases} \tag{4.42}$$

$\boldsymbol{Q}_{\texttt{HDG}}$ is the mixed variable representing the strain tensor in VOIGT notation scaled via the matrix $-\mathbf{D}_{\texttt{HDG}}^{1/2}$, whereas $\hat{\boldsymbol{u}}_{\texttt{HDG}}$ is the hybrid variable representing the trace of the primal solution $\boldsymbol{u}_{\texttt{HDG}}$ on the mesh skeleton. As explained for all HDG formulations throughout this thesis, the first equations in (4.42) represent the local DIRICHLET problems defined in each element $\Omega_{\texttt{HDG}}^e$, with $e = 1, \dots, \mathtt{n}_{\texttt{HDG}}^{\texttt{el}}$, while the last two equations define the transmission conditions imposing the continuity of the displacement field and the equilibrium of tractions across the interface $\Gamma_{\texttt{HDG}}$.

The strong form of the CG approximation of problem (4.41) follows a classical displacement-based formulation, discussed for instance by FISH and BELYTSCHKO [56], and reads

$$\begin{cases} -\boldsymbol{\nabla}_{\mathtt{S}}^T \mathbf{D}_{\mathtt{CG}} \boldsymbol{\nabla}_{\mathtt{S}} \boldsymbol{u}_{\mathtt{CG}} = \boldsymbol{f} & \text{in } \Omega_{\mathtt{CG}}, \\ \boldsymbol{u}_{\mathtt{CG}} = \boldsymbol{u}^D & \text{on } \Gamma_{\mathtt{CG}}^D, \\ \mathbf{N}_{\mathtt{CG}}^T \mathbf{D}_{\mathtt{CG}} \boldsymbol{\nabla}_{\mathtt{S}} \boldsymbol{u}_{\mathtt{CG}} = \boldsymbol{t}^N & \text{on } \Gamma_{\mathtt{CG}}^N. \end{cases} \tag{4.43}$$

On the one hand, CG methods provide computationally efficient discretizations for the solution of elasticity problems. On the other hand, however, it is commonly acknowledged that low-order displacement-based formulations fail to provide locking-free approximations when materials with nearly incompressible behaviors are involved, as discussed for instance by BABUŠKA and SURI [9]. To remedy this issue, several strategies have been proposed in literature, as briefly discussed in the introduction of this chapter.

The approach proposed in this thesis consists in the adoption of a hybrid HDG-CG discretization. In particular, the computationally cheap CG method is restricted to the compressible region, whereas the locking-free HDG method is employed in the nearly incompressible region. Therefore, let the domain Ω be split into two non-overlapping subdomains $\Omega_{\mathtt{HDG}}$ and $\Omega_{\mathtt{CG}}$ such that $\Omega = \Omega_{\mathtt{HDG}} \cup \Omega_{\mathtt{CG}}$, with interface $\Gamma^I = \Omega_{\mathtt{HDG}} \cap \Omega_{\mathtt{CG}}$. The efficient and minimally-intrusive NITSCHE-based coupling presented in Section 4.1.4 is exploited to enforce the transmission conditions

$$\begin{cases} \hat{\boldsymbol{u}}_{\mathtt{HDG}} = \boldsymbol{u}_{\mathtt{CG}} & \text{on } \Gamma^I, \\ \widehat{\mathbf{N}_{\mathtt{HDG}}^T \mathbf{D}_{\mathtt{HDG}}^{1/2} \boldsymbol{Q}_{\mathtt{HDG}}} = \widehat{\mathbf{N}_{\mathtt{CG}}^T \mathbf{D}_{\mathtt{CG}} \boldsymbol{\nabla}_{\mathtt{S}} \boldsymbol{u}_{\mathtt{CG}}} & \text{on } \Gamma^I. \end{cases} \tag{4.44}$$

A standard definition for the trace of the numerical normal fluxes is considered in the HDG subdomain according to

$$\widehat{\mathbf{N}_{\mathtt{HDG}}^T \mathbf{D}_{\mathtt{HDG}}^{1/2} \boldsymbol{Q}_{\mathtt{HDG}}} = \begin{cases} \mathbf{N}_{\mathtt{HDG}}^T \mathbf{D}_{\mathtt{HDG}}^{1/2} \boldsymbol{Q}_{\mathtt{HDG}} + \tau_u \left(\boldsymbol{u}_{\mathtt{HDG}} - \boldsymbol{u}^D \right) & \text{on } \partial\Omega_{\mathtt{HDG}}^e \cap \Gamma_{\mathtt{HDG}}^D, \\ \mathbf{N}_{\mathtt{HDG}}^T \mathbf{D}_{\mathtt{HDG}}^{1/2} \boldsymbol{Q}_{\mathtt{HDG}} + \tau_u \left(\boldsymbol{u}_{\mathtt{HDG}} - \hat{\boldsymbol{u}}_{\mathtt{HDG}} \right) & \text{on } \partial\Omega_{\mathtt{HDG}}^e \setminus \Gamma_{\mathtt{HDG}}^D. \end{cases} \tag{4.45}$$

An appropriate value for stabilization parameter τ_u to ensure the stability and the optimal convergence can be estimated as

$$\tau_u = C_u \frac{E}{l}, \tag{4.46}$$

with C_u being a positive scaling factor and l denoting a representative length scale. The trace of the CG normal stress along the interface is selected as

$$\widehat{\mathbf{N}_{\mathtt{CG}}^T \mathbf{D}_{\mathtt{CG}} \boldsymbol{\nabla}_{\mathtt{S}} \boldsymbol{u}_{\mathtt{CG}}} = \mathbf{N}_{\mathtt{CG}}^T \mathbf{D}_{\mathtt{CG}} \boldsymbol{\nabla}_{\mathtt{S}} \boldsymbol{u}_{\mathtt{CG}} - \frac{\gamma}{h} \left(\boldsymbol{u}_{\mathtt{CG}} - \hat{\boldsymbol{u}}_{\mathtt{HDG}} \right) \text{ on } \Gamma^I, \tag{4.47}$$

with h and γ denoting the characteristic element size and the NITSCHE penalty parameter, whose crucial role has been discussed in Section 4.1.4.

The HDG local problems are not affected by the hybrid coupling and they allow to compute the primal variable $\boldsymbol{u}_{\mathtt{HDG}}$ as a function of only the hybrid variable $\hat{\boldsymbol{u}}_{\mathtt{HDG}}$. Their weak form thus reads: given $\boldsymbol{u}^D$ on $\Gamma_{\mathtt{HDG}}^D$ and $\hat{\boldsymbol{u}}_{\mathtt{HDG}}$ on $\Gamma_{\mathtt{HDG}} \cup \Gamma_{\mathtt{HDG}}^N \cup \Gamma^I$, find $(\boldsymbol{Q}_{\mathtt{HDG}}, \boldsymbol{u}_{\mathtt{HDG}}) \in [\mathcal{W}^h(\Omega_{\mathtt{HDG}}^e)]^{\mathtt{msd}} \times$

$[\mathcal{W}^h(\Omega^e_{\texttt{HDG}})]^{\texttt{n}_{\texttt{sd}}}$ for $e = 1, \dots, \texttt{n}^{\texttt{el}}_{\texttt{HDG}}$ such that

$$\begin{aligned}
&-(\boldsymbol{W}, \boldsymbol{Q}_{\texttt{HDG}})_{\Omega^e_{\texttt{HDG}}} + \left(\boldsymbol{\nabla}^T_{\texttt{S}}\mathbf{D}^{1/2}_{\texttt{HDG}}\boldsymbol{W}, \boldsymbol{u}_{\texttt{HDG}}\right)_{\Omega^e_{\texttt{HDG}}} = \\
&\qquad \left\langle \mathbf{N}^T_{\texttt{HDG}}\mathbf{D}^{1/2}_{\texttt{HDG}}\boldsymbol{W}, \boldsymbol{u}^D \right\rangle_{\partial\Omega^e_{\texttt{HDG}}\cap\Gamma^D_{\texttt{HDG}}} + \left\langle \mathbf{N}^T_{\texttt{HDG}}\mathbf{D}^{1/2}_{\texttt{HDG}}\boldsymbol{W}, \hat{\boldsymbol{u}}_{\texttt{HDG}} \right\rangle_{\partial\Omega^e_{\texttt{HDG}}\setminus\Gamma^D_{\texttt{HDG}}},
\end{aligned} \tag{4.48a}$$

$$\begin{aligned}
&\left(\boldsymbol{w}, \boldsymbol{\nabla}^T_{\texttt{S}}\mathbf{D}^{1/2}_{\texttt{HDG}}\boldsymbol{Q}_{\texttt{HDG}}\right)_{\Omega^e_{\texttt{HDG}}} + \langle \boldsymbol{w}, \tau_u \boldsymbol{u}_{\texttt{HDG}} \rangle_{\partial\Omega^e_{\texttt{HDG}}} = (\boldsymbol{w}, \boldsymbol{f})_{\Omega^e_{\texttt{HDG}}} \\
&\qquad + \left\langle \boldsymbol{w}, \tau_u \boldsymbol{u}^D \right\rangle_{\partial\Omega^e_{\texttt{HDG}}\cap\Gamma^D_{\texttt{HDG}}} + \langle \boldsymbol{w}, \tau_u \hat{\boldsymbol{u}}_{\texttt{HDG}} \rangle_{\partial\Omega^e_{\texttt{HDG}}\setminus\Gamma^D_{\texttt{HDG}}},
\end{aligned} \tag{4.48b}$$

for all $(\boldsymbol{W}, \boldsymbol{w}) \in [\mathcal{W}^h(\Omega^e_{\texttt{HDG}})]^{\texttt{m}_{\texttt{sd}}} \times [\mathcal{W}^h(\Omega^e_{\texttt{HDG}})]^{\texttt{n}_{\texttt{sd}}}$.

In the philosophy of the proposed HDG-CG coupling strategy, the transmission conditions (4.44) are solely exploited in the global problem. In particular, owning to the definition (4.47), the traction equilibrium is enforced in the HDG subproblem as a NEUMANN-type boundary condition, whereas the continuity of the displacement is weakly imposed in the CG subproblem as a DIRICHLET-type boundary conditions, by means of NITSCHE's method. Consequently, the weak form of the global problem reads: find $(\hat{\boldsymbol{u}}_{\texttt{HDG}}, \boldsymbol{u}_{\texttt{CG}}) \in [\widehat{\mathcal{W}}^h(\Gamma_{\texttt{HDG}} \cup \Gamma^N_{\texttt{HDG}} \cup \Gamma^I)]^{\texttt{n}_{\texttt{sd}}} \times [\mathcal{V}^h(\Omega_{\texttt{CG}})]^{\texttt{n}_{\texttt{sd}}}$ such that

$$\begin{aligned}
&-\sum_{e=1}^{\texttt{n}^{\texttt{el}}_{\texttt{HDG}}} \left\{ \left\langle \hat{\boldsymbol{w}}, \mathbf{N}^T_{\texttt{HDG}}\mathbf{D}^{1/2}_{\texttt{HDG}}\boldsymbol{Q}_{\texttt{HDG}} + \tau_u \left(\boldsymbol{u}_{\texttt{HDG}} - \hat{\boldsymbol{u}}_{\texttt{HDG}}\right) \right\rangle_{\partial\Omega^e_{\texttt{HDG}}\setminus\Gamma^D_{\texttt{HDG}}} \right. \\
&\left. - \left\langle \hat{\boldsymbol{w}}, \left(-\mathbf{N}^T_{\texttt{HDG}}\right) \mathbf{D}_{\texttt{CG}}\boldsymbol{\nabla}_{\texttt{S}}\boldsymbol{u}_{\texttt{CG}} - \frac{\gamma}{h}\left(\boldsymbol{u}_{\texttt{CG}} - \hat{\boldsymbol{u}}_{\texttt{HDG}}\right) \right\rangle_{\partial\Omega^e_{\texttt{HDG}}\cap\Gamma^I} \right\} = \sum_{e=1}^{\texttt{n}^{\texttt{el}}_{\texttt{HDG}}} \left\langle \hat{\boldsymbol{w}}, \boldsymbol{t}^N \right\rangle_{\partial\Omega^e_{\texttt{HDG}}\cap\Gamma^N_{\texttt{HDG}}},
\end{aligned} \tag{4.49a}$$

$$\begin{aligned}
&(\boldsymbol{\nabla}_{\texttt{S}}\boldsymbol{v}, \mathbf{D}_{\texttt{CG}}\boldsymbol{\nabla}_{\texttt{S}}\boldsymbol{u}_{\texttt{CG}})_{\Omega_{\texttt{CG}}} - \left\langle \boldsymbol{v}, \mathbf{N}^T_{\texttt{CG}}\mathbf{D}_{\texttt{CG}}\boldsymbol{\nabla}_{\texttt{S}}\boldsymbol{u}_{\texttt{CG}} - \frac{\gamma}{h}\left(\boldsymbol{u}_{\texttt{CG}} - \hat{\boldsymbol{u}}_{\texttt{HDG}}\right) \right\rangle_{\Gamma^I} \\
&- \left\langle \mathbf{N}^T_{\texttt{CG}}\mathbf{D}_{\texttt{CG}}\boldsymbol{\nabla}_{\texttt{S}}\boldsymbol{v}, \boldsymbol{u}_{\texttt{CG}} - \hat{\boldsymbol{u}}_{\texttt{HDG}} \right\rangle_{\Gamma^I} = (\boldsymbol{v}, \boldsymbol{f})_{\Omega_{\texttt{CG}}} + \left\langle \boldsymbol{v}, \boldsymbol{t}^N \right\rangle_{\Gamma^N_{\texttt{CG}}},
\end{aligned} \tag{4.49b}$$

for all $(\hat{\boldsymbol{w}}, \boldsymbol{v}) \in [\widehat{\mathcal{W}}^h(\Gamma_{\texttt{HDG}} \cup \Gamma^N_{\texttt{HDG}} \cup \Gamma^I)]^{\texttt{n}_{\texttt{sd}}} \times [\mathcal{V}^h_0(\Omega_{\texttt{CG}})]^{\texttt{n}_{\texttt{sd}}}$.

In the HDG subdomain, a displacement field $\boldsymbol{u}^\star_{\texttt{HDG}}$ superconverging with order $k + 2$ can be obtained through an inexpensive element-by-element postprocessing procedure. The postprocessing reads: given $(\boldsymbol{Q}_{\texttt{HDG}}, \boldsymbol{u}_{\texttt{HDG}})$ in $\Omega^e_{\texttt{HDG}}$, $\boldsymbol{u}^D$ on $\Gamma^D_{\texttt{HDG}}$ and $\hat{\boldsymbol{u}}_{\texttt{HDG}}$ on $\Gamma_{\texttt{HDG}} \cup \Gamma^N_{\texttt{HDG}} \cup \Gamma^I$, find $\boldsymbol{u}^\star_{\texttt{HDG}} \in [\mathcal{W}^h_\star(\Omega^e_{\texttt{HDG}})]^{\texttt{n}_{\texttt{sd}}}$ for $e = 1, \dots, \texttt{n}^{\texttt{el}}_{\texttt{HDG}}$ such that

$$-\left(\boldsymbol{\nabla}_{\texttt{S}}\boldsymbol{w}^\star, \mathbf{D}^{1/2}_{\texttt{HDG}}\boldsymbol{\nabla}_{\texttt{S}}\boldsymbol{u}^\star_{\texttt{HDG}}\right)_{\Omega^e_{\texttt{HDG}}} = (\boldsymbol{\nabla}_{\texttt{S}}\boldsymbol{w}^\star, \boldsymbol{Q}_{\texttt{HDG}})_{\Omega^e_{\texttt{HDG}}}, \tag{4.50a}$$

$$(\boldsymbol{u}_{\texttt{T}}, \boldsymbol{u}^\star_{\texttt{HDG}})_{\Omega^e_{\texttt{HDG}}} = (\boldsymbol{u}_{\texttt{T}}, \boldsymbol{u}_{\texttt{HDG}})_{\Omega^e_{\texttt{HDG}}}, \tag{4.50b}$$

$$\begin{aligned}
(\boldsymbol{u}_{\texttt{R}}, \boldsymbol{\nabla}_{\texttt{W}}\boldsymbol{u}^\star_{\texttt{HDG}})_{\Omega^e_{\texttt{HDG}}} &= \left\langle \boldsymbol{u}_{\texttt{R}}, \mathbf{T}_{\texttt{HDG}}\boldsymbol{u}^D \right\rangle_{\partial\Omega^e_{\texttt{HDG}}\cap\Gamma^D_{\texttt{HDG}}} \\
&\quad + \langle \boldsymbol{u}_{\texttt{R}}, \mathbf{T}_{\texttt{HDG}}\hat{\boldsymbol{u}}_{\texttt{HDG}} \rangle_{\partial\Omega^e_{\texttt{HDG}}\setminus\Gamma^D_{\texttt{HDG}}},
\end{aligned} \tag{4.50c}$$

for all $(\boldsymbol{w}^\star, \boldsymbol{u}_{\texttt{T}}, \boldsymbol{u}_{\texttt{R}}) \in [\mathcal{W}^h_\star(\Omega^e_{\texttt{HDG}})]^{\texttt{n}_{\texttt{sd}}} \times [\mathcal{U}^h(\Omega^e_{\texttt{HDG}})]^{\texttt{n}_{\texttt{sd}}} \times [\mathcal{U}^h(\Omega^e_{\texttt{HDG}})]^{\texttt{q}_{\texttt{sd}}}$. The symbols $\boldsymbol{\nabla}_{\texttt{W}}$ and $\mathbf{T}$ denote the skew-symmetric part of the gradient and the tangent operator in VOIGT notation and they have been already defined in (3.15) and (3.20). The first equation in (4.50) is a least-squares fit to the mixed variable $\boldsymbol{Q}_{\texttt{HDG}}$, while the last two equations remove the underdetermination of the problem by constraining the rigid motions, i.e. $\texttt{n}_{\texttt{sd}}$ translations and $\texttt{q}_{\texttt{sd}}$ rotations.

4.3 Numerical examples

The numerical examples presented in this section investigate the effectiveness of the proposed strategy to couple HDG and CG discretizations in the context of thermal and elastic problems. The proposed technique is compared against the other coupling strategy available in literature and the influence of the NITSCHE parameter on the error is analyzed in the first two-dimensional numerical example. The following example instead assesses the optimal convergence of the HDG-CG coupling in a three-dimensional setting. The optimal global convergence of the stress and the superconvergence of the displacement field, together with a locking-free approximation, are then shown on two- and three-dimensional structural problems featuring multiple materials with compressible and nearly incompressible behaviors. The HDG-CG coupling techniques presented in this section have been implemented and tested in the `MATLAB` environment.

4.3.1 Two-dimensional thermal problem

The first numerical example considers a two-dimensional thermal problem, whose physical behavior is described by POISSON's equation (4.1). The main purpose is to assess the optimal convergence of the coupling strategies presented in Sections 4.1.3 and 4.1.4 and to analyze the influence of NITSCHE's parameter on the accuracy of the proposed hybrid HDG-CG coupling.

The analytical expression of the temperature field reads

$$T\left(x,y\right) = \cos\left(\frac{\pi}{2}\sqrt{x^2+y^2}\right), \tag{4.51}$$

whereas the source term is given by

$$s\left(x,y\right) = \frac{\pi}{2}\left[\frac{1}{\sqrt{x^2+y^2}}\sin\left(\frac{\pi}{2}\sqrt{x^2+y^2}\right) + \frac{\pi}{2}\cos\left(\frac{\pi}{2}\sqrt{x^2+y^2}\right)\right]. \tag{4.52}$$

The computational domain $\Omega = (-1,1) \times (-1,1)$ is decomposed into two non-overlapping subdomains, namely $\Omega_{\text{HDG}} = (-1,0) \times (-1,1)$ and $\Omega_{\text{CG}} = (0,1) \times (-1,1)$. The interface is therefore identified by $\Gamma^I = \{(x,y) \in \mathbb{R}^2 : x = 0\}$. DIRICHLET boundary conditions, corresponding to the restriction of the analytical solution to the domain boundary, are imposed on $\Gamma^D = \partial\Omega$. A unique thermal conductivity $\kappa = 1$ is considered in the whole domain.

The domain Ω is discretized using uniform meshes of triangular elements and five levels of refinement are considered for the convergence studies, i.e. $r = [1, 2, \ldots, 5]$. In Figure 4.3, the first three levels of mesh refinement are shown. The HDG subdomain is represented in blue and the CG one in red, whereas the black line denotes the interface. The two aforementioned coupling strategies are considered:

1. HDG-CG local-global coupling strategy according to Section 4.1.3,
2. HDG-CG NITSCHE-based coupling strategy according to Section 4.1.4.

In the following spatial convergence studies, the polynomial degree of approximation ranges from $k = 1$ to $k = 5$. For the stabilization of the HDG subproblem, a scaling factor $C_T = 10$ is considered. Given the thermal conductivity $\kappa = 1$ and the representative length scale $l = 1$,

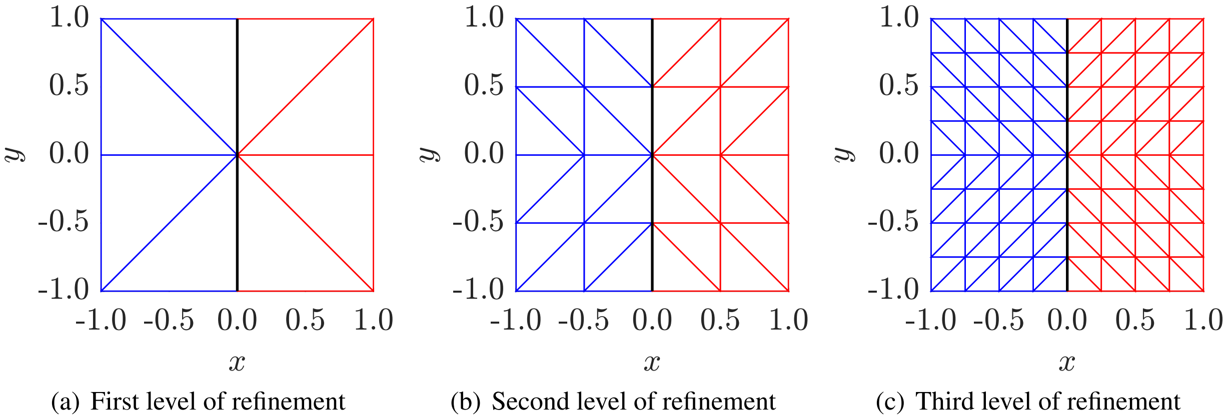

(a) First level of refinement (b) Second level of refinement (c) Third level of refinement

Figure 4.3: Computational mesh for two-dimensional thermal problem

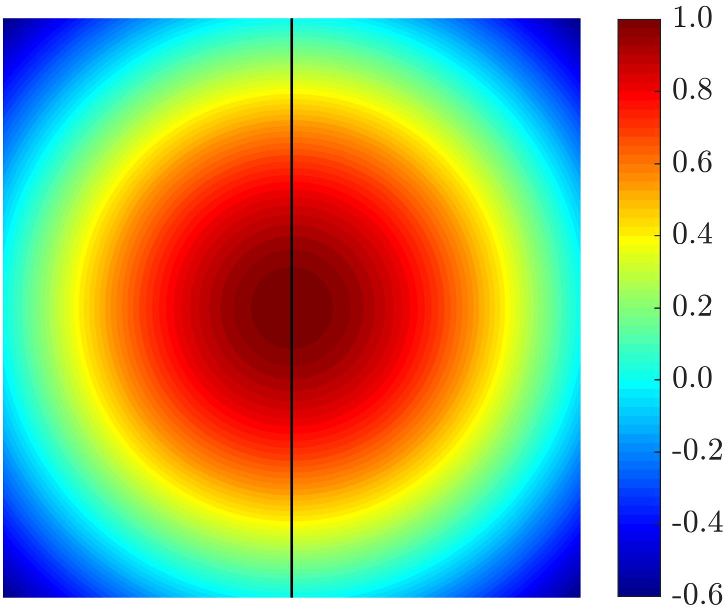

Figure 4.4: Solution of temperature for two-dimensional thermal problem

the stabilization parameter is considered equal to $\tau_T = 10$, according to equation (4.6). The NITSCHE parameter for the second case is instead taken as $\gamma = 100$.

The temperature field obtained with the NITSCHE-based coupling with $r = 5$ and $k = 5$ is exemplarily shown in Figure 4.4. The solution is obtained with a level of accuracy close to machine precision and no numerical oscillations are observed on the interface Γ^I.

The convergence of the error of the temperature measured in the $\mathcal{L}^2$ norm as a function of the characteristic element size h is presented in Figure 4.5 for the first case. Optimal convergence of order $k + 1$ is achieved in both the HDG subdomain (Figure 4.5(a)) and the CG subdomain (Figure 4.5(b)).

The convergence results obtained with the proposed NITSCHE-based coupling are presented in Figure 4.6, instead. Analogously to the first case, optimal convergence rates are obtained in both subdomains. It is worth point out that, given the higher number of DOFs in the HDG sub-

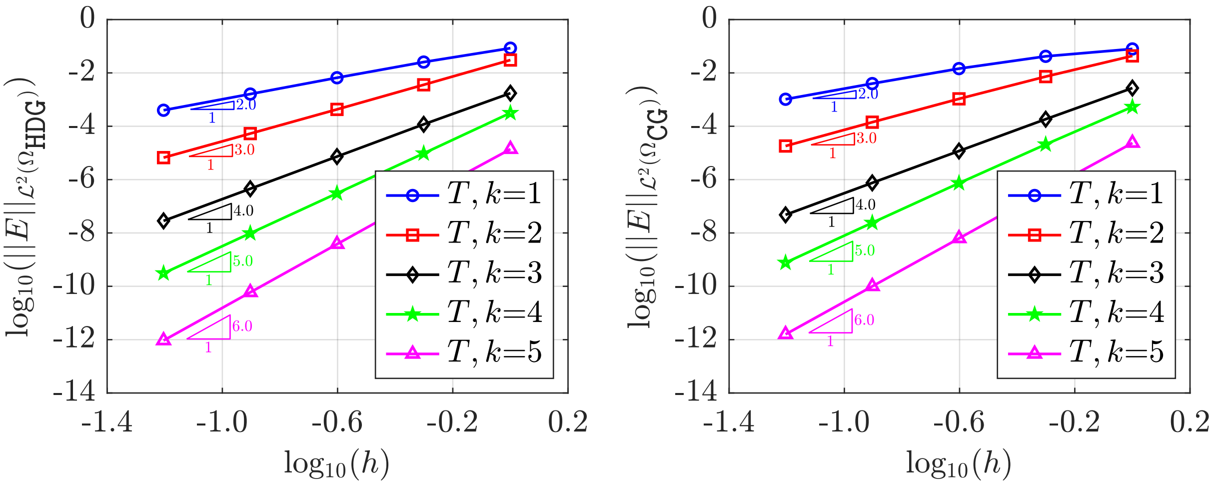

(a) HDG subdomain

(b) CG subdomain

Figure 4.5: Spatial convergence study for two-dimensional thermal problem via local-global coupling

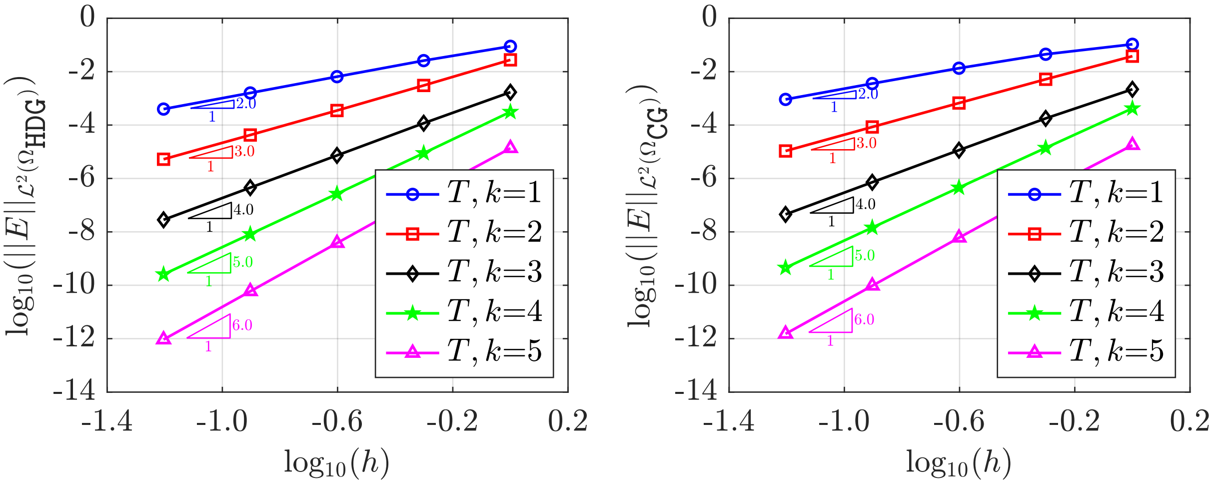

(a) HDG subdomain

(b) CG subdomain

Figure 4.6: Spatial convergence study for two-dimensional thermal problem via NITSCHE-based coupling

domain compared to the CG subdomain, the $\mathcal{L}^2$ error in Ω_{HDG} is systematically smaller than the corresponding one in Ω_{CG}, for a given level of mesh refinement r and polynomial degree k. Moreover, for high mesh refinements, the NITSCHE-based coupling produces slightly smaller errors compared to the local-global coupling. These differences are however minimal and the two coupling strategies can be considered to provide nearly identical accuracy. As explained in Section 4.1.4, the main advantage of the NITSCHE-based coupling is its minimally-intrusive nature, which makes this approach extremely easy to implement in existing HDG and CG libraries. Given the different treatment of the HDG global DOFs at the interface provided by the two cou-

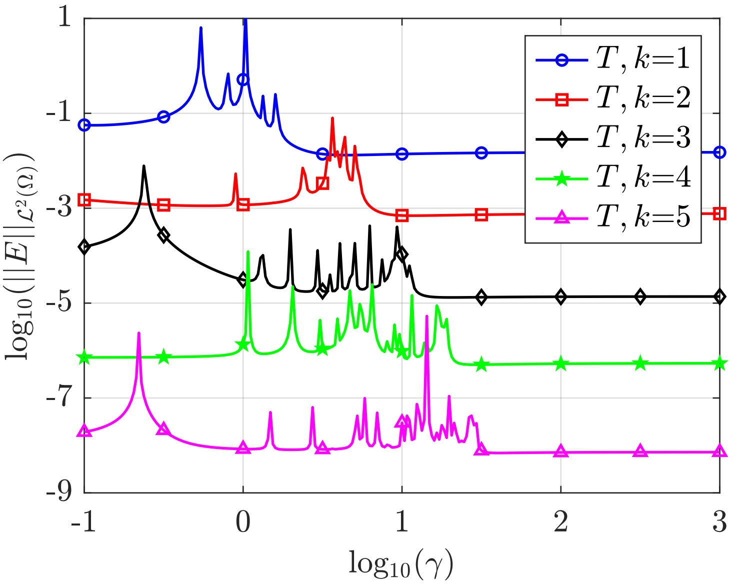

Figure 4.7: Plot of error as function of NITSCHE's parameter for two-dimensional thermal problem

pling strategies, a different size of the final linear system is expected. However, this difference is negligible for sufficiently fine meshes and high polynomial degrees. In fact, the number of global unknowns resulting from the NITSCHE-based coupling is about 33% larger than the corresponding one obtained with the local-global coupling for $r = 1$ and $k = 1$, but this difference reduces to less than 1% for $r = 5$ and $k = 5$.

This computationally inexpensive two-dimensional scalar problem constitutes a good benchmark for the analysis of the influence of NITSCHE's parameter on the accuracy of the proposed hybrid HDG-CG coupling. Figure 4.7 displays the evolution of the error, measured in the $\mathcal{L}^2$ norm, of the primal variable T on the whole domain Ω as a function of NITSCHE's parameter γ using the third level of mesh refinement ($r = 3$) and the same polynomial degrees adopted in the convergence studies, i.e. $k = [1, 2, \dots, 5]$. In particular, the range $\gamma \in (10^{-1}, 10^3)$ is subdivided into 256 equally spaced intervals in the logarithmic scale. It is well-known from literature that there exists a lower bound for γ below which the method is unstable, as observed by HANSBO [73] in the context general interface problems arising in computational mechanics. The spikes in Figure 4.7 clearly show the range in which NITSCHE's method provides unreliable results, due to an insufficient stabilization introduced by the numerical scheme. On the one hand, any value of γ above this lower bound could be chosen to ensure stability, since NITSCHE's method is consistent. On the other hand, however, very large values of γ may excessively increase the condition number of the resulting linear system, leading to ill-conditioned problems. An estimation of a lower bound of NITSCHE's parameter can be obtained by solving an auxiliary generalized eigenvalue problem, as suggested by GRIEBEL and SCHWEITZER [70]. It is worth noting that the value of γ ensuring stable results varies by about one order of magnitude in the range of polynomial degrees considered here. It is then clear that the value $\gamma = 100$, used for the convergence study in Figure 4.6, represents therefore a valid choice since it guaranties stability without compromising the condition number of the linear system.

4.3.2 Three-dimensional thermal problem

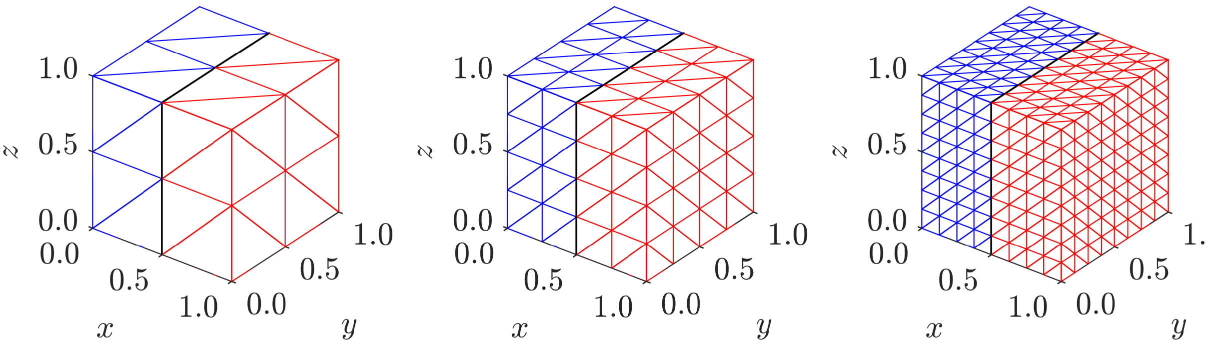

(a) First level of refinement (b) Second level of refinement (c) Third level of refinement

Figure 4.8: Computational mesh for three-dimensional thermal problem

The second numerical example consists of a three-dimensional thermal problem and the main goal is to assess the convergence properties of the proposed NITSCHE-based HDG-CG coupling in a three-dimensional setting.

The analytical solution is

$$T(x,y,z) = \sin(\pi x)\sin(\pi y)\sin(\pi z)\,, \tag{4.53}$$

and it is obtained by applying the following source in the right hand side of equation (4.1)

$$s(x,y,z) = 3\pi^2 \sin(\pi x)\sin(\pi y)\sin(\pi z)\,. \tag{4.54}$$

The computational domain is the unit cube $\Omega = (0,1)\times(0,1)\times(0,1)$ and it is decomposed into two non-overlapping subdomains, namely $\Omega_{\text{HDG}} = (0,0.5)\times(0,1)\times(0,1)$ and $\Omega_{\text{CG}} = (0.5,1)\times(0,1)\times(0,1)$. The resulting HDG-CG interface is represented by the plane $\Gamma^I = \{(x,y,z)\in\mathbb{R}^3 : x = 0.5\}$. Homogeneous DIRICHLET boundary conditions are applied on the whole boundary $\Gamma^D = \partial\Omega$. The thermal conductivity is considered $\kappa = 1$ in both subdomains.

Uniform meshes of tetrahedral elements are considered for the domain by splitting a regular $2^r \times 2^r \times 2^r$ Cartesian grid into a total of $6\cdot 2^{3r}$ tetrahedra, giving element sizes of $h = 1/2^r$. Five levels of mesh refinement are considered, i.e. $r = [1,2,\ldots,5]$, whereas only linear elements ($k = 1$) are taken into account. The first three levels of mesh refinement are shown in Figure 4.8, in which the HDG subdomain is represented in blue and the CG one in red. The interface plane is instead denoted in black. The stabilization parameter considered is $\tau_T = 1$ and the NITSCHE parameter for the coupling is taken as $\gamma = 100$.

Figure 4.9 depicts the solution of the temperature field obtained on the finest mesh, i.e. $r = 5$. The temperature has a zero value on the boundary and it reaches the maximum value of 1 in the center of the domain. From the cut in Ω_{CG}, the high regularity of the solution and the absence of any irregularity on the interface can be observed. The convergence of the temperature error in the $\mathcal{L}^2$ norm is then shown in Figure 4.10 with respect to the HDG subdomain (left) and the CG subdomain (right). Although the error in Ω_{HDG} is always smaller than the corresponding one in Ω_{CG}, given the higher total number of DOFs in the HDG discretization, optimal convergence rates with order $k+1$ are achieved in both subdomains, confirming the capability of the proposed hybrid coupling to accurately solve also three-dimensional problems.

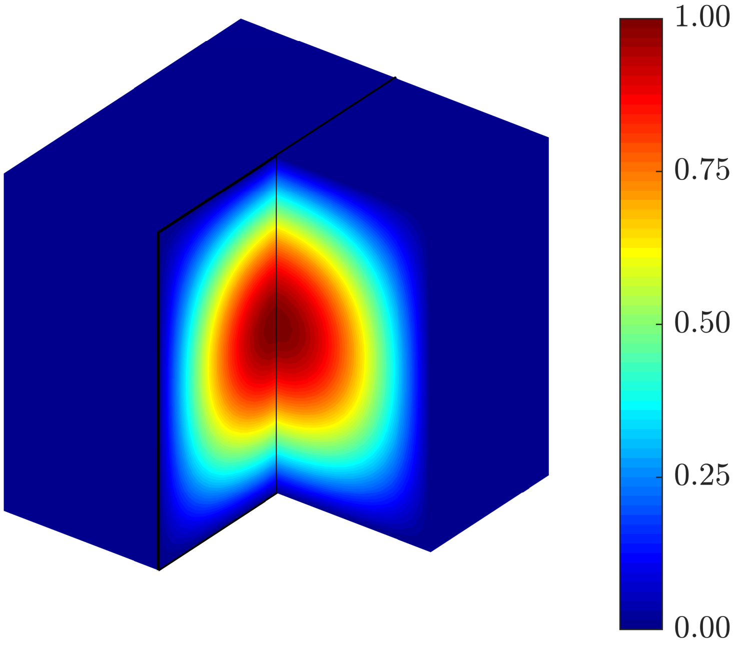

Figure 4.9: Solution of temperature for three-dimensional thermal problem

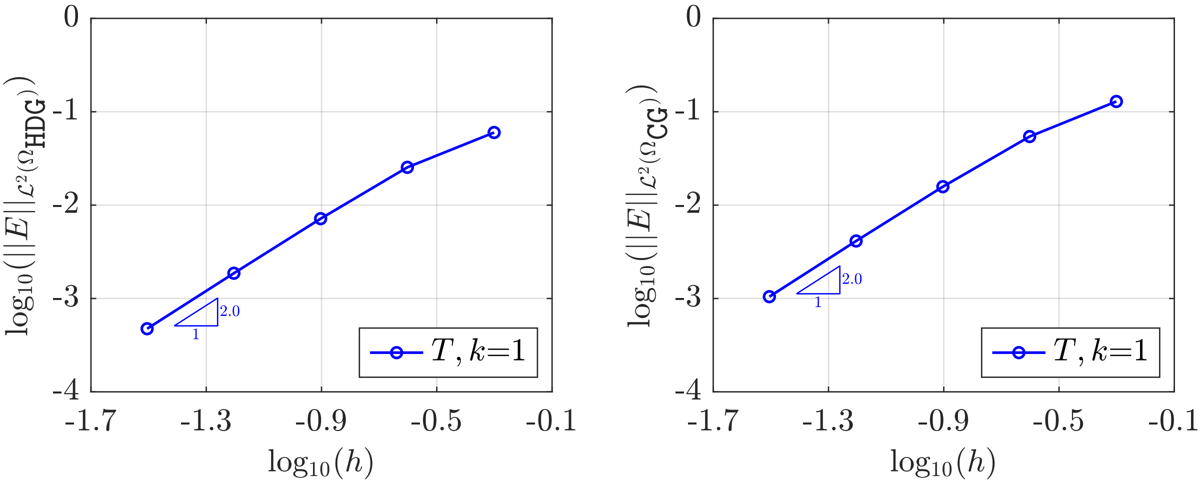

(a) HDG subdomain

(b) CG subdomain

Figure 4.10: Spatial convergence study for three-dimensional thermal problem

4.3.3 Two-dimensional elastic problem

This numerical experiment considers a two-dimensional elastic problem, involving compressible and nearly incompressible solids. It is inspired by the work of LAMICHHANE [98], who proposed a mortar finite element method for the coupling of inhomogeneous materials. This example serves as a benchmark for assessing the convergence properties of the NITSCHE-based coupling in the context of multimaterial elastic problems and for highlighting the benefits of adopting a nonuniform polynomial degrees of approximation.

The analytical solution in terms of displacement reads

$$\begin{cases} u_x(x,y) = -\dfrac{2(1+\nu)}{E}\left[1-\cos(2\pi x)\right]\sin(2\pi y) \\ \qquad\qquad + \dfrac{(1+\nu)(1-2\nu)}{(1+\nu)(1-2\nu)+\nu E} xy\sin(\pi x)\sin(\pi y), \\ u_y(x,y) = +\dfrac{2(1+\nu)}{E}\sin(2\pi x)\left[1-\cos(2\pi y)\right] \\ \qquad\qquad + \dfrac{(1+\nu)(1-2\nu)}{(1+\nu)(1-2\nu)+\nu E} xy\sin(\pi x)\sin(\pi y), \end{cases} \tag{4.55}$$

and the following forcing term is added in the right hand side of the governing equation in (4.33)

$$\begin{cases} f_x(x,y) = -4\pi^2\left[1-2\cos(2\pi x)\right]\sin(2\pi y) \\ \qquad -\dfrac{E}{2\left[(1+\nu)(1-2\nu)+\nu E\right]}\Big\{\left[1-\pi^2(3-4\nu)xy\right]\sin(\pi x)\sin(\pi y) \\ \qquad\qquad +\pi\left[2(1-2\nu)x+y\right]\sin(\pi x)\cos(\pi y) \\ \qquad\qquad +\pi\left[x+4(1-\nu)y\right]\cos(\pi x)\sin(\pi y) \\ \qquad\qquad +\pi^2 xy\cos(\pi x)\cos(\pi y)\Big\}, \\ f_y(x,y) = +4\pi^2\sin(2\pi x)\left[1-2\cos(2\pi y)\right] \\ \qquad -\dfrac{E}{2\left[(1+\nu)(1-2\nu)+\nu E\right]}\Big\{\left[1-\pi^2(3-4\nu)xy\right]\sin(\pi x)\sin(\pi y) \\ \qquad\qquad +\pi\left[4(1-\nu)x+y\right]\sin(\pi x)\cos(\pi y) \\ \qquad\qquad +\pi\left[x+2(1-2\nu)y\right]\cos(\pi x)\sin(\pi y) \\ \qquad\qquad +\pi^2 xy\cos(\pi x)\cos(\pi y)\Big\}. \end{cases} \tag{4.56}$$

The computational domain $\Omega = (-1,1)\times(-1,1)$ is decomposed into two non-overlapping subdomains, namely $\Omega_{\texttt{ninc}} = (-1,0)\times(0,1)\cup(0,1)\times(-1,0)$ and $\Omega_{\texttt{comp}} = (-1,0)\times(-1,0)\cup(0,1)\times(0,1)$, featuring nearly incompressible and compressible behaviors, respectively. The interface coincides with the Cartesian axes, i.e. $\Gamma^I = \{(x,y)\in\mathbb{R}^2 : x = 0 \text{ or } y = 0\}$. Homogeneous DIRICHLET boundary conditions are applied on the boundary $\Gamma^D = \partial\Omega$.

A nearly incompressible and soft material is considered in $\Omega_{\texttt{ninc}}$ with YOUNG's modulus $E_{\texttt{ninc}} = 25$ and POISSON's ratio $\nu_{\texttt{ninc}} = 0.49999$, whereas a compressible and stiff material is considered in $\Omega_{\texttt{comp}}$ with YOUNG's modulus $E_{\texttt{comp}} = 250$ and POISSON's ratio $\nu_{\texttt{comp}} = 0.3$.

For the convergence studies, the same triangular pattern of the two-dimensional thermal problem in Section 4.3.1 is used for meshing the computational domain and seven levels of refinement are adopted to observe the convergence rates in the asymptotic regime, i.e. $r = [1, 2, \ldots, 7]$. The meshes corresponding to the first three levels of refinement are shown in Figure 4.11, where the nearly incompressible and the compressible subdomains are drawn in blue and red, respectively, whereas the interface is denoted in black. In order to show the enhanced features of the hybrid coupling, four strategies are considered in the following:

1. HDG method with degree k in Ω,
2. CG method with degree k in Ω,
3. HDG method with degree k in $\Omega_{\texttt{ninc}}$ and CG method with degree k in $\Omega_{\texttt{comp}}$,
4. HDG method with degree k in $\Omega_{\texttt{ninc}}$ and CG method with degree $k+1$ in $\Omega_{\texttt{comp}}$ with HDG local postprocess.

The polynomial degree of approximation considered is $k = [1, 2, 3]$ and the coupling for the last two cases is performed via the NITSCHE-based coupling presented in Section 4.2. A unique stabilization parameter $\tau_u = 2.5 \cdot 10^2$, estimated according to equation (4.46) with scaling factor $C_u = 1$, representative length scale $l = 1$ and YOUNG's modulus $E = \max(E_{\texttt{ninc}}, E_{\texttt{comp}})$, is chosen whenever the HDG method is adopted. NITSCHE's parameter is set to $\gamma = 2.5 \cdot 10^3$ for the third case and it is amplified by a factor of 10 for the fourth case, where a nonuniform approximation is employed. It is worth recalling that, although some a priori estimates of the lower bound of NITSCHE's parameter may be derived as explained in Section 4.3.1, the value of γ is problem-dependent and is affected both by the equation under analysis and the material parameters considered.

Figure 4.12 depicts the displacement magnitude on the second level of mesh refinement ($r = 2$) with $k = 1$. The discontinuity of the material parameters is responsible for the displacement field in $\Omega_{\texttt{comp}}$ to be one order of magnitude smaller than the one in $\Omega_{\texttt{ninc}}$. Thus, the displacement values are magnified by a factor of 5, to appreciate the displacement in the CG subdomain as well. Figure 4.12 clearly shows that the solution in the HDG subdomain is approximated by means of polynomial functions discontinuous across the elements, whereas the displacement field in the CG subdomain is continuous by construction. Moreover, an improved solution is obtained in case 4 (Figure 4.12(b)) compared to case 3 (Figure 4.12(a)). In fact, the CG solution gains accuracy by using polynomial functions of one degree higher, whereas the HDG displacement improves through the inexpensive postprocessing in (4.50). The VON MISES stress obtained with the same polynomial degree of approximation ($k = 1$) on the fifth level of mesh refinement ($r = 5$) is shown in Figure 4.13. It is computed in two dimensions as

$$\sigma_{\text{VM}} = \sqrt{\sigma_{xx}^2 + \sigma_{yy}^2 - \sigma_{xx}\sigma_{yy} + 3\sigma_{xy}^2}. \tag{4.57}$$

The stress field is approximated with linear elements in the HDG subdomain, given the independent interpolation of the (scaled) symmetric part of the displacement gradient by means of the mixed variable $\boldsymbol{Q}_{\texttt{HDG}}$. In the CG subdomain, instead, the computed stress is only elementwise constant, leading to the rather coarse representation of σ_{VM} in Figure 4.13(a). Analogously to the displacement field, an improved approximation is achieved for the stress field by employing polynomial functions of one degree higher in the CG subdomain (Figure 4.13(b)).

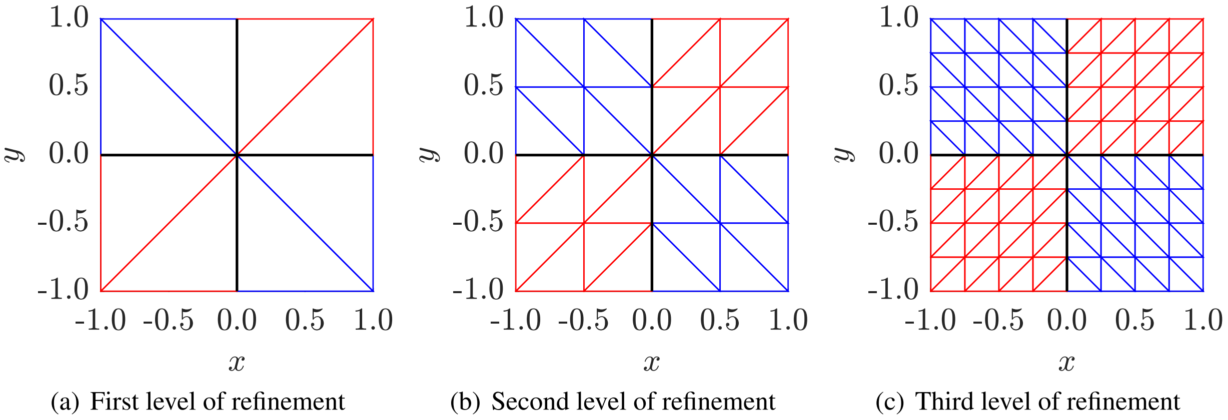

(a) First level of refinement (b) Second level of refinement (c) Third level of refinement

Figure 4.11: Computational mesh for two-dimensional elastic problem

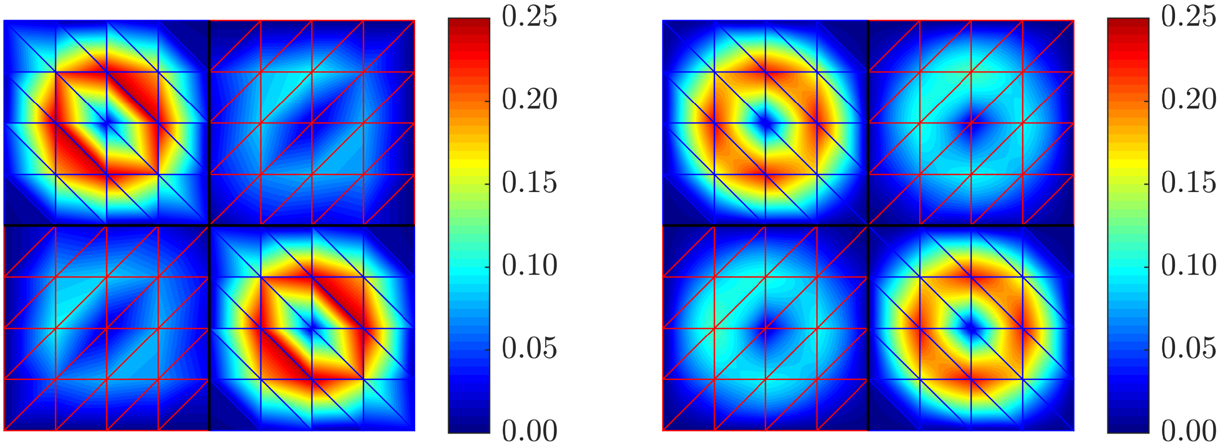

(a) HDG$_k$-CG$_k$ (b) HDG$_k$-CG$_{k+1}$ with postprocess

Figure 4.12: Solution of displacement for two-dimensional elastic problem

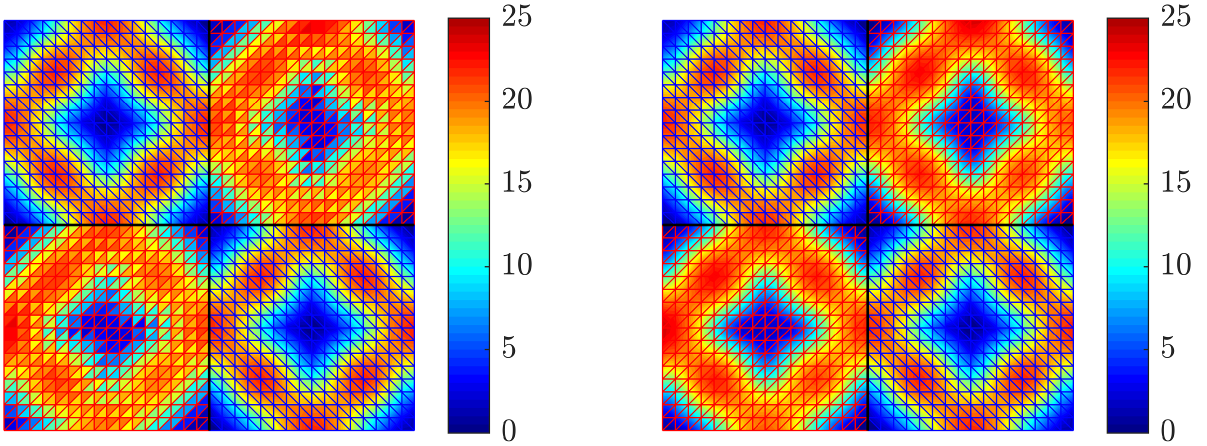

(a) HDG$_k$-CG$_k$ (b) HDG$_k$-CG$_{k+1}$

Figure 4.13: Solution of VON MISES stress for two-dimensional elastic problem

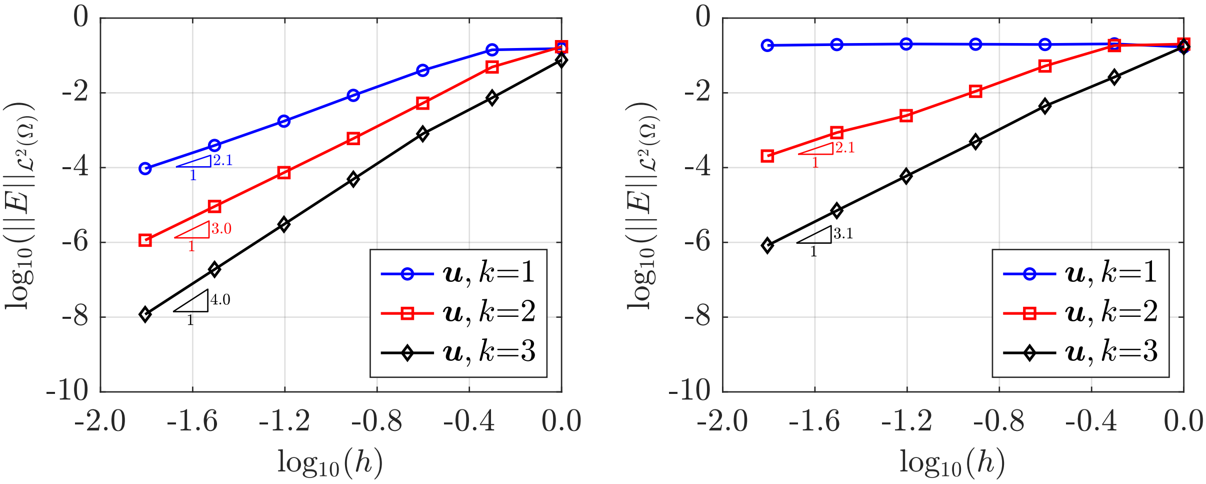

(a) HDG$_k$ (b) CG$_k$

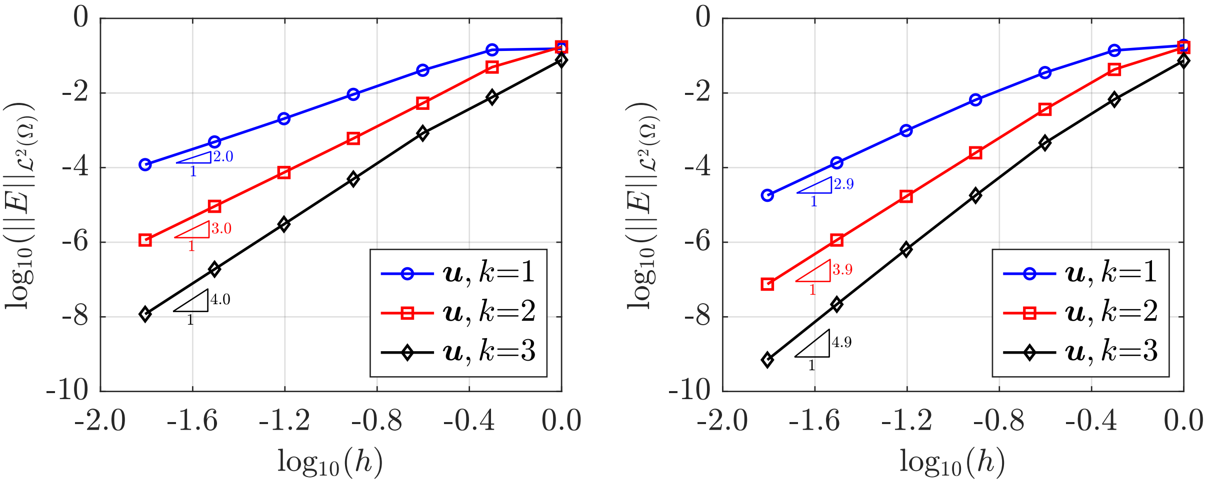

(c) HDG$_k$-CG$_k$ (d) HDG$_k$-CG$_{k+1}$ with postprocess

Figure 4.14: Spatial convergence study of displacement for two-dimensional elastic problem

The convergence of the error of the displacement on the whole domain Ω measured in the $\mathcal{L}^2$ norm as a function of the characteristic element size h is presented in Figure 4.14 for the four cases considered. The CG$_k$ approximation suffers from classical locking phenomena due to the presence of a nearly incompressible material in $\Omega_{\texttt{ninc}}$, preventing convergence for $k = 1$, whereas suboptimal rates of order k are obtained for higher polynomial degrees. On the contrary, both the HDG$_k$ and the hybrid HDG$_k$-CG$_k$ method exhibit optimal convergence of order $k + 1$ without locking effects. It is worth noting that the HDG$_k$-CG$_k$ coupling produces almost identical accuracy compared to the HDG$_k$ case in terms of displacement, but at a significantly reduced computational cost, given the smaller number of total DOFs. In fact, for the finest level of mesh refinement considered ($r = 7$), the number of global unknowns is $[195584, 293376, 391168]$ via HDG$_k$ and only $[115202, 214018, 345602]$ via HDG$_k$-CG$_k$ for $k = [1, 2, 3]$, respectively. Finally, considering a nonuniform degree of approximation via HDG$_k$-CG$_{k+1}$ and exploiting the HDG postprocessing strategy, superconvergence with order $k + 2$ is achieved.

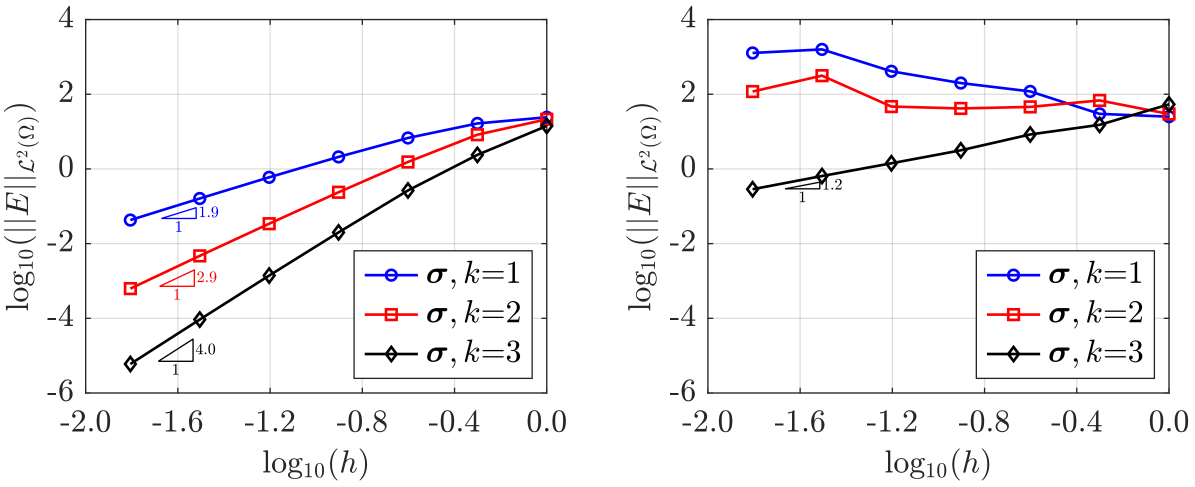

(a) HDG_k

(b) CG_k

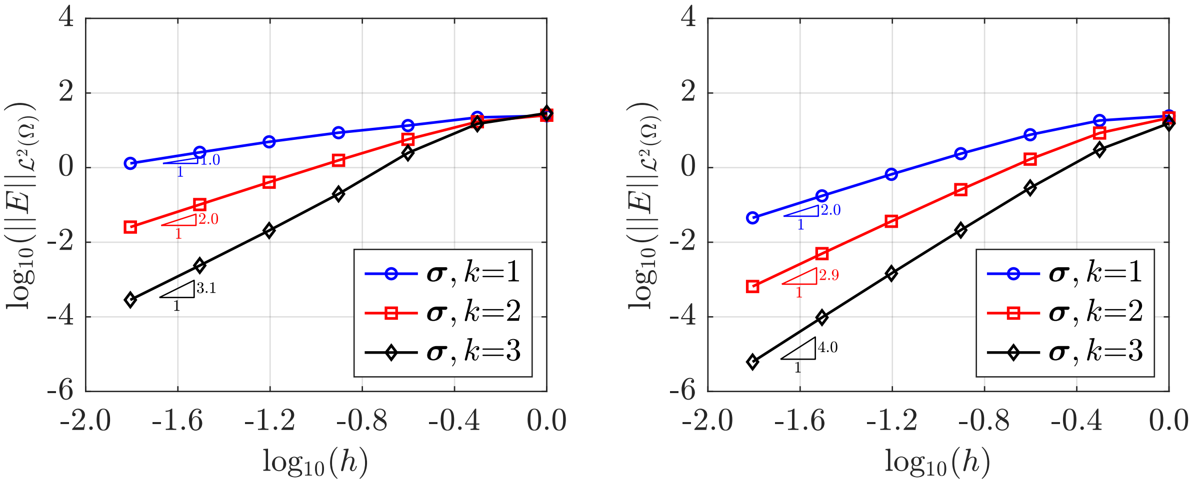

(c) HDG_k-CG_k

(d) HDG_k-CG_{k+1}

Figure 4.15: Spatial convergence study of stress for two-dimensional elastic problem

The convergence results of the stress field are then reported in Figure 4.15. The computation of the stress as a postprocessing of the displacement field leads to unreliable results, due to locking effects, when the CG_k approximation is adopted in the whole domain Ω. On the contrary, a direct approximation of the stress tensor is provided by mixed formulations. The HDG_k method, in particular, exploits the definition of the mixed variable $\boldsymbol{Q}_{\texttt{HDG}}$ to obtain optimal convergence of the stress with order $k+1$. Then, when the HDG_k-CG_k method is adopted, only suboptimal convergence of order k is obtained in the whole domain Ω, given the suboptimal convergence of the stress in $\Omega_{\texttt{comp}}$. Finally, optimal convergence of the stress with order $k+1$ can be globally recovered, by adopting the hybrid HDG_k-CG_{k+1} coupling.

4.3.4 Bimaterial COOK's membrane problem

This numerical example considers the classical bending-dominated problem of COOK's membrane. The problem is named after the author, who first reported it at COOK *et al.* [38]. After its introduction, this example has been used by several authors, especially to test the quality of finite element formulations in the presence of (nearly) incompressible solids. Here, a revisited setting is considered to take into account two materials with different mechanical properties, as proposed by LAMICHHANE [98]. The main objective is to show the locking-free behavior of the proposed NITSCHE-based coupling of HDG and CG discretizations, as the POISSON ratio tends to the incompressible limit, i.e. $\nu \to 0.5$.

The domain of the tapered plate is defined as $\Omega = \operatorname{hull}\{(0,0),(48,44),(48,60),(0,44)\}$, with $\operatorname{hull}\{\odot\}$ denoting the convex hull operator. A compressible material occupies the region $\Omega_{\texttt{comp}} = \operatorname{hull}\{(12,20.25),(36,38.75),(36,50.25),(12,38.75)\}$, whereas a nearly incompressible material is considered in the remaining space, i.e. $\Omega_{\texttt{ninc}} = \Omega \setminus \Omega_{\texttt{comp}}$. The plate is clamped on the left edge via homogeneous DIRICHLET boundary conditions ($\boldsymbol{u}^D = \boldsymbol{0}$) and it is subjected to the shear load

$$\begin{cases} t_x^N(48,y) = 0, \\ t_y^N(48,y) = 6.25, \end{cases} \tag{4.58}$$

applied on the right edge as a NEUMANN boundary condition. The geometry and the boundary conditions of the problem are sketched in Figure 4.16.

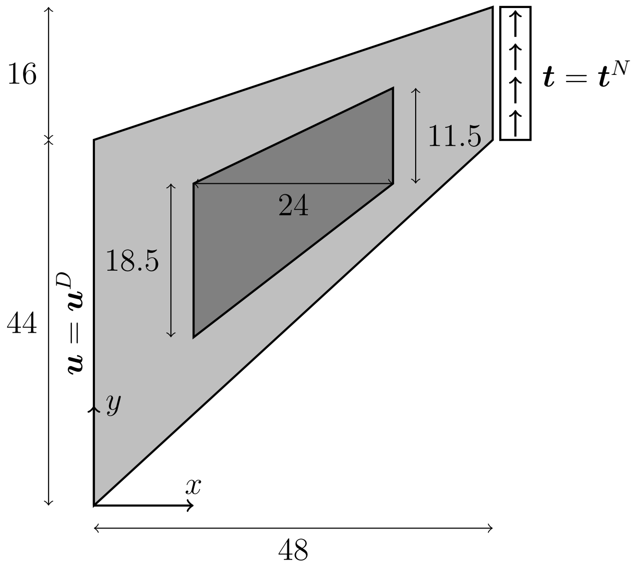

Figure 4.16: Geometry and boundary conditions for bimaterial COOK's membrane problem

The material in $\Omega_{\texttt{comp}}$ is characterized by YOUNG's modulus $E_{\texttt{comp}} = 250$ and POISSON's ratio $\nu_{\texttt{comp}} = 0.35$, whereas for the nearly incompressible material in $\Omega_{\texttt{ninc}}$ YOUNG's modulus is $E_{\texttt{ninc}} = 80$ and POISSON's ratio spans the values $\nu_{\texttt{ninc}} = [0.49, 0.4999, 0.499999]$.

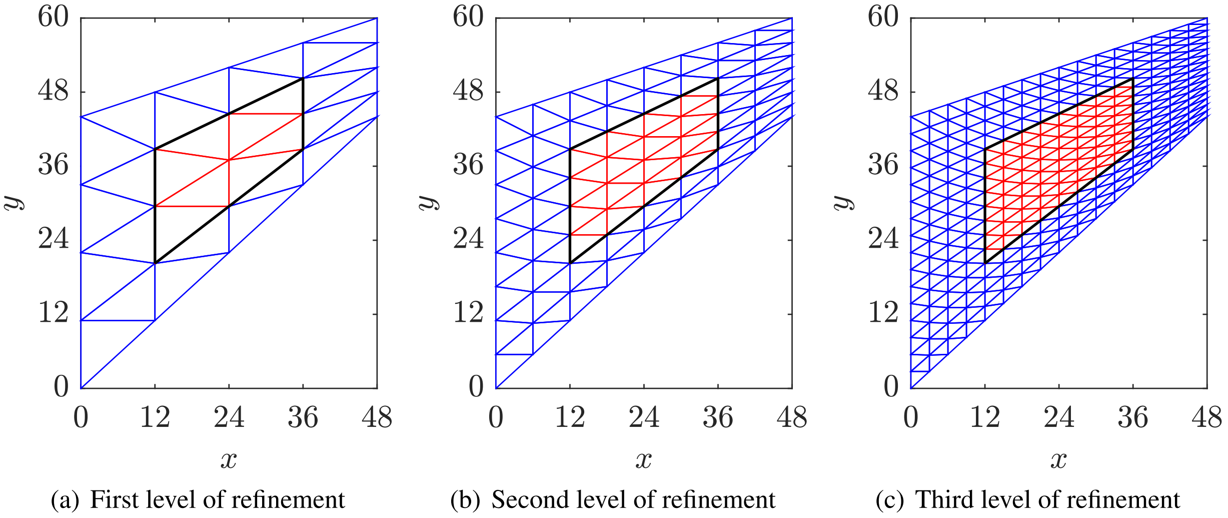

(a) First level of refinement (b) Second level of refinement (c) Third level of refinement

Figure 4.17: Computational mesh for bimaterial COOK's membrane problem

Uniform meshes of triangular elements are considered by subdividing the whole domain Ω into a total of $2 \cdot 2^{2r+2}$ triangles, with $r = [1, 2, \dots, 5]$. The first three levels of mesh refinement are shown in Figure 4.17, in which the blue, the red and the black lines denote the subdomains $\Omega_{\texttt{ninc}}$ and $\Omega_{\texttt{comp}}$ and the interface $\Gamma^I = \Omega_{\texttt{ninc}} \cap \Omega_{\texttt{comp}}$, respectively. As in the previous example, four strategies are considered:

1. HDG method with degree k in Ω,
2. CG method with degree k in Ω,
3. HDG method with degree k in $\Omega_{\texttt{ninc}}$ and CG method with degree k in $\Omega_{\texttt{comp}}$,
4. HDG method with degree k in $\Omega_{\texttt{ninc}}$ and CG method with degree $k+1$ in $\Omega_{\texttt{comp}}$.

A constant stabilization parameter $\tau_u = 10$ is considered on all HDG faces and the NITSCHE parameter $\gamma = 10^4$ is adopted for the hybrid HDG-CG coupling.

All the displacement and stress components obtained via the different strategies on the fifth level of mesh refinement with $\nu_{\texttt{ninc}} = 0.4999$ are compared in Figure 4.18. CG$_k$ provides unreliable results due to locking effects while similar values are obtained with the other approaches. In particular, a slightly more accurate stress approximation is achieved by the HDG$_k$-CG$_{k+1}$ coupling compared to the HDG$_k$-CG$_k$ one, due to the increased accuracy in the CG subdomain. The evolution of the vertical displacement of the top right corner is then plotted in Figure 4.19 as a function of the number of elements in Ω, for the various POISSON ratios. The closer the coefficient is to 0.5, the more severe is the underestimation of the displacement obtained via CG$_k$. By contrast, the other approaches are locking-free and lead to a tip vertical displacement of about 21, without loss of accuracy in the incompressible limit. In particular, a faster convergence is observed for the nonuniform HDG$_k$-CG$_{k+1}$ coupling, compared to the uniform counterpart.

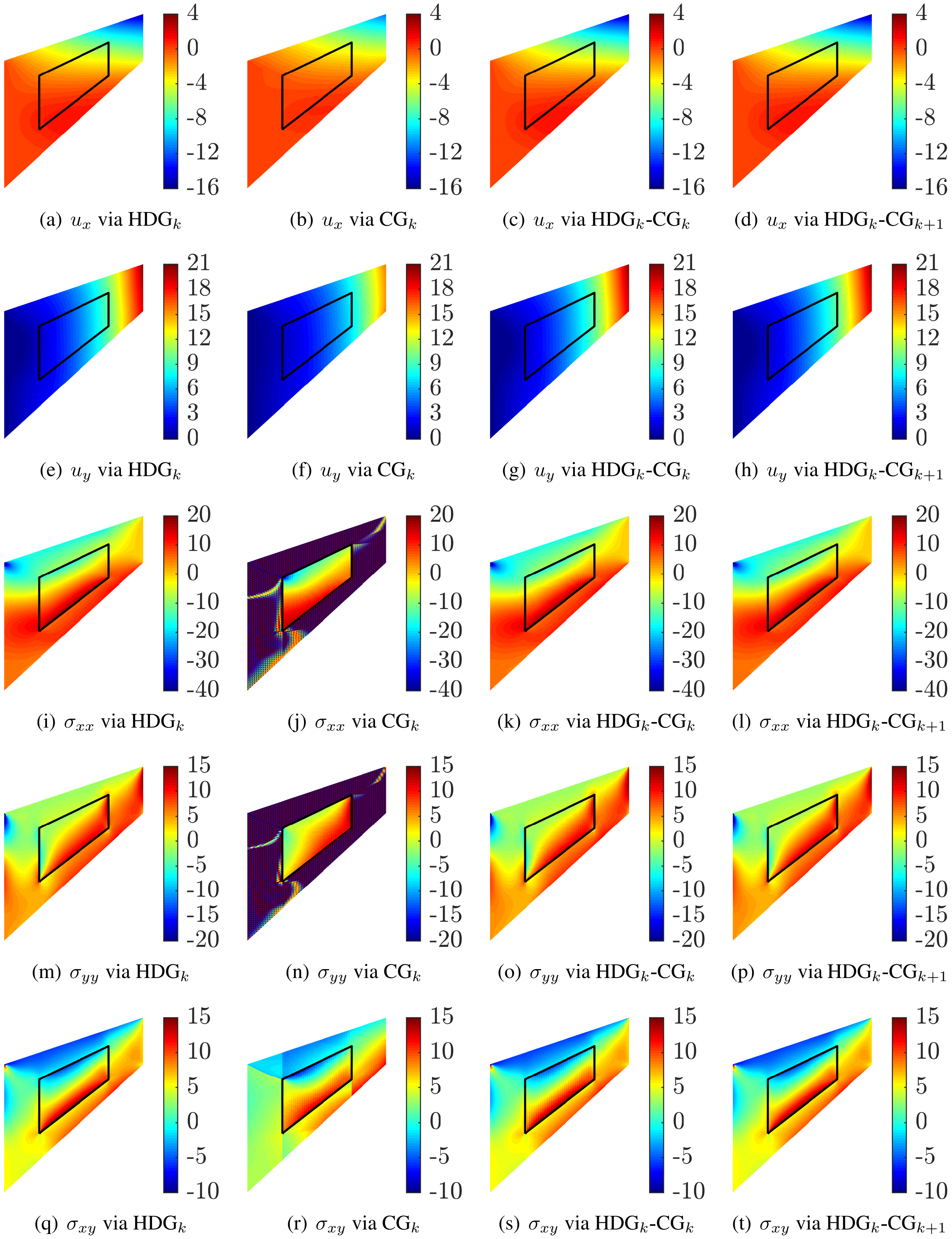

(a) u_x via HDG$_k$ (b) u_x via CG$_k$ (c) u_x via HDG$_k$-CG$_k$ (d) u_x via HDG$_k$-CG$_{k+1}$

(e) u_y via HDG$_k$ (f) u_y via CG$_k$ (g) u_y via HDG$_k$-CG$_k$ (h) u_y via HDG$_k$-CG$_{k+1}$

(i) σ_{xx} via HDG$_k$ (j) σ_{xx} via CG$_k$ (k) σ_{xx} via HDG$_k$-CG$_k$ (l) σ_{xx} via HDG$_k$-CG$_{k+1}$

(m) σ_{yy} via HDG$_k$ (n) σ_{yy} via CG$_k$ (o) σ_{yy} via HDG$_k$-CG$_k$ (p) σ_{yy} via HDG$_k$-CG$_{k+1}$

(q) σ_{xy} via HDG$_k$ (r) σ_{xy} via CG$_k$ (s) σ_{xy} via HDG$_k$-CG$_k$ (t) σ_{xy} via HDG$_k$-CG$_{k+1}$

Figure 4.18: Solution of displacement and stress for bimaterial COOK's membrane problem

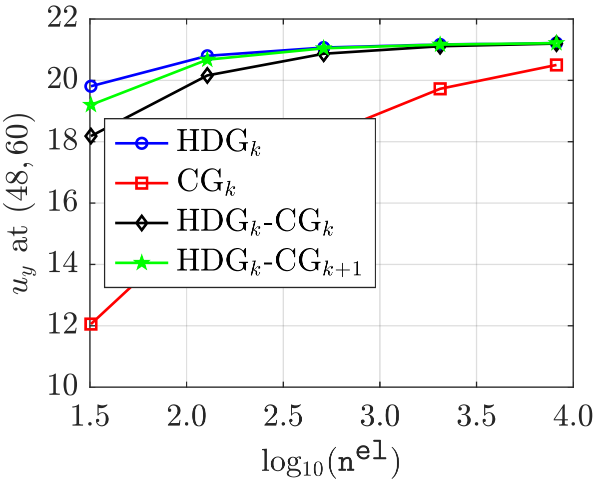

(a) $\nu_{\mathtt{ninc}} = 0.49$

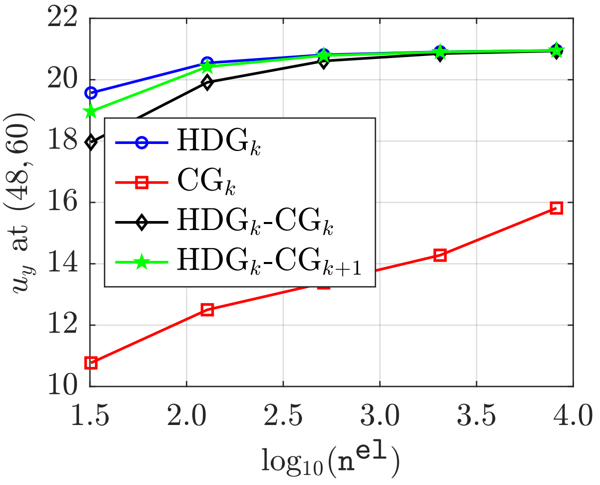

(b) $\nu_{\mathtt{ninc}} = 0.4999$

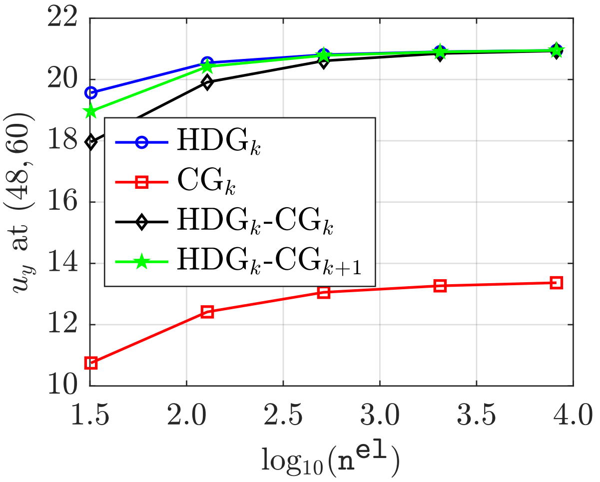

(c) $\nu_{\mathtt{ninc}} = 0.499999$

Figure 4.19: Plot of displacement for bimaterial COOK's membrane problem

4.3.5 Three-dimensional laminated composite beam

This numerical example considers a three-dimensional laminated composite beam to show the capability of the proposed HDG-CG coupling to treat problems of interest for engineering applications. Laminated composite beams are widely used in industry because of the possibility to assemble different materials in order to build new structures, exhibiting superior properties in terms of strength or stiffness to weight ratio and high resistance to external agents.

The domain of the beam is the parallelepiped $\Omega = (-1,1)\times(-1,1)\times(1,10)$ and it is obtained by stacking layers of alternating material properties. Two layers of a nearly incompressible material occupy the region $\Omega_{\texttt{ninc}} = (-1,1) \times (-1,-0.5) \times (0,10) \cup (-1,1) \times (0,0.5) \times (0,10)$, whereas other two layers of a compressible isotropic material are in considered in $\Omega_{\texttt{comp}} = (-1,1) \times (-0.5,0) \times (0,10) \cup (-1,1) \times (0.5,1) \times (0,10)$. The interface is thus defined as $\Gamma^I = \{(x,y,z) \in \mathbb{R}^3 : y = -0.5$ or $y = 0$ or $y = 0.5\}$. The beam is fixed at $z = 0$ by means of homogeneous DIRICHLET boundary conditions ($\boldsymbol{u}^D = \mathbf{0}$) and it is subjected to the uniformly distributed load

$$\begin{cases} t_x^N\,(x,1,z) = 0, \\ t_y^N\,(x,1,z) = -2.167 \cdot 10^{-3}, \\ t_z^N\,(x,1,z) = 0, \end{cases} \tag{4.59}$$

on the top surface of the beam via NEUMANN boundary conditions. The geometry and the boundary conditions of the problem are depicted in Figure 4.20.

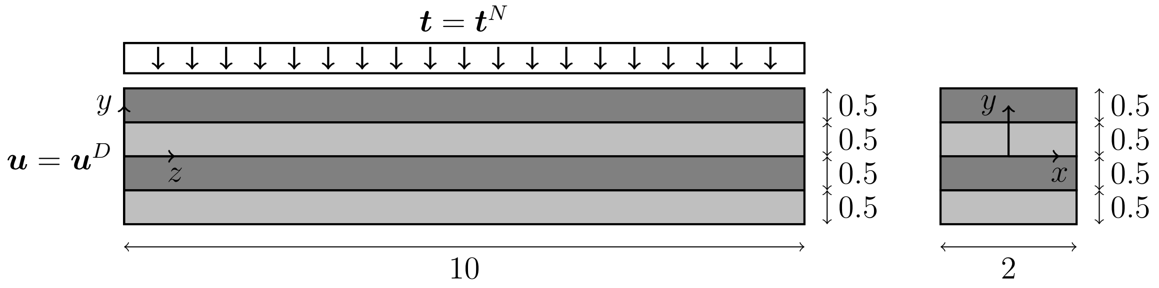

Figure 4.20: Geometry and boundary conditions for three-dimensional laminated composite beam

Analogously to the previous numerical examples, the nearly incompressible material is softer than the compressible one and the main resistance to bending comes from the compressible and stiffer material. In particular, YOUNG's modulus and POISSON's ratio are $E_{\texttt{ninc}} = 1$ and $\nu_{\texttt{ninc}} = 0.49999$ in $\Omega_{\texttt{ninc}}$ and $E_{\texttt{comp}} = 10$ and $\nu_{\texttt{comp}} = 0.3$ in $\Omega_{\texttt{comp}}$.

Three different mesh configurations are considered, whereas only elements of degree $k = 1$ are employed. The reference solution is computed using the HDG method on the mesh in Figure 4.21(c) featuring 414720 tetrahedral elements, for a total of 7568640 global DOFs, representing the displacement on the faces. As opposed to the strategy based on a nonuniform polynomial approximation adopted in Sections 4.3.3 and 4.3.4, here an improved solution is achieved by

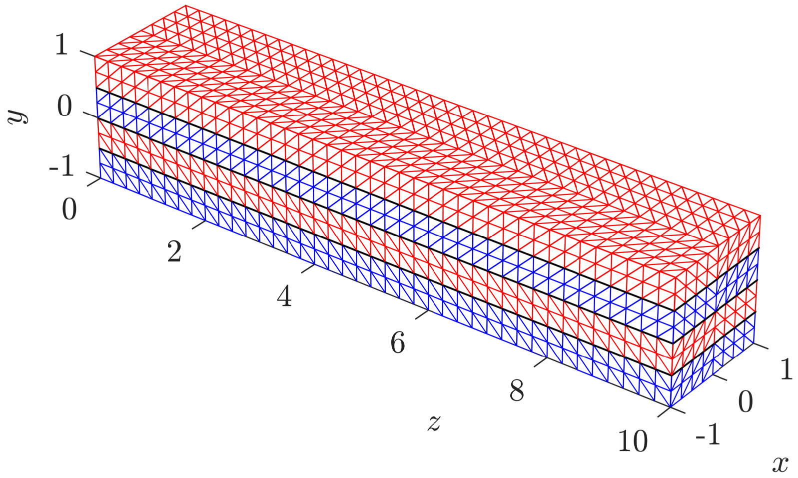

(a) Coarse mesh

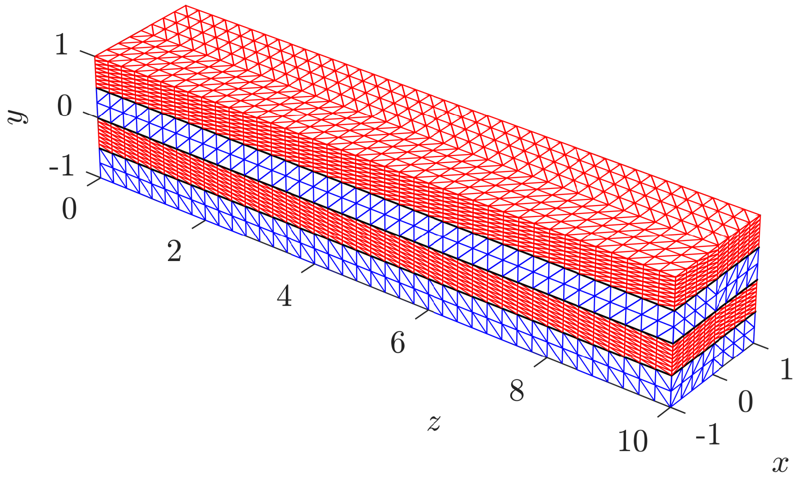

(b) Fine mesh

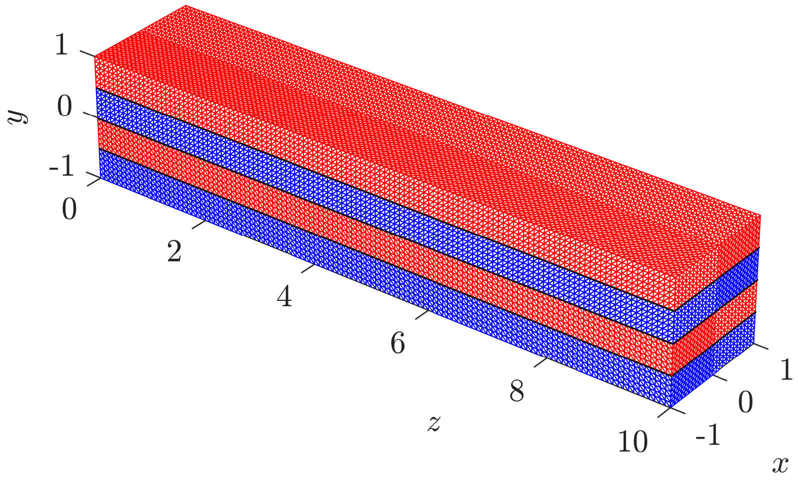

(c) Reference mesh

Figure 4.21: Computational mesh for three-dimensional laminated composite beam

	$\mathtt{n}^{\mathtt{dof}}$	$\left\lvert 1-u_y/u_y^{\mathtt{ref}}\right\rvert$	$\left\lvert 1-V_y/V_y^{\mathtt{ref}}\right\rvert$	$\left\lvert 1-M_x/M_x^{\mathtt{ref}}\right\rvert$
HDG coarse	288000	0%	0%	0%
CG coarse	9963	75%	0%	78%
HDG-CG coarse	159282	8%	2%	7%
HDG-CG fine	172566	4%	2%	2%

Table 4.1: Number of DOFs and error for three-dimensional laminated composite beam

increasing the number of DOFs in the subdomain $\Omega_{\mathtt{comp}}$. More precisely, the coarse mesh in Figure 4.21(a) counts 7680 elements both in $\Omega_{\mathtt{ninc}}$ and $\Omega_{\mathtt{comp}}$, whereas the fine mesh in Figure 4.21(b) features 7680 and 30720 tetrahedra in the two subdomains. The nearly incompressible material is represented in blue and the compressible material in red, while the interface planes are displayed in black. Five simulations are considered in total, by applying:

1. HDG method in Ω on the coarse mesh,
2. CG method in Ω on the coarse mesh,
3. HDG method in $\Omega_{\mathtt{ninc}}$ and CG method in $\Omega_{\mathtt{comp}}$ on the coarse mesh,
4. HDG method in $\Omega_{\mathtt{ninc}}$ and CG method in $\Omega_{\mathtt{comp}}$ on the fine mesh,
5. HDG method on the reference mesh.

The stabilization parameter in every HDG discretization is taken as $\tau_u = 10$ and the NITSCHE parameter $\gamma = 100$ is used for the hybrid HDG-CG coupling.

The relative error of the vertical displacement at the beam free end (point $(0, 0, 10)$) and of the shear and the bending moment at midspan ($z = 5$) is reported in Table 4.1 for the different strategies considered, together with the associated number of global DOFs in the resulting linear system. The displacement is directly obtained from the solution of the problem, while the shear and the bending moment are computed in postprocessing through the following formulas

$$V_y(z) = -\int_x \int_y \sigma_{zy}(x, y, z)\, dxdy, \tag{4.60}$$

and

$$M_x(z) = -\int_x \int_y \sigma_{zz}(x, y, z)(y - \bar{y})\, dxdy. \tag{4.61}$$

The y-coordinate of the neutral axis is evaluated as

$$\bar{y} = \frac{E_{\mathtt{comp}} - E_{\mathtt{ninc}}}{2\left(E_{\mathtt{comp}} + E_{\mathtt{ninc}}\right)}\bar{h}, \tag{4.62}$$

with $\bar{h} = 0.5$ being the thickness of a single layer of the beam. On the one hand, the HDG method on the coarse mesh produces the same results of the reference solution, but at a high computational cost ($\mathtt{n}^{\mathtt{dof}} = 288000$). On the other hand, the CG method applied on the whole domain produces completely unreliable results due to locking effects, except for the shear that

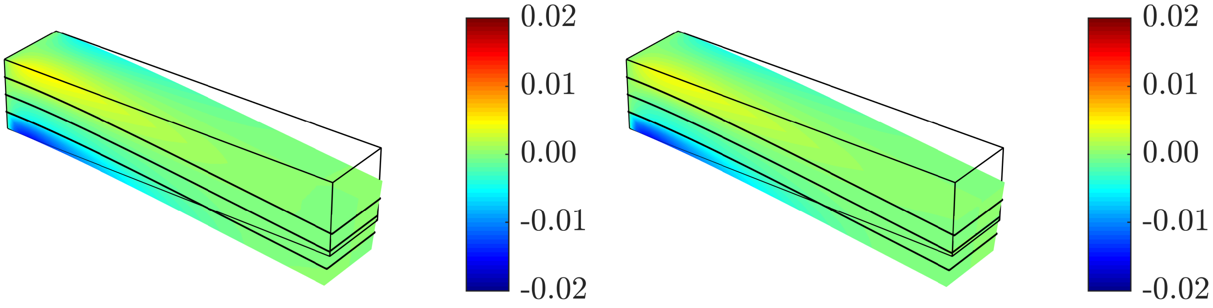

(a) x-displacement via HDG-CG on coarse mesh (b) x-displacement via HDG-CG on fine mesh

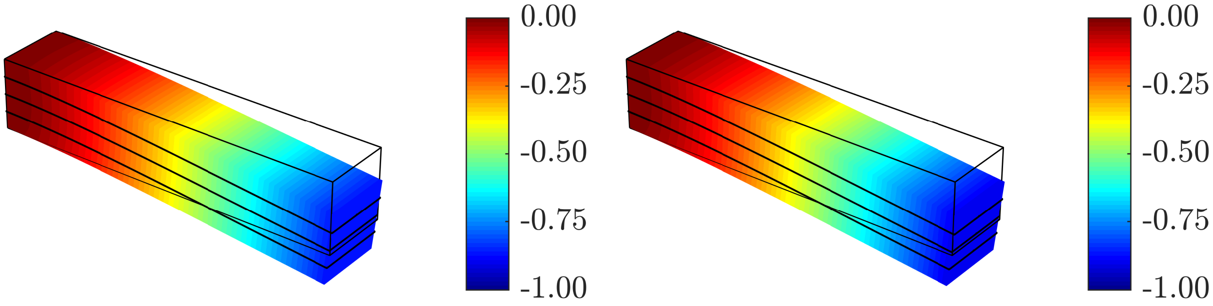

(c) y-displacement via HDG-CG on coarse mesh (d) y-displacement via HDG-CG on fine mesh

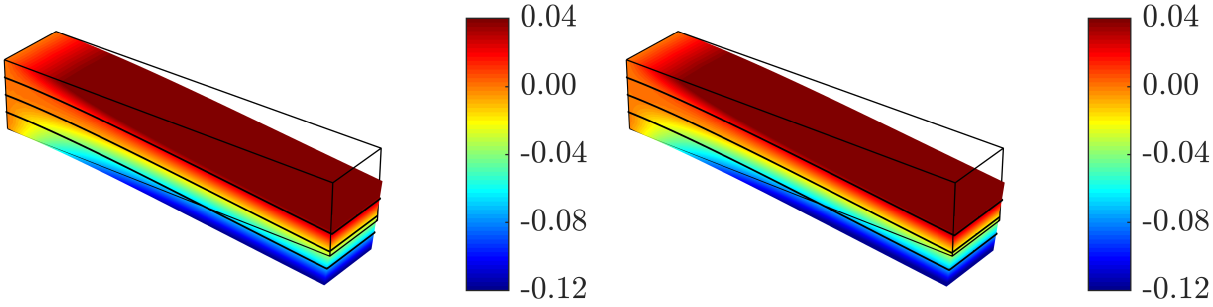

(e) z-displacement via HDG-CG on coarse mesh (f) z-displacement via HDG-CG on fine mesh

Figure 4.22: Solution of displacement for three-dimensional laminated composite beam

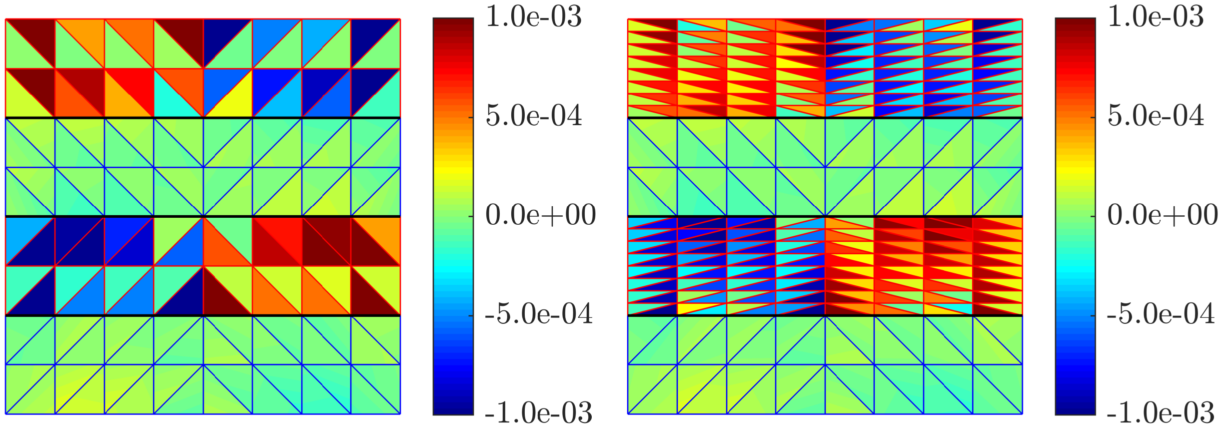

(a) zx-stress via HDG-CG on coarse mesh (b) zx-stress via HDG-CG on fine mesh

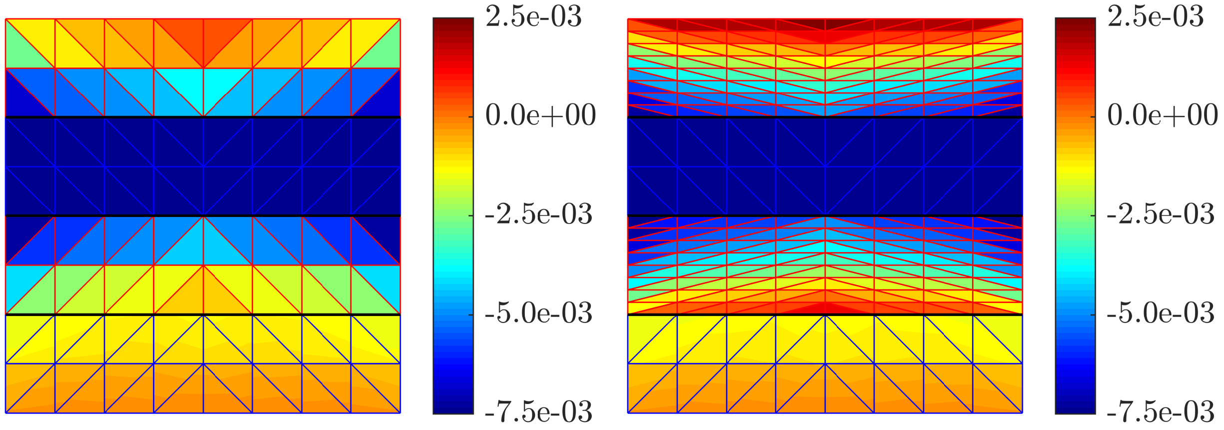

(c) zy-stress via HDG-CG on coarse mesh (d) zy-stress via HDG-CG on fine mesh

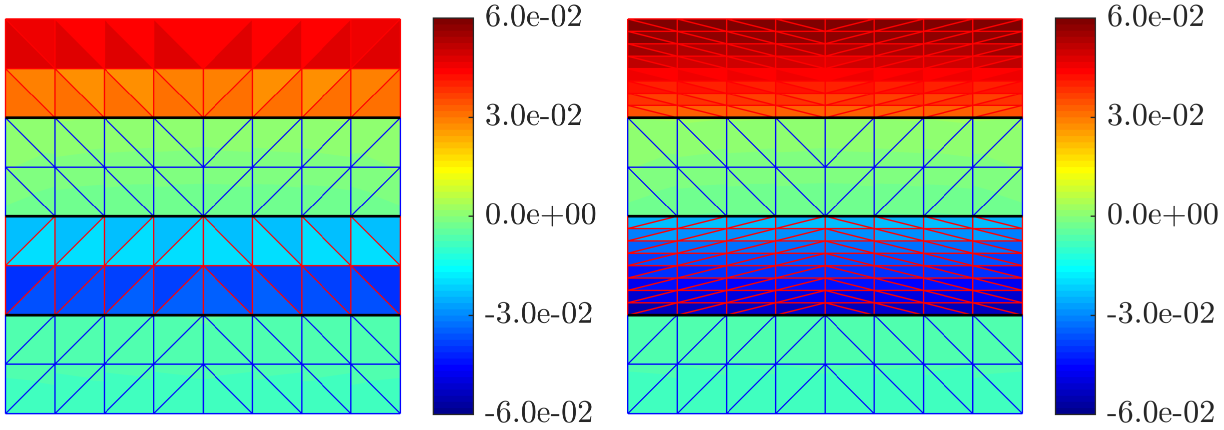

(e) zz-stress via HDG-CG on coarse mesh (f) zz-stress via HDG-CG on fine mesh

Figure 4.23: Solution of stress for three-dimensional laminated composite beam

is correctly resolved. By employing the computationally cheap CG method in the compressible region $\Omega_{\texttt{comp}}$ and restricting the more demanding HDG method in the nearly incompressible region $\Omega_{\texttt{ninc}}$, a physically reliable solution can be obtained at a reasonable computational cost.

Figure 4.22 shows the displacement components obtained with the hybrid formulation on the coarse mesh (left) and on the fine mesh (right). Although the results are qualitatively comparable in both cases, a slight improvement in the vertical displacement is achieved by adopting a finer mesh in the compressible region, as revealed in Table 4.1. In Figure 4.23 the approximation of the stress field is shown at the midspan section. Clearly, the compressible region is subjected to higher stress levels compared to the nearly incompressible region, since $E_{\texttt{comp}} > E_{\texttt{ninc}}$. The elementwise constant interpolation of the stress in the CG subdomain produces a rather tessellated representation on the coarse mesh, leading to a 7% error in the bending moment. The improved approximation on the fine mesh in the compressible region reduces the error to just 2%, at a small additional computational cost. The same level of accuracy is observed for the shear force. Finally, in Figure 4.24 the evolution of the vertical displacement, the shear and the bending moment along the beam axis is plotted. As anticipated in Table 4.1, the CG method severely underestimates the displacement and produces an unreliable bending moment, while preserving an accurate representation of the shear. On the contrary, the pure HDG method accurately reproduce the reference results. Similarly, the HDG-CG coupling strategies produce satisfactory results with improved accuracy when refining the compressible subdomain. It is worth noting the presence of small oscillations in the shear force and the bending moment near to the clamped face at $z = 0$, whenever a CG approach is adopted (cases 2, 3 and 4). These oscillations are not surprising and they are solely attributed to the strong imposition of DIRICHLET boundary conditions adopted in the CG framework.

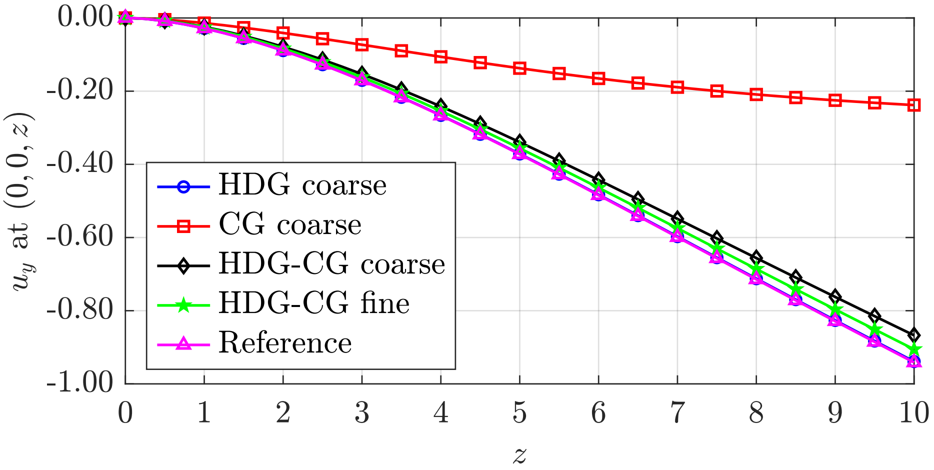

(a) Displacement

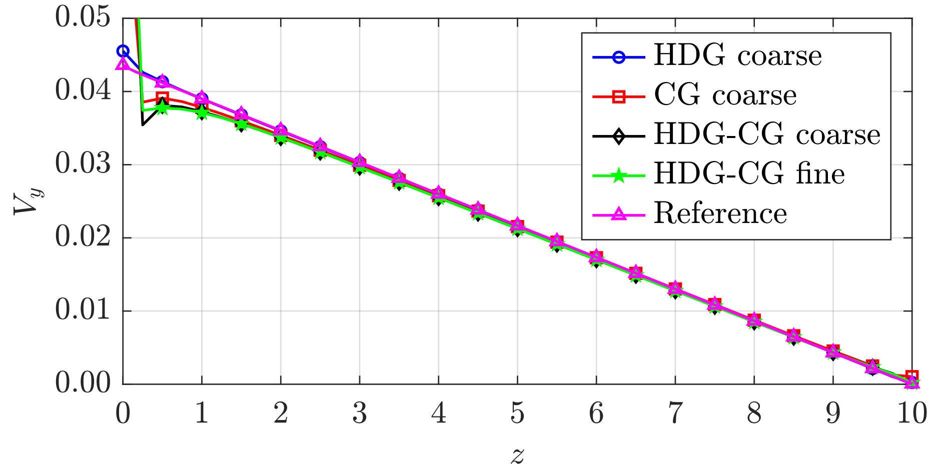

(b) Shear force

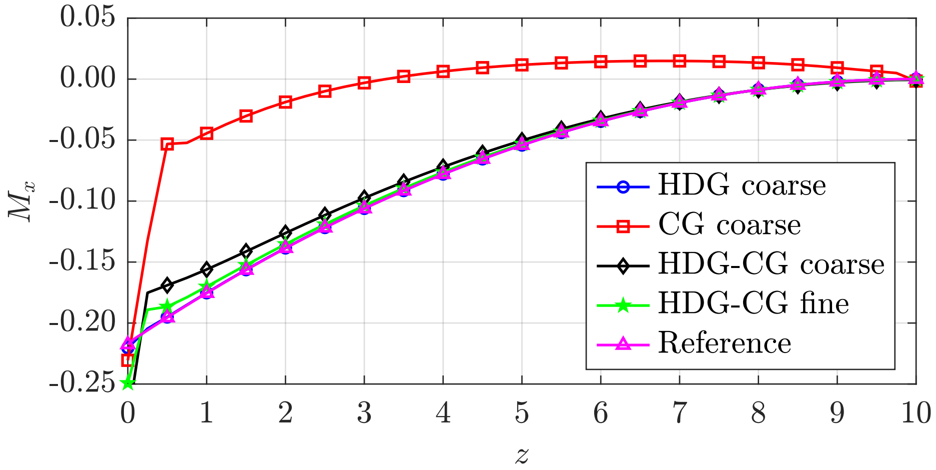

(c) Bending moment

Figure 4.24: Plot of displacement, shear force and bending moment for three-dimensional laminated composite beam

5 HDG-CG formulations for FSI

This final chapter presents novel robust and efficient schemes for the solution of fluid-structure interaction problems. The strategies proposed here exploit the findings of the previous chapters and build upon the algorithms presented therein. More precisely, a weak compressibility is considered in the fluid field, owing to the enhanced efficiency and robustness against the potential instability issues discussed in Chapter 2. The HDG method derived in Chapter 3 is then employed for the discretization of the fluid equations. In particular, the density-momentum formulation with the ALE description of motion is chosen owing to its ability to deal with deforming domains with high-order accuracy and to its flexibility in solving weakly compressible flow problems, as well as flows in the fully compressible regime with minimal changes. For the coupling of the HDG and the CG discretizations, the techniques presented in Chapter 4, generalized for the solution of more complex unsteady and nonlinear multiphysics problems, are adopted. More precisely, a partitioned DIRICHLET–NEUMANN scheme is formulated for the solution of FSI problems by applying the HDG-CG local-global coupling in a staggered fashion, hence circumventing the intrusive nature of this coupling by preserving the core structure of the single-field matrices. Finally, a minimally-intrusive monolithic FSI solver is constructed by employing the HDG-CG NITSCHE-based coupling to impose the coupling conditions in the global problem.

As already discussed in the introduction, a number of formulations have been proposed in literature for the solution of fluid-structure interaction problems through either partitioned or monolithic schemes. The procedure outlined by KÜTTLER and WALL [91] in the context of standard FEM constitutes the most representative example of strongly-coupled partitioned scheme, whereas notable monolithic schemes can be found in the works of MAYR *et al.* [104], HEIL [76], GEE *et al.* [61] and finally in the works of SHELDON *et al.* [144, 145] in the context of HDG methods. In this thesis, several key aspects remain unaddressed in the context of FSI, especially with regards to the development of efficient preconditioners for the resulting system of linear equations and to the employment of advanced time integration strategies tailored to the needs of the single fields. Indeed, the focus is on the spatial discretization and the novelty stems from the aforementioned advanced hybrid discretization techniques developed to simulate weakly compressible fluid flows interacting with nonlinear elastic structures undergoing large deformations.

After recalling in Section 5.1 the strong form of the fluid and the structural subproblems, in Sections 5.2 and 5.3 the partitioned DIRICHLET–NEUMANN coupling and the monolithic NITSCHE-based coupling for the solution of FSI problems are presented, respectively. Spatial and temporal convergence studies are presented in Section 5.4, together with two- and three-dimensional fluid-structure interaction benchmarks highlighting the advantages of the proposed approaches, as well as their capability to solve problems actual engineering interest. The content of this chapter is mainly based on the work of LA SPINA *et al.* [97].

5.1 Problem statement

The strong forms of the fluid and the structural single-field problems are briefly recalled here. Clearly, the subscripts $\odot_{\mathcal{F}}$ and $\odot_{\mathcal{S}}$ refer to the fluid and the structural quantities, respectively. The HDG density-momentum formulation of the fluid problem reads

$$
\begin{cases}
\boldsymbol{L}_{\mathcal{F}} + \mathbf{D}_{\mathcal{F}}^{1/2} \boldsymbol{\nabla}_{\mathrm{S}} \boldsymbol{v}_{\mathcal{F}} = \mathbf{0} & \text{in } \Omega_{\mathcal{F}}^{e} \times (t_i, t_f), \\
\dfrac{\partial \rho_{\mathcal{F}}}{\partial t} + \rho_{\mathcal{F}} \boldsymbol{\nabla} \cdot \boldsymbol{a}_{\mathcal{F}} + \boldsymbol{\nabla} \cdot (\rho \boldsymbol{c}_{\mathcal{F}}) = 0 & \text{in } \Omega_{\mathcal{F}}^{e} \times (t_i, t_f), \\
\dfrac{\partial \boldsymbol{\rho v}_{\mathcal{F}}}{\partial t} + \boldsymbol{\rho v}_{\mathcal{F}} \boldsymbol{\nabla} \cdot \boldsymbol{a}_{\mathcal{F}} + \boldsymbol{\nabla} \cdot (\boldsymbol{\rho v}_{\mathcal{F}} \otimes \boldsymbol{c}_{\mathcal{F}}) & \\
\qquad + \boldsymbol{\nabla}_{\mathrm{S}}^{T} \left(\mathbf{D}_{\mathcal{F}}^{1/2} \boldsymbol{L}_{\mathcal{F}} + \mathbf{E} p_{\mathcal{F}} (\rho_{\mathcal{F}}) \right) = \rho_{\mathcal{F}} \boldsymbol{b}_{\mathcal{F}} & \text{in } \Omega_{\mathcal{F}}^{e} \times (t_i, t_f), \\
\rho_{\mathcal{F}} = \rho_{\mathcal{F}}^{0} & \text{in } \Omega_{\mathcal{F}}^{e} \times (t_i), \\
\boldsymbol{\rho v}_{\mathcal{F}} = \boldsymbol{\rho v}_{\mathcal{F}}^{0} & \text{in } \Omega_{\mathcal{F}}^{e} \times (t_i), \\
\rho_{\mathcal{F}} = \rho_{\mathcal{F}}^{D} & \text{on } \partial \Omega_{\mathcal{F}}^{e} \cap \Gamma_{\mathcal{F}}^{D} \times (t_i, t_f), \\
\boldsymbol{\rho v}_{\mathcal{F}} = \boldsymbol{\rho v}_{\mathcal{F}}^{D} & \text{on } \partial \Omega_{\mathcal{F}}^{e} \cap \Gamma_{\mathcal{F}}^{D} \times (t_i, t_f), \\
\rho_{\mathcal{F}} = \hat{\rho}_{\mathcal{F}} & \text{on } \partial \Omega_{\mathcal{F}}^{e} \setminus \Gamma_{\mathcal{F}}^{D} \times (t_i, t_f), \\
\boldsymbol{\rho v}_{\mathcal{F}} = \widehat{\boldsymbol{\rho v}}_{\mathcal{F}} & \text{on } \partial \Omega_{\mathcal{F}}^{e} \setminus \Gamma_{\mathcal{F}}^{D} \times (t_i, t_f), \\
-\mathbf{N}_{\mathcal{F}}^{T} \left(\mathbf{D}_{\mathcal{F}}^{1/2} \boldsymbol{L}_{\mathcal{F}} + \mathbf{E} p_{\mathcal{F}} (\rho_{\mathcal{F}}) \right) = \boldsymbol{t}_{\mathcal{F}}^{N} & \text{on } \partial \Omega_{\mathcal{F}}^{e} \cap \Gamma_{\mathcal{F}}^{N} \times (t_i, t_f), \\
\llbracket \rho_{\mathcal{F}} \boldsymbol{n}_{\mathcal{F}} \rrbracket = \mathbf{0} & \text{on } \Gamma_{\mathcal{F}} \times (t_i, t_f), \\
\llbracket \boldsymbol{\rho v}_{\mathcal{F}} \otimes \boldsymbol{n}_{\mathcal{F}} \rrbracket = \mathbf{0} & \text{on } \Gamma_{\mathcal{F}} \times (t_i, t_f), \\
\llbracket \widehat{\rho \boldsymbol{c}_{\mathcal{F}} \cdot \boldsymbol{n}_{\mathcal{F}}} \rrbracket = 0 & \text{on } \Gamma_{\mathcal{F}} \times (t_i, t_f), \\
\left\llbracket \widehat{(\boldsymbol{\rho v}_{\mathcal{F}} \otimes \boldsymbol{c}_{\mathcal{F}}) \boldsymbol{n}_{\mathcal{F}}} \right\rrbracket = \mathbf{0} & \text{on } \Gamma_{\mathcal{F}} \times (t_i, t_f), \\
\left\llbracket \widehat{\mathbf{N}_{\mathcal{F}}^{T} \left(\mathbf{D}_{\mathcal{F}}^{1/2} \boldsymbol{L}_{\mathcal{F}} + \mathbf{E} p_{\mathcal{F}} (\rho_{\mathcal{F}}) \right)} \right\rrbracket = \mathbf{0} & \text{on } \Gamma_{\mathcal{F}} \times (t_i, t_f),
\end{cases}
\tag{5.1}
$$

with $\Omega_{\mathcal{F}}$ denoting the fluid domain, deforming in time according to the ALE description of motion. This time dependency is however not explicitly indicated here for the sake of readability. The CG displacement-based formulation of the structural problem reads

$$
\begin{cases}
\rho_{\mathcal{S}} \dfrac{d^2 \boldsymbol{u}_{\mathcal{S}}}{dt^2} - \boldsymbol{\nabla} \cdot \boldsymbol{P}_{\mathcal{S}} (\boldsymbol{\nabla} \boldsymbol{u}_{\mathcal{S}}) = \rho_{\mathcal{S}} \boldsymbol{b}_{\mathcal{S}} & \text{in } \Omega_{\mathcal{S}} \times (t_i, t_f), \\
\boldsymbol{u}_{\mathcal{S}} = \boldsymbol{u}_{\mathcal{S}}^{0} & \text{in } \Omega_{\mathcal{S}} \times (t_i), \\
\dfrac{d \boldsymbol{u}_{\mathcal{S}}}{dt} = \dot{\boldsymbol{u}}_{\mathcal{S}}^{0} & \text{in } \Omega_{\mathcal{S}} \times (t_i), \\
\boldsymbol{u}_{\mathcal{S}} = \boldsymbol{u}_{\mathcal{S}}^{D} & \text{on } \Gamma_{\mathcal{S}}^{D} \times (t_i, t_f), \\
\boldsymbol{P}_{\mathcal{S}} (\boldsymbol{\nabla} \boldsymbol{u}_{\mathcal{S}}) \boldsymbol{n}_{\mathcal{S}} = \boldsymbol{t}_{\mathcal{S}}^{N} & \text{on } \Gamma_{\mathcal{S}}^{N} \times (t_i, t_f),
\end{cases}
\tag{5.2}
$$

with $\Omega_{\mathcal{S}}$ denoting the undeformed structural domain, in the spirit of the total LAGRANGEan approach. The physical meaning of the variables in (5.1) and (5.2) has been extensively discussed in Chapters 2 and 3 and is not repeated here to avoid redundancy. The coupling conditions to close the FSI problem depend on the specific scheme adopted and are exposed in the following.

5.2 Partitioned DIRICHLET–NEUMANN coupling

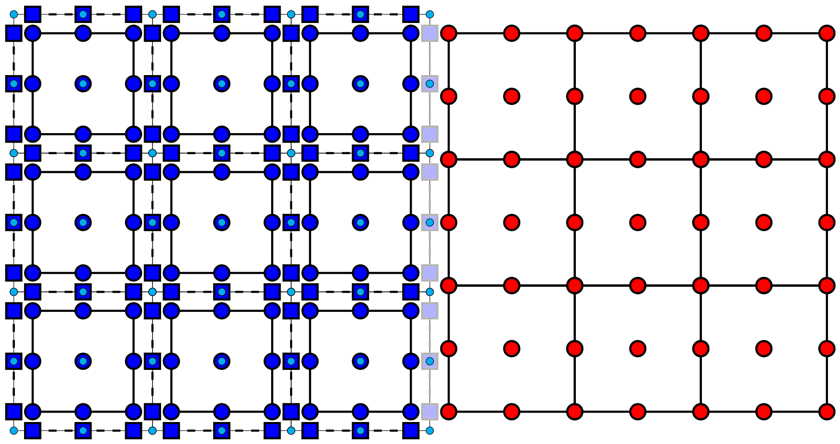

Figure 5.1: Degrees of freedom of the HDG-CG discretization for partitioned DIRICHLET–NEUMANN coupling

In this section, the HDG-CG formulation for fluid-structure interaction via the partitioned DIRICHLET–NEUMANN coupling is presented. This approach formally follows the methodology exposed by KÜTTLER and WALL [91] and adopted for instance in Chapter 2 in the context of standard finite element methods. However, several considerations are needed to deal with the hybrid discretization.

Figure 5.1 depicts the degrees of freedom of the HDG-CG discretization, for a polynomial degree of approximation $k = 2$ for both the fluid (left) and the structure (right). The HDG local DOFs are denoted with blue circles and include the fluid scaled strain rate tensor in VOIGT notation, the density and the momentum. The HDG global DOFs are indicated with blue squares and denote the trace of the fluid density and momentum. It is worth highlighting that, in the spirit of the local-global coupling presented in Section 4.1.3, the global DOFs at the interface are suppressed on the interface. More precisely, the DOFs associated to the trace of the momentum are eliminated, whereas those associated to the trace of the density (here indicated in transparency) need to be computed, according to the no-slip condition for moving boundaries discussed in Section 3.4. The circles in cyan refer to the displacement of the fluid mesh in the ALE framework and those in red denote the CG DOFs, i.e. the structural displacement.

The coupling conditions imposed at the fluid-structure interface can be written as

$$\begin{cases} \dfrac{\boldsymbol{\rho v}_{\mathcal{F}}}{\hat{\rho}_{\mathcal{F}}} - \dfrac{d\boldsymbol{u}_{\mathcal{S}}}{dt} = \boldsymbol{0} \quad \text{on } \Gamma^I \times (t_i, t_f), \\ \left[\widehat{\boldsymbol{P}_{\mathcal{F}}\left(\boldsymbol{L}_{\mathcal{F}}, p_{\mathcal{F}}\left(\rho_{\mathcal{F}}\right)\right)} - \boldsymbol{P}_{\mathcal{S}}\left(\boldsymbol{\nabla}\boldsymbol{u}_{\mathcal{S}}\right)\right]\boldsymbol{n}_{\mathcal{S}} = \boldsymbol{0} \quad \text{on } \Gamma^I \times (t_i, t_f). \end{cases} \tag{5.3}$$

The first condition prohibits a flow across the interface and a relative tangential movement of the fluid and the structure at the interface, whereas the second condition enforces the equilibrium of the fluid and the structural forces at the interface.

This partitioned scheme builds a DIRICHLET-to-NEUMANN map by taking the structural solution at the interface as a DIRICHLET boundary condition for the fluid problem and imposing the fluid normal flux as a NEUMANN boundary condition for the structural problem. The traction equilibrium in (5.3) is therefore consistently expressed in terms of the first PIOLA–KIRCHHOFF stress tensor. The fluid CAUCHY stress is transformed by means of the pull-back operation

$$\boldsymbol{P}_{\mathcal{F}}\left(\boldsymbol{L}_{\mathcal{F}}, p_{\mathcal{F}}\left(\rho_{\mathcal{F}}\right)\right)=\left|\boldsymbol{F}_{\mathcal{F}}\right| \boldsymbol{\sigma}_{\mathcal{F}}\left(\boldsymbol{L}_{\mathcal{F}}, p_{\mathcal{F}}\left(\rho_{\mathcal{F}}\right)\right) \boldsymbol{F}_{\mathcal{F}}^{-T}, \tag{5.4}$$

with $\boldsymbol{F}_{\mathcal{F}}$ denoting the deformation gradient, computed as a function of the displacement of the fluid mesh as

$$\boldsymbol{F}_{\mathcal{F}}=\boldsymbol{\nabla} \boldsymbol{d}_{\mathcal{F}}+\mathbf{I}_{\mathtt{n_{sd}}}. \tag{5.5}$$

The trace of the numerical normal fluxes in (5.1) are defined as in the pure fluid problem (3.39), but replacing the trace of the fluid momentum at the interface with the product of the trace of the fluid density and the time derivative of the structural displacement as

$$\begin{aligned}
&\widehat{\rho \boldsymbol{c}_{\mathcal{F}} \cdot \boldsymbol{n}_{\mathcal{F}}}= \\
&\qquad \begin{cases}
\left(\boldsymbol{\rho v}_{\mathcal{F}}^{D}-\rho_{\mathcal{F}}^{D} \boldsymbol{a}_{\mathcal{F}}\right) \cdot \boldsymbol{n}_{\mathcal{F}}+\tau_{\rho}\left(\rho_{\mathcal{F}}-\rho_{\mathcal{F}}^{D}\right) & \text{on } \partial \Omega_{\mathcal{F}}^{e} \cap \Gamma_{\mathcal{F}}^{D}, \\
\left(\widehat{\boldsymbol{\rho v}}_{\mathcal{F}}-\hat{\rho}_{\mathcal{F}} \boldsymbol{a}_{\mathcal{F}}\right) \cdot \boldsymbol{n}_{\mathcal{F}}+\tau_{\rho}\left(\rho_{\mathcal{F}}-\hat{\rho}_{\mathcal{F}}\right) & \text{on } \partial \Omega_{\mathcal{F}}^{e} \setminus \Gamma_{\mathcal{F}}^{D} \setminus \Gamma^{I}, \\
\hat{\rho}_{\mathcal{F}}\left(\dfrac{d \boldsymbol{u}_{\mathcal{S}}}{d t}-\boldsymbol{a}_{\mathcal{F}}\right) \cdot \boldsymbol{n}_{\mathcal{F}}+\tau_{\rho}\left(\rho_{\mathcal{F}}-\hat{\rho}_{\mathcal{F}}\right) & \text{on } \partial \Omega_{\mathcal{F}}^{e} \cap \Gamma^{I},
\end{cases}
\end{aligned} \tag{5.6a}$$

$$\begin{aligned}
&\widehat{\left(\boldsymbol{\rho v}_{\mathcal{F}} \otimes \boldsymbol{c}_{\mathcal{F}}\right) \boldsymbol{n}_{\mathcal{F}}}= \\
&\qquad \begin{cases}
\left[\boldsymbol{\rho v}_{\mathcal{F}}^{D} \otimes\left(\dfrac{\boldsymbol{\rho v}_{\mathcal{F}}^{D}}{\rho_{\mathcal{F}}^{D}}-\boldsymbol{a}_{\mathcal{F}}\right)\right] \boldsymbol{n}_{\mathcal{F}}+\tau_{\rho v}^{c}\left(\boldsymbol{\rho v}_{\mathcal{F}}-\boldsymbol{\rho v}_{\mathcal{F}}^{D}\right) & \text{on } \partial \Omega_{\mathcal{F}}^{e} \cap \Gamma_{\mathcal{F}}^{D}, \\
\left[\widehat{\boldsymbol{\rho v}}_{\mathcal{F}} \otimes\left(\dfrac{\widehat{\boldsymbol{\rho v}}_{\mathcal{F}}}{\hat{\rho}_{\mathcal{F}}}-\boldsymbol{a}_{\mathcal{F}}\right)\right] \boldsymbol{n}_{\mathcal{F}}+\tau_{\rho v}^{c}\left(\boldsymbol{\rho v}_{\mathcal{F}}-\widehat{\boldsymbol{\rho v}}_{\mathcal{F}}\right) & \text{on } \partial \Omega_{\mathcal{F}}^{e} \setminus \Gamma_{\mathcal{F}}^{D} \setminus \Gamma^{I}, \\
\left[\hat{\rho}_{\mathcal{F}} \dfrac{d \boldsymbol{u}_{\mathcal{S}}}{d t} \otimes\left(\dfrac{d \boldsymbol{u}_{\mathcal{S}}}{d t}-\boldsymbol{a}_{\mathcal{F}}\right)\right] \boldsymbol{n}_{\mathcal{F}}+\tau_{\rho v}^{c}\left(\boldsymbol{\rho v}_{\mathcal{F}}-\hat{\rho}_{\mathcal{F}} \dfrac{d \boldsymbol{u}_{\mathcal{S}}}{d t}\right) & \text{on } \partial \Omega_{\mathcal{F}}^{e} \cap \Gamma^{I},
\end{cases}
\end{aligned} \tag{5.6b}$$

$$\begin{aligned}
&\widehat{\mathbf{N}_{\mathcal{F}}^{T}\left(\mathbf{D}_{\mathcal{F}}^{1/2} \boldsymbol{L}_{\mathcal{F}}+\mathbf{E} p_{\mathcal{F}}\left(\rho_{\mathcal{F}}\right)\right)}= \\
&\qquad \begin{cases}
\mathbf{N}_{\mathcal{F}}^{T}\left(\mathbf{D}_{\mathcal{F}}^{1/2} \boldsymbol{L}_{\mathcal{F}}+\mathbf{E} p_{\mathcal{F}}\left(\rho_{\mathcal{F}}^{D}\right)\right)+\tau_{\rho v}^{d}\left(\boldsymbol{\rho v}_{\mathcal{F}}-\boldsymbol{\rho v}_{\mathcal{F}}^{D}\right) & \text{on } \partial \Omega_{\mathcal{F}}^{e} \cap \Gamma_{\mathcal{F}}^{D}, \\
\mathbf{N}_{\mathcal{F}}^{T}\left(\mathbf{D}_{\mathcal{F}}^{1/2} \boldsymbol{L}_{\mathcal{F}}+\mathbf{E} p_{\mathcal{F}}\left(\hat{\rho}_{\mathcal{F}}\right)\right)+\tau_{\rho v}^{d}\left(\boldsymbol{\rho v}_{\mathcal{F}}-\widehat{\boldsymbol{\rho v}}_{\mathcal{F}}\right) & \text{on } \partial \Omega_{\mathcal{F}}^{e} \setminus \Gamma_{\mathcal{F}}^{D} \setminus \Gamma^{I}, \\
\mathbf{N}_{\mathcal{F}}^{T}\left(\mathbf{D}_{\mathcal{F}}^{1/2} \boldsymbol{L}_{\mathcal{F}}+\mathbf{E} p_{\mathcal{F}}\left(\hat{\rho}_{\mathcal{F}}\right)\right)+\tau_{\rho v}^{d}\left(\boldsymbol{\rho v}_{\mathcal{F}}-\hat{\rho}_{\mathcal{F}} \dfrac{d \boldsymbol{u}_{\mathcal{S}}}{d t}\right) & \text{on } \partial \Omega_{\mathcal{F}}^{e} \cap \Gamma^{I}.
\end{cases}
\end{aligned} \tag{5.6c}$$

By combining the definition of the stress in (5.6) with the transformation (5.4), the actual expression of the flux in (5.3) takes the form

$$\begin{aligned}
&\widehat{\boldsymbol{P}_{\mathcal{F}}\left(\boldsymbol{L}_{\mathcal{F}}, p_{\mathcal{F}}\left(\rho_{\mathcal{F}}\right)\right) \boldsymbol{n}_{\mathcal{S}}}= \\
&\qquad \left|\boldsymbol{F}_{\mathcal{F}}\right| \mathrm{V}^{-1}\left(\mathbf{D}_{\mathcal{F}}^{1/2} \boldsymbol{L}_{\mathcal{F}}+\mathbf{E} p_{\mathcal{F}}\left(\hat{\rho}_{\mathcal{F}}\right)\right) \boldsymbol{F}_{\mathcal{F}}^{-T}\left(-\boldsymbol{n}_{\mathcal{S}}\right)+\tau_{\rho v}\left(\boldsymbol{\rho v}_{\mathcal{F}}-\hat{\rho}_{\mathcal{F}} \frac{d \boldsymbol{u}_{\mathcal{S}}}{d t}\right) \text{ on } \Gamma^{I},
\end{aligned} \tag{5.7}$$

with V^{-1} denoting the inverse VOIGT operator defined in (3.6).

The fluid HDG local problems provide the expression of $(\boldsymbol{L}_{\mathcal{F}}, \rho_{\mathcal{F}}, \boldsymbol{\rho v}_{\mathcal{F}})$ as a function of the hybrid variables $(\hat{\rho}_{\mathcal{F}}, \widehat{\boldsymbol{\rho v}}_{\mathcal{F}})$ and the CG solution $\boldsymbol{u}_{\mathcal{S}}$ at the interface. They are obtained as in the pure fluid problem (3.41), with the novel definition of the numerical fluxes in (5.6) Their weak form hence reads: given $(\rho^0_{\mathcal{F}}, \boldsymbol{\rho v}^0_{\mathcal{F}})$ in $\Omega^e_{\mathcal{F}} \times (t_i)$, $(\rho^D_{\mathcal{F}}, \boldsymbol{\rho v}^D_{\mathcal{F}})$ on $\Gamma^D_{\mathcal{F}}$, $\hat{\rho}_{\mathcal{F}}$ on $\Gamma_{\mathcal{F}} \cup \Gamma^N_{\mathcal{F}} \cup \Gamma^I$, $\widehat{\boldsymbol{\rho v}}_{\mathcal{F}}$ on $\Gamma_{\mathcal{F}} \cup \Gamma^N_{\mathcal{F}}$, $\boldsymbol{u}^0_{\mathcal{S}}$ on $\Gamma^I \times (t_i)$ and $\boldsymbol{u}_{\mathcal{S}}$ on Γ^I, find $(\boldsymbol{L}_{\mathcal{F}}, \rho_{\mathcal{F}}, \boldsymbol{\rho v}_{\mathcal{F}}) \in [\mathcal{W}^h(\Omega^e_{\mathcal{F}})]^{\mathtt{m_{sd}}} \times \mathcal{W}^h(\Omega^e_{\mathcal{F}}) \times [\mathcal{W}^h(\Omega^e_{\mathcal{F}})]^{\mathtt{n_{sd}}}$ for $e = 1, \dots, \mathtt{n}^{\mathtt{el}}_{\mathcal{F}}$ such that

$$
\begin{aligned}
&- (\boldsymbol{W}, \boldsymbol{L}_{\mathcal{F}})_{\Omega^e_{\mathcal{F}}} + \left(\boldsymbol{\nabla}^T_{\mathtt{S}} \mathbf{D}^{1/2}_{\mathcal{F}} \boldsymbol{W}, \frac{\boldsymbol{\rho v}_{\mathcal{F}}}{\rho_{\mathcal{F}}}\right)_{\Omega^e_{\mathcal{F}}} = \\
&\qquad \left\langle \mathbf{N}^T_{\mathcal{F}} \mathbf{D}^{1/2}_{\mathcal{F}} \boldsymbol{W}, \frac{\boldsymbol{\rho v}^D_{\mathcal{F}}}{\rho^D_{\mathcal{F}}} \right\rangle_{\partial\Omega^e_{\mathcal{F}} \cap \Gamma^D_{\mathcal{F}}} + \left\langle \mathbf{N}^T_{\mathcal{F}} \mathbf{D}^{1/2}_{\mathcal{F}} \boldsymbol{W}, \frac{\widehat{\boldsymbol{\rho v}}_{\mathcal{F}}}{\hat{\rho}_{\mathcal{F}}} \right\rangle_{\partial\Omega^e_{\mathcal{F}} \setminus \Gamma^D_{\mathcal{F}} \setminus \Gamma^I} \\
&\qquad + \left\langle \mathbf{N}^T_{\mathcal{F}} \mathbf{D}^{1/2}_{\mathcal{F}} \boldsymbol{W}, \frac{d\boldsymbol{u}_{\mathcal{S}}}{dt} \right\rangle_{\partial\Omega^e_{\mathcal{F}} \cap \Gamma^I},
\end{aligned}
\tag{5.8a}
$$

$$
\begin{aligned}
&\left(w, \frac{\partial \rho_{\mathcal{F}}}{\partial t}\right)_{\Omega^e_{\mathcal{F}}} + \left(w, \rho_{\mathcal{F}} \boldsymbol{\nabla} \cdot \frac{d\boldsymbol{d}_{\mathcal{F}}}{dt}\right)_{\Omega^e_{\mathcal{F}}} \\
&\quad - \left(\boldsymbol{\nabla} w, \boldsymbol{\rho v}_{\mathcal{F}} - \rho_{\mathcal{F}} \frac{d\boldsymbol{d}_{\mathcal{F}}}{dt}\right)_{\Omega^e_{\mathcal{F}}} + \langle w, \tau_\rho \rho_{\mathcal{F}} \rangle_{\partial\Omega^e_{\mathcal{F}}} = \\
&\quad - \left\langle w, \left(\boldsymbol{\rho v}^D_{\mathcal{F}} - \rho^D_{\mathcal{F}} \frac{d\boldsymbol{d}_{\mathcal{F}}}{dt}\right) \cdot \boldsymbol{n}_{\mathcal{F}} - \tau_\rho \rho^D_{\mathcal{F}} \right\rangle_{\partial\Omega^e_{\mathcal{F}} \cap \Gamma^D_{\mathcal{F}}} \\
&\quad - \left\langle w, \left(\widehat{\boldsymbol{\rho v}}_{\mathcal{F}} - \hat{\rho}_{\mathcal{F}} \frac{d\boldsymbol{d}_{\mathcal{F}}}{dt}\right) \cdot \boldsymbol{n}_{\mathcal{F}} - \tau_\rho \hat{\rho}_{\mathcal{F}} \right\rangle_{\partial\Omega^e_{\mathcal{F}} \setminus \Gamma^D_{\mathcal{F}} \setminus \Gamma^I} \\
&\quad - \left\langle w, \hat{\rho}_{\mathcal{F}} \left(\frac{d\boldsymbol{u}_{\mathcal{S}}}{dt} - \frac{d\boldsymbol{d}_{\mathcal{F}}}{dt}\right) \cdot \boldsymbol{n}_{\mathcal{F}} - \tau_\rho \hat{\rho}_{\mathcal{F}} \right\rangle_{\partial\Omega^e_{\mathcal{F}} \cap \Gamma^I},
\end{aligned}
\tag{5.8b}
$$

$$
\begin{aligned}
&\left(\boldsymbol{w}, \frac{\partial \boldsymbol{\rho v}_{\mathcal{F}}}{\partial t}\right)_{\Omega^e_{\mathcal{F}}} + \left(\boldsymbol{w}, \boldsymbol{\rho v}_{\mathcal{F}} \boldsymbol{\nabla} \cdot \frac{d\boldsymbol{d}_{\mathcal{F}}}{dt}\right)_{\Omega^e_{\mathcal{F}}} - \left(\boldsymbol{\nabla} \boldsymbol{w}, \boldsymbol{\rho v}_{\mathcal{F}} \otimes \left(\frac{\boldsymbol{\rho v}_{\mathcal{F}}}{\rho_{\mathcal{F}}} - \frac{d\boldsymbol{d}_{\mathcal{F}}}{dt}\right)\right)_{\Omega^e_{\mathcal{F}}} \\
&\quad + \left(\boldsymbol{w}, \boldsymbol{\nabla}^T_{\mathtt{S}} \left(\mathbf{D}^{1/2}_{\mathcal{F}} \boldsymbol{L}_{\mathcal{F}} + \mathbf{E} p_{\mathcal{F}}(\rho_{\mathcal{F}})\right)\right)_{\Omega^e_{\mathcal{F}}} + \langle \boldsymbol{w}, \tau_{\rho v} \boldsymbol{\rho v}_{\mathcal{F}} \rangle_{\partial\Omega^e_{\mathcal{F}}} - (\boldsymbol{w}, \rho_{\mathcal{F}} \boldsymbol{b}_{\mathcal{F}})_{\Omega^e_{\mathcal{F}}} = \\
&\quad - \left\langle \boldsymbol{w}, \left[\boldsymbol{\rho v}^D_{\mathcal{F}} \otimes \left(\frac{\boldsymbol{\rho v}^D_{\mathcal{F}}}{\rho^D_{\mathcal{F}}} - \frac{d\boldsymbol{d}_{\mathcal{F}}}{dt}\right)\right] \boldsymbol{n}_{\mathcal{F}} - \tau_{\rho v} \boldsymbol{\rho v}^D_{\mathcal{F}} \right\rangle_{\partial\Omega^e_{\mathcal{F}} \cap \Gamma^D_{\mathcal{F}}} \\
&\quad - \left\langle \boldsymbol{w}, \left[\widehat{\boldsymbol{\rho v}}_{\mathcal{F}} \otimes \left(\frac{\widehat{\boldsymbol{\rho v}}_{\mathcal{F}}}{\hat{\rho}_{\mathcal{F}}} - \frac{d\boldsymbol{d}_{\mathcal{F}}}{dt}\right)\right] \boldsymbol{n}_{\mathcal{F}} - \tau_{\rho v} \widehat{\boldsymbol{\rho v}}_{\mathcal{F}} \right\rangle_{\partial\Omega^e_{\mathcal{F}} \setminus \Gamma^D_{\mathcal{F}} \setminus \Gamma^I} \\
&\quad - \left\langle \boldsymbol{w}, \left[\hat{\rho}_{\mathcal{F}} \frac{d\boldsymbol{u}_{\mathcal{S}}}{dt} \otimes \left(\frac{d\boldsymbol{u}_{\mathcal{S}}}{dt} - \frac{d\boldsymbol{d}_{\mathcal{F}}}{dt}\right)\right] \boldsymbol{n}_{\mathcal{F}} - \tau_{\rho v} \hat{\rho}_{\mathcal{F}} \frac{d\boldsymbol{u}_{\mathcal{S}}}{dt} \right\rangle_{\partial\Omega^e_{\mathcal{F}} \cap \Gamma^I},
\end{aligned}
\tag{5.8c}
$$

for all $(\boldsymbol{W}, w, \boldsymbol{w}) \in [\mathcal{W}^h(\Omega^e_{\mathcal{F}})]^{\mathtt{m_{sd}}} \times \mathcal{W}^h(\Omega^e_{\mathcal{F}}) \times [\mathcal{W}^h(\Omega^e_{\mathcal{F}})]^{\mathtt{n_{sd}}}$. It is worth highlighting that, owing to the partitioned nature of this FSI scheme, no linearization of equations (5.8) with respect to the structural displacement needs to be performed for the computation of the structural stiffness matrix, hence circumventing the intrusiveness of the local-global coupling presented in Section 4.1.3.

The fluid HDG global problem remains substantially unchanged from the one in (3.42), with the only difference that the global DOFs associated to the trace of the momentum are removed not only of the DIRICHLET portion of the boundary, but also on the interface. The resulting weak form therefore reads: find $(\hat{\rho}_{\mathcal{F}}, \widehat{\boldsymbol{\rho v}}_{\mathcal{F}}) \in \widehat{\mathcal{W}}^h(\Gamma_{\mathcal{F}} \cup \Gamma_{\mathcal{F}}^N \cup \Gamma^I) \times [\widehat{\mathcal{W}}^h(\Gamma_{\mathcal{F}} \cup \Gamma_{\mathcal{F}}^N)]^{\mathtt{n_{sd}}}$ such that

$$\sum_{e=1}^{\mathtt{n}_{\mathcal{F}}^{\mathtt{el}}} \langle \hat{w}, \tau_\rho \left(\rho_{\mathcal{F}} - \hat{\rho}_{\mathcal{F}}\right) \rangle_{\partial\Omega_{\mathcal{F}}^e \setminus \Gamma_{\mathcal{F}}^D} = 0, \tag{5.9a}$$

$$\begin{aligned} -\sum_{e=1}^{\mathtt{n}_{\mathcal{F}}^{\mathtt{el}}} \Big\langle \hat{\boldsymbol{w}}, \mathbf{N}_{\mathcal{F}}^T \Big(\mathbf{D}_{\mathcal{F}}^{1/2} \boldsymbol{L}_{\mathcal{F}} + \mathbf{E} p_{\mathcal{F}}\left(\hat{\rho}_{\mathcal{F}}\right)\Big) + \tau_{\rho v} \left(\boldsymbol{\rho v}_{\mathcal{F}} - \widehat{\boldsymbol{\rho v}}_{\mathcal{F}}\right) \Big\rangle_{\partial\Omega_{\mathcal{F}}^e \setminus \Gamma_{\mathcal{F}}^D \setminus \Gamma^I} &= \\ \sum_{e=1}^{\mathtt{n}_{\mathcal{F}}^{\mathtt{el}}} \left\langle \hat{\boldsymbol{w}}, \boldsymbol{t}_{\mathcal{F}}^N \right\rangle_{\partial\Omega_{\mathcal{F}}^e \cap \Gamma_{\mathcal{F}}^N}&, \end{aligned} \tag{5.9b}$$

for all $(\hat{w}, \hat{\boldsymbol{w}}) \in \widehat{\mathcal{W}}^h(\Gamma_{\mathcal{F}} \cup \Gamma_{\mathcal{F}}^N \cup \Gamma^I) \times [\widehat{\mathcal{W}}^h(\Gamma_{\mathcal{F}} \cup \Gamma_{\mathcal{F}}^N)]^{\mathtt{n_{sd}}}$.

The structural CG problem stems from equation (2.20) with the inclusion of the fluid traction at the interface as a NEUMANN-type boundary condition. The resulting weak form then reads: given $\widetilde{\boldsymbol{P}_{\mathcal{F}}(\boldsymbol{L}_{\mathcal{F}}, p_{\mathcal{F}}(\rho_{\mathcal{F}}))\boldsymbol{n}_{\mathcal{S}}}$ on Γ^I and $(\boldsymbol{u}_{\mathcal{S}}^0, \dot{\boldsymbol{u}}_{\mathcal{S}}^0)$ in $\Omega_{\mathcal{S}} \times (t_i)$, find $\boldsymbol{u}_{\mathcal{S}} \in [\mathcal{V}^h(\Omega_{\mathcal{S}})]^{\mathtt{n_{sd}}}$ such that

$$\begin{aligned} &\left(\boldsymbol{v}, \rho_{\mathcal{S}} \frac{d^2 \boldsymbol{u}_{\mathcal{S}}}{dt^2}\right)_{\Omega_{\mathcal{S}}} + \left(\boldsymbol{\nabla v}, \boldsymbol{P}_{\mathcal{S}}\left(\boldsymbol{\nabla u}_{\mathcal{S}}\right)\right)_{\Omega_{\mathcal{S}}} = \left(\boldsymbol{v}, \rho_{\mathcal{S}} \boldsymbol{b}_{\mathcal{S}}\right)_{\Omega_{\mathcal{S}}} + \left\langle \boldsymbol{v}, \boldsymbol{t}_{\mathcal{S}}^N \right\rangle_{\Gamma_{\mathcal{S}}^N} \\ &\quad + \left\langle \boldsymbol{v}, |\boldsymbol{F}_{\mathcal{F}}| \, \mathrm{V}^{-1} \Big(\mathbf{D}_{\mathcal{F}}^{1/2} \boldsymbol{L}_{\mathcal{F}} + \mathbf{E} p_{\mathcal{F}}\left(\hat{\rho}_{\mathcal{F}}\right)\Big) \boldsymbol{F}_{\mathcal{F}}^{-T} \left(-\boldsymbol{n}_{\mathcal{S}}\right) + \tau_{\rho v} \left(\boldsymbol{\rho v}_{\mathcal{F}} - \hat{\rho}_{\mathcal{F}} \frac{d\boldsymbol{u}_{\mathcal{S}}}{dt}\right) \right\rangle_{\Gamma^I}, \end{aligned} \tag{5.10}$$

for all $\boldsymbol{v} \in [\mathcal{V}_0^h(\Omega_{\mathcal{S}})]^{\mathtt{n_{sd}}}$. As highlighted for the local problems (5.8), no linearization of the structural equation (5.10) with respect to either the global or the local fluid variables has to be performed.

Remark. *The strategy presented in this section to couple the fluid and the structure could also be implemented in a monolithic fashion, by simultaneously solving the problems* (5.8), (5.9) *and* (5.10) *in a large system of equations. An analogous method to couple HDG and CG discretization was introduced by PAIPURI et al. [127] to solve conjugate heat transfer problems and it has been adopted in Section 4.1.3 in the context of steady thermal problems. However, despite some attractive features, this monolithic coupling of local and global degrees of freedom of the HDG problem with the ones of the CG discretization would require the communication of the local solvers for the computation of the stiffness matrix and the residual vector of the structural problem, making the implementation of this strategy in existing HDG and CG libraries rather intrusive.*

The DIRICHLET–NEUMANN scheme presented in this section can more conveniently be expressed in matrix form. All the quantities are assumed to refer to the time step $n+1$, whereas i denotes the coupling iteration index of the related unknown vectors. Moreover, the barred terms in the following refer to a modified version of the corresponding single-field matrices or vectors and their definition is given in Appendix C. The solver coupling at each time step can therefore be schematized as:

1. Start with a predicted interface structural displacement $\left[\mathbf{u}_{\mathcal{S}}^{i}\right]$.
2. Update the fluid mesh by means of the ALE mapping $\left[\mathbf{d}_{\mathcal{F}}^{i}\right] = \boldsymbol{\varphi}\left(\left[\mathbf{u}_{\mathcal{S}}^{i}\right]\right)$.
3. Compute the fluid global solution $\left[\widehat{\mathbf{U}}_{\mathcal{F}}^{i}\right]$ by solving the global problem

$$\left[\bar{\mathbf{K}}_{\mathcal{F}\mathcal{F}}\right]\left[\delta\widehat{\mathbf{U}}_{\mathcal{F}}^{i}\right] = \left[\bar{\mathbf{f}}_{\mathcal{F}}\right] + \left[\bar{\mathbf{f}}_{\mathcal{I}}^{D}(\mathbf{u}_{\mathcal{S}}^{i})\right], \tag{5.11}$$

with

$$\left[\bar{\mathbf{K}}_{\mathcal{F}\mathcal{F}}\right] = \mathop{\mathsf{A}}\limits_{e=1}^{\mathtt{n}_{\mathcal{F}}^{\mathtt{el}}}\left\{\left[\bar{\mathbf{K}}_{\widehat{U}\widehat{U}}\right]_e - \left[\bar{\mathbf{K}}_{\widehat{U}L} \quad \bar{\mathbf{K}}_{\widehat{U}U}\right]_e \begin{bmatrix}\mathbf{K}_{LL} & \mathbf{K}_{LU}\\ \mathbf{K}_{UL} & \mathbf{K}_{UU}\end{bmatrix}_e^{-1}\begin{bmatrix}\bar{\mathbf{K}}_{L\widehat{U}}\\ \bar{\mathbf{K}}_{U\widehat{U}}\end{bmatrix}_e\right\}, \tag{5.12a}$$

$$\left[\bar{\mathbf{f}}_{\mathcal{F}}\right] = \mathop{\mathsf{A}}\limits_{e=1}^{\mathtt{n}_{\mathcal{F}}^{\mathtt{el}}}\left\{\left[\bar{\mathbf{f}}_{\widehat{U}}\right]_e - \left[\bar{\mathbf{K}}_{\widehat{U}L} \quad \bar{\mathbf{K}}_{\widehat{U}U}\right]_e \begin{bmatrix}\mathbf{K}_{LL} & \mathbf{K}_{LU}\\ \mathbf{K}_{UL} & \mathbf{K}_{UU}\end{bmatrix}_e^{-1}\begin{bmatrix}\bar{\mathbf{f}}_{L}\\ \bar{\mathbf{f}}_{U}\end{bmatrix}_e\right\}, \tag{5.12b}$$

$$\left[\bar{\mathbf{f}}_{\mathcal{I}}^{D}\right] = \mathop{\mathsf{A}}\limits_{e=1}^{\mathtt{n}_{\mathcal{I}}^{\mathtt{el}}}\left\{\qquad - \left[\bar{\mathbf{K}}_{\widehat{U}L} \quad \bar{\mathbf{K}}_{\widehat{U}U}\right]_e \begin{bmatrix}\mathbf{K}_{LL} & \mathbf{K}_{LU}\\ \mathbf{K}_{UL} & \mathbf{K}_{UU}\end{bmatrix}_e^{-1}\begin{bmatrix}\bar{\mathbf{f}}_{L}^{D}\\ \bar{\mathbf{f}}_{U}^{D}\end{bmatrix}_e\right\}, \tag{5.12c}$$

and $\left[\bar{\mathbf{f}}_{\mathcal{I}}^{D}(\mathbf{u}_{\mathcal{S}}^{i})\right]$ denoting the DIRICHLET coupling vector on the interface.

4. Compute the fluid local solution $\left[\mathbf{L}_{\mathcal{F}}^{i} \quad \mathbf{U}_{\mathcal{F}}^{i}\right]_e^T$ by solving the local problems

$$\begin{bmatrix}\mathbf{K}_{LL} & \mathbf{K}_{LU}\\ \mathbf{K}_{UL} & \mathbf{K}_{UU}\end{bmatrix}_e \begin{bmatrix}\delta\mathbf{L}_{\mathcal{F}}^{i}\\ \delta\mathbf{U}_{\mathcal{F}}^{i}\end{bmatrix}_e = \begin{bmatrix}\bar{\mathbf{f}}_{L}\\ \bar{\mathbf{f}}_{U}\end{bmatrix}_e + \begin{bmatrix}\bar{\mathbf{f}}_{L}^{D}\\ \bar{\mathbf{f}}_{U}^{D}\end{bmatrix}_e - \begin{bmatrix}\bar{\mathbf{K}}_{L\widehat{U}}\\ \bar{\mathbf{K}}_{U\widehat{U}}\end{bmatrix}_e \left[\delta\widehat{\mathbf{U}}_{\mathcal{F}}^{i}\right]_e, \tag{5.13}$$

for $e = 1, \ldots, \mathtt{n}_{\mathcal{F}}^{\mathtt{el}}$.

5. Repeat steps 3 and 4 until convergence of the fluid problem.
6. Compute a new structural solution $\left[\bar{\mathbf{u}}_{\mathcal{S}}^{i+1}\right]$ by solving the problem

$$\left[\bar{\mathbf{K}}_{\mathcal{S}\mathcal{S}}\right]\left[\delta\bar{\mathbf{u}}_{\mathcal{S}}^{i+1}\right] = \left[\bar{\mathbf{f}}_{\mathcal{S}}\right] + \left[\bar{\mathbf{f}}_{\mathcal{I}}^{N}(\mathbf{L}_{\mathcal{F}}^{i}, \mathbf{U}_{\mathcal{F}}^{i}, \widehat{\mathbf{U}}_{\mathcal{F}}^{i}, \mathbf{u}_{\mathcal{S}}^{i})\right], \tag{5.14}$$

with

$$\left[\bar{\mathbf{K}}_{\mathcal{S}\mathcal{S}}\right] = \mathop{\mathsf{A}}\limits_{e=1}^{\mathtt{n}_{\mathcal{S}}^{\mathtt{el}}}\left\{\left[\mathbf{K}_{uu}\right]_e\right\}, \quad \left[\bar{\mathbf{f}}_{\mathcal{S}}\right] = \mathop{\mathsf{A}}\limits_{e=1}^{\mathtt{n}_{\mathcal{S}}^{\mathtt{el}}}\left\{\left[\mathbf{f}_{u}\right]_e\right\}, \quad \left[\bar{\mathbf{f}}_{\mathcal{I}}^{N}\right] = \mathop{\mathsf{A}}\limits_{e=1}^{\mathtt{n}_{\mathcal{I}}^{\mathtt{el}}}\left\{\left[\bar{\mathbf{f}}_{u}^{N}\right]_e\right\}, \tag{5.15}$$

and $\left[\bar{\mathbf{f}}_{\mathcal{I}}^{N}(\mathbf{L}_{\mathcal{F}}^{i}, \mathbf{U}_{\mathcal{F}}^{i}, \widehat{\mathbf{U}}_{\mathcal{F}}^{i}, \mathbf{u}_{\mathcal{S}}^{i})\right]$ denoting the NEUMANN coupling vector on the interface.

7. Check the convergence of the interface displacement residual $\left\|\left[\mathbf{r}_{\mathcal{I}}^{i+1}\right]\right\| < \eta$ with

$$\left[\mathbf{r}_{\mathcal{I}}^{i+1}\right] = \left[\bar{\mathbf{u}}_{\mathcal{S}}^{i+1}\right] - \left[\mathbf{u}_{\mathcal{S}}^{i}\right]. \tag{5.16}$$

Continue with next time step if the algorithm is converged, otherwise return to step 2 with

$$\left[\mathbf{u}_{\mathcal{S}}^{i+1}\right] = \omega^{i+1}\left[\bar{\mathbf{u}}_{\mathcal{S}}^{i+1}\right] + \left(1 - \omega^{i+1}\right)\left[\mathbf{u}_{\mathcal{S}}^{i}\right], \tag{5.17}$$

where the relaxation parameter is updated by means of AITKEN's Δ^2 method

$$\omega^{i+1} = -\omega^{i}\left[\mathbf{r}_{\mathcal{I}}^{i}\right]^T\left(\left[\mathbf{r}_{\mathcal{I}}^{i+1}\right] - \left[\mathbf{r}_{\mathcal{I}}^{i}\right]\right) / \left\|\left[\mathbf{r}_{\mathcal{I}}^{i+1}\right] - \left[\mathbf{r}_{\mathcal{I}}^{i}\right]\right\|^2. \tag{5.18}$$

5.3 Monolithic NITSCHE-based coupling

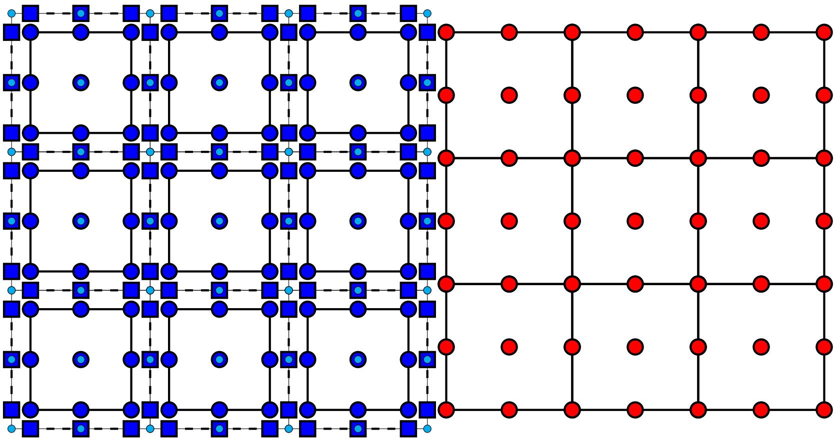

Figure 5.2: Degrees of freedom of the HDG-CG discretization for monolithic NITSCHE-based coupling

In this section, the HDG-CG formulation for FSI via the monolithic NITSCHE-based coupling is presented. This approach follows the methodology exposed in Sections 4.1.4 and 4.2 in the context of thermal and linear elastic problems, respectively, but extended to deal with the more complex unsteady, nonlinear and multiphysics nature of fluid-structure interaction.

The degrees of freedom of the hybrid HDG-CG discretization are shown in Figure 5.2 for a polynomial degree $k = 2$. The DOFs depicted therein refer to the same fluid and structural unknowns exposed in Section 5.2. However, owing to the global coupling provided by the NITSCHE-based approach, the HDG global DOFs are kept on the interface. As discussed in Section 4.1.4, this slightly increases the total DOFs count, but on the other hand it allows to enforce the coupling conditions in a much less invasive way. Moreover, it eases the treatment of potential nonuniform polynomial approximations as well as non-matching grids at the interface.

The coupling conditions needed to close the FSI problem defined by the single-field equations (5.1) and (5.2) read

$$\begin{cases} \dfrac{\widehat{\boldsymbol{\rho v}}_{\mathcal{F}}}{\hat{\rho}_{\mathcal{F}}} - \dfrac{d\boldsymbol{u}_{\mathcal{S}}}{dt} = \boldsymbol{0} & \text{on } \Gamma^I \times (t_i, t_f), \\ \left[\widehat{\boldsymbol{\sigma}_{\mathcal{F}}\left(\boldsymbol{L}_{\mathcal{F}}, p_{\mathcal{F}}\left(\rho_{\mathcal{F}}\right)\right)} - \widehat{\boldsymbol{\sigma}_{\mathcal{S}}\left(\boldsymbol{\nabla}\boldsymbol{u}_{\mathcal{S}}\right)}\right]\boldsymbol{n}_{\mathcal{F}} = \boldsymbol{0} & \text{on } \Gamma^I \times (t_i, t_f), \end{cases} \tag{5.19}$$

From a practical point of view, this scheme builds a NEUMANN-to-DIRICHLET map by imposing the traction equilibrium in (5.19) as a NEUMANN boundary condition in the fluid global problem and enforcing the velocity compatibility in (5.19) in the structural problem via the well-known NITSCHE method for the weak imposition of essential boundary conditions. The equilibrium of the normal fluxes has to be expressed in terms of the CAUCHY measure of the stress for consistency. The structural first PIOLA–KIRCHHOFF stress is transformed by means of the push-forward operation

$$\boldsymbol{\sigma}_{\mathcal{S}}\left(\boldsymbol{\nabla}\boldsymbol{u}_{\mathcal{S}}\right) = \left|\boldsymbol{F}_{\mathcal{S}}\right|^{-1}\boldsymbol{P}_{\mathcal{S}}\left(\boldsymbol{\nabla}\boldsymbol{u}_{\mathcal{S}}\right)\boldsymbol{F}_{\mathcal{S}}^{T}, \tag{5.20}$$

with $\boldsymbol{F}_{\mathcal{S}}$ being the structural deformation gradient, computed with respect to the reference configuration as

$$\boldsymbol{F}_{\mathcal{S}} = \boldsymbol{\nabla}\boldsymbol{u}_{\mathcal{S}} + \mathbf{I}_{\mathtt{n_{sd}}}. \tag{5.21}$$

The trace of the fluid normal fluxes remain unchanged from the single-field problem in (3.39). With the notation adopted for FSI problems, such fluxes can be written as

$$\widehat{\rho\boldsymbol{c}_{\mathcal{F}}\cdot\boldsymbol{n}_{\mathcal{F}}} =$$

$$\begin{cases} \left(\boldsymbol{\rho v}_{\mathcal{F}}^{D} - \rho_{\mathcal{F}}^{D}\boldsymbol{a}_{\mathcal{F}}\right)\cdot\boldsymbol{n}_{\mathcal{F}} + \tau_{\rho}\left(\rho_{\mathcal{F}} - \rho_{\mathcal{F}}^{D}\right) & \text{on } \partial\Omega_{\mathcal{F}}^{e}\cap\Gamma_{\mathcal{F}}^{D}, \\ \left(\widehat{\boldsymbol{\rho v}}_{\mathcal{F}} - \hat{\rho}_{\mathcal{F}}\boldsymbol{a}_{\mathcal{F}}\right)\cdot\boldsymbol{n}_{\mathcal{F}} + \tau_{\rho}\left(\rho_{\mathcal{F}} - \hat{\rho}_{\mathcal{F}}\right) & \text{on } \partial\Omega_{\mathcal{F}}^{e}\setminus\Gamma_{\mathcal{F}}^{D}, \end{cases} \tag{5.22a}$$

$$\widehat{\left(\boldsymbol{\rho v}_{\mathcal{F}}\otimes\boldsymbol{c}_{\mathcal{F}}\right)\boldsymbol{n}_{\mathcal{F}}} =$$

$$\begin{cases} \left[\boldsymbol{\rho v}_{\mathcal{F}}^{D}\otimes\left(\dfrac{\boldsymbol{\rho v}_{\mathcal{F}}^{D}}{\rho_{\mathcal{F}}^{D}} - \boldsymbol{a}_{\mathcal{F}}\right)\right]\boldsymbol{n}_{\mathcal{F}} + \tau_{\rho v}^{c}\left(\boldsymbol{\rho v}_{\mathcal{F}} - \boldsymbol{\rho v}_{\mathcal{F}}^{D}\right) & \text{on } \partial\Omega_{\mathcal{F}}^{e}\cap\Gamma_{\mathcal{F}}^{D}, \\ \left[\widehat{\boldsymbol{\rho v}}_{\mathcal{F}}\otimes\left(\dfrac{\widehat{\boldsymbol{\rho v}}_{\mathcal{F}}}{\hat{\rho}_{\mathcal{F}}} - \boldsymbol{a}_{\mathcal{F}}\right)\right]\boldsymbol{n}_{\mathcal{F}} + \tau_{\rho v}^{c}\left(\boldsymbol{\rho v}_{\mathcal{F}} - \widehat{\boldsymbol{\rho v}}_{\mathcal{F}}\right) & \text{on } \partial\Omega_{\mathcal{F}}^{e}\setminus\Gamma_{\mathcal{F}}^{D}, \end{cases} \tag{5.22b}$$

$$\widehat{\mathbf{N}_{\mathcal{F}}^{T}\left(\mathbf{D}_{\mathcal{F}}^{1/2}\boldsymbol{L}_{\mathcal{F}} + \mathbf{E}p_{\mathcal{F}}\left(\rho_{\mathcal{F}}\right)\right)} =$$

$$\begin{cases} \mathbf{N}_{\mathcal{F}}^{T}\left(\mathbf{D}_{\mathcal{F}}^{1/2}\boldsymbol{L}_{\mathcal{F}} + \mathbf{E}p_{\mathcal{F}}\left(\rho_{\mathcal{F}}^{D}\right)\right) + \tau_{\rho v}^{d}\left(\boldsymbol{\rho v}_{\mathcal{F}} - \boldsymbol{\rho v}_{\mathcal{F}}^{D}\right) & \text{on } \partial\Omega_{\mathcal{F}}^{e}\cap\Gamma_{\mathcal{F}}^{D}, \\ \mathbf{N}_{\mathcal{F}}^{T}\left(\mathbf{D}_{\mathcal{F}}^{1/2}\boldsymbol{L}_{\mathcal{F}} + \mathbf{E}p_{\mathcal{F}}\left(\hat{\rho}_{\mathcal{F}}\right)\right) + \tau_{\rho v}^{d}\left(\boldsymbol{\rho v}_{\mathcal{F}} - \widehat{\boldsymbol{\rho v}}_{\mathcal{F}}\right) & \text{on } \partial\Omega_{\mathcal{F}}^{e}\setminus\Gamma_{\mathcal{F}}^{D}. \end{cases} \tag{5.22c}$$

The trace of the structural normal stress along the interface is instead defined as

$$\widehat{\boldsymbol{P}_{\mathcal{S}}\left(\boldsymbol{\nabla}\boldsymbol{u}_{\mathcal{S}}\right)\boldsymbol{n}_{\mathcal{S}}} = \boldsymbol{P}_{\mathcal{S}}\left(\boldsymbol{\nabla}\boldsymbol{u}_{\mathcal{S}}\right)\boldsymbol{n}_{\mathcal{S}} - \frac{\gamma}{h}\left(\frac{d\boldsymbol{u}_{\mathcal{S}}}{dt} - \frac{\widehat{\boldsymbol{\rho v}}_{\mathcal{F}}}{\hat{\rho}_{\mathcal{F}}}\right) \text{ on } \Gamma^{I}, \tag{5.23}$$

with γ being the NITSCHE penalty parameter and h denoting a characteristic element size on the interface. It is worth reminding that the trace of the normal fluid stress in (5.22) is already written in terms of CAUCHY stress and consistently defined on the deformed domain. On the contrary, the trace of the structural normal stress in (5.23) has to be transformed according to (5.20). Hence, the actual expression of the flux in (5.19) can be written as

$$-\widehat{\boldsymbol{\sigma}_{\mathcal{S}}\left(\boldsymbol{\nabla}\boldsymbol{u}_{\mathcal{S}}\right)\boldsymbol{n}_{\mathcal{F}}} = \left|\boldsymbol{F}_{\mathcal{S}}\right|^{-1}\boldsymbol{P}_{\mathcal{S}}\left(\boldsymbol{\nabla}\boldsymbol{u}_{\mathcal{S}}\right)\boldsymbol{F}_{\mathcal{S}}^{T}\left(-\boldsymbol{n}_{\mathcal{F}}\right) - \frac{\gamma}{h}\left(\frac{d\boldsymbol{u}_{\mathcal{S}}}{dt} - \frac{\widehat{\boldsymbol{\rho v}}_{\mathcal{F}}}{\hat{\rho}_{\mathcal{F}}}\right) \text{ on } \Gamma^{I}. \tag{5.24}$$

A similar definition of the trace of the CG normal stress has been adopted in Section 4.2 in the context of linear elastic problems. However, some differences are worth highlighting. First, while in (4.47) the NITSCHE method penalizes the jump of the displacements among the HDG and the CG subdomains, here the penalization involves the structural velocity (computed as the time derivative of the structural displacement) and the fluid velocity (computed as the ratio of the traces of the fluid momentum and density). Secondly, the VOIGT notation is adopted in linear elasticity owing to the symmetry of the CAUCHY stress, whereas the non-symmetric nature of the first PIOLA–KIRCHHOFF stress tensor requires the computation of all its $\mathtt{n_{sd}} \times \mathtt{n_{sd}}$ components. Moreover, while in the single-physics problem in Section 4.2 the same stress measure is naturally chosen in the subdomains, here the adoption of a hybrid description of motion, i.e. the ALE description in the fluid field and the total LAGRANGEan description in the structural field, requires the aforementioned stress transformation for a consistent imposition of the coupling conditions. Then, no ambiguity in the definition of the characteristic element size arises in the case of linear elasticity, since the governing equations are written with respect to the undeformed configuration. In fluid-structure interaction involving fluid flows interacting with nonlinear elastic structures undergoing large deformations, the parameter h could refer to the size of either the deformed fluid elements or the undeformed structural elements on the interface. In the numerical examples presented in Section 5.4, the characteristic element size is computed with respect to the undeformed structural configuration.

Owing to the global nature of the NITSCHE-based coupling, the fluid HDG local problems are the same as in (3.41). With the new notation their weak form reads: given $(\rho^0_{\mathcal{F}}, \boldsymbol{\rho v}^0_{\mathcal{F}})$ in $\Omega^e_{\mathcal{F}} \times (t_i)$, $(\rho^D_{\mathcal{F}}, \boldsymbol{\rho v}^D_{\mathcal{F}})$ on $\Gamma^D_{\mathcal{F}}$ and $(\hat{\rho}_{\mathcal{F}}, \widehat{\boldsymbol{\rho v}}_{\mathcal{F}})$ on $\Gamma_{\mathcal{F}} \cup \Gamma^N_{\mathcal{F}} \cup \Gamma^I$, find $(\boldsymbol{L}_{\mathcal{F}}, \rho_{\mathcal{F}}, \boldsymbol{\rho v}_{\mathcal{F}}) \in [\mathcal{W}^h(\Omega^e_{\mathcal{F}})]^{\mathtt{m_{sd}}} \times \mathcal{W}^h(\Omega^e_{\mathcal{F}}) \times [\mathcal{W}^h(\Omega^e_{\mathcal{F}})]^{\mathtt{n_{sd}}}$ for $e = 1, \dots, \mathtt{n}^{\mathtt{el}}_{\mathcal{F}}$ such that

$$\begin{aligned}
&-\left(\boldsymbol{W}, \boldsymbol{L}_{\mathcal{F}}\right)_{\Omega^e_{\mathcal{F}}} + \left(\boldsymbol{\nabla}^T_{\mathtt{S}} \mathbf{D}^{1/2}_{\mathcal{F}} \boldsymbol{W}, \frac{\boldsymbol{\rho v}_{\mathcal{F}}}{\rho_{\mathcal{F}}}\right)_{\Omega^e_{\mathcal{F}}} = \\
&\qquad \left\langle \mathbf{N}^T_{\mathcal{F}} \mathbf{D}^{1/2}_{\mathcal{F}} \boldsymbol{W}, \frac{\boldsymbol{\rho v}^D_{\mathcal{F}}}{\rho^D_{\mathcal{F}}}\right\rangle_{\partial\Omega^e_{\mathcal{F}} \cap \Gamma^D_{\mathcal{F}}} + \left\langle \mathbf{N}^T_{\mathcal{F}} \mathbf{D}^{1/2}_{\mathcal{F}} \boldsymbol{W}, \frac{\widehat{\boldsymbol{\rho v}}_{\mathcal{F}}}{\hat{\rho}_{\mathcal{F}}}\right\rangle_{\partial\Omega^e_{\mathcal{F}} \setminus \Gamma^D_{\mathcal{F}}},
\end{aligned} \tag{5.25a}$$

$$\begin{aligned}
&\left(w, \frac{\partial \rho_{\mathcal{F}}}{\partial t}\right)_{\Omega^e_{\mathcal{F}}} + \left(w, \rho_{\mathcal{F}} \boldsymbol{\nabla} \cdot \frac{d\boldsymbol{d}_{\mathcal{F}}}{dt}\right)_{\Omega^e_{\mathcal{F}}} \\
&\quad - \left(\boldsymbol{\nabla} w, \boldsymbol{\rho v}_{\mathcal{F}} - \rho_{\mathcal{F}} \frac{d\boldsymbol{d}_{\mathcal{F}}}{dt}\right)_{\Omega^e_{\mathcal{F}}} + \left\langle w, \tau_\rho \rho_{\mathcal{F}} \right\rangle_{\partial\Omega^e_{\mathcal{F}}} = \\
&\quad - \left\langle w, \left(\boldsymbol{\rho v}^D_{\mathcal{F}} - \rho^D_{\mathcal{F}} \frac{d\boldsymbol{d}_{\mathcal{F}}}{dt}\right) \cdot \boldsymbol{n}_{\mathcal{F}} - \tau_\rho \rho^D_{\mathcal{F}} \right\rangle_{\partial\Omega^e_{\mathcal{F}} \cap \Gamma^D_{\mathcal{F}}} \\
&\quad - \left\langle w, \left(\widehat{\boldsymbol{\rho v}}_{\mathcal{F}} - \hat{\rho}_{\mathcal{F}} \frac{d\boldsymbol{d}_{\mathcal{F}}}{dt}\right) \cdot \boldsymbol{n}_{\mathcal{F}} - \tau_\rho \hat{\rho}_{\mathcal{F}} \right\rangle_{\partial\Omega^e_{\mathcal{F}} \setminus \Gamma^D_{\mathcal{F}}},
\end{aligned} \tag{5.25b}$$

$$\begin{aligned}
&\left(\boldsymbol{w}, \frac{\partial \boldsymbol{\rho v}_{\mathcal{F}}}{\partial t}\right)_{\Omega^e_{\mathcal{F}}} + \left(\boldsymbol{w}, \boldsymbol{\rho v}_{\mathcal{F}} \boldsymbol{\nabla} \cdot \frac{d\boldsymbol{d}_{\mathcal{F}}}{dt}\right)_{\Omega^e_{\mathcal{F}}} - \left(\boldsymbol{\nabla} \boldsymbol{w}, \boldsymbol{\rho v}_{\mathcal{F}} \otimes \left(\frac{\boldsymbol{\rho v}_{\mathcal{F}}}{\rho_{\mathcal{F}}} - \frac{d\boldsymbol{d}_{\mathcal{F}}}{dt}\right)\right)_{\Omega^e_{\mathcal{F}}} \\
&\quad + \left(\boldsymbol{w}, \boldsymbol{\nabla}^T_{\mathtt{S}} \left(\mathbf{D}^{1/2}_{\mathcal{F}} \boldsymbol{L}_{\mathcal{F}} + \mathbf{E} p_{\mathcal{F}}\left(\rho_{\mathcal{F}}\right)\right)\right)_{\Omega^e_{\mathcal{F}}} + \left\langle \boldsymbol{w}, \tau_{\rho v} \boldsymbol{\rho v}_{\mathcal{F}} \right\rangle_{\partial\Omega^e_{\mathcal{F}}} - \left(\boldsymbol{w}, \rho_{\mathcal{F}} \boldsymbol{b}_{\mathcal{F}}\right)_{\Omega^e_{\mathcal{F}}} = \\
&\quad - \left\langle \boldsymbol{w}, \left[\boldsymbol{\rho v}^D_{\mathcal{F}} \otimes \left(\frac{\boldsymbol{\rho v}^D_{\mathcal{F}}}{\rho^D_{\mathcal{F}}} - \frac{d\boldsymbol{d}_{\mathcal{F}}}{dt}\right)\right] \boldsymbol{n}_{\mathcal{F}} - \tau_{\rho v} \boldsymbol{\rho v}^D_{\mathcal{F}} \right\rangle_{\partial\Omega^e_{\mathcal{F}} \cap \Gamma^D_{\mathcal{F}}} \\
&\quad - \left\langle \boldsymbol{w}, \left[\widehat{\boldsymbol{\rho v}}_{\mathcal{F}} \otimes \left(\frac{\widehat{\boldsymbol{\rho v}}_{\mathcal{F}}}{\hat{\rho}_{\mathcal{F}}} - \frac{d\boldsymbol{d}_{\mathcal{F}}}{dt}\right)\right] \boldsymbol{n}_{\mathcal{F}} - \tau_{\rho v} \widehat{\boldsymbol{\rho v}}_{\mathcal{F}} \right\rangle_{\partial\Omega^e_{\mathcal{F}} \setminus \Gamma^D_{\mathcal{F}}},
\end{aligned} \tag{5.25c}$$

for all $(\boldsymbol{W}, w, \boldsymbol{w}) \in [\mathcal{W}^h(\Omega^e_{\mathcal{F}})]^{\mathtt{m_{sd}}} \times \mathcal{W}^h(\Omega^e_{\mathcal{F}}) \times [\mathcal{W}^h(\Omega^e_{\mathcal{F}})]^{\mathtt{n_{sd}}}$.

Exploiting the definition of the normal flux (5.23) and its transformed counterpart (5.24), the fluid-structure global problem reads: given $(\boldsymbol{u}_{\mathcal{S}}^0, \dot{\boldsymbol{u}}_{\mathcal{S}}^0)$ in $\Omega_{\mathcal{S}} \times (t_i)$, find $(\hat{\rho}_{\mathcal{F}}, \widehat{\boldsymbol{\rho v}}_{\mathcal{F}}, \boldsymbol{u}_{\mathcal{S}}) \in \widehat{\mathcal{W}}^h(\Gamma_{\mathcal{F}} \cup \Gamma_{\mathcal{F}}^N \cup \Gamma^I) \times [\widehat{\mathcal{W}}^h(\Gamma_{\mathcal{F}} \cup \Gamma_{\mathcal{F}}^N \cup \Gamma^I)]^{\mathtt{n_{sd}}} \times [\mathcal{V}^h(\Omega_{\mathcal{S}})]^{\mathtt{n_{sd}}}$ such that

$$\sum_{e=1}^{\mathtt{n}_{\mathcal{F}}^{\mathtt{el}}} \langle \hat{w}, \tau_\rho \left(\rho_{\mathcal{F}} - \hat{\rho}_{\mathcal{F}}\right) \rangle_{\partial\Omega_{\mathcal{F}}^e \setminus \Gamma_{\mathcal{F}}^D} = 0, \tag{5.26a}$$

$$\begin{aligned} - \sum_{e=1}^{\mathtt{n}_{\mathcal{F}}^{\mathtt{el}}} \Bigg\{ & \left\langle \hat{\boldsymbol{w}}, \mathbf{N}_{\mathcal{F}}^T \left(\mathbf{D}_{\mathcal{F}}^{1/2} \boldsymbol{L}_{\mathcal{F}} + \mathbf{E} p_{\mathcal{F}}\left(\hat{\rho}_{\mathcal{F}}\right) \right) + \tau_{\rho v}\left(\boldsymbol{\rho v}_{\mathcal{F}} - \widehat{\boldsymbol{\rho v}}_{\mathcal{F}}\right) \right\rangle_{\partial\Omega_{\mathcal{F}}^e \setminus \Gamma_{\mathcal{F}}^D} \\ & - \left\langle \hat{\boldsymbol{w}}, \left|\boldsymbol{F}_{\mathcal{S}}\right|^{-1} \boldsymbol{P}_{\mathcal{S}}\left(\boldsymbol{\nabla} \boldsymbol{u}_{\mathcal{S}}\right) \boldsymbol{F}_{\mathcal{S}}^T \left(-\boldsymbol{n}_{\mathcal{F}}\right) - \frac{\gamma}{h} \left(\frac{d\boldsymbol{u}_{\mathcal{S}}}{dt} - \frac{\widehat{\boldsymbol{\rho v}}_{\mathcal{F}}}{\hat{\rho}_{\mathcal{F}}} \right) \right\rangle_{\partial\Omega_{\mathcal{F}}^e \cap \Gamma^I} \Bigg\} = \\ & \sum_{e=1}^{\mathtt{n}_{\mathcal{F}}^{\mathtt{el}}} \left\langle \hat{\boldsymbol{w}}, \boldsymbol{t}_{\mathcal{F}}^N \right\rangle_{\partial\Omega_{\mathcal{F}}^e \cap \Gamma_{\mathcal{F}}^N}, \end{aligned} \tag{5.26b}$$

$$\begin{aligned} & \left(\boldsymbol{v}, \rho_{\mathcal{S}} \frac{d^2 \boldsymbol{u}_{\mathcal{S}}}{dt^2} \right)_{\Omega_{\mathcal{S}}} + \left(\boldsymbol{\nabla} \boldsymbol{v}, \boldsymbol{P}_{\mathcal{S}}\left(\boldsymbol{\nabla} \boldsymbol{u}_{\mathcal{S}}\right) \right)_{\Omega_{\mathcal{S}}} \\ & - \left\langle \boldsymbol{v}, \boldsymbol{P}_{\mathcal{S}}\left(\boldsymbol{\nabla} \boldsymbol{u}_{\mathcal{S}}\right) \boldsymbol{n}_{\mathcal{S}} - \frac{\gamma}{h} \left(\frac{d\boldsymbol{u}_{\mathcal{S}}}{dt} - \frac{\widehat{\boldsymbol{\rho v}}_{\mathcal{F}}}{\hat{\rho}_{\mathcal{F}}} \right) \right\rangle_{\Gamma^I} \\ & - \left\langle \frac{\partial \boldsymbol{P}_{\mathcal{S}}\left(\boldsymbol{\nabla} \boldsymbol{u}_{\mathcal{S}}\right)}{\partial \boldsymbol{\nabla} \boldsymbol{u}_{\mathcal{S}}} \boldsymbol{\nabla} \boldsymbol{v} \boldsymbol{n}_{\mathcal{S}}, \frac{d\boldsymbol{u}_{\mathcal{S}}}{dt} - \frac{\widehat{\boldsymbol{\rho v}}_{\mathcal{F}}}{\hat{\rho}_{\mathcal{F}}} \right\rangle_{\Gamma^I} = \left(\boldsymbol{v}, \rho_{\mathcal{S}} \boldsymbol{b}_{\mathcal{S}} \right)_{\Omega_{\mathcal{S}}} + \left\langle \boldsymbol{v}, \boldsymbol{t}_{\mathcal{S}}^N \right\rangle_{\Gamma_{\mathcal{S}}^N}, \end{aligned} \tag{5.26c}$$

for all $(\hat{w}, \hat{\boldsymbol{w}}, \boldsymbol{v}) \in \widehat{\mathcal{W}}^h(\Gamma_{\mathcal{F}} \cup \Gamma_{\mathcal{F}}^N \cup \Gamma^I) \times [\widehat{\mathcal{W}}^h(\Gamma_{\mathcal{F}} \cup \Gamma_{\mathcal{F}}^N \cup \Gamma^I)]^{\mathtt{n_{sd}}} \times [\mathcal{V}_0^h(\Omega_{\mathcal{S}})]^{\mathtt{n_{sd}}}$. In the spirit of the HDG-CG NITSCHE-based coupling introduced in Section 4.1.4, all the coupling information is exchanged solely in the global problem (5.26). It is worth highlighting that, owing to the nonlinear nature of the structural stress (contrarily to the linear elastic problems in Section 4.2), the evaluation of the directional derivatives of the first PIOLA–KIRCHHOFF stress tensor with respect to the structural displacement are needed here for the computation of the last term in the left hand side of the structural subproblem in (5.26). Considering the obvious non-symmetric nature of the overall FSI problem, the non-symmetric variant of NITSCHE's method discussed by BURMAN [20] could be adopted in this context to avoid the introduction of the penalty parameter γ. However, despite this attractive advantage, this variant has not been chosen because of the suboptimal convergence behavior experienced by the same author in the framework of simpler linear and scalar PDEs.

Remark. *The strategy presented in this section to couple the fluid and the structure could in theory be implemented in a partitioned fashion, by alternating the solution of pure fluid and structural problems and exchanging the interface information among the fields. This method can be referred to as partitioned NEUMANN–DIRICHLET coupling and it has been proposed for instance by KÜTTLER et al. [93] as a possible remedy for the so-called incompressibility dilemma, referring to the treatment of FSI problems with fully enclosed fluids. However, as stated by the same authors, despite the possibility to solve a number of academic examples, the method usually fails to solve real world problems, because the response of stiff structures to varying interface displacements is too sensitive for any numerical approach to find the equilibrium.*

After linearization of problems (5.25) and (5.26), discretized by means of a isoparametric formulation, and by performing a static condensation of the local DOFs, the global linear system that is solved in each NEWTON iteration to advance from the time step n to $n+1$ reads

$$\begin{bmatrix} \tilde{\mathbf{K}}_{\mathcal{F}\mathcal{F}} & \tilde{\mathbf{K}}_{\mathcal{F}\mathcal{S}} \\ \tilde{\mathbf{K}}_{\mathcal{S}\mathcal{F}} & \tilde{\mathbf{K}}_{\mathcal{S}\mathcal{S}} \end{bmatrix} \begin{bmatrix} \delta\widehat{\mathbf{U}}_{\mathcal{F}} \\ \delta\mathbf{u}_{\mathcal{S}} \end{bmatrix} = \begin{bmatrix} \tilde{\mathbf{f}}_{\mathcal{F}} \\ \tilde{\mathbf{f}}_{\mathcal{S}} \end{bmatrix}, \tag{5.27}$$

with the left hand side matrices computed as

$$\left[\tilde{\mathbf{K}}_{\mathcal{F}\mathcal{F}}\right] = \mathop{\mathsf{A}}_{e=1}^{\mathtt{n}^{\mathtt{el}}_{\mathcal{F}}} \left\{ \left[\tilde{\mathbf{K}}_{\widehat{U}\widehat{U}}\right]_e - \left[\mathbf{K}_{\widehat{U}L} \quad \mathbf{K}_{\widehat{U}U}\right]_e \begin{bmatrix} \mathbf{K}_{LL} & \mathbf{K}_{LU} \\ \mathbf{K}_{UL} & \mathbf{K}_{UU} \end{bmatrix}_e^{-1} \begin{bmatrix} \mathbf{K}_{L\widehat{U}} \\ \mathbf{K}_{U\widehat{U}} \end{bmatrix}_e \right\}, \tag{5.28a}$$

$$\left[\tilde{\mathbf{K}}_{\mathcal{F}\mathcal{S}}\right] = \mathop{\mathsf{A}}_{e=1}^{\mathtt{n}^{\mathtt{el}}_{\mathcal{I}}} \left\{ \left[\tilde{\mathbf{K}}_{\widehat{U}u}\right]_e \right\}, \tag{5.28b}$$

$$\left[\tilde{\mathbf{K}}_{\mathcal{S}\mathcal{F}}\right] = \mathop{\mathsf{A}}_{e=1}^{\mathtt{n}^{\mathtt{el}}_{\mathcal{I}}} \left\{ \left[\tilde{\mathbf{K}}_{u\widehat{U}}\right]_e \right\}, \tag{5.28c}$$

$$\left[\tilde{\mathbf{K}}_{\mathcal{S}\mathcal{S}}\right] = \mathop{\mathsf{A}}_{e=1}^{\mathtt{n}^{\mathtt{el}}_{\mathcal{S}}} \left\{ \left[\tilde{\mathbf{K}}_{uu}\right]_e \right\}, \tag{5.28d}$$

and the right hand side vectors computed as

$$\left[\tilde{\mathbf{f}}_{\mathcal{F}}\right] = \mathop{\mathsf{A}}_{e=1}^{\mathtt{n}^{\mathtt{el}}_{\mathcal{F}}} \left\{ \left[\tilde{\mathbf{f}}_{\widehat{U}}\right]_e - \left[\mathbf{K}_{\widehat{U}L} \quad \mathbf{K}_{\widehat{U}U}\right]_e \begin{bmatrix} \mathbf{K}_{LL} & \mathbf{K}_{LU} \\ \mathbf{K}_{UL} & \mathbf{K}_{UU} \end{bmatrix}_e^{-1} \begin{bmatrix} \mathbf{f}_{L} \\ \mathbf{f}_{U} \end{bmatrix}_e \right\}, \tag{5.29a}$$

$$\left[\tilde{\mathbf{f}}_{\mathcal{S}}\right] = \mathop{\mathsf{A}}_{e=1}^{\mathtt{n}^{\mathtt{el}}_{\mathcal{S}}} \left\{ \left[\tilde{\mathbf{f}}_{u}\right]_e \right\}. \tag{5.29b}$$

The tilted terms refer to a modified version of the corresponding single-field matrices and vectors. It can be noted that the proposed scheme requires only the inclusion of a small number of terms arising from the definitions (5.23) and (5.24) in the fluid matrix $\tilde{\mathbf{K}}_{\widehat{U}\widehat{U}}$ and in the structural matrix $\tilde{\mathbf{K}}_{uu}$, as well as in the corresponding residual vectors $\tilde{\mathbf{f}}_{\widehat{U}}$ and $\tilde{\mathbf{f}}_{u}$. Hence, the matrices $\tilde{\mathbf{K}}_{\mathcal{F}\mathcal{F}}$ and $\tilde{\mathbf{K}}_{\mathcal{S}\mathcal{S}}$ feature the usual structure of the fluid and structural global problem, respectively, whereas the blocks $\tilde{\mathbf{K}}_{\mathcal{F}\mathcal{S}}$ and $\tilde{\mathbf{K}}_{\mathcal{S}\mathcal{F}}$ are responsible for the coupling and solely involve the fluid hybrid variables and the structural unknown at the interface.

In the spirit of the NITSCHE-based coupling of HDG and CG discretizations, the fluid HDG local problems remain unchanged and they require, at each NEWTON iteration, the solution of the linear systems

$$\begin{bmatrix} \mathbf{K}_{LL} & \mathbf{K}_{LU} \\ \mathbf{K}_{UL} & \mathbf{K}_{UU} \end{bmatrix}_e \begin{bmatrix} \delta\mathbf{L}_{\mathcal{F}} \\ \delta\mathbf{U}_{\mathcal{F}} \end{bmatrix}_e = \begin{bmatrix} \mathbf{f}_{L} \\ \mathbf{f}_{U} \end{bmatrix}_e - \begin{bmatrix} \mathbf{K}_{L\widehat{U}} \\ \mathbf{K}_{U\widehat{U}} \end{bmatrix}_e \left[\delta\widehat{\mathbf{U}}_{\mathcal{F}}\right]_e, \tag{5.30}$$

for $e = 1, \dots, \mathtt{n}^{\mathtt{el}}_{\mathcal{F}}$. The expressions of all the matrices and vectors presented here are detailed in Appendix C.

5.4 Numerical examples

The numerical studies aim to assess the performance of the proposed HDG-CG formulations for the solution of weakly compressible fluid-structure interaction problems. The first example verifies the optimal convergence of both the partitioned DIRICHLET–NEUMANN coupling and the monolithic NITSCHE-based coupling using the method of manufactured solutions. The following examples highlight the enhanced robustness and efficiency of the proposed approaches by means of two- and three-dimensional simulations. On the one hand, the partitioned DIRICHLET–NEUMANN scheme has been implemented in the `C++` in-house research code `BACI` [167], by extending the capability of the fixed-point solver described in Chapter 2 to deal with hybrid HDG-CG discretizations. On the other hand, the monolithic NITSCHE-based coupling has been implemented in `MATLAB`, by merging the HDG fluid solver used in Chapter 3 with the CG structural solver used in Chapter 4, extended to the nonlinear regime.

5.4.1 FSI problem with manufactured solution

The first numerical example considers a two-dimensional fluid-structure interaction problem with manufactured solution. The generation of manufactured solutions for single-physics problems is a rather straightforward task and it simply consists in selecting a suitable continuous solution and adding an appropriate source term to cancel out any imbalance in the PDEs, caused by the arbitrary choice of the solution itself. Interestingly, this choice is often problem-independent and it is not affected by the structure of the code used. On the contrary, the derivation of manufactured solutions for the verification of FSI codes can be a quite complex task and a rigorous procedure to generate a class of non-trivial solutions has been developed by ÉTIENNE *et al.* [48]. Its main features are the rich structure of solution, ensuring that all terms of the differential equations are exercised, and the absence of artificial tractions on the fluid-structure interface, that would otherwise require substantial modifications for most codes. The problem considered consists of an unsteady incompressible flow interacting with a flexible structure and this flow configuration is simulated here by choosing a sufficiently small compressibility coefficient. The goal of this example is then to assess the convergence properties of the proposed HDG-CG formulations for fluid-structure interaction.

The parameters adopted to generate the solution according to [48] are

$$\begin{cases} \delta\left(t\right) = \delta_0 \sin\left[2\pi\left(t_0+t\right)\right], \\ f\left(x,t\right) = 1+\sin\left(2\pi x\right)\left[1-\cos\left(2\pi x\right)\right]\delta\left(t\right), \\ Q\left(\xi,t\right) = \xi\left[8-7\left(\delta\left(t\right)/\delta_0\right)^2\right], \\ q = 1, \\ a\left(x,y,t\right) = -\left(y-1\right)\left[1+10/3\cos\left(2\pi x\right)\delta\left(t\right)\right], \\ b\left(x,y,t\right) = 1, \end{cases} \tag{5.31}$$

with $\delta_0 = 1/20$ and $t_0 = 1/4$. The function $f(x,t)$ describes the shape of the deformed fluid-structure interface and its temporal variation is defined by $\delta(t)$. $Q(\xi,t)$ and q are user-supplied data characterizing the flow field. In particular, $q \leq 1$ produces a non-zero velocity profile along the bottom boundary, while $q > 1$ would generate a no-slip condition. Finally, $a(x,y,t)$ and $b(x,y,t)$ determine the structural solution.

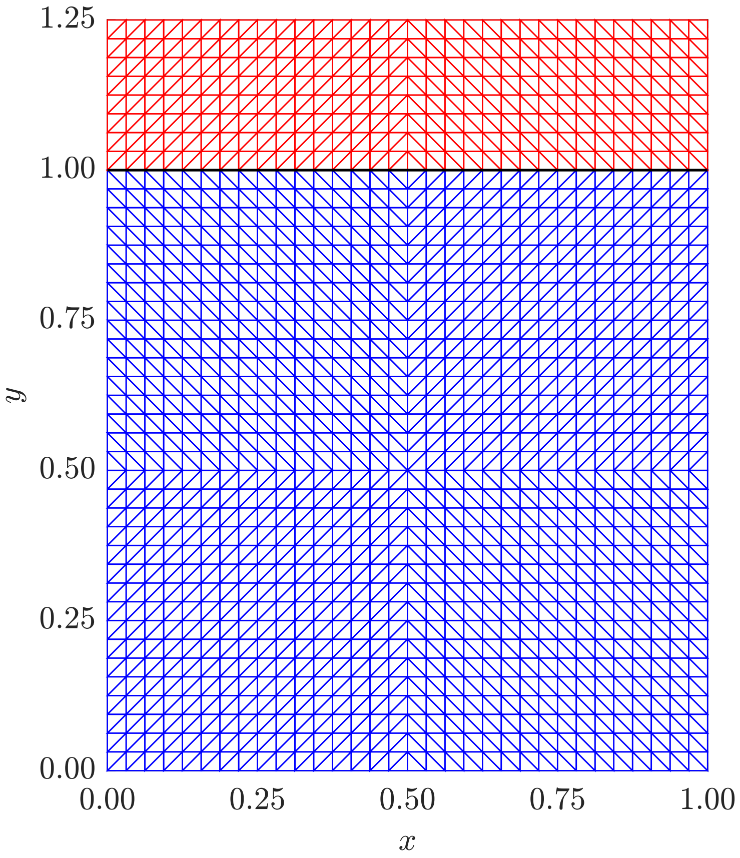

(a) Undeformed mesh

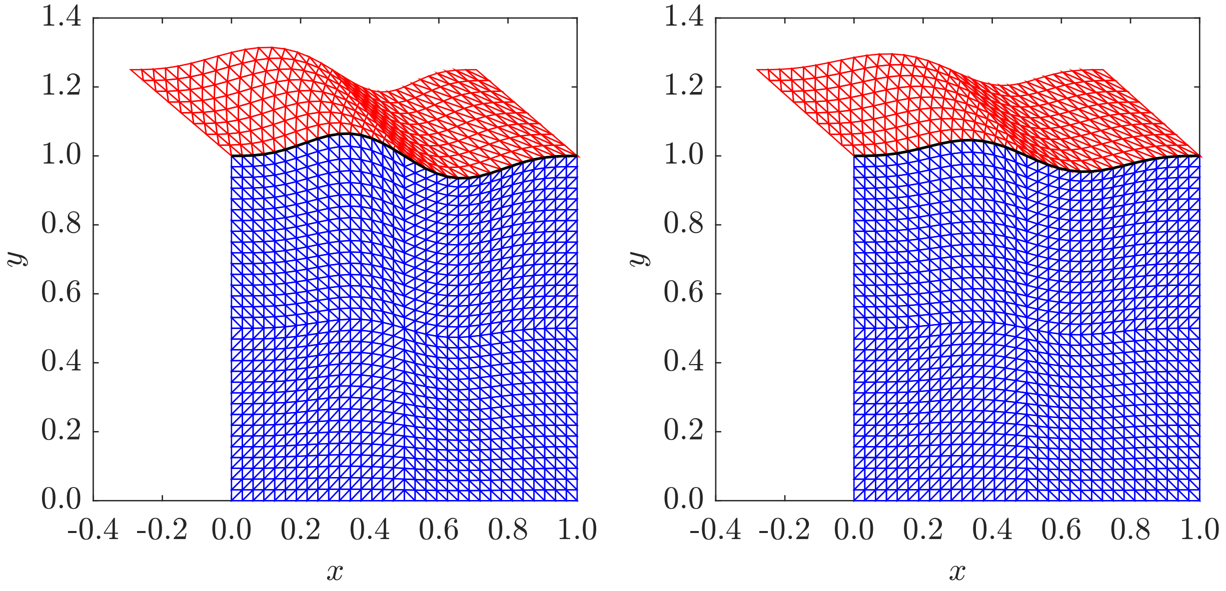

(b) Deformed mesh at $t = 0$

(c) Deformed mesh at $t = 0.125$

Figure 5.3: Computational mesh for FSI problem with manufactured solution

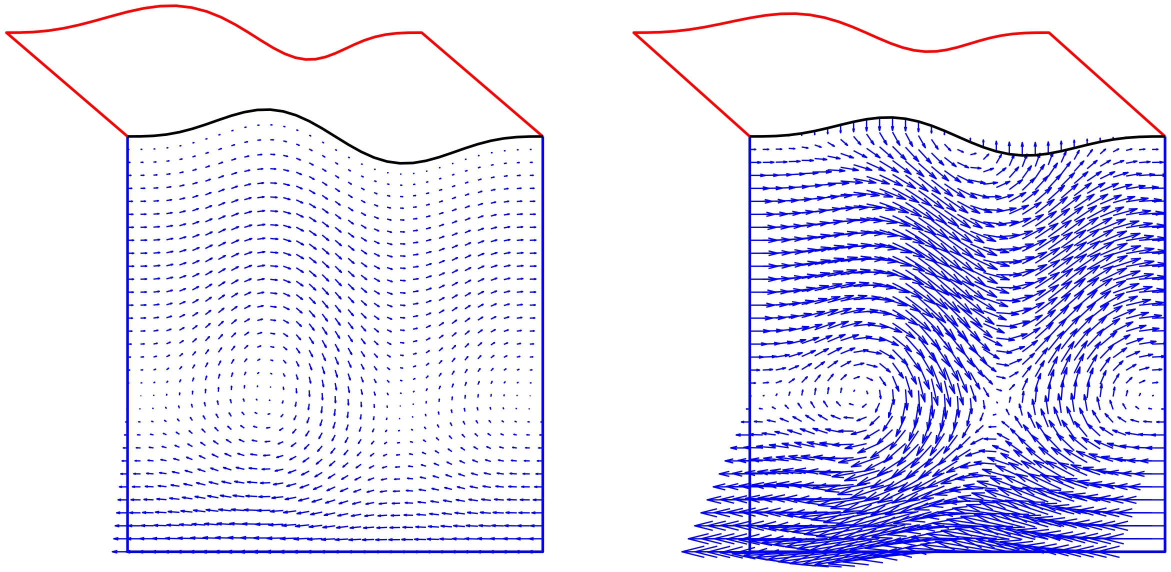

(a) $t = 0$ (b) $t = 0.125$

Figure 5.4: Solution of fluid velocity for FSI problem with manufactured solution

More specifically, the structural displacement with respect to the undeformed configuration $\Omega_{\mathcal{S}}$ is given by

$$\begin{cases} u_{\mathcal{S}x}\left(x,y,t\right) = a\left(x,y,t\right), \\ u_{\mathcal{S}y}\left(x,y,t\right) = b\left(x,y,t\right)\left(f\left(x,t\right)-1\right). \end{cases} \tag{5.32}$$

An appropriate body force, satisfying the structural PDEs, is then added to the right hand side of the governing equations. It is computed with standard techniques, as already done in Sections 3.5 and 4.3 for single-physics problems. The fluid velocity is evaluated with respect to the deformed configuration $\Omega_{\mathcal{F}}$ as

$$\begin{cases} \upsilon_{\mathcal{F}x}\left(x,y,t\right) = \left(q+1\right)y^{q}\left(R\left(\left[f\left(x,t\right),t\right]\right) - R\left(y,t\right)\right) \\ \qquad\qquad\qquad -qy^{q-1}\left(S\left(\left[f\left(x,t\right),t\right]\right) - S\left(y,t\right)\right), \\ \upsilon_{\mathcal{F}y}\left(x,y,t\right) = y^{q}\left(f\left(x,t\right)-y\right)Q\left[f\left(x,t\right),t\right]\dfrac{\partial f\left(x,t\right)}{\partial x} + \dfrac{\partial f\left(x,t\right)}{\partial t}, \end{cases} \tag{5.33}$$

with $R(\xi,t)$ and $S(\xi,t)$ representing two auxiliary functions, computed as

$$\begin{cases} R\left(\xi,t\right) = \displaystyle\int_{0}^{\xi} Q\left(\chi,t\right)d\chi, \\ S\left(\xi,t\right) = \displaystyle\int_{0}^{\xi} Q\left(\chi,t\right)\chi d\chi. \end{cases} \tag{5.34}$$

It is worth pointing out that the fluid velocity and the time derivative of the structural displacement exactly match on the interface, by construction. The parameters chosen induce a sufficiently complex flow, characterized by two pronounced vortices circulating in opposite directions. The flow field is shown in Figure 5.4 on the initial (left) and final (right) deformed configuration. The interface tractions on Γ^I are evaluated through the push-forward operation

$$\boldsymbol{t}\,(x,t) = \left(|\boldsymbol{F}_{\mathcal{S}}|^{-1}\boldsymbol{P}_{\mathcal{S}}\,(\boldsymbol{\nabla}\boldsymbol{u}_{\mathcal{S}})\,\boldsymbol{F}_{\mathcal{S}}^{T}\boldsymbol{n}\right)\Big|_{y=f(x,t)}, \tag{5.35}$$

with the deformation gradient $\boldsymbol{F}_{\mathcal{S}}$ and the first PIOLA–KIRCHHOFF stress tensor $\boldsymbol{P}_{\mathcal{S}}(\boldsymbol{\nabla}\boldsymbol{u}_{\mathcal{S}})$ computed from the given displacement field (5.32) according to equations (2.14) and (2.13), respectively. Then, $\boldsymbol{n}$ refers to the unit normal vector to the interface and its Cartesian components can be directly evaluated from the definition of the deformed interface $f(x,t)$ as

$$\begin{cases} n_x\,(x,t) = -\left[1+\left(\dfrac{\partial f\,(x,t)}{\partial x}\right)^2\right]^{-1/2}\dfrac{\partial f\,(x,t)}{\partial x}, \\ n_y\,(x,t) = +\left[1+\left(\dfrac{\partial f\,(x,t)}{\partial x}\right)^2\right]^{-1/2}. \end{cases} \tag{5.36}$$

The fluid pressure is given by

$$p_{\mathcal{F}}\,(x,t) = -\frac{At_yn_x - Bt_xn_x + Bt_yn_y - Ct_xn_y}{An_yn_x - Bn_xn_x + Bn_yn_y - Cn_xn_y}, \tag{5.37}$$

with $A(x,t)$, $B(x,t)$ and $C(x,t)$ being the independent components of the symmetric part of the velocity gradient at the interface

$$\begin{cases} A\,(x,t) = \left.\dfrac{\partial v_{\mathcal{F}x}}{\partial x}\right|_{y=f(x,t)}, \\ B\,(x,t) = \dfrac{1}{2}\left(\dfrac{\partial v_{\mathcal{F}x}}{\partial y} + \dfrac{\partial v_{\mathcal{F}y}}{\partial x}\right)\Big|_{y=f(x,t)}, \\ C\,(x,t) = \left.\dfrac{\partial v_{\mathcal{F}y}}{\partial y}\right|_{y=f(x,t)}. \end{cases} \tag{5.38}$$

The price paid to avoid fictitious interface tractions is the inclusion of the following spatially varying viscosity

$$\mu_{\mathcal{F}}\,(x,t) = \frac{t_xn_y - t_yn_x}{2\,(An_yn_x - Bn_xn_x + Bn_yn_y - Cn_xn_y)}. \tag{5.39}$$

This term can be easily handled by computing the fluid viscosity at the quadrature points and its implementation, if not already provided, does not represent a critical issue. As a last ingredient, a body force balancing the fluid momentum equation is calculated. The computation of this term is extremely complex and the symbolic math toolbox of `MATLAB` is therefore used for this purpose.

The computational domain Ω is composed by the union of the fluid subdomain $\Omega_{\mathcal{F}} = (0,1)\times(0,1)$ and the structural subdomain $\Omega_{\mathcal{S}} = (0,1)\times(1,1.25)$, such that the interface (in the undeformed configuration) is identified as $\Gamma^I = \{(x,y)\in\mathbb{R}^2 : y = 1\}$. The initial conditions and the DIRICHLET boundary conditions are computed from the analytical solution and are imposed on $\Omega\times(0)$ and $\Gamma^D = \partial\Omega$, respectively.

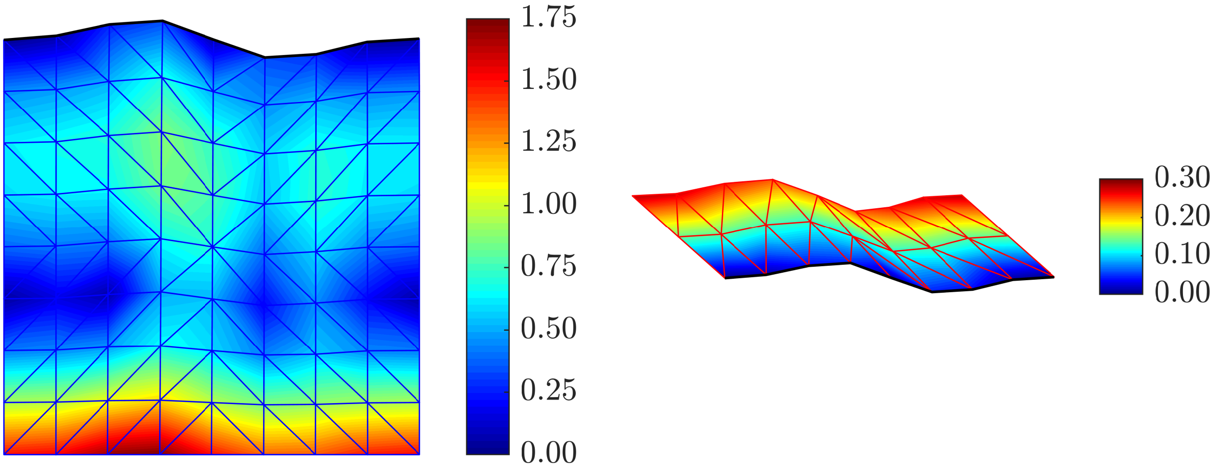

(a) Fluid velocity with $k = 1$

(b) Structural displacement with $k = 1$

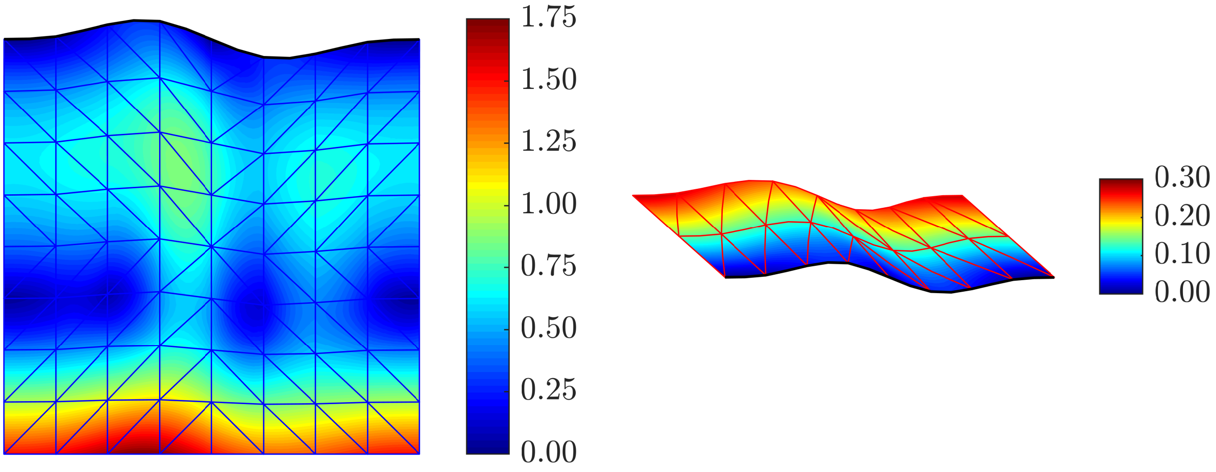

(c) Fluid velocity with $k = 2$

(d) Structural displacement with $k = 2$

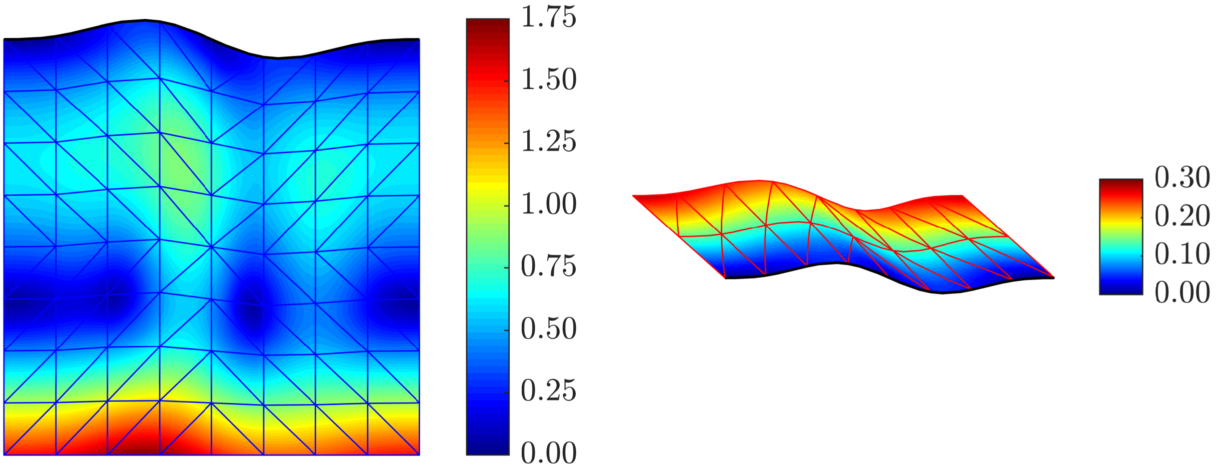

(e) Fluid velocity with $k = 3$

(f) Structural displacement with $k = 3$

Figure 5.5: Solution of fluid velocity and structural displacement for FSI problem with manufactured solution

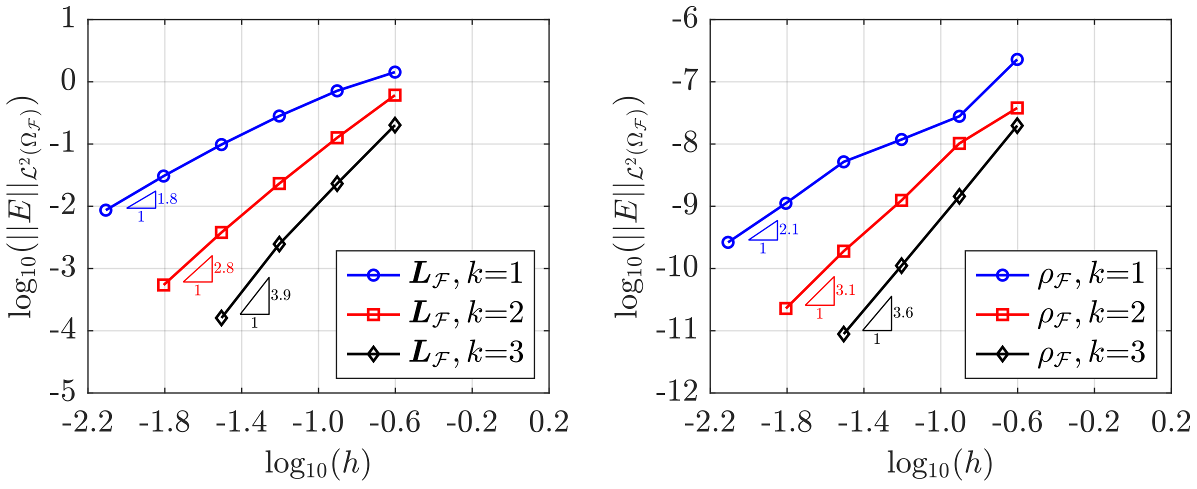

(a) Fluid scaled strain rate

(b) Fluid density

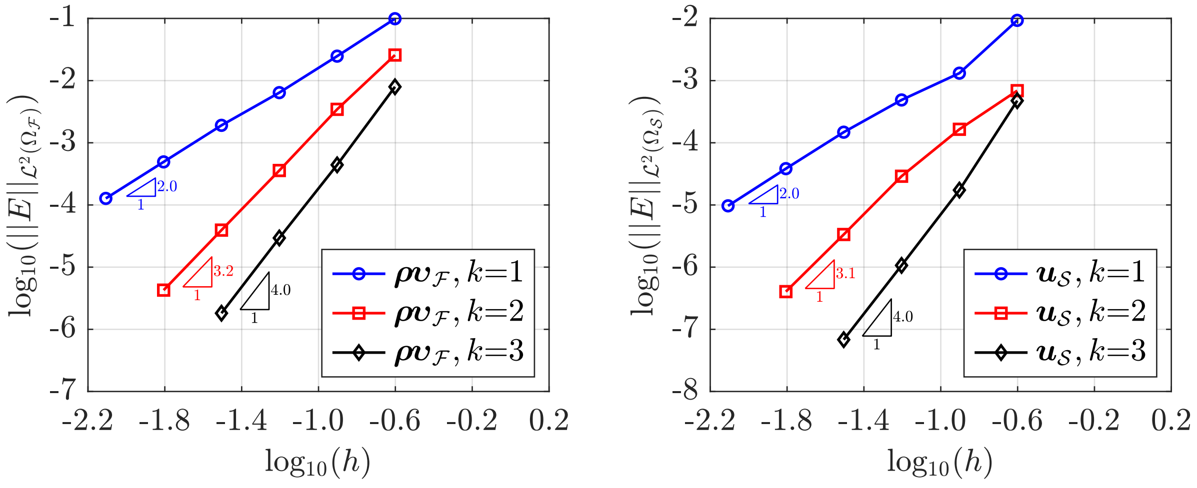

(c) Fluid momentum

(d) Structural displacement

Figure 5.6: Spatial convergence study for FSI problem with manufactured solution via partitioned DIRICHLET–NEUMANN coupling

The fluid reference density is $\rho_{\mathcal{F}}^{\mathtt{ref}} = 1$, computed at the reference pressure $p_{\mathcal{F}}^{\mathtt{ref}} = 0$. To mimic an incompressible flow, the compressibility coefficient is chosen extremely small, i.e. $\varepsilon_{\mathcal{F}} = 10^{-6}$. The structure is modelled as a ST. VENANT–KIRCHHOFF material with YOUNG's modulus $E_{\mathcal{S}} = 1$, POISSON's ratio $\nu_{\mathcal{S}} = 0.49$ and density $\rho_{\mathcal{S}} = 1$.

The meshes used for the convergence studies are obtained by splitting a Cartesian grid into a total number of triangles equal to $2 \cdot 2^{2r+2}$ and $2 \cdot 2^{2r}$ for the fluid and the structural subdomain respectively, producing the same element sizes of $h = 1/2^{r+1}$. In Figure 5.3, the fourth level of mesh refinement ($r = 4$) is displayed with respect to the undeformed (top), initial deformed (bottom-left) and final deformed (bottom-right) configuration. The fluid domain is plotted in blue, the structural domain in red and the interface is highlighted in black. The time interval analyzed is then $t \in (0, 1/8)$. The two HDG-CG formulations for FSI are considered in the following:

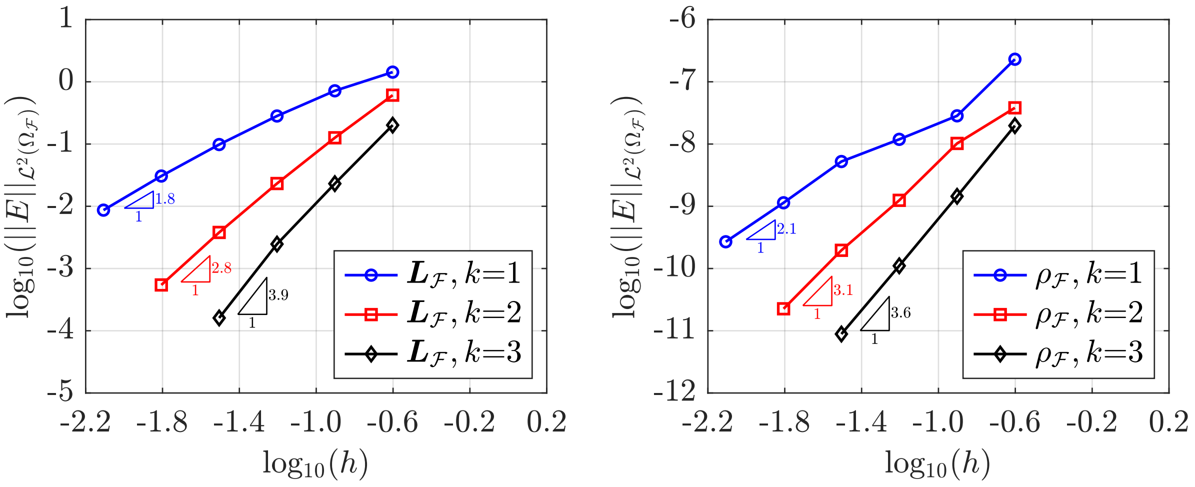

(a) Fluid scaled strain rate

(b) Fluid density

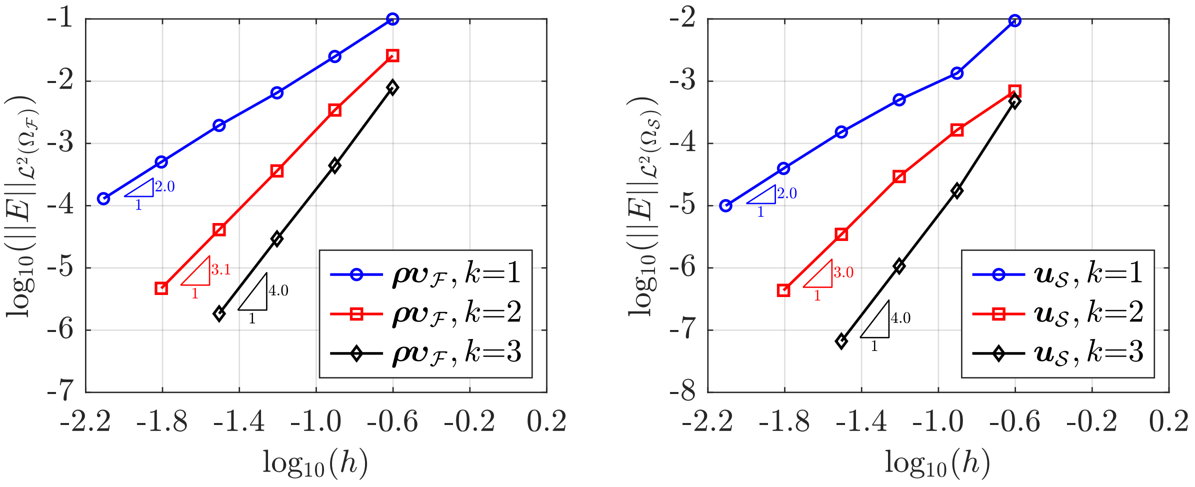

(c) Fluid momentum

(d) Structural displacement

Figure 5.7: Spatial convergence study for FSI problem with manufactured solution via monolithic NITSCHE-based coupling

1. partitioned DIRICHLET–NEUMANN coupling according to Section 5.2,
2. monolithic NITSCHE-based coupling according to Section 5.3.

The stabilization parameters for the fluid subproblem are taken as $\tau_\rho = 1/\varepsilon_\mathcal{F}$ and $\tau_{\rho v} = 10$. The convergence tolerance for the first case is set to $\eta = 10^{-7}$ whereas the NITSCHE parameter for the second case is $\gamma = 10^5$.

For the spatial convergence studies, the degrees of approximation considered are $k = [1, 2, 3]$ and the temporal integration is performed with BDF2 with a constant time step size of $\Delta t = 2^{-12}$. The level of mesh refinement sufficient to reach the asymptotic regime is $r = [1, 2, \dots, 6]$ for $k = 1$, $r = [1, 2, \dots, 5]$ for $k = 2$ and $r = [1, 2, \dots, 4]$ for $k = 3$. The approximation of the magnitude of the fluid velocity and the structural displacement obtained via the monolithic NITSCHE-based coupling on the second level of mesh refinement ($r = 2$) at $t = 1/8$

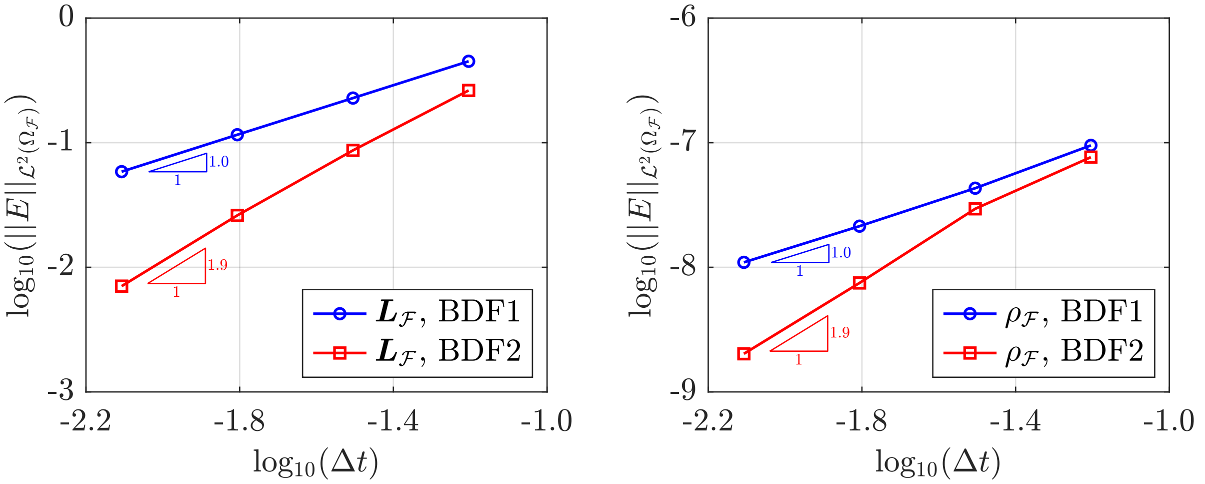

(a) Fluid scaled strain rate (b) Fluid density

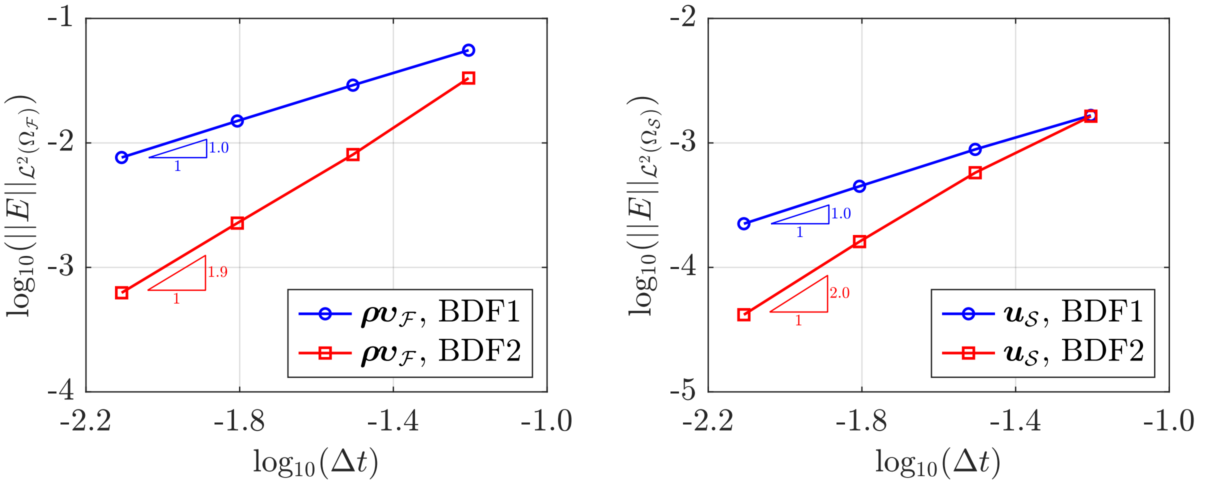

(c) Fluid momentum (d) Structural displacement

Figure 5.8: Temporal convergence study for FSI problem with manufactured solution via partitioned DIRICHLET–NEUMANN coupling

is exemplarily shown in Figure 5.5 for $k = 1$ (top), $k = 2$ (middle) and $k = 3$ (bottom). The improvement of the approximation brought by k-refinement can be clearly observed on this rather coarse mesh, especially with regards to the shape of the fluid-structure interface, denoted in black. The convergence of the error of the fluid and the structural variables in the $\mathcal{L}^2$ norm as a function of the characteristic element size h is shown in Figures 5.6 and 5.7 for the partitioned DIRICHLET–NEUMANN coupling and the monolithic NITSCHE-based coupling, respectively. Not surprisingly, the two formulations produce nearly identical results. In addition, the optimal convergence of order $k + 1$ of the single-fields variables observed in Section 3.5 for fluid problems and in Section 4.3 for structural problems is nicely preserved for the coupled FSI problem too. A small degradation of almost half order is only observed in the convergence rate of the fluid density error for $k = 3$, but at a level close to machine precision.

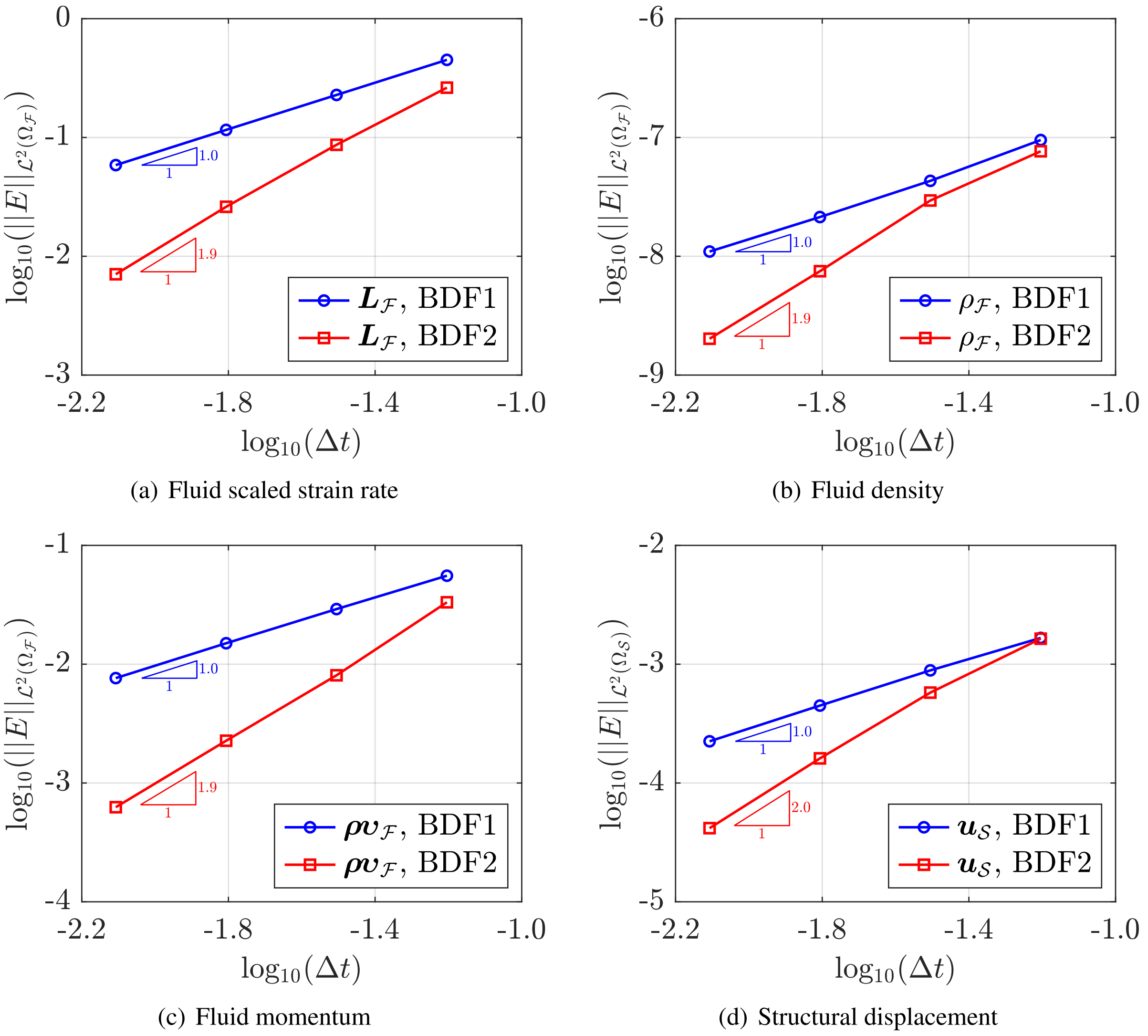

(a) Fluid scaled strain rate

(b) Fluid density

(c) Fluid momentum

(d) Structural displacement

Figure 5.9: Temporal convergence study for FSI problem with manufactured solution via monolithic NITSCHE-based coupling

For the temporal convergence studies, the time step sizes are $\Delta t = [1/16, 1/32, 1/64, 1/128]$ and the backward differentiation formulas are considered, with BDF$o = [1, 2]$. The error associated with the spatial discretization is kept sufficiently small by adopting the polynomial degree $k = 3$ on the mesh levels $r = 3$ and $r = 4$ for BDF1 and BDF2, respectively. The convergence of the $\mathcal{L}^2$ error as a function of the time step size Δt is shown in Figures 5.8 and 5.9 for the two coupling strategies. The theoretical convergence rates of order BDFo are achieved for all the fluid and structural unknowns with both coupling schemes.

In conclusion, both HDG-CG formulations accurately solve fluid-structure interaction problems with high-order accuracy and no loss of accuracy is observed for the fluid mixed and primal variables and for the structural displacement. However, no superconvergence of the postprocessed fluid velocity is achieved in this numerical example and further investigation would be required to understand the causes.

5.4.2 FSI benchmark

The second numerical experiment considers a complex two-dimensional fluid-structure interaction problem with large deformations. It was introduced by TUREK and HRON [159] and later used by several authors to test a great variety of FSI codes. The objective of this example is to show whether the developed HDG-CG formulations can deliver a meaningful coupled system response on a widely accepted benchmark.

The computational domain is the rectangle $\Omega = (0, 2.5) \times (0, 0.41)\ m$ in which a flexible structure $\Omega_{\mathcal{S}} = (0.25, 0.6) \times (0.19, 0.21)\ m$ is fully attached to a rigid circular block $\Omega_{\mathcal{C}}$ with radius $0.05\ m$ and centred at point $(0.2, 0.2)\ m$. The fluid region is identified by $\Omega_{\mathcal{F}} = \Omega \backslash \Omega_{\mathcal{S}} \backslash \Omega_{\mathcal{C}}$. It is worth highlighting that, as stated by TUREK and HRON [159], the setting is intentionally non-symmetric to prevent the dependence of the onset of any possible oscillation on the precision of the computation. A smoothly increasing parabolic profile is imposed on the inflow as

$$
\begin{cases}
\rho v^D_{\mathcal{F}x}(0, y, t) = \begin{cases} \dfrac{3}{2} \dfrac{y\,(0.41 - y)}{(0.41/2)^2} \dfrac{1 - \cos(\pi t / \bar{t})}{2} \rho^{\texttt{ref}}_{\mathcal{F}} U_{\mathcal{F}}\ kg/(m^2 \cdot s) & \text{if } t \leq \bar{t}, \\ \dfrac{3}{2} \dfrac{y\,(0.41 - y)}{(0.41/2)^2} \rho^{\texttt{ref}}_{\mathcal{F}} U_{\mathcal{F}}\ kg/(m^2 \cdot s) & \text{if } t > \bar{t}, \end{cases} \\
\rho v^D_{\mathcal{F}y}(0, y, t) = 0\ kg/(m^2 \cdot s),
\end{cases}
\tag{5.40}
$$

with $\bar{t} = 2\ s$ and $U_{\mathcal{F}} = 1\ m/s$, resulting in a REYNOLDS number of about 100 when the flow has completely developed. No-slip boundary conditions ($\boldsymbol{\rho v}^D_{\mathcal{F}} = \mathbf{0}$) are applied on the top and bottom, whereas the fluid density is imposed equal to its reference value ($\rho^D_{\mathcal{F}} = \rho^{\texttt{ref}}_{\mathcal{F}}$) at the outflow. The structure is considered clamped ($\boldsymbol{u}^D_{\mathcal{S}} = \mathbf{0}$) on the left edge. In addition, both the fluid and the structure are at rest at the beginning of the simulation. The geometry and the boundary conditions are depicted in Figure 5.10.

The fluid viscosity is $\mu_{\mathcal{F}} = 1\ kg/(m \cdot s)$, the reference density $\rho^{\texttt{ref}}_{\mathcal{F}} = 10^3\ kg/m^3$ evaluated at the reference pressure $p^{\texttt{ref}}_{\mathcal{F}} = 0\ N/m^2$. To mimic an incompressible flow, the compressibility coefficient is taken as $\varepsilon_{\mathcal{F}} = 10^{-5}\ s^2/m^2$. The structure is modelled as a ST. VENANT–KIRCHHOFF material with YOUNG's modulus $E_{\mathcal{S}} = 1.4 \cdot 10^6\ N/m^2$, POISSON's ratio $\nu_{\mathcal{S}} = 0.4$ and density $\rho_{\mathcal{S}} = 10^4\ kg/m^3$.

The fluid and the structural domains count 4189 and 1120 triangular elements, respectively. The fluid mesh is refined on the circular block and on the interface to match the structural nodes and the degree of approximation is $k = 2$ for both fields. The fluid mesh is constructed through the `MATLAB` code by PERSSON and STRANG [131], by providing a suitable mesh density function. The resulting computational mesh is shown in Figure 5.11, together with a close-up on the region around the structure for a better visualization. The evolution in time in the span $t \in (0, 15)\ s$ is performed with the BDF2 method with a time step size $\Delta t = 0.002\ s$. The two HDG-CG formulations are considered, i.e.:

1. partitioned DIRICHLET–NEUMANN coupling,
2. monolithic NITSCHE-based coupling.

The stabilization parameters in the fluid HDG discretization are taken as $\tau_\rho = 100/\varepsilon_{\mathcal{F}}$ and $\tau_{\rho v} = 10$. The convergence tolerance for the coupling iterations of the partitioned scheme in case 1 is then set as $\eta = 10^{-9}$, while the NITSCHE parameter for case 2 is $\gamma = 10^5$.

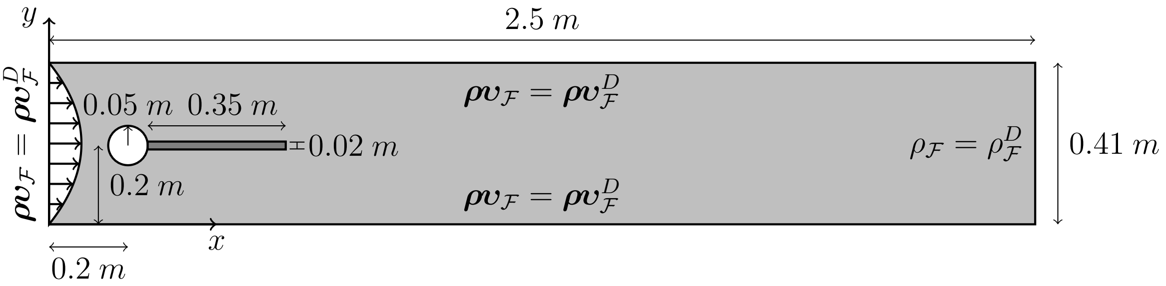

Figure 5.10: Geometry and boundary conditions for FSI benchmark

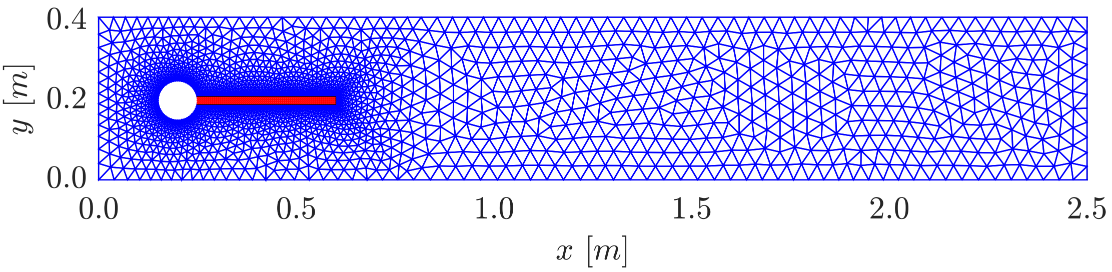

(a) Whole domain

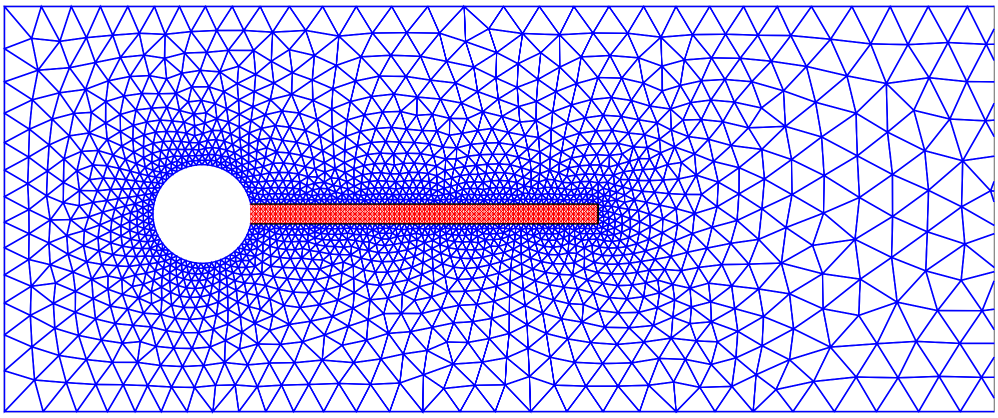

(b) Region around the structure

Figure 5.11: Computational mesh for FSI benchmark

Figures 5.12 and 5.13 show snapshots at different time instants for the fluid velocity magnitude and pressure, respectively. The flow exhibits a complex behavior and induces a significant structural deformation. The evolution of the tip structural displacement and of the lift and drag forces exerted by the fluid on the structure and on the circular block are shown in Figure 5.14. It is worth pointing out that the displacement is directly obtained from the solution of the structural subproblem, while the lift and the drag forces are computed in postprocessing through the following formula

$$\begin{bmatrix} f_{\mathrm{D}} \\ f_{\mathrm{L}} \end{bmatrix} = \int_{\partial\Omega_{\mathcal{F}} \cap (\partial\Omega_{\mathcal{S}} \cup \partial\Omega_{\mathcal{C}})} \mathbf{N}_{\mathcal{F}}^T \left(\mathbf{D}_{\mathcal{F}}^{1/2} \boldsymbol{L}_{\mathcal{F}} + \mathbf{E} p_{\mathcal{F}} \left(\hat{\rho}_{\mathcal{F}} \right) \right) d\Gamma. \tag{5.41}$$

An excellent agreement of the two HDG-CG coupling strategies is obtained in terms of both x-displacement (Figure 5.14(a)) and y-displacement (Figure 5.14(b)). No comparison is provided for the lift and drag forces, since their computation has been solely implemented in the `MATLAB` code for the monolithic NITSCHE-based coupling. However, given the practically indistinguishable displacement response in the two cases, no differences are expected with respect to these quantities too.

A detailed view of the displacement and the drag and lift forces over a time window of $1\ s$ for the fully developed flow is offered in Figures 5.15 and 5.16, respectively. The computed values are compared to the results obtained by TUREK and HRON [159] and SHELDON *et al.* [144]. On the one hand, TUREK and HRON adopted a monolithic CG method with a multigrid solver on different spatial and temporal discretization levels. On the other hand, SHELDON *et al.* employed a monolithic approach for the solution of the whole problem by means of the HDG method with a polynomial degree $k = 2$. Even though both the proposed HDG-CG coupling strategies provide overall meaningful results, some non-negligible differences can be noted in terms of the horizontal displacement and drag force with respect to the reference values reported by TUREK and HRON. In particular, the amplitude of the x-displacement and the amplitude of the computed drag force are overestimated by about 4% and 6%, respectively. The mismatch with the widely accepted results provided by TUREK and HRON might be attributed to an insufficient spatial resolution of the computational mesh adopted here. A summary of mean (`M`), amplitude (`A`) and frequency (`F`) of the compared quantities is offered in Table 5.1. These numbers are explicitly reported by TUREK and HRON [159], while the others are extrapolated from the plots in SHELDON *et al.* [144]. It is worth noting how the values presented here lie in between the ones provided by TUREK and HRON and the ones obtained by SHELDON *et al.* for all the compared quantities.

	$u_{\mathcal{S}x}\ [mm]$			$u_{\mathcal{S}y}\ [mm]$			$f_{\mathrm{L}}\ [N]$			$f_{\mathrm{D}}\ [N]$		
	`M`	`A`	`F`	`M`	`A`	`F`	`M`	`A`	`F`	`M`	`A`	`F`
DIRIC–NEUM	-15.1	12.9	3.8	1.2	82.2	1.9	–	–	–	–	–	–
NITSCHE	-15.1	12.9	3.8	1.2	82.2	1.9	1	239	1.9	215	78	3.8
SHELDON	-15.6	13.3	3.8	1.2	83.9	1.9	2	247	1.9	218	82	3.8
TUREK	-14.6	12.4	3.8	1.2	80.6	2.0	1	234	2.0	209	74	3.8

Table 5.1: Results comparison for FSI benchmark

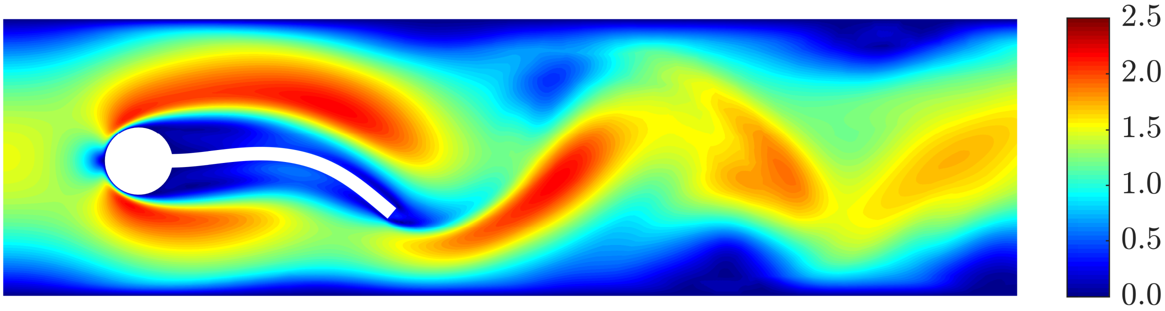

(a) $t = 14.6\ s$

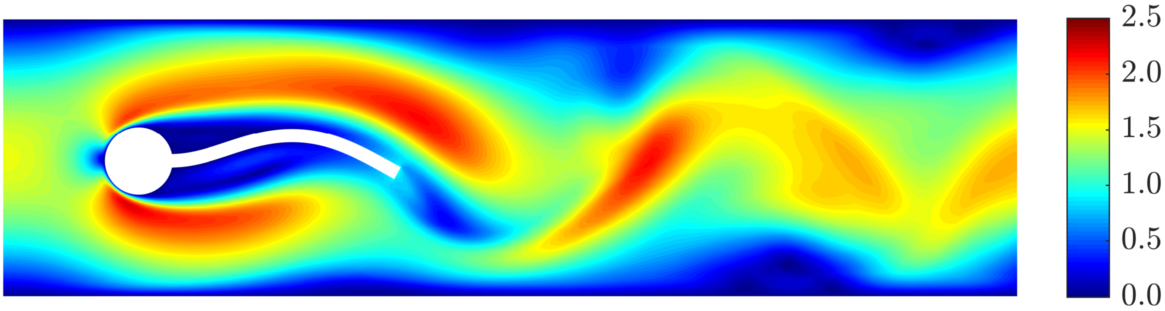

(b) $t = 14.7\ s$

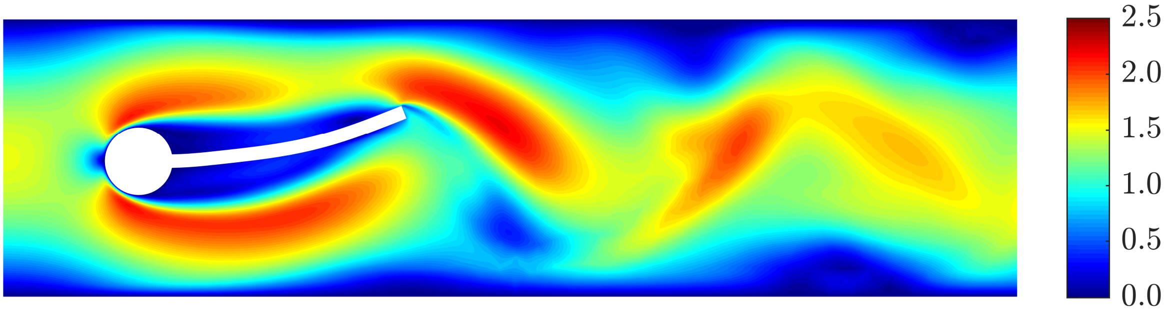

(c) $t = 14.8\ s$

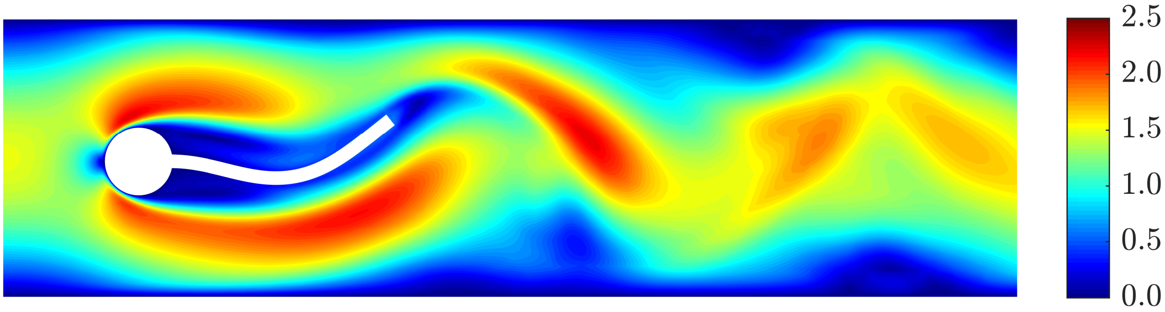

(d) $t = 14.9\ s$

Figure 5.12: Solution of fluid velocity for FSI benchmark

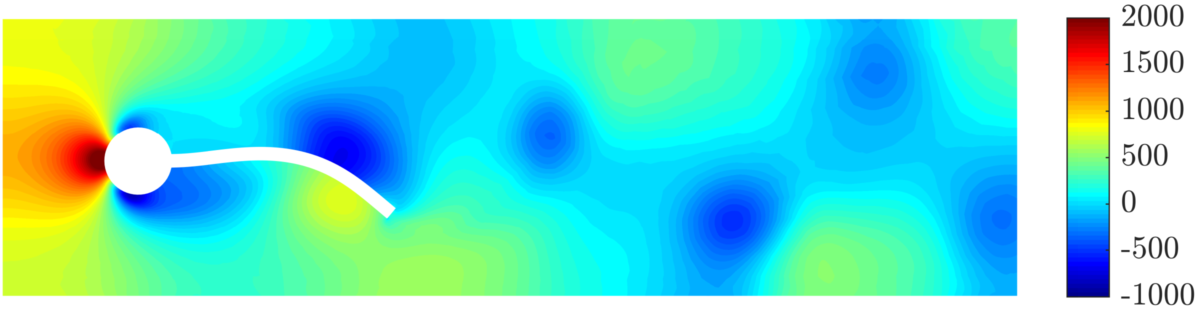

(a) $t = 14.6\ s$

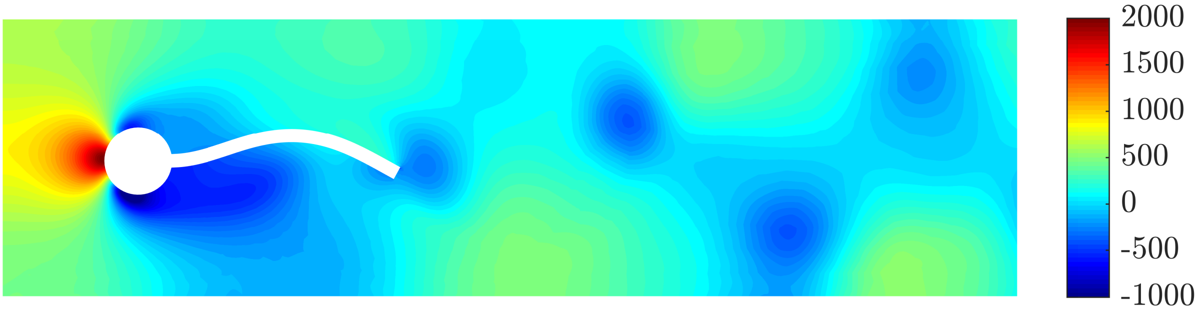

(b) $t = 14.7\ s$

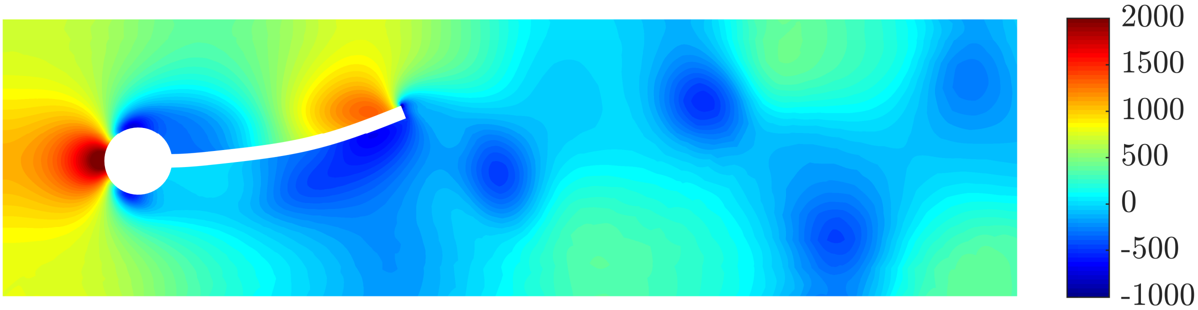

(c) $t = 14.8\ s$

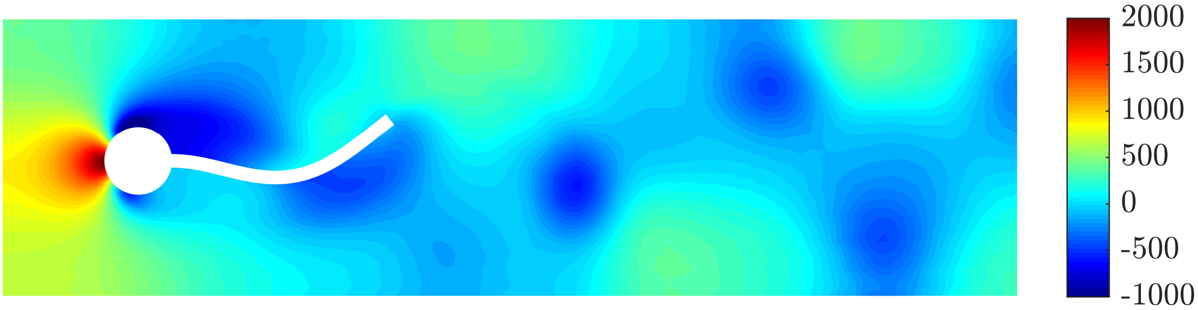

(d) $t = 14.9\ s$

Figure 5.13: Solution of fluid pressure for FSI benchmark

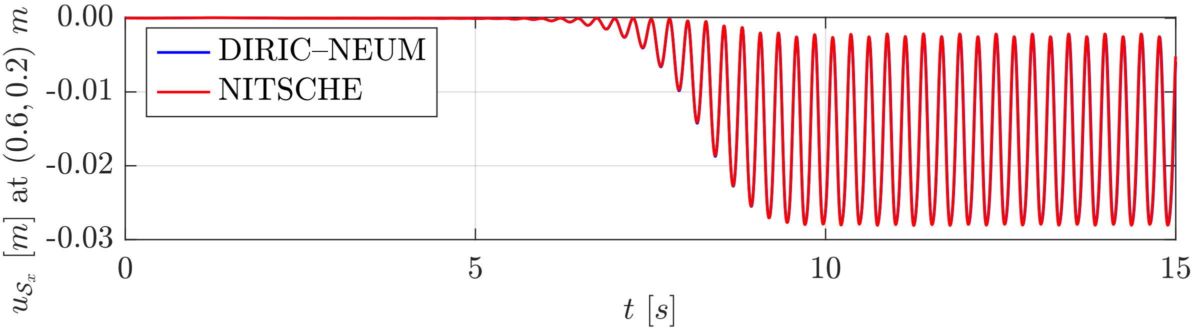

(a) x-displacement

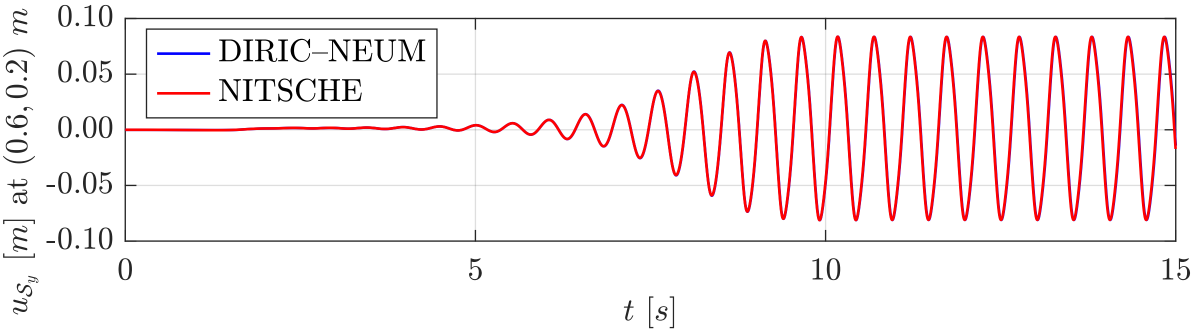

(b) y-displacement

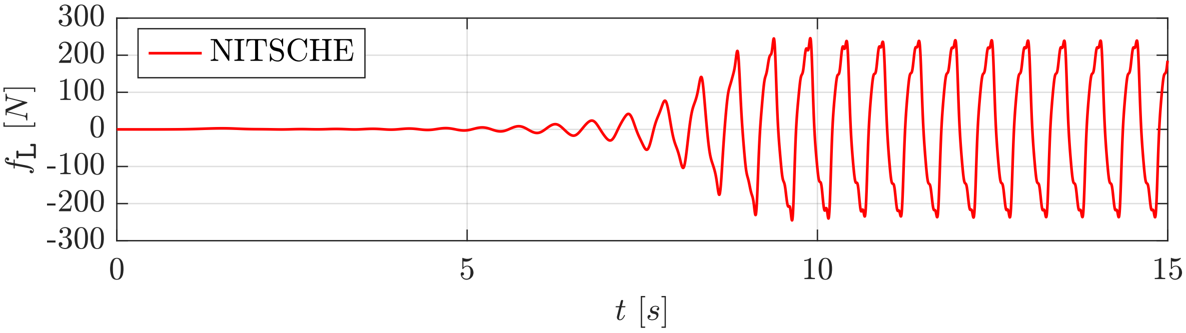

(c) Lift

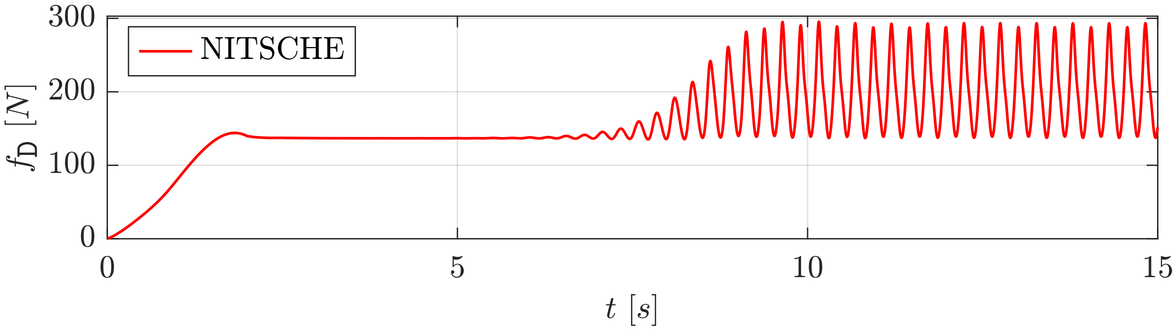

(d) Drag

Figure 5.14: Plot of displacement, lift and drag for FSI benchmark

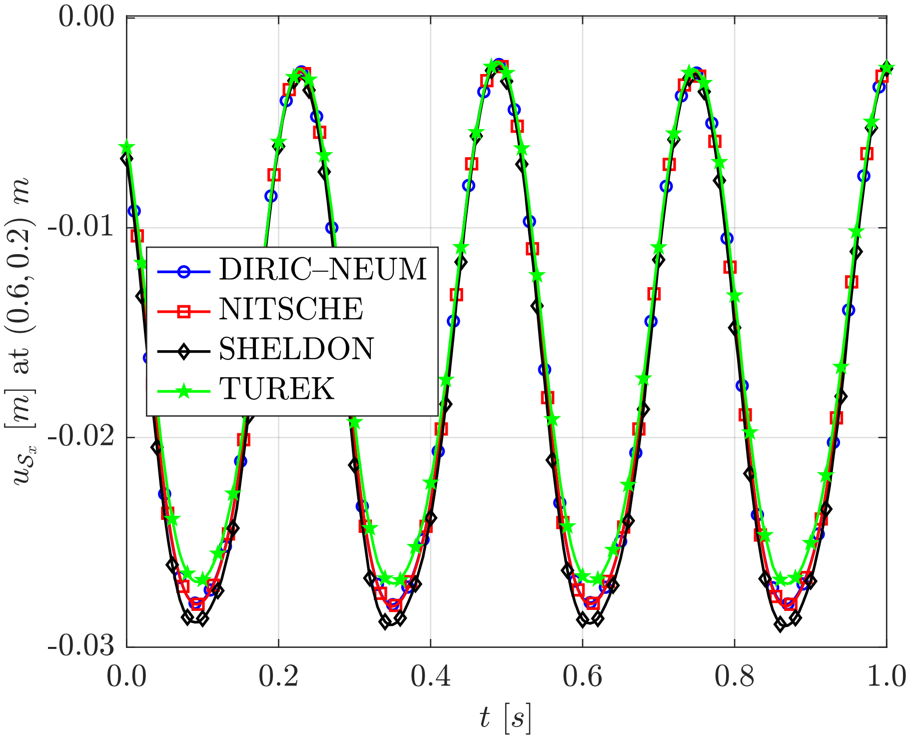

(a) x-displacement

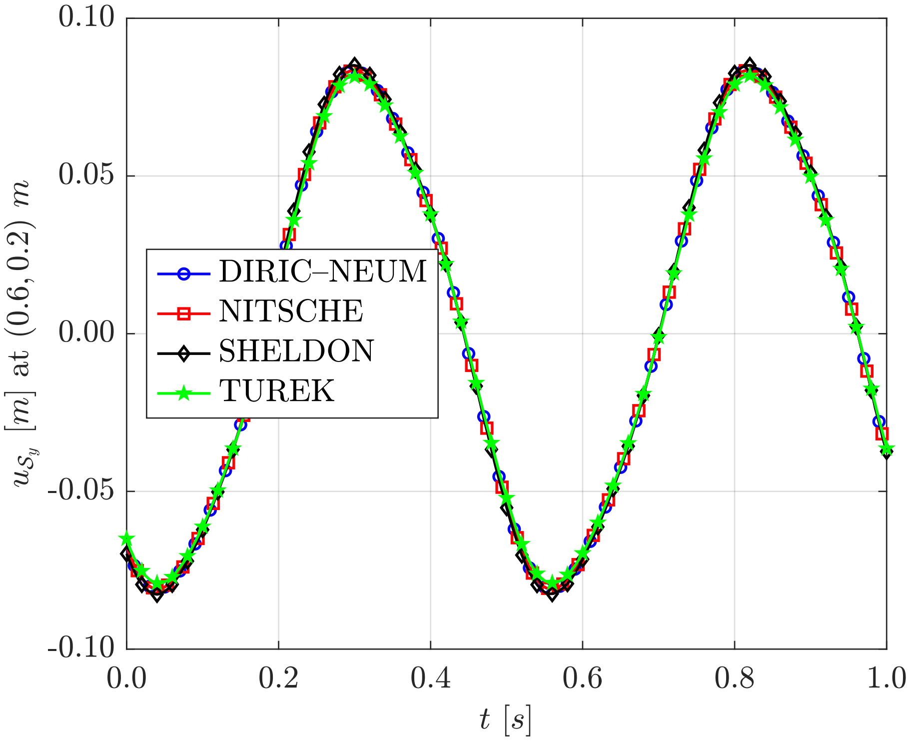

(b) y-displacement

Figure 5.15: Plot of displacement in detail for FSI benchmark

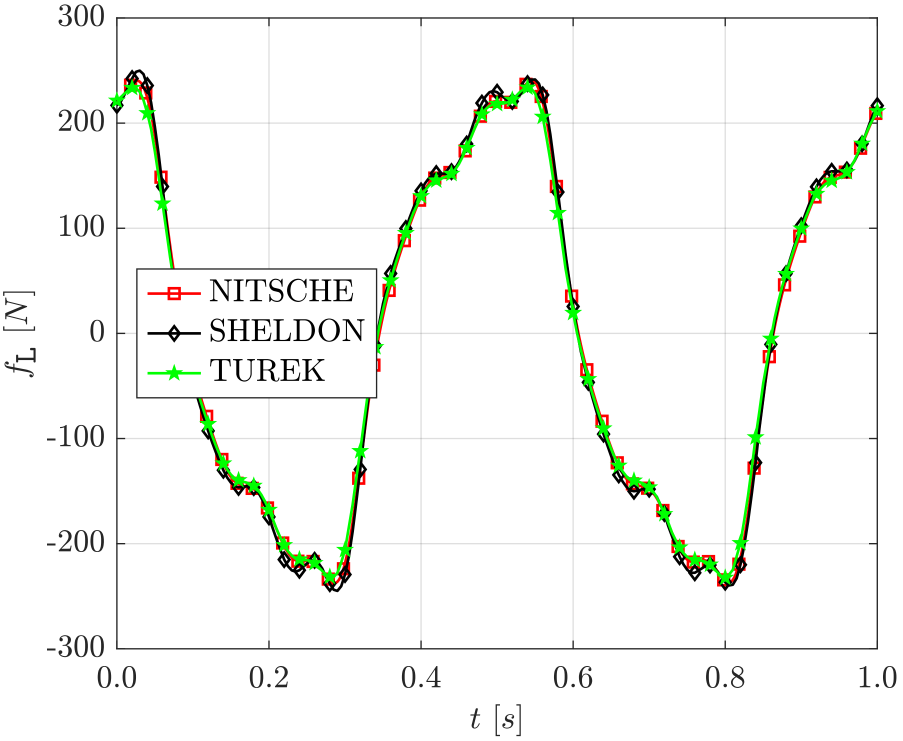

(a) Lift

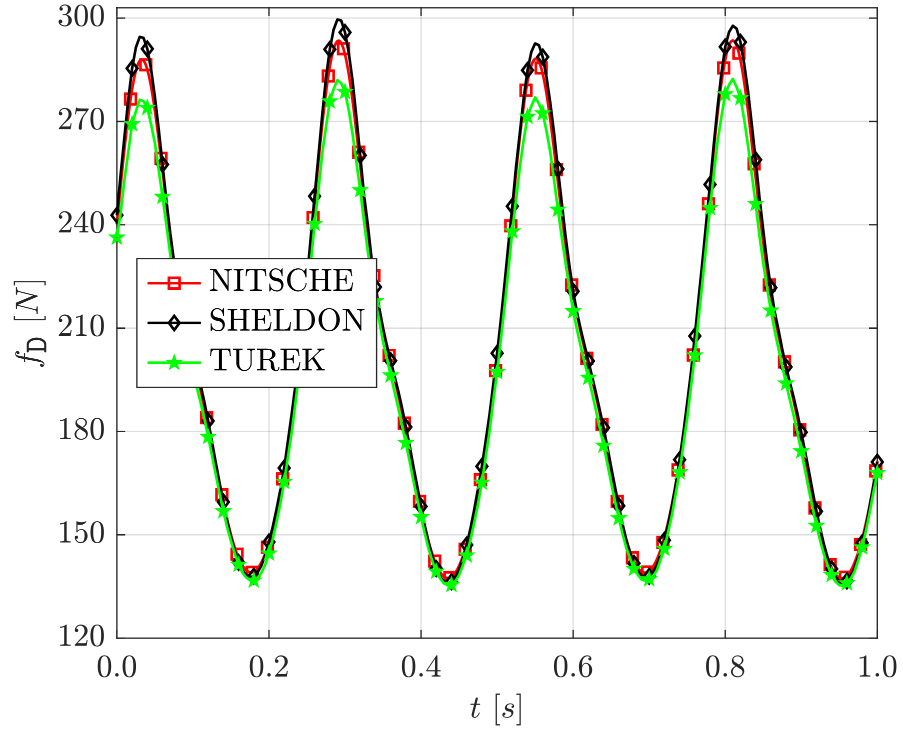

(b) Drag

Figure 5.16: Plot of lift and drag in detail for FSI benchmark

5.4.3 Two-dimensional channel with flexible wall

This numerical experiment considers a convergent fluid channel containing a flexible wall structure attached to its bottom. It was introduced by MOK [108] as a challenging test for the stability of FSI algorithms, due to the strong coupling between the fluid and structure given by their similar densities, i.e. $\rho_{\mathcal{F}}/\rho_{\mathcal{S}} \approx 1$. A similar setting has been later used by MOK and WALL [109] and by ROSSI and OÑATE [138], among others. The main goal of this example is to compare the proposed weakly compressible HDG-CG formulations for fluid-structure interaction on a challenging two-dimensional setting.

The fluid domain $\Omega_{\mathcal{F}}$ consists of a convergent channel with a total length of $1.75\ m$ and with a height of $0.5\ m$ at the inflow and $0.2\ m$ at the outflow. A parabolic momentum profile is imposed at the inflow according to

$$\begin{cases} \rho v^D_{\mathcal{F}x}(0,y,t) = \begin{cases} 4y\,(1-y)\,\dfrac{1-\cos\left(\pi t/\bar{t}\right)}{2}\rho^{\mathtt{ref}}_{\mathcal{F}}\bar{v}_{\mathcal{F}}\ kg/(m^2\cdot s) & \text{if } t \le \bar{t}, \\ 4y\,(1-y)\,\rho^{\mathtt{ref}}_{\mathcal{F}}\bar{v}_{\mathcal{F}}\ kg/(m^2\cdot s) & \text{if } t > \bar{t}, \end{cases} \\ \rho v^D_{\mathcal{F}y}(0,y,t) = 0\ kg/(m^2\cdot s), \end{cases} \tag{5.42}$$

with $\bar{t} = 10\ s$ and $\bar{v}_{\mathcal{F}} = 0.06067\ m/s$, resulting in a REYNOLDS number of about 100 when the flow is completely formed. No-slip ($\boldsymbol{\rho v}^D_{\mathcal{F}} = \mathbf{0}$) and free-slip ($\rho v^D_{\mathcal{F}y} = 0$) boundary conditions are considered on the bottom and on the top sides of the channel, respectively, whereas the fluid density is imposed equal to its reference value ($\rho^D_{\mathcal{F}} = \rho^{\mathtt{ref}}_{\mathcal{F}}$) at the outflow. The structural domain $\Omega_{\mathcal{S}}$ is then constituted by a thin wall with thickness $0.005\ m$ and height $0.25\ m$. It is located on the bottom of the channel at a distance of $0.5\ m$ from the inflow and it is considered fixed at the base ($\boldsymbol{u}^D_{\mathcal{S}} = \mathbf{0}$). Both the fluid and the structure are then considered at rest at the beginning of the simulation. A sketch of the geometry and the boundary conditions is given in Figure 5.17.

The weakly compressible fluid is characterized by a viscosity of $\mu_{\mathcal{F}} = 0.145\ kg/(m\cdot s)$ and a reference density of $\rho^{\mathtt{ref}}_{\mathcal{F}} = 956\ kg/m^3$, evaluated at the reference pressure $p^{\mathtt{ref}}_{\mathcal{F}} = 0\ N/m^2$. Three different orders of magnitude are considered for the compressibility coefficient, i.e. $\varepsilon_{\mathcal{F}} = [0.001, 0.01, 0.1]\ s^2/m^2$. The constitutive behavior of the structure is described by a ST. VENANT–KIRCHHOFF material with YOUNG's modulus $E_{\mathcal{S}} = 2.3\cdot 10^6\ N/m^2$, POISSON's ratio $\nu_{\mathcal{S}} = 0.45$ and density $\rho_{\mathcal{S}} = 1500\ kg/m^3$.

The fluid domain is discretized with 772 triangular elements, whereas the structural mesh is obtained by splitting a Cartesian grid into a total number of 200 triangles. A boundary layer mesh is constructed near the structure, such that the fluid and the structural nodes match at the interface. A polynomial degree of approximation $k = 2$ is considered in the whole domain. The computational mesh adopted in the following simulations is shown in Figure 5.18 with respect to the initial configuration. The interval analyzed is $t \in (0, 25)\ s$ and the BDF2 method is applied for the temporal integration. In order to assess the stability of the coupling strategies with respect to artificial added mass effect in the limit of vanishing time step size, three time step sizes are adopted, i.e. $\Delta t = [0.1, 0.01, 0.001]\ s$.

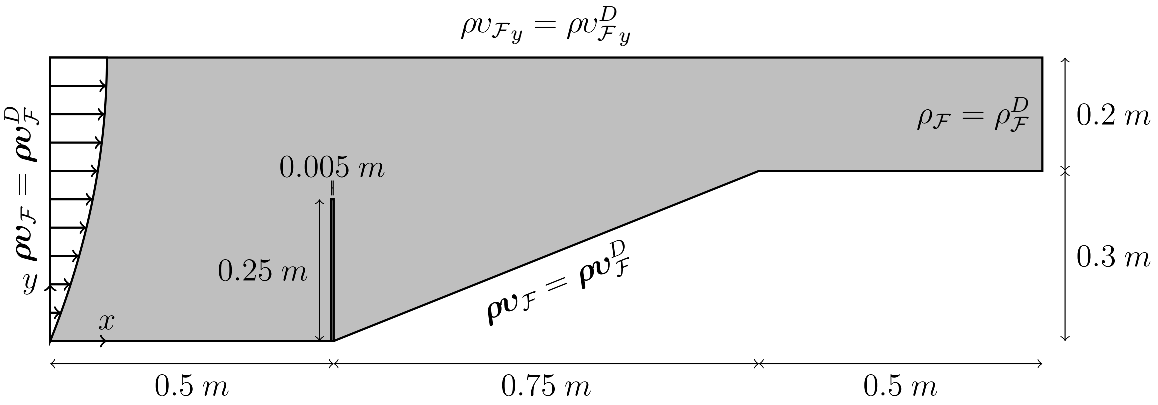

Figure 5.17: Geometry and boundary conditions for two-dimensional channel with flexible wall

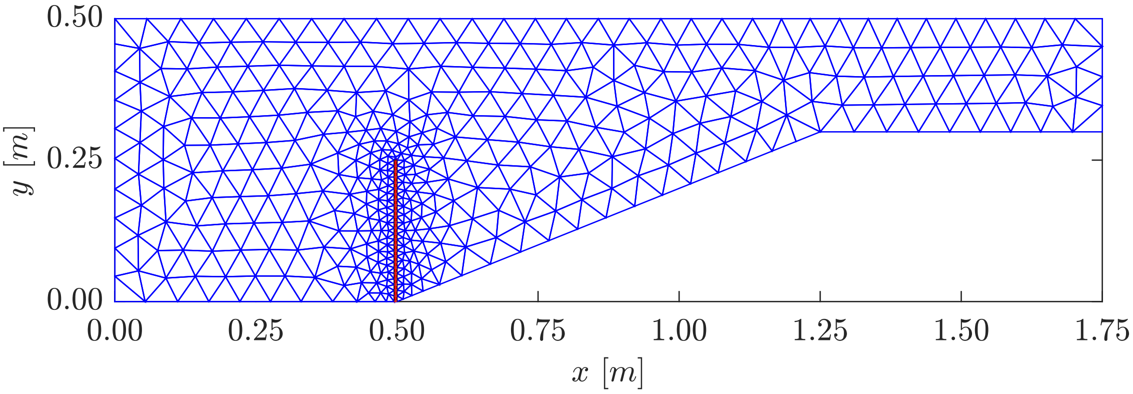

Figure 5.18: Computational mesh for two-dimensional channel with flexible wall

Three formulations are considered:

1. incompressible CG-CG partitioned DIRICHLET–NEUMANN coupling,
2. weakly compressible HDG-CG partitioned DIRICHLET–NEUMANN coupling,
3. weakly compressible HDG-CG monolithic NITSCHE-based coupling.

The stabilization parameters in the fluid HDG discretization are taken as $\tau_\rho = 10/\varepsilon_{\mathcal{F}}$ and $\tau_{\rho v} = 1$. The convergence tolerance for the coupling iterations of the partitioned scheme in cases 1 and 2 is then set as $\eta = 10^{-9}$, while the NITSCHE parameter for case 3 is $\gamma = 100$. It is worth reminding that the monolithic NITSCHE-based coupling is implemented in an independent `MATLAB` code, whereas the partitioned DIRICHLET–NEUMANN coupling approaches share a large number of libraries in the `BACI` platform. Therefore, the partitioned and the monolithic schemes are compared only on a qualitative level, while a comparison in terms of robustness can be fairly established between the incompressible CG-CG and the weakly compressible HDG-CG partitioned approaches.

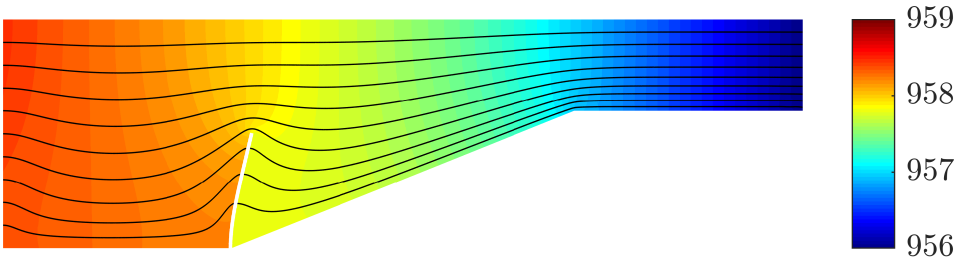

(a) $t = 5\ s$

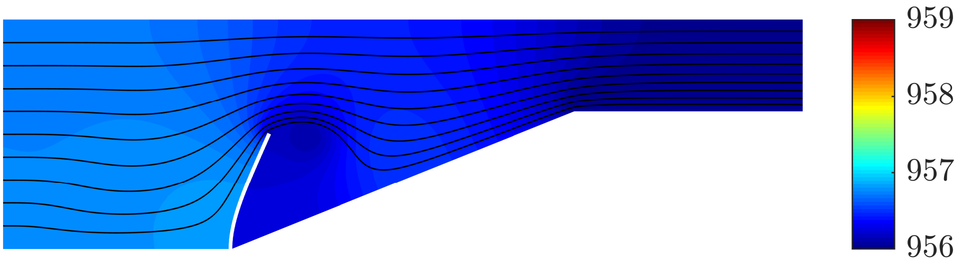

(b) $t = 10\ s$

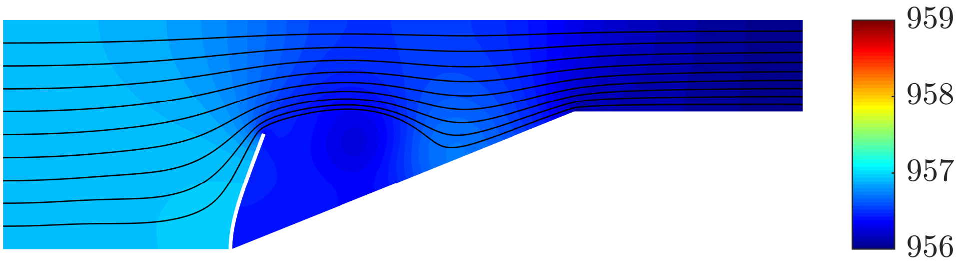

(c) $t = 15\ s$

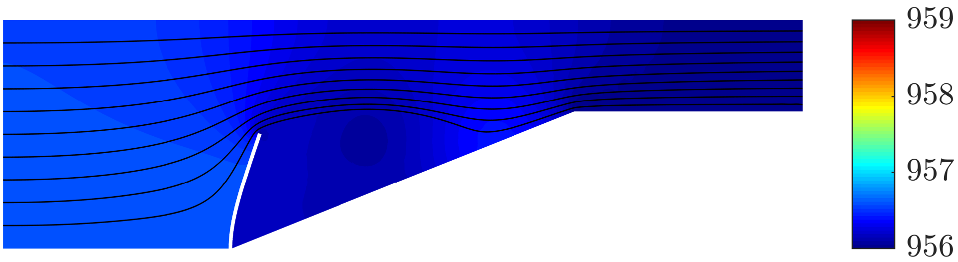

(d) $t = 20\ s$

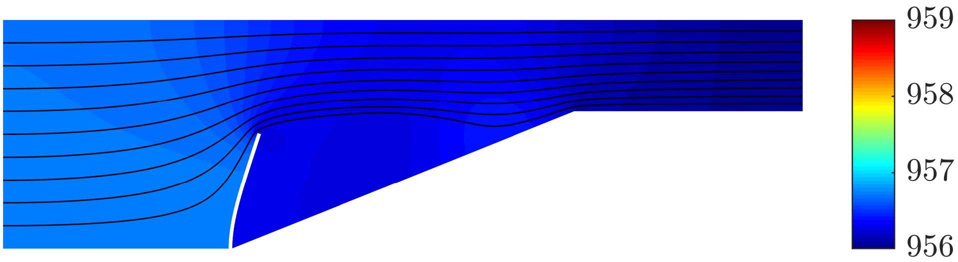

(e) $t = 25\ s$

Figure 5.19: Solution of fluid density for two-dimensional channel with flexible wall

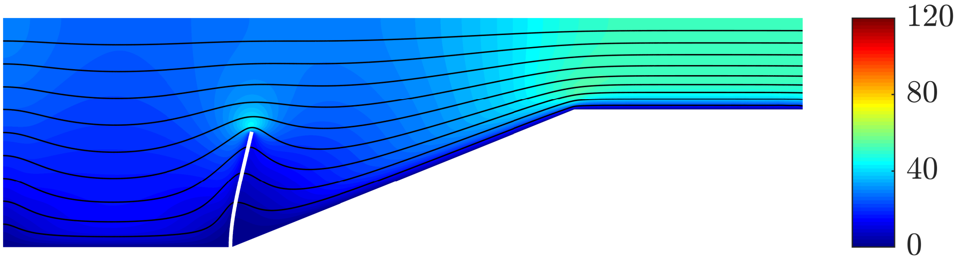

(a) $t = 5\ s$

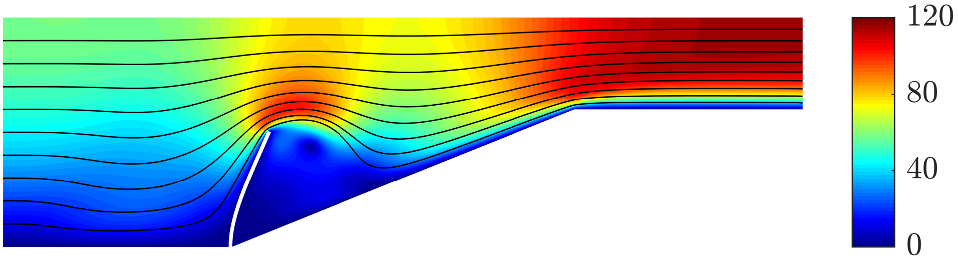

(b) $t = 10\ s$

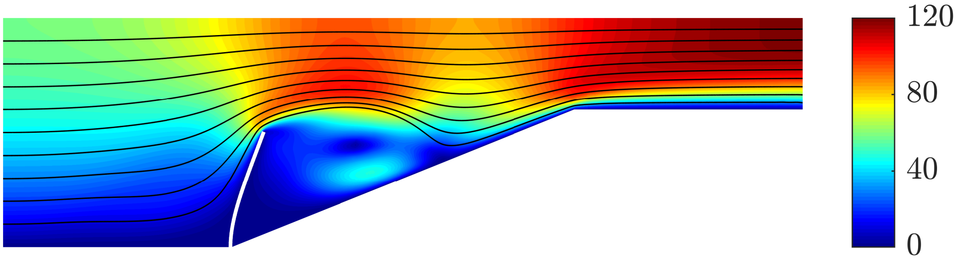

(c) $t = 15\ s$

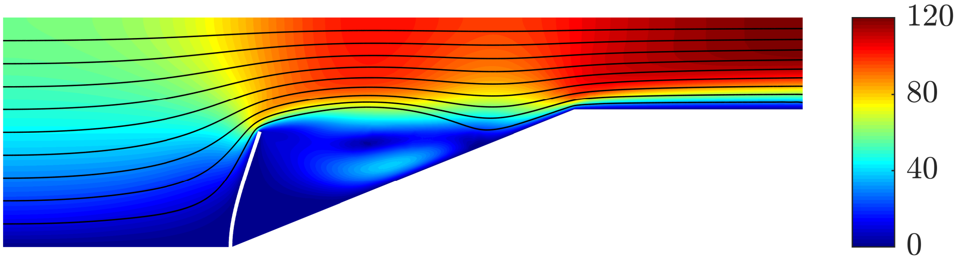

(d) $t = 20\ s$

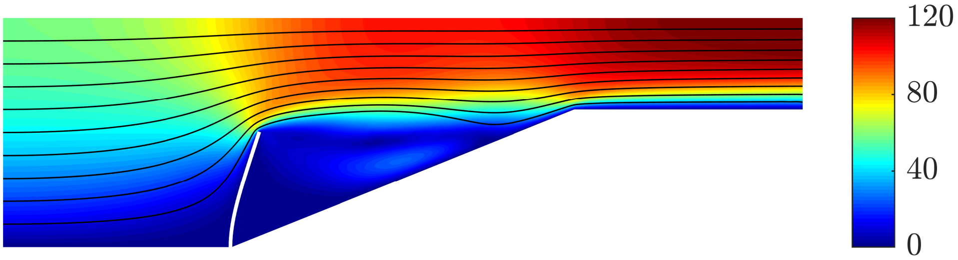

(e) $t = 25\ s$

Figure 5.20: Solution of fluid momentum for two-dimensional channel with flexible wall

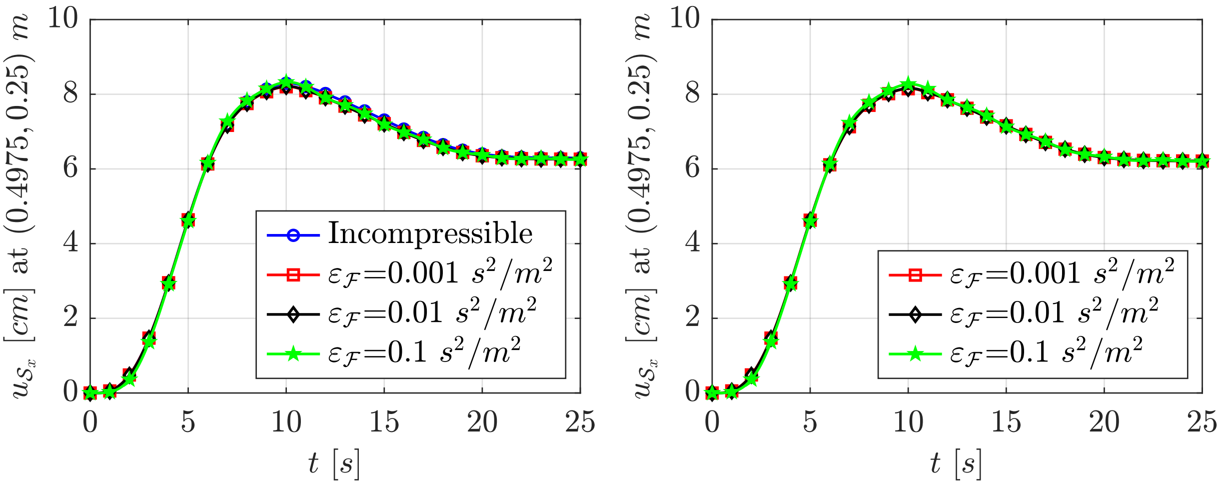

(a) Partitioned DIRICHLET–NEUMANN coupling

(b) Monolithic NITSCHE-based coupling

Figure 5.21: Plot of structural displacement for two-dimensional channel with flexible wall

The snapshots in Figures 5.19 and 5.20 depict the temporal evolution of the fluid density and momentum field, respectively, obtained for case 3 with $\varepsilon_{\mathcal{F}} = 0.1\ s^2/m^2$ and $\Delta t = 0.1\ s$. For largest compressibility level considered, the fluid density variation from its reference value is always below 1%. The momentum field highlights instead a strongly unsteady behavior characterized by the formation of a primary and a secondary vortex circulating in opposite directions in the wake of the wall during the $10\ s$ of start-up and for approximately additional $5\ s$, after which a steady flow is gradually established. In Figure 5.21 the horizontal displacement of the top-center of the structure is plotted for all the considered cases. The structural displacement closely matches the one obtained by considering the flow fully incompressible and the two coupling strategies provide nearly identical results. Table 5.2 reports the average value of the relaxation parameter and the average number of coupling iterations over the entire simulation. On the one hand, the incompressible solver requires a relatively small ω_{avg} and a large i_{avg} for $\Delta t = 0.1\ s$ and it fails to converge for smaller Δt. On the other hand, the weakly compressible HDG-CG partitioned DIRICHLET–NEUMANN coupling is always able to converge with an increase of ω_{avg} and a decrease of i_{avg} when increasing $\varepsilon_{\mathcal{F}}$ and decreasing Δt. Similarly, the monolithic NITSCHE-based coupling never fails, regardless of the time step size.

	$\Delta t = 0.1\ s$		$\Delta t = 0.01\ s$		$\Delta t = 0.001\ s$	
	ω_{avg}	i_{avg}	ω_{avg}	i_{avg}	ω_{avg}	i_{avg}
Incompressible	0.17	27.5	–	–	–	–
$\varepsilon_{\mathcal{F}} = 0.001\ s^2/m^2$	0.19	22.5	0.20	34.0	0.45	16.1
$\varepsilon_{\mathcal{F}} = 0.01\ s^2/m^2$	0.20	22.5	0.29	22.6	0.64	8.2
$\varepsilon_{\mathcal{F}} = 0.1\ s^2/m^2$	0.23	18.4	0.47	11.4	0.86	4.6

Table 5.2: Relaxation parameter and coupling iterations for two-dimensional channel with flexible wall

5.4.4 Three-dimensional channel with flexible wall

This numerical example considers a three-dimensional elastic wall embedded in a channel flow. It was first introduced by GERSTENBERGER and WALL [65] in the context of fixed-grid fluid-structure interaction problems and it was later used by MAYR [103] to discuss the properties of an adaptive time-stepping procedure for monolithic FSI solvers. More recently, this example was used by NITZLER *et al.* [124] to investigate the effects of an uncertainty in the model input on the final response of the coupled system. The goal of this problem is to show the enhanced robustness of the weakly compressible HDG-CG formulation on a three-dimensional setting.

The overall computational domain is given by $\Omega = (0,3) \times (-0.25, 0.25) \times (-0.5, 0.5)$. The structural domain is $\Omega_{\mathcal{S}} = (0.5, 0.55) \times (-0.25, 0.15) \times (-0.3, 0.3)$ and the fluid occupies the remaining region $\Omega_{\mathcal{F}} = \Omega \setminus \Omega_{\mathcal{S}}$. The inflow momentum is given by

$$\begin{cases} \rho v^D_{\mathcal{F}x}(0,y,z,t) = \begin{cases} \left(1-16y^2\right)\left(1-4z^2\right)\dfrac{1-\cos\left(\pi t/\bar{t}\right)}{2}\rho^{\mathtt{ref}}_{\mathcal{F}}\bar{v}_{\mathcal{F}} & \text{if } t \leq \bar{t}, \\ \left(1-16y^2\right)\left(1-4z^2\right)\rho^{\mathtt{ref}}_{\mathcal{F}}\bar{v}_{\mathcal{F}} & \text{if } t > \bar{t}, \end{cases} \\ \rho v^D_{\mathcal{F}y}(0,y,z,t) = 0, \\ \rho v^D_{\mathcal{F}z}(0,y,z,t) = 0, \end{cases} \tag{5.43}$$

with $\bar{t} = 5$ and $\bar{v}_{\mathcal{F}} = 0.1$. No-slip boundary conditions ($\boldsymbol{\rho v}^D_{\mathcal{F}} = \boldsymbol{0}$) are applied on the top and the bottom, as well as on the lateral walls, whereas the fluid density is imposed equal to its reference value ($\rho^D_{\mathcal{F}} = \rho^{\mathtt{ref}}_{\mathcal{F}}$) at the outflow. The structure is then considered clamped ($\boldsymbol{u}^D_{\mathcal{S}} = \boldsymbol{0}$) on the bottom face. A sketch of the geometry and the boundary conditions is given in Figure 5.22.

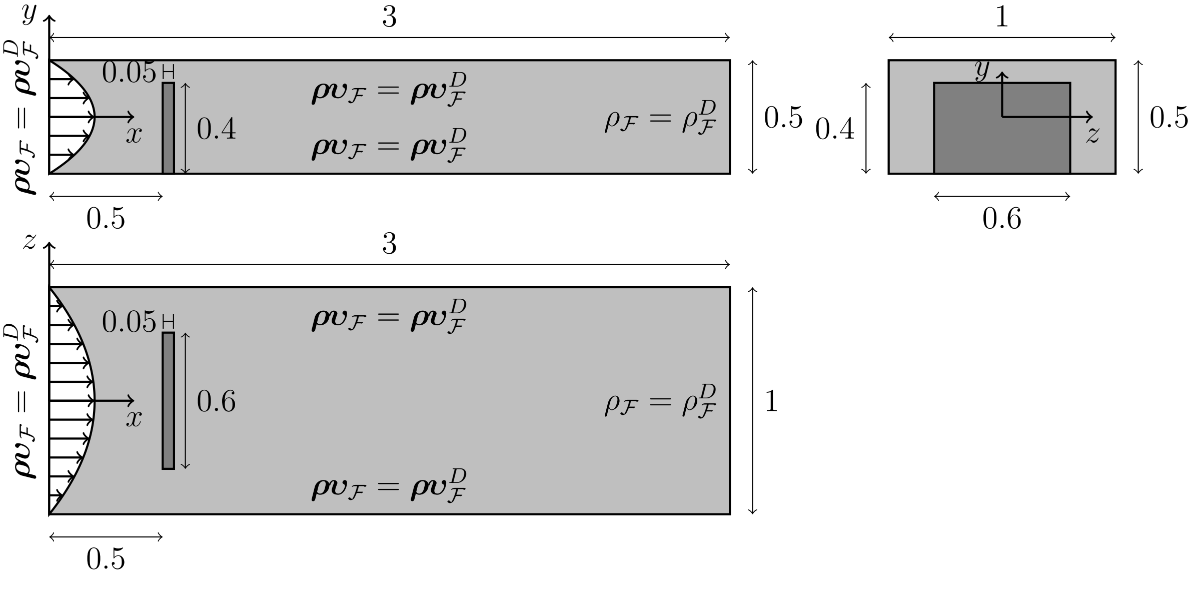

Figure 5.22: Geometry and boundary conditions for three-dimensional channel with flexible wall

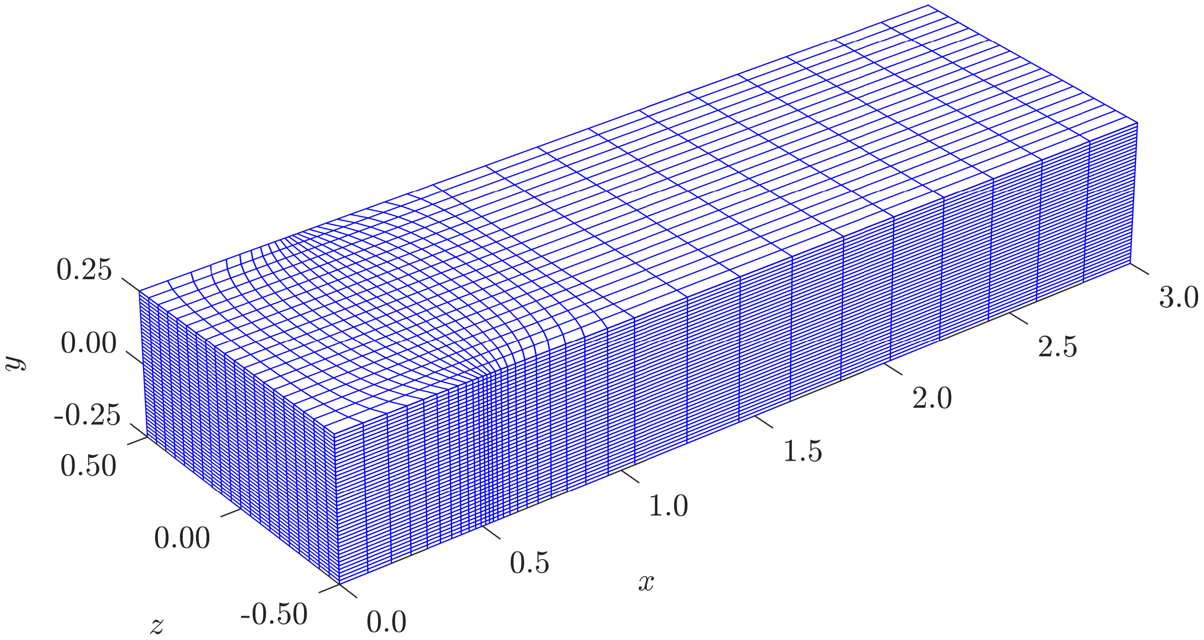

(a) Fluid mesh

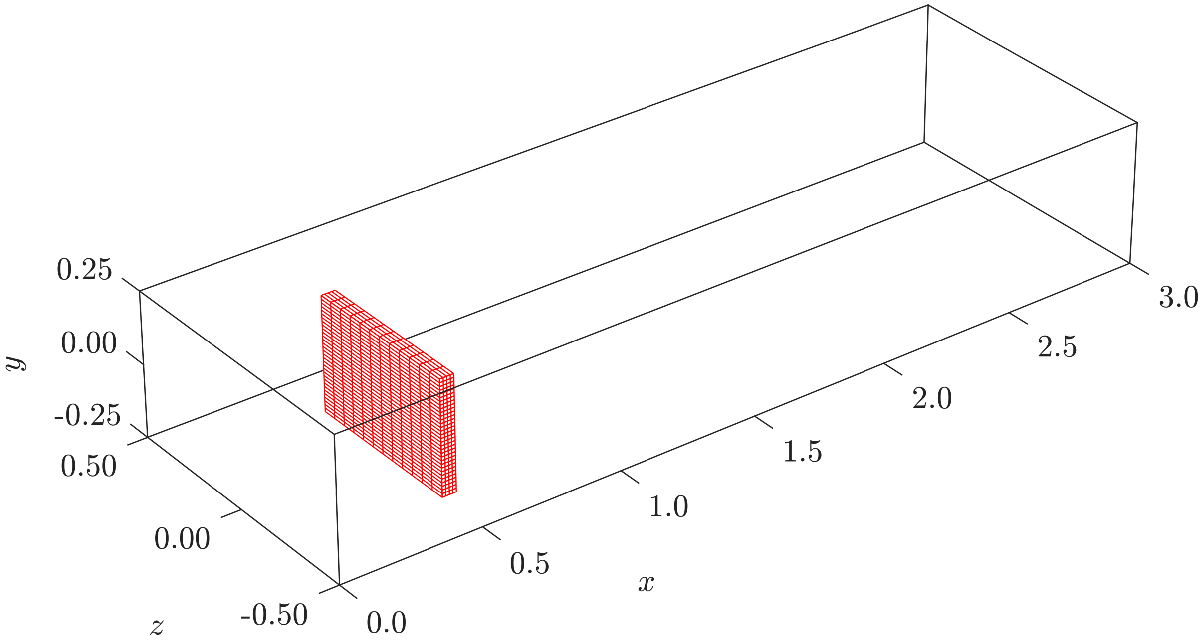

(b) Structural mesh

Figure 5.23: Computational mesh for three-dimensional channel with flexible wall

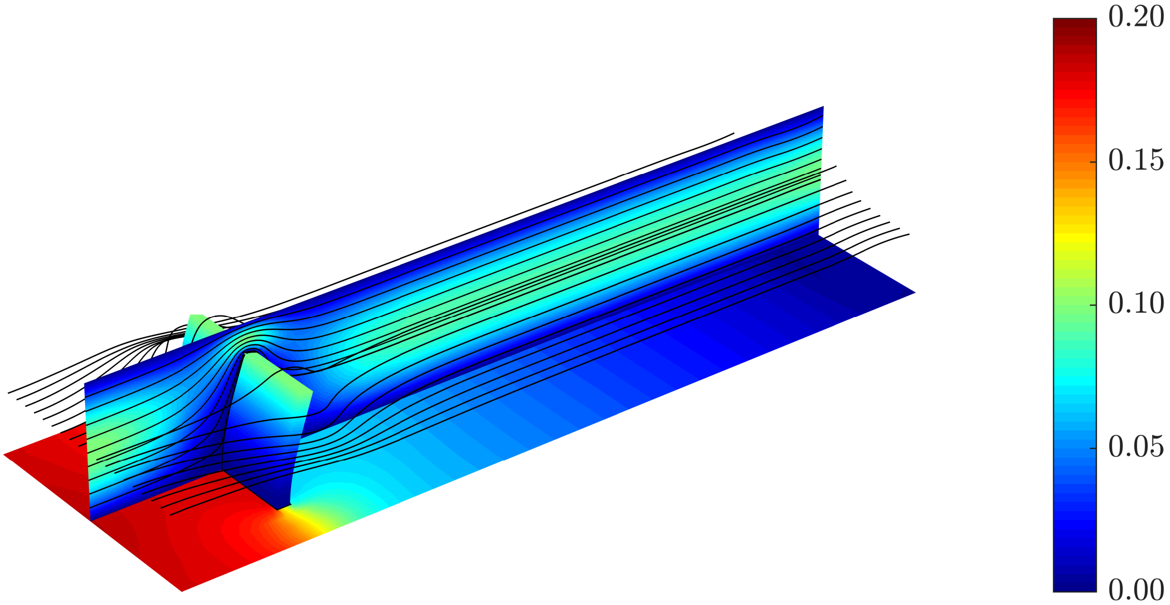

Figure 5.24: Solution of fluid velocity and pressure and structural displacement for three-dimensional channel with flexible wall

The fluid viscosity is $\mu_{\mathcal{F}} = 0.01$ and the reference density $\rho_{\mathcal{F}}^{\mathtt{ref}} = 1$, computed at the reference pressure $p_{\mathcal{F}}^{\mathtt{ref}} = 0$. Three orders of magnitude are considered for the compressibility coefficient, i.e. $\varepsilon_{\mathcal{F}} = [0.001, 0.01, 0.1]$. The structure is then modelled as a Neo-HOOKEan material with YOUNG's modulus $E_{\mathcal{S}} = 500$, POISSON's ratio $\nu_{\mathcal{S}} = 0$ and density $\rho_{\mathcal{S}} = 1$.

The fluid domain contains 25664 hexahedral elements, whereas the structural mesh is subdivided into $4 \times 32 \times 12$ hexahedrons, for a total number of 1536 elements. The fluid mesh is refined on the interface and it matches the structural one and the polynomial degree of approximation is $k = 1$ for both fields. Figure 5.23 depicts the fluid mesh on top and structural mesh on bottom. The time interval is $t \in (0, 10)$ and the integration in time is performed with the BDF2 method. Three different time step sizes are then considered, i.e. $\Delta t = [0.1, 0.01, 0.001]$. Two formulations are compared:

1. incompressible CG-CG partitioned DIRICHLET–NEUMANN coupling,
2. weakly compressible HDG-CG partitioned DIRICHLET–NEUMANN coupling.

It is worth pointing out that the monolithic NITSCHE-based coupling presented in Section 5.3 is implemented in an independent `MATLAB` code limited to two-dimensional geometries and it cannot therefore be applied for the example under analysis. The stabilization parameters are $\tau_\rho = 1/\varepsilon_{\mathcal{F}}$ and $\tau_{\rho v} = 1$ for the HDG subdomain and the tolerance for the coupling iterations is taken as $\eta = 10^{-7}$ for both cases.

The solution at $t = 10$ obtained via the weakly compressible formulation with $\varepsilon_{\mathcal{F}} = 0.01$ and $\Delta t = 0.1$ is exemplarily shown in Figure 5.24. The vertical and bottom planes illustrate the magnitude of the fluid velocity and pressure, respectively, whereas the structure is coloured according to its displacement magnitude. The x-component of the displacement of the structure center-top point (with coordinates $(0.525, 0.15, 0)$) is shown in Figure 5.25. The displacement at the steady-state condition differs from the incompressible and weakly compressible case

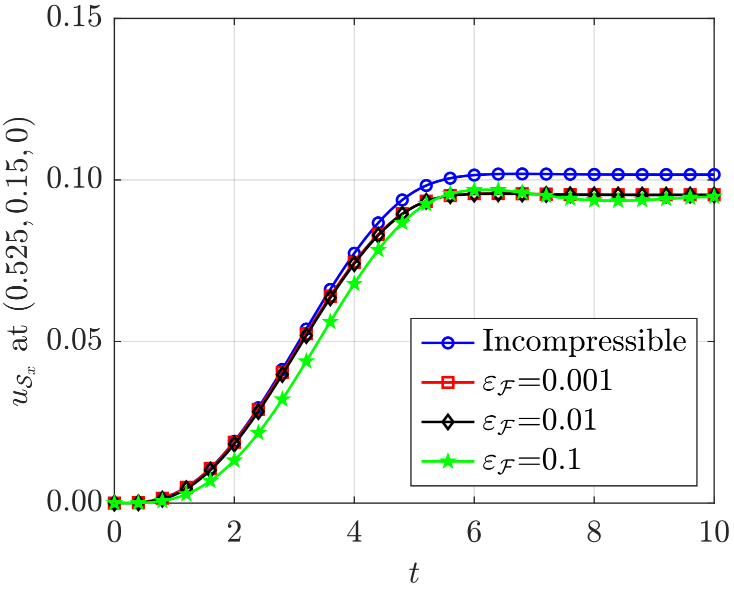

Figure 5.25: Plot of structural displacement for three-dimensional channel with flexible wall

by about 6%. The HDG stabilization parameters are observed to have a non-negligible influence on this gap and their role on the overall quality of the solution of the coupled problem would need further investigation. Finally, Table 5.3 summarizes the average relaxation parameter and the average number of coupling iterations required to meet the convergence criterion. Like the previous numerical example in Section 5.4.3, the incompressible partitioned scheme is able to convergence in a relatively large number of coupling iterations for a large time step size ($\Delta t = 0.1$). However, the incompressible solver fails before reaching the final time of the simulation for smaller time step sizes. On the contrary, the weakly compressible HDG-CG partitioned DIRICHLET–NEUMANN coupling is way more robust and exhibits an enhanced behavior when increasing the compressibility coefficient and decreasing the time step size. In the extreme case, for $\varepsilon_{\mathcal{F}} = 0.1$ and $\Delta t = 0.001$, no relaxation is needed at all since $\omega = 1$ in all steps and almost no coupling iterations are needed to satisfy the convergence criterion.

	$\Delta t = 0.1$		$\Delta t = 0.01$		$\Delta t = 0.001$	
	ω_{avg}	i_{avg}	ω_{avg}	i_{avg}	ω_{avg}	i_{avg}
Incompressible	0.33	10.9	–	–	–	–
$\varepsilon_{\mathcal{F}} = 0.001$	0.37	10.1	0.43	7.7	0.54	2.2
$\varepsilon_{\mathcal{F}} = 0.01$	0.39	8.7	0.57	4.2	0.74	0.8
$\varepsilon_{\mathcal{F}} = 0.1$	0.44	6.2	0.78	2.4	1.00	0.4

Table 5.3: Relaxation parameter and coupling iterations for three-dimensional channel with flexible wall

5.4.5 Micropump

The last numerical example simulates the functioning of a valveless micropump. Micropumps are devices operating at the micrometer level and are able to effectively control small fluid volumes. The interest in the design and development of reliable and efficient micropumps has increased over the last decades because of the potential applications in the industrial and biomedical field. Among many other applications, micropumps can be adopted for the smart drug delivery for the treatment of diabetes, cancer and ocular pathologies in forms of ultra-thin patches, implantable systems or intelligent pills. A comprehensive overview on micropump technologies can be found in the review articles by NGUYEN *et al.* [116], IVERSON and GARIMELLA [84] and AMIROUCHE *et al.* [4]. The specific setting adopted here, is taken from the model developed by HANCOCK *et al.* [71, 72] of *Veryst Engineering* and set up in the simulation software `COMSOL Multiphysics`. The goal of this example is to show the capability of the HDG-CG coupling for FSI to solve problems of actual engineering interest.

The fluid domain $\Omega_{\mathcal{F}}$ consists of a horizontal channel that is $600\ \mu m$ long and $100\ \mu m$ high. At the center of the top side of the channel, a vertical chamber with dimensions $80 \times 100\ \mu m$ is attached. A thickness of $10\ \mu m$ is considered in order to compute the fluid volume pumped over time by the micropump mechanism. However, since no edge effects due to out-of-plane walls are included in the model, this is equivalent to model a thin section of a much thicker channel. The action of an oscillatory piston is simulated by imposing a time-periodic parabolic momentum profile at the inflow on the top of the chamber according to

$$\begin{cases} \rho v^D_{\mathcal{F}x}\left(x, 2{\cdot}10^{-4}, t\right) = 0\ kg/(m^2 \cdot s), \\ \rho v^D_{\mathcal{F}y}\left(x, 2{\cdot}10^{-4}, t\right) = \dfrac{3}{2}\dfrac{\left(x + 4{\cdot}10^{-5}\right)\left(x - 4{\cdot}10^{-5}\right)}{\left(4{\cdot}10^{-5}\right)^2} \sin\left(2\pi t/\bar{t}\right) \rho^{\mathtt{ref}}_{\mathcal{F}} U_{\mathcal{F}}\ kg/(m^2 \cdot s), \end{cases} \tag{5.44}$$

with $\bar{t} = 1\ s$ and $U_{\mathcal{F}} = 0.16\ m/s$, resulting in a REYNOLDS number of 16. The fluid density is imposed equal to its reference value ($\rho^D_{\mathcal{F}} = \rho^{\mathtt{ref}}_{\mathcal{F}}$) on the left and the right sides of the channel, denoted in the following with $\Gamma^{\mathtt{Left}}_{\mathcal{F}}$ and $\Gamma^{\mathtt{Right}}_{\mathcal{F}}$, respectively, whereas no-slip ($\boldsymbol{\rho v}^D_{\mathcal{F}} = \mathbf{0}$) boundary conditions are considered on the remaining fluid walls. The structural domain $\Omega_{\mathcal{S}}$ is then constituted by two bendable microflaps $70\ \mu m$ long and $4\ \mu m$ wide, attached to the channel bottom ($\boldsymbol{u}^D_{\mathcal{S}} = \mathbf{0}$) with a tilt angle of $45°$ and whose center points are located $150\ \mu m$ far from the outflow sides. Both the fluid and the structures are considered at rest at the beginning of the simulation. A sketch of the geometry and the boundary conditions is given in Figure 5.26.

The fluid parameters represent water, characterized by a viscosity of $\mu_{\mathcal{F}} = 0.001\ kg/(m \cdot s)$ and a reference density of $\rho^{\mathtt{ref}}_{\mathcal{F}} = 1000\ kg/m^3$, evaluated at the reference pressure $p^{\mathtt{ref}}_{\mathcal{F}} = 0\ N/m^2$. A compressibility coefficient $\varepsilon_{\mathcal{F}} = 0.01\ s^2/m^2$ in considered to keep the density variation below 0.1%. The structure is made of polydimethylsiloxane (PDMS), a biocompatible polymer widely used for the fabrication of microfluidic devices. Its constitutive behavior can be described by a ST. VENANT–KIRCHHOFF model with YOUNG's modulus $E_{\mathcal{S}} = 3.6 \cdot 10^5\ N/m^2$, POISSON's ratio $\nu_{\mathcal{S}} = 0.499$ and density $\rho_{\mathcal{S}} = 970\ kg/m^3$.

The computational domain counts about 4000 triangular elements in the fluid region and nearly 300 triangular elements in the structural domain. The fluid mesh is refined on the fluid-structure interface and on the corners at the intersection between the horizontal channel and the vertical chamber to properly resolve the flow features in these areas. A polynomial degree

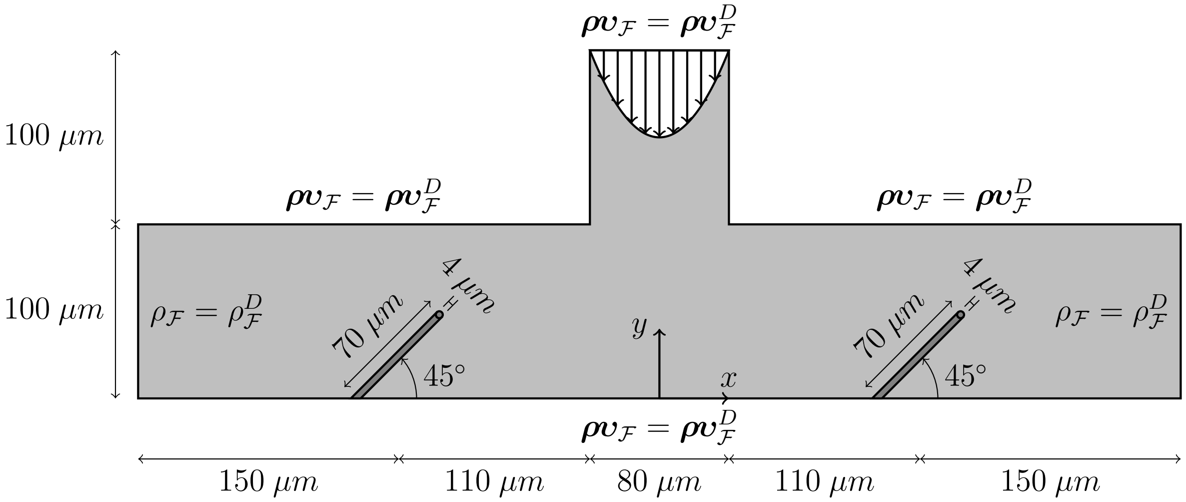

Figure 5.26: Geometry and boundary conditions for micropump

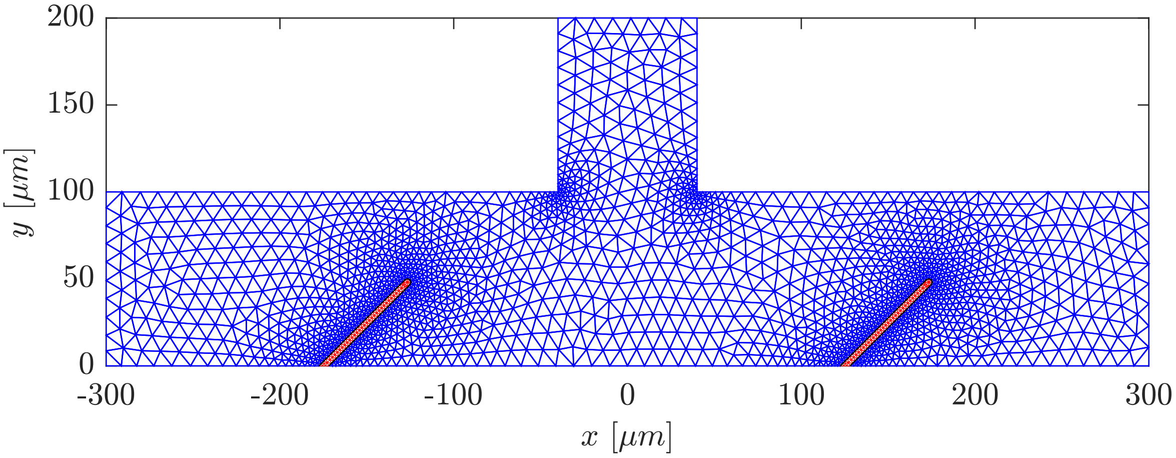

Figure 5.27: Computational mesh for micropump

$k = 3$ is considered in the whole domain. This degree allows to achieve an accurate flow solution without further mesh refinement and it moreover avoids potential locking effects in the nearly incompressible structures. The computational mesh is shown in Figure 5.27 with respect to the initial configuration. A total duration of $2\ s$ is analyzed, i.e. $t \in (0, 2)\ s$, corresponding to two full cycles of the pumping mechanism. The second order BDF2 method is applied for the temporal integration and a time step size $\Delta t = 0.01\ s$ is adopted, to capture the abrupt changes in the flow driven by the interaction with the flexible flaps. The stabilization parameters for the HDG fluid discretization are taken as $\tau_\rho = 100/\varepsilon_{\mathcal{F}}$ and $\tau_{\rho v} = 100$. The previous numerical examples of this chapter have systematically demonstrated how the two proposed formulations for fluid-structure interaction provide identical physical results. Hence, solely the computationally efficient monolithic HDG-CG formulation is here adopted for the simulation of the micropump functioning and the results are compared with those obtained by the creators of the model in `COMSOL`.

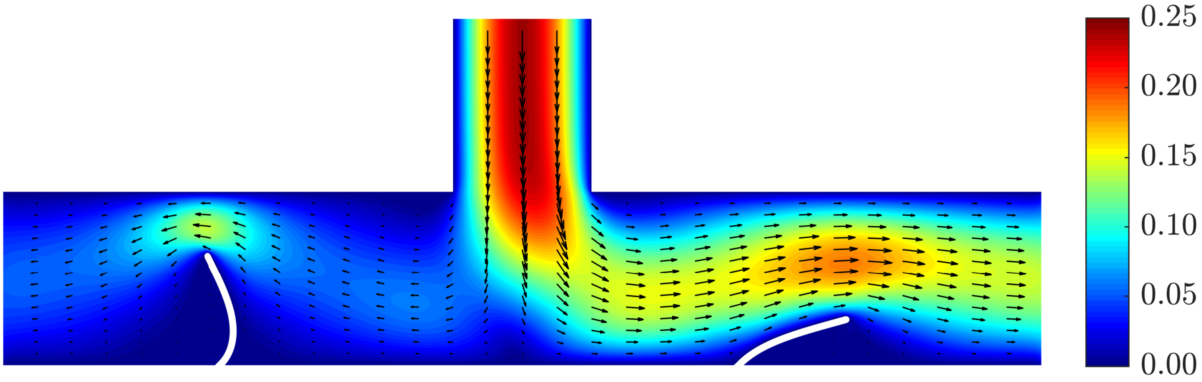

(a) $t = 0.25\ s$

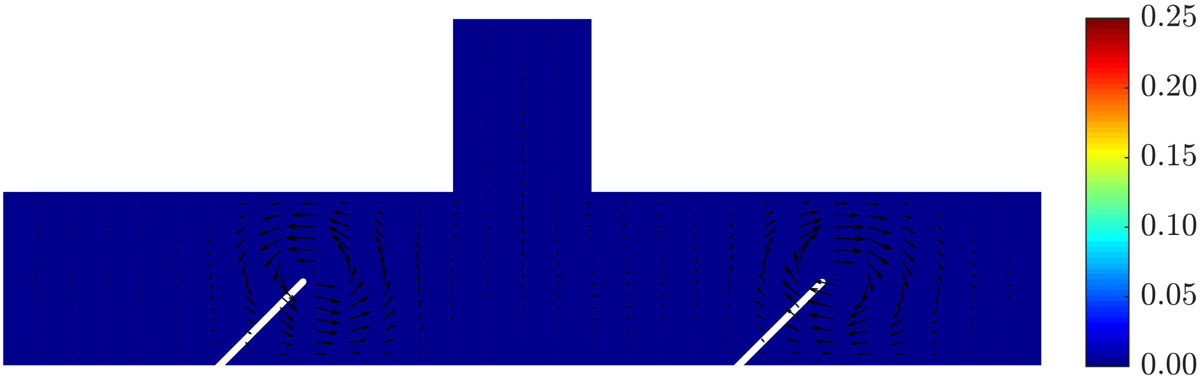

(b) $t = 0.50\ s$

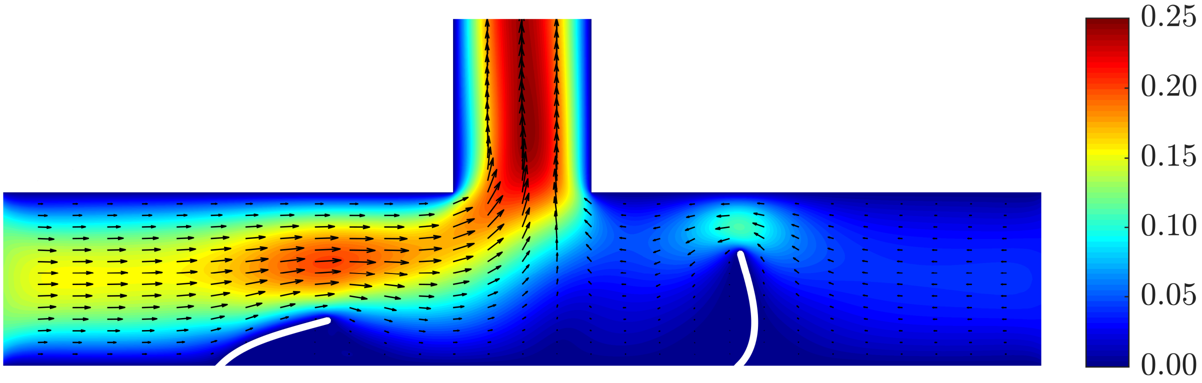

(c) $t = 0.75\ s$

Figure 5.28: Solution of fluid velocity for micropump

(a) $t = 0.25\ s$

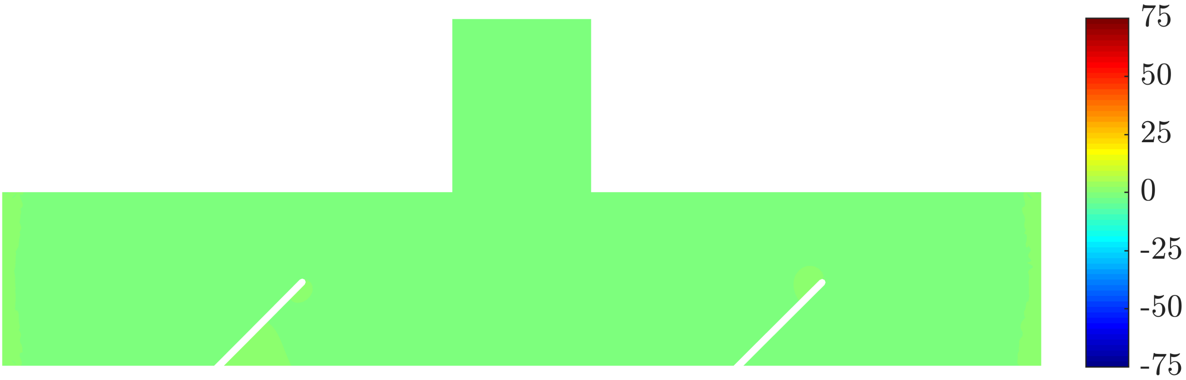

(b) $t = 0.50\ s$

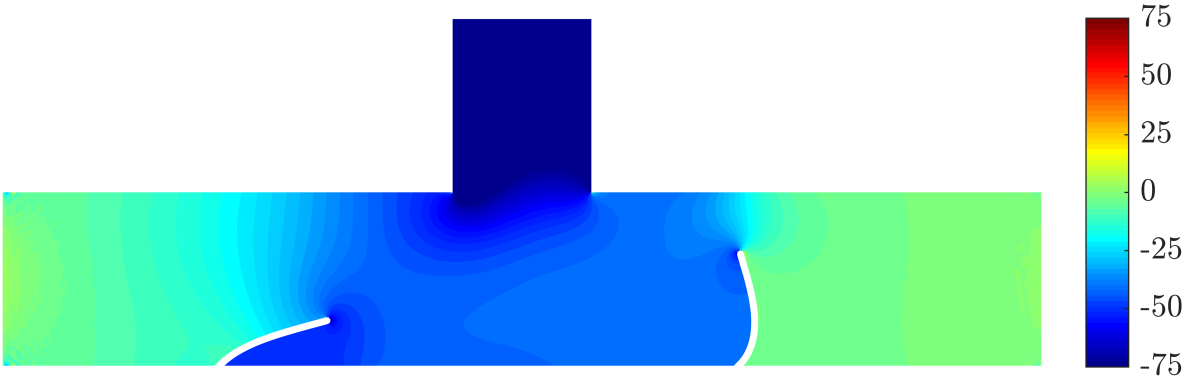

(c) $t = 0.75\ s$

Figure 5.29: Solution of fluid pressure for micropump

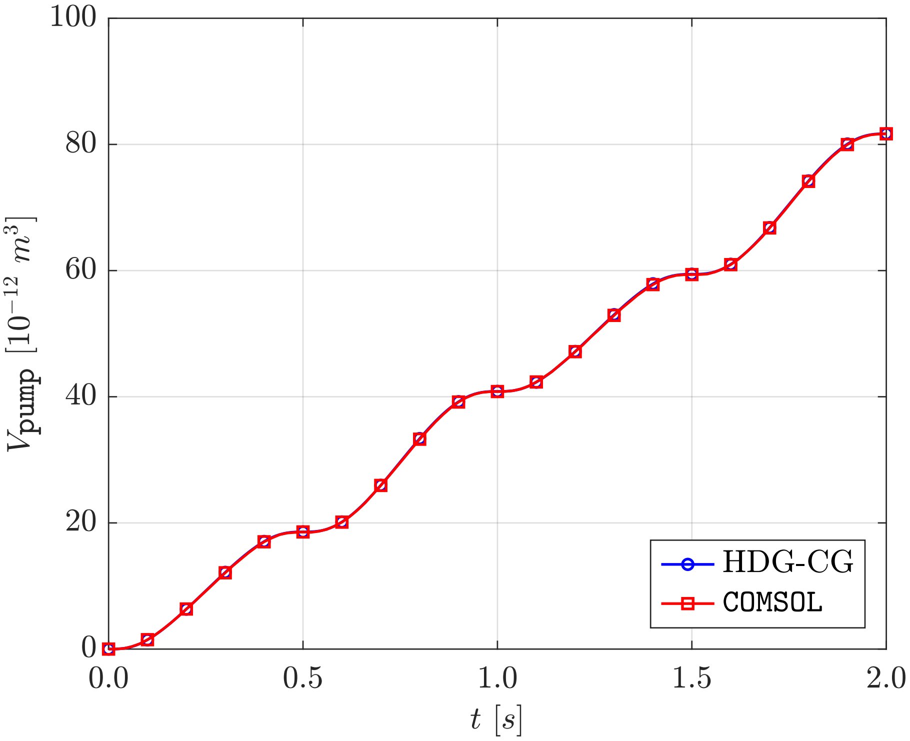

Figure 5.30: Plot of net volume pumped for micropump

Figures 5.28 and 5.29 exemplarily display the fluid velocity and pressure field, respectively, at times $t = [0.25, 0.50, 0.75]$ s, corresponding to $[1/4, 2/4, 3/4]$ of one period of the pumping mechanism. During the downstroke (Figures 5.28(a) and 5.29(a)), the left flap bends backward narrowing the channel and therefore significantly reducing the volume of fluid pumped out of the left boundary, while, on the contrary, the right flap bends forward widening the channel and easing the flow out of the right boundary. At half-cycle (Figures 5.28(b) and 5.29(b)) negligible pressure gradients instead arrest the flow and the structures return approximately to their original configuration. Finally, during the upstroke (Figures 5.28(c) and 5.29(c)), the left flap bends towards to bottom of the channel and the right flap bends towards the top of the channel pushing therefore most of the flow from left to right. As a consequence of the interaction between the fluid and the flexible cilia, a sustained flow is pumped in a consistent direction without the need of complex actuation mechanisms required in valve-based systems. The net volume pumped from left to right as a function of time can be computed by integrating the normal component of the velocity on the outflows and integrating the resulting flow rates in time. The contributions are then summed considering negative and positive signs for the left and right outflows, respectively, according to the formula

$$V_{\texttt{pump}}(t) = -\int_0^t \left(\int_{\Gamma_{\mathcal{F}}^{\texttt{Left}}} \boldsymbol{v}_{\mathcal{F}}(\tau) \cdot \boldsymbol{n}_{\mathcal{F}} d\Gamma \right) d\tau + \int_0^t \left(\int_{\Gamma_{\mathcal{F}}^{\texttt{Right}}} \boldsymbol{v}_{\mathcal{F}}(\tau) \cdot \boldsymbol{n}_{\mathcal{F}} d\Gamma \right) d\tau. \tag{5.45}$$

Figure 5.30 plots the computed net volume pumped that exhibits a consistent increase over time. The HDG-CG formulation for FSI produces accurate physical results that are indistinguishable from the ones provided by *Veryst Engineering* with `COMSOL`, confirming the capability of the proposed method to accurately solve problems of engineering interest.

6 Conclusion

Here, the achievements of this thesis are briefly summarized and an outlook on possible future research is then offered.

6.1 Achievements

In this thesis, novel robust and efficient schemes for the solution of fluid structure interaction problems have been proposed. The key features are the introduction of a weak compressibility in the flow field to alleviate potential instabilities related to the artificial added mass effect and the coupling of the fluid problem, discretized by means of the HDG method, with the structural one, discretized by means of the CG method.

The first part of the thesis has investigated the role of the fluid compressibility on the stability and the performance of FSI solvers in a classical CG framework. The stability is known to be heavily affected by the artificial added mass phenomenon, whose detrimental effect is closely related to the added mass operator. Through a rigorous analytical study, a discrete expression of this operator has been derived, by extending the analysis by FÖRSTER *et al.* [58] to the weakly compressible regime. Fundamental differences have thus been revealed between the incompressible and the weakly compressible regime. More precisely, it has been demonstrated that the instability condition is much more permissive in the weakly compressible model, explaining why artificial added mass effects have been rarely reported in literature for this case, and that, as opposed to incompressible solvers, time step reduction progressively stabilizes the partitioned FSI scheme. Numerical examples on two- and three-dimensional benchmarks confirmed the analytical findings. By means of a strongly-coupled partitioned scheme with either constant or dynamic relaxation, the most significant reduction of the coupling iterations and the consequent computational time has been obtained in the most challenging cases, when $m_{\mathcal{F}}/m_{\mathcal{S}} \approx 1$, and in the time step size limit, when $\Delta t \to 0$.

Two novel HDG formulations have been presented in the third chapter for the solution of weakly compressible flow problems. The first formulation features the velocity and the pressure and their trace representation as primal and hybrid variables, respectively, whereas the second one considers the conserved quantities, i.e. density and momentum. Both strategies adopt a scaled strain rate tensor as mixed variable to obtain a system of first-order equations. The adoption of the VOIGT notation to strongly enforce the symmetry of this tensor introduced by GIACOMINI *et al.* [67] and SEVILLA *et al.* [142] allows the use of an equal-order approximation for all the variables, hence simplifying the mathematical formulation and its computer implementation, and improves the efficiency of the HDG methods, by reducing the stored quantities and the size of the local problems. The convergence properties of the two formulations have been first assessed in a two-dimensional weakly compressible POISEUILLE flow, equipped with an analytical solution. This study has demonstrated the optimal convergence with order

$k+1$ of the mixed and the primal variables and the superconvergence with order $k+2$ for the postprocessed velocity field, as well as the robustness with respect to the compressibility level. While the velocity-pressure formulation has been restricted to steady and non-convective flows, the density-momentum counterpart has been formulated for unsteady and convective flows on deforming domains, to be then embedded in FSI codes. The convergence features of the latter formulation have been confirmed in a three-dimensional weakly compressible TAYLOR–COUETTE flow and in a problem with manufactured solution on a moving mesh.

The coupling of HDG and CG discretizations has been the focus of the fourth chapter of this thesis. The local-global coupling proposed by PAIPURI *et al.* [127] and the newly developed NITSCHE-based coupling have been first formulated and compared for the solution of the simple POISSON equation. Although both approaches have been demonstrated to provide the same level of accuracy with practically indistinguishable results, the discrete version of the associated weak forms has highlighted important differences. More precisely, the exploitation of the numerical flux and the trace of the solution on the mesh faces allows the NITSCHE-based coupling to enforce the transmission conditions solely in the global problem, hence preserving the core structure of the HDG and CG matrices. As a consequence, the proposed strategy leads to a minimally-intrusive coupling, suitable to be integrated in existing finite element libraries, and provides a flexible framework for the treatment of nonconforming meshes and nonuniform polynomial approximations. The latter aspect has been addressed in this thesis. The efficient NITSCHE-based coupling has been formulated for the solution of linear elastic problems featuring multiple materials with compressible and nearly incompressible behaviors. The adoption of the computationally efficient CG method on the compressible portion of the domain and the discretization of the nearly incompressible region by means of the HDG method has been shown to provide reliable and locking-free results with a relatively small number of globally coupled degrees of freedom, in both two and three dimensions. The numerical examples have demonstrated the possibility to obtain global optimal convergence of the stress with order $k+1$ and superconvergence of the displacement field with order $k+2$, if the polynomial degree in the CG discretization is chosen one degree higher than in the HDG one.

The first HDG-CG formulations for the solution of fluid-structure interaction problems have been presented in the last part of the thesis. Such formulations exploit the findings and the achievements of the previous chapters and build upon the algorithms developed therein. In particular, the partitioned DIRICHLET–NEUMANN scheme outlined by KÜTTLER and WALL [91] and adopted in the first part of the thesis in the context of standard FEM has been revisited to deal with the hybrid HDG-CG discretization. The local-global coupling analyzed in the previous chapter has been adopted in a staggered fashion, hence circumventing the intrusive nature of this approach. Moreover, a monolithic NITSCHE-based scheme has been proposed by exploiting the HDG-CG NITSCHE-based coupling to solely impose the coupling conditions in the global problem. The rigorous procedure proposed by ÉTIENNE *et al.* [48] has been used to derive a manufactured solution for the full FSI problem on a two-dimensional setting. The theoretical convergence rates have been verified on this artificial problem with respect to both the spatial and the temporal convergence. An extensive set of two- and three-dimensional problems have highlighted the high-order accuracy of the hybrid formulations and their enhanced robustness and efficiency compared to incompressible solvers, as well as their capability to solve problems of engineering interest.

6.2 Future work

Several aspects not addressed in this thesis could constitute the basis for future research. First, the NITSCHE-based strategy developed for the coupling of HDG and CG discretizations could be employed for handling non-matching meshes at the interface. Several works indeed show NITSCHE-related methodologies for the imposition of the interface conditions in fluid-structure interaction problems with nonconforming meshes, as in HANSBO and HERMANSSON [74], BURMAN and FERNÁNDEZ [22] and AGER *et al.* [1], among others. The extension of the proposed strategy to deal with non-matching meshes should be a straightforward task and it should mostly involve code development, rather than mathematical derivation. A successful implementation would allow a flexible and independent mesh generation for the fluid and the structural domains.

A second important aspect worth exploring is the adoption of the penalty-free non-symmetric NITSCHE method introduced by BURMAN [20] for the weak imposition of boundary conditions in convection-diffusion problems. On the one hand, this variant gets rid of the penalty parameter γ, whose evaluation is strongly problem-dependent and which might negatively affect the condition number of the resulting linear system. This feature would be of special interest for embedding the HDG-CG formulation in commercial finite element codes, in which the presence of user-provided parameters is undesired. On other hand, this penalty-free version of NITSCHE's method destroys the potential symmetry of the problem and it has been proven to be suboptimal by half an order. Therefore, the proposed NITSCHE-based coupling remains very competitive for the solution of the thermal and linear elastic problems considered in Chapter 4, owing to the symmetry of the underlying formulations which allows the use of efficient and specialized solvers for symmetric matrices. However, different considerations hold for the fluid-structure interaction problems considered in Chapter 5. For this class of problems the resulting linear system is in fact non-symmetric anyway because of the flow convection and compressibility and because of the large structural displacement and the flexibility offered by the absence of the penalty parameter could pay off the expected partial loss of accuracy.

Another topic worth investigating concerns the loss of the superconvergence of the postprocessed fluid velocity, experienced in the FSI problem with manufactured solution presented in Chapter 5. In fact, although the proposed NITSCHE-based coupling preserves the postprocessing procedure described in Chapter 3 for pure flow problems, the procedure fails to provide an improved approximation of the solution in the aforementioned numerical example. At the moment it is not clear whether this loss of superconvergence is ascribable to the deformation of the fluid domain according to the ALE description of motion or to the interaction with the structural field (or to a combination of both), although the postprocessing procedure is formally independent of these features.

A strategy that could provide a more accurate solution for a given computational effort or a faster computation for a given level of accuracy would be the implementation of a degree adaptivity procedure for the HDG discretization, as the one first proposed by GIORGIANI *et al.* [68, 69]. Such a technique uses the mismatch between the solution and the postprocessed counterpart as an a posteriori error estimator to drive an efficient local modification of the polynomial degree of approximation in the elements and the faces to obtain a uniform error distribution below a desired tolerance. A degree adaptivity would be particularly relevant in the context of fluid-structure interaction problems, for which much finer meshes are usually constructed near the structural interface to capture the relevant flow features. However, without a superconvergent solution this technique would fail in its objective and new estimators would need to be developed. The previously discussed superconvergence loss would alternatively need to be addressed before this strategy can be successfully employed.

Finally, an optimized implementation of the HDG-CG formulations for FSI could be developed, which would enable a fair comparison in terms of computational efficiency between the proposed schemes and the ones based on standard finite element discretizations. This comparison could be useful to understand under which circumstances and at which point high-order HDG methods can outperform classical CG methods.

A Finite element spaces

In this appendix, the discrete finite element spaces adopted in all the formulations are defined. The computational domain is denoted with Ω, while each finite element is indicated with Ω^e. Then, $\partial\Omega$ and Γ represent the boundary of the domain and the internal interface, respectively, Σ refers to the mesh skeleton, whereas each element edge/face is identified with Σ^f. Moreover, $\mathcal{P}^p$ denotes the space of polynomial functions of complete degree at most p, whereas $\mathcal{L}^l$ and $\mathcal{H}^h$ indicate the LEBESGUE and SOBOLEV spaces of order l and h, respectively. The finite element spaces associated to the HDG and CG discretizations are presented in the following.

A.1 HDG spaces

Each component of the mixed and the primal variables is sought in the space

$$\mathcal{W}^h(\Omega) = \left\{ w \in \mathcal{L}^2\left(\Omega\right) : w|_{\Omega^e} \in \mathcal{P}^k\left(\Omega^e\right) \forall \Omega^e \subset \Omega \right\},$$

whereas the hybrid variables belong to the space

$$\widehat{\mathcal{W}}^h(\Sigma) = \left\{ \hat{w} \in \mathcal{L}^2\left(\Sigma\right) : \hat{w}|_{\Sigma^f} \in \mathcal{P}^k\left(\Sigma^f\right) \forall \Sigma^f \subset \Sigma \subseteq \Gamma \cup \partial\Omega \right\}.$$

The postprocessed variables are then sought in the richer space

$$\mathcal{W}^h_\star(\Omega) = \left\{ w^\star \in \mathcal{L}^2\left(\Omega\right) : w^\star|_{\Omega^e} \in \mathcal{P}^{k+1}\left(\Omega^e\right) \forall \Omega^e \subset \Omega \right\},$$

while the following space is used to remove the underdetermination of the postprocessing

$$\mathcal{U}^h(\Omega) = \left\{ u \in \mathcal{L}^2\left(\Omega\right) : u|_{\Omega^e} \in \mathcal{P}^0\left(\Omega^e\right) \forall \Omega^e \subset \Omega \right\}.$$

Owing to the weak imposition of all boundary conditions, no distinction is made between the spaces of trial and test functions.

A.2 CG spaces

Each component of the solution variables is sought in the space

$$\mathcal{V}^h(\Omega) = \left\{ v \in \mathcal{H}^1\left(\Omega\right) : v|_{\Omega^e} \in \mathcal{P}^k\left(\Omega^e\right) \forall \Omega^e \subset \Omega,\ v|_{\Gamma^D} = v^D \right\},$$

with v^D denoting the boundary data imposed on the DIRICHLET portion of the boundary Γ^D. The test functions belong instead to space

$$\mathcal{V}^h_0(\Omega) = \left\{ v \in \mathcal{H}^1\left(\Omega\right) : v|_{\Omega^e} \in \mathcal{P}^k\left(\Omega^e\right) \forall \Omega^e \subset \Omega,\ v|_{\Gamma^D} = 0 \right\}.$$

Clearly, the two spaces coincide for the homogeneous boundary condition $v^D = 0$.

B Temporal discretization

While special effort has been devoted to the development of innovative spatial discretization strategies, the temporal discretization is performed in this thesis by means of standard and well-established techniques. More precisely, the BDF schemes are chosen for the approximation of the time derivatives appearing in all the formulations presented. Such implicit schemes belong to the family of linear multistep methods and they use information from previous time steps to compute a finite difference of the target function, with potential high-order accuracy. On the one hand, BDF solvers are relatively easy to implement, possess good stability properties and are often adopted for the solution of stiff differential equations. On the other hand, low-order BDF methods can produce severe damping effects. The formulas and the associated parameters needed for the approximation of first and second time derivatives are presented in the following.

B.1 BDF for first derivatives

The first temporal derivative of a function $\boldsymbol{u}$ at the time step $n+1$ can be approximated as

$$\frac{\partial \boldsymbol{u}^{n+1}}{\partial t} \approx \sum_{b=0}^{\mathrm{BDF}o} \frac{\alpha_b}{\Delta t} \boldsymbol{u}^{n+1-b}.$$

The coefficients α are reported in the following table for orders BDFo ranging from 1 to 6

	α_0	α_1	α_2	α_3	α_4	α_5	α_6
BDF1	1	-1	–	–	–	–	–
BDF2	$\frac{3}{2}$	-2	$\frac{1}{2}$	–	–	–	–
BDF3	$\frac{11}{6}$	-3	$\frac{3}{2}$	$-\frac{1}{3}$	–	–	–
BDF4	$\frac{25}{12}$	-4	3	$-\frac{4}{3}$	$\frac{1}{4}$	–	–
BDF5	$\frac{137}{60}$	-5	5	$-\frac{10}{3}$	$\frac{5}{4}$	$-\frac{1}{5}$	–
BDF6	$\frac{49}{20}$	-6	$\frac{15}{2}$	$-\frac{20}{3}$	$\frac{15}{4}$	$-\frac{6}{5}$	$\frac{1}{6}$

Table B.1: BDF coefficients for first derivatives

B.2 BDF for second derivatives

The second temporal derivative of a function $\boldsymbol{u}$ at the time step $n+1$ can be approximated as

$$\frac{\partial^2 \boldsymbol{u}^{n+1}}{\partial t^2} \approx \sum_{b=0}^{\mathrm{BDF}o+1} \frac{\beta_b}{\Delta t^2} \boldsymbol{u}^{n+1-b}.$$

The coefficients β are reported in the following table for orders BDFo ranging from 1 to 6

	β_0	β_1	β_2	β_3	β_4	β_5	β_6	β_7
BDF1	1	-2	1	–	–	–	–	–
BDF2	2	-5	4	-1	–	–	–	–
BDF3	$\frac{35}{12}$	$-\frac{26}{3}$	$\frac{19}{2}$	$-\frac{14}{3}$	$\frac{11}{12}$	–	–	–
BDF4	$\frac{15}{4}$	$-\frac{77}{6}$	$\frac{107}{6}$	-13	$\frac{61}{12}$	$-\frac{5}{6}$	–	–
BDF5	$\frac{203}{45}$	$-\frac{87}{5}$	$\frac{117}{4}$	$-\frac{254}{9}$	$\frac{33}{2}$	$-\frac{27}{5}$	$\frac{137}{180}$	–
BDF6	$\frac{469}{90}$	$-\frac{223}{10}$	$\frac{879}{20}$	$-\frac{949}{18}$	41	$-\frac{201}{10}$	$\frac{1019}{180}$	$-\frac{7}{10}$

Table B.2: BDF coefficients for second derivatives

C Definition of elemental matrices and vectors

In this appendix, the elemental matrices and vectors arising from the HDG and CG formulations are detailed. A generic variable $\left[\boldsymbol{u}\right]_e$ and its trace representation $\left[\hat{\boldsymbol{u}}\right]_e$ can be approximated over each element Ω^e and over each face of the element boundary $\partial\Omega^e$, respectively, as

$$\left[\boldsymbol{u}\left(\boldsymbol{\xi}\right)\right]_e = \left[\boldsymbol{\psi}\right]\left[\mathbf{u}\right]_e, \qquad \left[\hat{\boldsymbol{u}}\left(\widehat{\boldsymbol{\xi}}\right)\right]_e = \left[\widehat{\boldsymbol{\psi}}\right]\left[\hat{\mathbf{u}}\right]_e,$$

with $\boldsymbol{\xi}$ and $\widehat{\boldsymbol{\xi}}$ being the coordinates of the quadrature points in the reference element and face, respectively, whereas $\left[\mathbf{u}\right]_e$ and $\left[\hat{\mathbf{u}}\right]_e$ denote the elemental nodal column vectors. The variables appearing in the computation of the elemental matrices and vectors are computed on the integration points and the explicit dependence on $\boldsymbol{\xi}$ and $\widehat{\boldsymbol{\xi}}$ will be henceforth omitted for the sake of readability. Then, the matrices $\left[\boldsymbol{\psi}\right]$ and $\left[\widehat{\boldsymbol{\psi}}\right]$ gather the polynomial shape functions associated to each element/face node computed on each element/face integration point and they are built as

$$\left[\boldsymbol{\psi}\right] = \begin{bmatrix} \psi_{1,1} & \dots & \psi_{1,\mathtt{n}^{\mathtt{en}}} \\ \vdots & \ddots & \vdots \\ \psi_{\mathtt{n}^{\mathtt{eq}},1} & \dots & \psi_{\mathtt{n}^{\mathtt{eq}},\mathtt{n}^{\mathtt{en}}} \end{bmatrix}, \qquad \left[\widehat{\boldsymbol{\psi}}\right] = \begin{bmatrix} \widehat{\psi}_{1,1} & \dots & \widehat{\psi}_{1,\mathtt{n}^{\mathtt{fn}}} \\ \vdots & \ddots & \vdots \\ \widehat{\psi}_{\mathtt{n}^{\mathtt{fq}},1} & \dots & \widehat{\psi}_{\mathtt{n}^{\mathtt{fq}},\mathtt{n}^{\mathtt{fn}}} \end{bmatrix},$$

with $\mathtt{n}^{\mathtt{en}}$ and $\mathtt{n}^{\mathtt{fn}}$ denoting the number of element/face nodes and $\mathtt{n}^{\mathtt{eq}}$ and $\mathtt{n}^{\mathtt{fq}}$ being the number of element/face quadrature points. The matrix gathering the derivatives of the shape functions is then represented as

$$\left[\boldsymbol{\nabla}\left\{\mathtt{i}\right\}\boldsymbol{\psi}\right] = \begin{bmatrix} \partial_{\boldsymbol{x}\{\mathtt{i}\}}\psi_{1,1} & \dots & \partial_{\boldsymbol{x}\{\mathtt{i}\}}\psi_{1,\mathtt{n}^{\mathtt{en}}} \\ \vdots & \ddots & \vdots \\ \partial_{\boldsymbol{x}\{\mathtt{i}\}}\psi_{\mathtt{n}^{\mathtt{eq}},1} & \dots & \partial_{\boldsymbol{x}\{\mathtt{i}\}}\psi_{\mathtt{n}^{\mathtt{eq}},\mathtt{n}^{\mathtt{en}}} \end{bmatrix}.$$

The indices $\mathtt{i} = 1, 2, 3$ return the derivatives of the shape functions with respect to x, y, z, respectively. Similarly, the matrix $\left[\boldsymbol{\nabla}_{\mathtt{S}}^{T}\left\{i, j\right\}\boldsymbol{\psi}\right]$ provides the derivatives of the shape functions with the respect to the spatial coordinates, following the VOIGT notation ordering in Section 3.2. The notation $\{\mathtt{i}, \mathtt{j}\}$ and $\{\mathtt{i}\}$ is adopted in this section to extract a specific block of a generic matrix $\left[\mathbf{K}\right]$ and vector $\left[\mathbf{f}\right]$, respectively, as

$$\left[\mathbf{K}\right] = \begin{bmatrix} & \vdots & \\ \dots & \left[\mathbf{K}\left\{\mathtt{i}, \mathtt{j}\right\}\right] & \dots \\ & \vdots & \end{bmatrix}, \qquad \left[\mathbf{f}\right] = \begin{bmatrix} \vdots \\ \left[\mathbf{f}\left\{\mathtt{i}\right\}\right] \\ \vdots \end{bmatrix}.$$

Moreover, the KRONECKER delta $\delta_{\mathtt{i},\mathtt{j}}$ is used to access the diagonal blocks of a matrix. Finally, in the following definitions, the indices $\mathtt{d}, \mathtt{e}, \mathtt{f}, \mathtt{g}, \mathtt{h}$ span the values $1, \dots, \mathtt{n}_{\mathtt{sd}}$, whereas the indices $\mathtt{m}, \mathtt{n}$ span the values $1, \dots, \mathtt{m}_{\mathtt{sd}}$.

C.1 HDG formulations for weakly compressible flows

In this section, the elemental matrices and vectors appearing in the discrete form of the HDG formulations for weakly compressible flows in Chapter 3 are defined.

C.1.1 Velocity-pressure formulation

Here, the elemental contributions for the construction of the matrices and vectors in problems (3.30) and (3.31) are listed. It is worth reminding that in this formulation the density is computed as a function of the pressure level, i.e. $\rho = \rho(p)$, according to the equation of state (3.2). Alternative and more sophisticated relationships may be considered and hence this equation is not made explicit in the following definitions for the sake of generality. Analogously, the derivative of the density with respect to the pressure simply stems from the compressibility coefficient, i.e. $\partial\rho(p)/\partial p = \varepsilon$, but this coefficient is not explicitly written to easily accommodate potentially nonlinear equations of state. Only the steady-state problem in Section 3.5.1 is solved by means of this formulation. However, the intrinsic nonlinearity of the weakly compressible formulation requires the updating of the left and right hand sides of the discrete problem in every NEWTON iteration, denoted with the index j. The definition of the matrices and the vectors then reads

$$
\begin{aligned}
\left[\mathbf{K}_{LL}\{\mathtt{m},\mathtt{n}\}\right]_e^j &= -\,\delta_{\mathtt{m},\mathtt{n}}\left(\boldsymbol{\psi}^T,\boldsymbol{\psi}\right)_{\Omega^e}\\
\left[\mathbf{K}_{Lv}\{\mathtt{m},\mathtt{d}\}\right]_e^j &= +\sum_{\mathtt{n}=1}^{\mathtt{m_{sd}}}\left(\left(\boldsymbol{\nabla}_{\mathtt{S}}^T\{\mathtt{d},\mathtt{n}\}\,\mathbf{D}^{1/2}\{\mathtt{n},\mathtt{m}\}\,\boldsymbol{\psi}\right)^T,\boldsymbol{\psi}\right)_{\Omega^e}\\
\left[\mathbf{K}_{L\hat{v}}\{\mathtt{m},\mathtt{d}\}\right]_e^j &= -\sum_{\mathtt{n}=1}^{\mathtt{m_{sd}}}\left\langle\left(\mathbf{N}^T\{\mathtt{d},\mathtt{n}\}\,\mathbf{D}^{1/2}\{\mathtt{n},\mathtt{m}\}\,\boldsymbol{\psi}\right)^T,\widehat{\boldsymbol{\psi}}\right\rangle_{\partial\Omega^e\setminus\Gamma^D}\\
\left[\mathbf{K}_{vL}\{\mathtt{d},\mathtt{m}\}\right]_e^j &= +\sum_{\mathtt{n}=1}^{\mathtt{m_{sd}}}\left(\boldsymbol{\psi}^T,\boldsymbol{\nabla}_{\mathtt{S}}^T\{\mathtt{d},\mathtt{n}\}\,\mathbf{D}^{1/2}\{\mathtt{n},\mathtt{m}\}\,\boldsymbol{\psi}\right)_{\Omega^e}\\
\left[\mathbf{K}_{vv}\{\mathtt{d},\mathtt{e}\}\right]_e^j &= +\,\delta_{\mathtt{d},\mathtt{e}}\left\langle\boldsymbol{\psi}^T,\tau_v\boldsymbol{\psi}\right\rangle_{\partial\Omega^e}\\
\left[\mathbf{K}_{vp}\{\mathtt{d},1\}\right]_e^j &= +\left(\boldsymbol{\psi}^T,\boldsymbol{\nabla}\{\mathtt{d}\}\,\boldsymbol{\psi}\right)_{\Omega^e}\\
&\quad -\left(\boldsymbol{\psi}^T,\left.\frac{\partial\rho(p)}{\partial p}\right|_{p^j}\boldsymbol{b}\{\mathtt{d}\}\,\boldsymbol{\psi}\right)_{\Omega^e}\\
\left[\mathbf{K}_{v\hat{v}}\{\mathtt{d},\mathtt{e}\}\right]_e^j &= -\,\delta_{\mathtt{d},\mathtt{e}}\left\langle\boldsymbol{\psi}^T,\tau_v\widehat{\boldsymbol{\psi}}\right\rangle_{\partial\Omega^e\setminus\Gamma^D}\\
\left[\mathbf{K}_{pv}\{1,\mathtt{d}\}\right]_e^j &= -\left(\left(\boldsymbol{\nabla}\{\mathtt{d}\}\,\boldsymbol{\psi}\right)^T,\rho\left(p^j\right)\boldsymbol{\psi}\right)_{\Omega^e}\\
\left[\mathbf{K}_{pp}\{1,1\}\right]_e^j &= -\sum_{\mathtt{d}=1}^{\mathtt{n_{sd}}}\left(\left(\boldsymbol{\nabla}\{\mathtt{d}\}\,\boldsymbol{\psi}\right)^T,\left.\frac{\partial\rho(p)}{\partial p}\right|_{p^j}\boldsymbol{v}^j\{\mathtt{d}\}\,\boldsymbol{\psi}\right)_{\Omega^e}\\
&\quad +\left\langle\boldsymbol{\psi}^T,\tau_p\boldsymbol{\psi}\right\rangle_{\partial\Omega^e}\\
\left[\mathbf{K}_{p\hat{v}}\{1,\mathtt{d}\}\right]_e^j &= +\left\langle\boldsymbol{\psi}^T,\rho\left(\hat{p}^j\right)\boldsymbol{n}\{\mathtt{d}\}\,\widehat{\boldsymbol{\psi}}\right\rangle_{\partial\Omega^e\setminus\Gamma^D}
\end{aligned}
$$

$$\begin{aligned}
\big[\mathbf{K}_{p\hat{p}}\left\{1,1\right\}\big]_e^j &= + \sum_{\mathtt{d}=1}^{\mathtt{n}_{\mathtt{sd}}} \left\langle \boldsymbol{\psi}^T, \left.\frac{\partial\rho\left(\hat{p}\right)}{\partial\hat{p}}\right|_{\hat{p}^j} \hat{\boldsymbol{v}}^j\left\{\mathtt{d}\right\} \boldsymbol{n}\left\{\mathtt{d}\right\} \widehat{\boldsymbol{\psi}} \right\rangle_{\partial\Omega^e\setminus\Gamma^D} \\
&\quad - \left\langle \boldsymbol{\psi}^T, \tau_p \widehat{\boldsymbol{\psi}} \right\rangle_{\partial\Omega^e\setminus\Gamma^D} \\
\big[\mathbf{K}_{\hat{v}L}\left\{\mathtt{d},\mathtt{m}\right\}\big]_e^j &= - \sum_{\mathtt{n}=1}^{\mathtt{m}_{\mathtt{sd}}} \left\langle \widehat{\boldsymbol{\psi}}^T, \mathbf{N}^T\left\{\mathtt{d},\mathtt{n}\right\} \mathbf{D}^{1/2}\left\{\mathtt{n},\mathtt{m}\right\} \boldsymbol{\psi} \right\rangle_{\partial\Omega^e\setminus\Gamma^D} \\
\big[\mathbf{K}_{\hat{v}v}\left\{\mathtt{d},\mathtt{e}\right\}\big]_e^j &= - \,\delta_{\mathtt{d},\mathtt{e}} \left\langle \widehat{\boldsymbol{\psi}}^T, \tau_v \boldsymbol{\psi} \right\rangle_{\partial\Omega^e\setminus\Gamma^D} \\
\big[\mathbf{K}_{\hat{v}\hat{v}}\left\{\mathtt{d},\mathtt{e}\right\}\big]_e^j &= + \,\delta_{\mathtt{d},\mathtt{e}} \left\langle \widehat{\boldsymbol{\psi}}^T, \tau_v \widehat{\boldsymbol{\psi}} \right\rangle_{\partial\Omega^e\setminus\Gamma^D} \\
\big[\mathbf{K}_{\hat{v}\hat{p}}\left\{\mathtt{d},1\right\}\big]_e^j &= - \left\langle \widehat{\boldsymbol{\psi}}^T, \boldsymbol{n}\left\{\mathtt{d}\right\} \widehat{\boldsymbol{\psi}} \right\rangle_{\partial\Omega^e\setminus\Gamma^D} \\
\big[\mathbf{K}_{\hat{p}p}\left\{1,1\right\}\big]_e^j &= + \left\langle \widehat{\boldsymbol{\psi}}^T, \tau_p \boldsymbol{\psi} \right\rangle_{\partial\Omega^e\setminus\Gamma^D} \\
\big[\mathbf{K}_{\hat{p}\hat{p}}\left\{1,1\right\}\big]_e^j &= - \left\langle \widehat{\boldsymbol{\psi}}^T, \tau_p \widehat{\boldsymbol{\psi}} \right\rangle_{\partial\Omega^e\setminus\Gamma^D}
\end{aligned}$$

$$\begin{aligned}
\big[\mathbf{f}_L\left\{\mathtt{m}\right\}\big]_e^j = &+ \left(\boldsymbol{\psi}^T, \boldsymbol{L}^j\left\{\mathtt{m}\right\}\right)_{\Omega^e} \\
&- \sum_{\mathtt{d}=1}^{\mathtt{n}_{\mathtt{sd}}} \sum_{\mathtt{n}=1}^{\mathtt{m}_{\mathtt{sd}}} \Big(\left(\boldsymbol{\nabla}_{\mathtt{S}}^T\left\{\mathtt{d},\mathtt{n}\right\} \mathbf{D}^{1/2}\left\{\mathtt{n},\mathtt{m}\right\} \boldsymbol{\psi}\right)^T, \boldsymbol{v}^j\left\{\mathtt{d}\right\} \Big)_{\Omega^e} \\
&+ \sum_{\mathtt{d}=1}^{\mathtt{n}_{\mathtt{sd}}} \sum_{\mathtt{n}=1}^{\mathtt{m}_{\mathtt{sd}}} \Big\langle \left(\mathbf{N}^T\left\{\mathtt{d},\mathtt{n}\right\} \mathbf{D}^{1/2}\left\{\mathtt{n},\mathtt{m}\right\} \boldsymbol{\psi}\right)^T, \boldsymbol{v}^D\left\{\mathtt{d}\right\} \Big\rangle_{\partial\Omega^e\cap\Gamma^D} \\
&+ \sum_{\mathtt{d}=1}^{\mathtt{n}_{\mathtt{sd}}} \sum_{\mathtt{n}=1}^{\mathtt{m}_{\mathtt{sd}}} \Big\langle \left(\mathbf{N}^T\left\{\mathtt{d},\mathtt{n}\right\} \mathbf{D}^{1/2}\left\{\mathtt{n},\mathtt{m}\right\} \boldsymbol{\psi}\right)^T, \hat{\boldsymbol{v}}^j\left\{\mathtt{d}\right\} \Big\rangle_{\partial\Omega^e\setminus\Gamma^D} \\
\big[\mathbf{f}_v\left\{\mathtt{d}\right\}\big]_e^j = &- \sum_{\mathtt{m}=1}^{\mathtt{m}_{\mathtt{sd}}} \sum_{\mathtt{n}=1}^{\mathtt{m}_{\mathtt{sd}}} \left(\boldsymbol{\psi}^T, \boldsymbol{\nabla}_{\mathtt{S}}^T\left\{\mathtt{d},\mathtt{n}\right\} \mathbf{D}^{1/2}\left\{\mathtt{n},\mathtt{m}\right\} \boldsymbol{L}^j\left\{\mathtt{m}\right\}\right)_{\Omega^e} \\
&- \left(\boldsymbol{\psi}^T, \boldsymbol{\nabla}\left\{\mathtt{d}\right\} p^j\right)_{\Omega^e} \\
&- \left\langle \boldsymbol{\psi}^T, \tau_v \boldsymbol{v}^j\left\{\mathtt{d}\right\} \right\rangle_{\partial\Omega^e} \\
&+ \left(\boldsymbol{\psi}^T, \rho\left(p^j\right) \boldsymbol{b}\left\{\mathtt{d}\right\}\right)_{\Omega^e} \\
&+ \left\langle \boldsymbol{\psi}^T, \tau_v \boldsymbol{v}^D\left\{\mathtt{d}\right\} \right\rangle_{\partial\Omega^e\cap\Gamma^D} \\
&+ \left\langle \boldsymbol{\psi}^T, \tau_v \hat{\boldsymbol{v}}^j\left\{\mathtt{d}\right\} \right\rangle_{\partial\Omega^e\setminus\Gamma^D} \\
\big[\mathbf{f}_p\left\{1\right\}\big]_e^j = &+ \sum_{\mathtt{d}=1}^{\mathtt{n}_{\mathtt{sd}}} \Big(\left(\boldsymbol{\nabla}\left\{\mathtt{d}\right\} \boldsymbol{\psi}\right)^T, \rho\left(p^j\right) \boldsymbol{v}^j\left\{\mathtt{d}\right\} \Big)_{\Omega^e} \\
&- \left\langle \boldsymbol{\psi}^T, \tau_p p^j \right\rangle_{\partial\Omega^e} \\
&- \sum_{\mathtt{d}=1}^{\mathtt{n}_{\mathtt{sd}}} \left\langle \boldsymbol{\psi}^T, \rho\left(p^D\right) \boldsymbol{v}^D\left\{\mathtt{d}\right\} \boldsymbol{n}\left\{\mathtt{d}\right\} \right\rangle_{\partial\Omega^e\cap\Gamma^D} \\
&+ \left\langle \boldsymbol{\psi}^T, \tau_p p^D \right\rangle_{\partial\Omega^e\cap\Gamma^D}
\end{aligned}$$

$$
\begin{aligned}
& - \sum_{\mathtt{d}=1}^{\mathtt{n_{sd}}} \left\langle \boldsymbol{\psi}^T, \rho\left(\hat{p}^j\right) \hat{\boldsymbol{v}}^j \{\mathtt{d}\}\, \boldsymbol{n}\{\mathtt{d}\} \right\rangle_{\partial\Omega^e \setminus \Gamma^D} \\
& + \left\langle \boldsymbol{\psi}^T, \tau_p \hat{p}^j \right\rangle_{\partial\Omega^e \setminus \Gamma^D} \\
\left[\mathbf{f}_{\hat{v}}\{\mathtt{d}\}\right]_e^j & = + \sum_{\mathtt{m}=1}^{\mathtt{m_{sd}}} \sum_{\mathtt{n}=1}^{\mathtt{m_{sd}}} \left\langle \widehat{\boldsymbol{\psi}}^T, \mathbf{N}^T\{\mathtt{d},\mathtt{n}\}\, \mathbf{D}^{1/2}\{\mathtt{n},\mathtt{m}\}\, \boldsymbol{L}^j\{\mathtt{m}\} \right\rangle_{\partial\Omega^e \setminus \Gamma^D} \\
& + \left\langle \widehat{\boldsymbol{\psi}}^T, \hat{p}^j \boldsymbol{n}\{\mathtt{d}\} \right\rangle_{\partial\Omega^e \setminus \Gamma^D} \\
& + \left\langle \widehat{\boldsymbol{\psi}}^T, \tau_v \left(\boldsymbol{v}^j\{\mathtt{d}\} - \hat{\boldsymbol{v}}^j\{\mathtt{d}\}\right) \right\rangle_{\partial\Omega^e \setminus \Gamma^D} \\
& + \left\langle \widehat{\boldsymbol{\psi}}^T, \boldsymbol{t}^N\{\mathtt{d}\} \right\rangle_{\partial\Omega^e \cap \Gamma^N} \\
\left[\mathbf{f}_{\hat{p}}\{1\}\right]_e^j & = - \left\langle \widehat{\boldsymbol{\psi}}^T, \tau_p \left(p^j - \hat{p}^j\right) \right\rangle_{\partial\Omega^e \setminus \Gamma^D}
\end{aligned}
$$

C.1.2 Density-momentum formulation

Here the elemental matrices and vectors in problems (3.43) and (3.44) are detailed. These terms refer to pure flow problems, whereas a modified definition of such terms is presented in Sections C.3.2 and C.3.3 for the solution of fluid-structure interaction problems. As opposed to the velocity-pressure formulation, here the pressure is computed as a function of the density, i.e. $p = p(\rho)$, and its derivative with respect to the density equals the inverse of the compressibility coefficient, i.e. $\partial p(\rho)/\partial\rho = 1/\varepsilon$. For the sake of generality, such expressions are not made explicit. The stiffness matrices on the left hand side and the residual vectors on the right hand side to be computed at the j-th NEWTON iteration to advance from the time step n to the time step $n+1$ are defined as

$$
\begin{aligned}
\left[\mathbf{K}_{LL}\{\mathtt{m},\mathtt{n}\}\right]_e^{n+1,\,j} & = - \delta_{\mathtt{m},\mathtt{n}} \left(\boldsymbol{\psi}^T, \boldsymbol{\psi}\right)_{\Omega^e(t)} \\
\left[\mathbf{K}_{L\rho}\{\mathtt{m},1\}\right]_e^{n+1,\,j} & = - \sum_{\mathtt{d}=1}^{\mathtt{n_{sd}}} \sum_{\mathtt{n}=1}^{\mathtt{m_{sd}}} \left(\left(\boldsymbol{\nabla}_{\mathtt{S}}^T\{\mathtt{d},\mathtt{n}\}\, \mathbf{D}^{1/2}\{\mathtt{n},\mathtt{m}\}\, \boldsymbol{\psi}\right)^T, \frac{\boldsymbol{\rho v}^{n+1,\,j}\{\mathtt{d}\}}{\left(\rho^{n+1,\,j}\right)^2} \boldsymbol{\psi} \right)_{\Omega^e(t)} \\
\left[\mathbf{K}_{Lw}\{\mathtt{m},\mathtt{d}\}\right]_e^{n+1,\,j} & = + \sum_{\mathtt{n}=1}^{\mathtt{m_{sd}}} \left(\left(\boldsymbol{\nabla}_{\mathtt{S}}^T\{\mathtt{d},\mathtt{n}\}\, \mathbf{D}^{1/2}\{\mathtt{n},\mathtt{m}\}\, \boldsymbol{\psi}\right)^T, \frac{1}{\rho^{n+1,\,j}} \boldsymbol{\psi} \right)_{\Omega^e(t)} \\
\left[\mathbf{K}_{L\hat{\rho}}\{\mathtt{m},1\}\right]_e^{n+1,\,j} & = + \sum_{\mathtt{d}=1}^{\mathtt{n_{sd}}} \sum_{\mathtt{n}=1}^{\mathtt{m_{sd}}} \left\langle \left(\mathbf{N}^T\{\mathtt{d},\mathtt{n}\}\, \mathbf{D}^{1/2}\{\mathtt{n},\mathtt{m}\}\, \boldsymbol{\psi}\right)^T, \frac{\widehat{\boldsymbol{\rho v}}^{n+1,\,j}\{\mathtt{d}\}}{\left(\hat{\rho}^{n+1,\,j}\right)^2} \widehat{\boldsymbol{\psi}} \right\rangle_{\partial\Omega^e(t) \setminus \Gamma^D(t)} \\
\left[\mathbf{K}_{L\hat{w}}\{\mathtt{m},\mathtt{d}\}\right]_e^{n+1,\,j} & = - \sum_{\mathtt{n}=1}^{\mathtt{m_{sd}}} \left\langle \left(\mathbf{N}^T\{\mathtt{d},\mathtt{n}\}\, \mathbf{D}^{1/2}\{\mathtt{n},\mathtt{m}\}\, \boldsymbol{\psi}\right)^T, \frac{1}{\hat{\rho}^{n+1,\,j}} \widehat{\boldsymbol{\psi}} \right\rangle_{\partial\Omega^e(t) \setminus \Gamma^D(t)} \\
\left[\mathbf{K}_{\rho\rho}\{1,1\}\right]_e^{n+1,\,j} & = + \left(\boldsymbol{\psi}^T, \frac{\alpha_0}{\Delta t} \boldsymbol{\psi}\right)_{\Omega^e(t)} \\
& \quad + \sum_{\mathtt{d}=1}^{\mathtt{n_{sd}}} \left(\boldsymbol{\psi}^T, \boldsymbol{\nabla}\{\mathtt{d}\} \left(\sum_{b=0}^{\mathrm{BDF}o} \frac{\alpha_b}{\Delta t} \boldsymbol{d}^{n+1-b}\{\mathtt{d}\} \right) \boldsymbol{\psi} \right)_{\Omega^e(t)}
\end{aligned}
$$

$$
\begin{aligned}
&\quad + \sum_{\mathtt{d}=1}^{\mathtt{n_{sd}}} \left(\left(\boldsymbol{\nabla}\{\mathtt{d}\}\boldsymbol{\psi}\right)^T, \left(\sum_{b=0}^{\mathrm{BDF}o} \frac{\alpha_b}{\Delta t} \boldsymbol{d}^{n+1-b}\{\mathtt{d}\} \right) \boldsymbol{\psi} \right)_{\Omega^e(t)} \\
&\quad + \left\langle \boldsymbol{\psi}^T, \tau_\rho \boldsymbol{\psi} \right\rangle_{\partial\Omega^e(t)} \\
\left[\mathbf{K}_{\rho w}\{1,\mathtt{d}\}\right]_e^{n+1,\,j} &= - \left(\left(\boldsymbol{\nabla}\{\mathtt{d}\}\boldsymbol{\psi}\right)^T, \boldsymbol{\psi} \right)_{\Omega^e(t)} \\
\left[\mathbf{K}_{\rho\hat{\rho}}\{1,1\}\right]_e^{n+1,\,j} &= - \sum_{\mathtt{d}=1}^{\mathtt{n_{sd}}} \left\langle \boldsymbol{\psi}^T, \left(\sum_{b=0}^{\mathrm{BDF}o} \frac{\alpha_b}{\Delta t} \boldsymbol{d}^{n+1-b}\{\mathtt{d}\} \right) \boldsymbol{n}\{\mathtt{d}\} \widehat{\boldsymbol{\psi}} \right\rangle_{\partial\Omega^e(t)\setminus\Gamma^D(t)} \\
&\quad - \left\langle \boldsymbol{\psi}^T, \tau_\rho \widehat{\boldsymbol{\psi}} \right\rangle_{\partial\Omega^e(t)\setminus\Gamma^D(t)} \\
\left[\mathbf{K}_{\rho\hat{w}}\{1,\mathtt{d}\}\right]_e^{n+1,\,j} &= + \left\langle \boldsymbol{\psi}^T, \boldsymbol{n}\{\mathtt{d}\} \widehat{\boldsymbol{\psi}} \right\rangle_{\partial\Omega^e(t)\setminus\Gamma^D(t)} \\
\left[\mathbf{K}_{wL}\{\mathtt{d},\mathtt{m}\}\right]_e^{n+1,\,j} &= + \sum_{\mathtt{n}=1}^{\mathtt{m_{sd}}} \left(\boldsymbol{\psi}^T, \boldsymbol{\nabla}_{\mathtt{S}}^T\{\mathtt{d},\mathtt{n}\} \mathbf{D}^{1/2}\{\mathtt{n},\mathtt{m}\} \boldsymbol{\psi} \right)_{\Omega^e(t)} \\
\left[\mathbf{K}_{w\rho}\{\mathtt{d},1\}\right]_e^{n+1,\,j} &= + \sum_{\mathtt{e}=1}^{\mathtt{n_{sd}}} \left(\left(\boldsymbol{\nabla}\{\mathtt{e}\}\boldsymbol{\psi}\right)^T, \boldsymbol{\rho v}^{n+1,\,j}\{\mathtt{d}\} \frac{\boldsymbol{\rho v}^{n+1,\,j}\{\mathtt{e}\}}{\left(\rho^{n+1,\,j}\right)^2} \boldsymbol{\psi} \right)_{\Omega^e(t)} \\
&\quad + \left(\boldsymbol{\psi}^T, \left. \frac{\partial p(\rho)}{\partial \rho} \right|_{\rho^{n+1,\,j}} \boldsymbol{\nabla}\{\mathtt{d}\} \boldsymbol{\psi} \right)_{\Omega^e(t)} \\
&\quad - \left(\boldsymbol{\psi}^T, \boldsymbol{b}^{n+1}\{\mathtt{d}\} \boldsymbol{\psi} \right)_{\Omega^e(t)} \\
\left[\mathbf{K}_{ww}\{\mathtt{d},\mathtt{e}\}\right]_e^{n+1,\,j} &= + \delta_{\mathtt{d},\mathtt{e}} \left(\boldsymbol{\psi}^T, \frac{\alpha_0}{\Delta t} \boldsymbol{\psi} \right)_{\Omega^e(t)} \\
&\quad + \delta_{\mathtt{d},\mathtt{e}} \sum_{\mathtt{f}=1}^{\mathtt{n_{sd}}} \left(\boldsymbol{\psi}^T, \boldsymbol{\nabla}\{\mathtt{f}\} \left(\sum_{b=0}^{\mathrm{BDF}o} \frac{\alpha_b}{\Delta t} \boldsymbol{d}^{n+1-b}\{\mathtt{f}\} \right) \boldsymbol{\psi} \right)_{\Omega^e(t)} \\
&\quad - \delta_{\mathtt{d},\mathtt{e}} \sum_{\mathtt{f}=1}^{\mathtt{n_{sd}}} \left(\left(\boldsymbol{\nabla}\{\mathtt{f}\}\boldsymbol{\psi}\right)^T, \frac{\boldsymbol{\rho v}^{n+1,\,j}\{\mathtt{f}\}}{\rho^{n+1,\,j}} \boldsymbol{\psi} \right)_{\Omega^e(t)} \\
&\quad + \delta_{\mathtt{d},\mathtt{e}} \sum_{\mathtt{f}=1}^{\mathtt{n_{sd}}} \left(\left(\boldsymbol{\nabla}\{\mathtt{f}\}\boldsymbol{\psi}\right)^T, \left(\sum_{b=0}^{\mathrm{BDF}o} \frac{\alpha_b}{\Delta t} \boldsymbol{d}^{n+1-b}\{\mathtt{f}\} \right) \boldsymbol{\psi} \right)_{\Omega^e(t)} \\
&\quad - \left(\left(\boldsymbol{\nabla}\{\mathtt{e}\}\boldsymbol{\psi}\right)^T, \frac{\boldsymbol{\rho v}^{n+1,\,j}\{\mathtt{d}\}}{\rho^{n+1,\,j}} \boldsymbol{\psi} \right)_{\Omega^e(t)} \\
&\quad + \delta_{\mathtt{d},\mathtt{e}} \left\langle \boldsymbol{\psi}^T, \tau_{\rho v} \boldsymbol{\psi} \right\rangle_{\partial\Omega^e(t)} \\
\left[\mathbf{K}_{w\hat{\rho}}\{\mathtt{d},1\}\right]_e^{n+1,\,j} &= - \sum_{\mathtt{e}=1}^{\mathtt{n_{sd}}} \left\langle \boldsymbol{\psi}^T, \widehat{\boldsymbol{\rho v}}^{n+1,\,j}\{\mathtt{d}\} \frac{\widehat{\boldsymbol{\rho v}}^{n+1,\,j}\{\mathtt{e}\}}{\left(\hat{\rho}^{n+1,\,j}\right)^2} \boldsymbol{n}\{\mathtt{e}\} \widehat{\boldsymbol{\psi}} \right\rangle_{\partial\Omega^e(t)\setminus\Gamma^D(t)} \\
\left[\mathbf{K}_{w\hat{w}}\{\mathtt{d},\mathtt{e}\}\right]_e^{n+1,\,j} &= + \delta_{\mathtt{d},\mathtt{e}} \sum_{\mathtt{f}=1}^{\mathtt{n_{sd}}} \left\langle \boldsymbol{\psi}^T, \frac{\widehat{\boldsymbol{\rho v}}^{n+1,\,j}\{\mathtt{f}\}}{\hat{\rho}^{n+1,\,j}} \boldsymbol{n}\{\mathtt{f}\} \widehat{\boldsymbol{\psi}} \right\rangle_{\partial\Omega^e(t)\setminus\Gamma^D(t)}
\end{aligned}
$$

$$
\begin{aligned}
&- \delta_{\mathtt{d},\mathtt{e}} \sum_{\mathtt{f}=1}^{\mathtt{n}_{\mathtt{sd}}} \left\langle \boldsymbol{\psi}^T, \left(\sum_{b=0}^{\mathrm{BDF}o} \frac{\alpha_b}{\Delta t} \boldsymbol{d}^{n+1-b}\left\{\mathtt{f}\right\} \right) \boldsymbol{n}\left\{\mathtt{f}\right\} \widehat{\boldsymbol{\psi}} \right\rangle_{\partial\Omega^e(t)\setminus\Gamma^D(t)} \\
&+ \left\langle \boldsymbol{\psi}^T, \frac{\widehat{\boldsymbol{\rho v}}^{n+1,\,j}\left\{\mathtt{d}\right\}}{\hat{\rho}^{n+1,\,j}} \boldsymbol{n}\left\{\mathtt{e}\right\} \widehat{\boldsymbol{\psi}} \right\rangle_{\partial\Omega^e(t)\setminus\Gamma^D(t)} \\
&- \delta_{\mathtt{d},\mathtt{e}} \left\langle \boldsymbol{\psi}^T, \tau_{\rho v} \widehat{\boldsymbol{\psi}} \right\rangle_{\partial\Omega^e(t)\setminus\Gamma^D(t)}
\end{aligned}
$$

$$
\begin{aligned}
\left[\mathbf{K}_{\hat{\rho}\rho}\left\{1,1\right\}\right]_e^{n+1,\,j} &= + \left\langle \widehat{\boldsymbol{\psi}}^T, \tau_{\rho} \boldsymbol{\psi} \right\rangle_{\partial\Omega^e(t)\setminus\Gamma^D(t)} \\
\left[\mathbf{K}_{\hat{\rho}\hat{\rho}}\left\{1,1\right\}\right]_e^{n+1,\,j} &= - \left\langle \widehat{\boldsymbol{\psi}}^T, \tau_{\rho} \widehat{\boldsymbol{\psi}} \right\rangle_{\partial\Omega^e(t)\setminus\Gamma^D(t)} \\
\left[\mathbf{K}_{\hat{w}L}\left\{\mathtt{d},\mathtt{m}\right\}\right]_e^{n+1,\,j} &= - \sum_{\mathtt{n}=1}^{\mathtt{m}_{\mathtt{sd}}} \left\langle \widehat{\boldsymbol{\psi}}^T, \mathbf{N}^T\left\{\mathtt{d},\mathtt{n}\right\} \mathbf{D}^{1/2}\left\{\mathtt{n},\mathtt{m}\right\} \boldsymbol{\psi} \right\rangle_{\partial\Omega^e(t)\setminus\Gamma^D(t)} \\
\left[\mathbf{K}_{\hat{w}w}\left\{\mathtt{d},\mathtt{e}\right\}\right]_e^{n+1,\,j} &= - \delta_{\mathtt{d},\mathtt{e}} \left\langle \widehat{\boldsymbol{\psi}}^T, \tau_{\rho v} \boldsymbol{\psi} \right\rangle_{\partial\Omega^e(t)\setminus\Gamma^D(t)} \\
\left[\mathbf{K}_{\hat{w}\hat{\rho}}\left\{\mathtt{d},1\right\}\right]_e^{n+1,\,j} &= - \left\langle \widehat{\boldsymbol{\psi}}^T, \left.\frac{\partial p\left(\hat{\rho}\right)}{\partial \hat{\rho}}\right|_{\hat{\rho}^{n+1,\,j}} \boldsymbol{n}\left\{\mathtt{d}\right\} \widehat{\boldsymbol{\psi}} \right\rangle_{\partial\Omega^e(t)\setminus\Gamma^D(t)} \\
\left[\mathbf{K}_{\hat{w}\hat{w}}\left\{\mathtt{d},\mathtt{e}\right\}\right]_e^{n+1,\,j} &= + \delta_{\mathtt{d},\mathtt{e}} \left\langle \widehat{\boldsymbol{\psi}}^T, \tau_{\rho v} \widehat{\boldsymbol{\psi}} \right\rangle_{\partial\Omega^e(t)\setminus\Gamma^D(t)}
\end{aligned}
$$

$$
\begin{aligned}
\left[\mathbf{f}_L\left\{\mathtt{m}\right\}\right]_e^{n+1,\,j} = &+ \left(\boldsymbol{\psi}^T, \boldsymbol{L}^{n+1,\,j}\left\{\mathtt{m}\right\}\right)_{\Omega^e(t)} \\
&- \sum_{\mathtt{d}=1}^{\mathtt{n}_{\mathtt{sd}}} \sum_{\mathtt{n}=1}^{\mathtt{m}_{\mathtt{sd}}} \left(\left(\boldsymbol{\nabla}_{\mathtt{S}}^T\left\{\mathtt{d},\mathtt{n}\right\} \mathbf{D}^{1/2}\left\{\mathtt{n},\mathtt{m}\right\} \boldsymbol{\psi}\right)^T, \frac{\boldsymbol{\rho v}^{n+1,\,j}\left\{\mathtt{d}\right\}}{\rho^{n+1,\,j}} \right)_{\Omega^e(t)} \\
&+ \sum_{\mathtt{d}=1}^{\mathtt{n}_{\mathtt{sd}}} \sum_{\mathtt{n}=1}^{\mathtt{m}_{\mathtt{sd}}} \left\langle \left(\mathbf{N}^T\left\{\mathtt{d},\mathtt{n}\right\} \mathbf{D}^{1/2}\left\{\mathtt{n},\mathtt{m}\right\} \boldsymbol{\psi}\right)^T, \frac{\boldsymbol{\rho v}^{D,\,n+1}\left\{\mathtt{d}\right\}}{\rho^{D,\,n+1}} \right\rangle_{\partial\Omega^e(t)\cap\Gamma^D(t)} \\
&+ \sum_{\mathtt{d}=1}^{\mathtt{n}_{\mathtt{sd}}} \sum_{\mathtt{n}=1}^{\mathtt{m}_{\mathtt{sd}}} \left\langle \left(\mathbf{N}^T\left\{\mathtt{d},\mathtt{n}\right\} \mathbf{D}^{1/2}\left\{\mathtt{n},\mathtt{m}\right\} \boldsymbol{\psi}\right)^T, \frac{\widehat{\boldsymbol{\rho v}}^{n+1,\,j}\left\{\mathtt{d}\right\}}{\hat{\rho}^{n+1,\,j}} \right\rangle_{\partial\Omega^e(t)\setminus\Gamma^D(t)}
\end{aligned}
$$

$$
\begin{aligned}
\left[\mathbf{f}_{\rho}\left\{1\right\}\right]_e^{n+1,\,j} = &- \left(\boldsymbol{\psi}^T, \sum_{b=0}^{\mathrm{BDF}o} \frac{\alpha_b}{\Delta t} \rho^{n+1-b}\right)_{\Omega^e(t)} \\
&- \sum_{\mathtt{d}=1}^{\mathtt{n}_{\mathtt{sd}}} \left(\boldsymbol{\psi}^T, \rho^{n+1,\,j} \boldsymbol{\nabla}\left\{\mathtt{d}\right\} \left(\sum_{b=0}^{\mathrm{BDF}o} \frac{\alpha_b}{\Delta t} \boldsymbol{d}^{n+1-b}\left\{\mathtt{d}\right\} \right)\right)_{\Omega^e(t)} \\
&+ \sum_{\mathtt{d}=1}^{\mathtt{n}_{\mathtt{sd}}} \left(\left(\boldsymbol{\nabla}\left\{\mathtt{d}\right\} \boldsymbol{\psi}\right)^T, \boldsymbol{\rho v}^{n+1,\,j}\left\{\mathtt{d}\right\} \right)_{\Omega^e(t)} \\
&- \sum_{\mathtt{d}=1}^{\mathtt{n}_{\mathtt{sd}}} \left(\left(\boldsymbol{\nabla}\left\{\mathtt{d}\right\} \boldsymbol{\psi}\right)^T, \rho^{n+1,\,j} \left(\sum_{b=0}^{\mathrm{BDF}o} \frac{\alpha_b}{\Delta t} \boldsymbol{d}^{n+1-b}\left\{\mathtt{d}\right\} \right)\right)_{\Omega^e(t)} \\
&- \left\langle \boldsymbol{\psi}^T, \tau_{\rho} \rho^{n+1,\,j} \right\rangle_{\partial\Omega^e(t)}
\end{aligned}
$$

$$
\begin{aligned}
&- \sum_{\mathtt{d}=1}^{\mathtt{n_{sd}}} \left\langle \boldsymbol{\psi}^T, \boldsymbol{\rho v}^{D,\,n+1}\{\mathtt{d}\}\,\boldsymbol{n}\{\mathtt{d}\}\right\rangle_{\partial\Omega^e(t)\cap\Gamma^D(t)} \\
&+ \sum_{\mathtt{d}=1}^{\mathtt{n_{sd}}} \left\langle \boldsymbol{\psi}^T, \rho^{D,\,n+1}\left(\sum_{b=0}^{\mathrm{BDF}o}\frac{\alpha_b}{\Delta t}\boldsymbol{d}^{n+1-b}\{\mathtt{d}\}\right)\boldsymbol{n}\{\mathtt{d}\}\right\rangle_{\partial\Omega^e(t)\cap\Gamma^D(t)} \\
&+ \left\langle \boldsymbol{\psi}^T, \tau_\rho \rho^{D,\,n+1}\right\rangle_{\partial\Omega^e(t)\cap\Gamma^D(t)} \\
&- \sum_{\mathtt{d}=1}^{\mathtt{n_{sd}}} \left\langle \boldsymbol{\psi}^T, \widehat{\boldsymbol{\rho v}}^{n+1,\,j}\{\mathtt{d}\}\,\boldsymbol{n}\{\mathtt{d}\}\right\rangle_{\partial\Omega^e(t)\setminus\Gamma^D(t)} \\
&+ \sum_{\mathtt{d}=1}^{\mathtt{n_{sd}}} \left\langle \boldsymbol{\psi}^T, \hat{\rho}^{n+1,\,j}\left(\sum_{b=0}^{\mathrm{BDF}o}\frac{\alpha_b}{\Delta t}\boldsymbol{d}^{n+1-b}\{\mathtt{d}\}\right)\boldsymbol{n}\{\mathtt{d}\}\right\rangle_{\partial\Omega^e(t)\setminus\Gamma^D(t)} \\
&+ \left\langle \boldsymbol{\psi}^T, \tau_\rho \hat{\rho}^{n+1,\,j}\right\rangle_{\partial\Omega^e(t)\setminus\Gamma^D(t)}
\end{aligned}
$$

$$
\begin{aligned}
\left[\mathbf{f}_w\{\mathtt{d}\}\right]_e^{n+1,\,j} = &- \left(\boldsymbol{\psi}^T, \sum_{b=0}^{\mathrm{BDF}o}\frac{\alpha_b}{\Delta t}\boldsymbol{\rho v}^{n+1-b}\{\mathtt{d}\}\right)_{\Omega^e(t)} \\
&- \sum_{\mathtt{e}=1}^{\mathtt{n_{sd}}} \left(\boldsymbol{\psi}^T, \boldsymbol{\rho v}^{n+1,\,j}\{\mathtt{d}\}\,\boldsymbol{\nabla}\{\mathtt{e}\}\left(\sum_{b=0}^{\mathrm{BDF}o}\frac{\alpha_b}{\Delta t}\boldsymbol{d}^{n+1-b}\{\mathtt{e}\}\right)\right)_{\Omega^e(t)} \\
&+ \sum_{\mathtt{e}=1}^{\mathtt{n_{sd}}} \left(\left(\boldsymbol{\nabla}\{\mathtt{e}\}\,\boldsymbol{\psi}\right)^T, \boldsymbol{\rho v}^{n+1,\,j}\{\mathtt{d}\}\,\frac{\boldsymbol{\rho v}^{n+1,\,j}\{\mathtt{e}\}}{\rho^{n+1,\,j}}\right)_{\Omega^e(t)} \\
&- \sum_{\mathtt{e}=1}^{\mathtt{n_{sd}}} \left(\left(\boldsymbol{\nabla}\{\mathtt{e}\}\,\boldsymbol{\psi}\right)^T, \boldsymbol{\rho v}^{n+1,\,j}\{\mathtt{d}\}\left(\sum_{b=0}^{\mathrm{BDF}o}\frac{\alpha_b}{\Delta t}\boldsymbol{d}^{n+1-b}\{\mathtt{e}\}\right)\right)_{\Omega^e(t)} \\
&- \sum_{\mathtt{m}=1}^{\mathtt{m_{sd}}}\sum_{\mathtt{n}=1}^{\mathtt{m_{sd}}} \left(\boldsymbol{\psi}^T, \boldsymbol{\nabla}_{\mathtt{S}}^T\{\mathtt{d},\mathtt{n}\}\,\mathbf{D}^{1/2}\{\mathtt{n},\mathtt{m}\}\,\boldsymbol{L}^{n+1,\,j}\{\mathtt{m}\}\right)_{\Omega^e(t)} \\
&- \left(\boldsymbol{\psi}^T, \boldsymbol{\nabla}\{\mathtt{d}\}\,p\left(\rho^{n+1,\,j}\right)\right)_{\Omega^e(t)} \\
&- \left\langle \boldsymbol{\psi}^T, \tau_{\rho v}\boldsymbol{\rho v}^{n+1,\,j}\{\mathtt{d}\}\right\rangle_{\partial\Omega^e(t)} \\
&+ \left(\boldsymbol{\psi}^T, \rho^{n+1,\,j}\boldsymbol{b}^{n+1}\{\mathtt{d}\}\right)_{\Omega^e(t)} \\
&- \sum_{\mathtt{e}=1}^{\mathtt{n_{sd}}} \left\langle \boldsymbol{\psi}^T, \boldsymbol{\rho v}^{D,\,n+1}\{\mathtt{d}\}\,\frac{\boldsymbol{\rho v}^{D,\,n+1}\{\mathtt{e}\}}{\rho^{D,\,n+1}}\boldsymbol{n}\{\mathtt{e}\}\right\rangle_{\partial\Omega^e(t)\cap\Gamma^D(t)} \\
&+ \sum_{\mathtt{e}=1}^{\mathtt{n_{sd}}} \left\langle \boldsymbol{\psi}^T, \boldsymbol{\rho v}^{D,\,n+1}\{\mathtt{d}\}\left(\sum_{b=0}^{\mathrm{BDF}o}\frac{\alpha_b}{\Delta t}\boldsymbol{d}^{n+1-b}\{\mathtt{e}\}\right)\boldsymbol{n}\{\mathtt{e}\}\right\rangle_{\partial\Omega^e(t)\cap\Gamma^D(t)} \\
&+ \left\langle \boldsymbol{\psi}^T, \tau_{\rho v}\boldsymbol{\rho v}^{D,\,n+1}\{\mathtt{d}\}\right\rangle_{\partial\Omega^e(t)\cap\Gamma^D(t)} \\
&- \sum_{\mathtt{e}=1}^{\mathtt{n_{sd}}} \left\langle \boldsymbol{\psi}^T, \widehat{\boldsymbol{\rho v}}^{n+1,\,j}\{\mathtt{d}\}\,\frac{\widehat{\boldsymbol{\rho v}}^{n+1,\,j}\{\mathtt{e}\}}{\hat{\rho}^{n+1,\,j}}\boldsymbol{n}\{\mathtt{e}\}\right\rangle_{\partial\Omega^e(t)\setminus\Gamma^D(t)}
\end{aligned}
$$

$$
\begin{aligned}
&+\sum_{\mathtt{e}=1}^{\mathtt{n}_{\mathtt{sd}}}\left\langle \boldsymbol{\psi}^{T}, \widehat{\boldsymbol{\rho v}}^{n+1,\,j}\left\{\mathtt{d}\right\}\left(\sum_{b=0}^{\mathrm{BDF}o}\frac{\alpha_b}{\Delta t}\boldsymbol{d}^{n+1-b}\left\{\mathtt{e}\right\}\right)\boldsymbol{n}\left\{\mathtt{e}\right\}\right\rangle_{\partial\Omega^{e}(t)\setminus\Gamma^{D}(t)}\\
&+\left\langle \boldsymbol{\psi}^{T}, \tau_{\rho v}\widehat{\boldsymbol{\rho v}}^{n+1,\,j}\left\{\mathtt{d}\right\}\right\rangle_{\partial\Omega^{e}(t)\setminus\Gamma^{D}(t)}\\
\left[\mathbf{f}_{\hat{\rho}}\left\{1\right\}\right]_{e}^{n+1,\,j} ={}&-\left\langle \widehat{\boldsymbol{\psi}}^{T}, \tau_{\rho}\left(\rho^{n+1,\,j}-\hat{\rho}^{n+1,\,j}\right)\right\rangle_{\partial\Omega^{e}(t)\setminus\Gamma^{D}(t)}\\
\left[\mathbf{f}_{\hat{w}}\left\{\mathtt{d}\right\}\right]_{e}^{n+1,\,j} ={}&+\sum_{\mathtt{m}=1}^{\mathtt{m}_{\mathtt{sd}}}\sum_{\mathtt{n}=1}^{\mathtt{m}_{\mathtt{sd}}}\left\langle \widehat{\boldsymbol{\psi}}^{T}, \mathbf{N}^{T}\left\{\mathtt{d},\mathtt{n}\right\}\mathbf{D}^{1/2}\left\{\mathtt{n},\mathtt{m}\right\}\boldsymbol{L}^{n+1,\,j}\left\{\mathtt{m}\right\}\right\rangle_{\partial\Omega^{e}(t)\setminus\Gamma^{D}(t)}\\
&+\left\langle \widehat{\boldsymbol{\psi}}^{T}, p\left(\hat{\rho}^{n+1,\,j}\right)\boldsymbol{n}\left\{\mathtt{d}\right\}\right\rangle_{\partial\Omega^{e}(t)\setminus\Gamma^{D}(t)}\\
&+\left\langle \widehat{\boldsymbol{\psi}}^{T}, \tau_{\rho v}\left(\boldsymbol{\rho v}^{n+1,\,j}\left\{\mathtt{d}\right\}-\widehat{\boldsymbol{\rho v}}^{n+1,\,j}\left\{\mathtt{d}\right\}\right)\right\rangle_{\partial\Omega^{e}(t)\setminus\Gamma^{D}(t)}\\
&+\left\langle \widehat{\boldsymbol{\psi}}^{T}, \boldsymbol{t}^{N,\,n+1}\left\{\mathtt{d}\right\}\right\rangle_{\partial\Omega^{e}(t)\cap\Gamma^{N}(t)}
\end{aligned}
$$

C.2 HDG, CG and HDG-CG formulations for thermal problems

In this section, the elemental matrices and vectors appearing in the discrete form of the HDG, CG and the coupled HDG-CG formulations for thermal problems in Chapter 4 are defined.

C.2.1 HDG approximation

Here the elemental contributions to the HDG matrices and vectors in (4.9) and (4.10) are shown. Owing to the linear and steady-state nature of the problems considered, the computation of these terms is required only once and no iteration nor advancement in time has to be performed. Moreover, given the symmetry of the problem, only the independent blocks of the left hand side matrix are listed, whereas the remaining ones can be computed by simply transposing the corresponding blocks with inverted row and column indices. The matrices and vectors are thus defined as

$$
\begin{aligned}
\big[\mathbf{K}_{11}\{\mathtt{d},\mathtt{e}\}\big]_e &= -\,\delta_{\mathtt{d},\mathtt{e}}\left(\boldsymbol{\psi}^T_{\mathtt{HDG}},\boldsymbol{\psi}_{\mathtt{HDG}}\right)_{\Omega^e_{\mathtt{HDG}}}\\
\big[\mathbf{K}_{12}\{\mathtt{d},1\}\big]_e &= +\left(\left(\sqrt{\kappa}\boldsymbol{\nabla}\{\mathtt{d}\}\boldsymbol{\psi}_{\mathtt{HDG}}\right)^T,\boldsymbol{\psi}_{\mathtt{HDG}}\right)_{\Omega^e_{\mathtt{HDG}}}\\
\big[\mathbf{K}_{13}\{\mathtt{d},1\}\big]_e &= -\left\langle\left(\sqrt{\kappa}\boldsymbol{n}_{\mathtt{HDG}}\{\mathtt{d}\}\boldsymbol{\psi}_{\mathtt{HDG}}\right)^T,\widehat{\boldsymbol{\psi}}_{\mathtt{HDG}}\right\rangle_{\partial\Omega^e_{\mathtt{HDG}}\setminus\Gamma^D_{\mathtt{HDG}}}\\
\big[\mathbf{K}_{22}\{1,1\}\big]_e &= +\left\langle\boldsymbol{\psi}^T_{\mathtt{HDG}},\tau_T\boldsymbol{\psi}_{\mathtt{HDG}}\right\rangle_{\partial\Omega^e_{\mathtt{HDG}}}\\
\big[\mathbf{K}_{23}\{1,1\}\big]_e &= -\left\langle\boldsymbol{\psi}^T_{\mathtt{HDG}},\tau_T\widehat{\boldsymbol{\psi}}_{\mathtt{HDG}}\right\rangle_{\partial\Omega^e_{\mathtt{HDG}}\setminus\Gamma^D_{\mathtt{HDG}}}\\
\big[\mathbf{K}_{33}\{1,1\}\big]_e &= +\left\langle\widehat{\boldsymbol{\psi}}^T_{\mathtt{HDG}},\tau_T\widehat{\boldsymbol{\psi}}_{\mathtt{HDG}}\right\rangle_{\partial\Omega^e_{\mathtt{HDG}}\setminus\Gamma^D_{\mathtt{HDG}}}\\
\big[\mathbf{f}_1\{\mathtt{d}\}\big]_e &= +\left\langle\left(\sqrt{\kappa}\boldsymbol{n}_{\mathtt{HDG}}\{\mathtt{d}\}\boldsymbol{\psi}_{\mathtt{HDG}}\right)^T,T^D_{\mathtt{HDG}}\right\rangle_{\partial\Omega^e_{\mathtt{HDG}}\cap\Gamma^D_{\mathtt{HDG}}}\\
\big[\mathbf{f}_2\{1\}\big]_e &= +\left(\boldsymbol{\psi}^T_{\mathtt{HDG}},s\right)_{\Omega^e_{\mathtt{HDG}}}\\
&\quad+\left\langle\boldsymbol{\psi}^T_{\mathtt{HDG}},\tau_T T^D_{\mathtt{HDG}}\right\rangle_{\partial\Omega^e_{\mathtt{HDG}}\cap\Gamma^D_{\mathtt{HDG}}}\\
\big[\mathbf{f}_3\{1\}\big]_e &= +\left\langle\widehat{\boldsymbol{\psi}}^T_{\mathtt{HDG}},f^N\right\rangle_{\partial\Omega^e_{\mathtt{HDG}}\cap\Gamma^N_{\mathtt{HDG}}}
\end{aligned}
$$

C.2.2 CG approximation

The elemental contribution to the CG matrix and vector in (4.17) is simply given by

$$
\begin{aligned}
\big[\mathbf{K}_{44}\{1,1\}\big]_e &= +\sum_{\mathtt{d}=1}^{\mathtt{n_{sd}}}\left(\left(\boldsymbol{\nabla}\{\mathtt{d}\}\boldsymbol{\psi}_{\mathtt{CG}}\right)^T,\kappa\boldsymbol{\nabla}\{\mathtt{d}\}\boldsymbol{\psi}_{\mathtt{CG}}\right)_{\Omega^e_{\mathtt{CG}}}\\
\big[\mathbf{f}_4\{1\}\big]_e &= +\left(\boldsymbol{\psi}^T_{\mathtt{CG}},s\right)_{\Omega^e_{\mathtt{CG}}}\\
&\quad+\left\langle\boldsymbol{\psi}^T_{\mathtt{CG}},f^N\right\rangle_{\partial\Omega^e_{\mathtt{CG}}\cap\Gamma^N_{\mathtt{CG}}}
\end{aligned}
$$

C.2.3 Local-global coupling

The local-global coupling of HDG and CG discretizations requires a modification of the global matrices of the single discretizations $\left[\mathbf{K}_{33}\right]$ and $\left[\mathbf{K}_{44}\right]$, as well as the of the matrices connecting the HDG local and global DOFs $\left[\mathbf{K}_{13}\right]$ and $\left[\mathbf{K}_{14}\right]$, plus the introduction of the coupling blocks $\left[\bar{\mathbf{K}}_{14}\right]$ and $\left[\bar{\mathbf{K}}_{24}\right]$. The new terms in (4.23) are therefore defined as

$$
\begin{aligned}
\left[\bar{\mathbf{K}}_{13}\left\{\mathtt{d},1\right\}\right]_e &= -\left\langle\left(\sqrt{\kappa}\boldsymbol{n}_{\mathtt{HDG}}\left\{\mathtt{d}\right\}\boldsymbol{\psi}_{\mathtt{HDG}}\right)^T, \widehat{\boldsymbol{\psi}}_{\mathtt{HDG}}\right\rangle_{\partial\Omega^e_{\mathtt{HDG}}\setminus\Gamma^D_{\mathtt{HDG}}\setminus\Gamma^I} \\
\left[\bar{\mathbf{K}}_{14}\left\{\mathtt{d},1\right\}\right]_e &= -\left\langle\left(\sqrt{\kappa}\boldsymbol{n}_{\mathtt{HDG}}\left\{\mathtt{d}\right\}\boldsymbol{\psi}_{\mathtt{HDG}}\right)^T, \boldsymbol{\psi}_{\mathtt{CG}}\right\rangle_{\partial\Omega^e_{\mathtt{HDG}}\cap\Gamma^I} \\
\left[\bar{\mathbf{K}}_{23}\left\{1,1\right\}\right]_e &= -\left\langle\boldsymbol{\psi}^T_{\mathtt{HDG}}, \tau_T\widehat{\boldsymbol{\psi}}_{\mathtt{HDG}}\right\rangle_{\partial\Omega^e_{\mathtt{HDG}}\setminus\Gamma^D_{\mathtt{HDG}}\setminus\Gamma^I} \\
\left[\bar{\mathbf{K}}_{24}\left\{1,1\right\}\right]_e &= -\left\langle\boldsymbol{\psi}^T_{\mathtt{HDG}}, \tau_T\boldsymbol{\psi}_{\mathtt{CG}}\right\rangle_{\partial\Omega^e_{\mathtt{HDG}}\cap\Gamma^I} \\
\left[\bar{\mathbf{K}}_{33}\left\{1,1\right\}\right]_e &= +\left\langle\widehat{\boldsymbol{\psi}}^T_{\mathtt{HDG}}, \tau_T\widehat{\boldsymbol{\psi}}_{\mathtt{HDG}}\right\rangle_{\partial\Omega^e_{\mathtt{HDG}}\setminus\Gamma^D_{\mathtt{HDG}}\setminus\Gamma^I} \\
\left[\bar{\mathbf{K}}_{44}\left\{1,1\right\}\right]_e &= +\sum_{\mathtt{d}=1}^{\mathtt{n_{sd}}}\left(\left(\boldsymbol{\nabla}\left\{\mathtt{d}\right\}\boldsymbol{\psi}_{\mathtt{CG}}\right)^T, \kappa\boldsymbol{\nabla}\left\{\mathtt{d}\right\}\boldsymbol{\psi}_{\mathtt{CG}}\right)_{\Omega^e_{\mathtt{CG}}} \\
&\quad + \left\langle\boldsymbol{\psi}^T_{\mathtt{CG}}, \tau_T\boldsymbol{\psi}_{\mathtt{CG}}\right\rangle_{\Omega^e_{\mathtt{CG}}\cap\Gamma^I}
\end{aligned}
$$

C.2.4 NITSCHE-based coupling

The NITSCHE-based coupling of HDG and CG instead requires the addition of some terms in the global matrices $\left[\mathbf{K}_{33}\right]$ and $\left[\mathbf{K}_{44}\right]$ and the implementation of the coupling block $\left[\tilde{\mathbf{K}}_{34}\right]$ solely associated to the global DOFs on the interface. Such modified terms in (4.31) read

$$
\begin{aligned}
\left[\tilde{\mathbf{K}}_{33}\left\{1,1\right\}\right]_e &= +\left[\mathbf{K}_{33}\left\{1,1\right\}\right]_e \\
&\quad + \left\langle\widehat{\boldsymbol{\psi}}^T_{\mathtt{HDG}}, \frac{\gamma}{h}\widehat{\boldsymbol{\psi}}_{\mathtt{HDG}}\right\rangle_{\partial\Omega^e_{\mathtt{HDG}}\cap\Gamma^I} \\
\left[\tilde{\mathbf{K}}_{34}\left\{1,1\right\}\right]_e &= +\sum_{\mathtt{d}=1}^{\mathtt{n_{sd}}}\left\langle\widehat{\boldsymbol{\psi}}^T_{\mathtt{HDG}}, \kappa\left(-\boldsymbol{n}_{\mathtt{HDG}}\left\{\mathtt{d}\right\}\right)\boldsymbol{\nabla}\left\{\mathtt{d}\right\}\boldsymbol{\psi}_{\mathtt{CG}}\right\rangle_{\partial\Omega^e_{\mathtt{HDG}}\cap\Gamma^I} \\
&\quad - \left\langle\widehat{\boldsymbol{\psi}}^T_{\mathtt{HDG}}, \frac{\gamma}{h}\boldsymbol{\psi}_{\mathtt{CG}}\right\rangle_{\partial\Omega^e_{\mathtt{HDG}}\cap\Gamma^I} \\
\left[\tilde{\mathbf{K}}_{44}\left\{1,1\right\}\right]_e &= +\left[\mathbf{K}_{44}\left\{1,1\right\}\right]_e \\
&\quad - \sum_{\mathtt{d}=1}^{\mathtt{n_{sd}}}\left\langle\boldsymbol{\psi}^T_{\mathtt{CG}}, \kappa\boldsymbol{n}_{\mathtt{CG}}\left\{\mathtt{d}\right\}\boldsymbol{\nabla}\left\{\mathtt{d}\right\}\boldsymbol{\psi}_{\mathtt{CG}}\right\rangle_{\Omega^e_{\mathtt{CG}}\cap\Gamma^I} \\
&\quad - \sum_{\mathtt{d}=1}^{\mathtt{n_{sd}}}\left\langle\left(\kappa\boldsymbol{n}_{\mathtt{CG}}\left\{\mathtt{d}\right\}\boldsymbol{\nabla}\left\{\mathtt{d}\right\}\boldsymbol{\psi}_{\mathtt{CG}}\right)^T, \boldsymbol{\psi}_{\mathtt{CG}}\right\rangle_{\Omega^e_{\mathtt{CG}}\cap\Gamma^I} \\
&\quad + \left\langle\boldsymbol{\psi}^T_{\mathtt{CG}}, \frac{\gamma}{h}\boldsymbol{\psi}_{\mathtt{CG}}\right\rangle_{\Omega^e_{\mathtt{CG}}\cap\Gamma^I}
\end{aligned}
$$

C.3 HDG-CG formulations for FSI

In this section, the terms arising from the CG approximation of the structural equations are first recalled. Then, the elemental matrices and vectors appearing in the discrete form of the HDG-CG formulations for fluid-structure interaction in Chapter 5 are defined.

C.3.1 CG formulation for structural problems

The discretization of the structural problem is performed by means of the CG method, whereas the backward differentiation formula is adopted for the temporal integration. The elemental contributions to the stiffness matrix and the residual vector to be computed at the j-th NEWTON iteration to advance from the time step n to the time step $n+1$ are given by

$$\begin{aligned}
\big[\mathbf{K}_{uu}\left\{\mathtt{d},\mathtt{e}\right\}\big]_e^{n+1,\,j} &= +\,\delta_{\mathtt{d},\mathtt{e}}\left(\boldsymbol{\psi}_{\mathcal{S}}^T, \rho_{\mathcal{S}}\frac{\beta_0}{\Delta t^2}\boldsymbol{\psi}_{\mathcal{S}}\right)_{\Omega_{\mathcal{S}}^e} \\
&\quad + \sum_{\mathtt{f}=1}^{\mathtt{n_{sd}}}\sum_{\mathtt{g}=1}^{\mathtt{n_{sd}}}\left(\left(\boldsymbol{\nabla}\left\{\mathtt{f}\right\}\boldsymbol{\psi}_{\mathcal{S}}\right)^T, \left.\frac{\partial\left[\boldsymbol{P}_{\mathcal{S}}\left(\boldsymbol{\nabla}\boldsymbol{u}_{\mathcal{S}}\right)\right]\left\{\mathtt{d},\mathtt{f}\right\}}{\partial\left[\boldsymbol{F}_{\mathcal{S}}\left(\boldsymbol{\nabla}\boldsymbol{u}_{\mathcal{S}}\right)\right]\left\{\mathtt{e},\mathtt{g}\right\}}\right|_{\boldsymbol{\nabla}\boldsymbol{u}_{\mathcal{S}}^{n+1,\,j}}\boldsymbol{\nabla}\left\{\mathtt{g}\right\}\boldsymbol{\psi}_{\mathcal{S}}\right)_{\Omega_{\mathcal{S}}^e} \\
\big[\mathbf{f}_u\left\{\mathtt{d}\right\}\big]_e^{n+1,\,j} &= -\left(\boldsymbol{\psi}_{\mathcal{S}}^T, \rho_{\mathcal{S}}\left(\sum_{b=0}^{\mathrm{BDF}o+1}\frac{\beta_b}{\Delta t^2}\boldsymbol{u}_{\mathcal{S}}^{n+1-b}\left\{\mathtt{d}\right\}\right)\right)_{\Omega_{\mathcal{S}}^e} \\
&\quad - \sum_{\mathtt{e}=1}^{\mathtt{n_{sd}}}\left(\left(\boldsymbol{\nabla}\left\{\mathtt{e}\right\}\boldsymbol{\psi}_{\mathcal{S}}\right)^T, \left[\boldsymbol{P}_{\mathcal{S}}\left(\boldsymbol{\nabla}\boldsymbol{u}_{\mathcal{S}}^{n+1,\,j}\right)\right]\left\{\mathtt{d},\mathtt{e}\right\}\right)_{\Omega_{\mathcal{S}}^e} \\
&\quad + \left(\boldsymbol{\psi}_{\mathcal{S}}^T, \rho_{\mathcal{S}}\boldsymbol{b}_{\mathcal{S}}^{n+1}\left\{\mathtt{d}\right\}\right)_{\Omega_{\mathcal{S}}^e} \\
&\quad + \left\langle\boldsymbol{\psi}_{\mathcal{S}}^T, \boldsymbol{t}_{\mathcal{S}}^{N,\,n+1}\left\{\mathtt{d}\right\}\right\rangle_{\partial\Omega_{\mathcal{S}}^e\cap\Gamma_{\mathcal{S}}^N}
\end{aligned}$$

It is worth reminding that the first PIOLA–KIRCHHOFF stress tensor with size $\mathtt{n_{sd}}\times\mathtt{n_{sd}}$ is computed as a function of the displacement gradient, i.e. $\boldsymbol{P}_{\mathcal{S}} = \boldsymbol{P}_{\mathcal{S}}(\boldsymbol{\nabla}\boldsymbol{u}_{\mathcal{S}})$, according to equations (2.13), (2.14) and (2.15) and depending on the constitutive model adopted. In this thesis, both the ST. VENANT–KIRCHHOFF and the Neo-HOOKEan material models have been considered in the numerical studies. The derivative of the stress tensor with respect to the deformation gradient, i.e. $\partial\boldsymbol{P}_{\mathcal{S}}(\boldsymbol{\nabla}\boldsymbol{u}_{\mathcal{S}})/\partial\boldsymbol{F}_{\mathcal{S}}(\boldsymbol{\nabla}\boldsymbol{u}_{\mathcal{S}})$, has instead size $\mathtt{n_{sd}}\times\mathtt{n_{sd}}\times\mathtt{n_{sd}}\times\mathtt{n_{sd}}$ and is needed for the construction of the stiffness matrix in the structural problem and for the computation of a number of terms arising from the monolithic NITSCHE-based formulation for fluid-structure interaction in Section C.3.3. The resulting tensor is constant and solely contains the LAMÉ parameters in the linear case, whereas for the nonlinear models adopted here each component is a function of the deformation gradient (and therefore of the displacement gradient). Its derivation can be cumbersome and the symbolic math toolbox of `MATLAB` has been used for this purpose. In the following, the explicit definition of the first PIOLA–KIRCHHOFF stress tensor and its linearization is provided in the two-dimensional case for the aforementioned material models. The subscript $\odot_{\mathcal{S}}$ is omitted for the sake of readability.

ST. VENANT–KIRCHHOFF

$$\begin{aligned}
P_{xx} &= \mu\left[F_{xx}\left(F_{xx}^2+F_{yx}^2-1\right)+F_{xy}\left(F_{xx}F_{xy}+F_{yx}F_{yy}\right)\right]+\lambda F_{xx}\left(F_{xx}^2+F_{xy}^2+F_{yx}^2+F_{yy}^2-2\right)/2\\
P_{xy} &= \mu\left[F_{xy}\left(F_{xy}^2+F_{yy}^2-1\right)+F_{xx}\left(F_{xx}F_{xy}+F_{yx}F_{yy}\right)\right]+\lambda F_{xy}\left(F_{xx}^2+F_{xy}^2+F_{yx}^2+F_{yy}^2-2\right)/2\\
P_{yx} &= \mu\left[F_{yx}\left(F_{xx}^2+F_{yx}^2-1\right)+F_{yy}\left(F_{xx}F_{xy}+F_{yx}F_{yy}\right)\right]+\lambda F_{yx}\left(F_{xx}^2+F_{xy}^2+F_{yx}^2+F_{yy}^2-2\right)/2\\
P_{yy} &= \mu\left[F_{yy}\left(F_{xy}^2+F_{yy}^2-1\right)+F_{yx}\left(F_{xx}F_{xy}+F_{yx}F_{yy}\right)\right]+\lambda F_{yy}\left(F_{xx}^2+F_{xy}^2+F_{yx}^2+F_{yy}^2-2\right)/2
\end{aligned}$$

$$\begin{aligned}
\partial P_{xx}/\partial F_{xx} &= \mu\left(3F_{xx}^2+F_{xy}^2+F_{yx}^2-1\right)+\lambda\left(3F_{xx}^2+F_{xy}^2+F_{yx}^2+F_{yy}^2-2\right)/2\\
\partial P_{xx}/\partial F_{xy} &= \partial P_{xy}/\partial F_{xx} = \mu\left(2F_{xx}F_{xy}+F_{yx}F_{yy}\right)+\lambda F_{xx}F_{xy}\\
\partial P_{xx}/\partial F_{yx} &= \partial P_{yx}/\partial F_{xx} = \mu\left(2F_{xx}F_{yx}+F_{xy}F_{yy}\right)+\lambda F_{xx}F_{yx}\\
\partial P_{xx}/\partial F_{yy} &= \partial P_{yy}/\partial F_{xx} = \mu F_{xy}F_{yx}+\lambda F_{xx}F_{yy}\\
\partial P_{xy}/\partial F_{xy} &= \mu\left(F_{xx}^2+3F_{xy}^2+F_{yy}^2-1\right)+\lambda\left(F_{xx}^2+3F_{xy}^2+F_{yx}^2+F_{yy}^2-2\right)/2\\
\partial P_{xy}/\partial F_{yx} &= \partial P_{yx}/\partial F_{xy} = \mu F_{xx}F_{yy}+\lambda F_{xy}F_{yx}\\
\partial P_{xy}/\partial F_{yy} &= \partial P_{yy}/\partial F_{xy} = \mu\left(F_{xx}F_{yx}+2F_{xy}F_{yy}\right)+\lambda F_{xy}F_{yy}\\
\partial P_{yx}/\partial F_{yx} &= \mu\left(F_{xx}^2+3F_{yx}^2+F_{yy}^2-1\right)+\lambda\left(F_{xx}^2+F_{xy}^2+3F_{yx}^2+F_{yy}^2-2\right)/2\\
\partial P_{yx}/\partial F_{yy} &= \partial P_{yy}/\partial F_{yx} = \mu\left(F_{xx}F_{xy}+2F_{yx}F_{yy}\right)+\lambda F_{yx}F_{yy}\\
\partial P_{yy}/\partial F_{yy} &= \mu\left(F_{xy}^2+F_{yx}^2+3F_{yy}^2-1\right)+\lambda\left(F_{xx}^2+F_{xy}^2+F_{yx}^2+3F_{yy}^2-2\right)/2
\end{aligned}$$

Neo-HOOKE

$$\begin{aligned}
P_{xx} &= \mu\left(F_{xx}-F_{yy}/J\right)+\lambda F_{yy}\ln(J)/J\\
P_{xy} &= \mu\left(F_{xy}+F_{yx}/J\right)-\lambda F_{yx}\ln(J)/J\\
P_{yx} &= \mu\left(F_{yx}+F_{xy}/J\right)-\lambda F_{xy}\ln(J)/J\\
P_{yy} &= \mu\left(F_{yy}-F_{xx}/J\right)+\lambda F_{xx}\ln(J)/J
\end{aligned}$$

$$\begin{aligned}
\partial P_{xx}/\partial F_{xx} &= \mu\left(F_{yy}^2/J^2+1\right)+\lambda F_{yy}^2\left[1-\ln(J)\right]/J^2\\
\partial P_{xx}/\partial F_{xy} &= \partial P_{xy}/\partial F_{xx} = -\mu F_{yx}F_{yy}/J^2-\lambda F_{yx}F_{yy}\left[1-\ln(J)\right]/J^2\\
\partial P_{xx}/\partial F_{yx} &= \partial P_{yx}/\partial F_{xx} = -\mu F_{xy}F_{yy}/J^2-\lambda F_{xy}F_{yy}\left[1-\ln(J)\right]/J^2\\
\partial P_{xx}/\partial F_{yy} &= \partial P_{yy}/\partial F_{xx} = \mu\left(F_{xx}F_{yy}/J^2-1/J\right)+\lambda\left\{F_{xx}F_{yy}\left[1-\ln(J)\right]/J^2+\ln(J)/J\right\}\\
\partial P_{xy}/\partial F_{xy} &= \mu\left(F_{yx}^2/J^2+1\right)+\lambda F_{yx}^2\left[1-\ln(J)\right]/J^2\\
\partial P_{xy}/\partial F_{yx} &= \partial P_{yx}/\partial F_{xy} = \mu\left(F_{xy}F_{yx}/J^2+1/J\right)+\lambda\left\{F_{xy}F_{yx}\left[1-\ln(J)\right]/J^2-\ln(J)/J\right\}\\
\partial P_{xy}/\partial F_{yy} &= \partial P_{yy}/\partial F_{xy} = -\mu F_{xx}F_{yx}/J^2-\lambda F_{xx}F_{yx}\left[1-\ln(J)\right]/J^2\\
\partial P_{yx}/\partial F_{yx} &= \mu\left(F_{xy}^2/J^2+1\right)+\lambda F_{xy}^2\left[1-\ln(J)\right]/J^2\\
\partial P_{yx}/\partial F_{yy} &= \partial P_{yy}/\partial F_{yx} = -\mu F_{xx}F_{xy}/J^2-\lambda F_{xx}F_{xy}\left[1-\ln(J)\right]/J^2\\
\partial P_{yy}/\partial F_{yy} &= \mu\left(F_{xx}^2/J^2+1\right)+\lambda F_{xx}^2\left[1-\ln(J)\right]/J^2
\end{aligned}$$

$$J = F_{xx}F_{yy}-F_{xy}F_{yx}$$

C.3.2 Partitioned DIRICHLET–NEUMANN coupling

The partitioned DIRICHLET–NEUMANN scheme coupling HDG and CG discretizations for the solution of fluid-structure interaction problems is outlined in Section 5.2. Such strategy exchanges the coupling information by means of the interface vectors $\left[\bar{\mathbf{f}}_L^D\right]$, $\left[\bar{\mathbf{f}}_U^D\right]$ and $\left[\bar{\mathbf{f}}_u^N\right]$, with $\mathbf{U}_{\mathcal{F}}$ gathering the fluid density and momentum local DOFs. However, the suppression of the DOFs associated to the trace of the fluid momentum at the interface implies the modification of a number of terms in the fluid solver. By denoting with n the time step level, with i the coupling iteration index and with j the single-field NEWTON iteration, the elemental contributions to the modified terms in (5.12), (5.13) and (5.15) read

$$
\begin{aligned}
\left[\bar{\mathbf{K}}_{L\hat{\rho}}\left\{\mathtt{m},1\right\}\right]_e^{n+1,\,i,\,j} &= +\sum_{\mathtt{d}=1}^{\mathtt{n}_{\mathtt{sd}}}\sum_{\mathtt{n}=1}^{\mathtt{m}_{\mathtt{sd}}}\left\langle\left(\mathbf{N}_{\mathcal{F}}^T\left\{\mathtt{d},\mathtt{n}\right\}\mathbf{D}_{\mathcal{F}}^{1/2}\left\{\mathtt{n},\mathtt{m}\right\}\boldsymbol{\psi}_{\mathcal{F}}\right)^T,\right.\\
&\qquad\qquad\left.\frac{\widehat{\boldsymbol{\rho v}}_{\mathcal{F}}^{n+1,\,i,\,j}\left\{\mathtt{d}\right\}}{\left(\hat{\rho}_{\mathcal{F}}^{n+1,\,i,\,j}\right)^2}\widehat{\boldsymbol{\psi}}_{\mathcal{F}}\right\rangle_{\partial\Omega_{\mathcal{F}}^e\setminus\Gamma_{\mathcal{F}}^D\setminus\Gamma^I}\\
\left[\bar{\mathbf{K}}_{L\hat{w}}\left\{\mathtt{m},\mathtt{d}\right\}\right]_e^{n+1,\,i,\,j} &= -\sum_{\mathtt{n}=1}^{\mathtt{m}_{\mathtt{sd}}}\left\langle\left(\mathbf{N}_{\mathcal{F}}^T\left\{\mathtt{d},\mathtt{n}\right\}\mathbf{D}_{\mathcal{F}}^{1/2}\left\{\mathtt{n},\mathtt{m}\right\}\boldsymbol{\psi}_{\mathcal{F}}\right)^T,\frac{1}{\hat{\rho}_{\mathcal{F}}^{n+1,\,i,\,j}}\widehat{\boldsymbol{\psi}}_{\mathcal{F}}\right\rangle_{\partial\Omega_{\mathcal{F}}^e\setminus\Gamma_{\mathcal{F}}^D\setminus\Gamma^I}\\
\left[\bar{\mathbf{K}}_{\rho\hat{\rho}}\left\{1,1\right\}\right]_e^{n+1,\,i,\,j} &= -\sum_{\mathtt{d}=1}^{\mathtt{n}_{\mathtt{sd}}}\left\langle\boldsymbol{\psi}_{\mathcal{F}}^T,\left(\sum_{b=0}^{\mathrm{BDF}o}\frac{\alpha_b}{\Delta t}\boldsymbol{d}_{\mathcal{F}}^{n+1-b}\left\{\mathtt{d}\right\}\right)\boldsymbol{n}_{\mathcal{F}}\left\{\mathtt{d}\right\}\widehat{\boldsymbol{\psi}}_{\mathcal{F}}\right\rangle_{\partial\Omega_{\mathcal{F}}^e\setminus\Gamma_{\mathcal{F}}^D}\\
&\quad-\left\langle\boldsymbol{\psi}_{\mathcal{F}}^T,\tau_\rho\widehat{\boldsymbol{\psi}}_{\mathcal{F}}\right\rangle_{\partial\Omega_{\mathcal{F}}^e\setminus\Gamma_{\mathcal{F}}^D}\\
&\quad+\sum_{\mathtt{d}=1}^{\mathtt{n}_{\mathtt{sd}}}\left\langle\boldsymbol{\psi}_{\mathcal{F}}^T,\left(\sum_{b=0}^{\mathrm{BDF}o}\frac{\alpha_b}{\Delta t}\boldsymbol{u}_{\mathcal{S}}^{n+1-b}\left\{\mathtt{d}\right\}\right)\boldsymbol{n}_{\mathcal{F}}\left\{\mathtt{d}\right\}\widehat{\boldsymbol{\psi}}_{\mathcal{F}}\right\rangle_{\partial\Omega_{\mathcal{F}}^e\cap\Gamma^I}\\
\left[\bar{\mathbf{K}}_{\rho\hat{w}}\left\{1,\mathtt{d}\right\}\right]_e^{n+1,\,i,\,j} &= +\left\langle\boldsymbol{\psi}_{\mathcal{F}}^T,\boldsymbol{n}_{\mathcal{F}}\left\{\mathtt{d}\right\}\widehat{\boldsymbol{\psi}}_{\mathcal{F}}\right\rangle_{\partial\Omega_{\mathcal{F}}^e\setminus\Gamma_{\mathcal{F}}^D\setminus\Gamma^I}\\
\left[\bar{\mathbf{K}}_{w\hat{\rho}}\left\{\mathtt{d},1\right\}\right]_e^{n+1,\,i,\,j} &= -\sum_{\mathtt{e}=1}^{\mathtt{n}_{\mathtt{sd}}}\left\langle\boldsymbol{\psi}_{\mathcal{F}}^T,\widehat{\boldsymbol{\rho v}}_{\mathcal{F}}^{n+1,\,i,\,j}\left\{\mathtt{d}\right\}\frac{\widehat{\boldsymbol{\rho v}}_{\mathcal{F}}^{n+1,\,i,\,j}\left\{\mathtt{e}\right\}}{\left(\hat{\rho}_{\mathcal{F}}^{n+1,\,i,\,j}\right)^2}\boldsymbol{n}_{\mathcal{F}}\left\{\mathtt{e}\right\}\widehat{\boldsymbol{\psi}}_{\mathcal{F}}\right\rangle_{\partial\Omega_{\mathcal{F}}^e\setminus\Gamma_{\mathcal{F}}^D\setminus\Gamma^I}\\
&\quad+\sum_{\mathtt{e}=1}^{\mathtt{n}_{\mathtt{sd}}}\left\langle\boldsymbol{\psi}_{\mathcal{F}}^T,\left(\sum_{b=0}^{\mathrm{BDF}o}\frac{\alpha_b}{\Delta t}\boldsymbol{u}_{\mathcal{S}}^{n+1-b}\left\{\mathtt{d}\right\}\boldsymbol{u}_{\mathcal{S}}^{n+1-b}\left\{\mathtt{e}\right\}\right)\boldsymbol{n}_{\mathcal{F}}\left\{\mathtt{e}\right\}\widehat{\boldsymbol{\psi}}_{\mathcal{F}}\right\rangle_{\partial\Omega_{\mathcal{F}}^e\cap\Gamma^I}\\
&\quad-\sum_{\mathtt{e}=1}^{\mathtt{n}_{\mathtt{sd}}}\left\langle\boldsymbol{\psi}_{\mathcal{F}}^T,\left(\sum_{b=0}^{\mathrm{BDF}o}\frac{\alpha_b}{\Delta t}\boldsymbol{u}_{\mathcal{S}}^{n+1-b}\left\{\mathtt{d}\right\}\boldsymbol{d}_{\mathcal{F}}^{n+1-b}\left\{\mathtt{e}\right\}\right)\boldsymbol{n}_{\mathcal{F}}\left\{\mathtt{e}\right\}\widehat{\boldsymbol{\psi}}_{\mathcal{F}}\right\rangle_{\partial\Omega_{\mathcal{F}}^e\cap\Gamma^I}\\
&\quad-\left\langle\boldsymbol{\psi}_{\mathcal{F}}^T,\tau_{\rho v}\left(\sum_{b=0}^{\mathrm{BDF}o}\frac{\alpha_b}{\Delta t}\boldsymbol{u}_{\mathcal{S}}^{n+1-b}\left\{\mathtt{d}\right\}\right)\widehat{\boldsymbol{\psi}}_{\mathcal{F}}\right\rangle_{\partial\Omega_{\mathcal{F}}^e\cap\Gamma^I}\\
\left[\bar{\mathbf{K}}_{w\hat{w}}\left\{\mathtt{d},\mathtt{e}\right\}\right]_e^{n+1,\,i,\,j} &= +\delta_{\mathtt{d},\mathtt{e}}\sum_{\mathtt{f}=1}^{\mathtt{n}_{\mathtt{sd}}}\left\langle\boldsymbol{\psi}_{\mathcal{F}}^T,\frac{\widehat{\boldsymbol{\rho v}}_{\mathcal{F}}^{n+1,\,i,\,j}\left\{\mathtt{f}\right\}}{\hat{\rho}_{\mathcal{F}}^{n+1,\,i,\,j}}\boldsymbol{n}_{\mathcal{F}}\left\{\mathtt{f}\right\}\widehat{\boldsymbol{\psi}}_{\mathcal{F}}\right\rangle_{\partial\Omega_{\mathcal{F}}^e\setminus\Gamma_{\mathcal{F}}^D\setminus\Gamma^I}
\end{aligned}
$$

$$
\begin{aligned}
&- \delta_{\mathtt{d},\mathtt{e}} \sum_{\mathtt{f}=1}^{\mathtt{n}_{\mathtt{sd}}} \left\langle \boldsymbol{\psi}_{\mathcal{F}}^{T}, \left(\sum_{b=0}^{\mathrm{BDF}o} \frac{\alpha_b}{\Delta t} \boldsymbol{d}_{\mathcal{F}}^{n+1-b}\{\mathtt{f}\} \right) \boldsymbol{n}_{\mathcal{F}}\{\mathtt{f}\}\, \widehat{\boldsymbol{\psi}}_{\mathcal{F}} \right\rangle_{\partial\Omega^e_{\mathcal{F}}\setminus\Gamma^D_{\mathcal{F}}\setminus\Gamma^I} \\
&+ \left\langle \boldsymbol{\psi}_{\mathcal{F}}^{T}, \frac{\widehat{\boldsymbol{\rho v}}_{\mathcal{F}}^{n+1,\,i,\,j}\{\mathtt{d}\}}{\hat{\rho}_{\mathcal{F}}^{n+1,\,i,\,j}} \boldsymbol{n}_{\mathcal{F}}\{\mathtt{e}\}\, \widehat{\boldsymbol{\psi}}_{\mathcal{F}} \right\rangle_{\partial\Omega^e_{\mathcal{F}}\setminus\Gamma^D_{\mathcal{F}}\setminus\Gamma^I} \\
&- \delta_{\mathtt{d},\mathtt{e}} \left\langle \boldsymbol{\psi}_{\mathcal{F}}^{T}, \tau_{\rho v} \widehat{\boldsymbol{\psi}}_{\mathcal{F}} \right\rangle_{\partial\Omega^e_{\mathcal{F}}\setminus\Gamma^D_{\mathcal{F}}\setminus\Gamma^I}
\end{aligned}
$$

$$
\left[\bar{\mathbf{K}}_{\hat{w}L}\{\mathtt{d},\mathtt{m}\}\right]_e^{n+1,\,i,\,j} = - \sum_{\mathtt{n}=1}^{\mathtt{m}_{\mathtt{sd}}} \left\langle \widehat{\boldsymbol{\psi}}_{\mathcal{F}}^{T}, \mathbf{N}_{\mathcal{F}}^{T}\{\mathtt{d},\mathtt{n}\}\, \mathbf{D}_{\mathcal{F}}^{1/2}\{\mathtt{n},\mathtt{m}\}\, \boldsymbol{\psi}_{\mathcal{F}} \right\rangle_{\partial\Omega^e_{\mathcal{F}}\setminus\Gamma^D_{\mathcal{F}}\setminus\Gamma^I}
$$

$$
\left[\bar{\mathbf{K}}_{\hat{w}w}\{\mathtt{d},\mathtt{e}\}\right]_e^{n+1,\,i,\,j} = - \delta_{\mathtt{d},\mathtt{e}} \left\langle \widehat{\boldsymbol{\psi}}_{\mathcal{F}}^{T}, \tau_{\rho v} \boldsymbol{\psi}_{\mathcal{F}} \right\rangle_{\partial\Omega^e_{\mathcal{F}}\setminus\Gamma^D_{\mathcal{F}}\setminus\Gamma^I}
$$

$$
\left[\bar{\mathbf{K}}_{\hat{w}\hat{\rho}}\{\mathtt{d},1\}\right]_e^{n+1,\,i,\,j} = - \left\langle \widehat{\boldsymbol{\psi}}_{\mathcal{F}}^{T}, \left.\frac{\partial p_{\mathcal{F}}\left(\hat{\rho}_{\mathcal{F}}\right)}{\partial \hat{\rho}_{\mathcal{F}}}\right|_{\hat{\rho}_{\mathcal{F}}^{n+1,\,i,\,j}} \boldsymbol{n}_{\mathcal{F}}\{\mathtt{d}\}\, \widehat{\boldsymbol{\psi}}_{\mathcal{F}} \right\rangle_{\partial\Omega^e_{\mathcal{F}}\setminus\Gamma^D_{\mathcal{F}}\setminus\Gamma^I}
$$

$$
\left[\bar{\mathbf{K}}_{\hat{w}\hat{w}}\{\mathtt{d},\mathtt{e}\}\right]_e^{n+1,\,i,\,j} = + \delta_{\mathtt{d},\mathtt{e}} \left\langle \widehat{\boldsymbol{\psi}}_{\mathcal{F}}^{T}, \tau_{\rho v} \widehat{\boldsymbol{\psi}}_{\mathcal{F}} \right\rangle_{\partial\Omega^e_{\mathcal{F}}\setminus\Gamma^D_{\mathcal{F}}\setminus\Gamma^I}
$$

$$
\begin{aligned}
\left[\bar{\mathbf{f}}_{L}\{\mathtt{m}\}\right]_e^{n+1,\,i,\,j} = &+ \left(\boldsymbol{\psi}_{\mathcal{F}}^{T}, \boldsymbol{L}_{\mathcal{F}}^{n+1,\,i,\,j}\{\mathtt{m}\}\right)_{\Omega^e} \\
&- \sum_{\mathtt{d}=1}^{\mathtt{n}_{\mathtt{sd}}} \sum_{\mathtt{n}=1}^{\mathtt{m}_{\mathtt{sd}}} \left(\left(\boldsymbol{\nabla}_{\mathtt{S}}^{T}\{\mathtt{d},\mathtt{n}\}\, \mathbf{D}_{\mathcal{F}}^{1/2}\{\mathtt{n},\mathtt{m}\}\, \boldsymbol{\psi}_{\mathcal{F}}\right)^{T}, \frac{\boldsymbol{\rho v}_{\mathcal{F}}^{n+1,\,i,\,j}\{\mathtt{d}\}}{\rho_{\mathcal{F}}^{n+1,\,i,\,j}} \right)_{\Omega^e_{\mathcal{F}}} \\
&+ \sum_{\mathtt{d}=1}^{\mathtt{n}_{\mathtt{sd}}} \sum_{\mathtt{n}=1}^{\mathtt{m}_{\mathtt{sd}}} \left\langle \left(\mathbf{N}_{\mathcal{F}}^{T}\{\mathtt{d},\mathtt{n}\}\, \mathbf{D}_{\mathcal{F}}^{1/2}\{\mathtt{n},\mathtt{m}\}\, \boldsymbol{\psi}_{\mathcal{F}}\right)^{T}, \frac{\boldsymbol{\rho v}_{\mathcal{F}}^{D,\,n+1}\{\mathtt{d}\}}{\rho_{\mathcal{F}}^{D,\,n+1}} \right\rangle_{\partial\Omega^e_{\mathcal{F}}\cap\Gamma^D_{\mathcal{F}}} \\
&+ \sum_{\mathtt{d}=1}^{\mathtt{n}_{\mathtt{sd}}} \sum_{\mathtt{n}=1}^{\mathtt{m}_{\mathtt{sd}}} \left\langle \left(\mathbf{N}_{\mathcal{F}}^{T}\{\mathtt{d},\mathtt{n}\}\, \mathbf{D}_{\mathcal{F}}^{1/2}\{\mathtt{n},\mathtt{m}\}\, \boldsymbol{\psi}_{\mathcal{F}}\right)^{T}, \frac{\widehat{\boldsymbol{\rho v}}_{\mathcal{F}}^{n+1,\,i,\,j}\{\mathtt{d}\}}{\hat{\rho}_{\mathcal{F}}^{n+1,\,i,\,j}} \right\rangle_{\partial\Omega^e_{\mathcal{F}}\setminus\Gamma^D_{\mathcal{F}}\setminus\Gamma^I}
\end{aligned}
$$

$$
\begin{aligned}
\left[\bar{\mathbf{f}}_{\rho}\{1\}\right]_e^{n+1,\,i,\,j} = &- \left(\boldsymbol{\psi}_{\mathcal{F}}^{T}, \sum_{b=0}^{\mathrm{BDF}o} \frac{\alpha_b}{\Delta t} \rho_{\mathcal{F}}^{n+1-b}\right)_{\Omega^e_{\mathcal{F}}} \\
&- \sum_{\mathtt{d}=1}^{\mathtt{n}_{\mathtt{sd}}} \left(\boldsymbol{\psi}_{\mathcal{F}}^{T}, \rho_{\mathcal{F}}^{n+1,\,i,\,j} \boldsymbol{\nabla}\{\mathtt{d}\} \left(\sum_{b=0}^{\mathrm{BDF}o} \frac{\alpha_b}{\Delta t} \boldsymbol{d}_{\mathcal{F}}^{n+1-b}\{\mathtt{d}\}\right)\right)_{\Omega^e_{\mathcal{F}}} \\
&+ \sum_{\mathtt{d}=1}^{\mathtt{n}_{\mathtt{sd}}} \left(\left(\boldsymbol{\nabla}\{\mathtt{d}\}\, \boldsymbol{\psi}_{\mathcal{F}}\right)^{T}, \boldsymbol{\rho v}_{\mathcal{F}}^{n+1,\,i,\,j}\{\mathtt{d}\}\right)_{\Omega^e} \\
&- \sum_{\mathtt{d}=1}^{\mathtt{n}_{\mathtt{sd}}} \left(\left(\boldsymbol{\nabla}\{\mathtt{d}\}\, \boldsymbol{\psi}_{\mathcal{F}}\right)^{T}, \rho_{\mathcal{F}}^{n+1,\,i,\,j} \left(\sum_{b=0}^{\mathrm{BDF}o} \frac{\alpha_b}{\Delta t} \boldsymbol{d}_{\mathcal{F}}^{n+1-b}\{\mathtt{d}\}\right)\right)_{\Omega^e_{\mathcal{F}}} \\
&- \left\langle \boldsymbol{\psi}_{\mathcal{F}}^{T}, \tau_{\rho} \rho_{\mathcal{F}}^{n+1,\,i,\,j} \right\rangle_{\partial\Omega^e_{\mathcal{F}}} \\
&- \sum_{\mathtt{d}=1}^{\mathtt{n}_{\mathtt{sd}}} \left\langle \boldsymbol{\psi}_{\mathcal{F}}^{T}, \boldsymbol{\rho v}_{\mathcal{F}}^{D,\,n+1}\{\mathtt{d}\}\, \boldsymbol{n}_{\mathcal{F}}\{\mathtt{d}\} \right\rangle_{\partial\Omega^e_{\mathcal{F}}\cap\Gamma^D_{\mathcal{F}}}
\end{aligned}
$$

$$
\begin{aligned}
&+ \sum_{\mathtt{d}=1}^{\mathtt{n}_{\mathtt{sd}}} \left\langle \boldsymbol{\psi}_{\mathcal{F}}^{T}, \rho_{\mathcal{F}}^{D,\,n+1} \left(\sum_{b=0}^{\mathrm{BDF}o} \frac{\alpha_b}{\Delta t} \boldsymbol{d}_{\mathcal{F}}^{n+1-b} \{\mathtt{d}\} \right) \boldsymbol{n}_{\mathcal{F}} \{\mathtt{d}\} \right\rangle_{\partial\Omega_{\mathcal{F}}^{e} \cap \Gamma_{\mathcal{F}}^{D}} \\
&+ \left\langle \boldsymbol{\psi}_{\mathcal{F}}^{T}, \tau_{\rho} \rho_{\mathcal{F}}^{D,\,n+1} \right\rangle_{\partial\Omega_{\mathcal{F}}^{e} \cap \Gamma_{\mathcal{F}}^{D}} \\
&- \sum_{\mathtt{d}=1}^{\mathtt{n}_{\mathtt{sd}}} \left\langle \boldsymbol{\psi}_{\mathcal{F}}^{T}, \widehat{\boldsymbol{\rho v}}_{\mathcal{F}}^{n+1,\,i,\,j} \{\mathtt{d}\}\, \boldsymbol{n}_{\mathcal{F}} \{\mathtt{d}\} \right\rangle_{\partial\Omega_{\mathcal{F}}^{e} \setminus \Gamma_{\mathcal{F}}^{D} \setminus \Gamma^{I}} \\
&+ \sum_{\mathtt{d}=1}^{\mathtt{n}_{\mathtt{sd}}} \left\langle \boldsymbol{\psi}_{\mathcal{F}}^{T}, \hat{\rho}_{\mathcal{F}}^{n+1,\,i,\,j} \left(\sum_{b=0}^{\mathrm{BDF}o} \frac{\alpha_b}{\Delta t} \boldsymbol{d}_{\mathcal{F}}^{n+1-b} \{\mathtt{d}\} \right) \boldsymbol{n}_{\mathcal{F}} \{\mathtt{d}\} \right\rangle_{\partial\Omega_{\mathcal{F}}^{e} \setminus \Gamma_{\mathcal{F}}^{D}} \\
&+ \left\langle \boldsymbol{\psi}_{\mathcal{F}}^{T}, \tau_{\rho} \hat{\rho}_{\mathcal{F}}^{n+1,\,i,\,j} \right\rangle_{\partial\Omega_{\mathcal{F}}^{e} \setminus \Gamma_{\mathcal{F}}^{D}}
\end{aligned}
$$

$$
\begin{aligned}
\left[\bar{\mathbf{f}}_{w} \{\mathtt{d}\} \right]_{e}^{n+1,\,i,\,j} = &- \left(\boldsymbol{\psi}_{\mathcal{F}}^{T}, \sum_{b=0}^{\mathrm{BDF}o} \frac{\alpha_b}{\Delta t} \boldsymbol{\rho v}_{\mathcal{F}}^{n+1-b} \{\mathtt{d}\} \right)_{\Omega_{\mathcal{F}}^{e}} \\
&- \sum_{\mathtt{e}=1}^{\mathtt{n}_{\mathtt{sd}}} \left(\boldsymbol{\psi}_{\mathcal{F}}^{T}, \boldsymbol{\rho v}_{\mathcal{F}}^{n+1,\,i,\,j} \{\mathtt{d}\}\, \boldsymbol{\nabla} \{\mathtt{e}\} \left(\sum_{b=0}^{\mathrm{BDF}o} \frac{\alpha_b}{\Delta t} \boldsymbol{d}_{\mathcal{F}}^{n+1-b} \{\mathtt{e}\} \right) \right)_{\Omega_{\mathcal{F}}^{e}} \\
&+ \sum_{\mathtt{e}=1}^{\mathtt{n}_{\mathtt{sd}}} \left(\left(\boldsymbol{\nabla} \{\mathtt{e}\}\, \boldsymbol{\psi}_{\mathcal{F}} \right)^{T}, \boldsymbol{\rho v}_{\mathcal{F}}^{n+1,\,i,\,j} \{\mathtt{d}\} \frac{\boldsymbol{\rho v}_{\mathcal{F}}^{n+1,\,i,\,j} \{\mathtt{e}\}}{\rho_{\mathcal{F}}^{n+1,\,i,\,j}} \right)_{\Omega_{\mathcal{F}}^{e}} \\
&- \sum_{\mathtt{e}=1}^{\mathtt{n}_{\mathtt{sd}}} \left(\left(\boldsymbol{\nabla} \{\mathtt{e}\}\, \boldsymbol{\psi}_{\mathcal{F}} \right)^{T}, \boldsymbol{\rho v}_{\mathcal{F}}^{n+1,\,i,\,j} \{\mathtt{d}\} \left(\sum_{b=0}^{\mathrm{BDF}o} \frac{\alpha_b}{\Delta t} \boldsymbol{d}_{\mathcal{F}}^{n+1-b} \{\mathtt{e}\} \right) \right)_{\Omega_{\mathcal{F}}^{e}} \\
&- \sum_{\mathtt{m}=1}^{\mathtt{m}_{\mathtt{sd}}} \sum_{\mathtt{n}=1}^{\mathtt{m}_{\mathtt{sd}}} \left(\boldsymbol{\psi}_{\mathcal{F}}^{T}, \boldsymbol{\nabla}_{\mathtt{S}}^{T} \{\mathtt{d}, \mathtt{n}\}\, \mathbf{D}_{\mathcal{F}}^{1/2} \{\mathtt{n}, \mathtt{m}\}\, \boldsymbol{L}_{\mathcal{F}}^{n+1,\,i,\,j} \{\mathtt{m}\} \right)_{\Omega_{\mathcal{F}}^{e}} \\
&- \left(\boldsymbol{\psi}_{\mathcal{F}}^{T}, \boldsymbol{\nabla} \{\mathtt{d}\}\, p_{\mathcal{F}} \left(\rho_{\mathcal{F}}^{n+1,\,i,\,j} \right) \right)_{\Omega_{\mathcal{F}}^{e}} \\
&- \left\langle \boldsymbol{\psi}_{\mathcal{F}}^{T}, \tau_{\rho v} \boldsymbol{\rho v}_{\mathcal{F}}^{n+1,\,i,\,j} \{\mathtt{d}\} \right\rangle_{\partial\Omega_{\mathcal{F}}^{e}} \\
&+ \left(\boldsymbol{\psi}_{\mathcal{F}}^{T}, \rho_{\mathcal{F}}^{n+1,\,i,\,j} \boldsymbol{b}_{\mathcal{F}}^{n+1} \{\mathtt{d}\} \right)_{\Omega_{\mathcal{F}}^{e}} \\
&- \sum_{\mathtt{e}=1}^{\mathtt{n}_{\mathtt{sd}}} \left\langle \boldsymbol{\psi}_{\mathcal{F}}^{T}, \boldsymbol{\rho v}_{\mathcal{F}}^{D,\,n+1} \{\mathtt{d}\} \frac{\boldsymbol{\rho v}_{\mathcal{F}}^{D,\,n+1} \{\mathtt{e}\}}{\rho_{\mathcal{F}}^{D,\,n+1}} \boldsymbol{n}_{\mathcal{F}} \{\mathtt{e}\} \right\rangle_{\partial\Omega_{\mathcal{F}}^{e} \cap \Gamma_{\mathcal{F}}^{D}} \\
&+ \sum_{\mathtt{e}=1}^{\mathtt{n}_{\mathtt{sd}}} \left\langle \boldsymbol{\psi}_{\mathcal{F}}^{T}, \boldsymbol{\rho v}_{\mathcal{F}}^{D,\,n+1} \{\mathtt{d}\} \left(\sum_{b=0}^{\mathrm{BDF}o} \frac{\alpha_b}{\Delta t} \boldsymbol{d}_{\mathcal{F}}^{n+1-b} \{\mathtt{e}\} \right) \boldsymbol{n}_{\mathcal{F}} \{\mathtt{e}\} \right\rangle_{\partial\Omega_{\mathcal{F}}^{e} \cap \Gamma_{\mathcal{F}}^{D}} \\
&+ \left\langle \boldsymbol{\psi}_{\mathcal{F}}^{T}, \tau_{\rho v} \boldsymbol{\rho v}_{\mathcal{F}}^{D,\,n+1} \{\mathtt{d}\} \right\rangle_{\partial\Omega_{\mathcal{F}}^{e} \cap \Gamma_{\mathcal{F}}^{D}} \\
&- \sum_{\mathtt{e}=1}^{\mathtt{n}_{\mathtt{sd}}} \left\langle \boldsymbol{\psi}_{\mathcal{F}}^{T}, \widehat{\boldsymbol{\rho v}}_{\mathcal{F}}^{n+1,\,i,\,j} \{\mathtt{d}\} \frac{\widehat{\boldsymbol{\rho v}}_{\mathcal{F}}^{n+1,\,i,\,j} \{\mathtt{e}\}}{\hat{\rho}_{\mathcal{F}}^{n+1,\,i,\,j}} \boldsymbol{n}_{\mathcal{F}} \{\mathtt{e}\} \right\rangle_{\partial\Omega_{\mathcal{F}}^{e} \setminus \Gamma_{\mathcal{F}}^{D} \setminus \Gamma^{I}}
\end{aligned}
$$

$$
\begin{aligned}
&+\sum_{\mathtt{e}=1}^{\mathtt{n_{sd}}}\left\langle \boldsymbol{\psi}_{\mathcal{F}}^{T}, \widehat{\boldsymbol{\rho\upsilon}}_{\mathcal{F}}^{n+1,\,i,\,j}\left\{\mathtt{d}\right\}\left(\sum_{b=0}^{\mathrm{BDF}o}\frac{\alpha_b}{\Delta t}\boldsymbol{d}_{\mathcal{F}}^{n+1-b}\left\{\mathtt{e}\right\}\right)\boldsymbol{n}_{\mathcal{F}}\left\{\mathtt{e}\right\}\right\rangle_{\partial\Omega_{\mathcal{F}}^{e}\setminus\Gamma_{\mathcal{F}}^{D}\setminus\Gamma^{I}}\\
&+\left\langle \boldsymbol{\psi}_{\mathcal{F}}^{T}, \tau_{\rho\upsilon}\widehat{\boldsymbol{\rho\upsilon}}_{\mathcal{F}}^{n+1,\,i,\,j}\left\{\mathtt{d}\right\}\right\rangle_{\partial\Omega_{\mathcal{F}}^{e}\setminus\Gamma_{\mathcal{F}}^{D}\setminus\Gamma^{I}}
\end{aligned}
$$

$$
\begin{aligned}
\left[\bar{\mathbf{f}}_{\hat{w}}\left\{\mathtt{d}\right\}\right]_{e}^{n+1,\,i,\,j} =&+\sum_{\mathtt{m}=1}^{\mathtt{m_{sd}}}\sum_{\mathtt{n}=1}^{\mathtt{m_{sd}}}\left\langle \widehat{\boldsymbol{\psi}}^{T}, \mathbf{N}_{\mathcal{F}}^{T}\left\{\mathtt{d},\mathtt{n}\right\}\mathbf{D}_{\mathcal{F}}^{1/2}\left\{\mathtt{n},\mathtt{m}\right\}\boldsymbol{L}_{\mathcal{F}}^{n+1\,i,\,j}\left\{\mathtt{m}\right\}\right\rangle_{\partial\Omega_{\mathcal{F}}^{e}\setminus\Gamma_{\mathcal{F}}^{D}\setminus\Gamma^{I}}\\
&+\left\langle \widehat{\boldsymbol{\psi}}^{T}, p_{\mathcal{F}}\left(\hat{\rho}_{\mathcal{F}}^{n+1\,i,\,j}\right)\boldsymbol{n}\left\{\mathtt{d}\right\}\right\rangle_{\partial\Omega_{\mathcal{F}}^{e}\setminus\Gamma_{\mathcal{F}}^{D}\setminus\Gamma^{I}}\\
&+\left\langle \widehat{\boldsymbol{\psi}}^{T}, \tau_{\rho\upsilon}\left(\boldsymbol{\rho\upsilon}_{\mathcal{F}}^{n+1\,i,\,j}\left\{\mathtt{d}\right\}-\widehat{\boldsymbol{\rho\upsilon}}_{\mathcal{F}}^{n+1\,i,\,j}\left\{\mathtt{d}\right\}\right)\right\rangle_{\partial\Omega_{\mathcal{F}}^{e}\setminus\Gamma_{\mathcal{F}}^{D}\setminus\Gamma^{I}}\\
&+\left\langle \widehat{\boldsymbol{\psi}}^{T}, \boldsymbol{t}_{\mathcal{F}}^{N,\,n+1}\left\{\mathtt{d}\right\}\right\rangle_{\partial\Omega_{\mathcal{F}}^{e}\cap\Gamma_{\mathcal{F}}^{N}}
\end{aligned}
$$

$$
\left[\bar{\mathbf{f}}_{L}^{D}\left\{\mathtt{m}\right\}\right]_{e}^{n+1,\,i,\,j} =+\sum_{\mathtt{d}=1}^{\mathtt{n_{sd}}}\sum_{\mathtt{n}=1}^{\mathtt{m_{sd}}}\left\langle \left(\mathbf{N}_{\mathcal{F}}^{T}\left\{\mathtt{d},\mathtt{n}\right\}\mathbf{D}_{\mathcal{F}}^{1/2}\left\{\mathtt{n},\mathtt{m}\right\}\boldsymbol{\psi}_{\mathcal{F}}\right)^{T}, \sum_{b=0}^{\mathrm{BDF}o}\frac{\alpha_b}{\Delta t}\boldsymbol{u}_{\mathcal{S}}^{n+1-b}\left\{\mathtt{d}\right\}\right\rangle_{\partial\Omega_{\mathcal{F}}^{e}\cap\Gamma^{I}}
$$

$$
\left[\bar{\mathbf{f}}_{\rho}^{D}\left\{1\right\}\right]_{e}^{n+1,\,i,\,j} =-\sum_{\mathtt{d}=1}^{\mathtt{n_{sd}}}\left\langle \boldsymbol{\psi}_{\mathcal{F}}^{T}, \hat{\rho}_{\mathcal{F}}^{n+1,\,i,\,j}\left(\sum_{b=0}^{\mathrm{BDF}o}\frac{\alpha_b}{\Delta t}\boldsymbol{u}_{\mathcal{S}}^{n+1-b}\left\{\mathtt{d}\right\}\right)\boldsymbol{n}_{\mathcal{F}}\left\{\mathtt{d}\right\}\right\rangle_{\partial\Omega_{\mathcal{F}}^{e}\cap\Gamma^{I}}
$$

$$
\begin{aligned}
\left[\bar{\mathbf{f}}_{w}^{D}\left\{\mathtt{d}\right\}\right]_{e}^{n+1,\,i,\,j} =&-\sum_{\mathtt{e}=1}^{\mathtt{n_{sd}}}\left\langle \boldsymbol{\psi}_{\mathcal{F}}^{T}, \hat{\rho}_{\mathcal{F}}^{n+1,\,i,\,j}\left(\sum_{b=0}^{\mathrm{BDF}o}\frac{\alpha_b}{\Delta t}\boldsymbol{u}_{\mathcal{S}}^{n+1-b}\left\{\mathtt{d}\right\}\boldsymbol{u}_{\mathcal{S}}^{n+1-b}\left\{\mathtt{e}\right\}\right)\boldsymbol{n}_{\mathcal{F}}\left\{\mathtt{e}\right\}\right\rangle_{\partial\Omega_{\mathcal{F}}^{e}\cap\Gamma^{I}}\\
&+\sum_{\mathtt{e}=1}^{\mathtt{n_{sd}}}\left\langle \boldsymbol{\psi}_{\mathcal{F}}^{T}, \hat{\rho}_{\mathcal{F}}^{n+1,\,i,\,j}\left(\sum_{b=0}^{\mathrm{BDF}o}\frac{\alpha_b}{\Delta t}\boldsymbol{u}_{\mathcal{S}}^{n+1-b}\left\{\mathtt{d}\right\}\boldsymbol{d}_{\mathcal{F}}^{n+1-b}\left\{\mathtt{e}\right\}\right)\boldsymbol{n}_{\mathcal{F}}\left\{\mathtt{e}\right\}\right\rangle_{\partial\Omega_{\mathcal{F}}^{e}\cap\Gamma^{I}}\\
&+\left\langle \boldsymbol{\psi}_{\mathcal{F}}^{T}, \tau_{\rho\upsilon}\hat{\rho}_{\mathcal{F}}^{n+1,\,i,\,j}\left(\sum_{b=0}^{\mathrm{BDF}o}\frac{\alpha_b}{\Delta t}\boldsymbol{u}_{\mathcal{S}}^{n+1-b}\left\{\mathtt{d}\right\}\right)\right\rangle_{\partial\Omega_{\mathcal{F}}^{e}\cap\Gamma^{I}}
\end{aligned}
$$

$$
\begin{aligned}
\left[\bar{\mathbf{f}}_{u}^{N}\left\{\mathtt{d}\right\}\right]_{e}^{n+1,\,i,\,j} =&+\sum_{\mathtt{e}=1}^{\mathtt{n_{sd}}}\sum_{\mathtt{f}=1}^{\mathtt{n_{sd}}}\Big\langle \boldsymbol{\psi}_{\mathcal{S}}^{T}, \left|\boldsymbol{F}_{\mathcal{F}}\left(\boldsymbol{\nabla}\boldsymbol{d}_{\mathcal{F}}^{n+1,\,i}\right)\right|\left[\mathrm{V}^{-1}\left(\mathbf{D}_{\mathcal{F}}^{1/2}\boldsymbol{L}_{\mathcal{F}}^{n+1,\,i}\right)\right]\left\{\mathtt{d},\mathtt{e}\right\}\\
&\qquad\qquad\cdot\left[\boldsymbol{F}_{\mathcal{F}}\left(\boldsymbol{\nabla}\boldsymbol{d}_{\mathcal{F}}^{n+1,\,i}\right)\right]^{-T}\left\{\mathtt{e},\mathtt{f}\right\}\left(-\boldsymbol{n}_{\mathcal{S}}\left\{\mathtt{f}\right\}\right)\Big\rangle_{\partial\Omega_{\mathcal{S}}^{e}\cap\Gamma^{I}}\\
&+\sum_{\mathtt{e}=1}^{\mathtt{n_{sd}}}\Big\langle \boldsymbol{\psi}_{\mathcal{S}}^{T}, \left|\boldsymbol{F}_{\mathcal{F}}\left(\boldsymbol{\nabla}\boldsymbol{d}_{\mathcal{F}}^{n+1,\,i}\right)\right|p_{\mathcal{F}}\left(\hat{\rho}_{\mathcal{F}}^{n+1,\,i}\right)\\
&\qquad\qquad\cdot\left[\boldsymbol{F}_{\mathcal{F}}\left(\boldsymbol{\nabla}\boldsymbol{d}_{\mathcal{F}}^{n+1,\,i}\right)\right]^{-T}\left\{\mathtt{d},\mathtt{e}\right\}\left(-\boldsymbol{n}_{\mathcal{S}}\left\{\mathtt{e}\right\}\right)\Big\rangle_{\partial\Omega_{\mathcal{S}}^{e}\cap\Gamma^{I}}\\
&+\left\langle \boldsymbol{\psi}_{\mathcal{S}}^{T}, \tau_{\rho\upsilon}\left[\boldsymbol{\rho\upsilon}_{\mathcal{F}}^{n+1,\,i}\left\{\mathtt{d}\right\}-\hat{\rho}_{\mathcal{F}}^{n+1,\,i}\left(\sum_{b=0}^{\mathrm{BDF}o}\frac{\alpha_b}{\Delta t}\boldsymbol{u}_{\mathcal{S}}^{n+1-b}\left\{\mathtt{d}\right\}\right)\right]\right\rangle_{\partial\Omega_{\mathcal{S}}^{e}\cap\Gamma^{I}}
\end{aligned}
$$

C.3.3 Monolithic NITSCHE-based coupling

The monolithic HDG-CG NITSCHE-based coupling has been presented in Section 5.3. This minimally-intrusive strategy requires the inclusion of some additional terms in the global single-field matrices $\left[\mathbf{K}_{\widehat{U}\widehat{U}}\right]$ and $\left[\mathbf{K}_{uu}\right]$ and the implementation of the coupling blocks $\left[\tilde{\mathbf{K}}_{\widehat{U}u}\right]$ and $\left[\tilde{\mathbf{K}}_{u\widehat{U}}\right]$, with $\widehat{\mathbf{U}}_{\mathcal{F}}$ gathering the fluid density and momentum global DOFs. Moreover, owing to the unsteady and nonlinear nature of the equations involved, the global residuals $\left[\mathbf{f}_{\widehat{U}}\right]$ and $\left[\mathbf{f}_{u}\right]$ need to be computed accordingly. The elemental contributions to the updated matrices and vectors in (5.28) and (5.29) at each NEWTON iteration j, to advance from the time step n to the time step $n+1$, are

$$
\begin{aligned}
\left[\tilde{\mathbf{K}}_{\hat{w}\hat{\rho}}\left\{\mathtt{d},1\right\}\right]_e^{n+1,\,j} &= +\left[\mathbf{K}_{\hat{w}\hat{\rho}}\left\{\mathtt{d},1\right\}\right]_e^{n+1,\,j} \\
&\quad - \left\langle \widehat{\boldsymbol{\psi}}_{\mathcal{F}}^T, \frac{\gamma}{h}\frac{\widehat{\boldsymbol{\rho v}}_{\mathcal{F}}^{n+1,\,j}\left\{\mathtt{d}\right\}}{\left(\hat{\rho}_{\mathcal{F}}^{n+1,\,j}\right)^2}\widehat{\boldsymbol{\psi}}_{\mathcal{F}} \right\rangle_{\partial\Omega_{\mathcal{F}}^e\cap\Gamma^I} \\
\left[\tilde{\mathbf{K}}_{\hat{w}\hat{w}}\left\{\mathtt{d},\mathtt{e}\right\}\right]_e^{n+1,\,j} &= +\left[\mathbf{K}_{\hat{w}\hat{w}}\left\{\mathtt{d},\mathtt{e}\right\}\right]_e^{n+1,\,j} \\
&\quad + \delta_{\mathtt{d},\mathtt{e}}\left\langle \widehat{\boldsymbol{\psi}}_{\mathcal{F}}^T, \frac{\gamma}{h}\frac{1}{\hat{\rho}_{\mathcal{F}}^{n+1,\,j}}\widehat{\boldsymbol{\psi}}_{\mathcal{F}} \right\rangle_{\partial\Omega_{\mathcal{F}}^e\cap\Gamma^I} \\
\left[\tilde{\mathbf{K}}_{\hat{w}u}\left\{\mathtt{d},\mathtt{e}\right\}\right]_e^{n+1,\,j} &= \\
&\quad + \sum_{\mathtt{f}=1}^{\mathtt{n_{sd}}}\sum_{\mathtt{g}=1}^{\mathtt{n_{sd}}}\sum_{\mathtt{h}=1}^{\mathtt{n_{sd}}} \left\langle \widehat{\boldsymbol{\psi}}_{\mathcal{F}}^T, \left|\boldsymbol{F}_{\mathcal{S}}\left(\boldsymbol{\nabla}\boldsymbol{u}_{\mathcal{S}}^{n+1,\,j}\right)\right|^{-1} \left.\frac{\partial\left[\boldsymbol{P}_{\mathcal{S}}\left(\boldsymbol{\nabla}\boldsymbol{u}_{\mathcal{S}}\right)\right]\left\{\mathtt{d},\mathtt{f}\right\}}{\partial\left[\boldsymbol{F}_{\mathcal{S}}\left(\boldsymbol{\nabla}\boldsymbol{u}_{\mathcal{S}}\right)\right]\left\{\mathtt{e},\mathtt{g}\right\}}\right|_{\boldsymbol{\nabla}\boldsymbol{u}_{\mathcal{S}}^{n+1,\,j}} \right. \\
&\qquad\qquad \left. \cdot\left[\boldsymbol{F}_{\mathcal{S}}\left(\boldsymbol{\nabla}\boldsymbol{u}_{\mathcal{S}}^{n+1,\,j}\right)\right]^T\left\{\mathtt{f},\mathtt{h}\right\}\left(-\boldsymbol{n}_{\mathcal{F}}\left\{\mathtt{h}\right\}\right)\boldsymbol{\nabla}\left\{\mathtt{g}\right\}\boldsymbol{\psi}_{\mathcal{S}} \right\rangle_{\partial\Omega_{\mathcal{F}}^e\cap\Gamma^I} \\
&\quad - \delta_{\mathtt{d},\mathtt{e}}\left\langle \widehat{\boldsymbol{\psi}}_{\mathcal{F}}^T, \frac{\gamma}{h}\frac{\alpha_0}{\Delta t}\boldsymbol{\psi}_{\mathcal{S}} \right\rangle_{\partial\Omega_{\mathcal{F}}^e\cap\Gamma^I} \\
\left[\tilde{\mathbf{K}}_{u\hat{\rho}}\left\{\mathtt{d},1\right\}\right]_e^{n+1,\,j} &= + \left\langle \boldsymbol{\psi}_{\mathcal{S}}^T, \frac{\gamma}{h}\frac{\widehat{\boldsymbol{\rho v}}_{\mathcal{F}}^{n+1,\,j}\left\{\mathtt{d}\right\}}{\left(\hat{\rho}_{\mathcal{F}}^{n+1,\,j}\right)^2}\widehat{\boldsymbol{\psi}}_{\mathcal{F}} \right\rangle_{\partial\Omega_{\mathcal{S}}^e\cap\Gamma^I} \\
&\quad - \sum_{\mathtt{e}=1}^{\mathtt{n_{sd}}}\sum_{\mathtt{f}=1}^{\mathtt{n_{sd}}}\sum_{\mathtt{g}=1}^{\mathtt{n_{sd}}} \left\langle \left(\left.\frac{\partial\left[\boldsymbol{P}_{\mathcal{S}}\left(\boldsymbol{\nabla}\boldsymbol{u}_{\mathcal{S}}\right)\right]\left\{\mathtt{f},\mathtt{g}\right\}}{\partial\left[\boldsymbol{F}_{\mathcal{S}}\left(\boldsymbol{\nabla}\boldsymbol{u}_{\mathcal{S}}\right)\right]\left\{\mathtt{d},\mathtt{e}\right\}}\right|_{\boldsymbol{\nabla}\boldsymbol{u}_{\mathcal{S}}^{n+1,\,j}} \boldsymbol{n}_{\mathcal{S}}\left\{\mathtt{g}\right\}\boldsymbol{\nabla}\left\{\mathtt{e}\right\}\boldsymbol{\psi}_{\mathcal{S}} \right)^T, \right. \\
&\qquad\qquad \left. \frac{\widehat{\boldsymbol{\rho v}}_{\mathcal{F}}^{n+1,\,j}\left\{\mathtt{f}\right\}}{\left(\hat{\rho}_{\mathcal{F}}^{n+1,\,j}\right)^2}\widehat{\boldsymbol{\psi}}_{\mathcal{F}} \right\rangle_{\partial\Omega_{\mathcal{S}}^e\cap\Gamma^I} \\
\left[\tilde{\mathbf{K}}_{u\hat{w}}\left\{\mathtt{d},\mathtt{e}\right\}\right]_e^{n+1,\,j} &= -\delta_{\mathtt{d},\mathtt{e}}\left\langle \boldsymbol{\psi}_{\mathcal{S}}^T, \frac{\gamma}{h}\frac{1}{\hat{\rho}_{\mathcal{F}}^{n+1,\,j}}\widehat{\boldsymbol{\psi}}_{\mathcal{F}} \right\rangle_{\partial\Omega_{\mathcal{S}}^e\cap\Gamma^I} \\
&\quad + \sum_{\mathtt{f}=1}^{\mathtt{n_{sd}}}\sum_{\mathtt{g}=1}^{\mathtt{n_{sd}}} \left\langle \left(\left.\frac{\partial\left[\boldsymbol{P}_{\mathcal{S}}\left(\boldsymbol{\nabla}\boldsymbol{u}_{\mathcal{S}}\right)\right]\left\{\mathtt{e},\mathtt{f}\right\}}{\partial\left[\boldsymbol{F}_{\mathcal{S}}\left(\boldsymbol{\nabla}\boldsymbol{u}_{\mathcal{S}}\right)\right]\left\{\mathtt{d},\mathtt{g}\right\}}\right|_{\boldsymbol{\nabla}\boldsymbol{u}_{\mathcal{S}}^{n+1,\,j}} \boldsymbol{n}_{\mathcal{S}}\left\{\mathtt{f}\right\}\boldsymbol{\nabla}\left\{\mathtt{g}\right\}\boldsymbol{\psi}_{\mathcal{S}} \right)^T, \frac{1}{\hat{\rho}_{\mathcal{F}}^{n+1,\,j}}\widehat{\boldsymbol{\psi}}_{\mathcal{F}} \right\rangle_{\partial\Omega_{\mathcal{S}}^e\cap\Gamma^I} \\
\left[\tilde{\mathbf{K}}_{uu}\left\{\mathtt{d},\mathtt{e}\right\}\right]_e^{n+1,\,j} &= +\left[\mathbf{K}_{uu}\left\{\mathtt{d},\mathtt{e}\right\}\right]_e^{n+1,\,j}
\end{aligned}
$$

$$
\begin{aligned}
&- \sum_{\mathtt{f}=1}^{\mathtt{n_{sd}}} \sum_{\mathtt{g}=1}^{\mathtt{n_{sd}}} \left\langle \boldsymbol{\psi}_{\mathcal{S}}^{T}, \left. \frac{\partial \left[\boldsymbol{P}_{\mathcal{S}}\left(\boldsymbol{\nabla u}_{\mathcal{S}}\right)\right]\{\mathtt{d},\mathtt{f}\}}{\partial \left[\boldsymbol{F}_{\mathcal{S}}\left(\boldsymbol{\nabla u}_{\mathcal{S}}\right)\right]\{\mathtt{e},\mathtt{g}\}} \right|_{\boldsymbol{\nabla u}_{\mathcal{S}}^{n+1,\,j}} \boldsymbol{n}_{\mathcal{S}}\{\mathtt{f}\}\, \boldsymbol{\nabla}\{\mathtt{g}\}\, \boldsymbol{\psi}_{\mathcal{S}} \right\rangle_{\partial\Omega_{\mathcal{S}}^{e}\cap\Gamma^{I}} \\
&+ \delta_{\mathtt{d},\mathtt{e}} \left\langle \boldsymbol{\psi}_{\mathcal{S}}^{T}, \frac{\gamma}{h} \frac{\alpha_0}{\Delta t} \boldsymbol{\psi}_{\mathcal{S}} \right\rangle_{\partial\Omega_{\mathcal{S}}^{e}\cap\Gamma^{I}} \\
&- \sum_{\mathtt{f}=1}^{\mathtt{n_{sd}}} \sum_{\mathtt{g}=1}^{\mathtt{n_{sd}}} \left\langle \left(\left. \frac{\partial \left[\boldsymbol{P}_{\mathcal{S}}\left(\boldsymbol{\nabla u}_{\mathcal{S}}\right)\right]\{\mathtt{e},\mathtt{f}\}}{\partial \left[\boldsymbol{F}_{\mathcal{S}}\left(\boldsymbol{\nabla u}_{\mathcal{S}}\right)\right]\{\mathtt{d},\mathtt{g}\}} \right|_{\boldsymbol{\nabla u}_{\mathcal{S}}^{n+1,\,j}} \boldsymbol{n}_{\mathcal{S}}\{\mathtt{f}\}\, \boldsymbol{\nabla}\{\mathtt{g}\}\, \boldsymbol{\psi}_{\mathcal{S}} \right)^{T}, \frac{\alpha_0}{\Delta t} \boldsymbol{\psi}_{\mathcal{S}} \right\rangle_{\partial\Omega_{\mathcal{S}}^{e}\cap\Gamma^{I}}
\end{aligned}
$$

$$
\begin{aligned}
\left[\tilde{\mathbf{f}}_{\hat{w}}\{\mathtt{d}\}\right]_{e}^{n+1,\,j} = &+ \left[\mathbf{f}_{\hat{w}}\{\mathtt{d}\}\right]_{e}^{n+1,\,j} \\
&- \sum_{\mathtt{e}=1}^{\mathtt{n_{sd}}} \sum_{\mathtt{f}=1}^{\mathtt{n_{sd}}} \Big\langle \widehat{\boldsymbol{\psi}}_{\mathcal{F}}^{T}, \left|\boldsymbol{F}_{\mathcal{S}}\left(\boldsymbol{\nabla u}_{\mathcal{S}}^{n+1,\,j}\right)\right|^{-1} \left[\boldsymbol{P}_{\mathcal{S}}\left(\boldsymbol{\nabla u}_{\mathcal{S}}^{n+1,\,j}\right)\right]\{\mathtt{d},\mathtt{e}\} \\
&\qquad\qquad \cdot \left[\boldsymbol{F}_{\mathcal{S}}\left(\boldsymbol{\nabla u}_{\mathcal{S}}^{n+1,\,j}\right)\right]^{T}\{\mathtt{e},\mathtt{f}\} \left(-\boldsymbol{n}_{\mathcal{F}}\{\mathtt{f}\}\right) \Big\rangle_{\partial\Omega_{\mathcal{F}}^{e}\cap\Gamma^{I}} \\
&+ \left\langle \widehat{\boldsymbol{\psi}}_{\mathcal{F}}^{T}, \frac{\gamma}{h} \left[\left(\sum_{b=0}^{\mathrm{BDF}o} \frac{\alpha_b}{\Delta t} \boldsymbol{u}_{\mathcal{S}}^{n+1-b}\{\mathtt{d}\} \right) - \frac{\widehat{\boldsymbol{\rho v}}_{\mathcal{F}}^{n+1,\,j}\{\mathtt{d}\}}{\hat{\rho}_{\mathcal{F}}^{n+1,\,j}} \right] \right\rangle_{\partial\Omega_{\mathcal{F}}^{e}\cap\Gamma^{I}}
\end{aligned}
$$

$$
\begin{aligned}
\left[\tilde{\mathbf{f}}_{u}\{\mathtt{d}\}\right]_{e}^{n+1,\,j} = &+ \left[\mathbf{f}_{u}\{\mathtt{d}\}\right]_{e}^{n+1,\,j} \\
&+ \sum_{\mathtt{e}=1}^{\mathtt{n_{sd}}} \left\langle \boldsymbol{\psi}_{\mathcal{S}}^{T}, \left[\boldsymbol{P}_{\mathcal{S}}\left(\boldsymbol{\nabla u}_{\mathcal{S}}^{n+1,\,j}\right)\right]\{\mathtt{d},\mathtt{e}\}\, \boldsymbol{n}_{\mathcal{S}}\{\mathtt{e}\} \right\rangle_{\partial\Omega_{\mathcal{S}}^{e}\cap\Gamma^{I}} \\
&- \left\langle \boldsymbol{\psi}_{\mathcal{S}}^{T}, \frac{\gamma}{h} \left[\left(\sum_{b=0}^{\mathrm{BDF}o} \frac{\alpha_b}{\Delta t} \boldsymbol{u}_{\mathcal{S}}^{n+1-b}\{\mathtt{d}\} \right) - \frac{\widehat{\boldsymbol{\rho v}}_{\mathcal{F}}^{n+1,\,j}\{\mathtt{d}\}}{\hat{\rho}_{\mathcal{F}}^{n+1,\,j}} \right] \right\rangle_{\partial\Omega_{\mathcal{S}}^{e}\cap\Gamma^{I}} \\
&+ \sum_{\mathtt{e}=1}^{\mathtt{n_{sd}}} \sum_{\mathtt{f}=1}^{\mathtt{n_{sd}}} \sum_{\mathtt{g}=1}^{\mathtt{n_{sd}}} \Bigg\langle \left(\left. \frac{\partial \left[\boldsymbol{P}_{\mathcal{S}}\left(\boldsymbol{\nabla u}_{\mathcal{S}}\right)\right]\{\mathtt{d},\mathtt{g}\}}{\partial \left[\boldsymbol{F}_{\mathcal{S}}\left(\boldsymbol{\nabla u}_{\mathcal{S}}\right)\right]\{\mathtt{e},\mathtt{f}\}} \right|_{\boldsymbol{\nabla u}_{\mathcal{S}}^{n+1,\,j}} \boldsymbol{n}_{\mathcal{S}}\{\mathtt{f}\}\, \boldsymbol{\nabla}\{\mathtt{g}\}\, \boldsymbol{\psi}_{\mathcal{S}} \right)^{T}, \\
&\qquad\qquad\qquad\qquad \left(\sum_{b=0}^{\mathrm{BDF}o} \frac{\alpha_b}{\Delta t} \boldsymbol{u}_{\mathcal{S}}^{n+1-b}\{\mathtt{d}\} \right) - \frac{\widehat{\boldsymbol{\rho v}}_{\mathcal{F}}^{n+1,\,j}\{\mathtt{d}\}}{\hat{\rho}_{\mathcal{F}}^{n+1,\,j}} \Bigg\rangle_{\partial\Omega_{\mathcal{S}}^{e}\cap\Gamma^{I}}
\end{aligned}
$$

Bibliography

[1] C. Ager, B. Schott, M. Winter, and W. A. Wall, A Nitsche-based cut finite element method for the coupling of incompressible fluid flow with poroelasticity, *Computer Methods in Applied Mechanics and Engineering* 351, 253–280, 2019.

[2] M. Akköse, S. Adanur, A. Bayraktar, and A. A. Dumanoğlu, Elasto-plastic earthquake response of arch dams including fluid-structure interaction by the Lagrangian approach, *Applied Mathematical Modelling* 32(11), 2396–2412, 2008.

[3] J. A. C. Ambrósio and M. F. O. S. Pereira, Flexible multibody dynamics with nonlinear deformations: vehicle dynamics and crashworthiness applications, In *Computational Methods in Mechanical Systems*, 1998.

[4] F. Amirouche, Y. Zhou, and T. Johnson, Current micropump technologies and their biomedical applications, *Microsystem Technologies* 15(5), 647–666, 2009.

[5] J. D. Anderson, *Fundamentals of aerodynamics*, McGraw-Hill, 2017.

[6] C. Antoci, M. Gallati, and S. Sibilla, Numerical simulation of fluid-structure interaction by SPH, *Computers & Structures* 85(11–14), 879–890, 2007.

[7] D. N. Arnold and R. Winther, Mixed finite elements for elasticity, *Numerische Mathematik* 92(3), 401–419, 2002.

[8] D. N. Arnold, F. Brezzi, and J. Douglas, PEERS: A new mixed finite element for plane elasticity, *Japan Journal of Applied Mathematics* 1(2), 347, 1984.

[9] I. Babuška and M. Suri, Locking effects in the finite element approximation of elasticity problems, *Numerische Mathematik* 62(1), 439–463, 1992.

[10] S. Badia, F. Nobile, and C. Vergara, Fluid-structure partitioned procedures based on Robin transmission conditions, *Journal of Computational Physics* 227(14), 7027–7051, 2008.

[11] S. Badia, A. Quaini, and A. Quarteroni, Modular vs. non-modular preconditioners for fluid-structure systems with large added-mass effect, *Computer Methods in Applied Mechanics and Engineering* 197(49–50), 4216–4232, 2008.

[12] S. Badia, F. Nobile, and C. Vergara, Robin–Robin preconditioned Krylov methods for fluid-structure interaction problems, *Computer Methods in Applied Mechanics and Engineering* 198(33–36), 2768–2784, 2009.

[13] M. Bathe and R. D. Kamm, A fluid-structure interaction finite element analysis of pulsatile blood flow through a compliant stenotic artery, *Journal of Biomechanical Engineering* 121 (4), 361–369, 1999.

[14] Y. Bazilevs, V. M. Calo, Y. J. Zhang, and T. J. R. Hughes, Isogeometric fluid-structure interaction analysis with applications to arterial blood flow, *Computational Mechanics* 38 (4), 310–322, 2006.

[15] Y. Bazilevs, M.-C. Hsu, Y. J. Zhang, W. Wang, T. Kvamsdal, S. Støle-Hentschel, and J. G. Isaksen, Computational vascular fluid-structure interaction: methodology and application to cerebral aneurysms, *Biomechanics and Modeling in Mechanobiology* 9(4), 481–498, 2010.

[16] Y. Bazilevs, A. Korobenko, X. Deng, and J. Yan, Fluid-structure interaction modeling for fatigue-damage prediction in full-scale wind-turbine blades, *Journal of Applied Mechanics* 83(6), 061010, 2016.

[17] H. Braess and P. Wriggers, Arbitrary Lagrangian Eulerian finite element analysis of free surface flow, *Computer Methods in Applied Mechanics and Engineering* 190(1–2), 95–109, 2000.

[18] J. Bramwell, L. Demkowicz, J. Gopalakrishnan, and W. Qiu, A locking-free hp DPG method for linear elasticity with symmetric stresses, *Numerische Mathematik* 122(4), 671–707, 2012.

[19] A. N. Brooks and T. J. R. Hughes, Streamline upwind/Petrov–Galerkin formulations for convection dominated flows with particular emphasis on the incompressible Navier–Stokes equations, *Computer Methods in Applied Mechanics and Engineering* 32(1–3), 199–259, 1982.

[20] E. Burman, A penalty-free nonsymmetric Nitsche-type method for the weak imposition of boundary conditions, *SIAM Journal on Numerical Analysis* 50(4), 1959–1981, 2012.

[21] E. Burman and M. Á. Fernández, Stabilization of explicit coupling in fluid-structure interaction involving fluid incompressibility, *Computer Methods in Applied Mechanics and Engineering* 198(5–8), 766–784, 2009.

[22] E. Burman and M. Á. Fernández, An unfitted Nitsche method for incompressible fluid-structure interaction using overlapping meshes, *Computer Methods in Applied Mechanics and Engineering* 279, 497–514, 2014.

[23] F. Casadei, J. P. Halleux, A. Sala, and F. Chillé, Transient fluid-structure interaction algorithms for large industrial applications, *Computer Methods in Applied Mechanics and Engineering* 190(24–25), 3081–3110, 2001.

[24] P. Causin, J.-F. Gerbeau, and F. Nobile, Added-mass effect in the design of partitioned algorithms for fluid-structure problems, *Computer Methods in Applied Mechanics and Engineering* 194(42–44), 4506–4527, 2005.

[25] F. Celiker, B. Cockburn, and K. Shi, Hybridizable discontinuous Galerkin methods for Timoshenko beams, *Journal of Scientific Computing* 44(1), 1–37, 2010.

[26] A. Cesmelioglu, B. Cockburn, and W. Qiu, Analysis of a hybridizable discontinuous Galerkin method for the steady-state incompressible Navier–Stokes equations, *Mathematics of Computation* 86(306), 1643–1670, 2017.

[27] B. Cockburn and J. Cui, Divergence-free HDG methods for the vorticity-velocity formulation of the Stokes problem, *Journal of Scientific Computing* 52(1), 256–270, 2012.

[28] B. Cockburn and J. Gopalakrishnan, New hybridization techniques, *GAMM-Mitteilungen* 28(2), 154–182, 2005.

[29] B. Cockburn and J. Gopalakrishnan, The derivation of hybridizable discontinuous Galerkin methods for Stokes flow, *SIAM Journal on Numerical Analysis* 47(2), 1092–1125, 2009.

[30] B. Cockburn and K. Shi, Superconvergent HDG methods for linear elasticity with weakly symmetric stresses, *IMA Journal of Numerical Analysis* 33(3), 747–770, 2012.

[31] B. Cockburn and K. Shi, Conditions for superconvergence of HDG methods for Stokes flow, *Mathematics of Computation* 82, 651–671, 2012.

[32] B. Cockburn and K. Shi, Devising HDG methods for Stokes flow: an overview, *Computers & Fluids* 98, 221–229, 2014.

[33] B. Cockburn, G. E. Karniadakis, and C.-W. Shu, The development of discontinuous Galerkin methods, In *Discontinuous Galerkin Methods*, 2000.

[34] B. Cockburn, D. Schötzau, and J. Wang, Discontinuous Galerkin methods for incompressible elastic materials, *Computer Methods in Applied Mechanics and Engineering* 195(25–28), 3184–3204, 2006.

[35] B. Cockburn, B. Dong, and J. Guzmán, A superconvergent LDG-hybridizable Galerkin method for second-order elliptic problems, *Mathematics of Computation* 77(264), 1887–1916, 2008.

[36] B. Cockburn, J. Gopalakrishnan, and R. Lazarov, Unified hybridization of discontinuous Galerkin, mixed, and continuous Galerkin methods for second order elliptic problems, *SIAM Journal on Numerical Analysis* 47(2), 1319–1365, 2009.

[37] B. Cockburn, N.-C. Nguyen, and J. Peraire, A comparison of HDG methods for Stokes flow, *Journal of Scientific Computing* 45(1), 215–237, 2010.

[38] R. D. Cook, D. S. Malkus, M. E. Plesha, and R. J. Witt, *Concepts and applications of finite element analysis*, John Wiley & Sons, 2007.

[39] P. Crosetto, P. Reymond, S. Deparis, D. Kontaxakis, N. Stergiopulos, and A. Quarteroni, Fluid-structure interaction simulation of aortic blood flow, *Computers & Fluids* 43(1), 46–57, 2011.

[40] M. Crouzeix and P.-A. Raviart, Conforming and nonconforming finite element methods for solving the stationary Stokes equations I, *ESAIM: Mathematical Modelling and Numerical Analysis* 7(R3), 33–75, 1973.

[41] J. P. M. De Almeida and E. A. W. Maunder, *Equilibrium finite element formulations*, John Wiley & Sons, 2017.

[42] A. De Rosis, G. Falcucci, S. Ubertini, and F. Ubertini, A coupled lattice Boltzmann-finite element approach for two-dimensional fluid-structure interaction, *Computers & Fluids* 86, 558–568, 2013.

[43] J. Degroote, Partitioned simulation of fluid-structure interaction, *Archives of Computational Methods in Engineering* 20(3), 185–238, 2013.

[44] E. S. Di Martino, G. Guadagni, A. Fumero, G. R. Ballerini, R. Spirito, P. Biglioli, and A. Redaelli, Fluid-structure interaction within realistic three-dimensional models of the aneurysmatic aorta as a guidance to assess the risk of rupture of the aneurysm, *Medical Engineering & Physics* 23(9), 647–655, 2001.

[45] J. Donea and A. Huerta, *Finite element methods for flow problems*, John Wiley & Sons, 2003.

[46] J. Donea, A. Huerta, J.-P. Ponthot, and A. Rodriguez-Ferran, Arbitrary Lagrangian–Eulerian methods, In *Encyclopedia of Computational Mechanics*, 2004.

[47] M. Durand, A. Leroyer, C. Lothodé, F. Hauville, M. Visonneau, R. Floch, and L. Guillaume, FSI investigation on stability of downwind sails with an automatic dynamic trimming, *Ocean Engineering* 90, 129–139, 2014.

[48] S. Étienne, A. Garon, and D. Pelletier, Some manufactured solutions for verification of fluid-structure interaction codes, *Computers & Structures* 106–107, 56–67, 2012.

[49] C. Farhat, P. Geuzaine, and G. Brown, Application of a three-field nonlinear fluid-structure formulation to the prediction of the aeroelastic parameters of an F-16 fighter, *Computers & Fluids* 32(1), 3–29, 2003.

[50] C. Farhat, K. G. Van Der Zee, and P. Geuzaine, Provably second-order time-accurate loosely-coupled solution algorithms for transient nonlinear computational aeroelasticity, *Computer Methods in Applied Mechanics and Engineering* 195(17–18), 1973–2001, 2006.

[51] C. Farhat, A. Rallu, K. G. Wang, and T. Belytschko, Robust and provably second-order explicit-explicit and implicit-explicit staggered time-integrators for highly non-linear compressible fluid-structure interaction problems, *International Journal for Numerical Methods in Engineering* 84(1), 73–107, 2010.

[52] N. Fehn, W. A. Wall, and M. Kronbichler, A matrix-free high-order discontinuous Galerkin compressible Navier–Stokes solver: a performance comparison of compressible and incompressible formulations for turbulent incompressible flows, *International Journal for Numerical Methods in Fluids* 89(3), 71–102, 2019.

[53] M. Á. Fernández and M. Moubachir, A Newton method using exact jacobians for solving fluid-structure coupling, *Computers & Structures* 83(2–3), 127–142, 2005.

[54] M. Á. Fernández, J. Mullaert, and M. Vidrascu, Generalized Robin–Neumann explicit coupling schemes for incompressible fluid-structure interaction: stability analysis and numerics, *International Journal for Numerical Methods in Engineering* 101(3), 199–229, 2015.

[55] P. Fernandez, N.-C. Nguyen, and J. Peraire, The hybridized discontinuous Galerkin method for implicit large-eddy simulation of transitional turbulent flows, *Journal of Computational Physics* 336, 308–329, 2017.

[56] J. Fish and T. Belytschko, *A first course in finite elements*, John Wiley & Sons, 2007.

[57] L. Formaggia, J.-F. Gerbeau, F. Nobile, and A. Quarteroni, On the coupling of 3D and 1D Navier–Stokes equations for flow problems in compliant vessels, *Computer Methods in Applied Mechanics and Engineering* 191(6–7), 561–582, 2001.

[58] C. Förster, W. A. Wall, and E. Ramm, Artificial added mass instabilities in sequential staggered coupling of nonlinear structures and incompressible viscous flows, *Computer Methods in Applied Mechanics and Engineering* 196(7), 1278–1293, 2007.

[59] G. Fu, B. Cockburn, and H. Stolarski, Analysis of an HDG method for linear elasticity, *International Journal for Numerical Methods in Engineering* 102(3–4), 551–575, 2015.

[60] G. N. Gatica and F. A. Sequeira, A priori and a posteriori error analyses of an augmented HDG method for a class of quasi-Newtonian Stokes flows, *Journal of Scientific Computing* 69(3), 1192–1250, 2016.

[61] M. W. Gee, U. Küttler, and W. A. Wall, Truly monolithic algebraic multigrid for fluid-structure interaction, *International Journal for Numerical Methods in Engineering* 85(8), 987–1016, 2011.

[62] L. Gerardo-Giorda, F. Nobile, and C. Vergara, Analysis and optimization of Robin–Robin partitioned procedures in fluid-structure interaction problems, *SIAM Journal on Numerical Analysis* 48(6), 2091–2116, 2010.

[63] J.-F. Gerbeau and M. Vidrascu, A quasi-Newton algorithm based on a reduced model for fluid-structure interaction problems in blood flows, *ESAIM: Mathematical Modelling and Numerical Analysis* 37(4), 631–647, 2003.

[64] J.-F. Gerbeau, M. Vidrascu, and P. Frey, Fluid-structure interaction in blood flows on geometries based on medical imaging, *Computers & Structures* 83(2–3), 155–165, 2005.

[65] A. Gerstenberger and W. A. Wall, An embedded Dirichlet formulation for 3D continua, *International Journal for Numerical Methods in Engineering* 82(5), 537–563, 2010.

[66] S. Ghosh and N. Kikuchi, An arbitrary Lagrangian–Eulerian finite element method for large deformation analysis of elastic-viscoplastic solids, *Computer Methods in Applied Mechanics and Engineering* 86(2), 127–188, 1991.

[67] M. Giacomini, A. Karkoulias, R. Sevilla, and A. Huerta, A superconvergent HDG method for Stokes flow with strongly enforced symmetry of the stress tensor, *Journal of Scientific Computing* 77(3), 1679–1702, 2018.

[68] G. Giorgiani, S. Fernández-Méndez, and A. Huerta, Hybridizable discontinuous Galerkin p-adaptivity for wave propagation problems, *International Journal for Numerical Methods in Fluids* 72(12), 1244–1262, 2013.

[69] G. Giorgiani, S. Fernández-Méndez, and A. Huerta, Hybridizable discontinuous Galerkin with degree adaptivity for the incompressible Navier–Stokes equations, *Computers & Fluids* 98, 196–208, 2014.

[70] M. Griebel and M. A. Schweitzer, A particle-partition of unity method part V: boundary conditions, In *Geometric Analysis and Nonlinear Partial Differential Equations*, 2003.

[71] M. J. Hancock, N. H. Elabbasi, and M. C. Demirel, Simulations of micropumps based on tilted flexible fibers, *COMSOL Conference Boston*, 2014.

[72] M. J. Hancock, N. H. Elabbasi, and S. B. Brown, Micropump mechanism, *COMSOL Multiphysics® MEMS Module Application Library*, 2015.

[73] P. Hansbo, Nitsche's method for interface problems in computational mechanics, *GAMM-Mitteilungen* 28(2), 183–206, 2005.

[74] P. Hansbo and J. Hermansson, Nitsche's method for coupling non-matching meshes in fluid-structure vibration problems, *Computational Mechanics* 32(1), 134–139, 2003.

[75] P. Hansbo and M. G. Larson, Discontinuous Galerkin methods for incompressible and nearly incompressible elasticity by Nitsche's method, *Computer Methods in Applied Mechanics and Engineering* 191(17–18), 1895–1908, 2002.

[76] M. Heil, An efficient solver for the fully coupled solution of large-displacement fluid-structure interaction problems, *Computer Methods in Applied Mechanics and Engineering* 193(1–2), 1–23, 2004.

[77] M. Heil, A. L. Hazel, and J. Boyle, Solvers for large-displacement fluid-structure interaction problems: segregated versus monolithic approaches, *Computational Mechanics* 43 (1), 91–101, 2008.

[78] K. D. Housiadas and G. C. Georgiou, New analytical solutions for weakly compressible Newtonian Poiseuille flows with pressure-dependent viscosity, *International Journal of Engineering Science* 107, 13–27, 2016.

[79] J. Hron and S. Turek, A monolithic FEM/multigrid solver for an ALE formulation of fluid-structure interaction with applications in biomechanics, In *Fluid-Structure Interaction*, 2006.

[80] M.-C. Hsu and Y. Bazilevs, Fluid-structure interaction modeling of wind turbines: simulating the full machine, *Computational Mechanics* 50(6), 821–833, 2012.

[81] D. Z. Huang, P. Avery, C. Farhat, J. Rabinovitch, A. Derkevorkian, and L. D. Peterson, Modeling, simulation and validation of supersonic parachute inflation dynamics during Mars landing, *AIAA SciTech Forum*, 2020.

[82] T. J. R. Hughes, *The finite element method: linear static and dynamic finite element analysis*, Dover Publications, 2000.

[83] T. J. R. Hughes, L. P. Franca, and M. Balestra, A new finite element formulation for computational fluid dynamics: V. Circumventing the Babuška–Brezzi condition: a stable Petrov–Galerkin formulation of the Stokes problem accommodating equal-order interpolations, *Computer Methods in Applied Mechanics and Engineering* 59(1), 85–99, 1986.

[84] B. D. Iverson and S. V. Garimella, Recent advances in microscale pumping technologies: a review and evaluation, *Microfluidics and Nanofluidics* 5(2), 145–174, 2008.

[85] R. Jaiman, P. Geubelle, E. Loth, and X. Jiao, Stable and accurate loosely-coupled scheme for unsteady fluid-structure interaction, *45th AIAA Aerospace Sciences Meeting and Exhibit*, 2007.

[86] C. Jung-Ho and K. Noboru, An analysis of metal forming processes using large deformation elastic-plastic formulations, *Computer Methods in Applied Mechanics and Engineering* 49(1), 71–108, 1985.

[87] R. Kamakoti and W. Shyy, Fluid-structure interaction for aeroelastic applications, *Progress in Aerospace Sciences* 40(8), 535–558, 2004.

[88] N. Kambouchev, L. Noels, and R. Radovitzky, Nonlinear compressibility effects in fluid-structure interaction and their implications on the air-blast loading of structures, *Journal of Applied Physics* 100(6), 063519, 2006.

[89] B. Krank, N. Fehn, W. A. Wall, and M. Kronbichler, A high-order semi-explicit discontinuous Galerkin solver for 3D incompressible flow with application to DNS and LES of turbulent channel flow, *Journal of Computational Physics* 348, 634–659, 2017.

[90] U. Küttler, *Effiziente Lösungsverfahren für Fluid-Struktur-Interaktions-Probleme*, PhD thesis, Technische Universität München, 2009.

[91] U. Küttler and W. A. Wall, Fixed-point fluid-structure interaction solvers with dynamic relaxation, *Computational Mechanics* 43(1), 61–72, 2008.

[92] U. Küttler and W. A. Wall, Vector extrapolation for strong coupling fluid-structure interaction solvers, *Journal of Applied Mechanics* 76(2), 021205, 2009.

[93] U. Küttler, C. Förster, and W. A. Wall, A solution for the incompressibility dilemma in partitioned fluid-structure interaction with pure Dirichlet fluid domains, *Computational Mechanics* 38(4), 417–429, 2006.

[94] U. Küttler, M. W. Gee, C. Förster, A. Comerford, and W. A. Wall, Coupling strategies for biomedical fluid-structure interaction problems, *International Journal for Numerical Methods in Biomedical Engineering* 26(3-4), 305–321, 2010.

[95] A. La Spina, C. Förster, M. Kronbichler, and W. A. Wall, On the role of (weak) compressibility for fluid-structure interaction solvers, *International Journal for Numerical Methods in Fluids* 92(2), 129–147, 2020.

[96] A. La Spina, M. Giacomini, and A. Huerta, Hybrid coupling of CG and HDG discretizations based on Nitsche's method, *Computational Mechanics* 65(2), 311–330, 2020.

[97] A. La Spina, M. Kronbichler, M. Giacomini, W. A. Wall, and A. Huerta, A weakly compressible hybridizable discontinuous Galerkin formulation for fluid-structure interaction problems, *Computer Methods in Applied Mechanics and Engineering* 372, 2020.

[98] B. Lamichhane, Mortar finite elements for coupling compressible and nearly incompressible materials in elasticity, *International Journal of Numerical Analysis and Modeling* 6 (2), 177–192, 2009.

[99] A. Larsen, Aerodynamics of the Tacoma Narrows Bridge - 60 years later, *Structural Engineering International* 10(4), 243–248, 2000.

[100] M. G. Larson and F. Bengzon, *The finite element method: theory, implementation, and applications*, Springer, 2013.

[101] W. K. Liu, Finite element procedures for fluid-structure interactions and application to liquid storage tanks, *Nuclear Engineering and Design* 65(2), 221–238, 1981.

[102] H. G. Matthies and J. Steindorf, Partitioned but strongly coupled iteration schemes for nonlinear fluid-structure interaction, *Computers & Structures* 80(27–30), 1991–1999, 2002.

[103] M. Mayr, *A monolithic solver for fluid-structure interaction with adaptive time stepping and a hybrid preconditioner*, PhD thesis, Technische Universität München, 2016.

[104] M. Mayr, T. Klöppel, W. A. Wall, and M. W. Gee, A temporal consistent monolithic approach to fluid-structure interaction enabling single field predictors, *SIAM Journal on Scientific Computing* 37(1), B30–B59, 2015.

[105] M. McCormick, D. A. Nordsletten, D. Kay, and N. P. Smith, Simulating left ventricular fluid-solid mechanics through the cardiac cycle under LVAD support, *Journal of Computational Physics* 244, 80–96, 2013.

[106] C. Michler, E. H. Van Brummelen, and R. De Borst, An interface Newton–Krylov solver for fluid-structure interaction, *International Journal for Numerical Methods in Fluids* 47 (10–11), 1189–1195, 2005.

[107] N. Mitsume, S. Yoshimura, K. Murotani, and T. Yamada, Improved MPS-FE fluid-structure interaction coupled method with MPS polygon wall boundary model, *Computer Modeling in Engineering and Sciences* 101(4), 229–247, 2014.

[108] D. P. Mok, *Partitionierte Lösungsansätze in der Strukturdynamik und der Fluid-Struktur-Interaktion*, PhD thesis, Universität Stuttgart, 2001.

[109] D. P. Mok and W. A. Wall, Partitioned analysis schemes for the transient interaction of incompressible flows and nonlinear flexible structures, *Trends in Computational Structural Mechanics* 128, 689–698, 2001.

[110] D. S. Molony, A. Callanan, E. G. Kavanagh, M. T. Walsh, and T. M. McGloughlin, Fluid-structure interaction of a patient-specific abdominal aortic aneurysm treated with an endovascular stent-graft, *BioMedical Engineering OnLine* 8(1), 24, 2009.

[111] A. Montlaur, S. Fernández-Méndez, and A. Huerta, Discontinuous Galerkin methods for the Stokes equations using divergence-free approximations, *International Journal for Numerical Methods in Fluids* 57(9), 1071–1092, 2008.

[112] D. Moro, N.-C. Nguyen, and J. Peraire, Navier–Stokes solution using hybridizable discontinuous Galerkin methods, *20th AIAA Computational Fluid Dynamics Conference*, 2011.

[113] M. R. Motley, Z. Liu, and Y. L. Young, Utilizing fluid-structure interactions to improve energy efficiency of composite marine propellers in spatially varying wake, *Composite Structures* 90(3), 304–313, 2009.

[114] M. Movahhedy, M. S. Gadalá, and Y. Altintas, Simulation of the orthogonal metal cutting process using an arbitrary Lagrangian–Eulerian finite-element method, *Journal of Materials Processing Technology* 103(2), 267–275, 2000.

[115] I. Newton, *Philosophiae naturalis principia mathematica*, Royal Society of London, 1687.

[116] N.-T. Nguyen, X. Huang, and T. K. Chuan, MEMS-micropumps: a review, *Journal of Fluids Engineering* 124(2), 384–392, 2002.

[117] N.-C. Nguyen and J. Peraire, Hybridizable discontinuous Galerkin methods for partial differential equations in continuum mechanics, *Journal of Computational Physics* 231 (18), 5955–5988, 2012.

[118] N.-C. Nguyen, J. Peraire, and B. Cockburn, An implicit high-order hybridizable discontinuous Galerkin method for linear convection-diffusion equations, *Journal of Computational Physics* 228(9), 3232–3254, 2009.

[119] N.-C. Nguyen, J. Peraire, and B. Cockburn, An implicit high-order hybridizable discontinuous Galerkin method for nonlinear convection-diffusion equations, *Journal of Computational Physics* 228(23), 8841–8855, 2009.

[120] N.-C. Nguyen, J. Peraire, and B. Cockburn, A hybridizable discontinuous Galerkin method for Stokes flow, *Computer Methods in Applied Mechanics and Engineering* 199 (9–12), 582–597, 2010.

[121] N.-C. Nguyen, J. Peraire, and B. Cockburn, An implicit high-order hybridizable discontinuous Galerkin method for the incompressible Navier–Stokes equations, *Journal of Computational Physics* 230(4), 1147–1170, 2011.

[122] N.-C. Nguyen, J. Peraire, and B. Cockburn, High-order implicit hybridizable discontinuous Galerkin methods for acoustics and elastodynamics, *Journal of Computational Physics* 230(10), 3695–3718, 2011.

[123] P. Nithiarasu, An arbitrary Lagrangian Eulerian (ALE) formulation for free surface flows using the characteristic-based split (CBS) scheme, *International Journal for Numerical Methods in Fluids* 48(12), 1415–1428, 2005.

[124] J. Nitzler, J. Biehler, N. Fehn, P.-S. Koutsourelakis, and W. A. Wall, A generalized probabilistic learning approach for multi-fidelity uncertainty propagation in complex physical simulations, *Submitted to International Journal for Numerical Methods in Engineering*, 2020.

[125] F. Nobile, *Numerical approximation of fluid-structure interaction problems with application to haemodynamics*, PhD thesis, École Polytechnique Fédérale de Lausanne, 2001.

[126] F. Nobile and C. Vergara, An effective fluid-structure interaction formulation for vascular dynamics by generalized Robin conditions, *SIAM Journal on Scientific Computing* 30(2), 731–763, 2008.

[127] M. Paipuri, C. Tiago, and S. Fernández-Méndez, Coupling of continuous and hybridizable discontinuous Galerkin methods: application to conjugate heat transfer problem, *Journal of Scientific Computing* 78(1), 321–350, 2019.

[128] P. K. Pani and S. K. Bhattacharyya, Fluid-structure interaction effects on dynamic pressure of a rectangular lock-gate, *Finite Elements in Analysis and Design* 43(10), 739–748, 2007.

[129] N. Parolini and A. Quarteroni, Mathematical models and numerical simulations for the America's Cup, *Computer Methods in Applied Mechanics and Engineering* 194(9–11), 1001–1026, 2005.

[130] J. Peraire, N.-C. Nguyen, and B. Cockburn, A hybridizable discontinuous Galerkin method for the compressible Euler and Navier–Stokes equations, *48th AIAA Aerospace Sciences Meeting Including the New Horizons Forum and Aerospace Exposition*, 2010.

[131] P.-O. Persson and G. Strang, A simple mesh generator in MATLAB, *SIAM Review* 46(2), 329–345, 2004.

[132] P.-O. Persson, J. Bonet, and J. Peraire, Discontinuous Galerkin solution of the Navier–Stokes equations on deformable domains, *Computer Methods in Applied Mechanics and Engineering* 198(17–20), 1585–1595, 2009.

[133] A. Quaini, *Algorithms for fluid-structure interaction problems arising in hemodynamics*, PhD thesis, École Polytechnique Fédérale de Lausanne, 2009.

[134] W. H. Reed and T. R. Hill, Triangular mesh methods for the neutron transport equation, Technical report, Los Alamos National Laboratory, 1973.

[135] S. Rhebergen and B. Cockburn, A space-time hybridizable discontinuous Galerkin method for incompressible flows on deforming domains, *Journal of Computational Physics* 231(11), 4185–4204, 2012.

[136] A. Rodriguez-Ferran, A. Pérez-Foguet, and A. Huerta, Arbitrary Lagrangian–Eulerian (ALE) formulation for hyperelastoplasticity, *International Journal for Numerical Methods in Engineering* 53(8), 1831–1851, 2002.

[137] P. S. Rojas Fredini and A. C. Limache, Evaluation of weakly compressible SPH variants using derived analytical solutions of Taylor–Couette flows, *Computers & Mathematics with Applications* 66(3), 304–317, 2013.

[138] R. Rossi and E. Oñate, Analysis of some partitioned algorithms for fluid-structure interaction, *Engineering Computations* 27(1), 20–56, 2010.

[139] H. Schmucker, F. Flemming, and S. Coulson, Two-way coupled fluid structure interaction simulation of a propeller turbine, *International Journal of Fluid Machinery and Systems* 3(4), 342–351, 2010.

[140] R. Sevilla and A. Huerta, Tutorial on hybridizable discontinuous Galerkin (HDG) for second-order elliptic problems, In *Advanced Finite Element Technologies*, 2016.

[141] R. Sevilla and A. Huerta, HDG-NEFEM with degree adaptivity for Stokes flows, *Journal of Scientific Computing* 77(3), 1953–1980, 2018.

[142] R. Sevilla, M. Giacomini, A. Karkoulias, and A. Huerta, A superconvergent hybridisable discontinuous Galerkin method for linear elasticity, *International Journal for Numerical Methods in Engineering* 116(2), 91–116, 2018.

[143] M. R. Shekari, N. Khaji, and M. T. Ahmadi, A coupled BE-FE study for evaluation of seismically isolated cylindrical liquid storage tanks considering fluid-structure interaction, *Journal of Fluids and Structures* 25(3), 567–585, 2009.

[144] J. P. Sheldon, S. T. Miller, and J. S. Pitt, A hybridizable discontinuous Galerkin method for modeling fluid-structure interaction, *Journal of Computational Physics* 326, 91–114, 2016.

[145] J. P. Sheldon, S. T. Miller, and J. S. Pitt, An improved formulation for hybridizable discontinuous Galerkin fluid-structure interaction modeling with reduced computational expense, *Communications in Computational Physics* 24(5), 2018.

[146] S.-C. Soon, B. Cockburn, and H. K. Stolarskis, A hybridizable discontinuous Galerkin method for linear elasticity, *International Journal for Numerical Methods in Engineering* 80(8), 1058–1092, 2009.

[147] A. Soria and F. Casadei, Arbitrary Lagrangian–Eulerian multicomponent compressible flow with fluid-structure interaction, *International Journal for Numerical Methods in Fluids* 25(11), 1263–1284, 1997.

[148] M. Souli and J. P. Zolésio, Arbitrary Lagrangian–Eulerian and free surface methods in fluid mechanics, *Computer Methods in Applied Mechanics and Engineering* 191(3–5), 451–466, 2001.

[149] M. Souli, A. Ouahsine, and L. Lewin, ALE formulation for fluid-structure interaction problems, *Computer Methods in Applied Mechanics and Engineering* 190(5–7), 659–675, 2000.

[150] R. Stenberg, A family of mixed finite elements for the elasticity problem, *Numerische Mathematik* 53(5), 513–538, 1988.

[151] G. G. Stokes, On the theories of the internal friction of fluids in motion, and of the equilibrium and motion of elastic solids, *Transactions of the Cambridge Philosophical Society* 8, 287–319, 1845.

[152] G. Strang and G. J. Fix, *An analysis of the finite element method*, Prentice-Hall, 1973.

[153] K. Takizawa, S. Wright, C. Moorman, and T. E. Tezduyar, Fluid-structure interaction modeling of parachute clusters, *International Journal for Numerical Methods in Fluids* 65(1-3), 286–307, 2011.

[154] S. Terrana, N.-C. Nguyen, J. Bonet, and J. Peraire, A hybridizable discontinuous Galerkin method for both thin and 3D nonlinear elastic structures, *Computer Methods in Applied Mechanics and Engineering* 352, 561–585, 2019.

[155] T. E. Tezduyar, S. Sathe, M. Schwaab, J. Pausewang, J. Christopher, and J. Crabtree, Fluid-structure interaction modeling of ringsail parachutes, *Computational Mechanics* 43 (1), 133–142, 2008.

[156] R. Torii, M. Oshima, T. Kobayashi, K. Takagi, and T. E. Tezduyar, Fluid-structure interaction modeling of a patient-specific cerebral aneurysm: influence of structural modeling, *Computational Mechanics* 43(1), 151, 2008.

[157] P. Tricerri, L. Dedè, S. Deparis, A. Quarteroni, A. M. Robertson, and A. Sequeira, Fluid-structure interaction simulations of cerebral arteries modeled by isotropic and anisotropic constitutive laws, *Computational Mechanics* 55(3), 479–498, 2015.

[158] D. Trimarchi and C. M. Rizzo, A FEM-Matlab code for fluid-structure interaction coupling with application to sail aerodynamics of yachts, *13th International Congress of International Maritime Association of Mediterranean, Towards the Sustainable Marine Technology and Transportation*, 2009.

[159] S. Turek and J. Hron, Proposal for numerical benchmarking of fluid-structure interaction between an elastic object and laminar incompressible flow, In *Fluid-Structure Interaction*, 2006.

[160] E. H. Van Brummelen, Added mass effects of compressible and incompressible flows in fluid-structure interaction, *Journal of Applied Mechanics* 76(2), 021206, 2009.

[161] R. Van Loon, P. D. Anderson, and F. N. Van De Vosse, A fluid-structure interaction method with solid-rigid contact for heart valve dynamics, *Journal of Computational Physics* 217 (2), 806–823, 2006.

[162] G. Viccione, V. Bovolin, and E. P. Carratelli, Influence of the compressibility in fluid-structure interaction using weakly compressible SPH, *4th SPHERIC workshop*, 2009.

[163] G. Viccione, V. Bovolin, and E. P. Carratelli, Simulating fluid-structure interaction with SPH, *AIP Conference Proceedings* 1479(1), 209–212, 2012.

[164] J. Vierendeels, L. Lanoye, J. Degroote, and P. Verdonck, Implicit coupling of partitioned fluid-structure interaction problems with reduced order models, *Computers & Structures* 85(11–14), 970–976, 2007.

[165] S. C. Vigmostad, H. S. Udaykumar, J. Lu, and K. B. Chandran, Fluid-structure interaction methods in biological flows with special emphasis on heart valve dynamics, *International Journal for Numerical Methods in Biomedical Engineering* 26(3-4), 435–470, 2010.

[166] W. A. Wall, *Fluid-Struktur-Interaktion mit stabilisierten Finiten Elementen*, PhD thesis, Universität Stuttgart, 1999.

[167] W. A. Wall and M. W. Gee, Baci: a parallel multiphysics simulation environment, Technical report, Technische Universität München, 2010.

[168] W. A. Wall, A. Gerstenberger, P. Gamnitzer, C. Förster, and E. Ramm, Large deformation fluid-structure interaction – advances in ALE methods and new fixed grid approaches, In *Fluid-Structure Interaction*, 2006.

[169] W. A. Wall, S. Genkinger, and E. Ramm, A strong coupling partitioned approach for fluid-structure interaction with free surfaces, *Computers & Fluids* 36(1), 169–183, 2007.

[170] L. Wang, R. Quant, and A. Kolios, Fluid structure interaction modelling of horizontal-axis wind turbine blades based on CFD and FEA, *Journal of Wind Engineering and Industrial Aerodynamics* 158, 11–25, 2016.

[171] Y. L. Young, Fluid-structure interaction analysis of flexible composite marine propellers, *Journal of Fluids and Structures* 24(6), 799–818, 2008.

[172] O. C. Zienkiewicz, D. K. Paul, and E. Hinton, Cavitation in fluid-structure response (with particular reference to dams under earthquake loading), *Earthquake Engineering & Structural Dynamics* 11(4), 463–481, 1983.

[173] O. C. Zienkiewicz, R. L. Taylor, and J. Zhu, *The finite element method: its basis and fundamentals*, Butterworth-Heinemann, 2013.

[174] O. C. Zienkiewicz, R. L. Taylor, and D. Fox, *The finite element method for solid and structural mechanics*, Butterworth-Heinemann, 2014.

[175] O. C. Zienkiewicz, R. L. Taylor, and P. Nithiarasu, *The finite element method for fluid dynamics*, Butterworth-Heinemann, 2014.